

**Tectonic Evolution of the Thakkhola Graben
and Dhaulagiri Himalaya, Central Nepal**

by
José Miguel Hurtado, Jr.

B.S. with Honors
M.S. in Geology
California Institute of Technology, 1996

SUBMITTED TO THE DEPARTMENT OF EARTH, ATMOSPHERIC, AND
PLANETARY SCIENCES IN PARTIAL FULFILLMENT OF THE REQUIREMENTS
FOR THE DEGREE OF

DOCTOR OF PHILOSOPHY
AT THE
MASSACHUSETTS INSTITUTE OF TECHNOLOGY

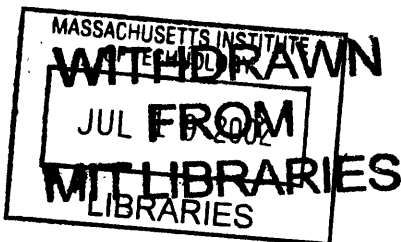
MARCH, 2002

©2001-2002 Massachusetts Institute of Technology. All rights reserved

Signature of Author: _____
Department of Earth, Atmospheric, and Planetary Sciences
March 13, 2002

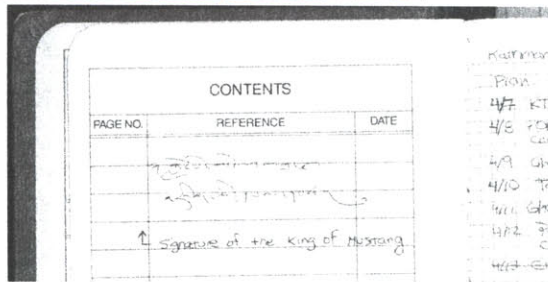
Certified by: _____
Kip V. Hodges, Ph.D.
Professor of Geology
Thesis Supervisor

Accepted by: _____
Ronald G. Prinn, Sc.D.
TEPCO Professor of Atmospheric Chemistry
Department Head



LINDGREN

Frontispiece



Top: I am seated between Raja Jigme Dorje (left), ruler of the Kingdom of Mustang, and Tsering Tendi Sherpa Lama (right), my good friend and sirdar during three field expeditions during 1998-2000. We are having tea in the 500-year-old residence of the Raja in Lo Mantang. Photograph by Mr. H. P. Khatiwada (May 7, 2000).

Middle Right: My field book was honored with the autograph of Raja Jigme Dorje in Tibetan script.

Bottom Left: Near Titi village, at the southern end of the Thakkhola graben, I take a location measurement using a handheld GPS receiver. The summit of Dhaulagiri I (8167 m), the seventh-tallest peak in the world, is in the background. Photograph by K. M. Viskupic (May 13, 1998).

Bottom Right: Seventy kilometers to the north, Mr. H. P. Khatiwada (left), and I (right) follow our porters (midground) to the walled city of Lo Mantang (background), the capital of Upper Mustang. Photograph by T. T. Sherpa Lama (May 7, 2000).

Tectonic Evolution of the Thakkhola Graben and Dhaulagiri Himalaya, Central Nepal

by

José Miguel Hurtado, Jr.

Submitted to the Department of Earth, Atmospheric, and Planetary Sciences on
March 13, 2002 in Partial Fulfillment of the Requirements for the Degree of Doctor of
Philosophy in Geology

ABSTRACT

Three extensional fault systems intersect in the central Nepal Himalaya: the *South Tibetan fault system (STFS)*; the *Thakkhola graben*; and structures bounding the *Upper Mustang Massif (UMM)*. Interactions between these systems are investigated using integrated field studies, remote sensing analyses, geodynamic modeling, and a wide variety of geochronologic tools. The goals are to characterize the relationships between the three extensional systems, document their neotectonic histories in relation to their older manifestations, and develop a model for how the geodynamic phenomena driving them have produced the observed patterns of tectonism and deformation.

^{14}C geochronology, remote sensing analyses, and field observations in the southern Thakkhola graben show that the STFS has been active in the Quaternary and that the kinematically-linked Thakkhola graben acts as a tear structure in its hanging wall. In the northern Thakkhola graben, neotectonic, structural, and $^{40}\text{Ar}/^{39}\text{Ar}$ and U-Pb geochronologic data from the UMM record its Late Miocene to Quaternary exhumational history and reveal a kinematic and geometric relationship between core-complex extension in the UMM and rift extension in the Thakkhola graben. This work shows that core-complex development and east-west extension in southern Tibet are closely related to the STFS. In the adjacent Dhaulagiri Himalaya, remote sensing and field analyses of several generations of STFS structures – some of which appear to be active – show that the most recently active fault traces do not necessarily follow pre-existing lithologic contacts defined by older strands, but instead follow less contorted traces, cutting across allochthons and even reactivating segments of the Main Central Thrust. The distribution of high-grade rocks and the interactions between the STFS, east-west extension, and core-complex development are hypothesized to reflect the response of the orogen to gravitational potential energy (GPE) anomalies. GPE anomalies in the Himalaya are calculated from geoid data and interpreted in terms of pressure gradients driving flow in an intracrustal channel. From the distribution of GPE anomalies, I suggest that orogen parallel flow may be as significant as orogen-perpendicular flow, indicating that both removal and redistribution of GPE is important in the development of extensional structures in the Himalayan orogen and in southern Tibet.

Thesis Supervisor: Kip V. Hodges, Ph.D.

Title: Professor of Geology

Foreword & Acknowledgements

Many individuals have supported me throughout my time at MIT and have contributed in some way to this dissertation. I apologize in advance to anyone I may forget to mention. Forgive me and know that my appreciation is strong all the same.

First, I would like to thank my advisor, Kip Hodges, for convincing me to come to MIT in the first place and for giving me the opportunity to do this project. The most important thing he taught me was the value of a multi-faceted approach to solving a problem, a lesson that I think is reflected in the wide range of topics and techniques in my dissertation. I would also like to thank Kelin Whipple for his enthusiasm and guidance. Both Kelin and Kip accompanied me to the field and I hope they enjoyed the experience as much as I did. I thank Clark Burchfiel, Sam Bowring, and Chris Duncan for reading my thesis and serving on my thesis committee. In particular I want to thank Sam for access to his lab and for motivating me to look at uraninite more carefully, a suggestion that grew into a chapter of this work.

Jahan Ramezani and Neel Chatterjee helped immensely with various analyses and their enthusiasm and expertise were invaluable. In particular I want to thank Jahan for his patience during my seemingly endless search for decent monazites for him to dissolve and run, and Neel for taking the time to work with me with the electron microprobe. My work in the $^{40}\text{Ar}/^{39}\text{Ar}$ lab would not have been possible without the tutelage of Mike Krol and Bill Oszewski. Although I only touch upon the work in progress, I express my appreciation to Darryl Granger, Mike Bourgeois, and Pankaj Sharma of Purdue University's PRIME laboratory, all of whom patiently offered invaluable assistance and advice regarding ^{10}Be - ^{26}Al nuclide geochronology. Finally, I wish to acknowledge the technical support staff at Research Systems, Inc., Phillip Cheng at PCI geomatics, and the customer service staffs at the USGS EROS Data Center and SPOT Image, Inc. for their help and advice.

Without the staff of Magic Mountain-Sundar Himali Treks in Kathmandu, Nepal, none of this work would have been possible. In particular I thank Ang Phuri Sherpa and Chandra Niraula for their assistance with making travel and logistical arrangements over email and fax and in person in Nepal. I very special thanks goes to my sirdar, Tsering Tendi Sherpa Lama. Tendi was my guide, translator, field assistant, and right-hand man.

And he will always be my friend. My hat's off to the many porters and cook-staff who went with us on our adventures and worked so incredibly hard to keep my expeditions going. I also owe a debt of gratitude to the staff of the Department of Mines and Geology of Nepal for their help in exporting my rock samples to the United States.

Graduate school would have been a far different and less worthwhile experience without my fellow students. I started at MIT with Arthur White and Noah Snyder, and, along with Eric Kirby, we were the "Gang of Four". As the last of that crew to finish, I want to thank them for their friendship, motivation, and encouragement. I knew that if they could do it, that I could do it too. In particular, I thank Eric for being a role model during the time we shared an office. Special thanks also go to Arthur who I have relied on the most as both a friend and a colleague, even though our field areas were half a world apart in time and space. I also thank Karen Viskupic for her friendship and for assisting me in the field during my 1998 field season. Thanks to Jeremy Boyce and Kate Ruhl for putting up with me (and all my stuff!) in the office. Finally, great appreciation goes out to the many other graduate students and post-docs I have come to know, have worked with, and have learned from during my tenure at MIT. In no particular order they include: Sinan Ackiz, Simon Brocklehurst, Lindsay Schoenbohm, Marin Clark, Nathan Niemi, Cam Wobus, Joel Johnson, Chris Studnicki-Gizbert, John Thurmond, Bill Lyons, Odin Smith, Jeff Parsons, Steve DiBenedetto, Ben Crosby, Blair Schoene, Mark Schmitz, Julie Baldwin, Jenny Matzel, Steve Singletary, Anke Friedrich, Jim Van Orman, Kirstin Nicolaysen, Fredrick Simons, and Mark Behn. In particular I want to sincerely thank Sinan, Simon, Lindsay, Nathan, Marin (and her sister, Marti) for their kind hospitality during the winter of 2001-2002 while I was completing my dissertation.

Finally, I express my gratitude to the Frank and Eva B. Buck Foundation for their generosity and financial support since my days as a freshman undergraduate. Above all, I thank my parents and my sister, to whom this work is dedicated, for their unending love, support, and understanding.

J. M. H.
Fairfield, California
Cambridge, Massachusetts
Winter, 2001-2002

To My Parents, Mike and Sonia, and My Sister, Elizabeth.

MBBK

Table of Contents

Title Page.....	1
Frontispiece.....	3
Abstract.....	5
Foreword & Acknowledgements.....	7
Dedication.....	9
Table of Contents.....	11
Chapter 1: Introduction.....	13
Chapter 2: Neotectonics of the Thakkhola graben and implications for Recent activity on the South Tibetan fault system in the central Nepal Himalaya.....	27
Chapter 3: Mapping the South Tibetan fault system between the Annapurna and Dhaulagiri Himalaya with integrated field geologic and remote sensing data.....	49
Chapter 4: Geochronologic and structural constraints on the exhumational history of the Mustang and Mugu granites: Implications for the development of the Thakkhola Graben, central Nepal Himalaya.....	163
Chapter 5: Electron microprobe chemical dating of uraninite as a reconnaissance tool for leucogranite geochronology.....	339
Chapter 6: Synthesis – Intracrustal channel flow, gravitational potential energy, and the tectonic development of the Himalaya.....	401
Biographical Note.....	457
Colophon.....	459

Chapter 1:

Introduction

Chapter 1: Introduction

The southern margin of the Tibetan plateau appears to represent a fundamental boundary between two deformational domains. On the plateau, active, east-west oriented extension is accommodated by numerous north-striking rift systems (Molnar and Tapponier, 1975; Molnar and Tapponier, 1978; Ni and York, 1978; Armijo *et al.*, 1986). To the south, within the Himalaya, active north-south shortening along east-striking thrust faults is the dominant process (Le Fort, 1975; Hodges, 2000). This simple observation requires mechanical decoupling between these two domains. Understanding this fundamental transition and the interactions between the tectonic processes on either side is the focus of this thesis.

Since the 1980's, workers throughout the Himalaya have documented the existence of a major system of east-striking, north-dipping, (predominately) normal-sense faults at the physiographic edge of the Tibetan plateau (Caby *et al.*, 1983; Burg *et al.*, 1984; Burchfiel and Royden, 1985; Searle, 1986; Herren, 1987; Valdiya, 1989; Burchfiel *et al.*, 1992; Brown and Nazarchuk, 1993; Coleman, 1996; Wu *et al.*, 1998; Godin *et al.*, 1999). This feature, the South Tibetan fault system, juxtaposes the high-grade metamorphic rocks of the Himalayan core against essentially unmetamorphosed Tethyan sedimentary rocks in its hanging wall. Spatially coincident with the strain transition and with the crest of the Himalaya, the South Tibetan fault system is an obvious candidate for the structure that decouples the Tibetan and Himalayan tectonic domains. However, most studies only emphasized the Miocene development of the South Tibetan detachment system. In fact, some field relationships and geochronologic results published in the past (e.g. Guillot *et al.*, 1994; Harrison *et al.*, 1995; Hodges *et al.*, 1998) are interpreted to

Chapter 1: Introduction

preclude post-Miocene activity on the system. Since a structure decoupling two active strain fields must, by definition, also be active, this implies a paradox, the resolution of which was the first objective of this work. The second objective was to determine the interactions between extensional processes in Tibet, the decoupling structure, and the deformational processes in the Himalaya.

To resolve the paradox required study of the South Tibetan fault system in an area where it was well known and mapped, but also where there were indications that it may still be active. Pursuit of the second objective required an area where Tibetan extension could be observed in close proximity to the Tibet-Himalaya transition. The central Nepal Himalaya is ideal on both counts. The Miocene evolution of the South Tibetan fault and the Himalayan metamorphic core has been well documented by previous work in the Annapurna Himalaya (e.g. Fort *et al.*, 1982; Iwata, 1984; Yoshida *et al.*, 1984; Colchen *et al.*, 1986; Fuchs *et al.*, 1988; Pêcher, 1991; Brown and Nazarchuk, 1993; Schneider and Masch, 1993; Garzanti *et al.*, 1994; Le Fort, 1994; Coleman, 1996; Hodges *et al.*, 1996; Vannay and Hodges, 1996; Godin, 1999; Garzzone *et al.*, 2000), whereas preliminary neotectonic observations in the nearby Dhaulagiri Himalaya has hinted at very recent South Tibetan fault activity (Nakata, 1989). Situated between these two ranges, the Thakkhola graben, one of the southernmost of the Tibetan rifts, cuts across most of the width of the Himalaya, extending southward from the Tibetan plateau almost to the range front. As such, the Thakkhola graben provides an excellent opportunity to evaluate kinematic relationships between east-west extensional strain in southern Tibet and north-south extensional strain in the Himalaya.

Chapter 1: Introduction

Study in the Thakkhola graben also affords other opportunities. Incision of the Kali Gandaki river into the basin fill sediments provides excellent exposure of the depositional history of the basin. Similarly, exhumation of datable metamorphic and igneous rocks in the footwall of the graben-bounding fault facilitates theochronologic studies of its slip history. As a result, the Thakkhola graben was ideal for pursuing a third objective: constraining the timing and history of east-west extension in this sector of southern Tibet. This temporal information is crucial in any interpretive model of the interactions between the Thakkhola graben and the South Tibetan fault system.

Finally, study in the Thakkhola-Dhaulagiri region presented the opportunity to examine one of the North Himalayan gneiss domes (Burg *et al.*, 1984; Chen *et al.*, 1990; Lee *et al.*, 2000). These structures are a chain of enigmatic metamorphic and igneous culminations that crop out among the Tibetan rifts north of the South Tibetan fault system. One of these, the Upper Mustang massif, is exposed at the northern end of the Thakkhola graben, in the footwall of the graben-bounding fault. Since the possibility exists that at least some of the North Himalayan gneiss domes are metamorphic core complexes (Chen *et al.*, 1990), their nature and development are crucial components to understanding the Tibet-Himalaya tectonic transition. Moreover, given the close proximity between the Upper Mustang massif the Thakkhola graben, it is clear that the development of one affected the other. As such any model for the interaction between the Thakkhola graben and the South Tibetan fault system would be incomplete without including the evolution of the Upper Mustang massif.

OVERVIEW

The dissertation is the compilation of the results of five separate projects in the Thakkhola graben and Dhaulagiri Himalaya undertaken over the course of five years between 1996 and 2001. They are presented in Chapters 2-6, the first four of which are written as manuscripts for submission to professional journals. As a result, there is some amount of redundancy in the presentation of background material. Each chapter, however, offers a distinct approach to the problems at hand, and together they involve a wide variety of analytical and quantitative techniques. This integrative approach has led to a more comprehensive understanding of the Thakkhola and Dhaulagiri regions and to a deeper appreciation for the orogenic processes there manifested (Chapter 6).

The linkage between the principal bounding structure of the Thakkhola graben – Dangardzong fault – and the STF system is described in *Chapter 2*. The highlight of my work on the intersection between these structures is that the Dangardzong fault is confined to and acts as a tear structure in the hanging wall of the STF system basal detachment. ¹⁴C constraints on the timing of Dangardzong fault activity not only document Pleistocene motion on that fault, but have important implications for the relationship between the Dangardzong fault and the STF system. The presence of an apparently young, brittle splay of the STF system that truncates the Dangardzong fault suggests that the youngest manifestations of STF system have also been active since the Pleistocene. Given the ca. 22-Myr history of STF system-related deformation documented in the Annapurna Himalaya, and the ca. >17.5-Myr history of extension in the structurally superjacent Thakkhola graben, I hypothesize that the two fault systems are kinematically and geometrically linked, with the Dangardzong fault plane merging

Chapter 1: Introduction

with the South Tibetan fault at depth. Thus, the South Tibetan fault decouples extension in the upper crust of southern Tibet from the processes occurring at deeper structural levels exposed in the Himalaya.

In *Chapter 3*, I extend the identification and mapping of recently active STF structures to the west of the Thakkhola graben, into the largely unmapped Dhaulagiri Himalaya. The principal results of my field and remote sensing studies of this area are four-fold. First, the Greater Himalayan Sequence experiences a significant, along-strike variation in thickness, one that mirrors a similar variation in the Annapurna Himalaya, wherein the Greater Himalayan Sequence thickens away from the Thakkhola graben. Second, the transitions from thick to thin coincide with anomalous stretches of north-striking strands of the STF system basal detachment. Third, the presence of an apparently contiguous chain of fresh normal fault scarps and top-to-the-north brittle deformational fabrics in the Dhaulagiri Himalaya suggests that the young STF system activity observed in the Thakkhola graben continues to the west. Finally, the observation that the young normal fault in the Dhaulagiri Himalaya cuts across the Greater Himalayan Sequence and reactivates stretches of older STF system structures as well as the Main Central Thrust (MCT) implies that normal faulting in the high Himalaya is not necessarily defined by pre-existing tectonostratigraphy. I hypothesize that lateral flow of the Greater Himalayan sequence can account the distribution of high-grade Greater Himalayan Sequence rocks and older STF system activity. I also speculate on the role GPE plays in the present-day distribution of fault activity.

In *Chapter 4* – having established linkages between the Thakkola graben and the STF system and between the STF system and lateral flow of the Greater Himalayan

Chapter 1: Introduction

Sequence – I concentrate on one of the North Himalayan gneiss domes, the Upper Mustang Massif (UMM) at the northern end of the Thakkhola graben. In addition to placing new constraints on the age of two plutons – the Mustang and Mugu granites – within the UMM, I develop an exhumation history for the UMM in the footwall of the Dangardzong fault. The exhumational history I reconstruct from structural observations and thermochronologic data, places a new constraint on the age of Thakkhola graben extension of ca. 18.3-17.5 Ma. These data also provide a glimpse at the linkage between the development of the UMM and the Thakkhola graben. In the kinematic model I propose, the granites and high-grade metamorphic rocks in the UMM originate in the middle crust beneath the STF system and were being exhumed in a core complex environment by ca. 21 Ma. The transition from the core complex mode to the rift mode of extension occurred at ca. 18.3-17.5 Ma when the Dangardzong fault began to open the Thakkhola graben, in the process splitting the Mustang granite and the UMM in two.

Chapter 5 is a departure from the large-scale tectonics that is the subject of the preceding chapters. In this study, I examine a single 200 μm grain of uraninite (UO_2) from the Mugu granite using an electron microprobe and obtain concentrations of U, Th, Pb, and Y along two core-to-rim transects across the crystal. I apply the U-Th-total Pb chemical dating method to obtain mean chemical dates which are compared to isotope-dilution thermal ionization mass spectrometry (ID-TIMS) U-Pb dates obtained from seven other uraninite grains and a monazite crystal from the same sample. I find that the chemical dates compare favorably with conventional ID-TIMS dates. More importantly, the electron microprobe provides a means to investigate the diffusivity of U, Th, Y, and Pb in uraninite and to evaluate the effect diffusion of these species (particularly Pb) has

Chapter 1: Introduction

had on both the chemical and ID-TIMS dates. This study is the only recent attempt to characterize U-Th-Pb systematics in uraninite and provides some of the only constraints on the diffusivities of U, Th, Pb, and Y in natural UO₂.

Finally, in *Chapter 6*, I propose a conceptual model for the tectonics of the Himalayan margin of the Tibetan plateau that combines the ideas of gravitational potential energy (GPE)-driven deformation and channelized flow of crustal material. I suggest that southward flow of lower crustal material out from the Tibetan interior can account for many of the features of Himalayan tectonics, including the kinematics of the South Tibetan fault system. In addition, I hypothesize that spatial and temporal variations in the efficiency of orogen-perpendicular flow can result in orogen-parallel flow. I conclude that orogen-parallel intracrustal flow in southern Tibet may be responsible for core-complex and rift development in southern Tibet.

REFERENCES CITED

- Armijo, R., Tapponier, P., Mercier, J., and Han, T., 1986, Quaternary extension in Southern Tibet: Field observations and tectonic implications: *Journal of Geophysical Research*, v. 91, p. 13803-13872.
- Brown, R. L., and Nazarchuk, J. H., 1993, Annapurna detachment fault in the Greater Himalaya of central Nepal, in Treloar, P. J., and Searle, M. P., eds., *Himalayan Tectonics*: London, Geological Society Special Publication, 47, p. 461-473.
- Burchfiel, B. C., Chen, Z., Hodges, K. V., Liu, Y., Royden, L. H., Deng, C., and Xu, J., 1992, The South Tibetan Detachment System, Himalayan Orogen: *Extension Contemporaneous With and Parallel to Shortening in a Collisional Mountain Belt*, Geological Society of America Special Paper 269: Boulder, CO, Geological Society of America, 41 p.

Chapter 1: Introduction

- Burchfiel, B. C., and Royden, L. H., 1985, North-south extension within the convergent Himalayan region: *Geology*, v. 13, p. 679-682.
- Burg, J. P., Brunel, M., Gapais, D., Chen, G. M., and Liu, G. H., 1984, Deformation of leucogranites of the crystalline Main Central Sheet in southern Tibet (China): *Journal of Structural Geology*, v. 6, p. 535-542.
- Caby, R., Pêcher, A., and LeFort, P., 1983, Le M.C.T. himalayan: nouvelles données sur le métamorphisme inverse à la base de la Dalle du Tibet: *Revue Géogr. phys. Géol. dynam.*, v. 24, p. 89-100.
- Colchen, M., LeFort, P., and Pêcher, A., 1986, *Recherches Géologiques dans l'Himalaya du Népal: Annapurna - Manaslu - Ganesh Himal* (Notice de la carte géologique au 1/200000): Paris, Centre National de la Recherche Scientifique, 136 p.
- Coleman, M. E., 1996, *The Tectonic Evolution of the Central Himalaya, Marsyandi Valley, Nepal* [Ph.D. thesis]: MIT, 221 p.
- Fort, M., Freytet, P., and Colchen, M., 1982, Structural and sedimentological evolution of the Thakkhola-Mustang graben (Nepal Himalayas): *Zeitschrift für Geomorphologie*, v. 42, p. 75-98.
- Fuchs, G., Widder, R., and Tuladhar, R., 1988, Contribution to the geology of the Manang area (Annapurna Himal, Nepal): *Jahrbuch der Geologischen Bundesanstalt*, Wien, v. 131, p. 593-607.
- Garzanti, E., Gorza, M., Martellini, L., and Nicora, A., 1994, Transition from diagenesis to metamorphism in the Paleozoic to Mesozoic succession of the Dolpo-Manang synclinorium and Thakkhola graben (Nepal Tethys Himalaya): *Eclogae Geologicae Helvetiae*, v. 87, p. 613-632.
- Garzione, C. N., Dettman, D. L., Quade, J., DeCelles, P. G., and Butler, R. F., 2000, High times on the Tibetan Plateau: Paleoelevation of the Thakkhola graben, Nepal: *Geology*, v. 28, no. 4, p. 339-342.

Chapter 1: Introduction

Godin, L., 1999, *Tectonic Evolution of the Tethyan Sedimentary Sequence in the Annapurna Area, Central Nepal Himalaya* [Ph.D. thesis]: Carleton University, 219 p.

Godin, L., Brown, R. L., and Hanmer, S., 1999, High strain zone in the hanging wall of the Annapurna detachment, central Nepal Himalaya, in Macfarlane, A., Sorkhabi, R. B., and Quade, J., eds., *Himalaya and Tibet: Mountain roots to mountain tops*: Denver, Colorado, Geological Society of America Special Paper 328, p. 199-210.

Guillot, S., Hodges, K. V., Le Fort, P., and Pêcher, A., 1994, New constraints on the age of the Manaslu leucogranite: Evidence for episodic tectonic denudation in the central Himalayas: *Geology*, v. 22, p. 559-562.

Harrison, T. M., McKeegan, K. D., and LeFort, P., 1995, Detection of inherited monazite in the Manaslu leucogranite by $^{208}\text{Pb}/^{232}\text{Th}$ ion microprobe dating: Crystallization age and tectonic implications: *Earth and Planetary Science Letters*, v. 133, p. 271-282.

Herren, E., 1987, Zaskar shear zone: Northeast-southwest extension within the Higher Himalayas (Ladakh, India). *Geology*, v. 15, p. 409-413.

Hodges, K., Bowring, S., Davidek, K., Hawkins, D., and Krol, M., 1998, Evidence for rapid displacement on Himalayan normal faults and the importance of tectonic denudation in the evolution of mountain ranges: *Geology*, v. 26, p. 483-486.

Hodges, K. V., 2000, Tectonics of the Himalaya and southern Tibet from two perspectives: *Geological Society of America Bulletin*, v. 112, no. 3, p. 324-350.

Hodges, K. V., Parrish, R. R., and Searle, M. P., 1996, Tectonic evolution of the central Annapurna Range, Nepalese Himalayas: *Tectonics*, v. 15, p. 1264-1291.

Iwata, S., 1984, Geomorphology of the Thakkhola-Muktinath Region, Central Nepal, and its Late Quaternary History: *Geographical Reports of the Tokyo Metropolitan University*, v. 19, p. 25-42.

Le Fort, P., 1975, Himalayas: the collided range: Present knowledge of the continental arc: *American Journal of Science*, v. 275-A, p. 1-44.

Chapter 1: Introduction

- Le Fort, 1994, *French Earth Sciences Research in the Himalaya Regions*: Kathmandu, Nepal, Alliance Française, p. 174.
- Molnar, P., and Tapponier, P., 1975, Cenozoic tectonics of Asia: Effects of a continental collision: *Science*, v. 189, p. 419-426.
- Molnar, P., and Tapponier, P., 1978, Active tectonics of Tibet: *Journal of Geophysical Research*, v. 83, p. 5361-5375.
- Nakata, T., 1989, Active faults of the Himalaya of India and Nepal, in Malinconico, L. L., and Lillie, R. J., eds., *Tectonics of the Western Himalayas*: Boulder, CO, Geological Society of America Special Paper 232, p. 243-264.
- Ni, J., and York, J. E., 1978, Cenozoic extensional tectonics of the Tibetan Plateau: *Journal of Geophysical Research*, v. 83, p. 5277-5384.
- Pêcher, A., 1991, The contact between the Higher Himalayan crystallines and the Tibetan sedimentary series: Miocene large-scale dextral shearing: *Tectonics*, v. 10, p. 587-599.
- Schneider, C., and Masch, L., 1993, The metamorphism of the Tibetan Series from the Manang area, Marsyandi Valley, Central Nepal, in Treloar, P. J., and Searle, M. P., eds., *Himalayan Tectonics*: London, Geological Society Special Publication, 47, p. 357-374.
- Searle, M. P., 1986, Structural evolution and sequence of thrusting in the High Himalayan, Tibetan-Tethys and Indus suture zones of Zaskar and Ladakh, Western Himalaya: *Journal of Structural Geology*, v. 8, p. 923-936.
- Valdiya, K. S., 1989, Trans-Himadri intracrustal fault and basement upwarps south of the Indus-Tsangpo Suture Zone, in Malinconico, L. L., and Lillie, R. J., eds., *Tectonics of the Western Himalayas*: Boulder, CO, *Geological Society of America Special Paper 232*, p. 153-168.
- Vannay, J.-C., and Hodges, K. V., 1996, Tectonometamorphic evolution of the Himalayan metamorphic core between Annapurna and Dhaulagiri, central Nepal: *Journal of Metamorphic Geology*, v. 14, p. 635-656.

Chapter 1: Introduction

Wu, C., Nelson, K. D., Wortman, G., Samson, S. D., Yue, Y., Li, J., Kidd, W. S. F., and Edwards, M. A., 1998, Yadong cross structure and South Tibetan detachment in the east central Himalaya (89°-90°E): *Tectonics*, v. 17, p. 28-45.

Yoshida, M., Igarashi, Y., Arita, K., Hayashi, D., and Sharma, T., 1984, Magnetostratigraphic and pollen analytic studies of the Thakmar series, Nepal Himalayas: *Journal of the Nepal Geological Society*, v. 4, p. 101-120.

Chapter 2:

Neotectonics of the Thakkhola graben and implications for Recent activity on the South Tibetan fault system in the Central Nepal Himalaya

Published in *Geological Society of America Bulletin*, February, 2001
(v. 113; no. 2; p. 222-240; 13 figures; 1 table)
© 2001 Geological Society of America

Neotectonics of the Thakkhola graben and implications for recent activity on the South Tibetan fault system in the central Nepal Himalaya

José M. Hurtado Jr.*

Kip V. Hodges

Kelin X Whipple

Department of Earth, Atmospheric, and Planetary Sciences, Massachusetts Institute of Technology, 77 Massachusetts Avenue, Cambridge, Massachusetts 02139-4307, USA

ABSTRACT

The Thakkhola graben is one of many north-trending rifts that define the Neogene structural pattern of the southern Tibetan Plateau. Lying at the southern margin of the plateau and extending to the crest of the Himalaya, the graben provides an opportunity to evaluate the kinematic relationships between east-west extensional strain in southern Tibet and north-south extensional strain in the Himalaya. Neotectonic and structural mapping of the Dangardzong fault along the western margin of the graben reveals a southward-decreasing component of normal slip coupled with a southward-increasing component of right-lateral slip that affects Pleistocene basin-fill sediments. We present ^{14}C ages for river terraces in the Thakkhola graben that provide a ca. 17.2 ka minimum age on the latest stage of Dangardzong fault movement. Near the southern termination of the graben, the Dangardzong fault apparently offsets the Annapurna detachment, an early (Miocene) strand of the east-striking South Tibetan fault system. However, the Dangardzong fault itself terminates against a young (i.e., younger than ca. 17.2 ka) strand of the South Tibetan fault system, the Dhumpu detachment. Structural relationships among the Dangardzong, Annapurna, and Dhumpu faults suggest that the Dangardzong structure is a tear fault in the South Tibetan allochthon that accommodates differential amounts and rates of displacement along the South Tibetan fault system. Thus, although the South Tibetan

fault system first developed as part of the structural architecture of the Himalaya in Miocene time, at least some strands have been active as recently as the Pleistocene. In a regional context, the South Tibetan fault system serves to accommodate the strain gradient between extension in Tibet and shortening in the Himalaya.

Keywords: ^{14}C , detachment faults, Himalaya, neotectonics, Nepal, normal faults, river terraces.

INTRODUCTION

Two different types of extensional structures have played important roles in the tectonic evolution of the Himalaya and Tibet. The first is the South Tibetan fault system, a family of approximately east-striking, shallowly to moderately north-dipping normal faults exposed near the crest of the Himalaya from Bhutan to northwest India (Burg and Chen, 1984; Burchfiel and Royden, 1985; Herren, 1987; Burchfiel et al., 1992; Brown and Nazarchuk, 1993; Coleman, 1996b; Godin et al., 1996; Wu et al., 1998) (Fig. 1). Thought to have developed as a gravitationally driven response to high topographic and crustal-thickness gradients in the developing orogen (Burchfiel et al., 1992), the South Tibetan fault system has a well-documented history of Miocene displacement (Hodges et al., 1996a, 1996b, 1998; Coleman, 1998; Wu et al., 1998), but the timing of movement on many strands remains unknown. The second class of extensional structures comprises numerous north-trending rift systems that largely dictate the topographic pattern of the southern Tibet-

an Plateau (Armijo et al., 1986) (Fig. 1). Whereas the seismic and sedimentary records clearly indicate Quaternary movement on these rift systems (Molnar and Tapponnier, 1978; Mercier et al., 1987; Molnar and Lyon-Caen, 1989), the age of inception of east-west extension in southern Tibet remains controversial. Thermochronologic data ($^{40}\text{Ar}/^{39}\text{Ar}$ thermochronology of muscovite, biotite, and K-feldspar, in addition to apatite fission-track work) from bedrock in the Nyainqentanghla Range of east-central Tibet, which constitutes an oblique (northeast-trending) uplift linking two segments of the Yadong-Gulu rift system, have been interpreted as dating the onset of widespread east-west extension at ca. 8 Ma (Harrison et al., 1992, 1995a; Pan and Kidd, 1992), but at least some faults related to east-west extension near the southern edge of the plateau developed prior to 14 Ma (Coleman and Hodges, 1995).

A few of the rift systems of southern Tibet extend southward to the crest of the Himalaya, offering an opportunity to investigate their developmental relationship with the South Tibetan fault system. One such study was that of Wu and coworkers (Wu et al., 1998) who mapped the southern end of the Yadong-Gulu rift at a transverse feature called the "Yadong cross structure" (Burchfiel et al., 1992) (Fig. 1). Across the Yadong cross structure there is an ~70 km, left-lateral strike separation of the South Tibetan fault system. The observations of Wu and coworkers show that this separation was produced by dip-slip movement on the cross structure, implying that most—if not all—of the displacement on the South Tibetan fault system preceded displacement on the cross structure and, by inference, on the south-

*E-mail. hurtado@mit.edu

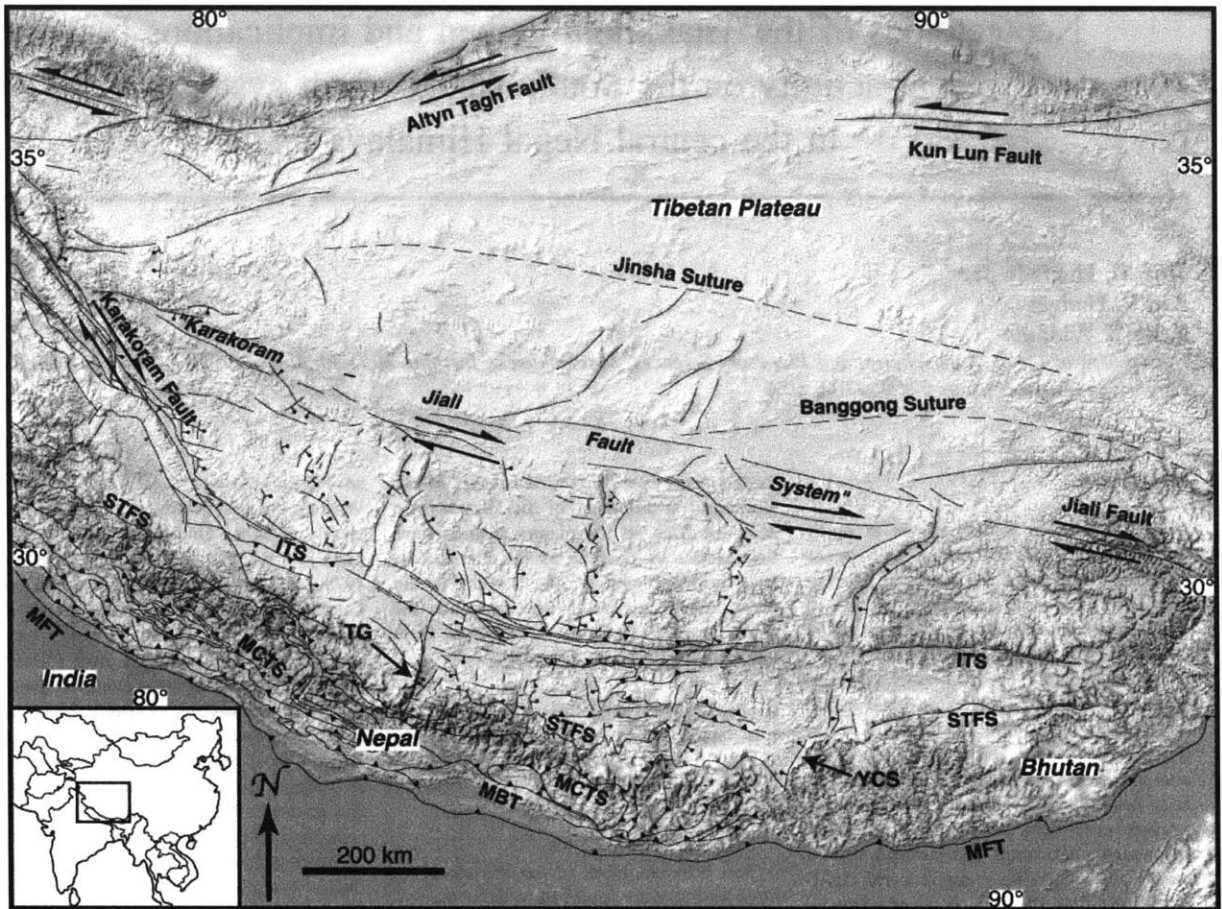


Figure 1. Generalized fault map of the Tibetan Plateau and the Himalayan orogen superimposed on GTOPO-30 DEM (1-km-resolution digital elevation model) shaded relief. Inset shows location within the Asian continent. Note the predominance of north-trending grabens in southern Tibet, south of the “Karakoram-Jiali” system of transcurrent faults. Each rift is defined by high-angle, east- and west-dipping normal faults that bound asymmetric grabens and are interconnected by left- and right-lateral transfer faults (Molnar and Tapponnier, 1975, 1978; Ni and York, 1978; Armijo et al., 1986, 1989). Fault locations are after Hodges (2000). Abbreviations are as follows: ITS—Indus-Tsangpo suture, STFS—South Tibetan fault system, MCTS—Main Central thrust system, MBT—Main Boundary thrust, MFT—Main Frontal thrust, TG—Thakkhola graben, YCS—Yadong cross structure.

ern Yadong-Gulu rift system (Wu et al., 1998). However, Wu et al. cautioned that their work did not include sufficiently detailed observations of the cross structure between offset segments of the South Tibetan fault system to evaluate whether the cross structure might have acted as a transfer fault during movement on the South Tibetan fault system.

In this paper, we further explore the relationships between east-west and north-south extension by presenting the results of a neotectonic investigation of a second critical study area, the southern termination of the Thakkhola graben in the Kali Gandaki valley

of north-central Nepal (Fig. 1). The Thakkhola graben is a long-lived feature, having been established in Miocene time (Yoshida et al, 1984; Coleman and Hodges, 1995; Garzzone et al, 1999), and it preserves a sedimentary and structural record of continuous development up to the present day. Previous work has shown that the South Tibetan fault system in this area also developed in early Miocene time (Brown, 1993; Vannay and Hodges, 1996; Godin et al., 1999a). Our research shows that the South Tibetan fault system was the locus of Pleistocene displacement in the Kali Gandaki valley during a movement phase that was

kinematically linked to displacement on the principal growth fault of the Thakkhola graben. In at least one section of the Himalayan-Tibetan orogenic system, therefore, east-west extension and north-south extension were related processes in recent geologic history.

GEOLOGIC SETTING OF THE CENTRAL NEPAL HIMALAYA

The tectonic stratigraphy of the central Himalaya comprises several subparallel, east-striking, north-dipping allochthons separated by major, north-dipping shear zones (Gansser,

Chapter 2: Neotectonics of the Thakkhola graben

HURTADO et al.

1964). Our study area resides primarily within rocks of the metamorphic core of the orogen—the Greater Himalayan Sequence—and the unmetamorphosed package of sedimentary rocks overlying it—the Tibetan Sedimentary Sequence (Fig. 2). The Greater Himalayan Sequence is composed of up to 10 km of amphibolite-facies schists, paragneisses, and orthogneisses (Colchen et al., 1986) with protolith ages ranging from Neoproterozoic to Ordovician (Colchen et al., 1986; Le Fort et al., 1986; Parrish and Hodges, 1996; Gehrels et al., 1999). Metamorphic grade increases within the Greater Himalayan Sequence from kyanite grade at the base up to sillimanite grade at higher structural levels. Two phases of metamorphism have been inferred from petrology and from $^{40}\text{Ar}/^{39}\text{Ar}$ and U-Th-Pb geochronology: a high-temperature, high-pressure “Eohimalayan” metamorphic event at ca. 35 Ma (Hodges et al., 1996b; Vannay and Hodges, 1996; Godin et al., 1999a), and a high-temperature, somewhat lower-pressure “Neohimalayan” metamorphic and anatexis melting event at ca. 22 Ma (Nazarchuk, 1993; Guillot et al., 1994; Harrison et al., 1995b; Coleman, 1996b; Hodges et al., 1996b; Vannay and Hodges, 1996; Godin, 1999). The latter was coeval with thrusting of the Greater Himalayan Sequence over lower-grade rocks to the south (Hubbard, 1989) and with north-directed extension at the base of the overlying Tibetan Sedimentary Sequence (Hodges et al., 1992).

The Tibetan Sedimentary Sequence crops out between the northern flank of the Himalaya and the Indus-Tsangpo suture (Fig. 2). The sequence includes a thick assortment of slightly metamorphosed to unmetamorphosed, lower Paleozoic to upper Mesozoic carbonate and siliciclastic rocks, the protoliths of which were deposited on the passive margin of the paleo-Indian subcontinent (Gansser, 1964; Le Fort, 1975; Colchen et al., 1986; Fuchs et al., 1988). Although largely unmetamorphosed above the high-strain zone marking its contact with the Greater Himalayan Sequence, the Tibetan Sedimentary Sequence has been subjected to at least three episodes of pervasive folding on submeter to kilometer scales (Bordet et al., 1971; Caby et al., 1983; Brown and Nazarchuk, 1993). The folding episodes are generally attributed to shortening during middle Eocene–early Oligocene crustal thickening and subsequent Oligocene–early Miocene “gravitational collapse” (Bordet et al., 1971; Burchfiel et al., 1992; Brown and Nazarchuk, 1993; Vannay and Hodges, 1996). Gravitational-collapse folding, however, has been disputed recently in favor of a contractional-fan

structure (Godin et al., 1999b). The abrupt metamorphic break across the contact with the Greater Himalayan Sequence is coincident with a structural discordance because these folds are truncated and not present in the Greater Himalayan Sequence.

The South Tibetan fault system (Fig. 1)—a family of shallowly to moderately north-dipping, east-striking, shear zones and brittle faults—marks the structural and metamorphic contact between the Greater Himalayan Sequence and the Tibetan Sedimentary Sequence

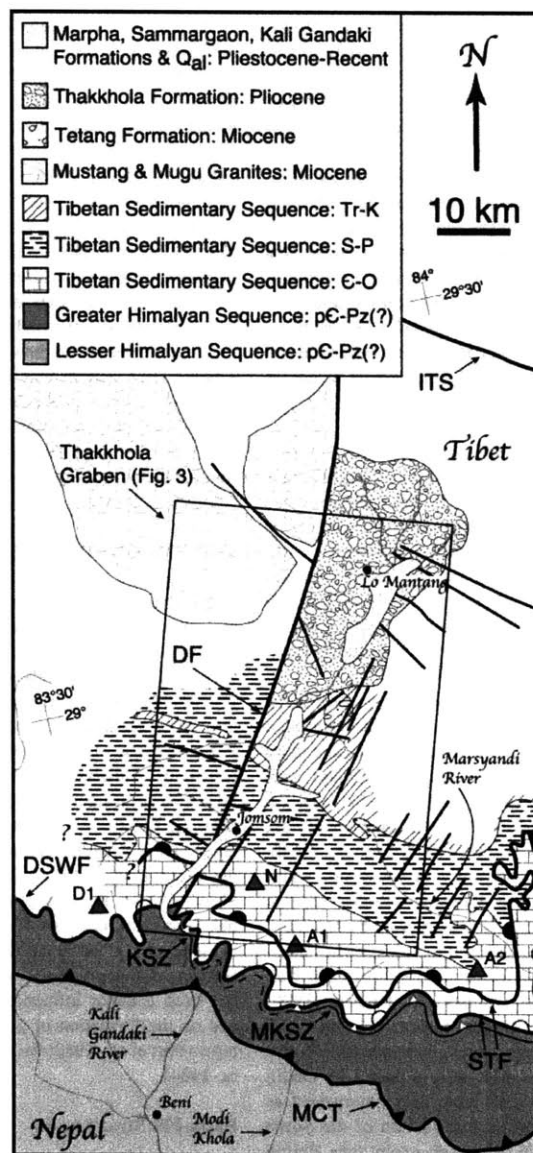


Figure 2. Simplified geologic map of the central Himalayas of Nepal modified from Colchchen et al. (1986) and Coleman (1996b). Abbreviations of major structures are as follows: ITS—Indus-Tsangpo suture, DF—Dangardzong fault, KSZ—Kalopani shear zone, MKSZ—Modi Khola shear zone, STF—normal faults of South Tibetan fault system, MCT—Main Central thrust, DSWF—Dhaulagiri Southwest fault. Triangles denote significant peaks: A1—Annapurna I, A2—Annapurna II, N—Nilgiri, D1—Dhaulagiri I.

(Burchfiel et al., 1992). Throughout its history, the South Tibetan fault system has moved episodically and has been dominantly a normal-sense structure, but its history also has included episodes of thrusting and orogen-parallel shear along the basal shear zone (Hodges et al., 1996b; Vannay and Hodges, 1996). Minimum normal-sense displacements of as much as 35 km have been documented along the basal detachment fault in the Everest region of Nepal, to the east of our study area (Hodges et al., 1992). The earliest-known motion (which is normal sense) on the South Tibetan fault system was coeval with metamorphism of the Greater Himalayan Sequence and motion on the Main Central thrust at ca. 22 Ma (Hubbard, 1989; Hodges et al., 1992; Nazarchuk, 1993; Coleman, 1996b; Godin, 1999), and ductile activity along the fault system continued until at least ca. 16 Ma (Hodges et al., 1998). The ca. 22 Ma timing comes from several places, including the Annapurna area (which includes the area where we did our work), the Manaslu area (east of Annapurna), Shisha Pangma (in the Langtang area of Nepal, east of Manaslu), Kula Kangri (in Bhutan), and Zaskar (in western India/southern Tibet).

Some strands of the basal shear zone of the South Tibetan fault system have been intruded by early to middle Miocene granites, and these intrusive relationships imply minimum ages for the basal part of the system between ca. 22 Ma (Guillot et al., 1994; Harrison et al., 1995b) and ca. 16 Ma (Hodges et al., 1998). However, the possibility of localized, younger—post-middle Miocene—South Tibetan fault system activity is supported by the range of cooling ages within the fault system's high-strain zone (Godin et al., 1999a) in the Kali Gandaki valley. Vannay and Hodges (1996) reported ages between 15.5 ± 0.3 and 13.02 Ma; even younger ages, between 12.7 ± 0.4 and 11.8 ± 0.4 Ma, were reported by Godin (1999). These data have been interpreted as indicative of brittle reactivation of the South Tibetan fault system high-strain zone during the interval 16–12 Ma, possibly related to extension in the Thakkhola graben (Godin, 1999).

The existence of north-dipping, brittle normal faults in the upper Modi Khola and Marsyandi valleys (Coleman, 1996b; Hodges et al., 1996b) presents the possibility that structurally higher parts of the South Tibetan fault system may have undergone even younger—post-Miocene—activity. These structures include brittle normal faults in the lowermost Tibetan Sedimentary Sequence structurally above the basal shear zone. Since the kilo-

meter-scale folds in their hanging walls cannot be traced into their footwalls, these faults represent major décollement horizons (Caby et al., 1983; Colchen et al., 1986). The structurally lowest of these normal faults in the Modi Khola and Marsyandi valleys also truncate ca. 18 Ma leucogranite dikes (Hodges et al., 1996b; Coleman, 1998). There are no other age constraints for these South Tibetan fault system structures, but, as noted by Hodges et al. (1996b), no geologic reason precludes their movement during the Pliocene or later.

Considering the range of cooling ages, and the existence of potentially young structures, it is appropriate to ask how recently the South Tibetan fault system was active and whether it is still active. Geologic relationships that may answer these questions and illuminate the interaction between Tibetan extension and the South Tibetan fault system can be found in the Thakkhola graben.

THE THAKKHOLA GRABEN

The Thakkhola graben is an asymmetric basin, measuring more than 70 km in length. Cutting across the tectonic grain of the Himalaya, the graben extends southward from the Tibetan Plateau, starting at the northern tip of the Mustang-Mugu leucogranite massif (Le Fort and France-Lanord, 1994), continuing between the Annapurna and Dhaulagiri Himalaya, and terminating near the Himalayan crest (Fig. 2). The graben has an angular shape that tapers from a width of more than 30 km in the north to a width of 2 km in the south. Flowing down the axis of the Thakkhola graben is the Kali Gandaki River, a drainage that is suspected to be antecedent to the modern Himalayan topography (Wager, 1937) and that has been a major influence on sedimentation and on the formation of geomorphologic features (Fort et al., 1982; Iwata et al., 1982; Iwata, 1984).

Basin-Fill Stratigraphy

Figures 3 and 4 summarize the geology and stratigraphy of the Thakkhola graben fill. The oldest sedimentary units in the Thakkhola graben are the middle Miocene to upper Pliocene Tetang and Thakkhola Formations. The upper Pliocene to upper Pleistocene Sammargaon and Marpha Formations lie disconformably above the Thakkhola and Tetang Formations. In a cut-and-fill relationship with all of these is the upper Pleistocene to Holocene Kali Gandaki Formation. The youngest sediments in the Thakkhola graben are the modern gravels in the alluviated bed of the Kali Gandaki

River. In addition, large volumes of landslide and moraine material of poorly determined age have been deposited in the Kali Gandaki valley (Fort et al., 1982; Iwata et al., 1982; Iwata, 1984). The type example of these deposits is the complex of terraced moraines and landslides near Larjung and Tuckuche villages and south of Lete village.

Tetang and Thakkhola Formations

The Tetang and Thakkhola Formations are in depositional and fault contact with the underlying Tibetan Sedimentary Sequence in the northern part of the Thakkhola graben (Fort et al., 1982; Colchen et al., 1986) (Fig. 3). These formations both comprise alternating sequences of alluvial and fluvial conglomerates that grade into lacustrine sediments, which are thickest toward the center of the graben (Fort et al., 1982; Garzzone et al., 1999) (Fig. 4). The distribution of coarse-grained facies in these deposits suggests deposition synchronous with active faulting along the margins of the Thakkhola graben, i.e., along the eastern margin during deposition of the Tetang Formation and along the western margin during deposition of the Thakkhola Formation (Fort et al., 1982; Garzzone et al., 1999). An angular unconformity that dips $\sim 10^\circ$ NW separates the Tetang Formation from the Thakkhola Formation (Colchen, 1980; Fort et al., 1982); the unconformity may mark the period of transition from faulting along the eastern margin to faulting along the western margin of the graben. Modern-day dips in the Tetang Formation of 25° NW probably reflect postdepositional faulting and tilting along the western edge of the Thakkhola graben during or after Thakkhola Formation deposition (Fort et al., 1982; Garzzone et al., 2000).

The best-available constraints for the age of the Tetang and Thakkhola Formations come from magnetostratigraphy and stable isotopes. The presence of magnetozones interpreted to be Neogene reversals suggests a 10.6–9.6 Ma age for the Tetang Formation (Yoshida et al., 1984; Garzzone et al., 2000). Carbon isotope characteristics ($\delta^{13}\text{C}$) of the lowermost Thakkhola Formation imply a maximum age of 8 Ma (Garzzone et al., 2000), and interpretation of the magnetostratigraphy led Yoshida et al. (1984) to conclude that deposition of the Thakkhola Formation continued until at least 2 Ma.

Sammargaon Formation

Unconformably overlying the Thakkhola Formation in the northern part of the Thakkhola graben is the Sammargaon Formation (Fort et al., 1982) (Fig. 3). Well exposed in an

~130-m-high cliff near Tangbe village, it is a package of breccia and conglomerate that was deposited into areas of high relief within the Tetang and Thakkhola Formations (Fig. 4). The basal unit consists of fine-grained lacustrine strata interbedded with fine-grained sandstone. Channels within this unit have been filled by conglomerates that include clasts of leucogranite, and clast imbrication suggests southward paleoflow. These fluvial conglomerates grade upward into sandstone, which is capped by a complex and very well-indurated, sandy, diamictic conglomerate that we interpret to be glacial till. The Sammargaon Formation is also associated with glacial moraines and is interpreted to be a glaciofluvial package deposited during middle Pleistocene glaciation (Fort et al., 1982; Fort, 1989).

Marpha Formation

The best exposures of glaciolacustrine sedimentary rocks belonging to the Marpha Formation are near the villages of Marpha and Syang (Fort et al., 1982; Iwata, 1984) (Fig. 3). The type section at Marpha features a >200-m-thick succession of poorly consolidated lacustrine claystone and siltstone intercalated with sandstone and conglomerate horizons (Fort et al., 1982) (Fig. 5). Most bedding planes are nearly horizontal, with maximum dips of 5°S. At Syang, however, the Marpha Formation is coarser grained and consists of poorly to well-indurated, massive, coarse-grained sandstone with a few 50-cm- to 1-m-sized clasts of Tibetan Sedimentary Sequence rocks, in addition to clasts of leucogranite (Fig. 5). These sandstones grade eastward into fine-grained, powdery, yellow, lacustrine siltstone and eventually into dark, carbonaceous siltstone (Fig. 6). Upsection, the massive, coarse sandstone grades into laminated, medium-grained sandstone and siltstone interbedded with 1–3-m-thick layers of muddy conglomerate. Bedding in the stratigraphically highest bedded material is flat lying, and individual laminae are ~10 cm thick.

Fort et al. (1982) correlated the lowermost Marpha Formation to the uppermost Sammargaon Formation, on the basis of the association of the Marpha Formation with an underlying glacial till (Fort et al., 1982). Later workers assigned a late Pleistocene (ca. 150 ka) maximum age to the Marpha Formation on the basis of reconnaissance magnetostratigraphic studies and correlations with moraines interpreted to be from the penultimate glacial maximum (Iwata, 1984; Yoshida et al., 1984). We have reanalyzed some of the paleomagnetic data presented by Yoshida et al. (1984) (Fig. 5). In the lowermost section of the Mar-

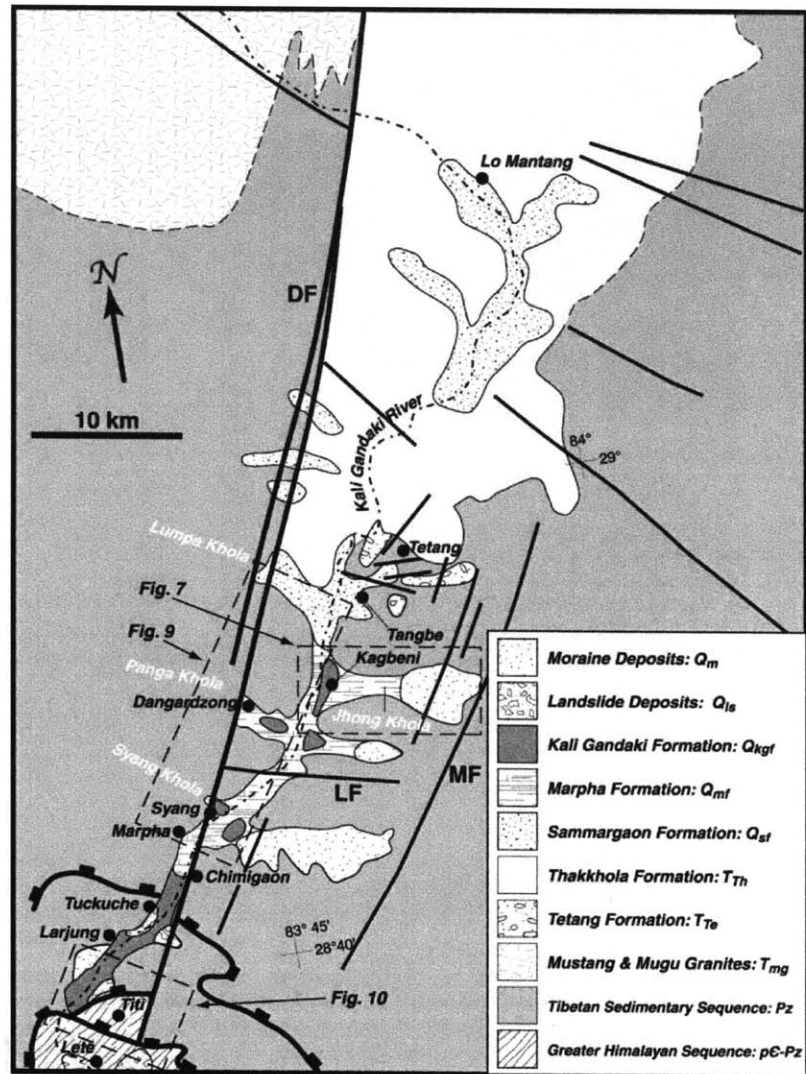


Figure 3. Detailed map of the Thakkhola graben showing the distribution of basin-fill units, modified from Fort et al. (1982). The ornamented faults between Lete and Tuckuche are various strands of the South Tibetan fault system. Abbreviations are as follows: DF—Dangardzong fault, MF—Muktinath fault, LF—Lupra fault.

pha Formation at Marpha, a small excursion to reversed polarity preceded by a zone of transitional directions yielding low VGP (virtual geomagnetic pole) latitudes may be the Laschamp Excursion, the best age estimate of which is ca. 33–37 ka (Nowaczyk and Antonow, 1997). The excursion places a maximum age on the part of the Marpha Formation overlying the excursion, which includes the correlative rocks 5 km to the north at Syang village.

Kali Gandaki Formation

Near Syang village, the Kali Gandaki Formation unconformably overlies the Marpha Formation in a cut-and-fill relationship and onlaps Devonian schists of the Tilicho Col Formation (Colchen, 1980) (Fig. 3). The type section is a 55-m-high cliff exposure at the mouth of the bedrock canyon of the Syang Khola, an east-flowing tributary drainage of the Kali Gandaki River (Fig. 6). The cliff is ~500 m in length and is contiguous with the

NEOTECTONICS OF THE THAKKHOLA GRABEN

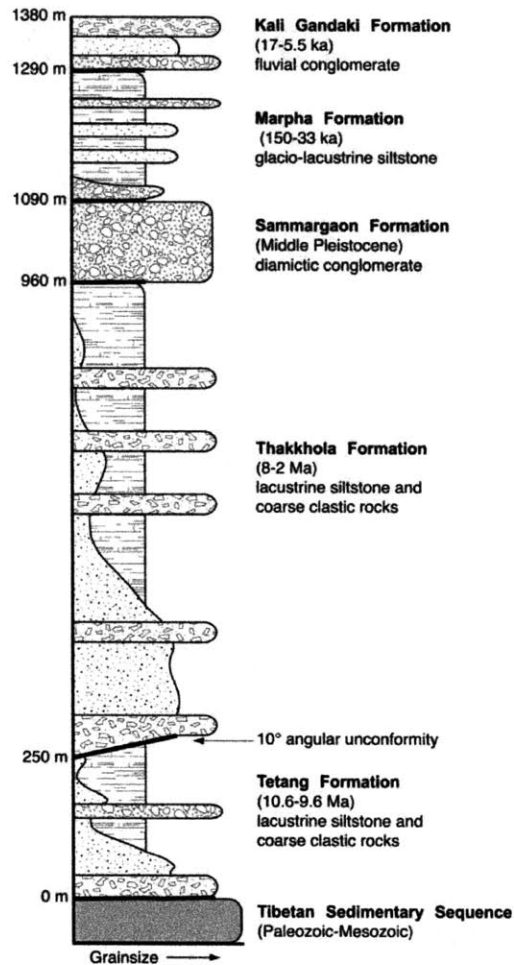


Figure 4. Generalized stratigraphy of the Thakkhola graben fill. Minimum thicknesses are shown. The units are separated from one another by major unconformities, shown by bold lines.

~1-km-long exposure of the Marpha Formation. The Kali Gandaki Formation includes three main units that are distinct from those of the adjacent, underlying Marpha Formation: a lower sandstone (KGF I), a middle fluvial conglomerate (KGF II), and an upper debris-flow breccia (KGF III) (Fig. 6). A terrace surface has been cut into the upper unit at the Syang Khola cliff, so no contiguous, stratigraphically higher Kali Gandaki Formation rocks are there exposed. Fluvial conglomerates stranded ~300 m above the Syang Khola, however, may be part of Kali Gandaki Formation. In addition, we correlate similar, coarse-grained fluvial conglomerates at the

mouth of the Jhong Khola at Kagbeni with the Kali Gandaki Formation.

Faults Related to Development of the Thakkhola Graben

The Thakkhola graben is bounded on its western edge by the Dangardzong fault, a N20°–40°E-striking, steeply (~60°SE) dipping, normal fault that is the principal growth structure for the basin (Hagen, 1968; Bordet et al., 1971; Colchen, 1980) (Fig. 3). The fault can be traced on the ground and via remote-sensing data for >100 km along strike (Colchen et al., 1986; Le Fort and France-Lanord,

1994). At its extreme northern end, the Dangardzong fault curves toward the west around a prominent massif—the topographic expression of the Mustang and Mugu plutons—and the Dangardzong forms its northeastern edge (Fig. 3). There is no trace of the Dangardzong fault north of the Indus-Tsangpo suture, which itself is a distinct lineament on Landsat imagery and digital elevation models. Along most of its length, the Dangardzong fault juxtaposes the Tibetan Sedimentary Sequence with Tertiary and Quaternary basin fill of the Thakkhola graben. The southernmost few kilometers of the fault, however, cut the Greater Himalayan Sequence (Fig. 3).

Previous researchers have reported a change in cumulative displacement of the Dangardzong fault along strike. In the north, at the latitude of Lo Mantang, more than 4 km of dip-slip displacement is estimated from the amount of topographic relief on the western margin of the graben (Fort et al., 1982). The amount of dip-slip displacement diminishes to almost zero toward the south, suggestive of scissors-like fault kinematics (Fort et al., 1982). The southward decrease in relief along the western margin of the basin and a decrease in the thickness of Thakkhola graben basin fill indicate this decrease in throw. In addition to this line of evidence, we note a progressive decrease in the metamorphic grade of the footwall of the Dangardzong fault, from the biotite zone of greenschist facies at the latitude of Tangbe village to the chlorite zone and lower south of Dangardzong village, suggestive of decreasing footwall exhumation toward the south.

Other normal faults and fracture sets with orientations similar to the Dangardzong fault have been observed and mapped up to 40 km to the east (Coleman, 1996b) (Fig. 2). A minimum age of ca. 14 Ma for east-west extension in the Thakkhola graben region is indicated by ⁴⁰Ar/³⁹Ar ages of hydrothermal muscovite that crystallized in one of these northeast-striking fractures (Coleman and Hodges, 1995). East-striking faults are also present in the Thakkhola graben area on several scales. On a regional scale, east-striking lineaments can be seen in remote-sensing imagery. Among these is the Lupra fault, which has been interpreted as a thrust fault that was later reactivated as a normal fault during development of the Thakkhola graben (Godin, 1999) (Fig. 3). On a smaller scale, we have mapped similarly oriented faults in the Tetang village area that appear to have been active at the time of inception of the graben (Fig. 3). These faults were active during deposition of the Tetang and Thakkhola Formations and may have been im-

portant controls on the development of the Tetang and Thakkhola basins.

¹⁴C TERRACE CHRONOLOGY

The Pleistocene and younger sedimentary rocks in the Kali Gandaki valley have important stratigraphic relationships with the Dangdanzong fault and with faults of the South Tibetan fault system. Dating these units and the river terraces developed upon them therefore provides a primary age constraint on the recent tectonic history of the area.

River terraces are cut into the Marpha, Sammargaon, and Kali Gandaki Formations along the course of the Kali Gandaki River in the Thakkhola graben (Hagen, 1968; Bordet et al., 1971; Fort, 1976). The highest of these terraces are more than 350 m above the riverbed. We mapped several of these terrace levels (K1–K5) at the mouth of the Jhong Khola, a tributary of the Kali Gandaki River (Fig. 7), and the terrace stratigraphy that we have inferred is shown in Figure 8. The substrate material becomes younger upward in a normal stratigraphic sense so that, during a single cycle of infilling and incision, the highest—and presumably oldest—cut terraces are developed on the youngest substrate. As shown by Iwata (1984), the terraces at Jhong Khola can be correlated throughout the Kali Gandaki valley.

Each terrace surface is mantled with a 1–5-m-thick layer of alluvium that is discordant to its substrate. Because such mantles were probably deposited at the time the terrace surface was the active flood plain, they provide a means of determining the maximum age for terrace formation and abandonment. In the alluvial mantles of three terraces (K2, K4, and K5) and in the substrate below the K1 terrace, we found organic material suitable for ¹⁴C dating. Sample locations are shown in Figure 7 and Figure 9. The appendix provides the details of the sample collection, preparation, and analysis, and the results of the age determinations are shown in Table 1.

The K5 sample (97KGW5/GX-23110-AMS) suggests that the flight of terraces between K1 and K5 in the area around the Jhong Khola and the correlative terraces downstream along the Kali Gandaki River are Holocene in age, having developed since 7490 ± 60 cal. yr B.P. Terrace development continued with the establishment of the K4 terrace at 5056 ± 56 cal. yr B.P. (97KGW7/GX-23112-AMS) and the K2 terrace at 2300 ± 250 cal. yr B.P. (97KGW2/GX-23107).

The sample obtained from the Kali Gandaki Formation fill beneath K1 provides a maximum age of 17 150 ± 150 cal. yr B.P.

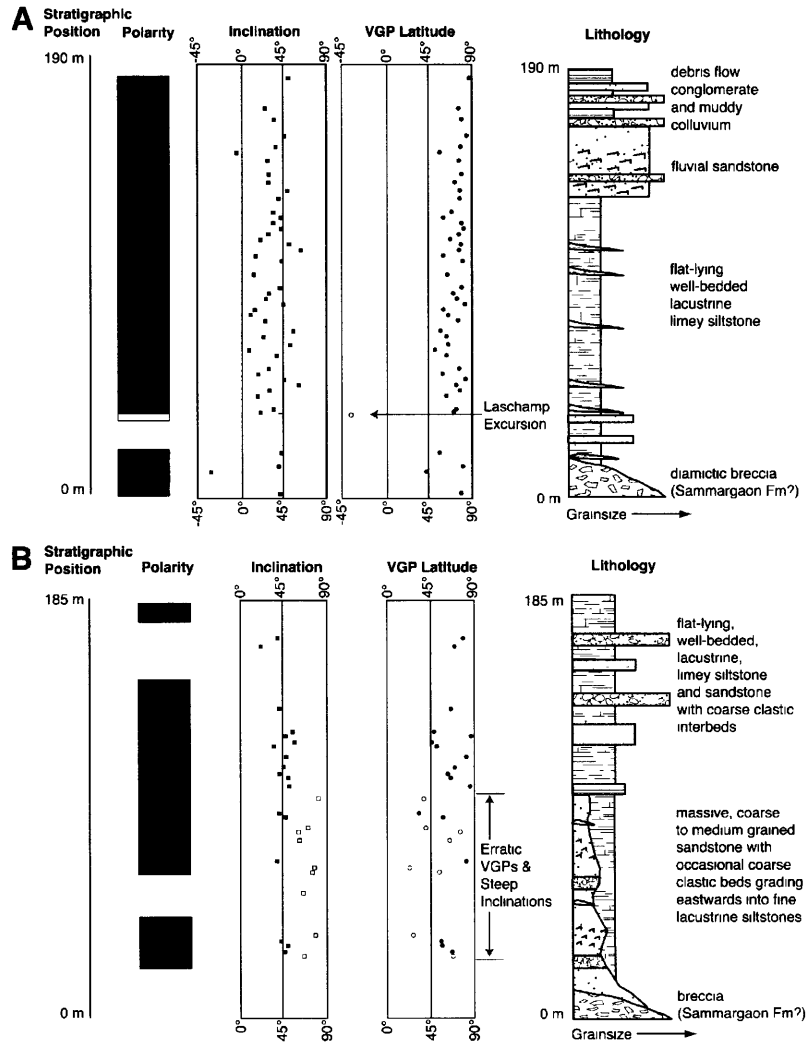


Figure 5. Stratigraphy of the Marpha Formation at (A) Marpha village and (B) Syang Khola, based partly on Fort et al. (1982). Magnetostratigraphic data are from Yoshida et al. (1984). The unfilled symbols in A show the possible location of the Laschamp Excursion in the lowermost part of the Marpha village section. The unfilled symbols in B represent erratic VGPs and correspondingly steep inclinations in the stratigraphically lowest samples at Syang Khola.

(97KGW1/GX-23106-AMS) for the Kali Gandaki Formation. A minimum age can be estimated if one recognizes that deposition of the Kali Gandaki Formation must have ceased when the latest episode of incision began. Because the K5 terrace is developed in part on Kali Gandaki Formation substrate, the terrace's 7490 ± 60 cal. yr B.P. age also provides a minimum age for that formation.

We postulate that the bulk of Kali Gandaki

Formation deposition would have occurred between ca. 17.2 ka and ca. 7.5 ka. This period of deposition may reflect a late Holocene glacial advance postdating the Last Glacial Maximum, similar to those documented in the Langtang Himalaya (Shiraiwa and Watanabe, 1991; Zhou et al., 1991; Shiraiwa, 1993). A similar advance may have occurred in the Kali Gandaki valley, and this episode of glaciation would have been followed by significant in-

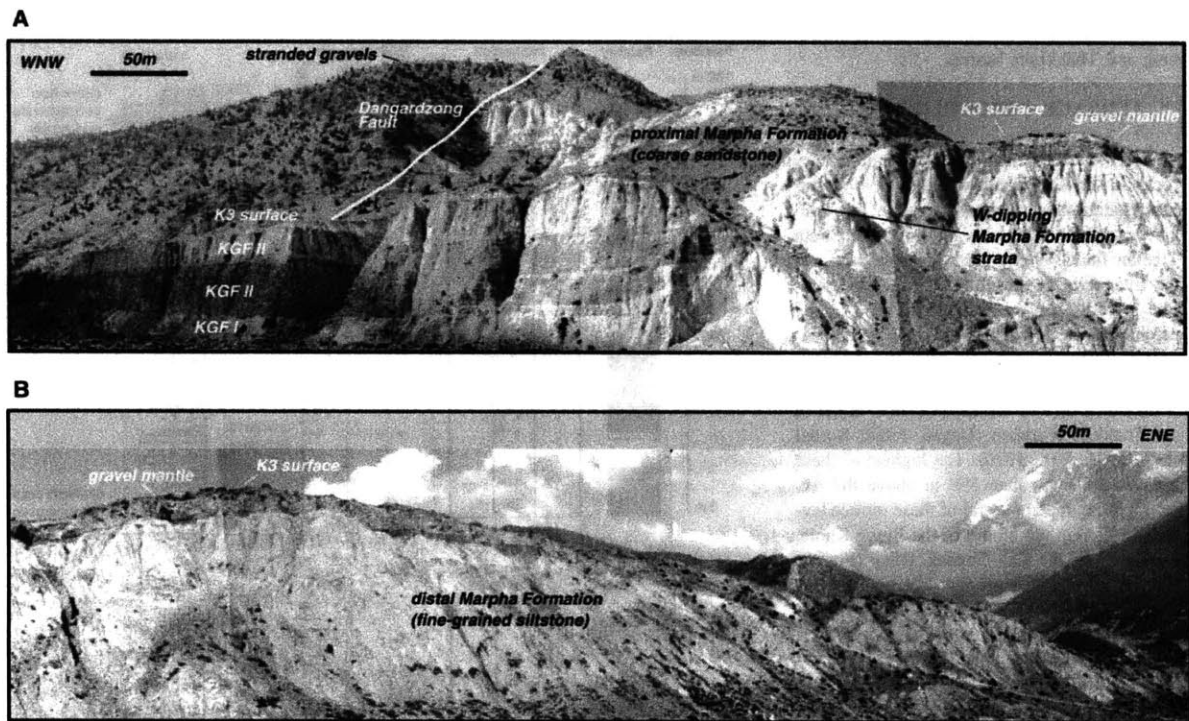


Figure 6. Panorama photographic mosaic of the northern bank of the Syang Khola, showing (A) the western half and (B) the eastern half. The type exposure of the Kali Gandaki Formation (units KGF I–KGF III) is the distinctly stratified cliff in the foreground of A. The height of the cliff is 55 m. In B, the Marpha Formation is seen to grade eastward from the sandy lithology that makes up the high cliffs above the Kali Gandaki Formation in A to progressively darker and more fine-grained siltstone. The flat surface developed on the Kali Gandaki Formation and the Marpha Formation is the K3 terrace level. Note the coarse-grained mantling layer of alluvium in B. The white line in A shows the trace of the Dangardzong fault. Neither the K3 terrace surface nor the Kali Gandaki Formation are offset by the Dangardzong fault.

cision as the volume of meltwater increased and sediment supply decreased. We regard the 332-m-high flight of K1–K5 terraces as a record of that process, and we estimate the rate of postglacial incision to be 44 mm/yr, averaged over the past ~7.5 k.y.

These results are important in their own right as the first quantitative ages for terraces in the Kali Gandaki valley. Combined with the field observations of the Dangardzong fault that we describe in the following section, they give an estimate for the age of neotectonic activity in the Thakkhola graben.

FIELD OBSERVATIONS ALONG THE DANGARDZONG FAULT

Field work was carried out in the Kali Gandaki valley between Tangbe and Titi villages, a distance of ~30 km (Fig. 9). Four localities were studied in detail (from north to south): Lumpa Khola (at the latitude of Tangbe vil-

lage), Dangardzong village, Syang village, and Titi village. Our field work was focused on the relationships between the Dangardzong fault, the K1–K5 river terraces, the fluvio-glacial deposits underlying the terraces, and the modern stream tributaries of the Kali Gandaki River. These relationships allowed us to estimate the age of latest movement on the Dangardzong fault. In addition, we employed a variety of digital remote-sensing data to aid in our field work and to augment our mapping and interpretations. These data sets include Landsat Thematic Mapper (TM), Landsat Multispectral Scanner (MSS), and SPOT (Satellite Pour l’Observation de la Terre) panchromatic scenes. We found the SPOT scenes more accurate than published topographic maps of the study area, so we used the SPOT imagery as a base for detailed field mapping. In addition, the highly detailed (10 m resolution) stereoscopic images that we were able to generate by using the SPOT scenes were in-

valuable in the recognition of small outcrops, lithologically controlled weathering and outcrop patterns, and critical geomorphic and neotectonic features such as fault scarps and offset drainages.

Lumpa Khola

At the northernmost locality visited, the Dangardzong fault is exposed at the head of an alluviated section of the Lumpa Khola, an east-flowing tributary of the Kali Gandaki River, 4 km west of their confluence (Fig. 9A). The fault zone coincides with an ~1000-m-high slope that is subparallel to the fault plane (N35°E, 50°SE) and approximates the exhumed fault surface (arrow i in Fig. 9A). Within the Lumpa Khola, the fault zone is ~100 m wide and contains cataclasite and fault gouge derived from the Tibetan Sedimentary Sequence bedrock. The fault places gray, fine-grained, Devonian schists of the Til-

Chapter 2: Neotectonics of the Thakkhola graben

HURTADO et al.

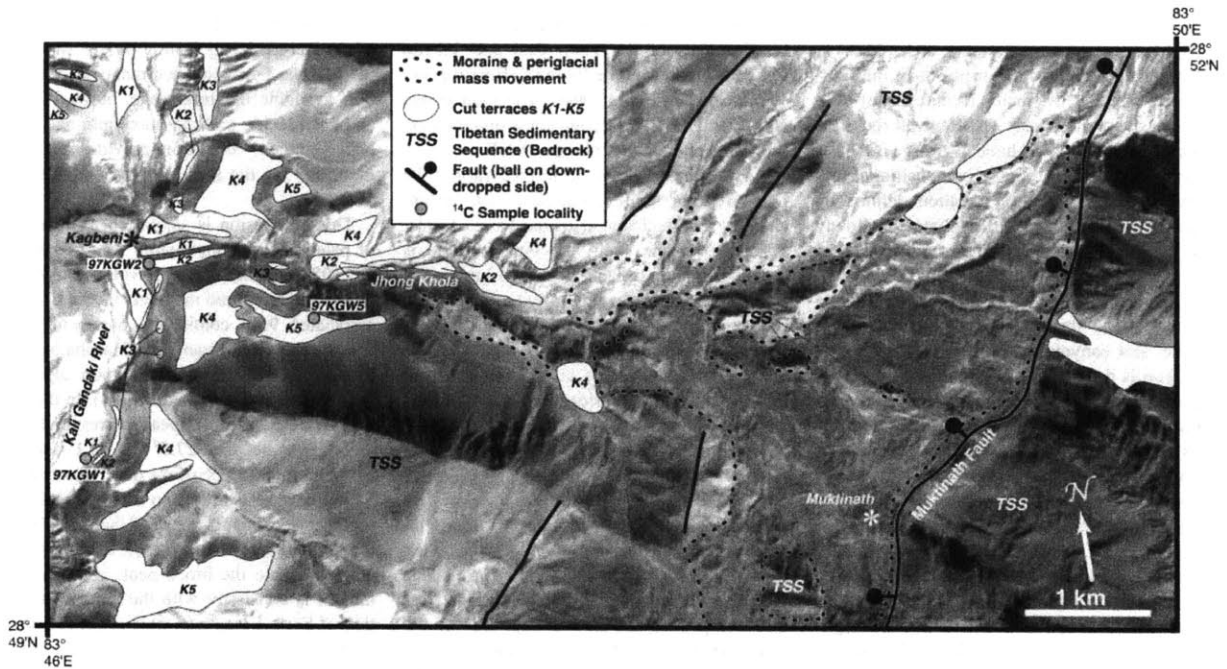


Figure 7. Geomorphologic map of the Jhong Khola between Kagbeni and Muktinath villages (see Fig. 3 for location). SPOT panchromatic imagery is used as the base. Note that lighting is from the south. The locations of ¹⁴C samples are indicated along with the mapped terrace levels and important faults.

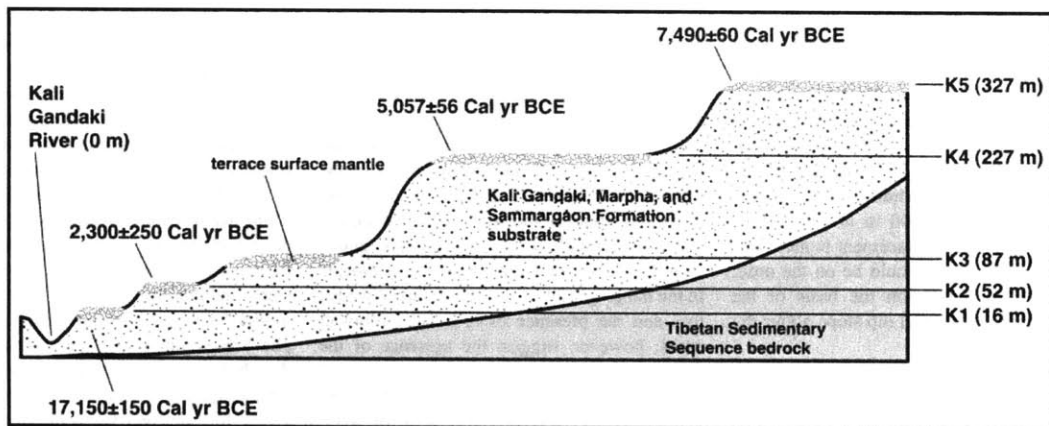


Figure 8. Schematic stratigraphy of the Kali Gandaki River terraces. Ages are corrected and calibrated ¹⁴C dates from organic material within the terrace surface and riser material. The 17 150 ± 150 cal. yr B.P. age is for the Kali Gandaki Formation. Heights given are relative altitudes above the Kali Gandaki River at Kagbeni village. The altitude given for the K4 terrace is that of K4 in the Jhong Khola east of Kagbeni village. The altitude of the K4 surface from which the 5057 ± 56 cal. yr B.P. age was acquired is higher because it is from the proximal part of a correlative alluvial-fan surface at Dangardzong village—see Table 1. Sample locations are shown in Figures 7 and 9.

icho Col Formation (Colchen et al., 1986) in the footwall against Cretaceous quartzites of the Chukh Formation (Colchen et al., 1986) in the hanging wall. Metamorphism in the footwall is greenschist facies (biotite zone) with neoblastic white micas. The footwall rocks directly below the fault have a strong northeast-striking, southeast-dipping compositional layering with a stretching lineation defined by quartzofeldspathic rods that plunge shallowly to the east, consistent with normal-sense, top-down-to-the-east movement.

Just upstream of the fault zone, the Lumpa Khola flows through a 100-m-deep, 10-m-wide, slot canyon cut into bedrock. The slot canyon is developed in the floor of a perched, glacially carved valley. In the fault zone, the Lumpa Khola channel widens considerably, its gradient shallows, and its bed becomes alluviated. Here, the stream takes a sudden right-angle bend to the south, following the trace of the fault for several hundred meters, after which it turns sharply to the east around a bedrock shutter ridge that has been partially covered by landslide material (arrow ii in Fig. 9A). On the slope south of the stream exposure, the fault trace coincides with a north-striking gully (arrow iii in Fig. 9A).

Although kinematic indicators in the bedrock show normal-sense movement, the sharp right-lateral bend in the Lumpa Khola coincident with the fault trace is suggestive of a component of dextral strike-slip displacement. In order to quantify the amount of cumulative strike-slip separation at Lumpa Khola, the lengths of both the bend in the river and the shutter ridge were measured with a laser range finder. A conservative estimate of 110 m of right-lateral offset was obtained by measuring the stream-parallel distance from the mouth of the bedrock slot canyon to the farthest extent of bedrock in the shutter ridge. Beyond that, the shutter-ridge obstruction is entirely landslide debris. Taking the entire length of the ridge, including the landslide section, yields a maximum estimate of 400 m of right-lateral separation. Dip-slip displacement is more difficult to determine, but could be on the order of hundreds of meters on the basis of the height of the fault-parallel dip slope above the Lumpa Khola.

Dangardzong Village

The Dangardzong fault is exposed at a sharp bend in the Panga Khola, another small tributary of the Kali Gandaki River, about 1 km west of Dangardzong village and 10 km south of Lumpa Khola (Fig. 9B). Here the fault places black schists of the Jurassic Lupra

Formation and quartzites of the Cretaceous Chukh Formation in the hanging wall against black schists of the Thini Chu and Tilicho Lake Formations in the footwall (Bordet et al., 1971; Colchen et al., 1986). The fault trends N43°E and dips 73°SE, and some outcrops exhibit slickenlines that plunge 16°SE.

As at Lumpa Khola, the surface trace of the Dangardzong fault coincides with abrupt changes in the character of the Panga Khola. Upstream of the fault, the Panga Khola is quite steep and is glacially carved (arrow i in Fig. 9B). Downstream, however, the stream gradient is shallower and the stream is alluviated. At the fault trace, the Panga Khola is deflected right laterally at an abrupt, 20-m-high bedrock-shutter ridge (arrow ii in Fig. 9B). An estimate of 300 m of right-lateral separation was made on the basis of laser range-finder measurements of the jog in the river, although it was not possible to correlate features across the fault. Similarly, we were unable to measure dip-slip displacement owing to the absence of displaced and correlatable features. An alluvial-fan terrace surface (K4) is developed on the downstream side of the shutter ridge, and a fragment of the same surface is preserved on the upstream side, in the footwall of the fault. Field surveys with a clinometer, altimeter, and laser range finder demonstrated that the K4 fan terrace surface and the smaller fragment are coplanar within measurement error and are not demonstrably offset from one another. Because the K4 terrace is undeformed, we infer that movement on the Dangardzong fault had ceased by ca. 5.1 ka at this location.

Syang Village

At the village of Syang, 5.5 km southwest of Dangardzong village (Fig. 9C), the Dangardzong fault places the Marpha Formation in fault contact with Devonian schists of the Tilicho Col Formation (Colchen et al., 1986). The fault zone is indistinct where exposed, and it is difficult to distinguish fault gouge from the debris flow and lacustrine sediments in the hanging wall. A distinct colluvial wedge unit and the presence of brecciated footwall rocks, however, suggest the presence of the fault.

The Dangardzong fault and the lower half of the Marpha Formation are buried by a 55-m-thick package of Kali Gandaki Formation sediments that clearly have not been offset by the fault (Fig. 9D). The K1–K3 terrace surfaces developed on the Kali Gandaki Formation and Marpha Formation also are not offset. These stratigraphic and structural relation-

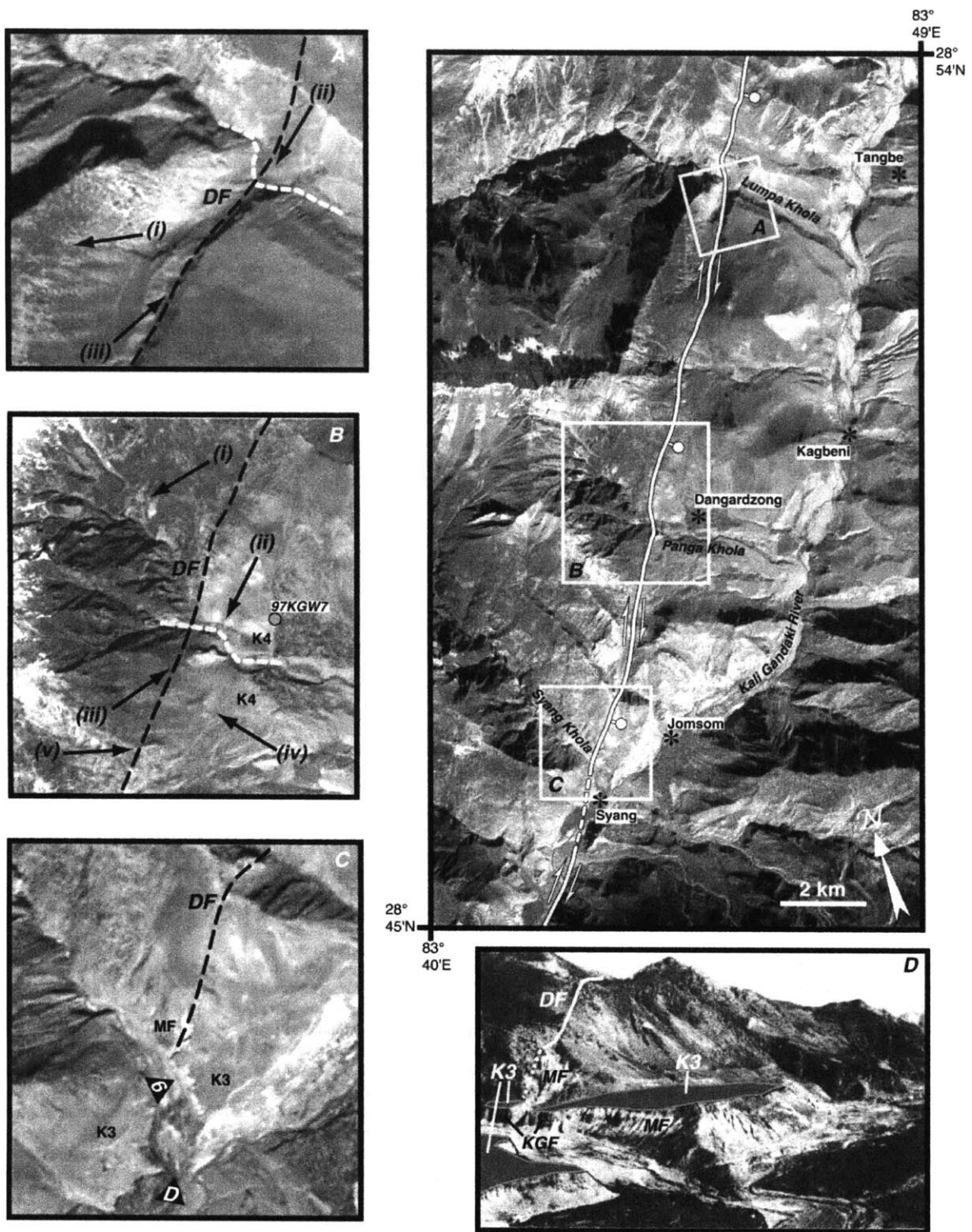
ships, combined with our ¹⁴C chronology, allow us to bracket the age of latest movement of the Dangardzong fault at Syang: the age of the Marpha Formation sediments provides the best available maximum age, between ca. 35 and ca. 150 ka, and the maximum age of the Kali Gandaki Formation provides the minimum age for the last episode of faulting, ca. 17.2 ka.

This conclusion is supported by reanalysis of paleomagnetic inclination data (Yoshida et al., 1984) for the Marpha Formation. We analyzed the measured magnetic inclinations and associated 95% confidence parameters (α_{95}) for samples from Syang and Marpha by using a maximum-likelihood estimation algorithm (Sambridge and Compston, 1994). In the Marpha data set, a broad peak corresponding to inclinations between 27.5° and 44.1° accounts for more than 71.6% of the data. However, the Syang data set shows two distinct peaks that together account for most of the data. One of the Syang peaks is centered about 44.3° ± 4.0°, and, like the broad peak in the Marpha data, it is consistent with the modern inclination of Earth's magnetic field at the latitude of Nepal (~43.2°; Barton, 1997). The mean of the other peak in the Syang data, however, is significantly steeper than these: 66.7° ± 2.7° (33.2% of the data).

The position of the Syang and Marpha sections with respect to the Dangardzong fault can explain the steepened inclinations in the Syang data and the absence of steep inclinations in the Marpha data. The Marpha Formation at Marpha village is located ~1 km west of the Dangardzong fault in map distance (Fig. 3). At this position, the Marpha strata would be spared from the most extreme post-depositional tilting due to motion on the Dangardzong fault and would therefore accurately preserve the correct inclination of Earth's magnetic field. In contrast, the correlative deposits at Syang crop out within and adjacent to the Dangardzong fault zone. Fault-related tilting would have locally steepened the magnetic inclinations; ~30° of backtilting is sufficient to create the population of anomalously steep inclinations in the Syang data. This model for the steepening of dips in the Marpha Formation is consistent with the spatial distribution of tilted strata; beds of the lowermost Marpha Formation north of Syang, between Jomsom and Kagbeni, are consistently backtilted by 10° and 25° to the northwest, with the degree of backtilting increasing as one moves north and away from the Dangardzong fault.

Recall that there are two inclination peaks in the Syang data, one consistent with the

HURTADO et al.



NEOTECTONICS OF THE THAKKHOLA GRABEN

TABLE 1 SUMMARY OF ^{14}C ANALYSES OF ORGANIC MATERIAL FROM THE KALI GANDAKI RIVER TERRACES

Sample number*	Sample location†		Terrace unit‡	Elevation* (m)	$\delta^{13}\text{C}$ (‰)	^{14}C age** (yr B P)	Libby-corrected age†† (yr B P)	Calibrated age‡‡ (cal yr B P)
	Latitude (°N)	Longitude (°E)						
97KGW1/GX-23106-AMS	N28°49 861'	83°42 026'	Kali Gandaki Formation below K1	16	-25.2	13890 ± 95	14307 ± 98	17150 ± 150
97KGW2/GX-23107	N28°49 955'	83°47 060'	Mantling gravel 2 m below K2	52	-24.7	2200 ± 200	2266 ± 206	2300 ± 250
97KGW5/GX-23110-AMS	N28°49 762'	83°48 109'	Mantling gravel 1 m below K5	331	-24.0	6490 ± 55	6685 ± 57	7490 ± 60
97KGW7/GX-23112-AMS	N28°49 581'	83°44 912'	Mantling gravel 5 m below K4	327	-22.4	4300 ± 55	4429 ± 57	5057 ± 56

Note Age determinations conducted by Geochron Laboratories, Cambridge, Massachusetts. See Appendix 1 for details of the sample collection and processing methods used. Stated uncertainties are $\pm 1\sigma$. Only the Libby correction** and ^{14}C calibration†† were performed, and uncertainties were propagated throughout.

*The sample number in parentheses is the sample identifier used by Geochron Laboratories.

†Global Positioning System (GPS) coordinates were determined with a hand-held GPS receiver with a horizontal uncertainty of ± 100 m.

‡Sample 99KGW2 was collected from the K2 terrace at Kagbeni village, and 99KGW5 was collected from the K5 terrace above Kagbeni village. 99KGW7 was collected from an alluvial-fan surface correlative with the K4 terrace level near Dangardzong village. 99KG1 was collected from the Kali Gandaki Formation below the K1 terrace south of Kagbeni village. See Figures 7 and 9 for locations.

*Elevations are above Kali Gandaki River. Elevations were measured using an electronic altimeter with an error of ± 10 m. A differential technique was used with the Kali Gandaki River at Kagbeni village as the datum (2773 m above sea level).

**The ^{14}C age is the uncorrected, uncalibrated age resulting from the ^{14}C analysis. Quoted errors are based solely on analytical uncertainty. The modern standard used is 95% of the activity of National Bureau of Standards oxalic acid, and the ages are referenced to the year A.D. 1950.

††The Libby correction is due to the 3% difference in the Libby half-life of ^{14}C (5568 yr) and the actual half-life (5735 yr). The Libby correction entails multiplication of the ^{14}C age by 1.03.

‡‡Calibrated (cal) ages were calculated from the Libby-corrected ages with the program OxCal 2.18 by using the calibration of Stuiver et al. (1993). Reported ages and uncertainties are the centroids of the 0.95 confidence age intervals.

modern-day magnetic inclination and one oversteepened. Figure 5 shows that VGP latitudes are smaller and more scattered for samples lower in the Syang section, mirroring the spatial distribution of steeper inclinations at stratigraphically lower—and therefore older—levels in the Syang section. If one accepts the hypothesis that the steep inclinations are due to postdepositional tilting, this pattern suggests that the steepening event occurred sometime during deposition of the Marpha Formation, but stopped before the end of the depositional period. This pattern is consistent with the dips of the uppermost Marpha Formation sedimentary units at Syang that appear to be flat lying. Unfortunately, because the lowermost Marpha Formation is buried by the Kali Gandaki Formation in the Syang Khola, we were unable to measure the dips in the lowermost Marpha Formation there, although photographs of the outcrop at Syang seem to indicate a westward dip to some of the lacustrine strata (Fig. 6). Thus, on the basis of magnetostratigraphy and the maximum age of the

Marpha Formation sedimentary units at Syang village, it is reasonable to estimate that steepening of the Marpha Formation—due to late-stage motion of the Dangardzong fault—occurred within the past ~ 35 k.y.

SOUTHERN TERMINATION OF THE DANGARDZONG FAULT

We mapped the Dangardzong fault to its southern termination, on a hill 3.5 km northeast of Lete village and 17 km southwest of Syang village, near the village of Titi (Fig. 10). South of Syang, our examination of SPOT satellite imagery reveals the trace of the fault on the east bank of the Kali Gandaki River. The Dangardzong fault can be traced in this fashion as far south as Titi village. Ground-based mapping of the Dangardzong fault in this area was difficult because the slopes around Titi are heavily forested and vegetated, and outcrop is quite poor. Surface morphology, SPOT imagery, and careful interpretation of talus and regolith lithologies

were crucial pieces of information where outcrop was absent. A compilation of previous mapping and the results of our ground survey of the area are shown in Figure 10 superimposed on SPOT imagery.

A good exposure of the Dangardzong fault is found at an elevation of 3000 m on the hill northeast of Titi (point a in Fig. 10). An ~ 100 -m-thick brecciated zone, trending approximately north, separates Greater Himalayan Sequence migmatitic calc-silicate gneiss in the footwall from muscovite-bearing sandy marbles of the Annapurna Yellow Formation, one of the lowermost units of the Tibetan Sedimentary Sequence, in the hanging wall (Fig. 11A). The fault zone, corresponding to a non-vegetated slope on the SPOT imagery, is marked on the ground by outcrops of rubbly blocks of brecciated and slickensided Annapurna Yellow Formation.

The fault plane is exposed again at an ~ 10 -m-high cliff of Annapurna Yellow Formation about 1 km farther south (point b in Fig. 10). Here a prominent, north-south-oriented spur

Figure 9. SPOT panchromatic image of the Dangardzong fault trace (white line in large image in upper right) between the Lumpa Khola and Syang Khola canyons (see Fig. 3 for location). In each inset, the Dangardzong fault (DF) is shown by a black, dashed line. (A) The right-lateral deflection of the Lumpa Khola (white dotted line) at the trace of the Dangardzong fault. Arrow i denotes the tall, steep dip slope above the Lumpa Khola. Arrow ii denotes the shutter-ridge obstruction, and arrow iii denotes the fault-controlled gully south of the Lumpa Khola. (B) The area around Dangardzong village near the headwaters of the Panga Khola (white dotted line). Note the steep upper reaches of the Panga Khola shown by arrow i; the Panga Khola becomes less steep and more alluviated east of the Dangardzong fault trace. Arrow ii denotes the right-lateral offset of the Panga Khola. Arrows iii–v show possible scarps. (C) The area around Syang village. Triangle 6 shows the Kali Gandaki Formation cliff exposure in Figure 6. Triangle D shows location of photograph in Figure 9D. The K3 terrace level, developed on the Kali Gandaki Formation, and the Marpha Formation (MF) are labeled. (D) Photograph from Iwata (1984) taken from approximately the position of triangle D in Figure 9C. Note that the Dangardzong fault (DF) offsets neither the Kali Gandaki Formation (KGF) nor the K3 surface, although it does place the Marpha Formation in fault contact with the Tibetan Sedimentary Sequence.

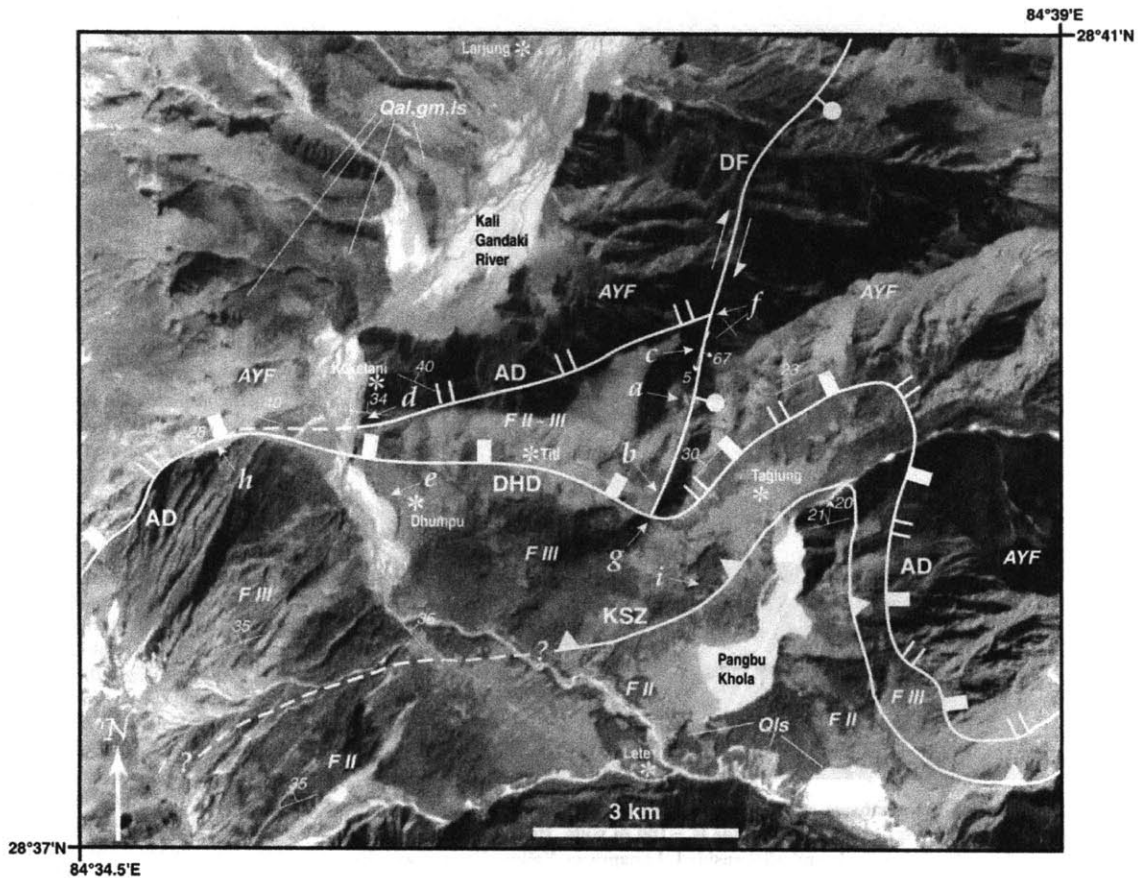


Figure 10. Geologic map of the Titi area on a panchromatic SPOT image base, showing the southern termination of the Dangardzong fault (see Fig. 3 for location). The data shown are the results of our geologic field mapping and our modifications of geologic mapping previously carried out by Colchen et al. (1986), Brown and Nazarchuk (1993), and Godin (1999). Abbreviations are as follows: DF—Dangardzong fault; AD—Annapurna detachment; DHD—Dhumpu detachment; KSZ—Kalopani shear zone; AYF—Annapurna Yellow Formation; F III, F II—Formations III (augen orthogneiss) and II (calc-silicate gneiss) of the Greater Himalayan Sequence; Qal, Qgm, Qls—Quaternary alluvium, glacial moraine, and landslide deposits. The arrows labeled a–i point to localities discussed in the text.

features an exhumed, subvertical fault plane that strikes N10°W with subhorizontal to slightly (~5°) south plunging slickenlines. Adjacent to this plane is an east-dipping, 10-m-wide cataclastic zone into which a gully has subsequently been incised (Fig. 11B). On the basis of the relative positions of outcrops in the foot-wall and hanging wall, the trend of the topography, and the exposed fault plane, our best estimate of the orientation of the fault zone is N10°W, 70° E. This is consistent with the orientation of the fault measured at a third outcrop 3 km to the north (point c in Fig. 10) where the fault plane is oriented N10°W and dips 67°E, again with subhorizontal slickenlines.

The Dangardzong fault outcrop at the north-

south-oriented spur coincides with an abrupt change in subsurface lithology and surface topography and morphology (Fig. 11B). The prominent, yellow-gray cliffs in the hanging wall just above and to the east of the Dangardzong fault, and those north of Taglung village, are composed of Annapurna Yellow Formation. North of Titi, however, the westward continuation of the same ridge displays no such cliffs, and the slope, although steep, is vegetated and subdued. Moreover, there is no outcrop of Annapurna Yellow Formation or any other Tibetan Sedimentary Sequence rocks in this area. Instead, there are sporadic, small outcrops and abundant, large boulders of Greater Himalayan Sequence paragneiss

and orthogneiss. Thus, the Dangardzong fault marks an abrupt, north-striking contact between Greater Himalayan Sequence and Tibetan Sedimentary Sequence that is nearly orthogonal to compositional layering in both units.

The Annapurna Yellow Formation crops out south of Koketani village, and orthogneiss of the Greater Himalayan Sequence crops out north of Dhumpu village. Their contact is located within the <1-km-wide zone between points d and e (Fig. 10). Because there is no outcrop of Annapurna Yellow Formation east of the area between points d and e (Fig. 10), the Tibetan Sedimentary Sequence–Greater Himalayan Sequence contact must project

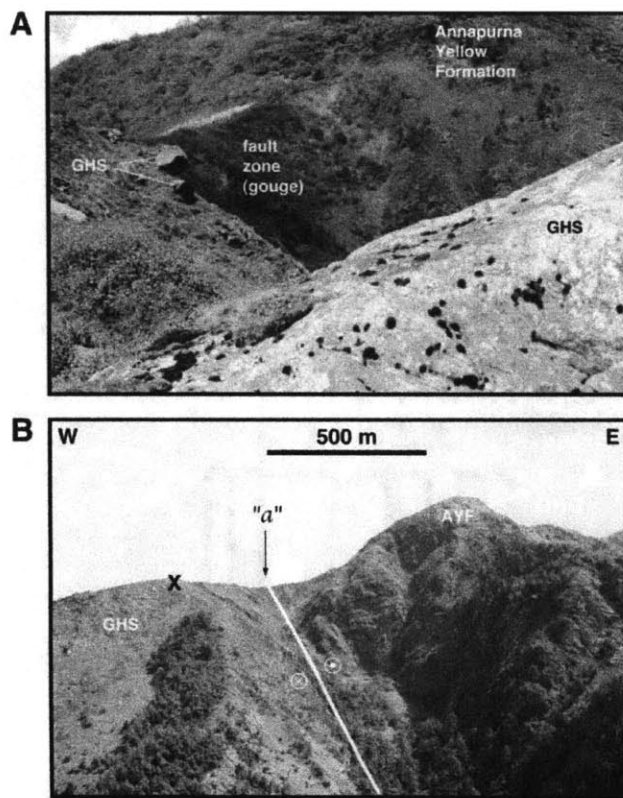


Figure 11. (A) View to the northeast of the Dangardzong fault exposure on the hill north of Titi village (point a in Fig. 10). The fault zone is ~100 m wide. Its surface exposure is a broad zone of sandy, pulverized, and slickensided Annapurna Yellow Formation. (B) View to the north of the hill north of Titi. The X marks the location where the photograph in A was taken, and location a is the same as point a in Figure 10. Note the change in the morphology of the ridge from east to west. The trace of the Dangardzong fault (white line) is defined by the abrupt change in lithology and morphology, outcrops of fault rocks, and a fault-controlled gully. The Dangardzong fault's kinematics are labeled showing right-lateral motion. At this location, it places Annapurna Yellow Formation (AYF) in the hanging wall against Greater Himalayan Sequence (GHS) in the footwall.

along a north-northeast strike until it is truncated at the trace of the Dangardzong fault at point f (Fig. 10). This is the last location where both the hanging wall and the footwall of the Dangardzong fault are composed of Annapurna Yellow Formation. The juxtaposition of Tibetan Sedimentary Sequence against Greater Himalayan Sequence across the Dangardzong fault continues south of point f for 3 km to point g (Fig. 10). From point g, the Tibetan Sedimentary Sequence–Greater Himalayan Sequence contact continues eastward as shown by other workers (Colchen et al., 1986; Brown and Nazarchuk, 1993; Godin, 1999).

On the basis of this mapping, we estimate

3 km of right-lateral separation of the contact between the Tibetan Sedimentary Sequence and the Greater Himalayan Sequence on the Dangardzong fault at the latitude of Titi village. For three reasons, this separation is best explained by mainly right-lateral displacement across the Dangardzong fault. First, this interpretation is compatible with the right-lateral displacements of tributary drainages observed farther north. Second, explaining the right-lateral separation by pure dip-slip displacement of north-dipping units would require an unreasonable amount of differential erosion, as much as 1.7 km. Third, there is no topographic expression of significant dip-slip displacement along the Dangardzong fault in this area.

However, despite having nearly 3 km of right-lateral offset in the Titi area, the fault terminates abruptly at the end of the north-south-oriented spur (point g in Fig. 10), and evidence for the fault's existence is lacking farther south.

The observation that the fault contact between the Greater Himalayan and Tibetan Sedimentary Sequences is offset right laterally is significant. Both in the area around Taglung (east of point g in Fig. 10) and in the Lang Khola (point h in Fig. 10), the contact has been interpreted to be the basal shear zone of the South Tibetan fault system, locally known as the Annapurna detachment (Brown and Nazarchuk, 1993; Godin et al., 1999a). Godin et al. (1999a) considered the Annapurna detachment to be a continuous structure between these two sites and projected the fault through the wind gap in which Titi village has been built. Although we agree that a South Tibetan fault system structure is located in the Titi wind gap, our mapping of the distribution of lithologies in the area leads us to make a modified interpretation. First, we have shown that the Dangardzong fault has offset the Annapurna detachment in a right-lateral sense. Our resulting geometry (Fig. 10) conforms to the distribution of rock types in the area and to the mapping of Colchen and coworkers who showed a thickened Greater Himalayan Sequence west of the Dangardzong fault (Colchen et al., 1986). Second, we conclude that a younger, brittle fault—which we term the Dhumpu detachment—has reactivated the South Tibetan fault system and cuts through the Titi wind gap. Both the east-southeast-trending Titi wind gap and the point of termination of the Dangardzong fault (point g in Fig. 10) are directly along strike with the mapped positions of the Annapurna detachment near Taglung (Godin et al., 1999a) and in Lang Khola (point h in Fig. 10; Brown and Nazarchuk, 1993). At both those locations, brittle deformation has also been reported (Brown and Nazarchuk, 1993; Godin et al., 1999a). Additionally, we observed east-striking zones of brittle deformation within the Greater Himalayan Sequence 2 km southeast of Titi on the north bank of the Pangbu Khola (point i in Fig. 10). The distribution of brittle deformational fabrics in the area supports our interpretation that the faults mapped by Brown and Nazarchuk (1993) and Godin et al. (1999a) are, in fact, segments of an older Annapurna detachment whose fault planes were subsequently reactivated at lower-temperature conditions when slip on the Dhumpu detachment began. A recently active structure in the Titi wind gap seems the simplest explanation

for this topographic feature, for the brittle deformation at this structural position, and, in particular, for the abrupt truncation of the Dangardzong fault

KINEMATIC MODELS OF THE THAKKHOLA GRABEN

The geometry of the intersection of the Dangardzong fault with the South Tibetan fault system in the area around Titi village suggests four possible kinematic relationships between the Dangardzong fault, Annapurna detachment, and Dhumpu detachment (Fig. 12). In each scenario, we assume that displacement on the Dangardzong fault began in the middle Miocene, perhaps at ca. 14 Ma (Coleman and Hodges, 1995), and, as demonstrated by our ¹⁴C geochronologic data, continued until the Pleistocene. Also common to each of the scenarios is the assumption that the Dhumpu detachment is the youngest structure in the area and that it was active until the Pleistocene. This interpretation is supported by apparently young, brittle deformation associated with the Dhumpu detachment, its inferred relationship to demonstrably young structures farther west (discussed subsequently), and the fact that it is not offset by the Dangardzong fault. The initial condition for each of the four scenarios in Figure 12 is a continuous Annapurna detachment that was active at ca. 22 Ma (Hodges et al., 1996b, Godin, 1999).

Two possibilities exist for the subsequent evolution of the area. Available data do not define the timing relationship between inception of the Dangardzong fault and movement on the Annapurna detachment. One possibility is that movement on the detachment ended before or during the early development of the Dangardzong fault at this latitude and that the Dangardzong fault subsequently offset the Annapurna detachment (Fig. 12A). Alternatively, the Dangardzong fault and the Annapurna detachment were synchronously active after initiation of the Dangardzong fault (Fig. 12B). We favor the latter relationship because (1) it is compatible with the thermal history of the detachment hanging wall and the age of Thakkhola graben extension as deduced from ⁴⁰Ar/³⁹Ar data (Coleman and Hodges, 1995; Vannay and Hodges, 1996; Godin, 1999) and (2) there is no field evidence that the Dangardzong fault penetrated into the Greater Himalayan sequence footwall of the South Tibetan fault system (Fort et al., 1982; Colchen et al., 1986; this work).

The relationship in Figure 12A would require the Dangardzong fault to continue into

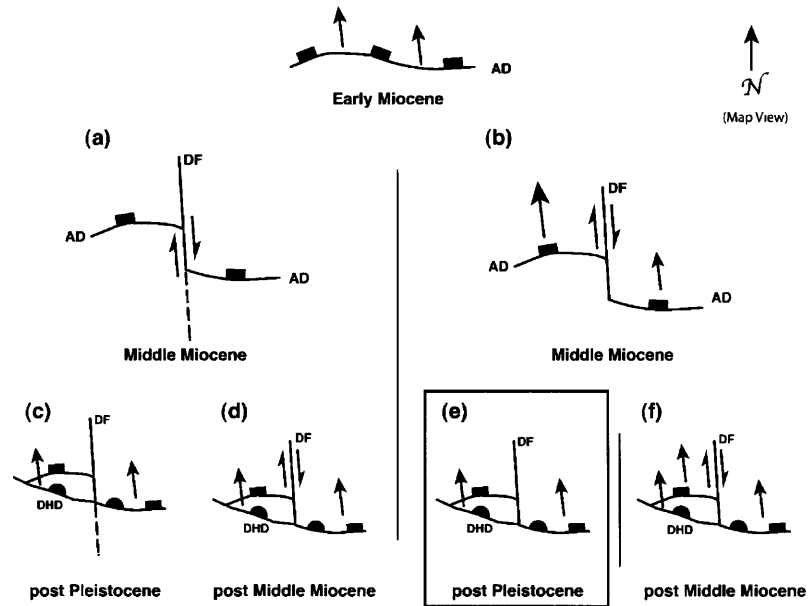


Figure 12. Possible kinematic scenarios for the interactions between the Annapurna detachment (AD), Dhumpu detachment (DHD), and the Dangardzong fault (DF). The initial condition was a continuous Annapurna detachment active in the early Miocene (ca. 22 Ma; Guillot et al., 1994; Harrison et al., 1995b). Subsequently, in the middle Miocene (ca. 14 Ma; Coleman and Hodges, 1995), the Annapurna detachment interacted with the Dangardzong fault either by (A) being passively offset or (B) allowing synchronous movement. Finally, the Dhumpu detachment became active sometime in the interval between the middle Miocene (ca. 14 Ma) and the Pleistocene. It moved either synchronously with the Dangardzong fault (D, F), or strictly after the last Dangardzong fault movement (C, E). Our favored model is E.

the footwall of the South Tibetan fault system. If the Dhumpu detachment strictly postdates the offset of the Annapurna detachment and latest movement of the Dangardzong fault, there should be evidence of prior penetration of the Dangardzong fault into the Dhumpu detachment footwall (Fig. 12C). Alternatively, if the Dhumpu detachment was active synchronously with the Dangardzong fault (Fig. 12D), it is conceivable that the Dhumpu detachment acted to decouple deformation in its hanging wall from its footwall, truncating the Dangardzong fault. Geometrically, however, it is difficult to imagine that the Dhumpu detachment, a north-dipping normal fault, could absorb the Dangardzong fault's substantial strike slip (~3 km) without the Dhumpu itself becoming offset. Therefore we consider the scenarios in Figure 12 (C and D) to be unlikely.

If we assume, then, that the Dangardzong fault moved synchronously with the Annapurna detachment (Fig. 12B), there are two further possibilities. Either motion on the Dhumpu detachment strictly postdates motion on the

Dangardzong fault (Fig. 12E), or the latest movements along both faults were synchronous (Fig. 12F). Both scenarios are consistent with the ⁴⁰Ar/³⁹Ar cooling ages for the hanging wall of the Annapurna detachment, with the geometric relationships we observe in the area around Titi village, and with the observation that the Dangardzong fault is confined to the hanging wall of the Dhumpu detachment. A testable difference between the two scenarios is the timing of movement along the Dhumpu detachment. In Figure 12F, the Dhumpu detachment may have had a long movement history, possibly going back as far as 14 Ma, whereas in Figure 12E, the Dhumpu detachment is a recently developed, Pleistocene structure. Studies yielding more detailed geochronology, including low-temperature thermochronology, for the area may be a means of testing which scenario is correct. In the absence of such a data set, we favor the simplest scenario, that illustrated in Figure 12E.

NEOTECTONICS OF THE THAKKHOLA GRABEN

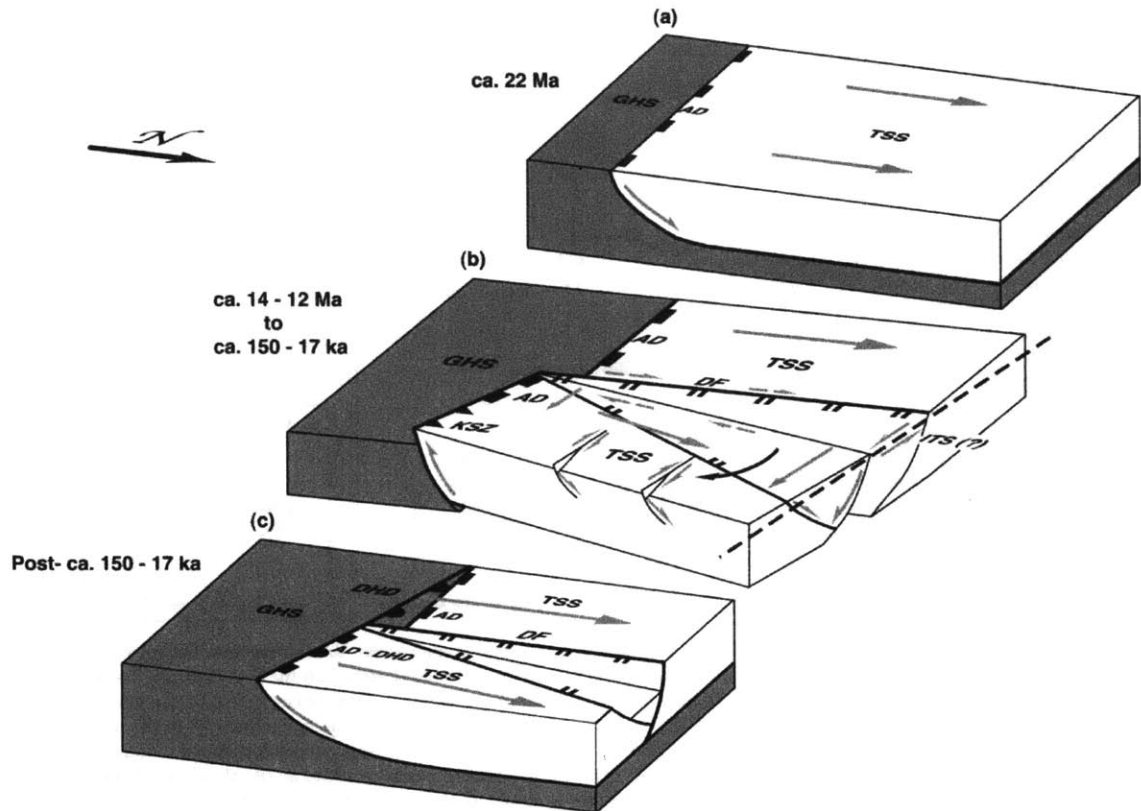


Figure 13. Kinematic model of the Thakkhola graben and the South Tibetan fault system. Three sequential views of a simple block model of the graben are shown, all viewed toward the southwest. Ornamented bold lines are faults, with ornaments on the hanging-wall side. Gray arrows denote fault-block kinematics, with rates of displacement (relative to the fixed GHS [Greater Himalayan Sequence] block) proportional to arrow length. Square ornaments denote the Annapurna detachment (AD), half circles denote the Dhumpu detachment (DHD), double bars denote the Dhangardzong fault (DF) and other Thakkhola graben faults, and triangular barbs denote out-of-sequence thrusting along the Kalopani shear zone (KSZ) (Vannay and Hodges, 1996). Other abbreviations: TSS—Tibetan Sedimentary Sequence; ITS—Indus-Tsangpo suture. (A) Condition during Miocene motion of the Annapurna detachment. (B) Condition during Thakkhola graben development, synchronous with motion on Annapurna detachment and Kalopani shear zone. Note the clockwise rotation of the Dhangardzong fault footwall (black arrow) due to its scissors-like kinematics during this time. Note also the segmentation of its footwall along east-striking, oblique-slip faults that accommodates some of the rotation. The rest is accommodated by shortening along the Kalopani shear zone. To the north, the Dhangardzong fault terminates at the Indus-Tsangpo suture, which should have a component (so far undetected) of left-lateral slip in order to accommodate Thakkhola extension. (C) Condition during Pleistocene motion on the Dhumpu detachment. Note that the Dhangardzong fault, the Kalopani shear zone, and the western part of the Annapurna detachment are inactive.

Figure 13 illustrates our model of the geometry and kinematics of the linked motion between the South Tibetan fault system (along its basal shear zone, i.e., the Annapurna detachment) and the Dhangardzong fault, based on this scenario. The model incorporates the observations that slip on the Dhangardzong fault is partitioned into components of normal-sense and dextral strike-slip motion and that the strike-slip component becomes more dom-

inant toward the south. It also shows that the Dhangardzong fault merges with the South Tibetan fault system décollement at depth in a listric geometry, an interpretation supported by the steepening of northwest dips with age within the Thakkhola and Tetang Formations (Fort et al., 1982; Garzzone et al., 1999) and the observation that the Dhangardzong fault is confined to the hanging wall of the South Tibetan fault system. We infer from these ge-

ometries that offset of the surface trace of the Annapurna detachment is due to coupled motion on the South Tibetan fault system and the Dhangardzong fault. Although the Thakkhola graben is a north-trending extensional structure, similar to others in southern Tibet, the Dhangardzong fault has also acted as a tear structure in the hanging wall of the South Tibetan fault system and, as such, has accommodated differential rates and amounts of

South Tibetan fault system displacement. This kinematic relationship may have lasted throughout the interval between 14 Ma and 17 ka. Subsequently, wholesale reactivation of the South Tibetan fault system along the Dhumpu detachment has occurred.

STRAIN COMPATIBILITY BETWEEN THE HIMALAYA AND SOUTHERNMOST TIBET

In the context of work done in other parts of the Himalaya, the results from the Kali Gandaki valley underscore the longevity of the South Tibetan fault system and the complexity of its movement history. Previous work in the Annapurna Range has documented a basal ductile shear zone and several generations of younger brittle normal faults and related out-of-sequence thrust-sense shear zones at the structural position of the South Tibetan fault system. The sense of motion of these faults ranges from normal-sense to thrust-sense to dextral shearing (Pêcher, 1991; Brown and Nazarchuk, 1993; Coleman, 1996a; Hodges et al., 1996b; Vannay and Hodges, 1996). Although the age of high-temperature displacement along the basal detachment in the Annapurna and Everest regions is well defined at 22–16 Ma (Hodges et al., 1992, 1998; Nazarchuk, 1993; Coleman, 1996b; Godin, 1999), the ages of the later stages of brittle faulting are less well known. Our work provides compelling evidence that the youngest South Tibetan fault system activity in the Annapurna area is of Quaternary age.

Direct evidence exists for even younger—Holocene—South Tibetan fault system activity to the west of the Thakkhola graben in the neighboring Dhaulagiri region. A prominent, normal-fault scarp cutting young glacial topography in the highlands to the southwest of the Dhaulagiri massif can be seen in aerial photography (Nakata, 1989). Using remote-sensing data, we have identified scarps and lineaments that extend the trace of this recently active normal fault—the Dhaulagiri Southwest fault (Nakata, 1989)—to the northwest and also to the southeast, toward the Dhumpu detachment (Hurtado and Hodges, 1998; Hurtado et al., 1999) (Fig. 2). In addition, recent field work at the foot of Dhaulagiri I has uncovered a potentially young brittle shear zone in the uppermost Greater Himalayan Sequence at the same structural position as both the Dhaulagiri Southwest fault and the Dhumpu detachment. These three structures appear to be a contiguous structure, the active

manifestation of the South Tibetan fault system west of the Thakkhola graben.

The long and continuing history of the South Tibetan fault system substantiates its regional importance as the kinematic boundary between the active extensional province of southern Tibet and the active contractional province of the Himalaya. Since the early Miocene, the rocks south of the Himalayan crest have been undergoing south-directed shortening accommodated by a southward-stepping progression of north-dipping thrust faults and shear zones (Fig. 1). Between ca. 22 and 18 Ma, the Main Central thrust system of top-to-the-south shear zones accommodated most of the shortening (Hubbard, 1989), perhaps 80–100 km since the early Miocene. Recent geochronologic work in the Main Central thrust zone suggests that the structure has been active as recently as the Pliocene (Harrison et al., 1998; Catlos et al., 1999). In addition, geodetic work in central Nepal has shown that 80% of the modern shortening rate of 17–18 mm/yr is concentrated just south of the Himalayan crest, near the surface trace of the Main Central thrust (Bilham et al., 1997). Although Bilham and coworkers interpreted these results as evidence for the buildup of strain on a ramp in the décollement between the Indian and Asian plates at depth (Bilham et al., 1997), another reasonable interpretation is that the Main Central thrust could still be active.

However, because Tibet has been in a state of east-west extension for much of this time and because both strain fields are still active, there is a substantial strain gradient between Tibet and the Himalaya that must be accommodated by some set of active structures. Given its location, physiographically at the edge of the Tibetan Plateau and structurally at the southernmost extent of east-west extension, the South Tibetan fault system is a good candidate. It is our interpretation that this fault system has played and is still playing the active role in accommodating the strain gradient between east-west extension in Tibet and north-south shortening in the Himalaya. Furthermore, we suspect that the situation at the Yadong cross structure may be analogous to the Thakkhola graben—South Tibetan fault system kinematic relationship. In both cases, the east-trending South Tibetan fault system and north-trending extensional structures are in intimate contact and interact, causing apparent offset of the South Tibetan fault system. Significant modern, normal-sense displacement in the high parts of the Himalayan ranges is generally not thought to be important. Our results imply that the episodic move-

ments of the South Tibetan fault system did not end in the middle Miocene but persisted, either episodically or continuously, into the Quaternary.

SUMMARY

Geomorphic data from neotectonic features in the Thakkhola graben demonstrate important crosscutting relationships between river terraces and the Dangardzong fault, requiring that the latest stage of displacement occurred during the Pleistocene. The Dangardzong fault exhibits dextral oblique slip and dip slip that decreases southward from ~4 km near the southern end of the Thakkhola graben to nearly zero at its southern terminus. About 3 km of right-lateral offset of the surface trace of the Annapurna detachment, coupled with the observation that tributary drainages of the Kali Gandaki River are right-laterally offset by hundreds of meters, lead us to infer a southward-increasing component of dextral strike-slip throughout much of the developmental history of the Dangardzong fault. One interpretation of the Annapurna detachment offset is that it resulted from the accommodation of differential rates of motion on the South Tibetan fault system. In our kinematic model, the Thakkhola graben began to develop during early middle Miocene time as a manifestation of east-west extension. Since then, the graben has evolved in response to two displacement vectors, a northward one related to extension along the South Tibetan fault system and a counterclockwise rotation related to oblique slip (east-directed extension coupled with dextral strike slip) on the Dangardzong fault. In this way, the Dangardzong fault has accommodated differential rates of northward displacement along the South Tibetan fault system between the Annapurna Himalaya and the rest of potentially very recent South Tibetan fault system activity in the Dhaulagiri Himalaya. The abrupt termination of the Dangardzong fault at the trace of the Dhumpu detachment implies that east-west extension in the Thakkhola graben is confined to the hanging wall of the South Tibetan fault system. The latest stage of movement on the Dhumpu detachment is younger than the latest stage of movement on the Dangardzong fault and demonstrates that the South Tibetan fault system has been active as late as the Pleistocene in the Thakkhola graben area.

APPENDIX

¹⁴C Method

Our samples consisted of organic materials—wood and humic soil—that were collected from

Chapter 2: Neotectonics of the Thakkhola graben

NEOTECTONICS OF THE THAKKHOLA GRABEN

within the topmost ~5 m of mantling gravel at each terrace-surface locality. Care was taken to minimize contamination from modern organic material, and samples were stored in airtight plastic bags after collection. Sample preparations and analyses were conducted by Geochron Laboratories, a division of Krueger Enterprises, in Cambridge, Massachusetts, USA.

Each sample was dispersed in a large volume of water, and the clays and organic matter were separated from sand, silt, and modern plant rootlets by a combination of decanting, agitation, ultrasound, and filtration through a fine nylon mesh. Once the organic material was isolated, it was treated with hot, dilute HCl to destroy any carbonates, and then filtered, washed, and dried. The remaining organic sample was then roasted in an atmosphere of pure oxygen to produce carbon dioxide for the analysis. The carbon dioxide gas was analyzed by using either conventional decay-counting techniques (97KGW2/GX-23107) at Geochron Laboratories or by accelerator mass spectrometry at Lawrence Livermore National Laboratory (97KGW1/GX-23106-AMS, 97KGW5/GX-23110-AMS, 97KGW7/GX-23112-AMS).

The resulting conventional radiocarbon ages (Table 1) are based on the Libby half-life (5570 yr) for ^{14}C and include a correction for $\delta^{13}\text{C}$. By convention, all ^{14}C errors are given at the 1σ level and are based on the analytical data alone. The modern standard used is 95% of the activity of NBS (National Bureau of Standards) oxalic acid, and the ages are referenced to the year A.D. 1950.

Table 1 also lists the ages after correction for the Libby half-life. Since the Libby half-life is 3% less than the actual value of the ^{14}C half-life (5735 yr), the correction requires ages to be multiplied by 1.03. Also given in Table 1 are the Libby-corrected ages further corrected against the ^{14}C calibration curve of Stuiver et al. (1993) by using the calibration program OxCal 2.18. The listed ages are the centroids of the 0.95 confidence age intervals calculated by the calibration program. For samples where the calibration resulted in more than one 0.95 confidence interval, the age given in Table 1 was found by taking a weighted mean. No other corrections or calibrations were performed on the data. The 1σ errors for both sets of corrected ages incorporate the required error propagations. Table 1 also gives the GPS (Global Positioning System) locations (± 100 m) for each sample locality, sample locations are given in Figures 7 and 9. We use the calibrated, Libby-corrected ages in our interpretations, as denoted by the "cal B.P." suffix. More information on the samples and data reduction is available from the corresponding author upon request.

ACKNOWLEDGMENTS

Our research was supported by a grant from the U.S. National Science Foundation awarded to K.V. Hodges, J.P. Grotzinger, and K.X. Whipple (EAR-9706216). Hurtado thanks the Frank and Eva B. Buck Foundation for their support. Dorjee Sherpa Lama, Tsering Tendi Sherpa Lama, Bom Magar, Lakpa Sherpa, Bharat Karki, Ang Phuri Sherpa, and all our friends at Magic Mountain-Sundar Himal Treks provided superb logistical support. We thank B.N. Upreti, Tribuvan University, and the personnel of the Department of Mines and Geology of the Kingdom of Nepal for assistance and advice. We

also thank M. Coleman, P. DeCelles, and L. Godin for very helpful reviews.

REFERENCES CITED

- Armijo, R., Tapponnier, P., Mercier, J., and Han, T., 1986. Quaternary extension in southern Tibet: Field observations and tectonic implications. *Journal of Geophysical Research*, v. 91, p. 13803–13872.
- Armijo, R., Tapponnier, P., and Han, T., 1989. Late Cenozoic right-lateral strike-slip faulting in southern Tibet. *Journal of Geophysical Research*, v. 94, p. 2787–2838.
- Barton, C.E., 1997. International Geomagnetic Reference Field: The seventh generation. *Journal of Geomagnetism and Geolectricity*, v. 49, p. 123–148.
- Bilham, R., Larson, K., Freymuller, J., and Members, P.I., 1997. GPS measurements of present-day convergence across the Nepal Himalaya. *Nature*, v. 386, p. 61–64.
- Bordet, P., Colchen, M., Krummenacher, D., Le Fort, P., Mouterde, R., and Remy, M., 1971. Recherches géologiques dans l'Himalaya du Népal, région de la Thakkhola. Paris, Centre National de la Recherche Scientifique, 279 p.
- Brown, M., 1993. *P-T-t* evolution of orogenic belts and the causes of regional metamorphism. *Geological Society [London] Journal*, v. 150, p. 227–241.
- Brown, R.L., and Nazarchuk, J.H., 1993. Annapurna detachment fault in the Greater Himalaya of central Nepal. *In* Treloar, P.J., and Searle, M.P., eds., *Himalayan tectonics*. Geological Society [London] Special Publication 47, p. 461–473.
- Burchfiel, B.C., and Royden, L.H., 1985. North-south extension within the convergent Himalayan region. *Geology*, v. 13, p. 679–682.
- Burchfiel, B.C., Chen, Z., Hodges, K.V., Liu, Y., Royden, L.H., Deng, C., and Xu, J., 1992. The South Tibetan detachment system: Himalayan orogen extension contemporaneous with and parallel to shortening in a collisional mountain belt. *Geological Society of America Special Paper* 269, 41 p.
- Burg, J.P., and Chen, G.M., 1984. Tectonics and structural zonation of southern Tibet. *China Nature*, v. 311, p. 219–223.
- Caby, R., Pêcher, A., and Le Fort, P., 1983. Le M.C.T. himalayen: Nouvelles données sur le métamorphisme inverse à la base de la Dalle du Tibet. *Revue de Géographie Physique et de Géologie Dynamique*, v. 24, p. 89–100.
- Catlos, E.J., Harrison, T.M., Searle, M.P., and Hubbard, M.S., 1999. Evidence for late Miocene reactivation of the Main Central thrust. From Garhwal to Nepal Himalaya [abs.]. *In* Sobel, E., et al., eds., *Terra Nostra*, no. 99/2, 14th Himalaya-Karakoram-Tibet Workshop, March 1999, Kloster Ettal, Germany. Cologne, Germany, Selbstverlag der Alfred-Wegener-Stiftung, abstract volume, p. 20–22.
- Colchen, M., 1980. Evolution paléogéographique et structurale du fossé de la Thakkhola-Mustang (Himalaya du Népal). Implications sur l'histoire récente de la chaîne himalayenne. Paris, Comptes Rendus des Académies des Sciences, v. 290, p. 311–314.
- Colchen, M., Le Fort, P., and Pêcher, A., 1986. Annapurna-Manaslu-Ganesh Himal. Paris, Centre National de la Recherche Scientifique, 136 p.
- Coleman, M.E., 1996a. Orogen-parallel and orogen-perpendicular extension in the central Nepalese Himalayas. *Geological Society of America Bulletin*, v. 108, p. 1594–1607.
- Coleman, M.E., 1996b. The tectonic evolution of the central Himalaya, Marsyandi Valley, Nepal [Ph.D. thesis]. Cambridge, Massachusetts Institute of Technology, 221 p.
- Coleman, M.E., 1998. U-Pb constraints on Oligocene-Miocene deformation and anatexis, Marsyandi Valley, central Nepalese Himalaya. *American Journal of Science*, v. 298, p. 553–571.
- Coleman, M.E., and Hodges, K.V., 1995. Evidence for Tibetan Plateau uplift before 14 Myr ago from a new minimum age for east-west extension. *Nature*, v. 374, p. 49–52.
- Fort, M., 1976. Quaternary deposits of the middle Kali Gandaki valley (central Nepal). *Himalayan Geology*, v. 6, p. 499–507.
- Fort, M., 1989. The Gongba conglomerates: Glacial or tectonic? *Zeitschrift für Geomorphologie*, v. 76, p. 181–194.
- Fort, M., Freyret, P., and Colchen, M., 1982. Structural and sedimentological evolution of the Thakkhola-Mustang graben (Nepal Himalayas). *Zeitschrift für Geomorphologie*, v. 42, p. 75–98.
- Fuchs, G., Widder, R., and Tuladhar, R., 1988. Contribution to the geology of the Manang area (Annapurna Himal, Nepal). Vienna, Jahrbuch der Geologischen Bundesanstalt, v. 131, p. 593–607.
- Gansser, A., 1964. *Geology of the Himalayas*. London, Wiley Interscience, 289 p.
- Garzzone, C.N., DeCelles, P.G., and Hodkinson, D.G., 1999. Late Miocene-Pliocene E-W extensional basin development in the southern Tibetan Plateau, Thakkhola graben, Nepal [abs.]. *In* Sobel, E., et al., eds., *Terra Nostra*, no. 99/2, 14th Himalaya-Karakoram-Tibet Workshop, March 1999, Kloster Ettal, Germany. Cologne, Germany, Selbstverlag der Alfred-Wegener-Stiftung, abstract volume, p. 51–53.
- Garzzone, C.N., Dettman, D.L., Quade, J., DeCelles, P.G., and Butler, R.F., 2000. High times on the Tibetan Plateau: Paleoelevation of the Thakkhola graben, Nepal. *Geology*, v. 28, p. 339–342.
- Gehrels, G.E., DeCelles, P.G., Quade, J., Lareau, B.N., and Spurlin, M.S., 1999. Tectonic implications of detrital zircon ages from the Himalayan orogen in Nepal. *Geological Society of America Abstracts with Programs*, v. 31, no. 7, p. 374.
- Godin, L., 1999. Tectonic Evolution of the Tethyan Sedimentary Sequence in the Annapurna Area, Central Nepal Himalaya [Ph.D. thesis]. Carleton University, 219 p.
- Godin, L., Brown, R.L., and Hamner, S., 1996. Ductile deformation along the Annapurna detachment fault, Kali Gandaki, central Nepal. *In* Macfarlane, A.M., Sorkhabi, R.B., and Quade, J., eds., *11th Himalaya-Karakoram-Tibet Workshop Abstracts*, p. 54–55.
- Godin, L., Brown, R.L., and Hamner, S., 1999a. High strain zone in the hanging wall of the Annapurna detachment, central Nepal Himalaya. *In* Macfarlane, A., Sorkhabi, R.B., and Quade, J., eds., *Himalaya and Tibet Mountain roots to mountain tops*. Geological Society of America Special Paper 328, p. 199–210.
- Godin, L., Brown, R.L., Hamner, S., and Parrish, R., 1999b. Back folds in the core of the Himalayan orogen: An alternative interpretation. *Geology*, v. 27, p. 151–154.
- Guillot, S., Hodges, K.V., Le Fort, P., and Pêcher, A., 1994. New constraints on the age of the Manaslu leucogranite: Evidence for episodic tectonic denudation in the central Himalayas. *Geology*, v. 22, p. 559–562.
- Hagen, T., 1968. Report on the Geological Survey of Nepal, Volume 2. *Geology of the Thakkhola*, including adjacent areas. Denkschriften der Schweizerischen Naturforschenden Gesellschaft, 160 p.
- Harrison, T.M., Copeland, P., Kidd, W.S.F., and Yin, A., 1992. Raising Tibet. *Science*, v. 255, p. 1663–1670.
- Harrison, T.M., Copeland, P., Kidd, W.S.F., and Lovera, O., 1995a. Activation of the Nyanquentanghla Shear Zone: Implications for uplift of the southern Tibetan Plateau. *Tectonics*, v. 14, p. 658–676.
- Harrison, T.M., McKeegan, K.D., and Le Fort, P., 1995b. Detection of inherited monazite in the Manaslu leucogranite by $^{209}\text{Pb}/^{233}\text{Th}$ ion microprobe dating. *Crystallization age and tectonic implications*. *Earth and Planetary Science Letters*, v. 133, p. 271–282.
- Harrison, T.M., Grove, M., Lovera, O.M., and Catlos, E.H., 1998. A model for the origin of Himalayan anatexis and inverted metamorphism. *Journal of Geophysical Research*, v. 103, no. B11, p. 27017–27032.
- Herren, E., 1987. Zaskar shear zone: Northeast-southwest extension within the Higher Himalayas (Ladakh, India). *Geology*, v. 15, p. 409–413.
- Hodges, K.V., 2000. Tectonics of the Himalaya and southern Tibet from two perspectives. *Geological Society of America Bulletin*, v. 112, no. 3, p. 324–350.
- Hodges, K.V., Parrish, R., Housh, T., Lux, D., Burchfiel, B.C., Royden, L., and Chen, Z., 1992. Simultaneous Miocene extension and shortening in the Himalayan orogen. *Science*, v. 258, p. 1466–1470.

Chapter 2: Neotectonics of the Thakkhola graben

HURTADO et al

- Hodges, K.V., Bowring, S., Hawkins, D., and Davidek, K., 1996a. The age of the Rongbuk granite and Qomolangma detachment, Mount Everest region, southern Tibet. *in* Macfarlane, A.M., Sorkhabi, R.B., and Quade, J., eds., 11th Himalaya-Karakoram-Tibet Workshop Abstracts, p. 63–64
- Hodges, K.V., Parrish, R.R., and Searle, M.P., 1996b. Tectonic evolution of the central Annapurna Range, Nepalese Himalayas. *Tectonics*, v. 15, p. 1264–1291
- Hodges, K., Bowring, S., Davidek, K., Hawkins, D., and Krol, M., 1998. Evidence for rapid displacement on Himalayan normal faults and the importance of tectonic denudation in the evolution of mountain ranges. *Geology*, v. 26, p. 483–486
- Hubbard, M.S., 1989. Thermobarometric constraints on the thermal history of the Main Central Thrust Zone and Tibetan Slab, eastern Nepal Himalaya. *Journal of Metamorphic Geology*, v. 7, p. 19–30
- Hurtado, J.M., and Hodges, K.V., 1998. The South Tibetan system in the Kali Gandaki Valley, Annapurna Himalaya, north central Nepal. A synthesis of structural geology and neotectonics. *Geological Society of America Abstracts with Programs*, v. 30, no. 7, p. 116–117
- Hurtado, J.M., Hodges, K.V., and Whipple, K.X., 1999. Evidence for ongoing tectonic activity at the position of the South Tibetan fault system and the Main Central thrust in the recent past [abs.]. *in* Sobel, E., et al., eds., *Terra Nostra*, no. 99/2, 14th Himalaya-Karakoram-Tibet Workshop, March 1999, Kloster Ettal, Germany. Cologne, Germany, Selbstverlag der Alfred-Wegener-Stiftung, abstract volume, p. 73–75
- Iwata, S., 1984. Geomorphology of the Thakkhola-Muktinath region, central Nepal, and its late Quaternary history. *Tokyo Metropolitan University Geographical Reports*, v. 19, p. 25–42
- Iwata, S., Yamanaka, H., and Yoshida, M., 1982. Glacial landforms and river terraces in the Thakkhola region, central Nepal. *Nepal Geological Society Journal*, v. 2, special issue, p. 81–94
- Le Fort, P., 1975. Himalayas: The collided range. Present knowledge of the continental arc. *American Journal of Science*, v. 275-A, p. 1–44
- Le Fort, P., and France-Lanord, C., 1994. Granites from Mustang and surrounding regions, central Nepal. *Nepal Geological Society Journal*, v. 10, p. 79–81
- Le Fort, P., Debon, F., Pêcher, A., Sonet, J., and Vidal, P., 1986. The 500 Ma magmatic event in Alpine southern Asia, a thermal episode at Gondwana scale. *Sciences de la Terre Mémoires*, v. 47, p. 191–209
- Mercier, J.-L., Armijo, R., Tapponnier, P., Carey-Gailhardis, E., and Han, T.L., 1987. Change from late Tertiary compression to Quaternary extension in southern Tibet during the India-Asia collision. *Tectonics*, v. 6, p. 275–304
- Molnar, P., and Lyon-Caen, H., 1989. Fault-plane solutions of earthquakes and active tectonics of the Tibetan Plateau and its margins. *Geophysical Journal International*, v. 99, p. 123–153
- Molnar, P., and Tapponnier, P., 1975. Cenozoic tectonics of Asia: Effects of a continental collision. *Science*, v. 189, p. 419–426
- Molnar, P., and Tapponnier, P., 1978. Active tectonics of Tibet. *Journal of Geophysical Research*, v. 83, p. 5361–5375
- Nakata, T., 1989. Active faults of the Himalaya of India and Nepal. *in* Mahnconico, L.L., and Lillie, R.J., eds., *Tectonics of the western Himalayas*. Geological Society of America Special Paper 232, p. 243–264
- Nazarchuk, J.H., 1993. Structure and geochronology of the Greater Himalaya, Kali Gandaki region, west-central Nepal [M.S. thesis]. Ottawa, Ontario, Carleton University, 157 p.
- Ni, J., and York, J.E., 1978. Cenozoic extensional tectonics of the Tibetan Plateau. *Journal of Geophysical Research*, v. 83, p. 5277–5384
- Nowaczyk, N., and Antonow, M., 1997. High-resolution magnetostratigraphy of four sediment cores from the Greenland Sea. 1. Identification of the Mono Lake Excursion, Laschamp and Biwa-I Jamaica geomagnetic polarity events. *Geophysical Journal International*, v. 131, no. 2, p. 310–324
- Pan, Y., and Kidd, W.S.F., 1992. Nyainqentanglha shear zone: A late Miocene extensional detachment in the southern Tibetan Plateau. *Geology*, v. 20, p. 775–778
- Parrish, R.R., and Hodges, K.V., 1996. Isotopic constraints on the age and provenance of the Lesser and Greater Himalayan sequences, Nepalese Himalaya. *Geological Society of America Bulletin*, v. 108, p. 904–911
- Pêcher, A., 1991. The contact between the Higher Himalayan crystallines and the Tibetan sedimentary series: Miocene large-scale dextral shearing. *Tectonics*, v. 10, p. 587–599
- Sambridge, M.S., and Compston, W., 1994. Mixture modeling of multicomponent data sets with application to ion probe zircon ages. *Earth and Planetary Science Letters*, v. 128, p. 373–390
- Shiraiwa, T., 1993. Glacial fluctuations and cryogenic environments in the Langtang Valley, Nepal Himalaya. Contributions from the Institution of Low Temperature Science, Hokkaido University, Japan, p. 1–98
- Shiraiwa, T., and Watanabe, T., 1991. Late Quaternary glacial fluctuations in the Langtang Valley, Nepal Himalaya, reconstructed by relative dating methods. *Arctic and Alpine Research*, v. 23, p. 404–416
- Stuiver, M., and Austin, L., editors, 1993. *Calibration 1993 Radiocarbon*, v. 35, p. 1–244
- Vannay, J.-C., and Hodges, K.V., 1996. Tectonometamorphic evolution of the Himalayan metamorphic core between Annapurna and Dhaulagiri, central Nepal. *Journal of Metamorphic Geology*, v. 14, p. 635–656
- Wager, L.R., 1937. The Arun River drainage pattern and the rise of the Himalaya. *Geographical Journal*, v. 89, p. 239–250
- Wu, C., Nelson, K.D., Wortman, G., Samson, S.D., Yue, Y., Li, J., Kidd, W.S.F., and Edwards, M.A., 1998. Yadong cross structure and South Tibetan detachment in the east central Himalaya (89°–90°E). *Tectonics*, v. 17, p. 28–45
- Yoshida, M., Igarashi, Y., Arita, K., Hayashi, D., and Sharma, T., 1984. Magnetostratigraphic and pollen analytic studies of the Thakkhola series, Nepal Himalayas. *Nepal Geological Society Journal*, v. 4, p. 101–120
- Zhou, S.Z., Chen, F.H., Pan, B.T., Cao, J.J.L., and Derbyshire, E., 1991. Environmental change during the Holocene in western China on a millennial timescale. *Holocene*, v. 1, p. 151–156

MANUSCRIPT RECEIVED BY THE SOCIETY OCTOBER 6, 1999
REVISED MANUSCRIPT RECEIVED MARCH 13, 2000
MANUSCRIPT ACCEPTED MARCH 24, 2000

Printed in the USA

Errata

I regret several typographical errors in the published version of this manuscript. Please take note the following corrections (highlighted in boldface).

- a) The caption for Figure 2 contains a misspelled name, and it should read:
“*Simplified geologic map of the central Himalayas of Nepal modified from **Colchen** et al. (1986) and Coleman (1996b)...*”

- b) The notes for Table 1 give incorrect sample numbers. Note § should read:
“*Sample **97KGW2** was collected from the K2 terrace at Kagbeni village, and **97KGW5** was collected from the K5 terrace above Kagbeni village. **97KGW7** was collected from an alluvial-fan surface correlative with the K4 terrace level near Dangardzong village. **97KGW1** was collected from the Kali Gandaki Formation below the K1 terrace south of Kagbeni village. See Figures 7 and 9 for locations.*”

- c) The bibliography and citations throughout the text list the incorrect year of publication for the paper by P. Le Fort and C. France-Lanord. The correct citation should read:
“*Le Fort, P., and France-Lanord, C., **1995**, Granites from Mustang and surrounding regions, central Nepal: Nepal Geological Survey Journal, v. 10, p. 79-81.*”

Chapter 3:

***Mapping the South Tibetan fault system
between the Annapurna and Dhaulagiri
Himalaya with integrated field geologic and
remote sensing data***

For submission to *Journal of Asian Earth Sciences*

Chapter 3: Mapping the South Tibetan fault system between the Annapurna and Dhaulagiri Himalaya with integrated field geologic and remote sensing data

José M. Hurtado, Jr. *
Kip V. Hodges

Department of Earth, Atmospheric, and Planetary Sciences
Massachusetts Institute of Technology
Cambridge, Massachusetts

* address: MIT EAPS 54-1022, 77 Massachusetts Avenue, Cambridge, MA 02139-4307
email: hurtado@MIT.EDU

ABSTRACT

The tectonic evolution of the Himalaya has been influenced to a large degree by the South Tibetan fault system, a family of primarily extensional structures that has accommodated significant tectonic denudation coeval with Miocene shortening along the Main Central thrust and metamorphism of the Greater Himalayan Sequence. Evidence from the central Nepal Himalaya and elsewhere, however, point to continuation of South Tibetan fault system activity into the Quaternary. Unfortunately, understanding the tectonic history of the South Tibetan fault system – in particular its neotectonics – is hampered by the geographic distribution of data, and valuable field geologic observations of structures like the South Tibetan fault system have been limited to a small number of accessible locations leaving large areas in between unknown. In this paper, we build upon field observations in the Annapurna and Dhaulagiri Himalaya of central Nepal using high-resolution satellite imagery and multispectral remote sensing data. Integrating these datasets into a regional map of the South Tibetan fault system, we attempt to understand the role of post-Miocene and active normal faulting in the Annapurna and Dhaulagiri Himalaya. We conclude that the modern day pattern of activity along the South Tibetan fault is not necessarily defined by pre-existing tectonostratigraphy. We hypothesize that lateral flow of material within the Himalaya can account for the pattern of faulting in the Annapurna and Dhaulagiri Himalaya, as well as the distribution of high-grade rocks and granitic bodies observed in the remote sensing data.

INTRODUCTION

One of the most valuable lessons learned from studying the Himalaya is the importance of extensional deformation in the tectonic evolution of convergent orogens. The extensional structures of the South Tibetan fault system (Caby *et al.*, 1983; Burg *et al.*, 1984; Burchfiel and Royden, 1985; Searle, 1986; Herren, 1987; Valdiya, 1989; Burchfiel *et al.*, 1992) have played key roles in the structural and thermal evolution of the Himalayan orogen, yet, while the Miocene, syn-metamorphic, ductile history of these faults has been the subject of numerous studies, their more recent tectonic history is still largely unknown in all but a few localities. One of these places is the Kali Gandaki valley in north central Nepal, where geomorphologic evidence and structural mapping show that the basal detachment was reactivated in the Pleistocene (Hurtado *et al.*, 2001). This work and observations in other locations in the Himalaya suggest that evidence of recent activity may be widespread yet under-appreciated, which has implications for the importance and longevity of extensional processes in compressional orogens. It is therefore important to address unresolved issues regarding the timing of the most recent South Tibetan fault system activity, the spatial extent of that activity, and whether recent displacement could be driven by the same processes that were dominant in the Miocene.

Although geologic fieldwork is the most direct way to tackle this problem, such research is often hampered by the logistical and topographic barriers posed by the mountains themselves. Because it is exposed at high elevations, the South Tibetan fault system is understood in great detail only in a few readily accessible places – invariably where major rivers have cut through the Himalaya – yet poorly known in the rugged areas between those transects. In many places in the Himalaya – and increasingly so in

Chapter 3: Integration of field geologic and remote sensing data

Nepal – a variety of political circumstances further impede fieldwork.

An alternative approach to exploring the geology of inaccessible areas is to use remote sensing data. In the Himalaya, for example, we can use these data to map the spatial distribution of rock types juxtaposed by the South Tibetan fault system and to identify landforms indicative of neotectonic activity along its trace. While the application of remote sensing technologies to geologic mapping is not new and has been successful in other parts of the world (e.g. Hook *et al.*, 1994), it has only been applied in a limited fashion in the Himalaya. With imagery from a variety of sensor systems including Landsat TM, Landsat MSS, SPOT, and Corona now widely available, and with next generation topographic multispectral, hyperspectral, and topographic data from Landsat 7, ASTER, Hyperion, and SRTM coming soon, we are entering an era when the integrative use of remote sensing and traditional field mapping can enhance dramatically our understanding of Himalayan tectonics.

Before we proceed, however, it seems prudent to explore the limitations of remote sensing geology in the Himalaya – by applying various interpretive tools to a region where the geology is well-known – and to assess the reliability of extrapolating the geology into adjacent, less well-known areas. In this paper, we present a tectonic analysis of remote sensing data for the Dhaulagiri Himalaya, a mountain range in north-central Nepal adjacent to and to the west of the Kali Gandaki valley and Annapurna Himalaya (Figure 1a). Surprisingly, while the Annapurna region has been the subject of numerous studies (e.g. Fort *et al.*, 1982; Iwata, 1984; Yoshida *et al.*, 1984; Colchen *et al.*, 1986; Fuchs *et al.*, 1988; Pêcher, 1991; Brown and Nazarchuk, 1993; Schneider and Masch, 1993; Garzanti *et al.*, 1994; Le Fort, 1994; Coleman, 1996b; Hodges *et al.*, 1996;

Chapter 3: Integration of field geologic and remote sensing data

Vannay and Hodges, 1996; Godin, 1999; Garzzone *et al.*, 2000; Hurtado *et al.*, 2001), the Dhaulagiri region is comparatively unknown (e.g. Gansser, 1964; Fuchs, 1967; Sako *et al.*, 1968; Sako *et al.*, 1973; Khule, 1982; Garzanti *et al.*, 1994).

We employ several lines of inquiry building upon the “ground truth” provided by these previous studies and by our own field observations in the Kali Gandaki valley and one of its tributaries, the Myagdi Khola (Figure 1a). We make correlations between South Tibetan fault system structures in the central Annapurna area (Pêcher, 1991; Brown and Nazarchuk, 1993; Coleman, 1996b; Hodges *et al.*, 1996; Vannay and Hodges, 1996; Godin *et al.*, 1999a), Pleistocene structures of the South Tibetan fault system in the Kali Gandaki valley (Hurtado *et al.*, 2001), structures mapped in the field in the eastern Dhaulagiri Himalaya (e.g. this study; Fuchs, 1967), and enigmatic, young normal faults in the western Dhaulagiri Himalaya (Yagi, personal communication; Nakata, 1989). Synthesizing the field and remote sensing data, we compile a map of the South Tibetan fault system and related neotectonic activity between the Marsyandi valley in the Annapurna Himalaya and Dunai village in the Dhaulagiri Himalaya (Figure 1a).

With respect to the broader problem of Himalayan tectonics, our analysis is directed towards two objectives. The first is to create a map of the South Tibetan fault system in the Dhaulagiri Himalaya based on lithologic and morphologic patterns discernable in remote sensing imagery and ground truth mapping in the field. The second is to identify locations in the Dhaulagiri Himalaya where surface morphology indicates recently active normal faulting and to determine what relationship, if any, that deformation has with the South Tibetan fault system.

THE SOUTH TIBETAN FAULT SYSTEM IN THE ANNAPURNA-DHAULAGIRI REGION

The South Tibetan fault system is a family of generally north-dipping, east-striking, and predominately extensional structures exposed at the crest of the Himalaya along much of the length of the orogen (Caby *et al.*, 1983; Burg *et al.*, 1984; Burchfiel and Royden, 1985; Searle, 1986; Herren, 1987; Valdiya, 1989; Burchfiel *et al.*, 1992; Brown and Nazarchuk, 1993; Coleman, 1996b; Wu *et al.*, 1998; Godin *et al.*, 1999a). Studies in central Nepal have found that it is characterized by a complex, polyphase architecture. Where the South Tibetan fault system has been studied in detail, it comprises the following succession of structural elements (Figure 2):

- STF1 – a basal, ductile detachment with evidence for orogen-normal, and, in places, orogen-parallel displacement (Pêcher, 1991; Coleman, 1996a). It is associated with a several-kilometer thick high-strain zone at the contact between silica-rich, migmatitic, amphibolite-facies gneisses of the Greater Himalayan Sequence in the footwall and lower grade, calcareous metasedimentary rocks of the Tibetan Sedimentary Sequence in the hanging wall (Brown and Nazarchuk, 1993; Coleman, 1996a; Hodges *et al.*, 1996; Godin *et al.*, 1999a).
- STF2 – a broad, out-of-sequence, thrust-sense shear zone that affects the entire basal detachment high strain zone, overprinting earlier extensional fabrics related to STF1 with fabrics related to shortening (Hodges *et al.*, 1996; Vannay and Hodges, 1996).
- STF3 – a structurally higher, brittle-ductile normal fault, subparallel to the basal detachment, that marks an abrupt metamorphic discontinuity between metasedimentary rocks in the footwall and unmetamorphosed sedimentary rocks in the hanging wall (Hodges *et al.*, 1996).
- STF4 – a series of brittle normal faults structurally higher within the hanging wall of STF3 (Coleman, 1996a; Hodges *et al.*, 1996).

Chapter 3: Integration of field geologic and remote sensing data

- STF5 – late-stage brittle faults at the structural position of STF1 (Godin, 1999; Hurtado *et al.*, 2001).

The STF_x nomenclature we present above is based on structural position as well as deformational history. In general, age and structural level are correlated, with the structurally highest STF faults being the youngest. However, for fault strands interpreted to have multiple stages of motion, the designation applied to it denotes the more recent stage. This is in particular the case with STF5 structures.

Geochronologic studies in central Nepal have shown that activity on the STF1 basal detachment had begun by ca. 22 Ma (Guillot *et al.*, 1994; Hodges *et al.*, 1996; Coleman, 1998), although minimum ages for STF1 from elsewhere in the Himalaya range from ca. 17-15 Ma (Schärer *et al.*, 1986; Xu, 1990; Searle *et al.*, 1997; Hodges *et al.*, 1998; Murphy and Harrison, 1999) to as young as ca. 12 Ma (Edwards and Harrison, 1997; Wu *et al.*, 1998). In the Modi Khola valley in central Nepal (Figure 1a), U-Pb dates on undeformed granite dikes require STF1 and STF2 activity to have ceased by 18 Ma, and the observation that STF3 truncates all granites constrains its age to be post-18 Ma (Hodges *et al.*, 1996). The lack of a ⁴⁰Ar/³⁹Ar cooling age discontinuity across the basal high strain zone in the adjacent Kali Gandaki valley (Figure 1a) led Vannay and Hodges (1996) to infer that STF1 and STF2 activity was completed by ca. 13-15 Ma, and that rapid cooling due to tectonic denudation at higher structural levels was occurring at this time. We attribute this cooling to STF3 activity. A third stage of extension (STF4) took place at low temperatures in the brittle regime following STF3, perhaps in the Pliocene (Hodges *et al.*, 1996). Finally, the STF5 structure in the Kali Gandaki valley may be Pleistocene in age (Hurtado *et al.*, 2001).

Chapter 3: Integration of field geologic and remote sensing data

The Greater Himalayan Sequence in the footwall of the South Tibetan fault system constitutes the high-grade metamorphic core of the orogen (Gansser, 1964; Le Fort, 1975; Hodges, 2000) (Figure 2). The tectonic stratigraphy of these rocks in central Nepal, defined by Colchen *et al.* (1986), comprises three major units. The basal unit, Formation I, ranges from 1 to 20 km thick in the region and includes amphibolite-facies psammitic schist with the assemblage quartz + K-feldspar + biotite + muscovite + garnet ± kyanite or sillimanite. In some places, Formation I shows abundant evidence for *in situ* anatectic melting. Conformably above is the ca. 2-4 km thick Formation II, composed primarily of distinctively banded, garnet + diopside calcisilicate gneiss. Intercalated within the uppermost part of Formation II – in places in the immediate footwall of the basal detachment – is a 100 to 1000 m thick sheet of granitic augen orthogneiss called Formation III. Primary foliations in all three units strike approximately northwest and dip shallowly northeast.

The hanging wall rocks of STF1 in central Nepal are amphibolite- to greenschist-facies calcareous gneisses similar to Formation II, a rock-type colloquially termed the “Larjung Formation” in the Annapurna area (Bordet *et al.*, 1971; Colchen *et al.*, 1986; Vannay and Hodges, 1996) (Figure 2). Outside of the high strain zone of the basal detachment, the rocks grade upwards into the lowermost units of the Tibetan Sedimentary Sequence. In some places, though, the upper termination of the amphibolite-facies rocks is quite abrupt and the metamorphic discontinuity coincides with a second, brittle-ductile detachment (STF3).

Above STF3, the bulk of the essentially unmetamorphosed Tibetan Sedimentary Sequence forms a nearly continuous, > 10-km thick, section of early Paleozoic to late

Chapter 3: Integration of field geologic and remote sensing data

Mesozoic sedimentary rocks interpreted to have been deposited on the Tethyan passive margin of Indian subcontinent prior to collision with Asia (Gansser, 1964; Hodges, 2000). The base of the Tibetan Sedimentary Sequence in the Annapurna region is the Cambrian-Ordovician Sanctuary Formation. It consists of dark shale and quartzite, which is overlain by muscovite-bearing, sandy marble of the Cambrian Annapurna Yellow Formation, which itself is below gray limestone of the Ordovician Nilgiri Formation (Colchen *et al.*, 1986). The entire Tibetan Sedimentary Sequence has been pervasively folded – and refolded – into north- and south-verging folds a kilometer or more in amplitude that invert the section in some localities (Colchen *et al.*, 1986; Godin, 1999; Godin *et al.*, 1999b) (Figure 2). The most spectacular of these is the Fang-Nilgiri nappe exposed on the east side of the Kali Gandaki valley which is cored by the Sanctuary Formation (Colchen *et al.*, 1986). This structural inversion of the stratigraphy places the Annapurna Yellow Formation in the immediate hanging wall of STF1 (Figure 2). Several subparallel, moderately north-dipping faults cut the lowermost units of the Tibetan Sedimentary Sequence. These STF4 brittle normal faults lie several kilometers structurally above the basal STF1 detachment within the Annapurna Yellow, Sanctuary, and Nilgiri Formations, sometimes following interformational contacts (Figure 2).

GEOLOGIC TRANSECTS IN THE ANNAPURNA AND DHAULAGIRI HIMALAYA

In this section, we briefly describe the field relations observed in four transects within the Annapurna and Dhaulagiri Himalaya (Figure 1a). Noting the structural correlations that can be made, we review previous work in the Marsyandi valley by

Chapter 3: Integration of field geologic and remote sensing data

Coleman (1996a), investigations in the Modi Khola valley by Hodges *et al.* (1996), and mapping in the Kali Gandaki valley by Vannay and Hodges (1996), Godin (1999), and Hurtado *et al.* (2001). We also describe our own structural analyses for a section in the Kali Gandaki valley near Tuckuche village and a transect in the Myadgi Khola valley. These geologic transects constitute the “ground truth” upon which our remote sensing analyses are based.

The Marsyandi Valley Area

The Dudh Khola valley is a tributary of the Marsyandi valley adjacent to the main body of the Manaslu pluton (Figure 3). Coleman (1996a) reported that the contact between Greater Himalayan Sequence and Tibetan Sedimentary Sequence in this valley has been obscured to a large degree by the intrusion of leucogranites comparable in composition to the nearby 17-22 Ma Manaslu leucogranite (Guillot, 1993). In a small, unintruded section, however, Coleman (1996a) observed the Annapurna Yellow Formation above Formation III, the two juxtaposed by a ca. 300-m thick mylonitic zone. Within this zone, both Formation III and the Annapurna Yellow Formation display well-developed, north-plunging stretching lineations and asymmetric shear-sense indicators indicative of top-to-the-north-northeast displacement. Coleman (1996a) refers to this structure as the Dudh Khola detachment and we classify it an STF1 structure.

The Dudh Khola detachment is correlative with the basal detachment at Chame village, ca. 15 km to the west (Figure 3). The Chame detachment is characterized by a 1.2-km thick, north-northwest dipping, normal-sense shear zone that places Annapurna Yellow Formation over Formation II (Colchen *et al.*, 1986; Coleman, 1996a). Kinematic

Chapter 3: Integration of field geologic and remote sensing data

indicators imply an early phase of deformation characterized by north-plunging lineations and top-to-the-north, normal-sense motion. These features are overprinted by a second set of west-plunging lineations and mylonitic fabrics consistent with top-to-the-west normal motion. Sillimanite defining the west-plunging lineations imply that the second, west-directed, orogen-parallel deformational phase occurred at close to peak metamorphic conditions and continued during the retrogression that followed (Coleman, 1996b). We interpret the Chame detachment as an STF1 structure, although we note that the kinematic indicators imply at least two distinct phases of motion (STF1a and STF1b).

Coleman (1996a) reports a second, 300-m thick, unnamed shear zone within the Annapurna Yellow Formation west of Chame village (Figure 3). The structure truncates leucogranitic dikes crosscutting the Annapurna Yellow Formation, transposing them into parallelism with the mylonitic fabric in the shear zone. The shear zone exhibits locally intensified strain with lineations and kinematic indicators showing top-to-the-west-southwest-sense displacement, consistent with the development of associated tight, west-southwest verging folds. Since this structure shares the same transport direction as the second phase of STF1 activity, it is possible that they are coeval. We classify the unnamed shear zone as an STF3 structure, and it is mapped by Coleman (1996a) as being contiguous with structures at the same structural level within the Tibetan Sedimentary Sequence in the Modi Khola valley (Hodges *et al.*, 1996), 50 km west of Chame.

The Modi Khola Valley

The contact between the Tibetan Sedimentary Sequence and the Greater Himalayan Sequence is exposed near Deorali village in the Modi Khola valley (Colchen

Chapter 3: Integration of field geologic and remote sensing data

et al., 1986; Hodges *et al.*, 1996) (Figure 3). Hodges *et al.* (1996) report that the contact strikes west-northwest and is sharp, marked by a shallowly north-dipping structure they named the Deorali detachment. Although normal sense kinematic indicators were obscured by younger fabrics, Hodges *et al.* (1996) correlated the Deorali detachment to the Chame and Dudh Khola detachments, and, we therefore interpret it as an STF1 structure. The normal-sense STF1 fabrics are obscured by younger fabrics related to top-to-the-southwest, out-of-sequence thrusting along the Modi Khola Shear Zone (Hodges *et al.*, 1996). This structure manifests itself as a 1.5 km thick mylonitic zone that overprints the Deorali detachment, affecting all of Formation III and the uppermost section of Formation II, in addition to the Annapurna Yellow Formation (Hodges *et al.*, 1996). We classify the Modi Khola Shear Zone as an STF2 structure.

The uppermost extent of STF2 fabrics is marked by a second detachment, the Machhapuchhare detachment, at the top of the Annapurna Yellow Formation (Figure 3). This structure crops out as a sharp, west-northwest-striking, shallowly north-dipping normal fault with Sanctuary Formation in its hanging wall, and it marks an abrupt decrease in metamorphic grade. Structurally above the Machhapuchhare detachment, the greenschist-facies Tibetan Sedimentary Sequence rocks display pervasive north-vergent fold sets that are absent in the footwall (Hodges *et al.*, 1996). We interpret this fault as an STF3 structure.

Within the hanging wall of STF3, Hodges *et al.* (1996) identified at least two brittle-ductile normal faults, one of which they named the Hiunchuli detachment (Figure 3), that we classify as STF4 structures. Since they truncate kilometer-scale folds, these shallow- to moderately- north-dipping faults represent detachment horizons within the

Chapter 3: Integration of field geologic and remote sensing data

Tibetan sedimentary sequence. Their geometry suggests that they may root downward into a single detachment surface that coincides with the down-dip projection of STF3 (Hodges *et al.*, 1996). The ages of the STF4 faults are unconstrained, but they are possibly very young (cf. Hodges *et al.*, 1996).

The Kali Gandaki Valley

Colchen *et al.* (1986) mapped the Greater Himalayan Sequence-Tibetan Sedimentary Sequence contact near Taglung village, ca. 30 km west of the Modi Khola valley (Figure 3). The contact was first recognized as a normal-sense structure by Brown and Nazarchuk (1993) who studied its dip-slope exposure near Dhumpu and named it the Annapurna detachment. At the type locality, the Annapurna detachment is a shallowly-dipping (ca. 30°), brittle normal fault underlain by a 500 to 1000 m thick mylonitic zone, all within a several kilometer thick high-strain zone (Brown and Nazarchuk, 1993). The brittle fault marks a sharp contact between intercalated Formations II and III in the footwall and the Larjung Formation in the hanging wall. Godin *et al.* (1999a) mapped the Annapurna detachment to the east in the vicinity of Taglung village (Figure 3), and identified a ca. 1.5 km-thick high-strain zone straddling both sides of the structure, affecting both its footwall and hanging wall. Penetrative fabrics within this high-strain zone indicate top-to-the-northeast displacement and have coherent orientations throughout the footwall and hanging wall (Godin *et al.*, 1999a). The ductile fabrics of the Annapurna detachment are correlated to the Deorali, Chame, and Dudh Khola detachments, and as is the case with the latter structures, we classify it as an STF1 feature.

Chapter 3: Integration of field geologic and remote sensing data

Compared with the impressive Dhumpu locality, the location of the Annapurna detachment on the east bank of the Kali Gandaki River is not as clear, and field relationships imply that movement on the Dangardzong fault – the northeast-striking, southeast-dipping, oblique normal structure responsible for the opening of the Thakkhola graben further north (Figure 1a) (Fort *et al.*, 1982; Hurtado *et al.*, 2001) – has complicated the tectonic stratigraphy. Hurtado *et al.* (2001) reported ca. 3 km of right-lateral separation of the Annapurna detachment at the southern termination of the Dangardzong fault. In addition, localized, late-stage brittle deformation near Taglung village reported by both Godin (1999) and Hurtado *et al.* (2001), as well as the brittle fault at the type locality (Brown and Nazarchuk, 1993), suggest post-Miocene activity at the position of the STF1 structure. Godin (1999) interprets these features as related to the southern termination of the Dangardzong fault, whereas Hurtado *et al.* (2001) suggest that the brittle deformation is related to a Pleistocene-aged splay of the South Tibetan fault they refer to as the Dhumpu detachment. Following this latter interpretation, we regard the Dhumpu detachment as an STF5 fault.

Vannay and Hodges (1996) described a top-to-the-south shear zone within the upper part of the Greater Himalayan Sequence in the Kali Gandaki valley (Figure 3). The Kalopani Shear Zone, as it is called, pervasively deforms the upper part of Formation II and all of Formation III. Kinematic indicators show dextral shear as well as top-to-the-south thrusting (Vannay and Hodges, 1996). Vannay and Hodges (1996) place the structure at the same structural position as the Modi Khola Shear Zone (Hodges *et al.*, 1996), correlating the two. We therefore also interpret the Kalopani Zone as STF2.

Structural Geology near Tuckuche Village in the Kali Gandaki Valley

The westward continuation of STF3 from the Modi Khola valley into the Kali Gandaki valley is exposed north of Dhumpu village and south of Tuckuche village (Figure 3). Figure 4a is a photograph taken of the STF3 structure on the east side of the Kali Gandaki valley in the cliffs adjacent to Thulobugin ridge and Nimek Danda (point “A”, Figure 3). The STF3 fault can be seen truncating a recumbent fold in its hanging wall, putting Sanctuary Formation over Annapurna Yellow Formation in the footwall. Further north, (point “B”, Figure 3), the STF3 fault can be seen in the cliffs above Taglung village south of where it must intersect the Dangardzong fault (Figure 4b). The area between “B” and the Kali Gandaki River is densely wooded, precluding detailed mapping of the intersection relationship. Offset of the STF3 fault across the Dangardzong fault, appears to be ca. 1 km in a right-lateral sense, however, consistent with the amount and sense of displacement of the basal detachment near Dhumpu village (Hurtado *et al.*, 2001).

We studied deformational fabrics at the structural position of STF3 on the west side of the Kali Gandaki River in a cliff exposure between Tuckuche and Kobang villages (point “C”, Figure 3), ca. 1 km upstream from the Dangardzong fault intersection. At this location, STF3 places Nilgiri Formation over the Annapurna Yellow Formation, both of which have been injected by at least five generations of sulfide-bearing, calcite and quartz veins (Figure 4c-f; Table 1) that attest to significant hydrothermal activity. The outcrop is also cut by several meter-thick, east-striking, brittle shear zones that dip ca. 45° N that we assume are related to brittle STF3 faulting (Figure 4g). At least three stages of ductile STF3 fault activity are manifested in deformation of the veins, which we

Chapter 3: Integration of field geologic and remote sensing data

interpret in light of the veins' orientations with respect to STF3 (Figure 5; Table 1). We conclude from our structural analysis that this part of the Tibetan Sedimentary Sequence in the Kali Gandaki had an early phase of extensional activity which was punctuated by a phase of shortening, followed by renewed extension, a similar chronology to that of the basal detachment (Hodges *et al.*, 1996; Vannay and Hodges, 1996) and consistent with the more general chronology of deformation within the Tibetan Sedimentary Sequence put forward by Godin (1999).

We correlate the STF3 fault in the Kali Gandaki to the Machhapuchhare detachment in the Modi Khola valley (Hodges *et al.*, 1996). We also regard the shortening episode at this structural position as the manifestation of STF2 at this structural level. The style and sequence of deformational events we document is localized to the area near Tuckuche, and is observed no farther north than Chokhopani Khola or south of Kobang village (Figure 3). West of Tuckuche village, visual inspection of the Dhaulagiri I and Tuckuche Peak massif constrains the trace of the STF3 structure as shown in Figure 4i. Note the change in orientation of layering within the Tibetan Sedimentary Sequence across STF3, in particular the prominent folding in the hanging wall on the east face of Tuckuche peak that is not present structurally below STF3.

Structural Geology along the Myagdi Khola Valley Transect

In order to investigate the westward continuation of South Tibetan fault system structures from the Kali Gandaki valley, in particular the Pleistocene-aged STF5 reactivation described by (Hurtado *et al.*, 2001), a traverse was made along the south-flowing Myadgi Khola, a river draining the west flank of Dhaulagiri I, ca. 16 km west of

Chapter 3: Integration of field geologic and remote sensing data

the Kali Gandaki valley (Figure 1a). A generalized map showing the geology in this area is shown in Figure 6. The Greater Himalayan Sequence in this transect is relatively thin, ca. 10 km compared to ca. 30 km in the Manaslu-Ganesh Himalaya and < 15 km in the Kali Gandaki valley. Because the structure in this area has not been described previously, we present it in some detail here.

At the base of the Greater Himalayan Sequence, the ca. 5 km-thick Main Central thrust zone is exposed between the villages of Muri and Boghara (Figure 6). Geomorphologically, the Main Central thrust zone is expressed as a dramatic increase in the steepness of the Myagdi Khola resulting in bedrock incision and abundant waterfalls near Boghara village. Outcrops in this area contain interleaved low-grade schist, limestone, and quartzite from the Lesser Himalayan Sequence structurally below, and lower-amphibolite facies garnet + muscovite + biotite \pm kyanite schists from structurally above the Main Central thrust zone. The higher-grade schists are correlative to Greater Himalayan Sequence Formation I which are ca. 4 km-thick in the Myagdi Khola (Figure 6). Original compositional layering has been completely transposed by moderately northeast-dipping deformational fabrics that strike northwest. Kinematic indicators within the Main Central thrust zone and in outcrops of Formation I, include lineations, mylonitic fabrics, shear bands, and folds all indicating top-to-the-southwest sense of shear (Figure 7a).

Structurally above Formation I is a ca. 4 km-thick unit comprising biotite-bearing calcsilicate gneiss intercalated with sills of tourmaline-bearing leucogranitic augen gneiss, correlative with Greater Himalayan Sequence Formations II and III. The structurally lowest outcrops of the calcsilicate gneiss are at Dobang village (Figure 6).

Chapter 3: Integration of field geologic and remote sensing data

Within them, compositional layering strikes east and dips moderately to the north. Transposition fabrics and kinematic indicators within these gneisses, such as asymmetric boudinage, indicate top-to-the-northeast sense of shear at this structural level (Figure 7b). However, deformation appears to have been heterogeneous towards the top of the Greater Himalayan Sequence. In places, the rocks have been affected by a phase of top-to-the-southwest shortening as evidenced by southwest-vergent folding. (Figure 7c). Boudinaged, north-dipping leucogranitic sills that have been subsequently refolded and faulted in a top-to-the-north sense (Figure 7d) may indicate a second phase of to north-directed extension (e.g. Figure 5).

The complex deformational fabrics in Formation II are exposed at the structural position of the basal detachment of the South Tibetan fault system – STF1 – just north of the “Jungle Camp” at Chartare (point “A”, Figure 6). While poorly exposed at river level due to extensive landslide and rock glacier deposits, STF1 manifests itself on the steep cliffs high above the river as an abrupt 10° change in the dip of rocks in the hanging wall relative to those in the footwall (Figure 7d) and a distinct color change (Figure 7e). Lithologically, STF1 marks the northernmost extent of the Formation III sills; the hanging wall is composed of a yellow-weathering, calcsilicate gneiss identical to the Larjung Formation in the Kali Gandaki valley. Outcrops near STF1 show abundant migmatization and some contain in excess of 50% granitic leucosome by volume (Figure 7f). Meter-scale, concordant sills of fine- to medium-grained tourmaline-bearing leucogranite dikes intruding the hanging wall rocks are extensively boudinaged, although shear sense is difficult to determine (Figure 7g).

A second normal fault is exposed about 2 km north of the basal detachment, in a

Chapter 3: Integration of field geologic and remote sensing data

small bedrock stream, just west of the Puchare “Italy Base Camp” at an elevation of 3500 m (point “B”, Figure 6). The fault crops out as a ca. 2-m thick horizon of intensely brecciated Larjung Formation (Figure 7h), and faint lineations and striae on exposed compositional layering planes below the brittle zone suggest displacement to the northwest. Caught within the brecciated zone is part of a steeply northwest-dipping leucogranite dike discordant to the compositional layering (Figure 7i). The dike is folded into a north-vergent fold train consistent with top-to-northwest, normal-sense shear and has been shattered by the cataclastic deformation in the brittle fault zone. The dike is truncated by brittle shear zone and cannot be traced into the hanging wall of the fault. The brittle fault, which we call the Myagdi Khola fault, can be followed in the streambed for ca. 2 km to the west before being buried by young moraines around Puchare (Figure 6). Based on its structural position, we classify the Myagdi Khola fault as an STF3 structure, and in the following sections we substantiate and expand upon this correlation with remote sensing data.

REMOTE SENSING

In this section we describe the remote sensing data sets and methodologies we employed to augment the field geologic data. We used morphologic analysis of high-resolution satellite imagery as well as multispectral analyses, both of which rely on the field geology for ground truth.

Datasets

Our high spatial resolution imagery includes three digital SPOT satellite scenes

Chapter 3: Integration of field geologic and remote sensing data

and four declassified “Corona” satellite photographs of the Dhaulagiri and Annapurna Himalaya (Table 2; Figure 1a & b). The SPOT and Corona imagery were used for photogeologic mapping of faults and lithology, and the Corona images provided the capability to map areas in the far western Dhaulagiri Himalaya not covered by the SPOT scenes. Our digital multispectral data include one Landsat Multispectral Scanner (MSS) scene and one Landsat Thematic Mapper (TM) scene (Table 3). Each Landsat image shows approximately the same area centered on the Kali Gandaki valley, and together they include most of the Dhaulagiri and Annapurna Himalaya (Figure 1a). We used the Landsat TM data in our multispectral analyses.

Digital image analysis and multispectral processing were done using the remote sensing software package ENVI®. In order to better visualize the data, SPOT stereo imagery was displayed 3-dimensionally using blue-red anaglyph technology and epipolar images created using PCI/OrthoEngine SE® software. Photointerpretive maps based on stereo SPOT and Landsat MSS digital imagery were exported from ENVI® into a GIS created using ArcView®. Landsat TM multispectral analysis and interpretation was also done in ENVI® and the results were exported to the GIS. Corona stereo photography was inspected with an optical stereoscope and the interpretive maps were later added to the GIS database.

All images used as mapping bases in the GIS were orthorectified with PCI/OrthoEngine SE® to remove distortion due to high relief. For orthorectification, we used the GTOPO-30 1 km-resolution digital elevation model (DEM) (USGS, 1993) along with a set of ground-control points (GCPs) collected in the field using Trimble® differential GPS (global positioning system) survey equipment. Our GCPs have sub-

Chapter 3: Integration of field geologic and remote sensing data

meter horizontal uncertainties and 1-2 meter vertical uncertainties. After orthorectification, the various digital datasets were mosaicked and co-registered in the UTM 44R coordinate grid referenced to the WGS-84 ellipsoid using ENVI® before adding them to the GIS database.

In addition to the various remote sensing datasets, several published – albeit low-quality – topographic maps were included in the GIS along with the GTOPO-30 DEM. Finally, previous geologic mapping by Colchen *et al.* (1986), Coleman (1996b), Hodges *et al.* (1996), Godin (1999), Fuchs (1967), Hashimoto *et al.* (1973), and Nakata (1989) was incorporated into the GIS and reinterpreted in light of our own field mapping and remote sensing analyses.

Spectral Characteristics of Geologic Materials

The spectral reflectance and emissivity spectra of geologic materials provide a means for remote identification (see Hunt, 1980). Absorbance features in these spectra are the direct result of electronic and vibrational processes arising from the interaction between electromagnetic energy and the atoms and molecules in the imaged material. The various electronic and vibrational interactions require different quanta of energy to proceed, so the absorbance features they create are manifest at specific wavelengths. Because the absence or presence of specific absorption features is dependent on the chemistry of the material, spectral information can be used to infer composition.

Carbonate minerals display absorbance features between 0.4 μm and 2.5 μm . Calcite, for example, shows characteristic absorptions at 0.5 μm and at 2.5 μm with flat reflectance in between (Figure 8a). By contrast, silicate minerals such as quartz generally

Chapter 3: Integration of field geologic and remote sensing data

have flat spectra in the visible to mid-infrared (Figure 8b). In the thermal infrared between 8.5 μm and 12 μm – the so-called Reststrahlen band – silicate minerals have emission spectra that are diagnostic of silica content. In this region, absorption minima occur at short wavelengths (8.5 μm) for framework silicates (such as quartz) and at progressively longer wavelengths for sheet, chain, and isolated tetrahedral mineral structures (Hunt, 1980). Carbonate minerals also have spectral features in the thermal infrared; in particular calcite has a strong absorption at 11.2 μm due to C-O bond vibration. Aside from this feature, though, carbonate rocks – such as marble – have relatively flat emission spectra in the thermal infrared between 8.5 μm and 12 μm (Figure 8c), whereas silicate rocks – such as garnet gneiss, mica schist, and granite – exhibit higher emissivity in the Reststrahlen band below 10 μm and lower emissivity above 10 μm (Figure 8d).

These spectral differences between silicate and carbonate minerals allow discrimination between the two. We are fortunate that the base of the Tibetan Sedimentary Sequence is primarily calcareous whereas the upper Greater Himalayan Sequence contains a much higher proportion of siliceous rocks (Gansser, 1964; Le Fort, 1975; Hodges, 2000). Because of this, the two sequences have sufficiently distinctive spectral signatures between 0.4 μm and 2.5 μm that can be exploited with Landsat TM data (Figure 8a-d). For instance, Bands 2 and 7 encapsulate the carbonate minima at ca. 0.5 μm and ca. 2.5 μm while Band 6 contains the sharp carbonate minimum at ca. 11 μm . Moreover, the spectral signatures of both siliceous and carbonate rocks in the visible and near-infrared wavelengths are, in turn, distinct from those of vegetation (Figure 8e) and snow, the latter of which has far higher reflectance in the visible and near-infrared than

Chapter 3: Integration of field geologic and remote sensing data

rocks or vegetation (Figure 8f). At thermal infrared wavelengths, both vegetation and snow have significantly lower and flatter reflectance than either siliceous or carbonate rocks (Figure 8c, d, & f).

Multispectral Analysis Methods

The Landsat TM scene we use for quantitative spectral analysis was originally processed with basic radiometric and geometric corrections (USGS EROS Data Center Level 08 processing). Before orthorectification and registration, we calibrated the data for secular variation in the TM detector and converted the data from radiance to reflectance (EOSAT, 1986). We did not, however, convert the thermal infrared band (TM Band 6) to emissivity and interpretations based on this band do not take into account the competing effects of surface temperature, thermal inertia, and thermal emission (Hook *et al.*, 1992). Atmospheric corrections to the data were not performed, as data on atmospheric aerosol and water content at the time of data acquisition were not available. We tried to apply a Dark Object Subtraction (DOS) algorithm to the data to approximate the removal of atmospheric scattering (RSI, 2000), but this process yielded unacceptable results and was not used in the final data processing.

The calibrated reflectance data were processed in two ways. The first was a decorrelation stretch (DCS) transformation that removes the high correlation commonly found when multispectral datasets are displayed as false color images in red-green-blue (RGB) color space (RSI, 2000). As noted in the previous discussion, we chose Landsat TM bands 7, 5, and 2, as the RGB input channels for the DCS because they accentuate the spectral differences between the calcareous Tibetan Sedimentary Sequence and the

Chapter 3: Integration of field geologic and remote sensing data

siliceous rocks of the Greater Himalayan Sequence (see Figure 8). The result is shown in Figure 9a. This image was used in interpreting the trace of the Greater Himalayan Sequence-Tibetan Sedimentary Sequence lithologic contact.

The second technique involves the classification of all pixels in the Landsat TM image based on the mean spectra of a set of training classes. This was accomplished using a supervised classification algorithm which assumes that the training classes are endmembers and that linear combinations of them can produce the spectral characteristics of every pixel in the image (Richards, 1994). The supervised classification algorithm we employ is the Spectral Angle Mapper (SAM) (RSI, 2000). This particular algorithm was chosen because it is relatively insensitive to illumination and albedo effects when applied to calibrated reflectance data (Kruse *et al.*, 1993). Such effects are substantial in regions of high relief and high altitude like the Himalaya, where both extreme shadowing and extensive snow cover are prevalent.

Given a multispectral image with n bands, a classification algorithm will operate on it in n -dimensional “spectral space” wherein each pixel can be represented by an n -dimensional vector. Similarly, a set of j training classes yields j n -dimensional vectors, each of which is the mean vector – with an associated n -dimensional standard deviation – of the pixels included in the corresponding training class (Richards, 1994). The SAM algorithm calculates the n -dimensional angles between the vector representations of each training class and each pixel in the image. Smaller angles represent closer matches, and the closest match, within a user-defined threshold, determines to which training class a given pixel is assigned. The more orthogonal the training spectra are to each other in n -

Chapter 3: Integration of field geologic and remote sensing data

dimensional vector space, the more effective this classification technique becomes (Kruse *et al.*, 1993; RSI, 2000).

To select the training classes, we defined regions-of-interest in the Landsat TM image for which we knew the composition *a priori*. Our user-defined training classes included field corroborated outcrop localities of the Greater Himalayan Sequence and the Tibetan Sedimentary Sequence (Figures 8g & 9b). We also chose various areas known to be covered by vegetation and by snow and extracted training spectra from them (Figures 8g & 9b). We evaluated the separability and orthogonality of our $j = 4$ training classes in $n = 7$ vector space using the n -D Visualizer™ utility in ENVI® (Boardman, 1993), and we computed the spectral separability between each combination of training class pairs using both the Jeffries-Matusita and Transformed Divergence separability measures (Richards, 1994; RSI, 2000) (Table 4). Since values in Table 4 close to 2 indicate good spectral separability, our training classes are distinct enough to be used as robust endmembers in the SAM classification.

The result of the supervised classification is a false-color map with pixels color-coded according to the training class to which they are assigned. It was post-processed to reduce noise, and statistical analyses of the classification were performed to evaluate its fidelity (Jensen, 1986; Richards, 1994; RSI, 2000) (Table 4). In Figure 9b, we overlay the results of the SAM classification onto Landsat TM band 1. Generally, the SAM result compares favorably with the DCS image, although there are discrepancies (compare Figure 9a & b). In addition, because the SAM algorithm is a quantitative process with predefined tolerances and is dependent on the choice of user-defined training classes, it will normally leave unclassified a (sometimes significant) portion of

Chapter 3: Integration of field geologic and remote sensing data

the pixels in the input image that do not fit the user-defined spectral angle criteria. The quality of the training classes also greatly affects the quality of the result. By contrast, while the DCS process is dependent on the choice of input bands, it reflects the inherent spectral variability of all the pixels within those bands and therefore is not prone to the loss of information due to unclassified or misclassified pixels as is the case with the SAM classification. In the case of the data processing we present, the success of our SAM result is likely to have been affected by the quality of our training classes. While we were careful in our choices, implicit in using training classes is the assumption of homogeneity. We do not take into account effects such as spectral mixing within single pixels and multi-pixel spectral heterogeneity. Therefore, while perhaps less quantitative, the DCS result may be more informative than the SAM result. Indeed, we find that our photointerpretive efforts described in the following sections agree best with the DCS result.

Photointerpretive Techniques

The resolution of the SPOT and Corona images approaches the resolution afforded by aerial photography, making SPOT and Corona adequate for detailed examination of fault traces and kilometer-scale outcrops such as are common along the southern flank of the Himalaya. Analysis of the high-resolution images focused on mapping morphologies and grayscale variations indicative of structures and rock type. Highly detailed, 3-dimensional visualization of stereo imagery combined with the multispectral analyses, was effective for mapping the contact between Greater Himalayan Sequence and Tibetan Sedimentary Sequence rocks.

Chapter 3: Integration of field geologic and remote sensing data

In addition to the outcrop morphologies of the Greater Himalayan Sequence and Tibetan Sedimentary Sequence, we concentrated on features indicative of neotectonic deformation in our effort to map out young South Tibetan fault system structures. These features include scarps and fault-controlled drainage and ridge patterns. We also focused on the geometry of the South Tibetan fault system and how both the fault's orientation and the topography of the Dhaulagiri Himalaya constrain its trace. Specifically we considered measurements of fault orientation from field mapping, the orientation of kilometer-scale lithologic features such as dip-slopes discernable in the stereo imagery, and the topography of the Dhaulagiri Himalaya as seen in the stereo imagery.

TESTING THE METHOD IN THE ANNAPURNA AND EASTERN DHAULAGIRI HIMALAYA

The Basal Detachment Between the Marsyandi and the Kali Gandaki Valleys

Using previous studies in the Annapurna area and our own mapping in the Kali Gandaki and Myagdi Khola valleys as “ground truth”, we were able to study the high-resolution SPOT and Corona imagery of those areas and characterize changes in grayscale and outcrop morphology related to lithology. In the area between the Marsyandi valley and the Kali Gandaki, the Tibetan Sedimentary Sequence forms steep, dark, banded cliffs and dip-slopes that prominently exhibit large-scale sedimentary layering (Figure 10a). In contrast, the Greater Himalayan Sequence appears homogenous, with little indication of compositional layering at this scale, and does not form high cliffs and ramparts. Instead, it forms relatively subdued topography, in some places with well-developed dip-slopes that are significantly steeper than those of the

Chapter 3: Integration of field geologic and remote sensing data

Tibetan Sedimentary Sequence (Figure 10a). The assignment of these terrain types to lithologies is consistent with ground observations of outcrop patterns in the Kali Gandaki valley, where a distinct topographic transition is seen across the basal detachment from steep cliffs of relatively flat-lying Tibetan Sedimentary Sequence above to kilometer-scale dip-slopes of the Greater Himalayan Sequence below.

The contact between the Greater Himalayan terrain types, however, varies widely in its expression on the SPOT and Corona imagery. In some places, it marks an abrupt transition between the two morphologies described above (Figure 10a), whereas it is a more subtle change in grayscale in other places (Figure 10a). In several places, identification of the contact is hindered by cloud cover, shadowing, vegetation, or by permanent snow cover. Where the basal detachment is not completely obscured, these shortcomings can be addressed by using the Landsat TM imagery to distinguish between quartz-rich gniesses of the Greater Himalayan Sequence and carbonate-rich strata of the Tibetan Sedimentary Sequence. In the DCS image (Figure 9a), the Tibetan Sedimentary Sequence appears orange-red, snow is dark blue, and both the Greater Himalayan Sequence and vegetative cover appear green to yellow. The trace of the Greater Himalayan Sequence-Tibetan Sedimentary Sequence contact between the Marsyandi and the Kali Gandaki valley as drawn by Colchen *et al.* (1986) is in good agreement with the orange-red to green-yellow transition.

Other Faults in the Annapurna Himalaya

Although structures corresponding to STF3 have been mapped in the Kali Gandaki valley (this study) and those corresponding to STF3 and STF4 have been

Chapter 3: Integration of field geologic and remote sensing data

mapped in the Modi Khola valley (Hodges *et al.*, 1996), exactly how they project along strike has not been addressed in the course of mapping studies in the western Annapurna Himalaya. The Machhapuchhare detachment (STF3) in the Modi Khola marks the contact between greenschist-facies Annapurna Yellow formation in the footwall and unmetamorphosed Sanctuary Formation in the hanging wall. Spectrally, the Annapurna Yellow Formation and the Sanctuary Formation are not sufficiently different to be distinguishable from one another in the Landsat TM imagery. In the SPOT and Corona imagery, however, the Sanctuary Formation appears somewhat darker and is a slope-forming unit, whereas the Annapurna Yellow Formation forms steep dip-slopes and near-vertical cliffs (Figure 10b). These differences, the geometry of STF3 in the Modi Khola valley, and our ground observations allow us to map the STF3 structure as shown in Figures 3 and 10c.

Our data cannot constrain the trace of STF4 (e.g. the Hiunchuli detachment – Hodges *et al.*, 1996) west of the Modi Khola because it is intraformational to the Sanctuary Formation and it is thought to merge with STF3 near the summits of Hiunchuli and Machhapuchhare peaks (Hodges *et al.*, 1996) (Figure 3). However, the trace of another, unnamed STF4 structure mapped by Hodges *et al.* (1996), if extrapolated to the northeast into the Marsyandi valley (Figure 3), would correlate with a steep normal fault mapped by Colchen *et al.* (1986) and Coleman (1996b). That fault is one of a family of north- to northeast-striking, steeply west-dipping brittle faults cutting the Tibetan Sedimentary Sequence between Chame and the Kali Gandaki valley (Colchen *et al.*, 1986; Coleman, 1996b) (Figure 3).

Chapter 3: Integration of field geologic and remote sensing data

North of the crest of the Annapurna Himalaya, a second, orthogonal set of east-striking oblique normal faults (Figure 3) can be mapped using the Corona stereo photographs. One example is a previously unrecognized structure we call the Tilicho Lake fault which can be mapped for ca. 20 km to the east of Tilicho Lake towards Chame village and for ca. 15 km to the west to Jomsom village (Figure 10c). This fault can be seen in the field at Jomsom, where it has created water springs, sag ponds, and has disrupted bedding within poorly consolidated Plio-Pleistocene basin fill of the Marpha and Kali Gandaki Formations (Hurtado *et al.*, 2001). Where it cuts Tibetan Sedimentary Sequence bedrock of the Thini Chu Formation (Colchen *et al.*, 1986), there is abundant hydrothermal mineralization of calcite, and east-striking, north-dipping brittle shear zones associated with the fault have demonstrable normal-sense displacement on the order of ten meters (Figure 4h). In the Corona imagery, the intersection of the fault trace with topography implies that this fault is a near-vertical, north dipping fault, although it appears to have a shallower dip towards its western end (Figure 10c), consistent with the more moderate (ca. 45°) northward dip seen in the field (Figure 4h).

Offset ridges and other features imply that the Tilicho Lake fault has both left-lateral and normal-sense components of offset (Figure 10c). In some cases, east-striking faults, including the Tilicho Lake fault, have been offset by north-striking faults, but the reverse is true in other cases, as in the case of the Lupra fault (Figure 3). These relationships suggest that the east- and north-striking sets of faults were active concurrently. There is no indication in the Corona imagery that the Tilicho Lake fault continues into the footwall of the Dangardzong fault in the Kali Gandaki valley, as is also the case with most of the east-striking faults we have identified (this study; Hurtado *et*

Chapter 3: Integration of field geologic and remote sensing data

al., 2001). Due to insufficient high-resolution image coverage and lack of field data, however, we similarly have no constraints on the intersection between the basal detachment at Chame and east-striking faults like the Tilicho Lake fault.

Correlation of Structures Between the Kali Gandaki and the Myagdi Khola Valleys

Based on their geometries and structural positions, we correlate the Myagdi Khola fault to the STF3 fault in the Kali Gandaki valley (Figure 6). Similarly, we correlate the top-to-the-south deformational fabrics within the STF zone in the Myagdi Khola to those of the Kalopani/Modi Khola Shear Zone, although we note that the pervasive mylonitic fabrics and overprinting of pre-existing fabrics in the Greater Himalayan sequence are not as severe as they are further east in the Kali Gandaki valley.

The Landsat TM imagery and photointerpretive analysis of the Corona and SPOT data can constrain the trace of the basal detachment (STF1) between the Kali Gandaki valley and the Myadgi Khola valley. In the DCS Landsat TM image (Figure 9a), the red-orange indicative of the Tibetan Sedimentary Sequence colors the high peaks south of Dhaulagiri I. The transition to green-yellow indicative of Greater Himalayan Sequence follows a trace consistent with the orientation of the basal detachment in the Kali Gandaki valley and correlates well with where the basal detachment is observed in the field in the Myagdi Khola valley (Figure 6).

RESULTS FROM THE WESTERN DHAULAGIRI HIMALAYA

Having tested our capabilities to map effectively the distribution of Greater Himalayan Sequence and Tibetan Sedimentary Sequence rocks and to identify

Chapter 3: Integration of field geologic and remote sensing data

morphologic features indicative of South Tibetan fault system structures in the Annapurna and eastern Dhaulagiri Himalaya, we apply these techniques to the western Dhaulagiri Himalaya. Our interpretive mapping of this area based on our image analysis and incorporating ground truth from previous work (Yagi, personal communication; Fuchs, 1967; Ando and Ohta, 1973; Hashimoto *et al.*, 1973; Sako *et al.*, 1973; Nakata, 1989) is shown in Figure 6.

Mapping the Tibetan Sedimentary Sequence-Greater Himalayan Sequence Contact

Based on the Landsat TM DCS imagery (Figure 9a) for the Dhaulagiri Himalaya west of the Myagdi Khola valley, we can locate the contact between Tibetan Sedimentary Sequence and Greater Himalayan Sequence at the base of the cliffs marking the south face of Gurja Himal and Churen Himal (Figure 6). Confidence in our assessment of the location of the basal detachment is provided by photographs of the southern flank of Dhaulagiri range which show the base of the Tibetan Sedimentary Sequence exposed at ca. 4000 m (Figure 7j), consistent with our multispectral imagery (Figure 9).

Since SPOT and Corona imagery have higher resolution than the Landsat TM data, we used photointerpretation to refine the trace of the basal detachment. As in the Annapurna area, the Tibetan Sedimentary Sequence crops out in banded, light and dark colored cliffs and, in places, prominent, dark, northwest-dipping dip-slopes (Figure 11a). The Greater Himalayan Sequence is characterized by more subdued topography, without the light to dark compositional banding, and with more steeply northwest-dipping dip-slopes (Figure 11a). In some localities, large-scale folds in the Tibetan Sedimentary Sequence can be seen in the Corona imagery, and this aided us in making our

Chapter 3: Integration of field geologic and remote sensing data

interpretation of the distribution of the unit (e.g. Figure 11b). In some places in the Dhaulagiri area, where both have dip-slope exposures, the Tibetan Sedimentary Sequence and Greater Himalayan Sequence look very much alike, and only a subtle difference in outcrop attitude – the Greater Himalayan Sequence typically dips more steeply – can be discerned in stereo images (Figure 11c).

Uncertainty in the mapped trace of the basal detachment as shown in Figure 6 increases to the west, away from the Myagdi Khola valley. Ground control in the far northwestern part of the Dhaulagiri Himalaya is provided by mapping by Fuchs (1967) who reported a contact between “crystalline igneous gneisses” and “metamorphic carbonate gneisses” north and east of Tarakot village in the Barbung Khola (Figure 6). In the Corona imagery of the Barbung Khola, the Greater Himalayan Sequence appears to dip moderately to the east-southeast. However, the orientation of the Greater Himalayan Sequence systematically changes along the western edge of the Dhaulagiri Himalaya, becoming east-dipping, and ultimately northeast- to northwest-dipping, along the southern flank of the range (Figure 11d). Compositional layering in the Tibetan Sedimentary Sequence, by contrast, is generally north-dipping throughout the Dhaulagiri Himalaya, with the exception of large, long-wavelength, folds developed in the immediate hanging wall of the South Tibetan fault system in the Barbung Khola (Figures 6 & 11d; Fuchs, 1967). This divergence in orientation along with the distinct morphologies of the two units allowed us to map the Greater Himalayan Sequence-Tibetan Sedimentary Sequence contact with reasonable confidence and to infer that it is a tectonic boundary, as is the case in other parts of the Himalaya.

Mapping the Main Central Thrust

Unfortunately, the multispectral analysis does not place constraints on the location of the Main Central thrust west of the Myagdi Khola. This is due in part to the thick vegetative cover at elevations below 2500 m where the Main Central thrust is exposed. One solution is to project the fault west of the Myagdi Khola toward Seng Khola with a constant strike and dip, and, in doing so, we estimate that the Greater Himalayan Sequence may be no more than 2 km thick in the westernmost Dhaulagiri Himalaya (Figure 6). This is in accord with previous observations by (Sako *et al.*, 1973), who, in their reconnaissance of the area just to the east, noted that the Main Central thrust and “Tuchucha thrust” (as they call the basal detachment of the South Tibetan fault system) are in “close proximity” along the southern flank of Churen Himal.

Photointerpretation of the Corona and SPOT imagery yield some constraints based on outcrop morphology consistent with a remarkably thin Greater Himalayan Sequence. For example, in Figures 11b and 12, apparently bedded cliff outcrops between Ghustung Khola and Dogari Khola are located ca. 2-5 km south of what appear to be dip-slope outcrops of Greater Himalayan Sequence. Based on their structural position and morphology, one hypothesis is that the bedded outcrops are Lesser Himalayan Sequence. However, these outcrops are located in the hanging wall of an active normal fault (Figures 11b & 12; Nakata, 1989), and given that the area in question is so close to established Tibetan Sedimentary Sequence outcrops along the south face of Gurja Himal (Figure 6; Fuchs, 1967), an equally reasonable interpretation is that these are outcrops of the Tibetan Sedimentary Sequence. Unfortunately, without ground truth, we do not have enough information to say which is correct based purely on the image analysis, and so the

Chapter 3: Integration of field geologic and remote sensing data

trace of the Main Central thrust east of Seng Khola we depict in Figure 6 is based on extrapolation of the Hashimoto *et al.* (1973) and Fuchs (1967) mapping.

We are then faced with a situation where reconnaissance field mapping projects the Main Central thrust into an area where, based on photointerpretation, the fault has normal sense displacement and is located within a few kilometers of the Tibetan Sedimentary Sequence-Greater Himalayan Sequence contact. Not surprisingly, the close proximity of the South Tibetan fault system to the Main Central thrust in this area complicates the interpretation of neotectonic features as well as the bedrock geology.

Mapping Neotectonic Features

Nakata (1989) produced a compilation of active normal faults, one of which, the Dhaulagiri Southwest fault, is exposed at ca. 4000 m elevation at the far western end of the Dhaulagiri Himalaya (Figures 1 & 6). This is the fault shown in Figures 11b and 12 near the structural position of the Greater Himalayan Sequence-Tibetan Sedimentary Sequence contact. Using the original mapping by Nakata (1989) and the SPOT and Corona satellite photographs, we extended the mapped trace of the Dhaulagiri Southwest fault. The result of the photointerpretation is incorporated into Figure 6, and it is based on the recognition of active fault segments from prominent scarps and offset ridges, glacial features, and streams. We have identified nine stretches of fresh normal fault scarps that form a contiguous structure traceable for 50 km along a west-northwest strike from Dunai village (point “C” in Figure 6) to point “D” in Figure 6, and the result is in general agreement with independent mapping by H. Yagi (personal communication). Unfortunately, in the stretch between point “D” and the Myagdi Khola, the Dhaulagiri

Chapter 3: Integration of field geologic and remote sensing data

Southwest fault becomes poorly defined in all images. Several factors may contribute to this: vegetative cover, sub-optimal illumination conditions, shallowing of the fault plane's dip, or simply fault inactivity in that area.

Figure 12 shows a particularly well-exposed segment of the Dhaulagiri Southwest fault that illustrates many of its neotectonic features (see also Figure 11b & e). The fault displaces the surface in a top-to-the-north sense with some degree of right-lateral slip, and close inspection of how it crosses topography suggests that it is a northeast-dipping structure, striking approximately northwest. The fault trace is extremely sharp, has numerous sag ponds in depressions along its length, and has produced triangularly-faceted, ca. 10 m high scarps in the footwall, as well as ca. 100 m offsets of ridges in the hanging wall. The fault cuts across glacially sculpted cirques and is responsible for prominent, relatively unincised knick-points in the headwaters of streams draining the cirques. The Dhaulagiri Southwest fault also offsets periglacial surfaces that are correlated with the last glacial advance (H. Yagi, personal communication; Nakata, 1989). Based on luminescence age estimates of the recent glacial advances in the Khumbu Himalaya of Nepal (Richards *et al.*, 2000), this implies slip sometime in the past 25 kyr. Along some portions of the fault trace, there are several sets of degraded scarps that may reflect co-seismic slip during several earthquake cycles within this period (Figure 11e).

Where well exposed, the Dhaulagiri Southwest fault is clearly a young fault, and, given its kinematics and youth, our main interest is how this structure relates geometrically to STF1 and to the Main Central thrust. Field mapping of the Dhaulagiri Southwest fault and its structural position within the Himalayan tectonostratigraphy is

Chapter 3: Integration of field geologic and remote sensing data

limited to observations by H. Yagi (personal communication) near Dogari Khola (Figure 6) who reports that top-to-the-north normal faulting occurs along 30-35° north-dipping “sedimentary-metamorphic structure plane(s)”. This description however, is ambiguous as it can be compatible with the Dhaulagiri Southwest fault marking the contact between Greater Himalayan Sequence gneisses and Tibetan Sedimentary Sequence strata or the contact between Lesser Himalayan Sequence metasediments and Greater Himalayan Sequence gneisses. In the former case, the Dhaulagiri Southwest fault is coincident with STF1 whereas in the latter case it is coincident with the Main Central thrust.

As discussed in the previous section, if we accept the mapping by Hashimoto *et al.* (1973) and Fuchs (1967), the Dhaulagiri Southwest fault in the area between Seng Khola and Ghustung Khola is coincident with the trace of the Main Central thrust, in agreement with the interpretations of both Nakata (1989) and H. Yagi (personal communication). East of Ghustung Khola, though, the Dhaulagiri Southwest fault strikes away from the Main Central thrust and towards the Dhaulagiri Himalaya range-front. At its easternmost extent (point “D” in Figure 6), the fault is essentially at the position of the South Tibetan fault basal detachment (Figure 11f).

To the west of Seng Khola, between Seng Khola and Dunai village (Figure 6), the Dhaulagiri Southwest fault is very clearly exposed (Figure 11d & e), and along this stretch, we can propose two endmember hypotheses for the tectonostratigraphic position of the Dhaulagiri Southwest fault (Figure 6). One possibility, as shown in regional mapping compiled by Fuchs (1982) and Hodges (2000) is that the Main Central thrust maintains its strike. This geometry suggests that the traces of the Dhaulagiri Southwest fault and the Main Central thrust diverge from one another, resulting in a dramatic

Chapter 3: Integration of field geologic and remote sensing data

increase in the thickness of the Greater Himalayan Sequence west of the Dhaulagiri Himalaya (striped and solid fields in Figure 6). The alternative is that the Dhaulagiri Southwest fault and Main Central thrust do not diverge (solid field in Figure 6), which reduces the thickness attained by the Greater Himalayan Sequence thickness immediately west of the Dhaulagiri Himalaya. However, with the exception of the Kali Gandaki transect, it would still be thicker than it is anywhere in the Annapurna or Dhaulagiri Himalaya.

We favor the latter interpretation as there are substantial differences in the terrain and outcrop morphologies in the area between Seng Khola and Dubai village that we can attribute to both the Main Central thrust and the South Tibetan fault. These include cliffs northwest of the fault trace that are morphologically and geometrically identical to and contiguous with cliffs of Tibetan Sedimentary Sequence at higher elevations (Figure 11d & e). Similarly, dip-slope outcrops in the immediate hanging wall of the Dhaulagiri Southwest fault have attitudes and morphology consistent with those of the Greater Himalayan Sequence (Figure 11d & e). These are separated from the Tibetan Sedimentary Sequence outcrops by a distinct contact structurally above the Dhaulagiri Southwest fault that we interpret to be STF1 (Figure 11d & e). Finally, in the footwall of the Dhaulagiri Southwest fault near Tarakot village, cliff outcrops of banded material are visible (Figure 11e). Again, we are faced with the same ambiguity as in the Ghustung Khola (Figures 11b & 12) since these cliffs can be interpreted as either Lesser Himalayan Sequence or Tibetan Sedimentary Sequence. In this case, however, the outcrops in question are in the footwall, consistent with Himalayan tectonostratigraphy; in addition, we have more confidence in our photointerpretation in this area due to better exposure

Chapter 3: Integration of field geologic and remote sensing data

and ground truth provided by mapping in the nearby Burbang Khola by Fuchs (1967). Therefore, our preferred interpretation of these outcrops is that they are Lesser Himalayan Sequence below the Main Central thrust and that the Dhaulagiri Southwest fault between Seng Khola and Dunai is spatially coincident with the Main Central thrust.

Our mapping of the Dhaulagiri Southwest fault ends just west of Dunai, although Nakata (1989) correlates the Dhaulagiri Southwest fault to oblique faults in far western Nepal at Tibrikot and Jumla villages. The relationship between the Dhaulagiri Southwest fault and the Main Central thrust and STF1 in this area is not well known, though we offer a hypothesis in the following sections.

DISCUSSION

Geometry of the South Tibetan Fault System in Central Nepal

The architecture of the South Tibetan fault system in the Dhaulagiri Himalaya matches that of the Annapurna Himalaya. Using the Landsat TM data and high-resolution satellite imagery, we have linked the STF1 detachment in the Marsyandi valley to that in the Myadgi Khola and to the Greater Himalayan Sequence-Tibetan Sedimentary Sequence lithologic contact mapped by Fuchs (1967) in the Barbung Khola (Figures 3 & 6). We have also documented STF2 and STF3 structures and fabrics in the field that can be similarly identified in the remotely sensed data as throughgoing South Tibetan fault system elements between Chame village and the Myadgi Khola (Figures 3 & 6). Other studies of the South Tibetan fault system point to similar structures elsewhere in the Himalaya. For example, in the Everest region of Nepal, Searle (1999) has described three faults in the Everest-Lhotse-Nuptse massif. The lowermost one, the Khumbu thrust

Chapter 3: Integration of field geologic and remote sensing data

may be comparable to the STF2 out-of-sequence thrust, whereas the structurally higher Lhotse and Qomolangma detachments may be analogous to STF1 and STF3, respectively. Steep normal faults north of the northernmost exposures of the Qomolangma detachment (Burchfiel, *et al.*, 1992; Lombardo *et al.*, 1993) may be comparable to STF4. Other examples of polyphase, progressively brittle, northward-stepping normal faults, including potentially young STF4 features, are found in Zaskar, India (Herren, 1987), Giyrong, Tibet (Burchfiel *et al.*, 1992), and Khula Kangri, east-central Tibet (Edwards *et al.*, 1996).

Despite the apparent cross-sectional structural coherence of the South Tibetan fault system, our correlations have brought to light considerable complexity. In both the Marsyandi valley and in the Barbung Khola, for instance, the South Tibetan fault system changes orientation dramatically, from east- to north-striking (Figures 3 & 6). Attitudes in the Greater Himalayan Sequence below the detachment mirror this change in both localities (this study; Coleman, 1996a), yet attitude variations in the Tibetan Sedimentary Sequence above the basal detachment are not as extreme. The Tibetan Sedimentary Sequence, instead, is warped into broad, kilometer-wavelength, synformal structures in both the Annapurna (Schneider and Masch, 1993; Garzanti *et al.*, 1994; Coleman, 1996a) and the Dhaulagiri Himalaya (this study). Another important observation is the variation in thickness of the Greater Himalayan Sequence throughout the Annapurna and Dhaulagiri Himalaya. For instance, Coleman (1996a) noted that the Greater Himalayan Sequence abruptly thins from 12 km in the Marsyandi valley to 5 km in the Kali Gandaki valley (Figure 1a). East of the Marsyandi valley, the Greater Himalayan Sequence becomes in excess of 20 km thick (e.g. compilation tectonic map by Hodges, 2000)

Chapter 3: Integration of field geologic and remote sensing data

(Figure 1a). Our mapping of the area west of the Kali Gandaki valley shows even greater extremes: the Greater Himalayan Sequence thins to as little as 2 km before abruptly thickening to 20 km at the longitude of the Barbung Khola (Figures 6 & 11). It is important to note that these thickness variations are spatially associated with the major embayments in the trace of the South Tibetan fault system in the Marsyandi valley and Burbang Khola (Figure 1a).

Geometrically, thinning of the Greater Himalayan Sequence can be accommodated by the assumption of a shallower dip by the upper boundary – the South Tibetan fault system basal detachment – and/or a steeper dip by the lower boundary – the Main Central thrust. These changes in fault plane orientation would have predictable consequences. For instance, shallowing of the basal detachment would cause the structure to crop out at lower elevations and further south than otherwise; steepening of the Main Central thrust would cause that feature to crop out at higher elevations and further north. This may be the case in the Annapurna and Dhaulagiri areas where, for instance, STF1 crops out between 2500 m and 3500 m. This is in comparison to the ca. 5000 m elevation of STF1 exposures in the Everest region and the ca. 3500 m elevation of STF1 exposures near Manaslu, both of which are – taking into account the northeasterly strike of the orogen – ca. 30 farther north. More significantly, orogen-parallel thickness variations in the Greater Himalayan Sequence and concomitant variations in fault plane orientation require lateral ramps in the South Tibetan fault system and the Main Central thrust. When cut by topography, these ramps would crop out as very large-scale, three-dimensional antiforms and synforms, very much like those observed at the transitions from thick to thin Greater Himalayan Sequence in the

Chapter 3: Integration of field geologic and remote sensing data

Marsyandi valley and Barbung Khola. The overall effect is reminiscent of boudinage, although on an unusually large scale.

It is important to note that this outcrop pattern is not necessarily due to post-slip folding of the South Tibetan fault system, but is more likely a primary feature of the orogen and the product of concurrent warping of the South Tibetan fault hanging wall and thickening of its footwall during STF1 activity. This is supported by the association of Greater Himalayan Sequence thickness variations, the structural disparity between the footwall and hanging wall of the South Tibetan detachment (this study), and kinematic evidence for west-directed lateral flow concurrent with a phase of STF1 activity in the Annapurna area (Coleman, 1996a). Coleman (1996a) hypothesized that lateral flow in the Greater Himalayan sequence may be responsible for the observed geometry and kinematics in the Greater Himalayan Sequence. One possibility is that the natural fluid-dynamical evolution of a relatively low-viscosity channel within the crust represented by the Greater Himalayan Sequence (see Chapter 6) would include undulatory instabilities similar to those seen at the interface between two fluids of significantly different density. Such instabilities could be responsible for local variations in the thickness of the Greater Himalayan Sequence and for the embayed geometries of the STF and MCT systems (e.g. Hurtado *et al.*, submitted – see Chapter 3). The development of these geometries in the Greater Himalayan Sequence is remarkable as they resemble those predicted in geodynamic models of convergent orogens (Beaumont *et al.*, 2001; Jamieson *et al.*, 2002)

We further hypothesize that the flow conjectured by Coleman (1996a) reflects orogen-parallel redistribution of material under the influence of lateral gravitational potential energy gradients (see Chapter 6). If we consider the kinematics of the STF

Chapter 3: Integration of field geologic and remote sensing data

system in this context, it may provide a way to reconcile a kinematic difficulty posed by the geometry of STF1 in the Annapurna and Dhaulagiri Himalaya. In these areas, more-or-less temporally coincident transport directions documented on STF1 are radially distributed. In the Annapurna Himalaya, for instance, transport direction shifts from top to the west in the Marsyandi (Coleman, 1996a), to top to the north in the Modi Khola (Hodges *et al.*, 1996), with intermediate orientations – presumably normal to the strike of STF1 – in between. Clearly, a strain accommodation and space problem becomes apparent if these kinematics are thought of in terms of displacement of the hanging wall of a fault relative to its footwall. However, if we instead consider STF1 as a shear interface accommodating outward flow of low-viscosity material, the kinematics make sense as the divergent flow of a fluid in a channel (see Chapter 6).

Nature of the Dhaulagiri Southwest Fault

Nakata (1989) correlated the Dhaulagiri Southwest fault to an en echelon set of faults between Dunai village and Jumla village (Figure 13), all of which he observed to be steep, north-dipping faults with normal-sense displacement. He interpreted them as a throughgoing reactivation of the Main Central thrust. Others (e.g. H. Yagi, personal communication) have interpreted this system as a transfer structure in a releasing bend that shifts displacement to the Bari Gad fault, an oblique, north-northwest-striking strike-slip fault south of the Dhaulagiri Himalaya (Figure 1a). Since the Dhaulagiri Southwest fault does not change orientation drastically, it is difficult to reconcile its geometry with that of a releasing bend. While we recognize that faults need not be contiguous to interact, the releasing-bend interpretation is weakened by the observation that the

Chapter 3: Integration of field geologic and remote sensing data

Dhaulagiri Southwest fault at its southernmost extent is tens of kilometers north of the Bari Gad fault and the two should not intersect given their observed orientations (Figure 1a).

Another way to interpret the Dhaulagiri Southwest fault is as an “out-of-sequence normal fault” element of the South Tibetan fault system. In this interpretation, the Dhaulagiri Southwest fault is STF5, correlative to the STF5 structure in the Kali Gandaki valley (Hurtado *et al.*, 2001). It is important to realize that STF5 does not strictly reactivate any particular pre-existing tectonostratigraphic contact. It is however the manifestation of active normal faulting in the vicinity of STF1. Whereas in the Kali Gandaki valley STF5 is essentially coplanar with the Greater Himalayan Sequence-Tibetan Sedimentary Sequence contact, our observations of the Dhaulagiri Southwest fault show that it is coincident with the trace of the Main Central thrust along some parts of its length, whereas along others it is within just a few kilometers of STF1 (e.g. Figure 11f). These observations imply that the processes responsible for active normal faulting in the Himalaya have less to do with pre-established lithologic patterns and more to do with other characteristics of the orogen such as the distribution of potential energy, crustal thickness, topography, erosion rates, or the subsurface geometry of structures. In fact, the trace of the Dhaulagiri Southwest fault correlates well with the northern edge of a zone of steep gravitational potential energy anomaly gradient south of the gravitational potential energy anomaly highs coincident with metamorphic core complexes at Mustang and Gurla Mandahta (see Chapter 6) (Figure 13). Gravitational potential energy is a measure of the contribution made by buoyancy forces to the deformation of the lithosphere (e.g. Molnar and Lyon-Caen, 1988), and Hodges *et al.* (2001) argue that areas

Chapter 3: Integration of field geologic and remote sensing data

with high gradients in gravitational potential energy are expected to be sites of efficient dissipation of excess gravitational potential energy. The Himalayan margin of the Tibetan plateau has the highest gravitational potential energy anomaly gradients in the region, and dissipation by aggressive erosion and coupled motion on the Main Central thrust and South Tibetan fault – thereby extruding the Greater Himalayan Sequence to the south – is considered to be a critical tectonic process in the Himalayan orogen (Hodges, 2000; Hodges *et al.*, 2001). We consider the Dhaulagiri Southwest fault to be the modern day manifestation of this ongoing process.

Also associated with the gravitational potential energy anomalies in northwestern Nepal are a set of parallel faults that strike southeastward (Remy, 1973; Fuchs, 1982), away from the Gurla Mandahta core complex (Murphy, 2000) in southern Tibet (Figure 13). According to mapping by Murphy (2000), the southernmost of these faults – which separates Greater Himalayan Sequence rocks from Tibetan Sedimentary Sequence rocks – should be contiguous with the Dhaulagiri Southwest fault near Jumla village (Figure 13). We suggest that the Dhaulagiri Southwest fault STF5 structure links active extensional deformation in the Gurla Mandahta area to that in the Dhaulagiri and Kali Gandaki areas. We hypothesize that the development of core complexes like Gurla Mandahta is driven by gravitational potential energy anomalies in the Tibetan crust (see Chapter 6). Following this interpretation, development of the gravitational potential energy anomaly at Gurla Mandahta has caused extension in the High Himalaya to abandon old traces of the South Tibetan fault system in western Nepal in favor of less contorted traces, with the resulting STF5 structures cutting across lithologic boundaries and reactivating strands of both STF1 and the Main Central thrust (Figure 13).

Relationship Between the South Tibetan Fault and Faults within the Tibetan Sedimentary Sequence

The two sets of structures in the hanging wall of STF1 in the Marsyandi valley together have significantly dismembered and extended the Tibetan Sedimentary Sequence between Chame village and the Dangardzong fault (Figure 3). Our observations of their crosscutting relationships demonstrates that the east- and north-striking faults were active concurrently. The question remains, however, as to the processes creating the stress field responsible for the faulting.

The east-striking faults include the Tilicho Lake fault (this study), the Lupra fault (Godin, 1999) and a number of other structures that segment the hanging wall of the Dangardzong fault (Hurtado *et al.*, 2001). Collectively, these faults appear to have been an important part of the development of the Thakkhola graben, accommodating the “scissors” geometry of the Dangardzong fault during Late Miocene to Recent rifting (Hurtado *et al.*, 2001). Some of the north-striking faults in the Marsyandi valley have been interpreted as Middle-Miocene (ca. 14 Ma) structures related to the earliest stages of Thakkhola graben extension (Coleman and Hodges, 1995). The easternmost of the north-striking faults in the Marsyandi, however, can also be included in the South Tibetan fault system and we correlate one of them to an STF4 structure in the Modi Khola (Figure 3). Although these faults have not been studied in great detail, there is no *a priori* reason to segregate them into those that are related strictly to Thakkhola extension and those that are purely STF4 faults. Indeed, the orientations and displacement geometries of all the north-striking faults as can be discerned from the Corona imagery are uniform.

Chapter 3: Integration of field geologic and remote sensing data

We suggest a close geometric and kinematic relationship between the north- and east-striking high angle faults in the Annapurna area. Because of these relationships, and the observation that east- and north-striking faults were active synchronously, we hypothesize that at least late-stage extensional activity on the South Tibetan fault system in the Marsyandi valley was intimately related to the beginning of extension in the Thakkhola graben. A kinematic link between Thakkhola graben extension and South Tibetan fault system activity is consistent with the observation in the Kali Gandaki valley that the Dangardzong fault acted as a tear structure in the hanging wall of the South Tibetan fault (Hurtado *et al.*, 2001).

Kinematic Model for the Evolution of the Dhaulagiri and Annapurna Himalaya

Kinematic models for this process should explain the faulting in the Tibetan Sedimentary Sequence and opening of the Thakkhola graben in light of flow in the Greater Himalayan Sequence. A quantitative model for core complex formation by Chéry (2001) may be applicable (Figure 14a). In this model, the initial development of a core complex occurs in a half-graben geometry. A steep breakaway fault bounding the graben triggers the development of a “synthetic”, low-angle décollement at depth (steps 1-2, Figure 14a). Upwelling of material from below the brittle-ductile transition warps the décollement upwards and severely thins the hanging wall, all in the footwall of a new, steep normal fault antithetic to the original breakaway (steps 3-4, Figure 14a).

We apply the Chéry (2001) model in a qualitative manner as a hypothesis for the development of several features of the Annapurna and Dhaulagiri Himalaya. In the case of the Annapurna-Dhaulagiri region, we envision a symmetrical situation wherein

Chapter 3: Integration of field geologic and remote sensing data

sequential activity along two sets of normal faults, one on either side of the Thakkhola graben, triggers slip on a low angle detachment and synkinematic extension in its hanging wall and synkinematic flow in its footwall (Figure 14b). The process begins with South Tibetan fault system activity the Marsyandi valley (step 1, Figure 14b). In this area, the second phase of activity on the west-dipping STF1 is characterized by top-to-the-west motion, and, similarly, the west-dipping STF3 exhibits top-to-the-west-southwest sense of shear (Coleman, 1996a). At depth, these structures are interpreted to be low-angle detachments, and according to the Chéry (2001) model, continued slip on the low-angle structure results in uplift of the STF detachment surface and thinning of its hanging wall west of the Thakkhola graben (steps 1-2, Figure 14b). This, in turn, occurs in the footwall of a new, steep normal fault that has developed antithetic to STF1 and STF3. In this case, the new normal fault is the east-dipping Dangardzong fault (step 2, Figure 14). Following the Chéry (2001) model, continued slip on the Dangardzong fault results in further upward warping and exhumation of the detachment as well as opening of the Thakkhola graben (steps 2-3, Figure 14b).

So far, this is directly analogous to the Chéry (2001) model. However, we now can employ the sequence of events again to account for the continued tectonic evolution of the area. We note, for instance, that the Chéry (2001) model predicts that continued slip along the steeply-dipping Dangardzong fault – which is interpreted to root into the STF detachment at depth (e.g. Hurtado and Hodges, 2000; Hurtado *et al.*, submitted – see Chapter 4) – leads to uplift of the STF detachment surface east of the Thakkhola graben. It also results in the development of a second steep normal fault, STF4, which is synthetic with respect to STF1 and STF3 and antithetic to the Dangardzong fault (step 3, Figure

Chapter 3: Integration of field geologic and remote sensing data

14b). Thereafter, slip along both STF4 and the Dangardzong fault leads to continued Thakkhola graben extension as well as further doming of the STF detachment surface and thinning of the Tibetan Sedimentary Sequence in the hanging wall (step 4, Figure 14b).

Concomitant tectonic denudation would have also driven relatively rapid exhumation of both the Mugu and Manaslu plutons (Figure 1a). Since the Greater Himalayan Sequence may have been relatively mobile during this process, thinning of the Tibetan Sedimentary Sequence also may have facilitated the development of features suspected to be core complexes (step 4, Figure 14b). Two of these have been identified in the study area, the Mustang massif exposed in the northern footwall of the Dangardzong fault (Hurtado and Hodges, 2000; Hurtado *et al.*, submitted – see Chapter 4) and the Chako dome exposed in the Naur valley in the footwall of the Chame detachment (Godin, 2001) (Figure 1a). Both feature exhumed rocks similar to those in the Greater Himalayan Sequence (Hurtado and Hodges, 2000; Godin, 2001; Hurtado *et al.*, submitted – see Chapter 4).

Flow of the Greater Himalayan Sequence away from the central Annapurna and Dhaulagiri Himalaya is also a result of the modified Chéry (2001) model (step 4, Figure 14b). Flow toward outlying areas to the west and the east of the Thakkhola graben accounts for the observed lateral thickness variations in the Greater Himalayan Sequence, and for the kinematic indicators of eastward, orogen-parallel flow reported by Coleman (1996a) and Pêcher (1991). We predict similar indicators of westward transport to exist in the Dhaulagiri area (Burbang Khola). The development of synclinal structures within the Tibetan Sedimentary Sequence in the Marsyandi valley and Burbang Khola (Figures 3 & 6) are also the result of the lateral flow of the Greater Himalayan Sequence, perhaps due

Chapter 3: Integration of field geologic and remote sensing data

to mechanical relaxation or “deflation” of the hanging wall as the Greater Himalayan Sequence is thinned.

The relative sequence of events illustrated in Figure 14b is compatible with $^{40}\text{Ar}/^{39}\text{Ar}$ and U-Pb geochronologic data from throughout the Annapurna and Dhaulagiri area. The west-directed STF1 activity and eastward flow of the Greater Himalayan Sequence (step 1, Figure 14b) is constrained to ca. 22-18 Ma in the Marsyandi valley (Coleman, 1996a, 1998). As predicted by the model, initiation of Thakkhola graben extension and inception of the Dangardzong fault postdates this and is estimated to have occurred by ca. 17 Ma, but it may have begun several million years earlier (Garzione *et al.*, 2000; Hurtado and Hodges, 2000; Hurtado *et al.*, submitted – see Chapter 4) (step 2, Figure 14b). Subsequent STF4 activity triggered by the Dangardzong fault and Thakkhola graben extension is estimated to be 14 Ma (Coleman and Hodges, 1995) and younger (Hodges *et al.*, 1996), coincident with continued Dangardzong fault activity (Hurtado and Hodges, 2000; Hurtado *et al.*, 2001; Hurtado *et al.*, submitted – see Chapter 4). The geochronology, then, complements the remote sensing analyses and is consistent with there being a kinematic relationship between Thakkhola graben faults and STF4 structures.

Thermochronologic estimates for the timing of rapid Mustang massif and Mugu leucogranite exhumation, between ca. 20 Ma and ca. 15 Ma (Hurtado and Hodges, 2000; Hurtado *et al.*, submitted – see Chapter 4), are consistent with the above sequence of events. In fact, the absolute age of the Mugu granite, estimated to be between ca. 20.8 Ma (Hurtado *et al.*, submitted – see Chapter 4) and ca. 17.6 Ma (Harrison *et al.*, 1997a), coincides with the beginning of Thakkhola extension, and it is possible that

Chapter 3: Integration of field geologic and remote sensing data

decompression-assisted melting of the Greater Himalayan Sequence occurred during tectonic denudation (stage 2, Figure 14b). We cannot infer the same for the Manaslu pluton since it is estimated to have been emplaced prior to ca. 22 Ma (Guillot *et al.*, 1994). Thermochronology of the Manaslu pluton, however, is consistent with rapid denudation between ca. 19 Ma and ca. 16 Ma (Guillot *et al.*, 1994) and fits the sequence of events predicted by our developmental model.

Implications of Recent Faulting in the High Himalaya

The observation that some strands of the STF1 basal detachment are intruded by undeformed granite plutons (e.g. the Manaslu granite – Guillot, 1993) has led many researchers to consider the entire South Tibetan fault system a currently inactive structure. However, geomorphic evidence for Recent activity on the Dhaulagiri Southwest fault, field evidence for Recent extension related to opening of the Thakkhola graben, and the documentation of potentially young STF4 and STF5 brittle normal faulting in several places in the Himalaya, suggests to us that activity on the entire South Tibetan fault system continued into post-Miocene time. Recent activity at the structural position of the basal detachment may not be unique to the Annapurna-Dhaulagiri area, though. For example, seismic data from the INDEPTH geophysical profile also suggest an association between Quaternary basins in southern Tibet and strands of the STF1 basal detachment (Hauck *et al.*, 1998). These observations are significant because they imply that the same fault system has been active on a regional scale, at least episodically, over much of the past 22 million years.

The corollary to this is that the tectonic processes responsible for the South

Chapter 3: Integration of field geologic and remote sensing data

Tibetan fault system in the Miocene may still be at work today. However, just as activity on these faults has shown itself to be long-lived, albeit episodic, we suspect that the South Tibetan fault may be kinematically segmented. Therefore, while young normal faults are prevalent on the scale of the Dhaulagiri Himalaya, it is still unclear if this is the case on the scale of the entire orogen. In the case of the Main Central thrust, for instance, geomorphologic and topographic evidence point to its being recently active – perhaps even with normal sense displacement – along some stretches, yet inactive along others (e.g. Duncan, 1997; Whipple and Brocklehurst, 2000; Hodges *et al.*, 2001). Thermochronologic data from central Nepal also imply Pliocene and younger Main Central thrust activity (e.g. Harrison *et al.*, 1997b). If recent tectonism in the Himalaya is spatially variable, the question then becomes: why are contiguous structures active in one part of the orogen, and less active in another? The answer may lie in the lateral distribution of potential energy in the orogen and the manner in which it is redistributed (Hodges *et al.* 2001; see Chapter 6).

Evaluation of the Integrative Method

As the quantity and quality of accessible remote sensing data for remote areas like the Himalaya increases, application and refinement of the techniques we describe should prove invaluable in understanding both regional and local tectonics. We feel that the use of remote sensing data complements and effectively extends the spatially limited amount of fieldwork that can be done. It also is an effective guide for identifying areas where focused and detailed fieldwork is needed. In particular, we found the combined use of high-resolution stereo imagery with multispectral data to be a very powerful tool. As

Chapter 3: Integration of field geologic and remote sensing data

with any developing technology, problems and uncertainties do exist. The primary limitations in this regard are spatial and spectral data coverage and spectral resolution. In order to do concurrent, high-spatial resolution morphologic analysis and multispectral lithologic identification, the proper datasets must be available. Our high-resolution data coverage was excellent, and we were fortunate that the Landsat TM data was capable of discriminating between the Tibetan Sedimentary Sequence and Greater Himalayan Sequence. However, ASTER (Advanced Spaceborne Thermal Emission and Radiance imaging spectroradiometer – ERSDAC, 2001) data, with its superior spectral resolution and coverage of the thermal infrared, where the most spectral information relating to lithology is manifest, would have even been better suited for detailed mapping of geologic units. For example, we could have been able to distinguish individual formations within the Greater Himalayan and Tibetan Sedimentary Sequences. Unfortunately, research-quality data from ASTER are not yet available for the Dhaulagiri Himalaya.

Beyond the technological considerations, there will always be observational impediments to overcome. Not least among these are the masking effects of extensive vegetation and permanent snow cover. These effects are mitigated in many remote sensing studies carried out in desert areas, but they limit applicability of multispectral remote sensing data in temperate to tropical mountainous regions like the Himalaya. In the Dhaulagiri Himalaya, there are also local geologic uncertainties to overcome. Fieldwork is required in the far western Dhaulagiri Himalaya – and in the area between it and Gurla Mandahta – to confirm our interpretations of the relationship between Gurla Mandahta, the South Tibetan fault system, and the Dhaulagiri Southwest fault and to re-

Chapter 3: Integration of field geologic and remote sensing data

evaluate the original mapping by Fuchs (1967). Field work should in particular be directed towards documenting meso- and microscopic kinematic evidence for orogen-parallel flow in the Burbang Khola, which is expected if our hypothesis is correct and there is symmetry between that area and the Marsyandi valley (e.g. Coleman, 1996a). Finally, thermo- and geochronologic studies, crucial to understanding the tectonic development of any area and impossible to conduct remotely, need to be carried out to understand the thermal history of the far western Dhaulagiri region and especially the neotectonic history of the Dhaulagiri Southwest fault, a structure that may be an important seismic hazard.

CONCLUSION

We have described an architectural framework for the South Tibetan fault system in the Annapurna Himalaya (Figure 2) comprising STF1 – the oldest, Miocene phase – to STF5 – the most recent, Pleistocene phase. Within this framework, we have synthesized our own field observations along two transects across the South Tibetan fault system with the fieldwork of previous researchers in the Annapurna and Dhaulagiri Himalaya. Using both as ground truth, we have attempted to extend the field geology with our interpretation of various high-resolution and multispectral remote sensing datasets. The result (Figures 6 & 9) is a map of the South Tibetan fault system and the outcrop pattern of the Greater Himalayan Sequence throughout the Annapurna and Dhaulagiri Himalaya. In addition, we have paid special attention to the geomorphologic expression of recent normal faulting in the Dhaulagiri Himalaya, and we have documented the trace of one set of young normal faults – collectively called the Dhaulagiri Southwest fault – which we

Chapter 3: Integration of field geologic and remote sensing data

correlate with STF5 in the Annapurna region.

From these maps and our structural interpretations, we conclude that the recently to currently active extensional faults in the Dhaulagiri Himalaya are contiguous with the mapped traces of the South Tibetan fault system further east. However, young extensional faulting does not everywhere coincide with the lithologic contact traditionally defined as the basal detachment of the South Tibetan fault system. In the far western Dhaulagiri Himalaya, for example, extension is active at the structural position of the Main Central thrust. The location of young faulting does, however coincide with areas of high gradients in gravitational potential energy (Figure 13). We argue that extension in the Himalaya is a regional characteristic of the orogen rather than a localized phenomenon and is fundamentally related to the distribution of gravitational potential energy in the orogen. Finally, we describe a model for the Annapurna and Dhaulagiri Himalaya that results in the formation of metamorphic culminations, fast exhumation of leucogranite plutons, distension of the Tibetan Sedimentary Sequence, lateral flow of the Greater Himalayan Sequence, and syn-kinematic warping of the South Tibetan fault (Figure 14b). We hypothesize that flow of material within the crust as dictated by the distribution of gravitational potential energy may account for the kinematics, interactions, and timing of the faults whose geometries remote sensing data has allowed us to map.

ACKNOWLEDGEMENTS

Our research was supported by a grant from the U. S. National Science Foundation (NSF) awarded to KVH, J. P. Grotzinger, and Kelin X Whipple (EAR-9706216) and an NSF graduate fellowship awarded to JMH. JMH thanks the Frank and Eva B. Buck Foundation for their continuing financial support. JMH also thanks the

Chapter 3: Integration of field geologic and remote sensing data

technical support staff at Research Systems Inc., Phillip Cheng at PCI Geomatics, and the customer service staff at the USGS EROS Data Center and SPOT Image Inc. for their help and advice. We also thank B. N. Upreti, Tribuvan University, and the personnel of the Department of Mines and Geology of the Government of Nepal for their assistance. Ang Phuri Sherpa, Tsering Tendi Sherpa Lama, Makar Girial, Chhatra Girial, Pasang Sherpa, Lakpa Sherpa, Tendi Sherpa, Bharat Karki, Ang Kami Sherpa, Neema Taman, Ang Ringi Sherpa, Doro Lama, Loang Taman, Pasang Chhri Taman, Dorgee Sherpa Lama, Bom Magar, the “Jomsom Mule Wrangler”, and all our friends at Magic Mountain-Sundar Himali Treks provided superb logistical support in the field. Products and brand names may be trademarks or registered trademarks of their respective owners, and reference herein to any specific commercial product, process, or service does not imply endorsement by the Massachusetts Institute of Technology.

REFERENCES CITED

- Ando, H., and Ohta, Y., 1973, Chapter 8: Karnali Region, in Hashimoto, S., Ohta, Y., Akiba, C., and Arita, K., eds., *Geology of the Nepal Himalayas* (Hokkaido University Report): *Geology of the Nepal Himalayas* (Hokkaido University Report), Saikon Publishing Co., Ltd., p. 219-231.
- Beaumont, C., Jamieson, R. A., Nguyen, M. H., and Lee, B., 2001, Himalayan Tectonics explained by extrusion of a low-viscosity crustal channel coupled to focused surface denudation: *Nature*, v. 20, p. 738-742.
- Boardman, J. W., 1993, Automated spectral unmixing of AVIRIS data using convex geometry concepts, in *Summaries, Fourth JPL Airborne Geoscience Workshop*, JPL Publication 93-26, p. 11-14.
- Bordet, P., Colchen, M., Krummenacher, D., Le Fort, P., Mouterde, R., and Remy, M., 1971, *Recherches géologiques dans l'Himalaya du Népal, région de la Thakkhola*: Paris, Centre National de la Recherche Scientifique, 279 p.
- Brown, R. L., and Nazarchuk, J. H., 1993, Annapurna detachment fault in the Greater Himalaya of central Nepal, in Treloar, P. J., and Searle, M. P., eds., *Himalayan Tectonics*: London, Geological Society Special Publication, 47, p. 461-473.
- Burchfiel, B. C., Chen, Z., Hodges, K. V., Liu, Y., Royden, L. H., Deng, C., and Xu, J., 1992, *The South Tibetan Detachment System, Himalayan Orogen: Extension Contemporaneous With and Parallel to Shortening in a Collisional Mountain*

Chapter 3: Integration of field geologic and remote sensing data

Belt, Geological Society of America Special Paper 269: Boulder, CO, Geological Society of America, 41 p.

Burchfiel, B. C., and Royden, L. H., 1985, North-south extension within the convergent Himalayan region: *Geology*, v. 13, p. 679-682.

Burg, J. P., Brunel, M., Gapais, D., Chen, G. M., and Liu, G. H., 1984, Deformation of leucogranites of the crystalline Main Central Sheet in southern Tibet (China): *Journal of Structural Geology*, v. 6, p. 535-542.

Caby, R., Pêcher, A., and Le Fort, P., 1983, Le M.C.T. himalayen: nouvelles données sur le métamorphisme inverse à la base de la Dalle du Tibet: *Revue Géogr. Phys. Géol. Dynam.*, v. 24, p. 89-100.

Chéry, J., 2001, Core complex mechanics: From the Gulf of Corinth to the Snake Range: *Geology*, v. 29, no. 5, p. 439-442.

Clark, R. N., Swayze, G. A., Gallagher, A. J., King, T. V. V., and Calvin, W. M., 1993, The U. S. Geological Survey, *Digital Spectral Library: Version 1: 0.2 to 3.0 microns*, U. S. Geological Survey Open File Report 93-592, 1340 p.

Coblentz, D. D., Richardson, R. M., and Sandiford, M., 1994, On the gravitational potential of the Earth's lithosphere: *Tectonics*, v. 13, no. 4, p. 929-945.

Colchen, M., Le Fort, P., and Pêcher, A., 1986, *Recherches Géologiques dans l'Himalaya du Népal: Annapurna - Manaslu - Ganesh Himal* (Notice de la carte géologique au 1/200000): Paris, Centre National de la Recherche Scientifique, 136 p.

Coleman, M. E., 1996a, Orogen-parallel and orogen-perpendicular extension in the central Nepalese Himalayas: *Geological Society of America Bulletin*, v. 108, p. 1594-1607.

Coleman, M. E., 1996b, *The Tectonic Evolution of the Central Himalaya, Marsyandi Valley, Nepal* [Ph.D. thesis]: MIT, 221 p.

Coleman, M. E., 1998, U-Pb constraints on Oligocene-Miocene deformation and anatexis, Marsyandi Valley, central Nepalese Himalaya: *American Journal of Science*, v. 298, p. 553-571.

Coleman, M. E., and Hodges, K. V., 1995, Evidence for Tibetan plateau uplift before 14 Myr ago from a new minimum age for east-west extension: *Nature*, v. 374, p. 49-52.

Coleman, M. E. and Hodges, K. V., 1998, Contrasting Oligocene and Miocene thermal histories from the hanging wall and footwall of the South Tibetan detachment in

Chapter 3: Integration of field geologic and remote sensing data

- the central Himalaya from $^{40}\text{Ar}/^{39}\text{Ar}$ thermochronology, Marsyandi Valley, central Nepal: *Tectonics*, v. 17, no. 5 (October, 1998), p. 726-740.
- Duncan, C. C., 1997, *Tectonics, topography, climate, and erosion: Analysis of Himalayan digital elevation model data and numerical modeling* [Ph.D. thesis]: Cornell University, 208 p.
- Edwards, M. A., and Harrison, T. M., 1997, When did the roof collapse? Late Miocene north-south extension in the high Himalaya revealed by Th-Pb monazite dating of the Khula Kangri granite: *Geology*, v. 25, p. 543-546.
- Edwards, M. A., Kidd, W. S. F., Li, J., Yue, Y., and Clark, M., 1996, Multi-stage development of the southern Tibetan detachment system near Khula Kangri. New data from Gonto La: *Tectonophysics*, v. 260, p. 1-19.
- EOSAT, 1986, *Landsat Technical Notes, 1*.
- ERSDAC, 2001, *ASTER User's Guide, Part I: General: Earth Remote Sensing Data Analysis Center*, v. 3.0.
- Fort, M., Freytet, P., and Colchen, M., 1982, Structural and sedimentological evolution of the Thakkhola-Mustang graben (Nepal Himalayas): *Zeitschrift für Geomorphologie*, v. 42, p. 75-98.
- Fuchs, G., 1967, *Geological Map of the Dolpo region and the Dhaul Himal: Osterr. Akad. Wiss.*, scale 1:100000.
- Fuchs, G., 1982, *Geologic-tectonic map of the Himalaya: Geological Survey of Austria*, scale 1:2000000.
- Fuchs, G., Widder, R., and Tuladhar, R., 1988, Contribution to the geology of the Manang area (Annapurna Himal, Nepal): *Jahrbuch der Geologischen Bundesanstalt, Wien*, v. 131, p. 593-607.
- Gansser, A., 1964, *Geology of the Himalayas*: London, Wiley Interscience, 289 p.
- Garzanti, E., Gorza, M., Martellini, L., and Nicora, A., 1994, Transition from diagenesis to metamorphism in the Paleozoic to Mesozoic succession of the Dolpo-Manang synclinorium and Thakkhola graben (Nepal Tethys Himalaya): *Eclogae Geologicae Helveticae*, v. 87, p. 613-632.
- Garzione, C. N., Dettman, D. L., Quade, J., DeCelles, P. G., and Butler, R. F., 2000, High times on the Tibetan Plateau: Paleoelevation of the Thakkhola graben, Nepal: *Geology*, v. 28, no. 4, p. 339-342.

Chapter 3: Integration of field geologic and remote sensing data

- Godin, L., 1999, *Tectonic Evolution of the Tethyan Sedimentary Sequence in the Annapurna Area, Central Nepal Himalaya* [Ph.D. thesis]: Carleton University, 219 p.
- Godin, L., 2001, The Chako dome: an enigmatic structure in the hanging wall of the South Tibetan detachment, Nar valley, central Nepal, in *16th Himalaya-Karakoram-Tibet Workshop*, Gratz, Austria.
- Godin, L., Brown, R. L., and Hanmer, S., 1999a, High strain zone in the hanging wall of the Annapurna detachment, central Nepal Himalaya, in Macfarlane, A., Sorkhabi, R. B., and Quade, J., eds., *Himalaya and Tibet: Mountain roots to mountain tops*: Denver, Colorado, GSA, Geological Society of America Special Paper 328, p. 199-210.
- Godin, L., Brown, R. L., Hanmer, S., and Parrish, R., 1999b, Back folds in the core of the Himalayan orogen: An alternative interpretation: *Geology*, v. 27, p. 151-154.
- Grove, C. I., Hook, S. J., and Paylor, E. D., 1992, *Laboratory reflectance spectra for 160 minerals: 0.4 - 2.5 micrometers*, JPL Publication 92-2: Pasadena, CA., Jet Propulsion Laboratory.
- Guillot, S., 1993, *Le granite du Manaslu (Nepal central) marqueur de la subduction et de l'extension intracontinentale Himalayenne* [D.Sc. thesis]: Joseph Fourier - Grenoble.
- Guillot, S., Hodges, K. V., Le Fort, P., and Pêcher, A., 1994, New constraints on the age of the Manaslu leucogranite: Evidence for episodic tectonic denudation in the central Himalayas: *Geology*, v. 22, p. 559-562.
- Hanmer, S., and Passchier, C., 1991, *Shear-Sense Indicators: A Review*: Ottawa, Geological Survey of Canada Paper 90-17, 72 p.
- Harrison, T. M., Lovera, O. M., and Grove, M., 1997a, New insights into the origin of two contrasting Himalayan granite belts: *Geology*, v. 25, p. 899-902.
- Harrison, T. M., Ryerson, F. J., Le Fort, P., Yin, A., Lovera, O., and Catlos, E. J., 1997b, A Late Miocene-Pliocene origin for the central Himalayan inverted metamorphism: *Earth and Planetary Science Letters*, v. 146, p. E1-E7.
- Hashimoto, S., Ohta, Y., Akiba, C., Arita, K., Amma, S., Ando, H., Endo, T., Ishida, T., Kano, T., Koshiro, K., Yuji, M., Minoru, M., Sako, S., Soma, T., Tanaka, H., and Watanabe, O., 1973, *Geology of the Nepal Himalayas* (Hokkaido University Compilation): Saikon Publishing Co, Ltd., scale 1:500000.

Chapter 3: Integration of field geologic and remote sensing data

- Hauck, M. L., Nelson, K. D., Brown, L. D., Zhao, W., and Ross, A. R., 1998, Crustal structure of the Himalayan Orogen at approximately 90° east longitude from Project INDEPTH deep reflection profiles: *Tectonics*, v. 17, p. 481-500.
- Herren, E., 1987, Zaskar shear zone: Northeast-southwest extension within the Higher Himalayas (Ladakh, India). *Geology*, v. 15, p. 409-413.
- Hodges, K., Bowring, S., Davidek, K., Hawkins, D., and Krol, M., 1998, Evidence for rapid displacement on Himalayan normal faults and the importance of tectonic denudation in the evolution of mountain ranges: *Geology*, v. 26, p. 483-486.
- Hodges, K. V., 2000, Tectonics of the Himalaya and southern Tibet from two perspectives: *Geological Society of America Bulletin*, v. 112, no. 3, p. 324-350.
- Hodges, K. V., Hurtado, J. M., and Whipple, K. X., 2001, Southward extrusion of Tibetan crust and its effect on Himalayan tectonics: *Tectonics*, v. 20 (6), p. 799-809.
- Hodges, K. V., Parrish, R. R., and Searle, M. P., 1996, Tectonic evolution of the central Annapurna Range, Nepalese Himalayas: *Tectonics*, v. 15, p. 1264-1291.
- Hook, S. J., Gabell, A. R., Green, A. A., and Kealy, P. S., 1992, A comparison of techniques for extracting emissivity information from thermal infrared data for geologic studies: *Remote Sens. Environ.*, v. 42, p. 123-135.
- Hook, S. J., Karlstrom, K. E., Miller, C. F., and McCaffrey, K. J. W., 1994, Mapping the Piute Mountains, California, with thermal infrared multispectral scanner (TIMS) images: *Journal of Geophysical Research*, v. 99, no. B8, p. 15605-15622.
- Hunt, G. R., 1980, Electromagnetic radiation: The communication link in remote sensing, in Siegal, B. S., and Gillespie, A. R., eds., *Remote Sensing in Geology*: New York, John Wiley, p. 5-45.
- Hurtado, J. M., and Hodges, K. V., 2000, Exhumational history of the Mustang and Mugu granites of the central Nepal Himalaya: *EOS*, v. 81, no. 48, p. 1070.
- Hurtado, J. M., Hodges, K. V., and Whipple, K. X., 2001, Neotectonics of the Thakkhola graben and implications for Recent activity on the South Tibetan fault system in the central Nepal Himalaya: *Geological Society of America Bulletin*, v. 113, no. 2, p. 222-240.
- Iwata, S., 1984, Geomorphology of the Thakkhola-Muktinath region, central Nepal, and its Late Quaternary history: *Geographical Reports of the Tokyo Metropolitan University*, v. 19, p. 25-42.

Chapter 3: Integration of field geologic and remote sensing data

- Jamieson, R. A., Beaumont, C., Nguyen, M. H., and Lee, B., 2002, Interaction of metamorphism, deformation, and exhumation in large convergent orogens: *Journal of Metamorphic Geology*, v. 20, p. 1-16.
- Jensen, J. R., 1986, *Introductory Digital Image Processing*: Englewood Cliffs, New Jersey, Prentice-Hall, 379 p.
- Jones, C. H., Unruh, J. R., and Sonder, L. J., 1996, The role of gravitational potential energy in active deformation in the southwestern United States: *Nature*, v. 381, p. 37-41.
- Khule, M., 1982, *Der Dhaulagiri- und Annapurna-Himalaya; Ein Beitrag zur Geomorphologie extremer Hochgebirge, Zeitschrift fuer Geomorphologie Supplementband*, 299 p.
- Kruse, F. A., Lefkoff, A. B., Boardman, J. B., Heidebrecht, K. B., Shapiro, A. T., Barloon, P. J., and Goetz, A. F. H., 1993, The Spectral Image Processing System (SIPS) - Interactive visualization and analysis of imaging spectrometer data: *Remote Sens. of Environ.*, v. 44, p. 145-163.
- Le Fort, P., 1975, Himalayas: the collided range: Present knowledge of the continental arc: *American Journal of Science*, v. 275-A, p. 1-44.
- Le Fort, P., 1994, *French Earth Sciences Research in the Himalaya Regions*: Kathmandu, Nepal, Alliance Française, p. 174.
- Le Fort, P., and France-Lanord, C., 1995, Granites from Mustang and surrounding regions, central Nepal: *Journal of the Nepal Geological Society*, v. 10, p. 79-81.
- Lemoine, F. G., Kenyon, S. C., Factor, J. K., Trimmer, R. G., Pavlis, N. K., Chinn, D. S., Cox, S. M., Klosko, S. M., Luthcke, S. B., Torrence, M. H., Wang, Y. M., Williamson, R. G., Pavlis, E. C., Rapp, R. H., and Olson, T. R., 1998, *The development of the joint NASA GSFC and the National Imagery and Mapping Agency (NIMA) geopotential model EGM96*, NASA Technical Paper NASA/TP-1998-206861: Greenbelt, MD, Goddard Space Flight Center, p. 600.
- Lombardo, B., Pertusati, P., and Borghi, S., 1993, Geology and tectonomagmatic evolution of the eastern Himalaya along the Chomolungma-Makalu transect, in Treloar, P. J., and Searle, M. P., eds., *Himalayan Tectonics*: London, Geological Society Special Publication, 47, p. 341-355.
- Molnar, P., and Lyon-Caen, H., 1988, Some simple physical aspects of the support, structure, and evolution of mountain belts, in Clark, S., Burchfiel, B. C., and Suppe, J., eds., *Processes in Continental Lithospheric Deformation*: Boulder, CO, Geological Society of America Special Paper 218, p. 179-207.

Chapter 3: Integration of field geologic and remote sensing data

- Murphy, M. A., 2000, *Tectonic Evolution of southwest Tibet* [Ph.D. thesis]: University of California, Los Angeles, 216 p.
- Murphy, M. A., and Harrison, T. M., 1999, The relationship between leucogranites and the South Tibetan detachment system, Rongbuk Valley, southern Tibet: *Geology*, v. 27, no. 9, p. 831-834.
- Nakata, T., 1989, Active faults of the Himalaya of India and Nepal, in Malinconico, L. L., and Lillie, R. J., eds., *Tectonics of the Western Himalayas*: Boulder, CO, Geological Society of America Special Paper 232, p. 243-264.
- Pêcher, A., 1991, The contact between the Higher Himalayan crystallines and the Tibetan sedimentary series: Miocene large-scale dextral shearing: *Tectonics*, v. 10, p. 587-599.
- Remy, J. M., 1973, *Carte Geologique du Népal (Ouest du Népal)*: Centre National de la Recherche Scientifique, scale 1:5068
- Richards, B. W. M., Benn, D. I., Owen, L. A., Rhodes, E. J., and Spencer, J. Q., 2000, Timing of late Quaternary glaciations south of Mount Everest in the Khumbu Himal, Nepal: *Geological Society of America Bulletin*, v. 112, no. 10, p. 1621-1632.
- Richards, J. A., 1994, *Remote Sensing Digital Image Analysis*: Berlin, Springer-Verlag, 340 p.
- RSI, 2000, *ENVI User's Guide 3.4*, Research Systems, Inc., 930 p.
- Sako, S., Ishida, T., Masuda, M., Watanabe, O., and Fushimi, H., 1968, Geology of the Central Nepal Himalaya: *Report - Geological Survey of Hokkaido*, v. 38, p. 1-23.
- Sako, S., Ishida, T., and Yoshihide, O., 1973, Chapter 7: Dhaulagiri Region, in Hashimoto, S., Ohta, Y., Akiba, C., and Arita, K., eds., *Geology of the Nepal Himalayas* (Hokkaido University Report): Tokyo, Japan, Saikon Publishing Co., Ltd., p. 189-218.
- Salisbury, J. W., Walter, L. S., Vergo, N., and D'Aria, D. M., 1991, *Infrared (2.1-25 micrometers) Spectra of Minerals*, Johns Hopkins University Press, 294 p.
- Schärer, U., Xu, R., and Allegre, C., 1986, U-(Th)-Pb systematics and ages of Himalayan leucogranites, South Tibet: *Earth and Planetary Science Letters*, v. 77, p. 35-48.
- Schneider, C., and Masch, L., 1993, The metamorphism of the Tibetan Series from the Manang area, Marsyandi Valley, Central Nepal, in Treloar, P. J., and Searle, M. P., eds., *Himalayan Tectonics*: London, Geological Society Special Publication, 47, p. 357-374.

Chapter 3: Integration of field geologic and remote sensing data

- Searle, M. P., 1986, Structural evolution and sequence of thrusting in the High Himalayan, Tibetan-Tethys and Indus suture zones of Zaskar and Ladakh, Western Himalaya: *Journal of Structural Geology*, v. 8, p. 923-936.
- Searle, M. P., 1999, Extensional and compressional faults in the Everest-Lhotse massif, Khumbu Himalaya, Nepal: *Journal of the Geological Society of London*, v. 156, p. 227-240.
- Searle, M. P., Parrish, R. R., Hodges, K. V., Hurford, A., Ayers, M. W., and Whitehouse, M. J., 1997, Shisha Pangma leucogranite, South Tibetan Himalaya: Field relations, geochemistry, age, origin, and emplacement: *Journal of Geology*, v. 105, p. 295-317.
- USGS, 1993, *Digital elevation models, data user guide, 5*: Reston, Virginia, United States Geological Survey, p. 1-50.
- Valdiya, K. S., 1989, Trans-Himadri intracrustal fault and basement upwarps south of the Indus-Tsangpo Suture Zone, in Malinconico, L. L., and Lillie, R. J., eds., *Tectonics of the Western Himalayas*: Boulder, CO, Geological Society of America Special Paper 232, p. 153-168.
- Vannay, J.-C., and Hodges, K. V., 1996, Tectonometamorphic evolution of the Himalayan metamorphic core between Annapurna and Dhaulagiri, central Nepal: *Journal of Metamorphic Geology*, v. 14, p. 635-656.
- Whipple, K. X., and Brocklehurst, S. H., 2000, Estimating glacial relief production in the Nepal Himalaya: *GSA Abstracts with Programs*, v. 32, no. 7 (Reno 2000 Annual Meeting), p. 330.
- Wu, C., Nelson, K. D., Wortman, G., Samson, S. D., Yue, Y., Li, J., Kidd, W. S. F., and Edwards, M. A., 1998, Yadong cross structure and South Tibetan detachment in the east central Himalaya (89°-90°E): *Tectonics*, v. 17, p. 28-45.
- Xu, R. H., 1990, Age and geochemistry of granites and metamorphic rocks in south-central Xizang (Tibet), in C. A. o. G. Sciences, ed., *Igneous and Metamorphic Rocks of the Tibetan Plateau*: Beijing, Science Press, p. 287-302.
- Yoshida, M., Igarashi, Y., Arita, K., Hayashi, D., and Sharma, T., 1984, Magnetostratigraphic and pollen analytic studies of the Thakmar series, Nepal Himalayas: *Journal of the Nepal Geological Society*, v. 4, p. 101-120.

FIGURE CAPTIONS

Table 1.

Deformational history of the Nilgiri Formation south of Tuckuche Village in the Kali Gandaki valley.

Table 2.

Characteristics of the SPOT and Corona high-resolution imagery.

Table 3.

Characteristics of the Landsat MSS and Landsat TM multispectral imagery.

Table 4.

Summary of separability measures for the training classes used in the Spectral Angle Mapper classification (Figure 9b).

Table 5.

Statistics for the Spectral Angle Mapper Classification result.

Figure 1.

Location maps.

a. Map of the Central Nepal Himalaya showing the Dhaulagiri, Thakkhola, and Annapurna regions. The base is the GTOPO-30 Digital Elevation Model (DEM) with 1 km pixel resolution (USGS, 1993). The various boxed areas show the ground coverage of our remote sensing imagery, and the shaded areas numbered “1”-“4” indicate field geologic traverses from which we derive ground truth observations. Note the traces of the Main Central thrust (MCT) and the basal detachment of the South Tibetan fault system (STF1). The intervening area is the extent of the Greater Himalayan Sequence in the core of the Himalayan ranges. Note the along strike thickness variation in the Greater Himalayan Sequence which attains minimum thickness in the Dhaulagiri-Thakkhola-Annapurna region between the Barbung Khola and the Marsyandi River. To the west and east of this area, the Greater Himalayan Sequence is substantially thicker (≥ 30 km) as

Chapter 3: Integration of field geologic and remote sensing data

reflected by the prominent embayments in the trace of STF1. Also shown on the map is the map trace of the Dhaulagiri Southwest fault and several metamorphic and plutonic massifs. These include the Mugu and Manaslu plutons, leucogranitic batholiths within the Tibetan Sedimentary Sequence (e.g. Guillot, 1993; Le Fort and France-Lanord, 1995), and the Mustang and Chako domes, enigmatic structures that may be core complexes (Hurtado and Hodges, 2000; Godin, 2001; Hurtado *et al.*, submitted – see Chapter 4).

b. Index of SPOT and Corona images in Figures 10, 11, and 12. Dashed boxes show the extent of the images.

Figure 2.

Simplified cross section showing the architecture of the central Nepal Himalaya. The basic structure is that of a north-dipping monocline consisting of a stack of allochthonous units (from south to north): the Lesser Himalayan Sequence (LHS), the Greater Himalayan Sequence (GHS), and the Tibetan Sedimentary Sequence (TSS). They are separated from one another by faults as shown. The Main Central thrust (MCT) separates LHS from GHS, and is actually a broad, several kilometer thick zone of shortening rather than a single fault. In this study, we will refer to the uppermost fault in the zone as “MCT” (although in Figures 3 and 6, we also map the basal thrust fault in the MCT zone in addition to the upper fault, labeling them as such). In the cross section we have schematically shown the geometry of the South Tibetan fault (STF) system with each element as described in the text along with its approximate age.

Figure 3.

Geologic map of the Annapurna range incorporating our image interpretation, multispectral remote sensing analyses, and field observations as well as previously published mapping. In particular, we have incorporated mapping by Coleman (1996b), Colchen *et al.* (1986), Godin (1999), and Hodges *et al.* (1996) with some reinterpretations. Note the network of intersecting north- and east-striking steep faults within the Tibetan Sedimentary Sequence that we have mapped primarily with the stereo Corona and SPOT imagery. Also note the large-scale synformal structure in the Tibetan

Sedimentary Sequence in the far eastern Annapurna range (Schneider and Masch, 1993; Garzanti *et al.*, 1994; Coleman, 1996a). Points “A”-“C” are discussed in the text.

Figure 4.

Photographs taken during field work in the Kali Gandaki valley.

a. STF3 in the hill-slopes between Thulobugin Ridge and Nimek Danda summit (at point “A” in Figure 3). View to the east. Fold structures depicted have ca. 500-m wavelengths. SF = Sanctuary Formation. AYW = Annapurna Yellow Formation.

b. STF3 near Taglung village (at point “B” in Figure 3). View to the northeast. Relief on the ridge behind Taglung is ca. 1 km. NF = Nilgiri Formation. AYW = Annapurna Yellow Formation. DF = Dangardzong fault. Note that the apparent shallow dip of the Dangardzong fault is an illusion due to topography and the view angle; the same is true of the apparent geometry of STF3. The Dangardzong fault actually dips steeply to the west and STF3 dips north.

c. North-dipping generation 1 vein (see Table 1) in the Nilgiri Formation south of Tuckuche village (at point “C” in Figure 3). It has been isoclinally folded along with the host rock by $F1_{NF}$ folding prior to being warped by $F2_{NF}$ and boudinaged by $B3_{NF}$. Black dot-dashed lines show fold closures. Lens cap for scale is 5.5 cm in diameter.

d. North-dipping generation 2 vein (see Table 1) in the Nilgiri Formation south of Tuckuche village (at point “C” in Figure 3). It has been folded by $F2_{NF}$ prior to being boudinaged by $B3_{NF}$. Lens cap for scale is 5.5 cm in diameter.

e. North-dipping generation 3 vein (see Table 1) in the Nilgiri Formation south of Tuckuche village (at point “C” in Figure 3). It has been not been folded, but is boudinaged by $B3_{NF}$. Field book for scale is 12 cm x 19 cm.

f. Subhorizontal generation 4 vein in the Nilgiri Formation. It has been boudinaged by $B2_{NF}$ prior to being folded by $F3_{NF}$.

g. Brittle shear zone cutting the Nilgiri Formation outcrop south of Tuckuche village (at point “C” in Figure 3). Arrows show width of the cataclastic zone.

h. Easternmost extent of the Tilicho Lake fault (see Figures 3 & 10d) as exposed at the edge of Jomsom village. Hill is ca. 50 m tall. Stratum outlined in black and labeled “ α ” has been offset in a normal sense by ca. 10 m across the shear zone shown by the

Chapter 3: Integration of field geologic and remote sensing data

white solid lines. The fault strikes approximately 045° and dips ca. 45°NW . Dashed lines show folding in the upper half of the hill and an apparent lithologic contact between the top and bottom of the hill. According to the stratigraphy defined by Colchen *et al.* (1986) the Tilicho Lake fault cuts through Permo-Carboniferous black, fossiliferous shale of the Thini Chu Formation at this location. View towards south.

i. *Top*: Panoramic view to the west of the Dhaulagiri I – Tuckuche Peak massif. White dashed lines show the trend of large-scale compositional layering displayed on the cliffs. The wall in the center panel of the image is ca. 2 km high. Solid lines adorned with arrows denote the inferred trace of the STF3 structure. *Bottom*: Dhaulagiri I and Tuckuche Peak from different perspectives. *Bottom left*: Dhaulagiri I taken from Thulobugin ridge showing the traces of both STF1 and STF3. *Bottom right*: Tuckuche peak shows the trace of STF3 south of point “C” in Figure 3. Note that the large scale folding in the hanging wall of STF3 does not continue into the footwall.

Figure 5.

Schematic representation of the response of north-dipping and subhorizontal veins to deformation within a north-dipping shear zone (orientation shown schematically by the dotted gray line). Two cases, shortening and extension, are considered, with the orientation of σ_1 and σ_3 indicated for each. In the case of shortening (left panel), north-dipping veins become boudinaged whereas subhorizontal veins are folded. Conversely, in the case of extension (right panel), north-dipping veins become folded whereas subhorizontal veins are boudinaged. In either case, the response of the vein to the shear zone is dependent on the orientation of the vein with respect to σ_1 and σ_3 (e.g. Hanmer and Passchier, 1991; Hodges *et al.*, 1996).

Figure 6.

Geologic map of the Dhaulagiri range incorporating our image interpretation, multispectral remote sensing analyses, and field observations as well as previously published mapping – with substantial reinterpretations – by Nakata (1989), Hashimoto *et al.* (1973) and Fuchs (1967). In particular, our mapping and reinterpretation was aimed towards extending the geology of the Annapurna Himalaya (see Figure 3) to the west,

Chapter 3: Integration of field geologic and remote sensing data

linking and interrelating the various strands of the South Tibetan fault system. Note the large-scale anti- and synformal structures that we infer in the far western Dhaulagiri range based on the orientation of the basal detachment of the South Tibetan fault system (STF1) and photointerpretive assessments of the orientation of compositional layering within the Tibetan Sedimentary Sequence (TSS). Also note the progressive change in the thickness and strike of the Greater Himalayan Sequence (GHS) in the far western Dhaulagiri range that mirrors the similar transition in the far eastern Annapurna range. Finally, note the two possible traces for the Main Central thrust (MCT) as discussed in the text. The geometry shown by the solid red field results in a GHS thickness of ca. 30 km in western Nepal versus as little as ca. 2 km in the Dhaulagiri Himalaya. Requiring the MCT and Dhaulagiri Southwest fault (DSWF) to remain coplanar (red, ruled field) results in a minimum thickness of ca. 15-20 km in western Nepal, still substantially thicker than elsewhere in the Annapurna and Dhaulagiri Himalaya (with the exception of the Kali Gandaki River transect). Points “A”-“D” are discussed in the text. The asterisk (*) corresponds to the location of Figure 11e. The eye symbol (<) denotes the location from which the photograph in Figure 7j was taken.

Figure 7.

Photographs taken during field work in the Kali Gandaki valley.

a. Greater Himalayan Sequence Formation I migmatitic garnet-mica gneiss between Dobang and Boghara villages. Arrow denotes top-to-the-south shear sense as indicated by the shear band, asymmetric folding, and sigmoidal porphyroblasts. View to the southeast. Lens cap for scale is 5.5 cm in diameter.

b. Greater Himalayan Sequence Formation II calcsilicate gneiss at Dobang village. Note deformed leucosomes. Arrow denotes top-to-the-north shear sense as indicated by asymmetric boudinage. View to the northwest. Lens cap for scale is 5.5 cm in diameter.

c. Greater Himalayan Sequence Formation II calcsilicate gneiss ca. 3 km north of Dobang village. South vergent fold trains indicate shortening at this structural level. Author’s hand for scale. View to the west.

Chapter 3: Integration of field geologic and remote sensing data

d. Deformation at the position of the South Tibetan fault system basal detachment (STF1). Note the difference in the dip of compositional layering between the Tibetan Sedimentary Sequence (TSS) at the top and the Greater Himalayan Sequence (GHS) at the bottom of the image (shown by angle symbols). Also, note the deformed dike, outlined in black that has been boudinaged prior to being folded and faulted in a top to the north sense. View to the west. Fold indicated by dashed white lines is approximately 2-m-across.

e. The South Tibetan fault system basal detachment (STF1) in the cliffs above Chartare. Note the distinct color change between the dark weathering Greater Himalayan Sequence (GHS) and the yellow weathering lower Tibetan Sedimentary Sequence (TSS). View to the southwest. Cliffs in the mid-ground are ca. 1.5 km tall.

f. Larjung Formation outcrop in the immediate hanging wall of the South Tibetan fault system basal detachment. The outcrop at this location contains a significant amount of discordant tourmaline-bearing granitic leucosome. Handheld GPS unit (12-cm-long) and head of geologic hammer (17-cm-long) for scale.

g. Larjung Formation outcrop in the immediate footwall of the Myagdi Khola fault (STF3). Note the boudinaged sills of tourmaline-bearing leucogranite. The boudinage is symmetric with no asymmetric shear sense indicators and appear to reflect coaxial strain. Lens cap for scale is 5.5 cm in diameter.

h. The Myagdi Khola fault (STF3) as exposed at point “B” in Figure 6. Arrows denote the width of the zone of cataclasite. Height of the waterfall in the background is ca. 5 m. View to the east.

i. The Myagdi Khola fault (STF3). Photograph taken of the fault exposed behind the waterfall in Figure 7h. Note the folded granitic dike below the brittle shear zone. A portion of it is caught within the brittle shear zone but it is truncated and cannot be followed into the hanging wall of the Myagdi Khola fault. View to the south.

j. The south face of Gurja Himal (7193 m). The Tibetan Sedimentary Sequence (TSS) and Greater Himalayan Sequence (GHS) are labeled based on their outcrop morphologies and color. The basal detachment of the South Tibetan fault system (STF1) is drawn at the approximate transition between the two morphologies. This assessment is consistent with those based on photointerpretation of SPOT (see Figure 11a) and Corona

Chapter 3: Integration of field geologic and remote sensing data

imagery (see Figure 11c) as well as the TSS-GHS contact as seen in the decorrelation stretched Landsat TM image (see Figure 9a). Photograph taken ca. 10 km from mountain front (location shown by eye symbol (<) in Figure 6). STF1 as drawn crops out at ca. 4000 m altitude. Height of escarpment in background is ca. 3500 m.

Figure 8.

Reflectance spectra plots. Plots “a”-“f” are hemispherical reflectance laboratory spectra referenced to the HALON standard. They are taken from various sources and are labeled accordingly. Plots in “g” are spectra of the training classes selected for the Spectral Angle Mapper (SAM) supervised classification. USGS = USGS Mineral Spectral Library (see <http://speclab.cr.usgs.gov/> for details; Clark *et al.*, 1993); JPL = Jet Propulsion Laboratory Spectral Library (see <http://asterweb.jpl.nasa.gov/speclib/> for details; Grove *et al.*, 1992); JHU = Johns Hopkins University Spectral Library (see <ftp://rocky.eps.jhu.edu> for details; Salisbury *et al.*, 1991).

a. Visible and near-infrared reflectance spectra for calcite. Several different grainsizes and calcite polymorphs are shown. Shaded strips indicate locations of Landsat TM bands 2, 5, and 7. Note the absorption features at ca. 0.5 μm (near Landsat TM band 2) and ca. 2.5 μm (near Landsat TM band 7).

b. Visible and near-infrared reflectance spectra for quartz. Several different grain-sizes and quartz polymorphs are shown. Shaded strips indicate locations of Landsat TM bands 2, 5, and 7. Note the very flat spectra over the entire interval.

c. Calcite and quartz visible and near-infrared to thermal-infrared spectra. Shaded strip indicates position of Landsat TM band 6. Note that calcite is relatively more reflective in this interval, but has a very prominent absorption at ca. 11 μm .

d. Visible and near-infrared to thermal-infrared spectra for siliceous and calcareous rocks. Shaded strip indicates position of Landsat TM band 6. Note that limestone marble exhibits a prominent absorption at ca. 11 μm whereas the siliceous rocks exhibit monotonically decreasing reflectance.

e. Visible and near-infrared spectra for various types of vegetation. Shaded strips indicate locations of Landsat TM bands 2, 5, and 7. Note that despite the variety of plant types, all have nearly identical absorption features.

Chapter 3: Integration of field geologic and remote sensing data

f. Visible and near-infrared to thermal-infrared spectra of snow and vegetation. Note that both are similar to one another above ca. 1 μm . Snow is highly reflective below 1 μm . Both vegetation and snow have low reflectance beyond ca. 3 μm , and in particular have much lower reflectance than either siliceous or carbonate rocks at ca. 11 μm .

g. Landsat TM spectra of the four training classes – snow, Greater Himalayan Sequence (GHS), Tibetan Sedimentary Sequence (TSS), and vegetation – used in the SAM supervised classification. The top center panel is a comparison of the mean spectra for each training class. The four panels below correspond to the individual training classes and show the mean spectrum, the $\pm 1\sigma$ error envelope, and minimum and maximum spectra of the pixels in the region of interest defining the training class. The vertical bars in each panel denote Landsat TM bands 2, 5, and 7. Note that, while the mean spectra of TSS, GHS, and snow are quite distinct from each other, the spectra of GHS and vegetation bear some similarity to one another.

Figure 9.

a. Decorrelation stretched image of Landsat TM Bands 7, 5, and 2 in the red, blue, and green channels, respectively. Area shown is the southern portion of the entire Landsat TM scene outlined in Figure 3. White boxes in the center panel indicate the areas shown in detail in the insets: the upper Modi Khola in the Annapurna Himalaya, and the southern flank of the Gurja Himal-Putha Hiunchuli massif in the Dhaulagiri Himalaya. The white line is the trace of the South Tibetan fault system basal detachment (STF1). Solid line denotes areas where the trace of STF1 is based on ground truth. Dashed segments are based on interpretation of the decorrelation stretch. Dotted lines are stretches where photointerpretation in addition to multispectral data interpretation was used. In the decorrelation stretch, reds and oranges correspond to pixels with spectral signatures like that of the Tibetan Sedimentary Sequence (TSS). Blue corresponds to snow and ice. Green corresponds in part to vegetation, but also may indicate Greater Himalayan Sequence (GHS) since their spectra are similar (see Figure 8g). Yellow also corresponds to GHS. Note the correspondence between the trace of STF1 determined by ground truth and the red/orange to yellow/green transition in the Annapurna region (e.g.

Chapter 3: Integration of field geologic and remote sensing data

Modi Khola inset). Based on this correlation and our Corona and SPOT satellite image interpretation, we extend the trace of STF1 west into the Dhaulagiri Himalaya as shown (e.g. Gurja Himal inset). DK = Dudh Khola; NK = Naur Khola; MR = Marsyandi River; MK = Modi Khola; A = Annapurna I (8091 m); KGR = Kali Gandaki River; D = Dhaulagiri I (8167 m); MyK = Myagdi Khola; BK = Barbung Khola.

b. Result of the Spectral Angle Mapper supervised classification. Area shown in the main panel is the same as that in the decorrelation stretched image (Figure 9a). Yellow boxes show the areas detailed in the insets. TSS = blue; GHS = red; snow = white; undifferentiated = black. Solid black lines show the approximate trace of the GHS-TSS contact based on mapping by previous workers (e.g. Colchen *et al.*, 1986; Coleman, 1996b; Hodges *et al.*, 1996; Godin, 1999), satellite image interpretation (this study), and the decorrelation stretched image (this study) (see Figure 9a). Question marks denote areas where the classification algorithm has resulted in pixel identifications inconsistent with the trace of the STF1 as shown. DK = Dudh Khola; NK = Naur Khola; MR = Marsyandi River; MK = Modi Khola; MyK = Myagdi Khola; BK = Barbung Khola; KGR = Kali Gandaki River; A = Annapurna I (8091 m); D = Dhaulagiri I (8167 m).

Figure 10.

a. SPOT image of the Kali Gandaki valley between Dana and Kalopani (see Figure 1b for location). On the west bank of the Kali Gandaki River, outcrop morphologies of the Tibetan Sedimentary Sequence (TSS) and the Greater Himalayan Sequence (GHS) are sufficiently distinct to allow mapping based on photointerpretation. Outcrops of TSS units are steep banded cliffs, typically lighter in color than dip-slope outcrops of GHS. On the east bank of the Kali Gandaki River, however, outcrop morphologies are less useful, and the mapping shown is based on field observations. AYW = Annapurna Yellow Formation. NF = Nilgiri Formation; STF1 = South Tibetan fault system basal detachment; STF3 = South Tibetan fault system upper brittle-ductile detachment; STF5 = South Tibetan fault system basal detachment reactivation (Hurtado *et al.*, 2001); DF = Dangardzong fault.

b. SPOT image of the Miristi Khola (see Figure 1b for location) showing outcrop morphologies of the Sanctuary Formation (SF), Annapurna Yellow Formation (AYF),

Chapter 3: Integration of field geologic and remote sensing data

and Nilgiri Formation (NF). Note that SF typically manifests itself as a dark, slope-forming unit, whereas AYF forms cliffs and dip-slopes, and NF forms high, steep cliffs. Bold, ornamented lines are faults. Other lines are formational contacts. Faults and contacts are based on analysis of SPOT imagery and reinterpretation of mapping by Colchen *et al.* (1986). GHS = Greater Himalayan Sequence; STF1 = South Tibetan fault system basal detachment; STF3 = South Tibetan fault system upper brittle-ductile detachment.

c. Corona images of the Tilicho Lake fault (TLF) near Tilicho Lake (see Figure 1b for location) *Top*: Portion of the Corona strip showing the main extent of TLF. Note that it is cut by several north-striking faults. Conversely, other east-striking faults, have offset the north-striking faults (see the Lupra fault in Figure 3). *Bottom*: Detailed stereo image of the area around Tilicho Lake. Point “a” denotes a shutter ridge indicative of left-lateral displacement along the fault. Points “b” and “c” denote localities where north-facing normal fault scarps are evident and where the fault cuts topography in a fashion consistent with it being a steep, slightly north-dipping structure.

Figure 11.

a. Portion of the SPOT image for the Dhaulagiri Himalaya showing the south face of Gurja Himal (7193 m) (See Figure 1b for location). Dashed line shows the transition (STF1) between terrain types corresponding to the Tibetan Sedimentary Sequence (TSS) and the Greater Himalayan Sequence (GHS). TSS crops out as light colored, banded steep cliffs forming kilometers scale walls and the summits of the highest peaks. GHS crops out at lower elevations, and it is typically darker in color and exhibits large-scale dip-slopes.

b. *Top*: Corona stereo imagery of the area between the Dogari Khola and Ghustung Khola in the western Dhaulagiri Himalaya (see Figure 1b for location). Black line is the trace of STF1 as defined by the transition between Tibetan Sedimentary Sequence (TSS) and Greater Himalayan Sequence (GHS) terrain types and the multispectral imagery in Figure 9. Arrows point to the trace of the Dhaulagiri Southwest fault (DSWF) as defined by well-developed scarps (see Figure 12). LHS = Lesser Himalayan Sequence. *Bottom*: Detailed view of the area outlined by the black box in the

Chapter 3: Integration of field geologic and remote sensing data

stereo view. TSS and LHS crop out as banded cliffs. GHS crops out as darker dip-slopes. Note in particular the folded outcrop of TSS at middle right.

c. Corona stereo imagery of the area between Gurja Himal (7193 m) and the Myadgi Khola (see Figure 1b for location). The white dashed line labeled STF1 marks the trace of the basal detachment of the South Tibetan fault system as defined by field observations, multispectral analysis (see Figure 9), and photointerpretation of outcrop morphology. In this area, photointerpretation is made difficult by the presence of extensive cloud coverage, extreme shadowing, and vegetation at the relatively low elevations where STF1 is exposed. Based on its trace in the Myadgi Khola, STF1 should be exposed on the ridge in the center of the image (see arrow). Unfortunately, TSS and GHS have similar morphologies in this area and both form prominent dip-slopes. Exposures at the highest elevations north of Konabon glacier are certainly TSS and are contiguous with the dip-slopes at lower elevations (see arrow). However a subtle change in dip – steeper dips in GHS – that can be discerned using the stereo images allows us to draw STF1 as shown.

d. Corona stereo imagery of the Burbang Khola in the northwestern Dhaulagiri Himalaya (see Figure 1b for location). Black dashed line is the trace of STF1 as defined by field observations (Fuchs, 1967), multispectral analysis (this study; see Figure 9), and photointerpretation of outcrop morphology (this study). White dashed line is the trace of the Dhaulagiri Southwest fault (DSWF) as defined by our image interpretation and that of previous workers (Yagi, personal communication; Nakata, 1989). Strike and dip symbols schematically represent the attitude of large-scale layering as can be discerned in the Corona imagery. Black dashed curves in the TSS denote a kilometer scale fold closure within the TSS in the immediate hanging wall of STF1. Note how attitudes in the GHS change along strike in this area, mirroring the embayment of the trace of STF1. Attitudes in the TSS, however, do not change as dramatically.

e. *Top*: Corona stereo imagery of the area between Seng Khola and Saunre Khola in the western Dhaulagiri Himalaya (see Figure 1b for location). In this stretch, northwest of the area where (Nakata, 1989) mapped the Dhaulagiri Southwest fault (DSWF), several generations of fault scarps related to DSWF activity can be discerned as well as features such as sag ponds along the fault trace. White dashed lines are the traces of STF1

Chapter 3: Integration of field geologic and remote sensing data

and the DSWF. TSS = Tibetan Sedimentary Sequence. GHS = Greater Himalayan Sequence. LHS = Lesser Himalayan Sequence. Boxed areas show areas detailed in bottom frames. *Bottom left:* Well-developed triangular facet in the footwall of the DSWF. The facet has been developed on a hill composed of light-colored, banded material that may be LHS. *Bottom right:* From south to north, points “a”-“h” denote the various generations of DSWF fault scarp that can be discerned in the Corona imagery within the GHS.

f. SPOT scene of the area between Ghustung Khola and Dhola Khola in the western Dhaulagiri Himalaya (see Figure 1b for location). Along this stretch, the Dhaulagiri Southwest fault (DSWF) strikes to the northeast, away from the Main Central Thrust (MCT) and towards the South Tibetan fault system basal detachment (STF1). Arrows denote the trace of the DSWF based on identifiable fault scarps. Dashed lines show the traces of STF1 and the MCT. Note that the Greater Himalayan Sequence (GHS) is between 5 km and 2 km in this area. TSS = Tibetan Sedimentary Sequence.

Figure 12.

SPOT image of the Dhaulagiri Southwest fault between the between the Dogari Khola and Ghustung Khola in the western Dhaulagiri Himalaya (see Figure 1b for location). Note the fault trace, well defined by scarps, triangular facets, offset ridgelines, and the morphologic transition between steep fluvial streams in the footwall and glacial cirques in the hanging wall.

Figure 13.

The area between Gurla Mandahta and the Dhaulagiri Himalaya. *Top:* Geologic map incorporating mapping from this study (see Figures 3 & 5), Colchen *et al.* (1986), Fuchs (1967), and Hodges (2000). Base is the GTOPO-30 Digital Elevation Model (DEM) with 1-km pixel resolution (USGS, 1993). STF1 = South Tibetan fault system basal detachment; MCT = Main Central thrust; DSWF = Dhaulagiri Southwest fault; STF5 = Pleistocene South Tibetan fault system; TSS = Tibetan Sedimentary Sequence; GHS = Greater Himalayan Sequence; LHS = Lesser Himalayan Sequence. Note the interpreted trace of the DSWF west of Dunai (see text). Dashed lines show possible

linkages between the DSWF and STF1 in the Gurla Mandahta area. *Bottom left:* Geologic mapping on a plot of gravitational potential energy anomaly calculated from the NASA-NIMA EGM96/WGS-84 global geoid model (Lemoine *et al.*, 1998) using the technique described by Coblenz *et al.* (1994) and Jones *et al.* (1996). See Chapter 6 and Hodges *et al.* (2001) for details. Note the correspondence between the gravitational potential energy anomaly highs at the top of the image and the massifs at Gurla Mandahta, Mugu, and Mustang. *Bottom right:* Geologic mapping overlain on a map of gravitational potential energy anomaly gradient. The gradient map is computed as described in Chapter 6 and by Hodges *et al.* (2001). Note that the active trace of the DSWF and the trace of STF1 coincide with the northern edges of the gravitational potential energy gradient highs whereas the MCT coincides with their southern edges.

Figure 14.

a. Model for core complex development after (Chéry, 2001). Schematic cross sectional views with time progressing downward. Process begins with extension along a steep breakaway fault (1) that at depth develops into a low-angle detachment synthetic to the original breakaway due to rotation of the principal stress axes, perhaps resulting from increased pore fluid pressure (2). As activity on the low-angle detachment progresses, it is uplifted and its hanging wall thinned, and a second breakaway, antithetic to the first develops (3-4).

b. Symmetric model. Schematic east-west cross sectional views through the Thakkhola graben and the adjacent areas as seen facing north. Time progresses downward. (1) Slip along STF1, STF3, or both at ca. 22-18 Ma during eastward flow of the Greater Himalayan Sequence (GHS) (Coleman, 1996a; Coleman and Hodges, 1998). (2) Slip along the STF detachment leads to thinning of its hanging wall and uplift of the detachment surface. This occurs in the footwall of the Dangardzong fault (DF) and marks the start of Thakkhola graben extension at ca. 17-14 Ma (Coleman and Hodges, 1995; Hurtado and Hodges, 2000; Hurtado *et al.*, submitted – see Chapter 4). (3) Continued slip along DF leads to uplift of the STF detachment surface and development of a second steep normal fault, STF4. (4) Slip along both STF4 and DF leads to: further Thakkhola graben extension; continued doming of the STF detachment surface; thinning

Chapter 3: Integration of field geologic and remote sensing data

of the Tibetan Sedimentary Sequence (TSS); flow of GHS away from the central Annapurna and Dhaulagiri Himalaya; exhumation of metamorphic rocks and granites at Mustang and Chako (Hurtado and Hodges, 2000; Godin, 2001; Hurtado *et al.*, submitted – see Chapter 4); and exhumation of leucogranitic bodies such as the Mugu and Manaslu plutons.

TABLE 1. DEFORMATIONAL HISTORY: NILGIRI FORMATION SOUTH OF TUCKUCHE VILLAGE, KALI GANDAKI VALLEY

Deformational Phase (interpretation)	Schistosity S/D (°)	Lineations P-T (°)	Folds Axial Plane S/D, Axis T -> P (°)	Boudinage	Quartz & Calcite Veins					
					N-dipping			S-dipping		
					1*	2†	3§	4#	5**	
-	S _{0NF} comp. layering; ca. 300/15-20° N									
D _{1NF} (pre-STF3 ?) compression)	S _{1NF} transposed S _{0NF} axial planar to F _{1NF} ; ca. 300/15-20°N	L _{1NF} mineral lineation; ca. 12 -> 020	F _{1NF} recumbent folds transposing S _{0NF} ; ca. 300/15-20°N, ca. 10 -> 090			F _{1NF}				
D _{2NF} (STF4 extension)	S _{2NF} crenulation cleavage axial planar to F _{2NF} ; ca. 300/65°N		F _{2NF} broad to tight, upright, N-vergent, disharmonic folds & crenulations; affects N-dipping fabrics & veins; ca. 300/65°N, ca. 25 -> 090	B _{2NF} max. extension to N; affects subhoriz. to S-dipping veins		F _{2NF}	F _{2NF}		B _{2NF}	
D _{3NF} (STF3 compression)			F _{3NF} S-vergent disharmonic folding of subhoriz. to S-dipping veins	B _{3NF} max. extension to N; affects N-dipping fabrics & veins; asymmetric w/ CCW _w rotation		B _{3NF}	B _{3NF}	B _{3NF}	F _{3NF}	
D _{4NF} (STF3 extension)				B _{4NF} max. extension to N; affects subhoriz. to S-dipping veins						B _{4NF}
D _{5NF} (STF3)	Brittle shear zones; ca. 270/45°N	N-plunging slickenlines								

Note: Schistosity (S), lineations (L), folds (F), and boudinage (B) formed during specific deformational events (D) are numbered sequentially based on interpreted age relationships as observed in the field. NF = Nilgiri Formation. S/D = strike and dip of a planar fabric element. P-T = plunge and trend of a linear fabric element. Comp. layering = compositional layering. Max = maximum. Subhoriz. = subhorizontal. CCW_w = counterclockwise (when viewed towards W).

*Population 1: concordant with S_{0NF} and are transposed into parallelism with S_{1NF} by F_{1NF}. Dip less steeply N than STF3 and intersect it at ca. 30°. See Fig. 4c.

†Population 2: subconcordant with – but dip ca. 10° more steeply N than – S_{0NF} & S_{1NF}. Dip less steeply N than STF3 and intersect it at ca. 15°. See Fig. 4d.

§Population 3: have the same orientation as population 1 and 2 veins. See Fig. 4e.

#Population 4: subhoriz. or dip slightly S, and, therefore, are discordant with respect to S_{0NF} & S_{1NF}. They intersect STF3 at a high angle (ca. 45°). See Fig. 4f.

**Population 5: have the same orientation as population 4 veins.

Table 1

TABLE 2. DATA CHARACTERISTICS: HIGH RESOLUTION IMAGERY

Instrument and Spacecraft	Data Type*	Wavelength (µm)	Ground Resolution† (m)	Ground Coverage N-S x E-W (km x km)	Image Entity Identifier and Acquisition Date§	Stereo Coverage Notes	Latitude / Longitude# Upper Right, Lower Left (degrees, WGS-84)
SPOT 3 **	panchromatic, level 1B digital radiance	0.51 - 0.73 (visible green - red)	10	60 x 60	00401 219/292 910131-6 Jan. 31, 1991	Dhaulagiri; look angle: R 0.5° no stereo pair	N028°57.7' / E083°09.5', N028°20.5' / E083°37.0'
SPOT 3	panchromatic, level 1B digital radiance	0.51 - 0.73 (visible green - red)	10	60 x 70	00201 220/292 961020-2 Oct. 20, 1996	‡Kali Gandaki; look angle: R 24.8° overlap: ca. 90%	N029°09.6' / E083°37.1', N028°33.3' / E084°11.9'
SPOT 3	panchromatic, level 1B digital radiance	0.51 - 0.73 (visible green - red)	10	64 x 60	00301 221/292 931123-3 Nov. 23, 1993	‡Kali Gandaki; look angle: L 17.7° overlap: ca. 90%	N029°06.9' / E083°40.1', N028°29.5' / E084°09.8'
Corona KH-4B §§	black & white, panoramic 70-mm film positive	visible	ca. 2	ca. 14 x 188	DS1112-1007DF177 Nov. 19, 1970	##N. Dhaulagiri & Annapurna; forward looking	N029°01.9' / E082°39.9', N029°09.0' / E085°30.9'
Corona KH-4B	black & white, panoramic 70-mm film positive	visible	ca. 2	ca. 14 x 188	DS1112-1007DA182 Nov. 19, 1970	##N. Dhaulagiri & Annapurna; aft looking	N028°52.9' / E082°40.9', N029°00.0' / E085°31.9'
Corona KH-4B	black & white, panoramic 70-mm film positive	visible	ca. 2	ca. 14 x 188	DS1112-1007DF178 Nov. 19, 1970	***S. Dhaulagiri & Annapurna; forward looking	N028°52.9' / E082°40.9', N029°00.0' / E085°31.9'
Corona KH-4B	black & white, panoramic 70-mm film positive	visible	ca. 2	ca. 14 x 188	DS1112-1007DA183 Nov. 19, 1970	***S. Dhaulagiri & Annapurna; aft looking	N028°54.0' / E082°37.9', N029°00.9' / E085°27.9'

*Panchromatic = single-, wide-band image. SPOT Level 1B digital data is provided by SPOT Image, Inc. has been radiometrically corrected and has minimal geometric processing to correct for earth's rotation and the panoramic effects associated with oblique viewing angles. Radiance = amount of electromagnetic radiation leaving or arriving at a point on a surface (in Watts per meter per steradian). Corona images are "analog" data provided on film transparencies.

†SPOT ground resolution based on absolute characteristics of the solid state imaging system and its optics. Nominal ground resolution given for Corona which, in addition to camera optics, is dependent on characteristics of the film emulsion, development process, interpreter, and, if digitized, the scan resolution.

§Entity ID numbers are unique to the image and are assigned by the agency providing the data, in this case either SPOT Image, Inc. or the United States Geological Survey EROS Data Center (for Corona). Corona mission and frame numbers are those originally assigned by United States Department of Defense.

#Estimated georeferencing error is ca. 1 km for SPOT scenes and up to ca. 16 km for Corona scenes. WGS-84 (UTM zone 44R) is the datum used.

**SPOT 3 denotes the spacecraft that acquired the imagery. It was launched on Sept. 26, 1993 from Kourou, French Guiana by the European Space Agency and Arianespace for the French firm SPOT Image, Inc. The spacecraft was disabled in a collision with orbital debris on Nov. 14, 1997 and is no longer in operation.

‡These images are a stereo pair. R & L denote off-nadir direction in which the incidence, or look angle, is measured. Overlap is the ground area in both scenes.

§§KH-4B denotes the spacecraft type that acquired the imagery and returned the film to earth via air-retrievable deorbit "buckets". Mission 1112 was launched from Cape Canaveral Air Force Station by the United States Air Force for the Central Intelligence Agency on Nov. 18, 1970. Corona was the United States' first space photoreconnaissance program (1960-1972) from which over 860 000 images were declassified by President Clinton by Executive Order on Feb. 22, 1995.

##These images are a stereo pair. Forward- and aft- looking cameras with 30°-separation angle provided off-nadir stereo capability. Overlap is ca. 100%.

***These images are a stereo pair. Forward- and aft- looking cameras with 30°-separation angle provided off-nadir stereo capability. Overlap is ca. 100%.

Table 2

Chapter 3: Integration of field geologic and remote sensing data

TABLE 3. DATA CHARACTERISTICS: MULTISPECTRAL DATA

Instrument and Spacecraft	Coverage	Band	Wavelength (μm)	Ground Resolution§ (m)	
Landsat 2 MSS# Multispectral Scanner	Image Entity Identifier*	LM2153040007507490	4: visible green**	0.5 - 0.6	57
	Acquisition Date	May 31, 1975			
	Latitude / Longitude† Upper Left, Lower Right	N029°52.2' / E082°49.2', N027°52.8' / E084°25.9'	5: visible red	0.6 - 0.7	57
	Ground Coverage N-S x E-W (km x km)	187 x 181	6: reflected near-infrared	0.7 - 0.8	57
			7: reflected near-infrared	0.8 - 0.9	57
			1: visible blue	0.45 - 0.52	28.5
			2: visible green	0.52 - 0.60	28.5
Landsat 4 TM‡ Thematic Mapper	Image Entity Identifier*	LT4142040008901510	3: visible red	0.63 - 0.69	28.5
	Acquisition Date	Jan. 15, 1989			
	Latitude / Longitude† Upper Left, Lower Right	N029°48.9' / E083°13.3', N027°54.2' / E082°49.2'	4: reflected near-infrared	0.76 - 0.90	28.5
	Ground Coverage N-S x E-W (km x km)	181 x 181	5: reflected mid-infrared	1.55 - 1.75	28.5
			6: thermal infrared	10.4 - 12.5	120
			7: reflected mid-infrared§§	2.08 - 2.35	28.5

*Entity ID numbers are unique to the image and are assigned by the United States Geological Survey EROS Data Center.

†Estimated error in georeferencing is ca. 1 km. WGS-84 (UTM zone 44R) is the datum used.

§Ground resolution is based on the absolute characteristics of the solid state imaging system and its optics.

#Landsat 2 denotes the spacecraft carrying the MSS instrument. It was in operation from Jan. 22, 1975 until 1981.

**MSS bands 4-7 were renumbered MSS bands 1-4 beginning with the Landsat 4 mission.

‡Landsat 4 is the spacecraft carrying the first TM class system. It has been in operation since July 16, 1982.

§§TM band 7 is out of sequence because it was added late in the design process, after the other bands were established.

TABLE 4. TRAINING CLASS SEPARABILITY

Training Class	Training Class	Jeffries-Matusita	Transformed Divergence
Tibetan Sedimentary Sequence	Greater Himalayan Sequence	1.89588952	1.99967897
	Vegetation	1.99918218	2.00000000
	Snow	NaN*	2.00000000
Greater Himalayan Sequence	Tibetan Sedimentary Sequence	1.89588952	1.99967897
	Vegetation	1.99644786	2.00000000
	Snow	NaN	2.00000000
Vegetation	Tibetan Sedimentary Sequence	1.99918218	2.00000000
	Greater Himalayan Sequence	1.99644786	2.00000000
	Snow	NaN	2.00000000
Snow	Tibetan Sedimentary Sequence	NaN	2.00000000
	Greater Himalayan Sequence	NaN	2.00000000
	Vegetation	NaN	2.00000000

Note: Both the Jeffries-Matusita and Transformed Divergence separability measures are reported. These values range from 0 to 2.0 and indicate how well the selected ROI pairs are statistically separate. Values greater than 1.9 indicate that the ROI pairs have good separability. For more information, see Richards (1994) and RSI (2000).

*NaN = Not a Number. These values are artifacts of the Jeffries-Matusita method in instances where there is complete separability between the endmembers in question.

Tables 3 & 4

Chapter 3: Integration of field geologic and remote sensing data

TABLE 5. SPECTRAL ANGLE MAPPER (SAM) CLASSIFICATION STATISTICS

Spectral Angle Threshold* (radians)	Overall Accuracy† (%)	Kappa (κ) Coefficient§	Image Size (pixels) x Number of Bands
0.2	78.3093 (1686/2153)	0.7230	13 732 720 x 6 (TM Bands 1-5, 7)

<i>Class Statistics#</i>			
Training Class	Pixels in Training Class (no. of pixels)	Image Pixels Classified (no. of pixels)	Image Pixels Classified (% of total in image)
TSS	637	535 471	3.8992
GHS	513	735 160	5.3533
Vegetation	658	644 617	4.6940
Snow	345	3 488 784	25.4049

<i>Contingency Matrix**</i>					
Class	TSS	GHS	Vegetation	Snow	Total
Unclassified	111 (17.34%)	84 (16.37%)	136 (20.67%)	0 (0%)	331 (15.37%)
TSS	449 (70.49%)	18 (3.51%)	1 (0.15%)	0 (0%)	468 (21.74%)
GHS	69 (10.83%)	409 (79.73%)	38 (5.78%)	0 (0%)	516 (23.97%)
Vegetation	6 (0.94%)	0 (0%)	483 (73.40%)	0 (0%)	489 (22.71%)
Snow	2 (0.31%)	2 (0.39%)	0 (0%)	345 (100%)	349 (16.21%)
Total	637 (100%)	513 (100%)	658 (100%)	345 (100%)	2153 (100%)

<i>Accuracy Assessment</i>				
Class	Commission‡	Omission§§	Producer Accuracy##	User Accuracy***
TSS	19/637 (4.06%)	188/637 (29.51%)	449/637 (70.49%)	449/468 (95.94%)
GHS	107/513 (20.74%)	104/513 (20.27%)	409/513 (79.93%)	409/416 (79.26%)
Vegetation	6/658 (1.23%)	175/658 (26.60%)	483/658 (73.40%)	483/489 (98.77%)
Snow	4/345 (1.15%)	0/345 (0%)	345/345 (100%)	345/349 (98.85%)

Note: Pixels not classified into any training class are omitted in this analysis. Statistics computed with ENVI® (RSI, 2000). TSS = Tibetan Sedimentary Sequence. GHS = Greater Himalayan Sequence. TM Band 6 not used in the SAM classification.

*The maximum spectral angle allowed between the *n*-dimensional mean vector of a given training class and the *n*-dimensional vector representation of a given pixel for the SAM algorithm to classify the pixel as belonging to that class.

†Calculated by summing the no. of endmember pixels classified correctly, divided by the total no. of endmember pixels.

§Measures the accuracy of the SAM classification. $\kappa = (N \sum_{(k)} X_{kk} - \sum_{(k)} X_{k\Sigma} X_{\Sigma k}) / (N^2 - \sum_{(k)} X_{k\Sigma} X_{\Sigma k})$, where: N is the number of training classes; $\sum_{(k)} X_{kk}$ is the sum of the diagonal elements of the Contingency Matrix**; $\sum_{(k)} X_{k\Sigma} X_{\Sigma k}$ denotes the sum of ground truth pixels in a class times the sum of the classified pixels in that class, summed over all classes (RSI, 2000).

#Statistics include sizes of the training classes and the number of image pixels assigned to them by the SAM algorithm.

**Also known as the "Confusion Matrix". See Jensen (1986) for details. It is computed for the pixels in the training classes by comparing the location and class of each ground truth pixel with the corresponding location and class in the SAM result. Each column corresponds to a training class; values in the column indicate the algorithm's labeling of training class pixels.

‡For a given Class "A", errors of commission represent pixels that belong to other classes but were incorrectly labeled as belonging to Class "A" by the SAM algorithm. It is based on the algorithm's performance with respect to the training classes.

§§For a given Class "A", errors of omission represent pixels that belong to Class "A" but were incorrectly classified into another class by the SAM algorithm. It is based on the algorithm's performance with respect to the training classes.

##Probability that the algorithm has labeled a pixel into Class "A" given that the ground truth is Class "A".

***Probability that a pixel belongs in Class "A" given that the algorithm has labeled the pixel into Class "A".

Table 5

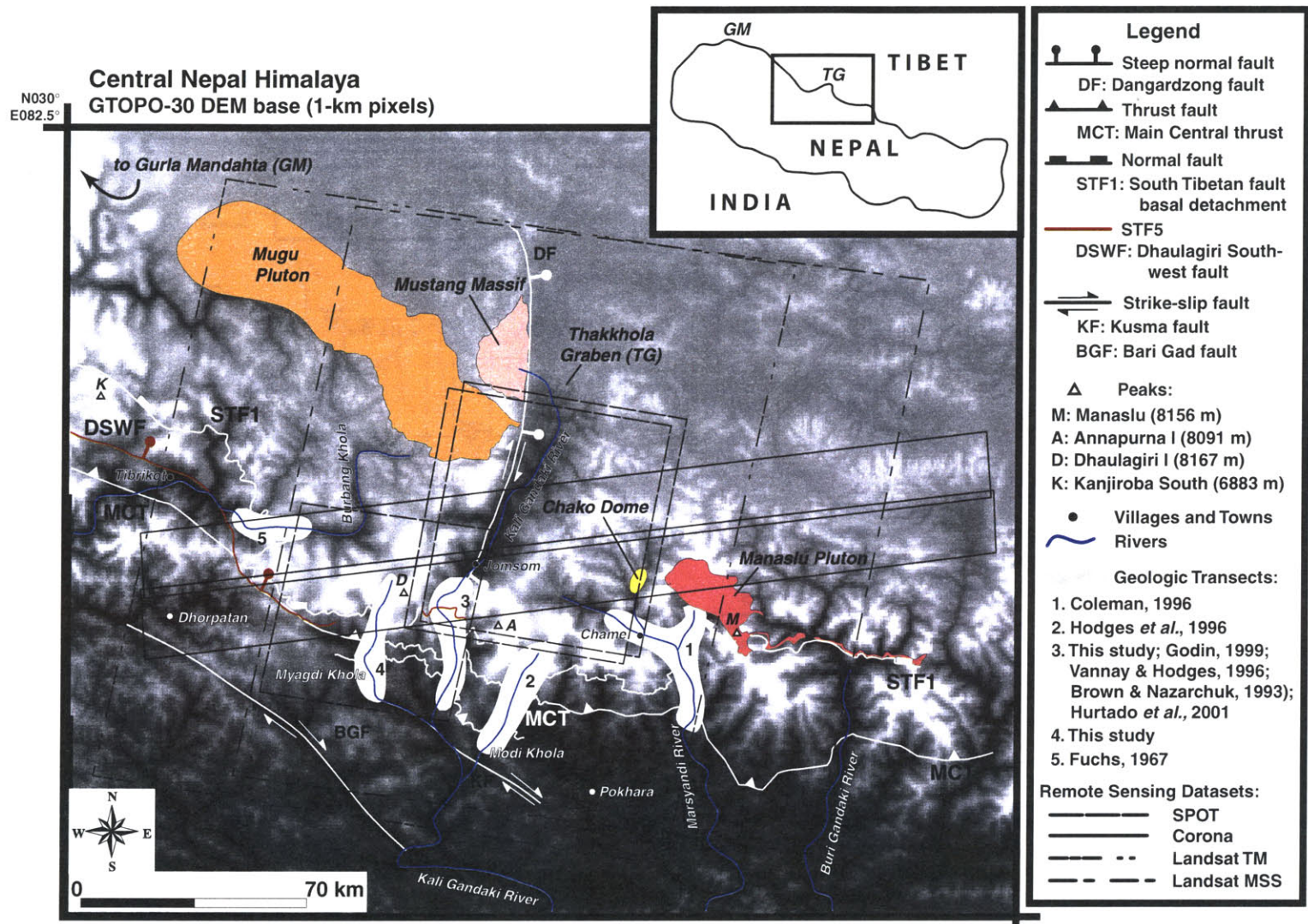


Figure 1a

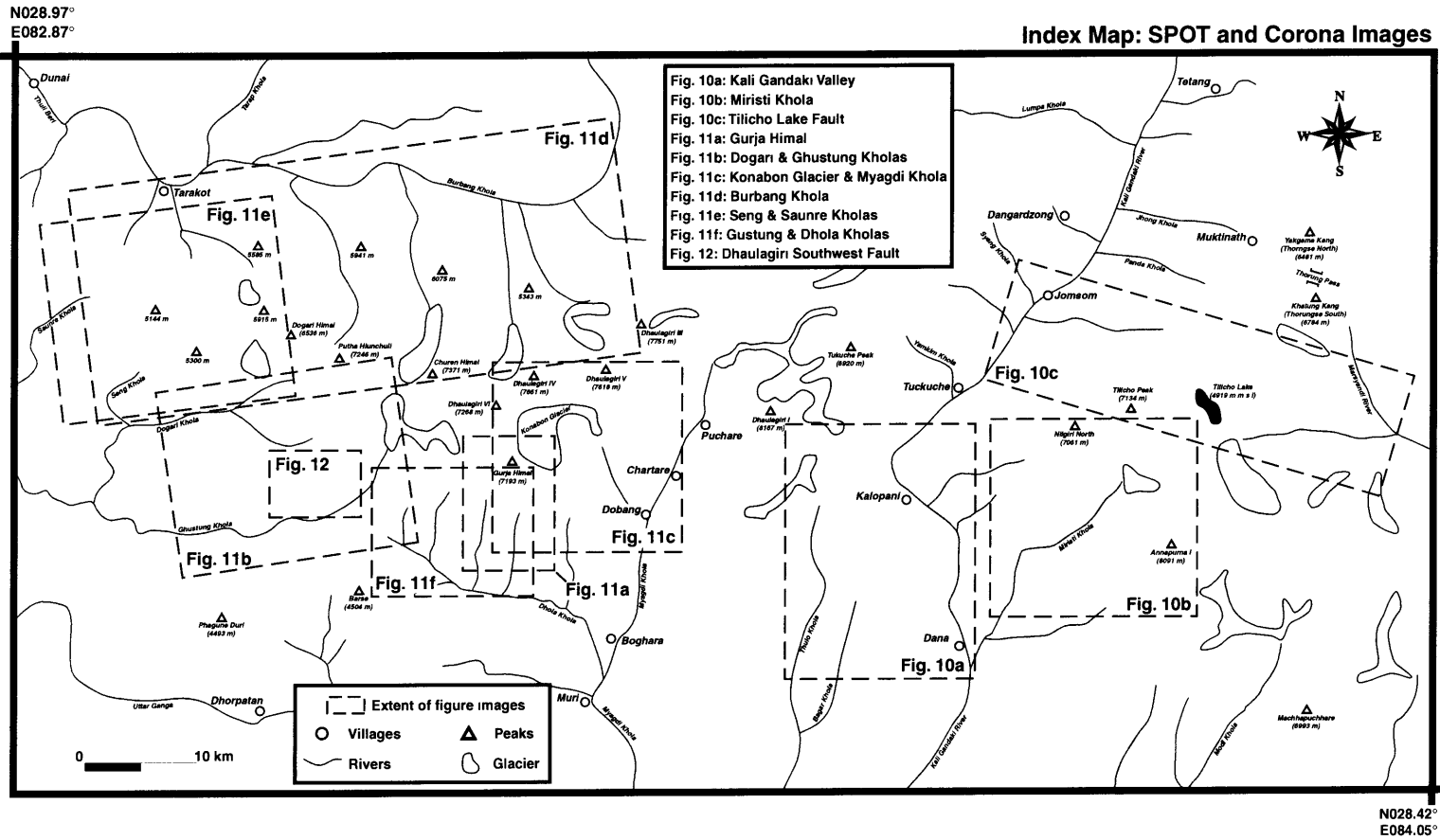


Figure 1b

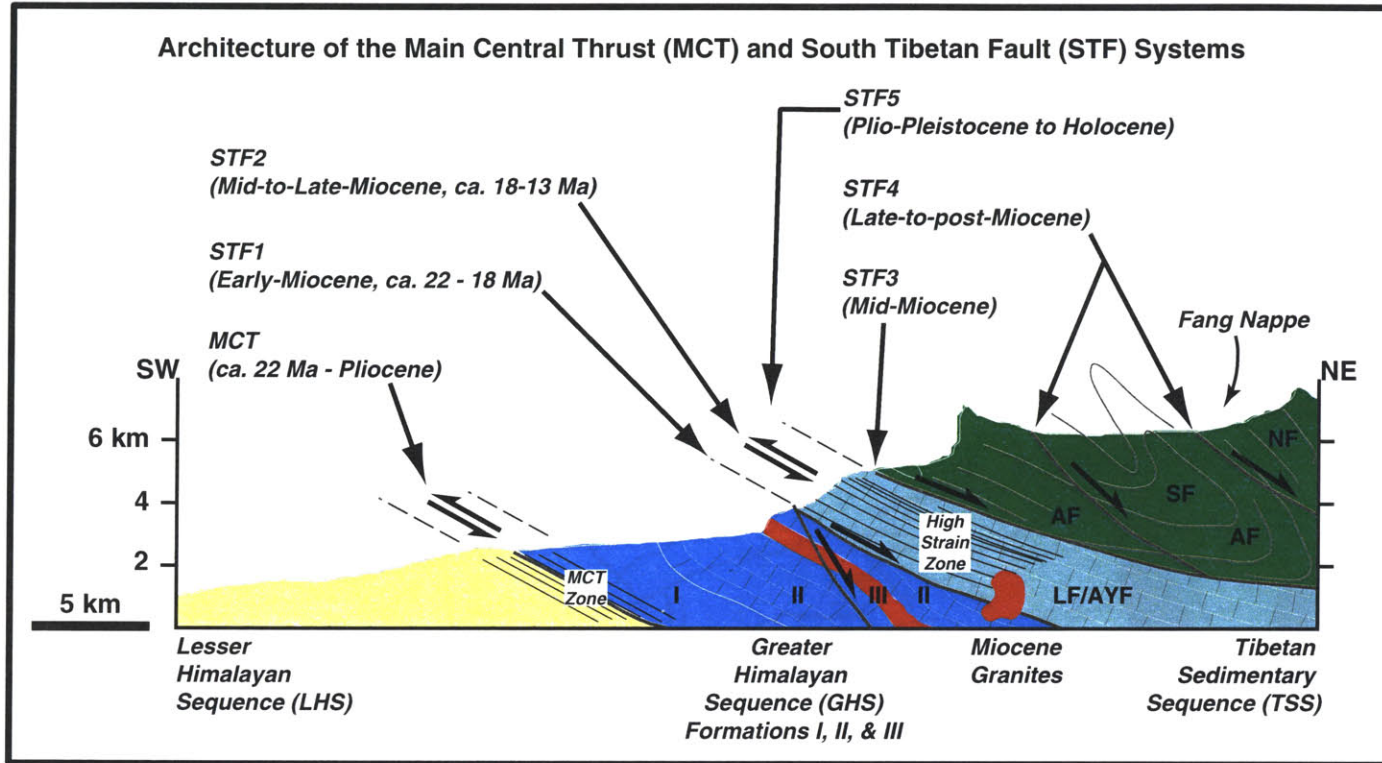


Figure 2

N029.00°
E083.43°

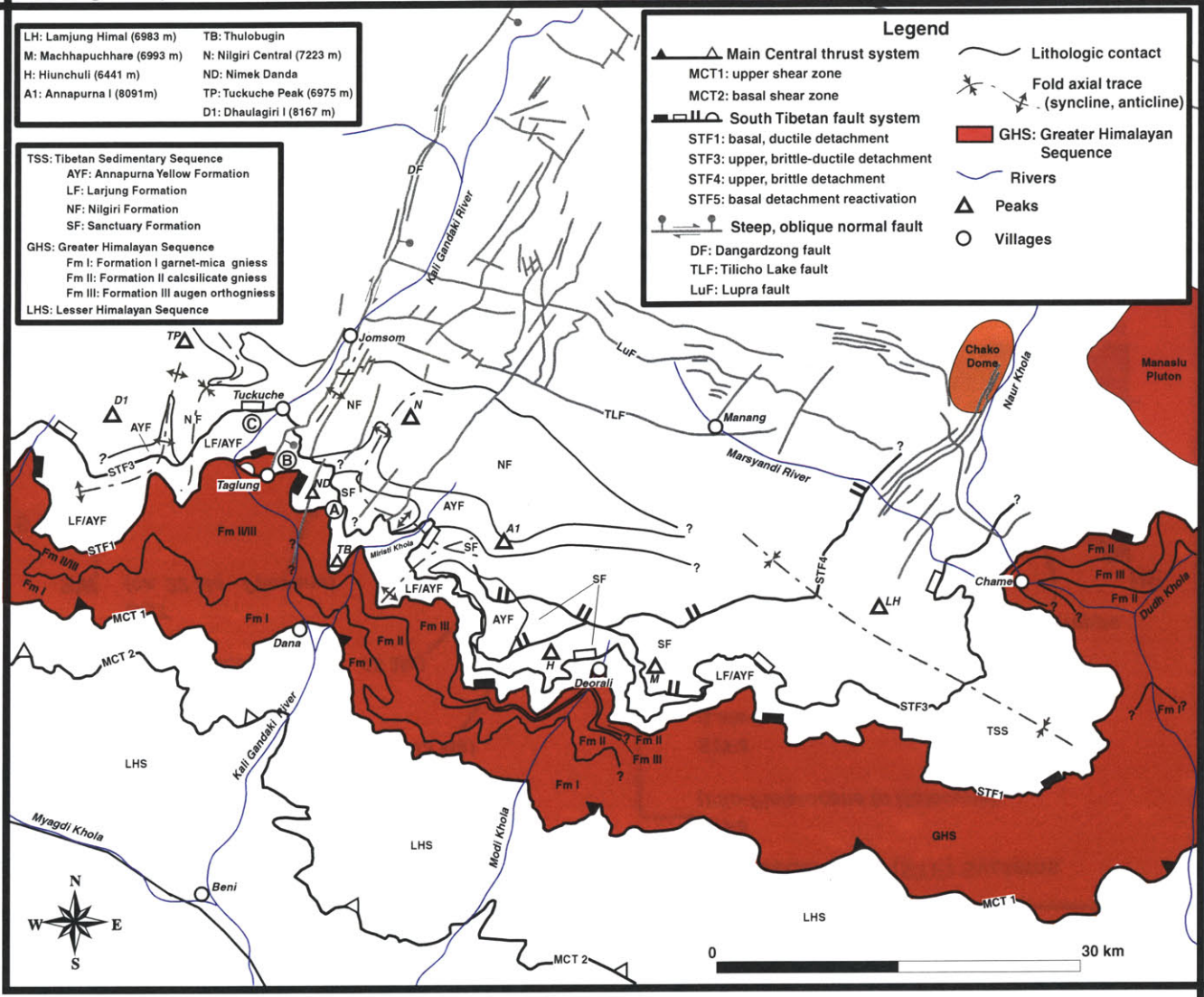
Geologic Map of the Annapurna Himalaya, Central Nepal

- | | |
|----------------------------|-----------------------------|
| LH: Lamjung Himal (6983 m) | TB: Thulobugin |
| M: Machhapuchhare (6993 m) | N: Nilgiri Central (7223 m) |
| H: Hiunchuli (6441 m) | ND: Nimek Danda |
| A1: Annapurna I (8091m) | TP: Tuckuche Peak (6975 m) |
| | D1: Dhaulagiri I (8167 m) |

- TSS: Tibetan Sedimentary Sequence**
 AYF: Annapurna Yellow Formation
 LF: Larjung Formation
 NF: Nilgiri Formation
 SF: Sanctuary Formation
- GHS: Greater Himalayan Sequence**
 Fm I: Formation I garnet-mica gneiss
 Fm II: Formation II calcisilicate gneiss
 Fm III: Formation III augen orthogneiss
- LHS: Lesser Himalayan Sequence**

Legend

- ▲▲ Main Central thrust system
- MCT1: upper shear zone
- MCT2: basal shear zone
- ▬ South Tibetan fault system
- STF1: basal, ductile detachment
- STF3: upper, brittle-ductile detachment
- STF4: upper, brittle detachment
- STF5: basal detachment reactivation
- ↗ Steep, oblique normal fault
- DF: Dangardzong fault
- TLF: Tilicho Lake fault
- LuF: Lupa fault
- Lithologic contact
- ✱ Fold axial trace (syncline, anticline)
- GHS: Greater Himalayan Sequence
- Rivers
- ▲ Peaks
- Villages



N028.25°
E084.38°

Figure 3

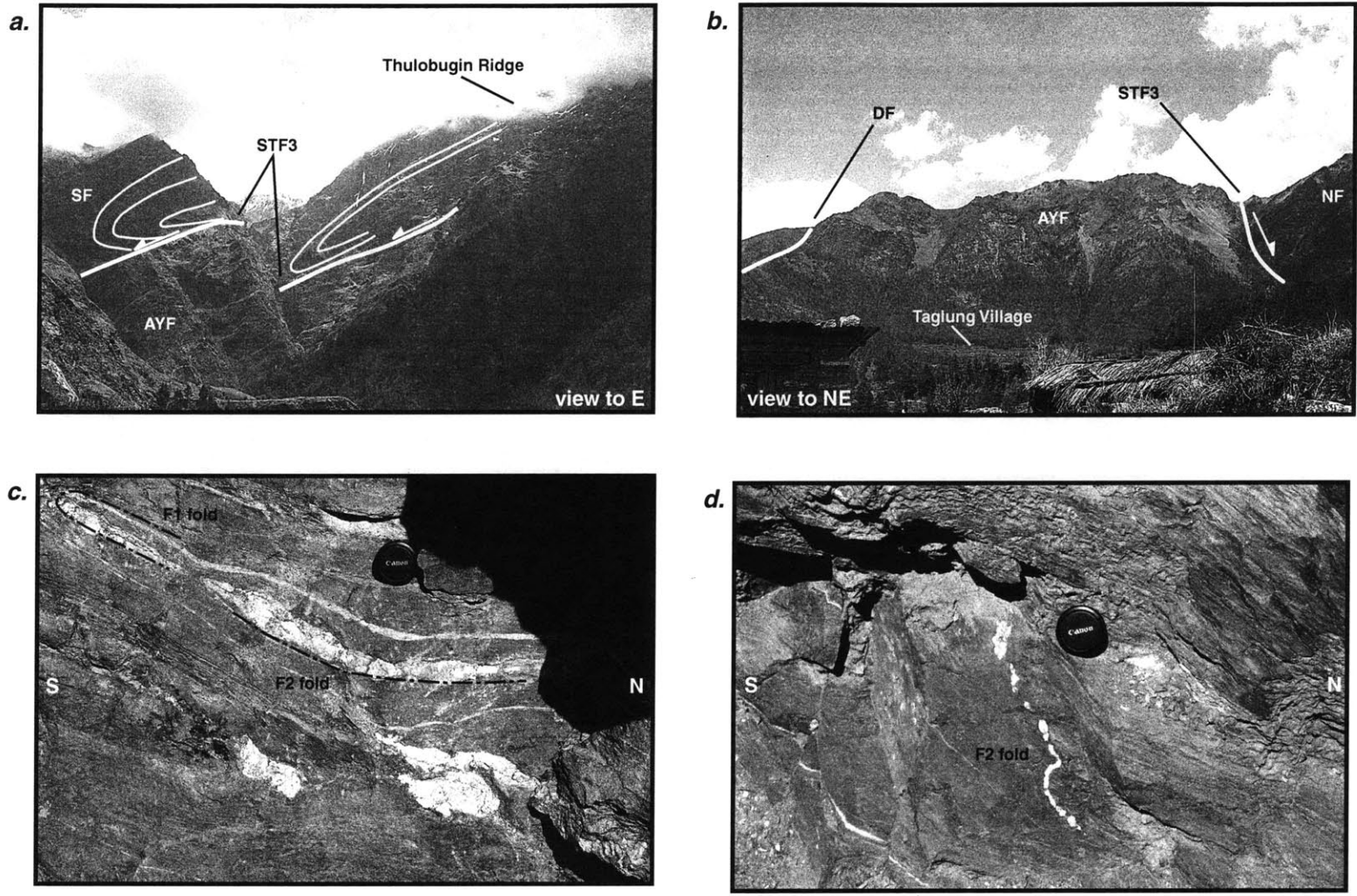


Figure 4

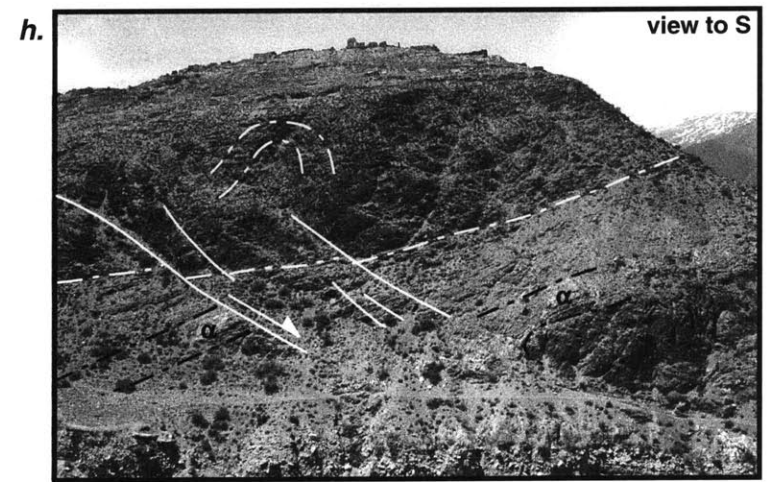
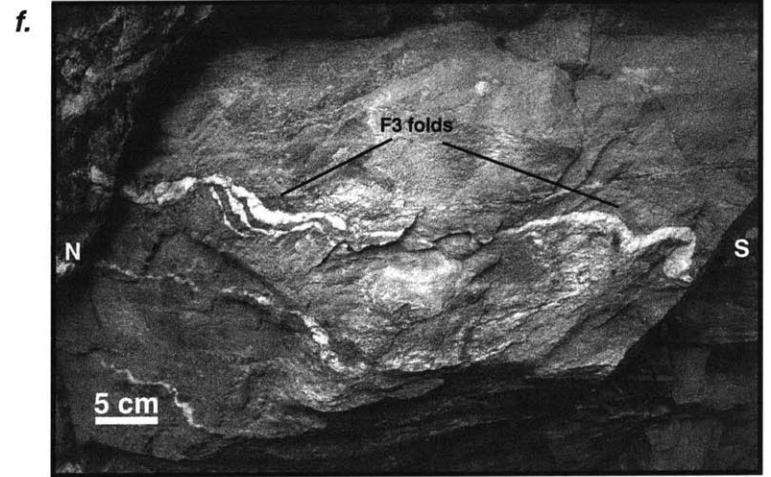


Figure 4 <continued>

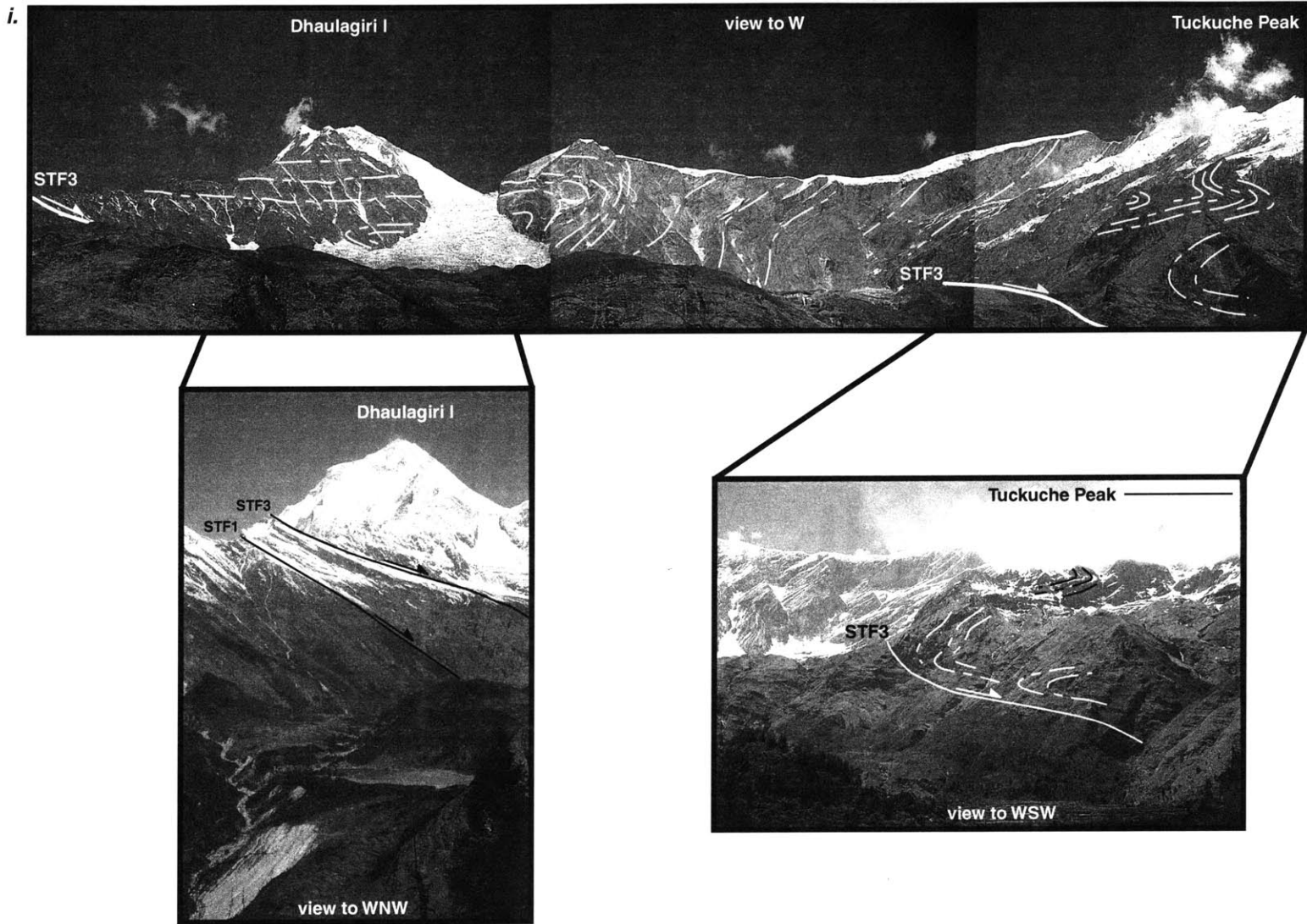


Figure 4 <continued>

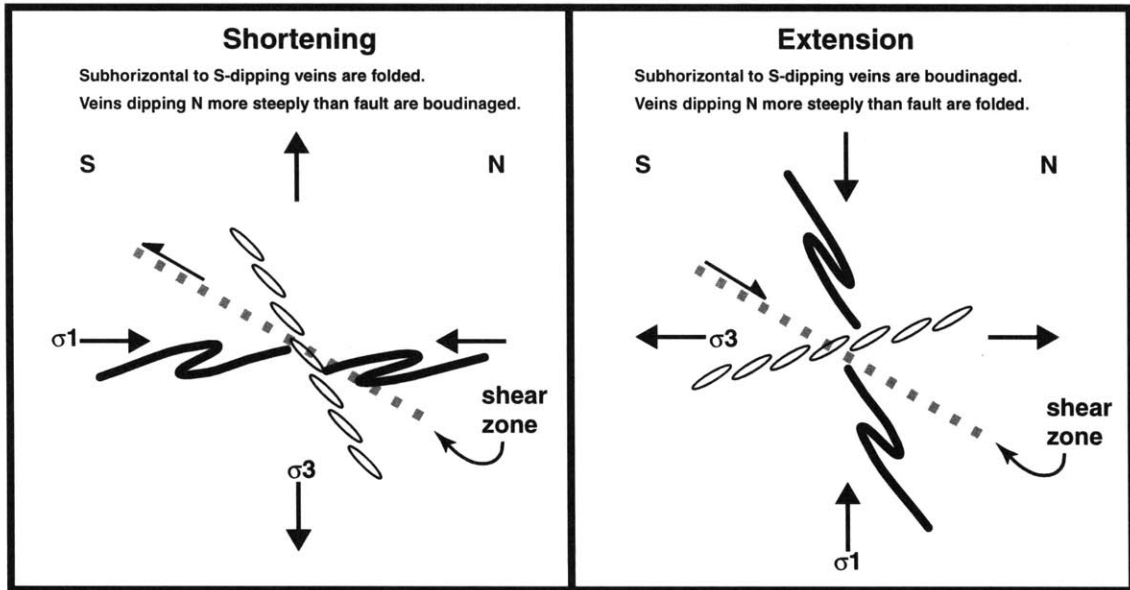
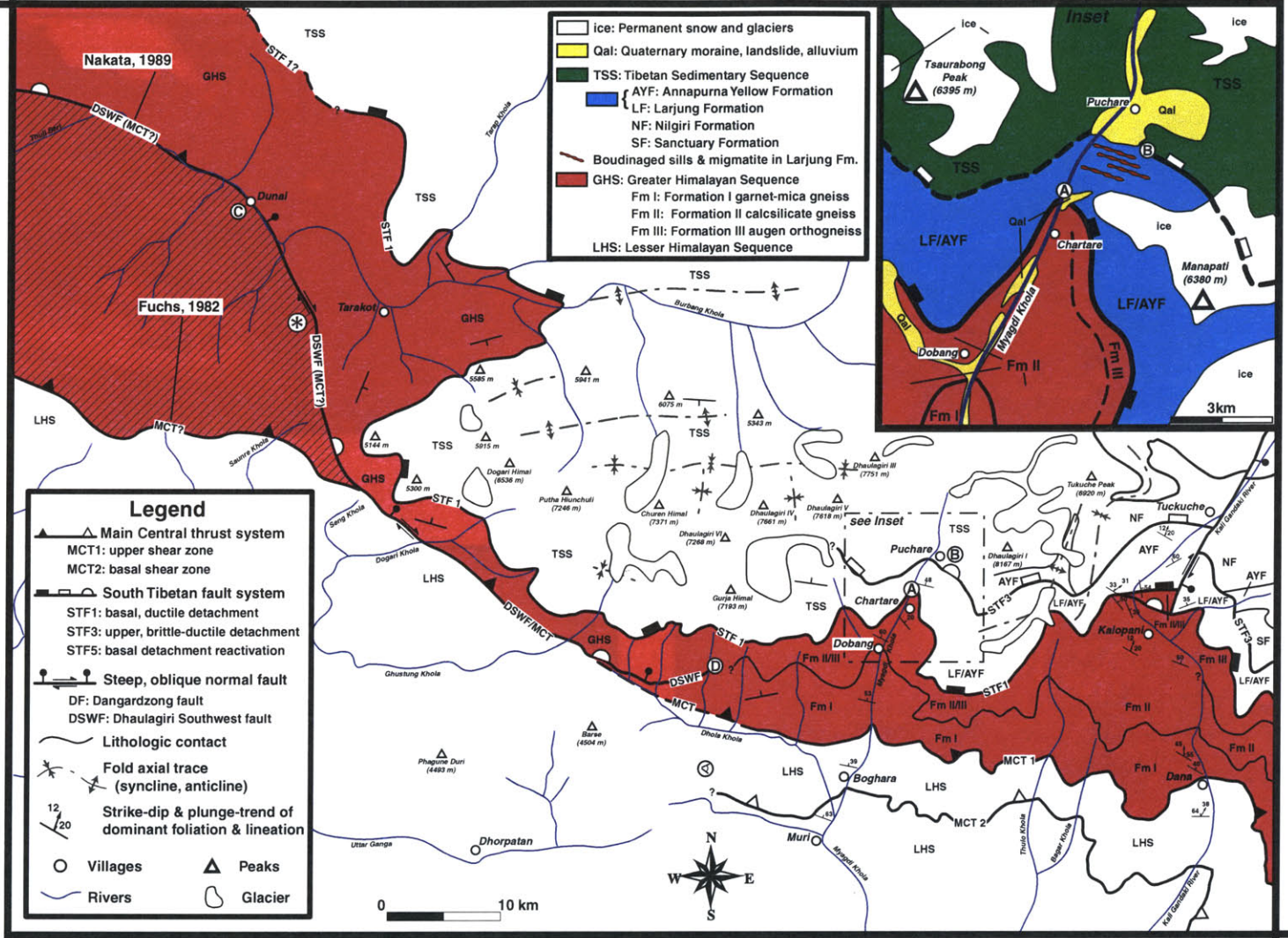


Figure 5

N029.08°
E082.66°

Geologic Map of the Dhaulagiri Himalaya, Central Nepal



139

Figure 6

N028.43°
E083.70°

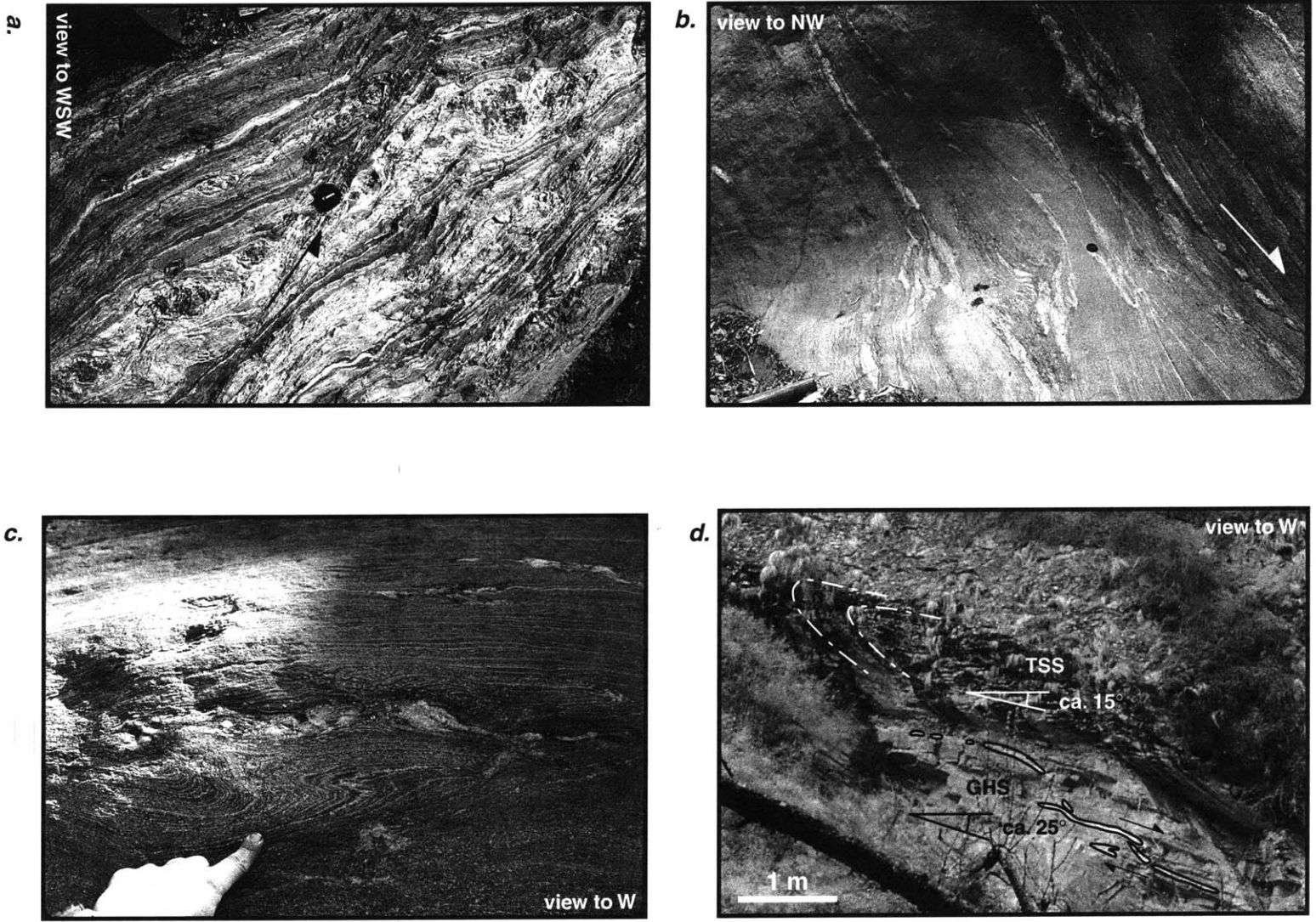


Figure 7

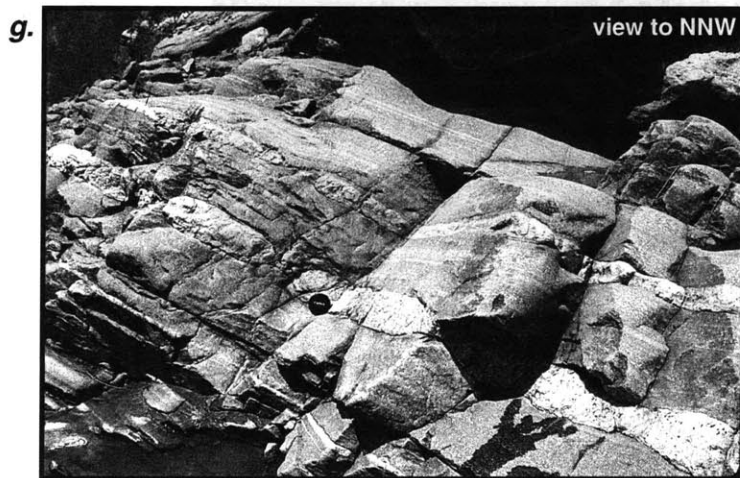
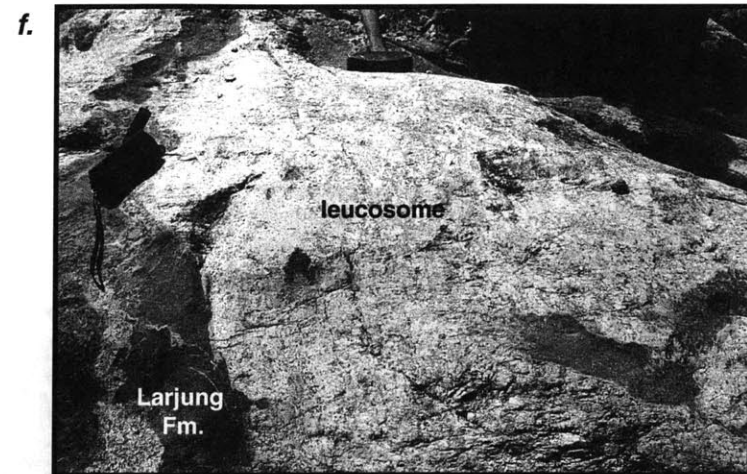
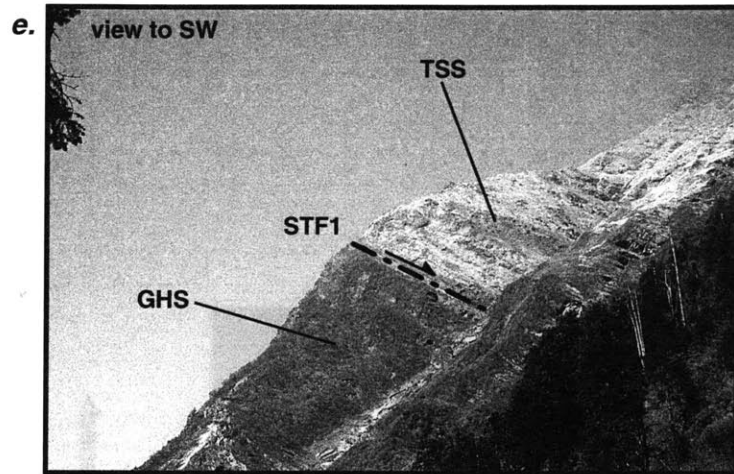


Figure 7 <continued>

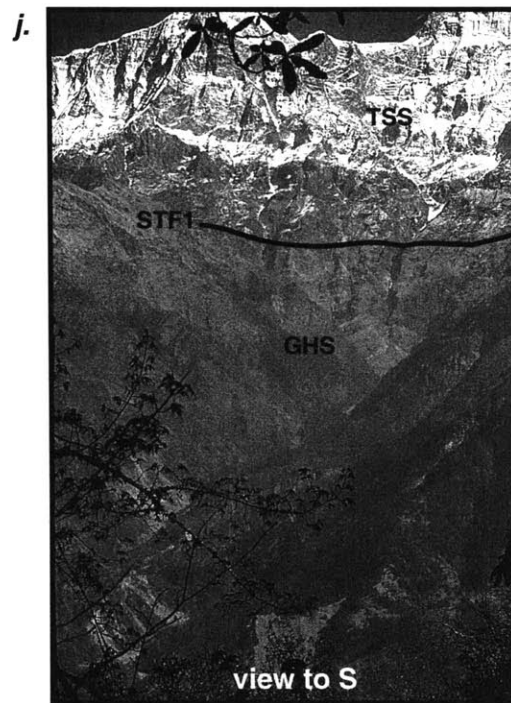
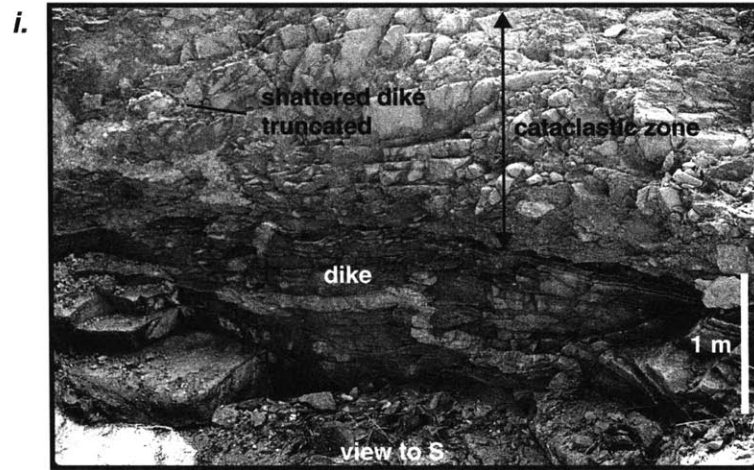


Figure 7 <continued>

Chapter 3: Integration of field geologic and remote sensing data

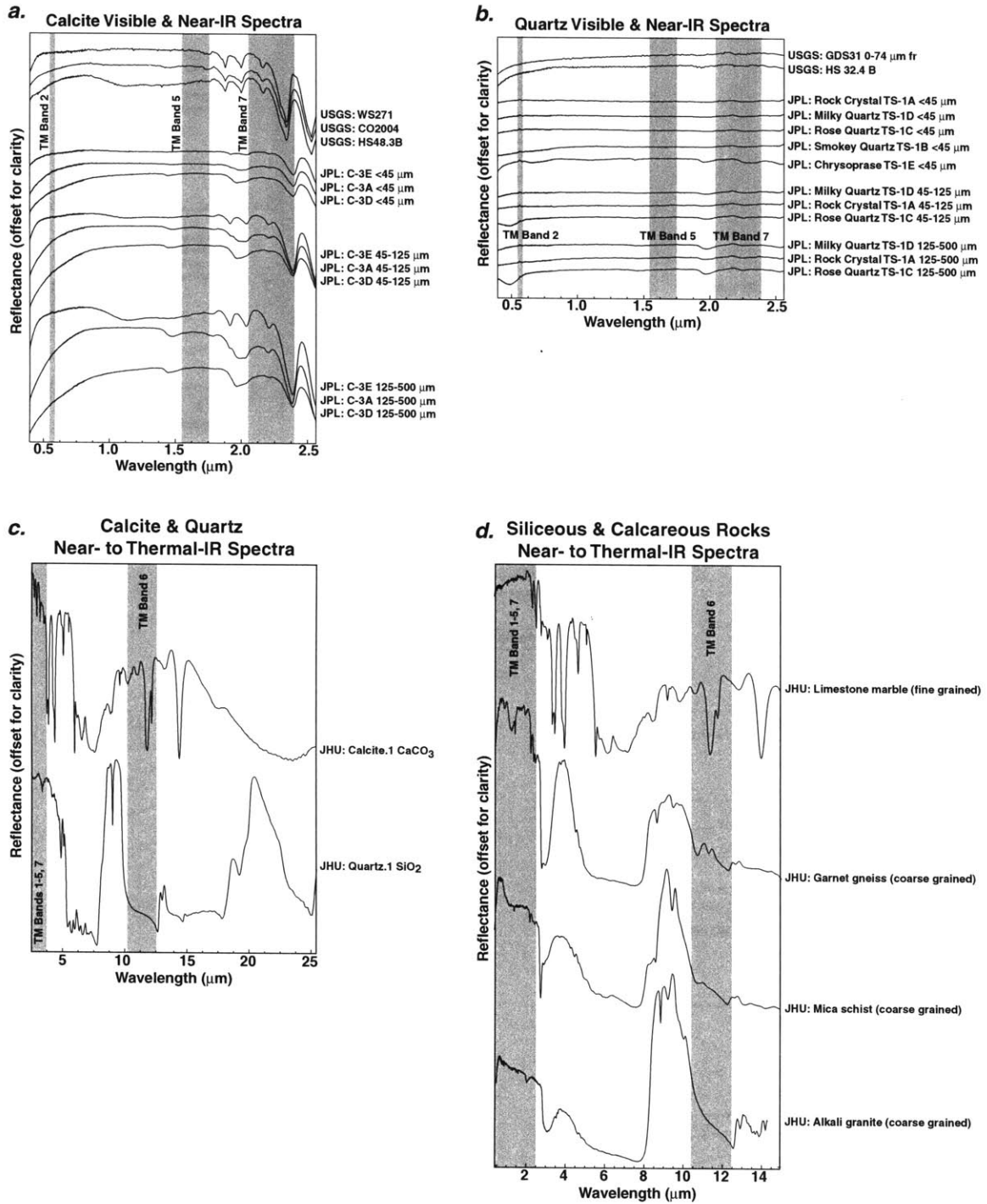


Figure 8

Chapter 3: Integration of field geologic and remote sensing data

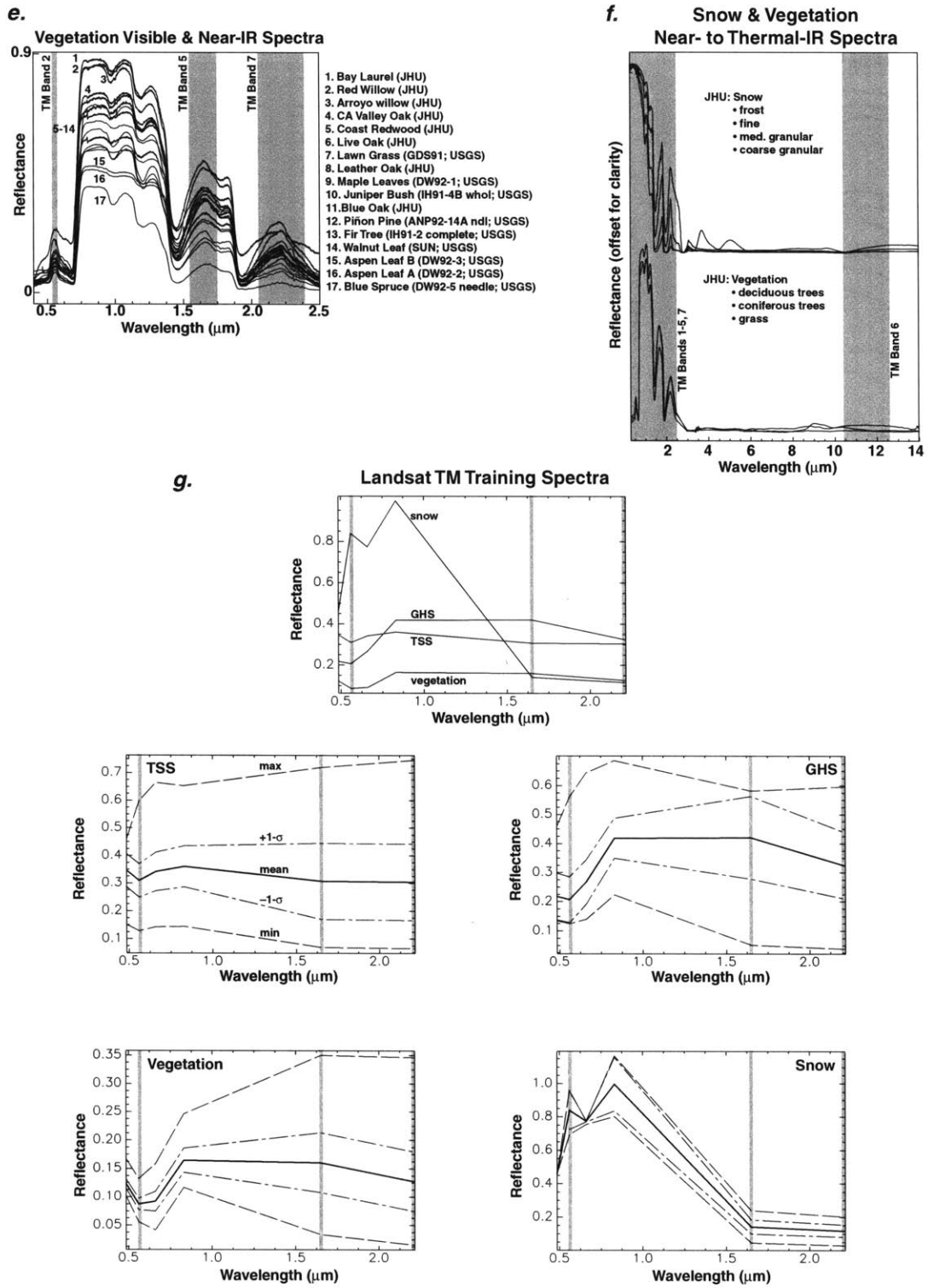
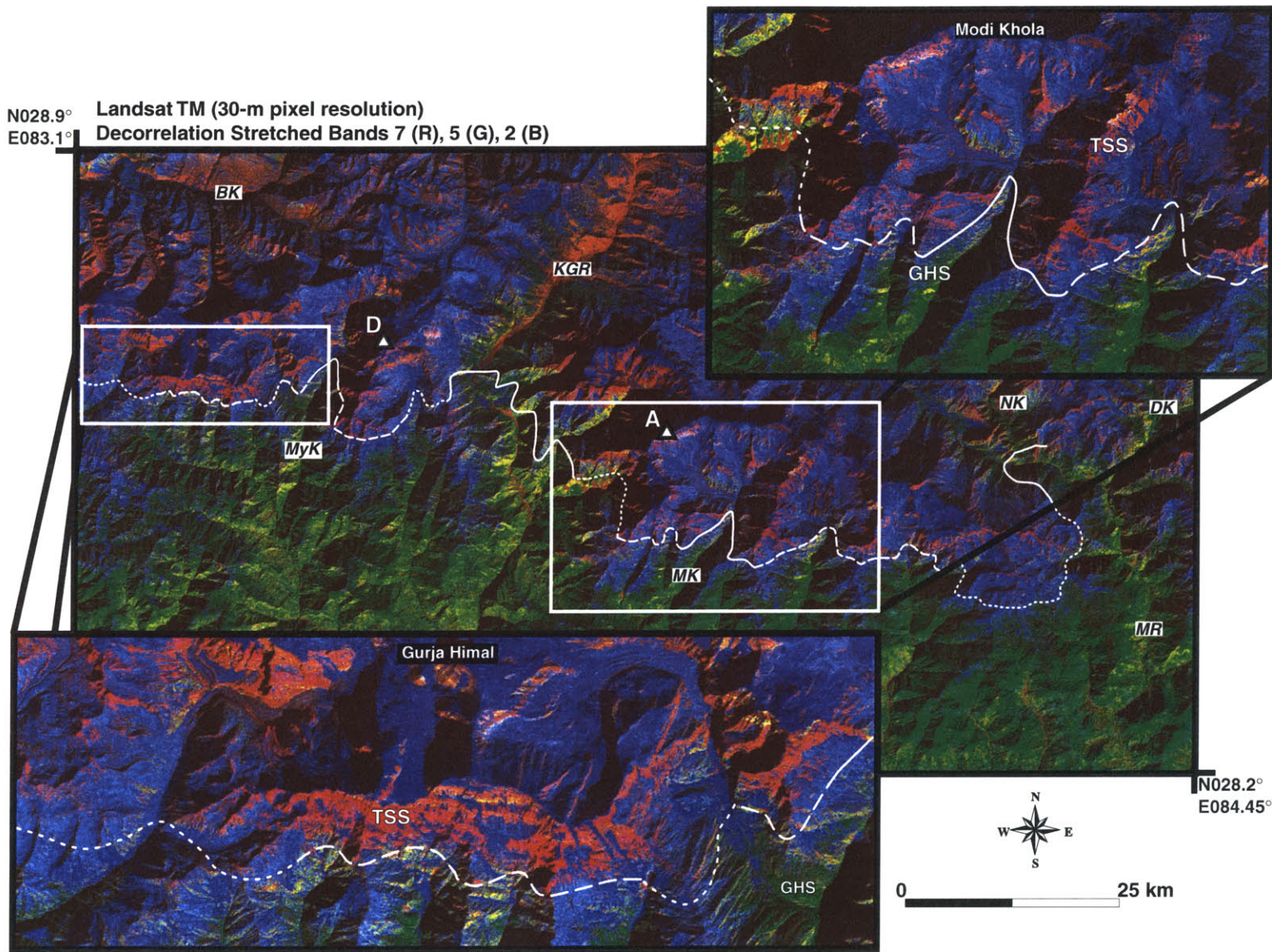
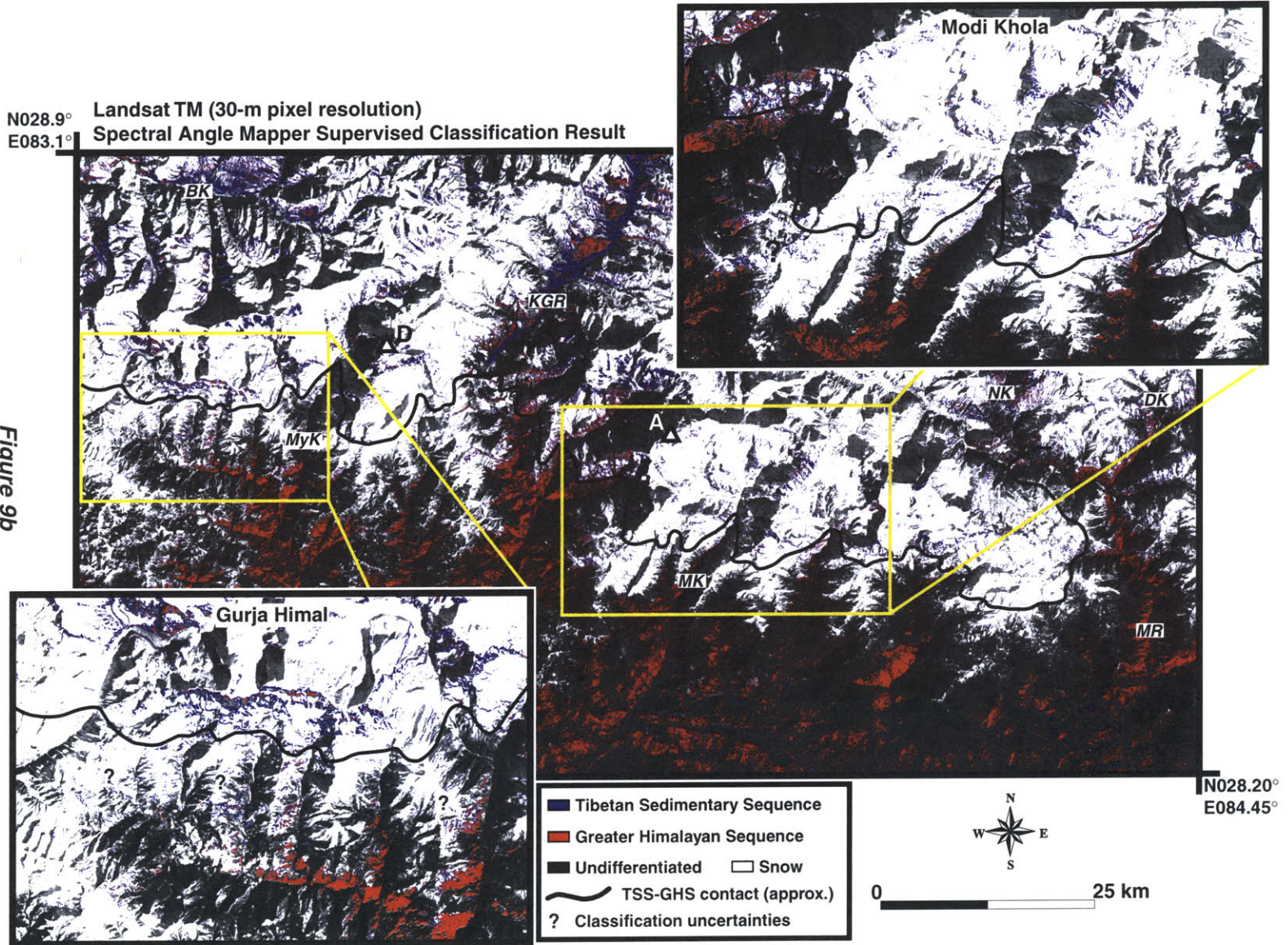


Figure 8 <continued>





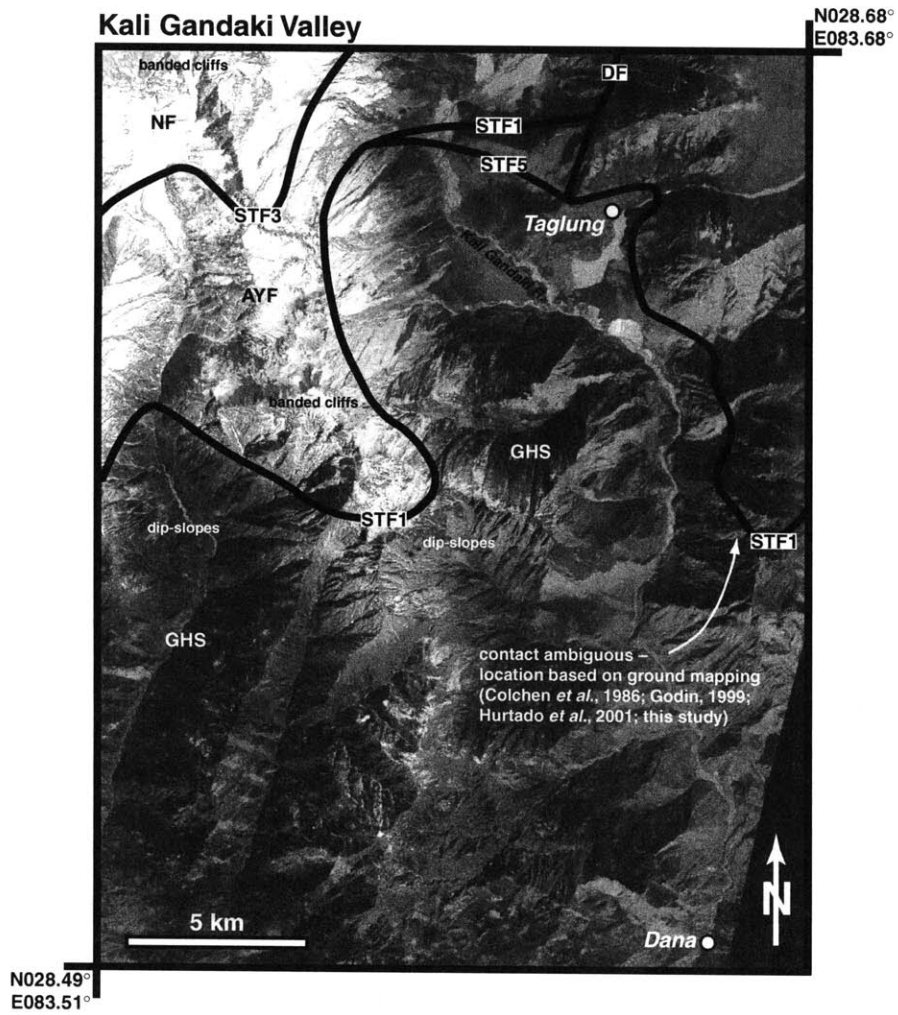


Figure 10a

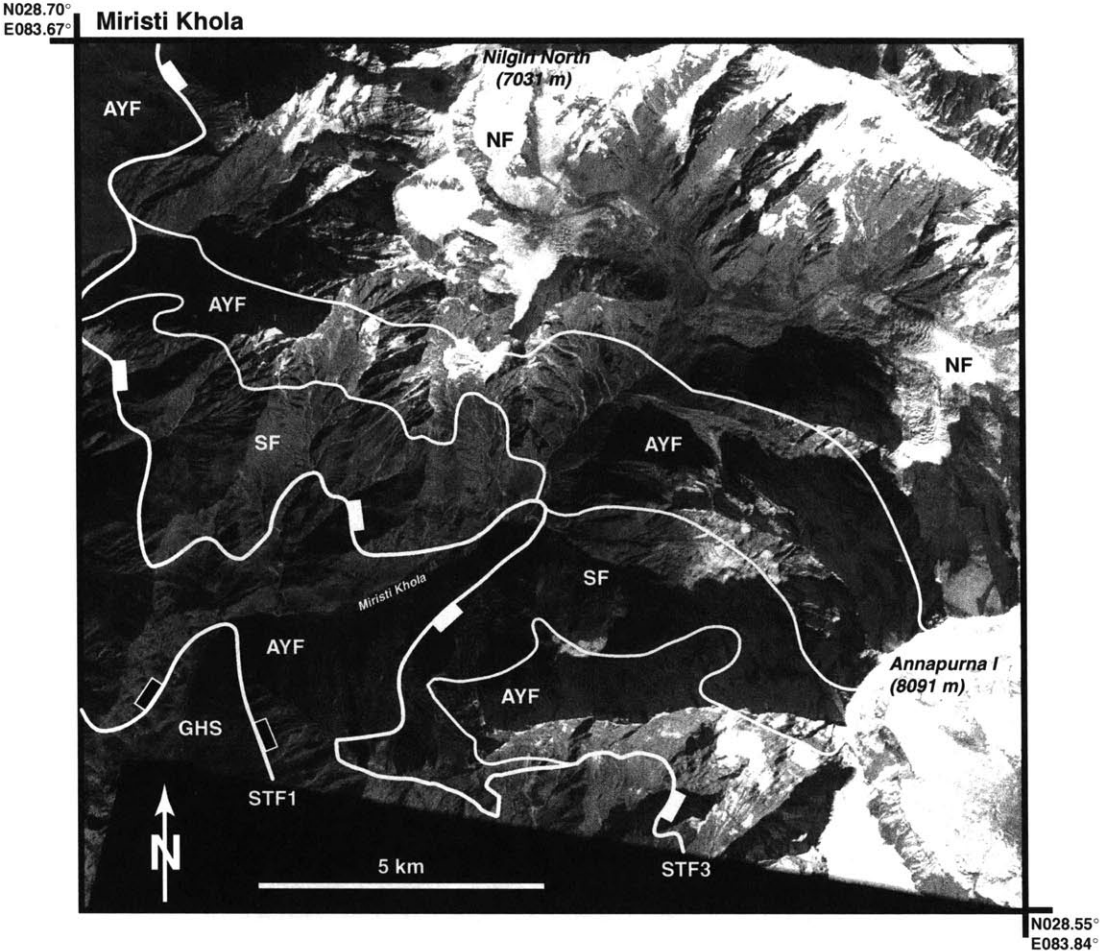


Figure 10b



Figure 10c

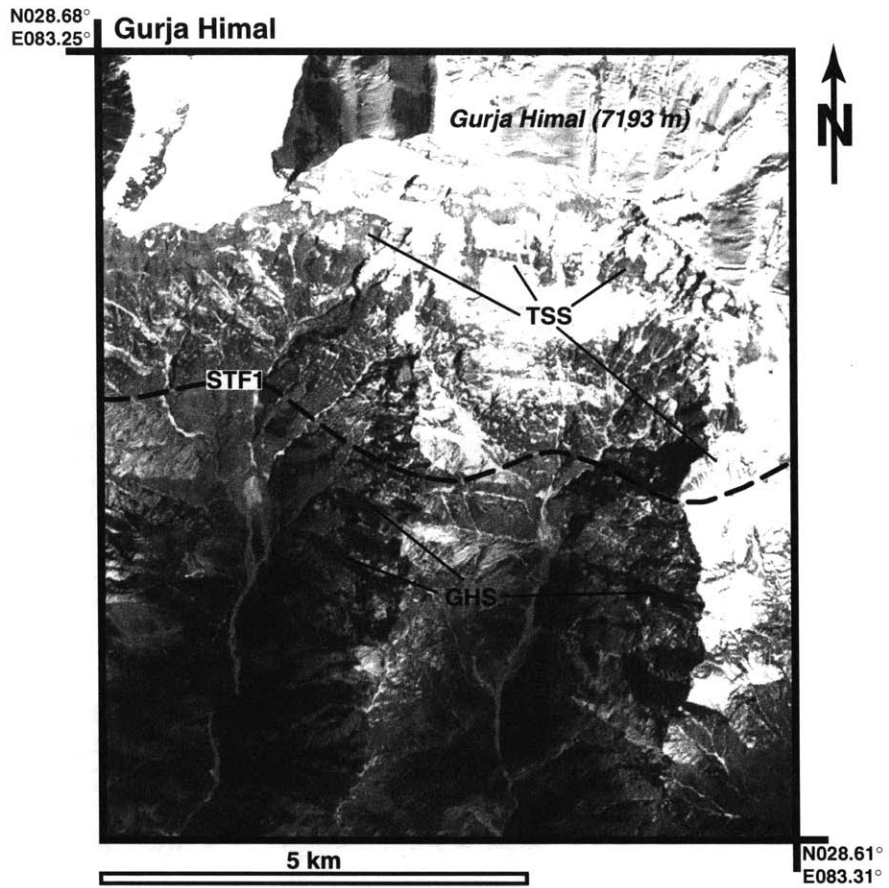


Figure 11a

Dogari Khola and Ghustung Khola

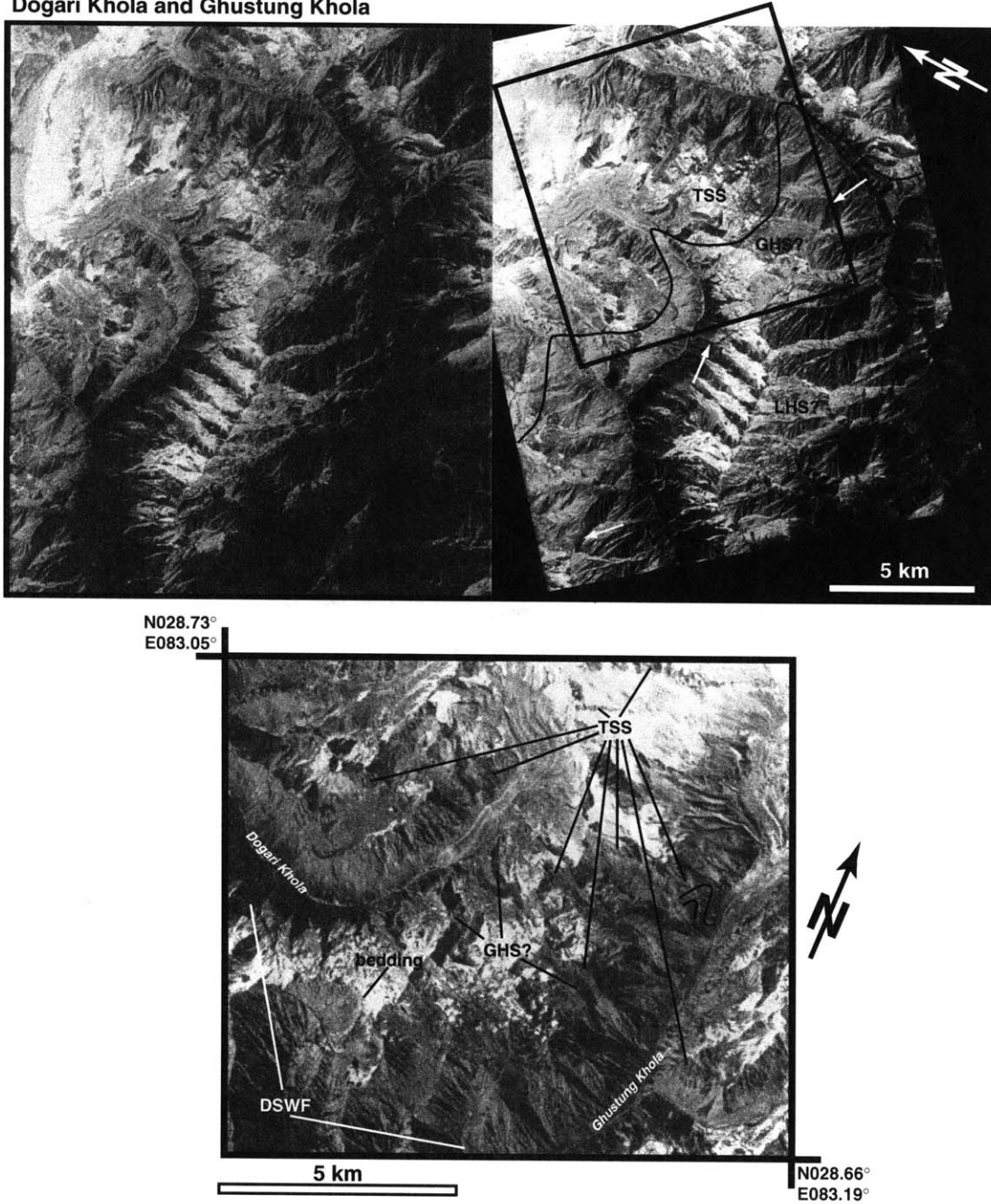


Figure 11b

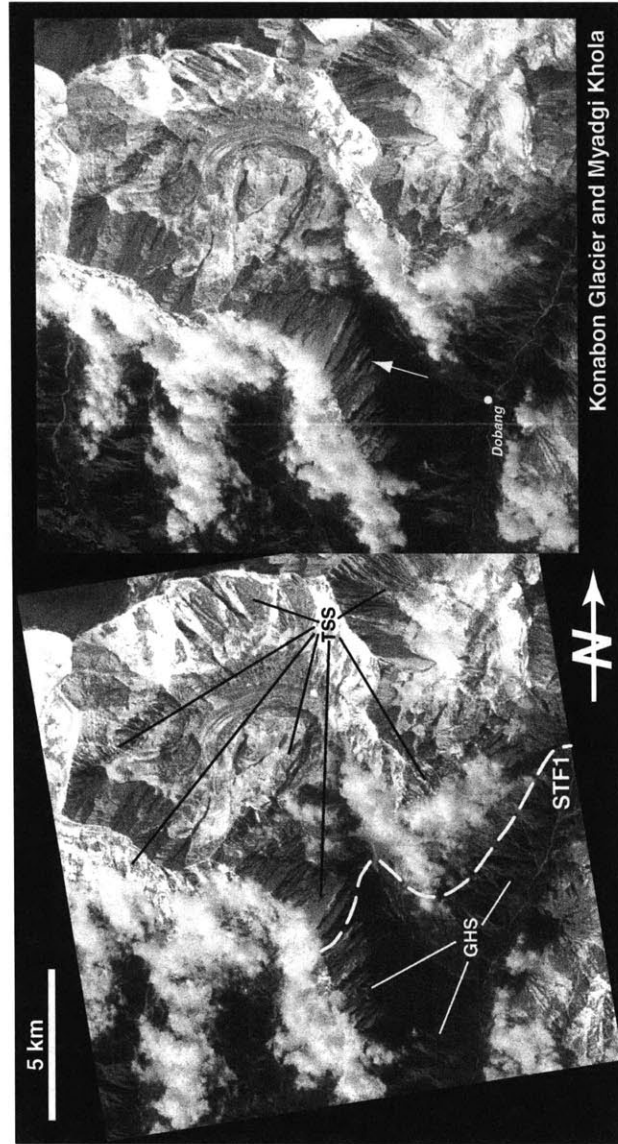


Figure 11c

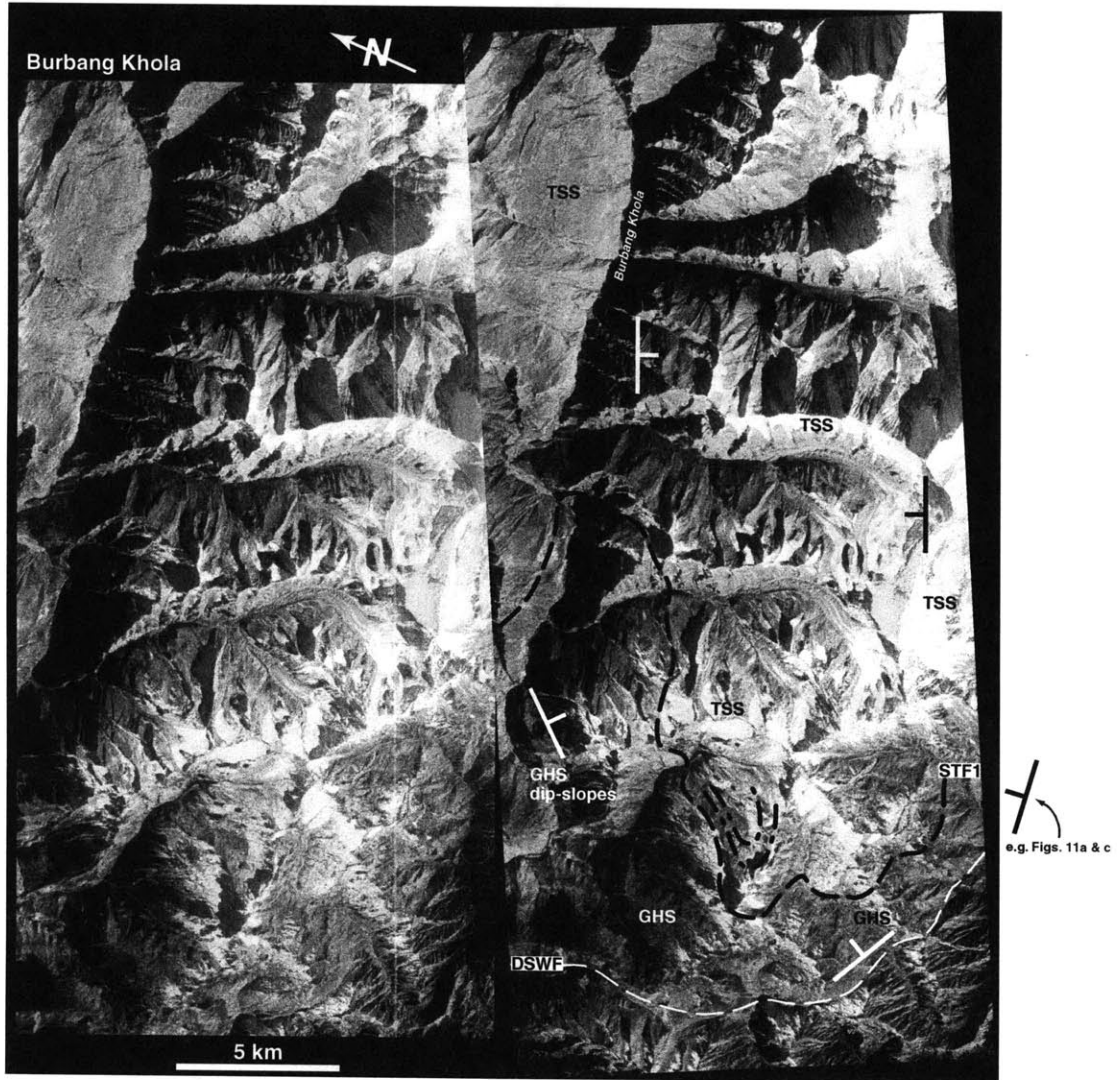


Figure 11d

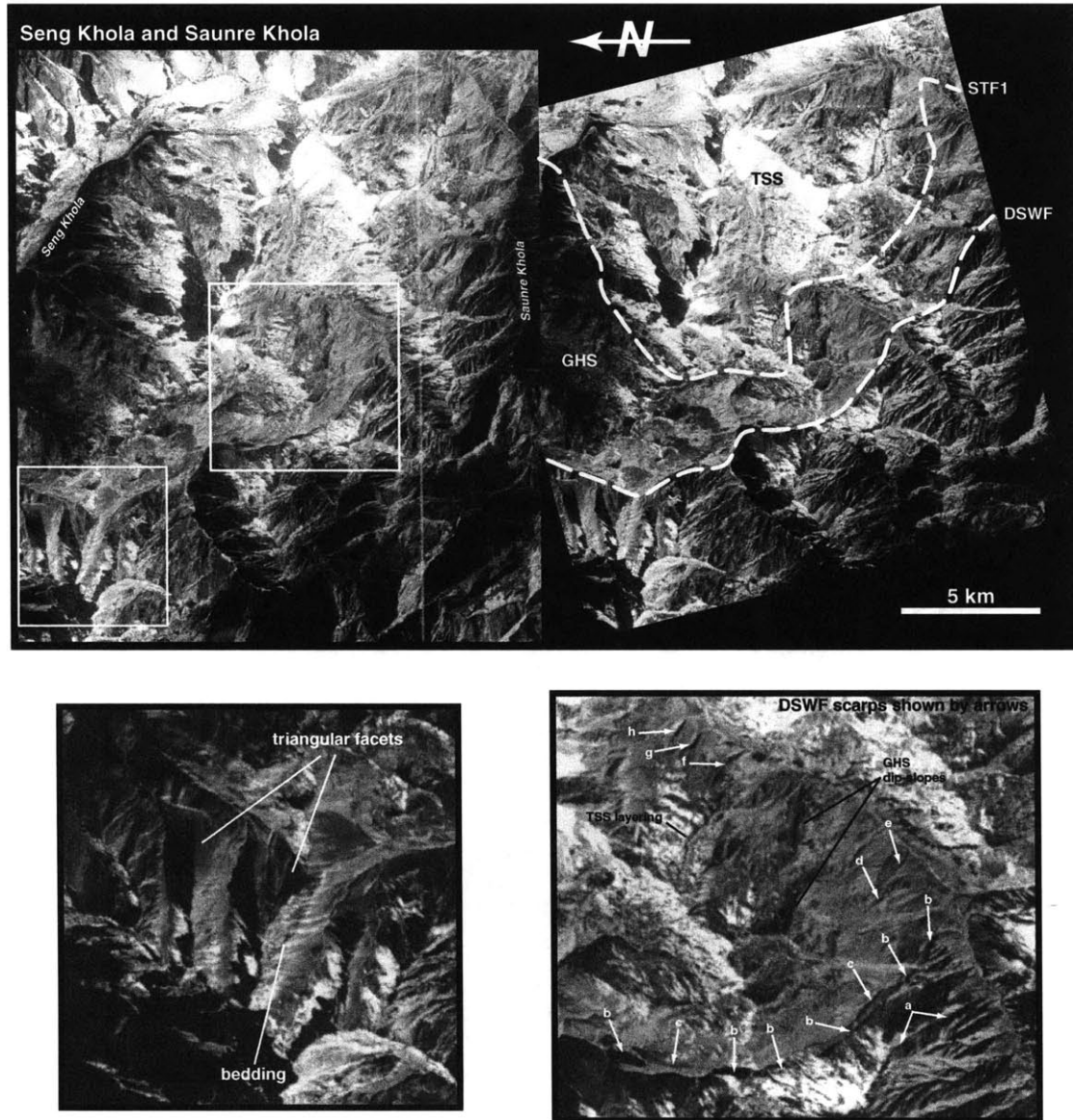


Figure 11e

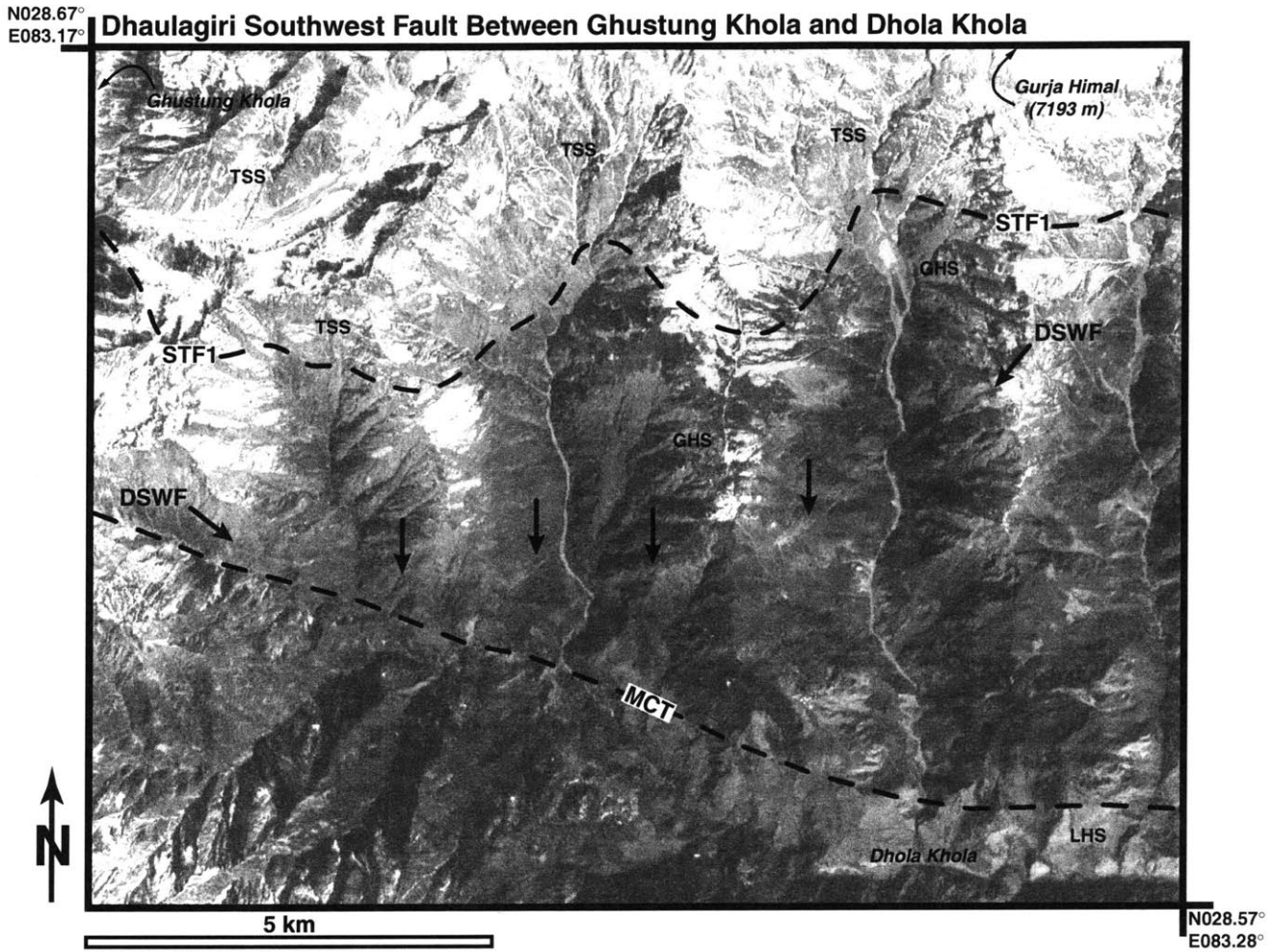


Figure 11f

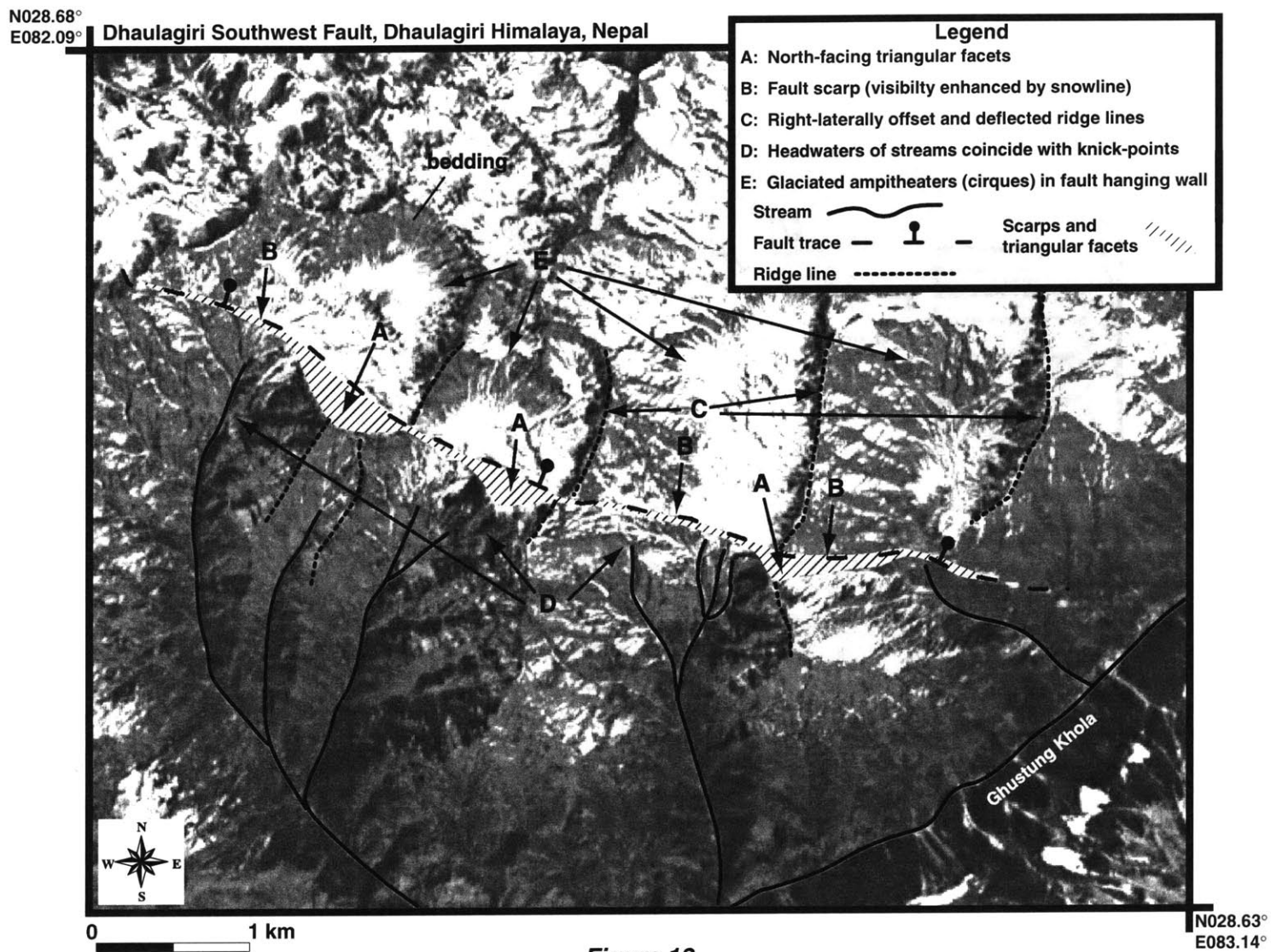
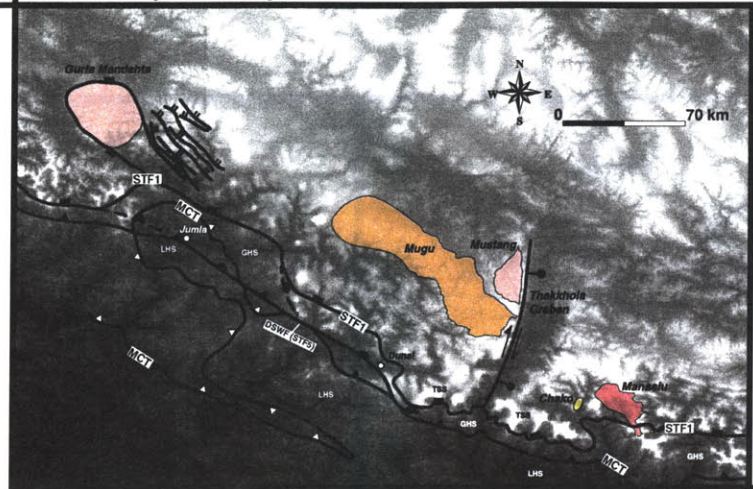
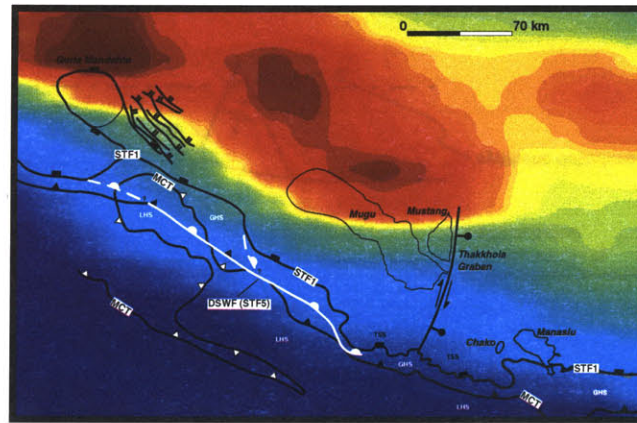


Figure 12

N031°
E080.89° Western Nepal Himalaya

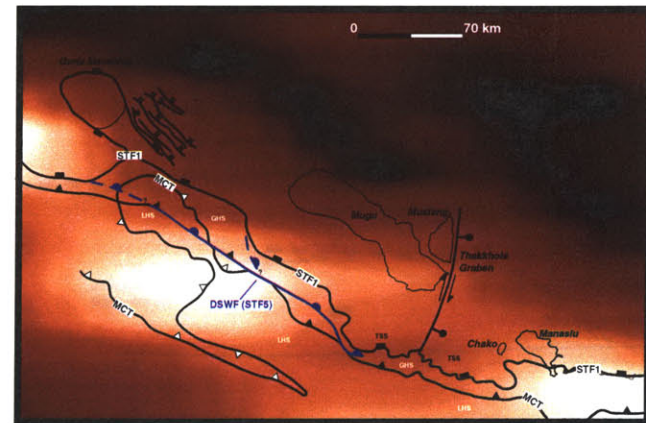


N028.21°
E085.22°



-4.29e12 N m⁻¹ 5.14e12 N m⁻¹

Gravitational Potential Energy Anomaly



4.54e8 N m⁻¹ km⁻¹ 5.68e10 N m⁻¹ km⁻¹

Gravitational Potential Energy Anomaly Gradient

Figure 13

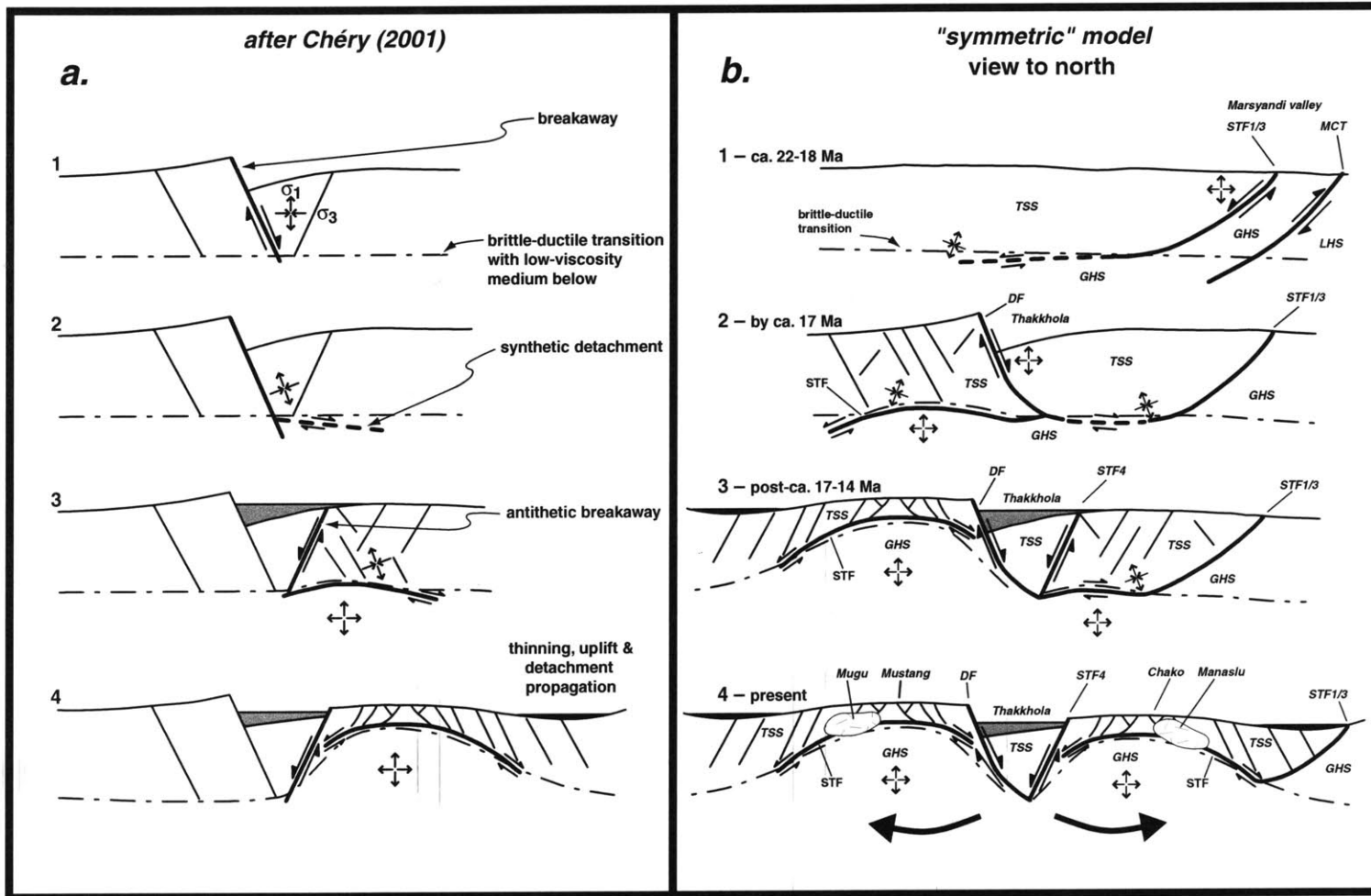


Figure 14

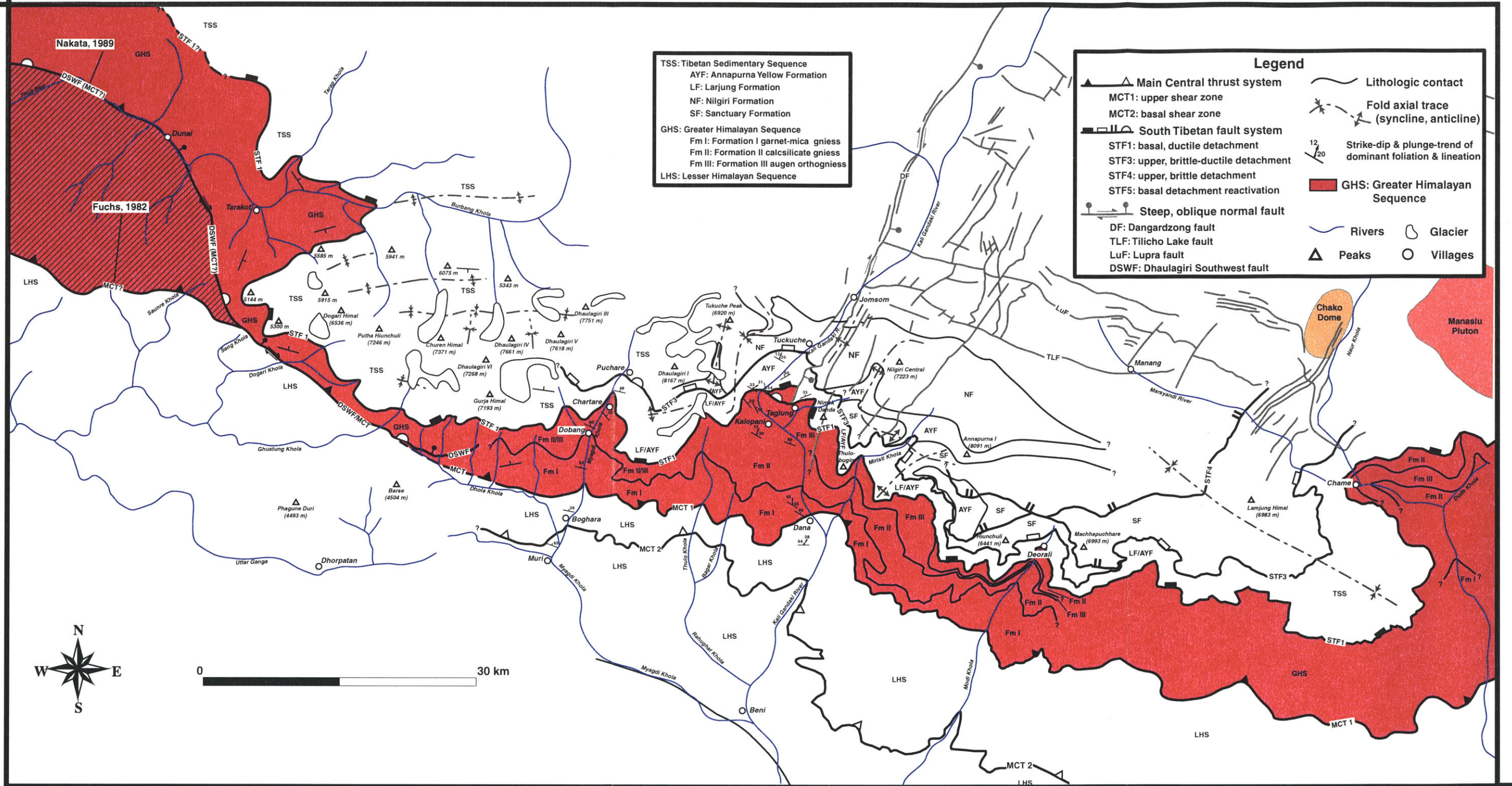
APPENDIX

Figure A1. Geologic map of the Dhaulagiri-Thakkhola-Annapurna region of the central Nepal Himalaya. This map is a composite of Figures 3 and 6 of Chapter 3, and incorporates our image interpretation, multispectral remote sensing analyses, and field observations as well as previously published mapping. In particular, we have incorporated mapping – with substantial reinterpretations – by Coleman (1996b), Colchen *et al.* (1986), Godin (1999), Hodges *et al.* (1996), Nakata (1989), Hashimoto *et al.* (1973) and Fuchs (1967). In particular, our mapping and reinterpretation was aimed towards extending the geology of the Annapurna Himalaya to the west, linking and interrelating the various strands of the South Tibetan fault system. The legend describes the symbology used to depict the stratigraphy, structure, and geography. Note that the STF nomenclature used for the South Tibetan fault system (see Chapter 3 text) is complicated by the fact that the youngest component, STF5, is structurally transgressive, reactivating or cutting across older structures at a range of structural levels. As such, the rounded ornament (see legend), when used in conjunction with other ornaments and label, denotes an MCT or STF structure that has been modified or reactivated by STF5.

Note the large-scale synformal structure in the Tibetan Sedimentary Sequence in the far eastern Annapurna range (Schneider and Masch, 1993; Garzanti *et al.*, 1994; Coleman, 1996a). There are similar, large-scale anti- and synformal structures in the far western Dhaulagiri range. A progressive change in the thickness and strike of the Greater Himalayan Sequence (GHS) is also evident in the far western Dhaulagiri range, one that mirrors the similar transition in the far eastern Annapurna range. These transitions are marked by stretches of STF1 with anomalous orientations. Finally, note the two possible traces for the Main Central thrust (MCT) and the relationships between the thin GHS, STF1, the MCT, and the Dhaulagiri Southwest fault (DSWF). The geometry shown by the solid red field results in a GHS thickness of ca. 30 km in western Nepal versus as little as ca. 2 km in the Dhaulagiri Himalaya. Requiring the MCT and DSWF to remain coplanar (red, ruled field) results in a minimum thickness of ca. 15-20 km in western Nepal, still substantially thicker than elsewhere in the Annapurna and Dhaulagiri Himalaya (with the exception of the Kali Gandaki River transect).

Geologic Map of the Dhaulagiri-Thakkhola-Annapurna Region, Central Nepal Himalaya

N029.08°
E082.66°



N028.25°
E084.38°

Figure A1

Chapter 4:

Geochronologic and structural constraints on the exhumational history of the Mustang and Mugu granites: Implications for the development of the Thakkhola graben, central Nepal Himalaya

For submission to *Tectonics*

Chapter 4: Geochronologic and structural constraints on the exhumational history of the Mustang and Mugu granites: Implications for the development of the Thakkhola graben, central Nepal Himalaya

José M. Hurtado, Jr. *
Kip V. Hodges
Jahandar Ramezani
Samuel A. Bowring

Department of Earth, Atmospheric, and Planetary Sciences
Massachusetts Institute of Technology
Cambridge, Massachusetts

* address: MIT EAPS 54-1022, 77 Massachusetts Avenue, Cambridge, MA 02139-4307
email: hurtado@MIT.EDU

ABSTRACT

The Thakkhola graben intersects the South Tibetan fault (STF) system and bounds one of the North Himalayan gneiss domes, the Upper Mustang massif (UMM). These structures, representative of the three major types of extensional systems in the Himalayan-Tibetan orogen, are structurally and kinematically linked. The UMM comprises a half-domical mountain range cored by amphibolite-facies metasedimentary rocks and an igneous complex including two plutons, the Mugu and Mustang granites. The eastern margin of the UMM is defined by the main bounding structure of the Thakkhola graben – the Dangardzong fault – so it is clear that development of the graben has greatly affected the exhumational history of the UMM. We report structural and geochronologic data from two transects across the Dangardzong fault into the southeastern part of the UMM. We found evidence for several generations of granitic magmatism and five generations of tectonite fabrics that record the progressive structural evolution of the Upper Mustang region from a metamorphic core complex setting to a rift setting. Isotope dilution-thermal ionization mass spectrometry (ID-TIMS) U-Pb analyses yield the first constraint on the age of the Mustang granite (23.35 ± 0.17 Ma), provide a new age constraint for the Mugu intrusive complex (20.76 ± 0.67 Ma), and demonstrate that Mugu magmatism was protracted, spanning a period of at least 3 Myr. U-Pb and $^{40}\text{Ar}/^{39}\text{Ar}$ cooling dates also place constraints on the deformational history, indicating that

Chapter 4: Exhumational history of the Mustang and Mugu granites

ductile east-west extension in the region began between ca. 23.4 Ma and ca. 20.8 Ma and that top-to-the east brittle-ductile normal faulting was ongoing by ca. 18.3-17.5 Ma. Our thermochronologic data show that rapid cooling (ca. 100 °C/Myr) and denudation (ca. 2.7 mm/yr) of the UMM in the Dangardzong fault footwall occurred between ca. 18.3-17.5 Ma and ca. 15.5-12 Ma. We infer that this period of rapid tectonic denudation reflects the initiation of slip on the modern Dangardzong fault as extension in the region evolved from a core complex mode to a rift mode. Our results suggest a new minimum age for the initiation of the rift-mode of extension in the Thakkhola graben of ca. 18.3-17.5 Ma. Based on the map extent of Mustang granite and our thermochronologic data, we estimate a maximum of ca. 30 km of horizontal extension at an integrated rate of about 1.7 mm/yr since graben inception. Finally, we propose a kinematic model for the evolution of upper Mustang which ties Thakkhola graben extension to the structural evolution of the UMM and activity on the STF system. Our model predicts that the material being exhumed in the UMM originates from below the STF system and that the low angle detachment active during the core complex phase was an up-warped portion of the STF basal detachment.

INTRODUCTION

Within the Himalaya and Tibet, the prototypical continent-continent collision zone, three classes of extensional structures have been identified. They have played integral roles in the development of the orogen, and their kinematics offer important insights into the geodynamic processes at work. The southernmost set of structures, the South Tibetan fault (STF) system, comprises an orogen-scale family of predominately normal-sense faults exposed along the crest of the high Himalayan ranges from Bhutan to northwest India (Burg and Chen, 1984; Burchfiel and Royden, 1985; Herren, 1987; Burchfiel *et al.*, 1992; Brown and Nazarchuk, 1993; Coleman, 1996b; Wu *et al.*, 1998; Godin, 1999) (Figure 1). Evidence points to an episodic history of activity along this system of faults that began ca. 22 Ma, continued throughout the Miocene (Hodges *et al.*,

Chapter 4: Exhumational history of the Mustang and Mugu granites

1996a; Hodges *et al.*, 1996b; Coleman, 1998; Hodges *et al.*, 1998; Wu *et al.*, 1998), and persisted until at least the Pleistocene (Hurtado *et al.*, 2001 ; Hurtado *et al.*, submitted – see Chapter 3). Active synchronously with north-south shortening along the Main Central thrust system (Hodges *et al.*, 1992), the STF system is hypothesized to have developed as a gravitationally driven response to high topographic and crustal thickness gradients in the developing orogen (Burchfiel *et al.*, 1992), and its kinematics are thought to have been controlled largely by the redistribution and removal of potential energy from the orogen (Hodges *et al.*, 2001; see Chapter 6).

North of the STF system, numerous Neogene rift systems in the southern part of Tibet comprise a second set of extensional structures (Tapponier *et al.*, 1981; Armijo *et al.*, 1986; Mercier *et al.*, 1987; Burchfiel *et al.*, 1991; Pan and Kidd, 1992; Ratschbacher *et al.*, 1994; Harrison *et al.*, 1995; Wu *et al.*, 1998) (Figure 1). These north-striking grabens help define the topographic grain of the otherwise flat plateau and are thought to accommodate roughly 10 mm/yr of regional east-west extension along high-angle east- and west-dipping normal faults and associated transcurrent faults (Molnar and Tapponier, 1975; Molnar and Tapponier, 1978; Ni and York, 1978; Armijo *et al.*, 1986). Seismic, sedimentary, and neotectonic records indicate Quaternary movement on these rift systems (Molnar and Tapponier, 1978; Mercier *et al.*, 1987; Molnar and Lyon-Caen, 1989; Hurtado *et al.*, 2001), but the age of inception of E-W extension in southern Tibet remains controversial, with estimates ranging from as recently as the Pleistocene (Armijo *et al.*, 1986) to as early as the middle Miocene (Coleman and Hodges, 1995; Blisniuk *et al.*, 2001; Williams, 2001).

Various hypotheses have been put forward to explain Tibetan extension including

Chapter 4: Exhumational history of the Mustang and Mugu granites

“gravitational collapse” of the Tibetan plateau (Molnar and Tapponnier, 1978; Ni and York, 1978; Armijo *et al.*, 1986; England and Houseman, 1989; Harrison *et al.*, 1992; Molnar *et al.*, 1993), arc-parallel strain partitioning (Buck and Sokoutis, 1994; McCaffrey, 1996), variations in elastic thickness along strike (Judge and McNutt, 1991), and basal shear of India beneath Tibet (McCaffrey and Nabelek, 1998). Moreover, research on two of the southernmost Tibetan grabens – the Thakkhola graben (Hurtado *et al.*, 2001) and the Yadong Gulu rift (Wu *et al.*, 1998) – suggest that the kinematics of the grabens and the STF system were linked. Still unclear, however, is the relationship between the STF system, the Tibetan grabens, and a third class of extensional structures that frame a series of gneiss domes that lie north of the physiographic Himalaya (Figure 1).

The North Himalayan gneiss domes form a discontinuous belt of at least twenty enigmatic metamorphic culminations. Most are situated in the central part of the orogen between 83°E and 89°E longitude, although the largest of the domes – the Tso Morari complex and the Gurla Mandahta massif – are located in the western Himalaya between 77°E and 82°E longitude (Figure 1). Cored by orthogneisses and paragneisses, many of the domes include large granite plutons. This infrastructure is often in ambiguous contact with a superstructure of lower-grade metasedimentary rocks (Burg *et al.*, 1984). While only a handful of these domes have been studied in detail, research at several of the domes has shown the contact to be a tectonic rather than intrusive one (e.g. Chen *et al.*, 1990; Lee *et al.*, 2000) and at least two – the Gurla Mandahta and Kangmar domes (Chen *et al.*, 1990; Murphy *et al.*, in review) (Figure 1) – have been hypothesized to be metamorphic core complexes exhumed along systems of detachment faults.

Chapter 4: Exhumational history of the Mustang and Mugu granites

Another potential core complex among the North Himalayan gneiss domes is the Upper Mustang massif (UMM), located in the Upper Mustang region at the northern end of the Thakkhola graben (ca. 29.5°N, 83.5°E; Figures 1 & 2). One of the southernmost of the Tibetan rifts, the Thakkhola graben penetrates through the higher Himalaya, forming the prominent Kali Gandaki valley between the Annapurna and Dhaulagiri ranges of central Nepal (Figure 2). Hurtado *et al.* (2001) studied the intersection between the principal growth fault of the Thakkhola graben – the Dangardzong fault (Hagen, 1968; Bordet *et al.*, 1971; Colchen, 1980) – and the STF system in the Lower Mustang region at the southern end of the Thakkhola graben (Figure 2). As described in detail in Chapter 2, the two systems are kinematically linked (Hurtado *et al.*, 2001). Since the northern end of the Dangardzong fault also forms the eastern edge of the UMM, the Thakkhola graben offers an excellent opportunity to see how all three classes of extensional features interact.

In the Thakkhola graben, the intimate relationship between the STF system, the Dangardzong fault, and the UMM have important implications for the tectonic and geodynamic evolution of the central Himalaya. Of specific interest is the extent to which exhumation of the UMM is related to Thakkhola extension and the displacement history of the Dangardzong fault. To address this problem, we conducted geological investigations of the Dangardzong fault at Lumpa Khola and of the UMM in the Tsarang Khola and near Thinker village (Figure 2). In the latter two areas, we made several transects across the Dangardzong fault into the southeastern part of the igneous and metamorphic core of the MMF. We report field geologic, structural, and remote sensing data which suggest that the Mustang granite and surrounding rocks in the UMM may

Chapter 4: Exhumational history of the Mustang and Mugu granites

have been exhumed in a metamorphic core complex setting. With U-Pb geochronology of monazite and xenotime and $^{40}\text{Ar}/^{39}\text{Ar}$ thermochronology of muscovite, biotite, and K-feldspar, we place constraints on the crystallization ages of the granites, the timing of deformational events, and the cooling and exhumational history of the UMM. We interpret our results in terms of the displacement history of the Dangardzong fault and the amount and rate of Thakkhola graben extension. We present a model that features the progressive evolution of the UMM from a metamorphic core complex to a rift-flank uplift such that the Thakkhola graben is kinematically related to a developing extensional core complex. Finally, we relate this to previous models for the kinematic link between Thakkhola graben extension and STF system activity (Hurtado *et al.*, 2001 ; Hurtado *et al.*, submitted – see Chapter 3).

GEOLOGIC SETTING

The Thakkhola graben is bounded on its west side by a system of N20°-40°E striking, steeply ($\geq 60^\circ$) east-dipping normal faults that have served as growth structures and the major control on the development of the basin (Hagen, 1968; Bordet *et al.*, 1971; Fort *et al.*, 1982; Colchen *et al.*, 1986) (Figure 2). This system is called the Dangardzong fault system, and it can be traced with satellite remote sensing data for 100 km along strike from the surface trace of the STF system near Taglung village to the Tibetan border north of Thinker village (Colchen *et al.*, 1986; Le Fort and France-Lanord, 1995; Hurtado *et al.*, 2001) (Figure 2).

The master Dangardzong fault separates unmetamorphosed Paleozoic to Mesozoic strata of the Tibetan Sedimentary Sequence (Garzanti, 1987) in its footwall

Chapter 4: Exhumational history of the Mustang and Mugu granites

from Tertiary and Quaternary basin fill in its hanging wall (Hagen, 1968; Bordet *et al.*, 1971; Fort *et al.*, 1982; Colchen *et al.*, 1986) (Figure 2). Field mapping demonstrates that slip on the Dangardzong fault resulted in dextral, oblique offset with a scissors geometry, such that cumulative dip-slip displacement decreases and cumulative right-lateral displacement increases southward along strike (Hurtado *et al.*, 2001). For example, the structure exhibits more than 4 km of dip-slip separation in the Upper Mustang region (Fort *et al.*, 1982) to essentially no dip-slip separation but ca. 3 km of strike-slip separation at the outcrop trace of the South Tibetan fault system at Taglung village (Hurtado *et al.*, 2001). In addition, a progressive decrease in the metamorphic grade of the footwall – from biotite-grade at the latitude of Lumpa Kholā to sub-chlorite grade south of Dangardzong village (Garzanti *et al.*, 1994) – suggests decreasing footwall exhumation towards the south. East-striking oblique transcurrent faults are also present in the Thakkhola graben area (Figure 2). Hurtado *et al.* (submitted – see Chapter 3) interpret these faults to be coeval with the Dangardzong fault system and hypothesize that the two sets of structures accommodate a clockwise rotational component to Thakkhola graben extension (e.g. Hurtado *et al.*, 2001).

Faults and fracture sets of similar orientation and kinematics to the Dangardzong fault system have been mapped 40 km to the east of the Kali Gandaki valley (Coleman, 1996b ; Hurtado *et al.*, submitted – see Chapter 3) where they disrupt the rocks of the Tibetan Sedimentary Sequence in the Marsyandi valley (Figure 2). A minimum age of ca. 14 Ma for east-west extension in the Thakkhola graben region is indicated by $^{40}\text{Ar}/^{39}\text{Ar}$ ages of hydrothermal muscovite that crystallized in one of these north-striking fracture sets (Coleman and Hodges, 1995). ^{14}C ages of alluvial and fluvial fill terraces in

Chapter 4: Exhumational history of the Mustang and Mugu granites

the Kali Gandaki valley indirectly show that the most recent Dangardzong fault activity occurred during the Pleistocene (Hurtado *et al.*, 2001). Combined with the observed geometry of the intersection between the Dangardzong fault and two strands of the South Tibetan fault system, these data further imply that Pleistocene activity also occurred on the South Tibetan fault system (Hurtado *et al.*, 2001).

Situated in the footwall of the northern end of the Dangardzong fault near the Nepal-China border (Figure 2), the UMM exposes deformed and metamorphosed Tibetan Sedimentary Sequence strata and a deformed granitic pluton – the Mustang granite – as well as dikes from the adjacent Mugu leucogranite pluton. The Mustang granite defines a ca. 325 km², half-domical massif in the immediate footwall of the Dangardzong fault, whereas the Mugu granite, a north-northwest-striking elongated batholith, is much larger (ca. 1600 km²) and is possibly the largest single leucogranite exposed in the Himalaya (Figures 1 & 2). The southeastern end of the Mugu granite is in the immediate footwall of the Dangardzong fault, where it crops out less than 3 km away from the Mustang granite (Figure 2). In the study area, along the Dangardzong fault escarpment between Tsarang and Thinker villages (Figure 2), deformed and undeformed dikes of Mugu affinity cut both the Mustang granite and the surrounding country rock.

Previous work in the Upper Mustang area has been limited due to its remoteness. Although distinctive, tourmaline-bearing leucogranite clasts are common in the sedimentary fill of the Thakkhola graben, and granite intrusions were mentioned by early workers in the region (Fuchs, 1967; Hagen, 1968; Hagen, 1969; Krummenacher, 1971), Le Fort and France-Lanord (1995) were the first to describe the Mugu and Mustang granites in any detail and the first to identify them as separate bodies. Structurally, little

Chapter 4: Exhumational history of the Mustang and Mugu granites

has been known about the granites' contacts with the surrounding Tibetan Sedimentary Sequence, although previous researchers (Fuchs, 1967; Le Fort and France-Lanord, 1995) have assumed them to be intrusive. Previous work also has not specifically addressed the relationships between the Dangardzong fault and the granites, although Le Fort and France-Lanord (1995) hypothesized that the Mustang granite may have originally been circular in plan and that part of it was faulted away during subsequent movement on the Dangardzong fault.

Geochemical data for the Mugu granite shows it to be similar to the Manaslu pluton and other "High Himalayan granites", although richer in Si, Ca, and Na (Le Fort and France-Lanord, 1995). Estimates of the P-T conditions of emplacement are 2.6 ± 0.6 kbar to 4.0 ± 1.0 kbar and 575 ± 25 °C, similar to the emplacement conditions of the Manaslu granite (Guillot *et al.*, 1995a; Guillot *et al.*, 1995c). The few published age estimates for the Mugu pluton cluster at range between ca. 24 Ma and ca. 15 Ma (see Table 1 and references therein), although no age estimates have been published for the Mustang granite. Given estimated P-T conditions for emplacement, an age of ca. 20 Ma, and an assumption of exposure at the surface by ca. 5 Ma, Le Fort and France-Lanord (1995) estimated the rate of denudation of the Mugu and Mustang granites to be ca. 1 mm/yr between 20 Ma and 5 Ma. They suggested that tectonic denudation is necessary to produce such unroofing rates, but maintained that extension related to Thakkhola graben formation was a separate event that began after principal denudation of the Mugu-Mustang (Le Fort and France-Lanord, 1995).

BEDROCK LITHOLOGIES IN THE MUSTANG REGION

In the Mustang region north of the outcrop trace of the STF system, bedrock lithologies can be subdivided into three packages: (1) metamorphosed to unmetamorphosed rocks of the Tibetan Sedimentary Sequence; (2) porphyritic two-mica granite of the Mustang pluton; and (3) a suite of fine- to medium-grained leucogranites that includes the large Mugu batholith

Tibetan Sedimentary Sequence

The Tibetan Sedimentary Sequence in Mustang includes an assortment of early Paleozoic to late Mesozoic carbonate and fine-grained siliciclastic sedimentary rocks deposited on the passive Tethyan margin of the paleo-Indian subcontinent prior to collision with Asia (Gansser, 1964; Le Fort, 1975; Colchen *et al.*, 1986; Fuchs *et al.*, 1988). In Lower Mustang, near the intersection between the Dangardzong fault and the South Tibetan fault system (Figure 2), these rocks are metamorphosed to amphibolite facies, but the metamorphic grade quickly decreases to below biotite grade within a kilometer north of the South Tibetan fault system. Near the boundary between Lower and Upper Mustang – at about the latitude of Dangardzong village (ca. 28.8°N; Figure 2) – illite crystallinity and vitrinite reflectance data suggest maximum metamorphic temperatures of 200 °C to 250 °C in the hanging wall of the Dangardzong fault, although they increase to about 350 °C in the footwall (Garzanti *et al.*, 1994).

Substantially higher metamorphic grade was established in the Dangardzong fault footwall farther north, in Upper Mustang. In the Panga Khola – a small tributary of the Kali Gandaki river near Dangardzong village (Figure 2) – the Dangardzong fault places

Chapter 4: Exhumational history of the Mustang and Mugu granites

black schists of the Jurassic Lupra Formation and quartzites of the Cretaceous Chukh Formation in the hanging wall in contact with black schists and quartzite of the Permo-Carboniferous Thini Chu Formation in the footwall (Bordet *et al.*, 1971; Colchen *et al.*, 1986). In hand-sample and thin section, the footwall rocks display a higher degree of deformational fabric development, and protomylonitic fabrics are discernable in some samples collected near the fault. Quartz and calcite veins are common in these rocks, implying significant hydrothermal fluid flow within and around the fault zone.

Approximately 10 km northwest of Dangardzong village, at Lumpa Khola (Figure 2) – another tributary of the Kali Gandaki river – the Dangardzong fault places Chukh Formation in the hanging wall in contact with dark-gray, fine-grained, schist intercalated with carbonate of the Devonian Tilicho Col Formation (Bordet *et al.*, 1971; Colchen *et al.*, 1986) in the footwall. At this latitude, metamorphism in the footwall has increased to biotite grade. Hydrothermal quartz and calcite veins are also common in this area and along the range front north of Lumpa Khola. Along this stretch, Tibetan Sequence rocks are typically hydrothermally altered and brecciated, and some outcrops (e.g. Figure 7h) display well-developed S-C cataclasites (Lin, 1999). Extensive Quaternary fan deposits and older basin fill bury the Tibetan Sedimentary Sequence along the Dangardzong fault north of Lumpa Khola. However, mapping by Colchen *et al.* (1986) shows the footwall of the Dangardzong fault as Tilicho Col Formation as far north as Samar village, (Figure 2) beyond which the footwall comprises dark, graptolitic schist of the Silurian Sombre Formation.

By the latitude of Tsarang Khola (ca. 29.1°N; Figures 2 & 5), at the southern edge of the UMM, the Tibetan Sedimentary Sequence is metamorphosed to amphibolite facies.

Chapter 4: Exhumational history of the Mustang and Mugu granites

The spatial association of high metamorphic grade and the Mugu and Mustang intrusive bodies suggests that metamorphism of the Tibetan Sedimentary Sequence was temporally related to granitic plutonism in the Upper Mustang region, much as it was in the vicinity of the Manaslu pluton in the eastern Annapurna range (e.g. Guillot *et al.*, 1995a). Within the UMM, the Tibetan Sedimentary Sequence is a black, fine-grained gneiss we informally refer to as Lo Mantang gneiss (Figure 3a). Le Fort and France-Lanord (1995) interpreted the protolith of the Lo Mantang gneiss as Silurian to Devonian gray, graptolitic schist of the Sombre and Tilicho Col Formations and Permo-Carboniferous intercalated quartzite and schist of the Thini Chu Formation. However, since we observed few preserved, primary sedimentary features and since the stratigraphy in this part of Upper Mustang is not well known, we suspect that the metamorphic rocks in the UMM may also include metamorphosed upper Paleozoic to Mesozoic formations (c.f. Colchen *et al.*, 1986).

The mineralogy of the Lo Mantang gneiss can be summarized as: biotite + quartz + K-feldspar + plagioclase + garnet + opaque oxides ± Al-silicate ± muscovite ± staurolite ± diopside. Biotite grains are typically ≤ 1 mm in diameter and garnets are up to 2 mm in diameter. We only observed staurolite and sillimanite (after kyanite) in float blocks within moraines interpreted to have been derived from deeper structural levels of the UMM. In outcrops away from the core of the massif, kyanite is present instead of sillimanite, suggesting that rocks of the core may have attained significantly higher temperatures than those of the margins during regional metamorphism.

The gneiss has a strong planar fabric (Figure 3a) that consistently strikes east and is defined by biotite fish and sillimanite (where present). Dips, however, vary as most

Chapter 4: Exhumational history of the Mustang and Mugu granites

outcrops have moderate to steep southerly dips while some have northerly orientations, consistent with the large-scale folding observed in unmetamorphosed sections of Tibetan Sedimentary Sequence elsewhere in the Thakkhola graben (e.g. Bordet *et al.*, 1971; Caby *et al.*, 1983; Godin *et al.*, 1999). In thin section, some samples of Lo Mantang gneiss (e.g. 00KG10 used for $^{40}\text{Ar}/^{39}\text{Ar}$ thermochronology – see below) exhibit partially resorbed garnet porphyroblasts armored with biotite. The garnets have symmetric pressure shadows filled with quartz, feldspar and biotite. Other samples (e.g. 00KG07) exhibit sigmoidal- and deltoidal-shaped, relatively euhedral garnet porphyroblasts with asymmetric pressure shadows.

Mustang Granite

Intruded into the upper Paleozoic to Mesozoic part of the Tibetan Sedimentary Sequence along the range front northwest of Thinker village (Figure 5), the medium gray Mustang granite is porphyritic and contains the assemblage: quartz + K-feldspar + plagioclase + biotite + muscovite \pm garnet \pm sillimanite. Characteristic of the Mustang granite are large, ca. 1 cm diameter, sheared sigmoidal and back-rotated deltoidal augen of polycrystalline K-feldspar aggregates (Figure 3b). Outcrops display strong ductile S-C fabrics (Lister and Snoke, 1984) with C-planes, defined by biotite and quartz ribbons, that strike northeast and dip moderately to steeply to the southeast (Figure 3b). A weak, subhorizontal, east-west trending stretching lineation is evident on many C-planes and is occasionally accompanied by a subparallel mineral lineation defined by sillimanite and linear aggregates of biotite. Muscovite is almost exclusively found as inclusions within the feldspar augen, often either as kinked books or in tabular sheets oriented subparallel

Chapter 4: Exhumational history of the Mustang and Mugu granites

to the S-planes.

Mugu Granites

Although previous publications have not emphasized the distinction, we found the Mugu pluton to be both mineralogically and texturally different from the Mustang pluton. Mugu granite samples are more leucocratic than Mustang samples and are fine- to medium-grained rather than porphyritic (Figure 3c). Typical minerals include quartz + K-feldspar + plagioclase + muscovite + tourmaline ± garnet ± biotite ± sillimanite ± xenocrystic diopside. Intrusions of Mugu granite into the surrounding Lo Mantang gneiss occur on a variety of scales, from the dekameter- to kilometer-scale bodies that make up the bulk of the Mugu batholith (Figure 3d), to dikes and sills a meter or less in width (Figure 3e). Most dikes strike east and dip moderately north or south. Given the enormous areal extent of the batholith (Figures 1 & 2) and the wide variety of field relationships we observed in outcrop, it is clear that the Mugu granite is polyphase and both mineralogically and texturally heterogeneous. On the hand-sample scale, most samples are equigranular and isotropic, with grain sizes not exceeding 0.5 cm in size and no significant deformational fabric, although some, in particular those within the Dangardzong fault zone, have experienced moderate degrees of mylonitization and deformational grain-size reduction. Mugu dikes and sills are also variably deformed on the mesoscopic scale; some are folded and boudinaged in outcrop (e.g. Figure 3f & g), whereas others are entirely undeformed and cut across earlier, deformed Mugu dikes as well as the deformed country rock (e.g. Figure 3e).

Many Mugu samples possess few fabric-defining platy minerals (e.g. 00KG06, -

Chapter 4: Exhumational history of the Mustang and Mugu granites

16, -18, -24, -29, -31, all used for geochronology – see below), and in thin section they lack a fabric. Some samples, however, possess muscovite and biotite fish and/or sigmoidal feldspars (e.g. 00KG08, -09, -14, -20, all used for geochronology – see below). Tourmaline also defines a prominent, although variably-oriented lineation in some samples. A few samples (e.g. 00KG12, -23 used for $^{40}\text{Ar}/^{39}\text{Ar}$ thermochronology – see below) even have complex migmatitic and schlieren textures. One dike sample in particular (00KG12) has a very fine-grained core that comprises several round pods, some with anomalously high concentrations of millimeter-sized tourmaline grains. A significantly coarser rind surrounds this, with tourmaline crystals up to a few centimeters in length. The interface between the two is intensely sheared, and we interpret these fabrics to be magmatic, with the finer-grained pods representing faster-cooled marginal material that was partially re-incorporated into the melt. From sample to sample, the orientation of shear and flow fabrics in the Mugu granite is highly variable.

GEOLOGIC MAPPING

As our field mapping in the UMM was limited to the small areas in the Tsarang Khola and near Thinker village, we augmented our field observations with a simple analysis of Landsat TM imagery. The goal of the remote sensing work was to characterize, in a crude way, the distribution of rock types and the geometry of the contacts between them throughout the Upper Mustang area. Figure 4 shows perspective views of a decorrelation-stretched Landsat TM image of the northern Thakkhola graben (entity ID LT4142040008901510; see Chapter 3 for imagery details) draped over

Chapter 4: Exhumational history of the Mustang and Mugu granites

DTED® digital topography (NIMA, 1996)¹. Using ENVI® image analysis software (RSI, 2000), the stretch was calculated from the original image with band 7 (middle infrared: 2.08 μm to 2.35 μm) in the red channel and band 6 (thermal infrared: 10.4 μm to 12.5 μm) in both the blue and green channels. The resulting “binary false color” image was merged with the digital elevation data and rendered in three dimensions to produce the perspective views in Figure 4. Due to their distinct spectral signatures in the infrared, the Mustang and Mugu granites appear bright red, and the Tibetan Sedimentary Sequence appears aqua blue. Thakkhola graben basin fill derived from these rocks also appears red and aqua blue, respectively, while other material appears muddy red and pink.

Several things become apparent in these visualizations. First, the half-domical morphology of the Mustang granite is well defined, although the eastern margin of the dome appears to be missing (Figure 4a). The hypothesis that the Mustang granite has been faulted into two separate blocks (e.g. Le Fort and France-Lanord, 1995) is supported by the decorrelation-stretched image, which indicates a second area of half-domical topography and Mustang granite-like spectral signature lying ca. 30 km east of the UMM (Figures 4a & b). The occurrence of granite on this side of the Thakkhola graben was briefly described by Hagen (1968; 1969), although that observation was questioned by Le Fort and France-Lanord (1995). We interpret this second half-dome as the eastern portion of the Mustang granite, and that the extensional faulting responsible for the Thakkhola graben also led to the eastward displacement of the Mustang outlier. Figure 4b shows a magnified view of the inferred Mustang granite-cored dome on the east side of the Thakkhola graben. Upon close inspection, one can see what appears to be a

¹ For publication, DTED® topography was resampled to ca. 1 km/pixel (Level 0 resolution) from the original ca. 90 m/pixel (Level 1 resolution) as required by NIMA (National Imagery and Mapping Agency).

Chapter 4: Exhumational history of the Mustang and Mugu granites

shallowly east-dipping contact between the granite and a thin carapace of presumably Tibetan Sedimentary Sequence rocks. This is in contrast to the steep contact along the rest of the granite's perimeter (Figure 4a). One viable interpretation, which we tentatively favor, is that this low-angle contact represents the extensional fault responsible for exhumation of the Mustang granite. Fieldwork in this remote area will be necessary to substantiate this. However, for logistical and political reasons, such an expedition is unlikely in the near future.

Shown in Figure 5 is a geologic map of the northern Thakkhola graben incorporating work by Colchen *et al.* (1986) and Le Fort and France-Lanord (1995), as well as our remote sensing image interpretation and field observations in the Tsarang Khola and Thinker areas. It shows the distribution of the main lithologies and the geometries of the granites in the UMM and of the Thakkhola graben faults. Because access to Upper Mustang is limited for foreigners, we were only able to study two areas of the UMM in detail. In both areas, we conducted transects across the Dangardzong fault that proceeded approximately 3 km into the footwall (boxed areas in Figure 5). The first area lies within deeply incised bedrock canyons at the mouth of the Tsarang Khola west of Tsarang village (Figure 5). It is characterized by an abundance of variably-deformed leucogranite dikes and sills along the periphery of the main body of the Mugu granite that intrude the Lo Mantang gniesses and their unmetamorphosed Tibetan Sedimentary Sequence counterparts. We observed no Mustang granite in the Tsarang Khola. The second area we studied lies in the mountains near Thinker village, ca. 11 km to the north of the Tsarang Khola (Figure 5). Here vast exposures of highly deformed Mustang granite dominate the escarpment along the Dangardzong fault. The Mustang

Chapter 4: Exhumational history of the Mustang and Mugu granites

granite is cut by several Mugu granite dikes, but neither Tibetan Sedimentary Sequence rocks nor large bodies of Mugu granite are exposed in this area.

STRUCTURAL GEOLOGY

A total of five generations of tectonite fabrics and at least four generations of granitic rocks were observed during our structural traverses. We use these observations to construct an interpretive deformational history for the UMM (Figure 6). The earliest deformational episodes occurred under ductile conditions and represent a progression from broadly north-south oriented compression to east-west oriented extension. The most recent episode occurred under brittle conditions and was characterized by top-down-to-the-east normal faulting that may be temporally and dynamically related to slip on the Dangardzong fault system. Despite the close proximity of the Tsarang and Thinker areas, correlation of deformational and magmatic events between the two is difficult, and in the following sections we present our observations for these areas separately before describing the interpretations that allow us to construct the history illustrated in Figure 6.

Tsarang Khola

D₁

Tibetan Sedimentary Sequence rocks in the Tsarang Khola have been deformed and metamorphosed to Lo Mantang gneiss under lower amphibolite-facies conditions. These rocks are characterized by the development of a schistosity (S_1) into which compositional layering (S_0) is transposed (Figure 7a). Subparallel S_0 and S_1 planes

Chapter 4: Exhumational history of the Mustang and Mugu granites

consistently strike east-west, although dips are somewhat variable (Figure 8a). Most foliation planes dip moderately-to-steeply southward, although a few dip moderately to the north. Mugu granite sills concordant to S_0 and S_1 (hereafter referred to as $Mugu_1$ – Figure 3g) intrude the Lo Mantang gneiss, and their parallelism suggests that they are pre- or syn-kinematic with respect to D_1 (Figure 7a).

D_2

The second deformational event resulted in a set of complex isoclinal folds (F_2) with moderately west-plunging axes and east-west striking, moderately-to-steeply south-dipping axial planes (S_2) parallel to S_1 . The folds deform both the Lo Mantang gneiss and the concordant $Mugu_1$ sills (Figure 7b).

D_3

Evidence for a third ductile event is found in some Tsarang Khola outcrops where S_0 , S_1 , and F_2 have been asymmetrically boudinaged (B_3) (Figure 7c). The boudinage is best developed in $Mugu_1$ sills as well as in a second set of near-concordant dikes that are undeformed by D_1 or D_2 ($Mugu_{II}$ – Figure 3f). The orientation of boudin necklines is consistent with east-west oriented extension and the asymmetry implies top-to-the-east shear.

East-west oriented transport during this phase is also demonstrated by generally horizontal, consistently east-west trending (Figure 8b) stretching lineations (L_3), defined by acicular sillimanite and linear aggregates of biotite developed on S_0 and S_1 planes. These lineations are ubiquitous in the Tsarang Khola outcrops of Lo Mantang gneiss, and

Chapter 4: Exhumational history of the Mustang and Mugu granites

their consistent orientation implies that they must be younger than F_2 . In thin sections oriented parallel to L_3 and perpendicular to S_0 and S_1 , some specimens of deformed Lo Mantang gneiss from the Tsarang Khola show top-to-the-east sense of shear. For example, biotite pressure shadow tails developed around garnet as well as biotite inclusion trails within garnets indicate rotation and back-rotation consistent with east- and west-directed shear synchronous with garnet growth. Microstructural analysis of mica fish in other samples, however, does not give as clear an indication of shear sense. Biotite fish form symmetric micro-boudinage structures, while muscovite, where present, is isoclinally folded and kinked in geometries consistent with east-directed shear.

D_4

In some outcrops, a second set of folds (F_4) refolds both the Lo Mantang gneiss and boudinaged Mugu_I and Mugu_{II} sills (Figure 7d). They are asymmetric and upright, with steeply northeast-plunging axes and northeast-striking, moderately west-dipping axial planes (S_{4a}). The fold orientation, however, varies widely. A poorly defined axial planar cleavage (S_{4b}) is also found in some outcrops (Figure 7d). Trains of these folds verge to the east, consistent with top-to-the-east sense of shear, the same transport direction inferred for D_3 . The folds, however, were not pervasive in the Tsarang Khola and are disharmonic. Where present, their age relative to earlier deformation events is clear, as they fold previously boudinaged (B_3) and isoclinally folded (F_2) Mugu_{I-II} sills (Figure 7d). A third generation of Mugu granite, ductily undeformed, discordant Mugu_{III} dikes (Figure 3e), truncates all D_4 and earlier fabrics.

***D*₅**

Unlike older deformational structures in the UMM, those of the *D*₅ generation developed under brittle conditions. They include northeast-striking normal faults and northeast-striking, shallowly-to-steeply southeast-dipping (Figure 8c) cataclastic shear zones (*S*₅) associated with the modern Dangardzong fault system (Figure 7e). The *D*₅ shear zones cut all classes of rock types – including Mugu_I-Mugu_{III} granites – and all *D*₁-*D*₄ structures within the Dangardzong fault zone in the Tsarang Khola. Abundant slickenlines (*L*₅) and tool-marked bedrock fault planes (Figures 7f & 8d), along with offset leucogranite dikes and sills indicate that faulting was normal-sense, with top-to-the-southeast displacement. Most of the brittle shear zones in the UMM have small displacements, on the order of a meter. The cumulative offset across the entire Dangardzong fault zone in upper Mustang could not be estimated due to the lack of features that could be correlated between the hanging wall and footwall.

Structures of *D*₅ age are not confined to the UMM. For example, outcrops of the Dangardzong fault outside of the UMM near Dangardzong village in Lower Mustang and Lumpa Khola in Upper Mustang (c.f. Hurtado *et al.*, 2001) (Figure 2) display similar cataclastic features with the same kinematics as those in the UMM. Displacements for individual structures within the Dangardzong fault zone in Upper and Lower Mustang range from meter-scale on the smallest cataclastic shear zones, to several hundreds of meters on the main strands of the Dangardzong fault (e.g. Hurtado *et al.*, 2001).

Some of the best-exposed brittle shear fabrics are found along the Dangardzong fault between Lumpa Khola and Tsarang village (Figures 2 & 5). Buried beneath Quaternary fans and exposed in 50-m deep canyons incised into the old alluvial fan

Chapter 4: Exhumational history of the Mustang and Mugu granites

surfaces are sets of eastward-stepping, moderate to steeply (ca. 60°) east-dipping brittle faults (Figure 7g) that sole into shallowly (ca. 30°) east dipping-brittle zones (e.g. Figure 7h). The shallowly-dipping zones exhibit well-developed brittle S-C cataclasites (Lin, 1999) that indicate top-to-the-southeast kinematics (Figure 7h). Some exposures along the Dangardzong fault zone include paleo-colluvial cones developed against steeply-dipping buried fault scarps (Figure 7g).

Thinker Village

The range of lithologies and deformational fabrics in the Thinker area was narrower than that in the Tsarang Khola, preventing us from constructing a deformational and intrusive sequence as detailed as that for the Tsarang Khola. Nevertheless, the Thinker area is dominated by a strong and consistently oriented mylonitic foliation developed within the border facies of the Mustang granite. It includes northeast-striking, moderately-to-steeply southeast-dipping S-C composite fabrics with lineations that plunge steeply to the southeast (Figures 9ab & 10a-f). Kinematic indicators – including mica fish, rotated K-feldspar porphyroblasts, and shear bands – indicate top-down-to-the-southeast (normal-sense) deformational kinematics. Examples of the various kinematic indicators observed in the field are shown in Figure 10a-f. The only other deformational structures observed in the Mustang granite are cataclasites within the Dangardzong fault zone (Figure 10g) with orientations and kinematics that are similar to those of the ductile fabrics and which also are indistinguishable from the D_5 cataclasites in the Tsarang Khola.

Chapter 4: Exhumational history of the Mustang and Mugu granites

We saw no evidence for multiple episodes of Mustang granite intrusion. However, three types of Mugu granite were observed to intrude the Mustang granite. The first comprise pods of gray leucogranite at the foot of our age-elevation transect (Figure 3h). Unfortunately, this leucogranite is very homogenous with few discernable fabrics in hand sample or in thin section, and talus deposits obscure its contact with the Mustang granite. We therefore know little about its age relative to the deformational sequence or other intrusive bodies. Examples of the second type of Mugu granite are seen in large boulders of Mustang granite in the Thinker area (Figure 3i). These sills of coarse-grained, tourmaline-bearing leucogranite and fine-grained, gray, tourmaline-free granite cut across the mylonitic fabric in the Mustang granite, but are themselves intensely folded and boudinaged, most likely during high-temperature deformation synchronous with intrusion. The third type comprises undeformed, fine-grained granite dikes that steeply cut across the Mustang granite fabric and the earlier Mugu granites (Figure 3j).

Structural Interpretations

Figure 6 illustrates our interpretation of the relative structural and intrusive history of the UMM based on our field observations. The orientation of D_1 and D_2 fabrics suggests north-south oriented compression. Granites in Upper Mustang, particularly those of the Mugu suite, display a spectrum of deformational intensities, implying that granitic intrusion began before D_1 and outlasted D_4 . Based on their pre-kinematic relationships to D_1 structures, the oldest observed granites in the Tsarang Khola area are early dikes and sills of the Mugu suite ($Mugu_1$). However, since no D_1 fabrics are preserved in the Mustang granite, field relations alone do not demonstrate the relative age

Chapter 4: Exhumational history of the Mustang and Mugu granites

of Mustang granite intrusion with respect to D_1 or $Mugu_1$. We note that the pervasive mylonitic fabric developed in the Mustang granite may have completely transposed any D_1 or D_2 fabrics originally present, so the issue of whether the Mustang granite pre- or post-dates those deformational phases and the earliest Mugu granites requires geochronologic constraints. By the same token, the main part of the Mugu granite lies outside of the Dangardzong fault zone and is largely homogeneous where we studied and sampled it. We presume it is correlative to $Mugu_{III}$, although we note that the main part of the Mugu batholith is polyphase and likely includes deformed components as well.

Because they are not isoclinally folded but are boudinaged, the second set of Mugu dikes in the Tsarang Khola ($Mugu_{II}$) demonstrably post-date D_2 and pre-date D_3 . We note that the kinematics of D_3 and D_4 are broadly similar, with both showing southeastward extension. Moreover, while D_3 is ubiquitous in the Tsarang Khola outcrops we investigated, D_4 features were less common. One possibility is that D_3 and D_4 were nearly synchronous or otherwise closely spaced in time and represent spatially heterogeneous responses to progressive, increasingly non-coaxial, top-to-the-east shear.

The mylonitic fabric affecting the Mustang granite indicates top-to-the-southeast shear, so it seems likely that it is correlative with D_3 or D_4 (or both) in the Tsarang Khola. We note, however, that L_3 in the Tsarang Khola does not plunge as steeply as the lineation associated with the Mustang granite mylonitic fabric. We hypothesize that fabrics identical to the Mustang granite mylonitic fabric are not present in the Tsarang Khola because the scissors-like kinematics of the Dangardzong fault (Hurtado *et al.*, 2001) has caused the fault to subsequently cut down section in the footwall in that direction, excising the mylonitic carapace. If correct, this interpretation suggests that the

Chapter 4: Exhumational history of the Mustang and Mugu granites

less steeply-plunging Tsarang Khola fabrics may have formed at deeper structural levels.

We have no structural control on which generation of Mugu granite is represented by the first type of gray leucogranite pods in the Thinker area. Because they intrude the deformed Mustang granite, truncating the mylonitic fabric, the deformed sills of the second type of Mugu granite in the Thinker area must be post- or late- syn-kinematic with respect to $D_{3,4}$ and we classify them as late Mugu_{II} to early Mugu_{III}. In the simplest interpretation, the undeformed crosscutting dikes of the third Mugu granite type in the Thinker area are correlative to the latest of Mugu granite dikes in the Tsarang Khola (Mugu_{III}) and they all post-date D_4 .

Finally, we can easily correlate the cataclastic fabrics of the Dangardzong fault zone in the Tsarang Khola to those in the Thinker area, assigning them all to D_5 . We note that shallowly-dipping brittle D_5 structures such as those in Figure 7h are subparallel with – and have similar kinematics to – D_3 and D_4 ductile east-west extending structures. These relationships imply the overprinting of deeper level, ductile structures in the footwall of the Dangardzong fault system by progressively lower temperature structures during tectonic denudation. Based on ^{14}C dating of river terraces in the Thakkhola graben, Hurtado, *et al.* (2001) showed that D_5 activity along the Dangardzong fault system in Lower Mustang occurred as recently as ca. 17 ka. Preliminary ^{26}Al and ^{10}Be cosmogenic nuclide surface exposure dating of the undeformed surface² burying D_5 faults (e.g. Figure 7g) in the vicinity of Samar village (Figure 2) suggests that the surface is ca. 11 ka in age, and places a further minimum constraint on late D_5 activity (Hurtado, unpublished).

² With the aid of aerial photography, the surface was classified in the field as K6 within the terrace stratigraphy defined by Hurtado *et al.* (2001) (see Chapter 2 for details).

U-Pb GEOCHRONOLOGY OF THE MUSTANG AND MUGU GRANITES

The pre-, syn-, and post-kinematic relationships among the various phases of granite intrusion and deformational structures in Upper Mustang provide an opportunity to bracket the absolute ages of D_1 and D_5 through U-Pb geochronology. We were able to obtain suitable mineral separates from a sample of the Mustang granite (00KG28), and three samples of Mugu_{III} (00KG18, -20 and -31). Unfortunately, we were unable to isolate appropriate phases for U-Pb analyses from our samples of Mugu_I or Mugu_{II}. In this section, we report the results of isotope dilution, thermal ionization mass spectrometry (ID-TIMS) analyses of accessory minerals separated from these four samples.

U-Pb Analytical Procedures

Pure separates of monazite [(Ce, La, Y, Th)PO₄] and xenotime [YPO₄] were obtained from the four samples using standard magnetic and gravimetric separation techniques and hand picking under a binocular microscope. Backscattered electron (BSE) images of selected grains were obtained using the JEOL 733 electron microprobe at the Massachusetts Institute of Technology in order to characterize intracrystal structure and, in a qualitative way, compositional zonation. Point measurements using energy dispersive spectrometry (EDS) were also performed on most grains to confirm mineralogy, in particular to distinguish between xenotime and monazite.

After electron microprobe study, grains were removed from their mounts, thoroughly washed, and measured using a binocular microscope with calibrated reticule

Chapter 4: Exhumational history of the Mustang and Mugu granites

and video display in order to estimate their weights. Experience in our facility suggests that the estimated values have a nominal error of roughly 20%. The grains were dissolved in Teflon capsules and spiked with a mixed ^{205}Pb - ^{233}U - ^{235}U tracer solution. U and Pb were isolated and extracted from the samples by anion exchange chromatography. U and Pb were then loaded on Re filaments and measured by isotope-dilution, thermal-ionization mass spectrometry (ID-TIMS) on a VG Sector 54 mass spectrometer at the Massachusetts Institute of Technology. Details regarding dissolution, chromatography, spectrometry, and other analytical procedures can be found in Hawkins and Bowring (1997). See Table 2 for further details, including total procedural blanks, and complete isotopic data for each grain analyzed.

The isotopic composition of Pb in most of the grains we analyzed was highly radiogenic (Table 2), such that calculated U-Pb dates are not strongly dependent on our choice of a common Pb correction scheme. The dates reported in this paper were calculated following the Stacey and Kramers (1975) model for common Pb, but we explored the effect of alternative approaches by recalculating the dates using Pb isotopic compositions for HF-leached feldspars from other Himalayan leucogranites (e.g. Gariépy *et al.*, 1985; Hodges *et al.*, 1998; Viskupic and Hodges, 2001). Those rocks display a relatively wide range of common Pb compositions, but the assumption of even the most radiogenic of those values produced minor changes in the plotting coordinates in concordia space of most of the Mugu-Mustang accessory minerals we analyzed. The singular exception to this is a relatively non-radiogenic monazite from the Mustang granite sample (00KG28, grain m2; Table 2). However, the analytical uncertainties for this grain are large in any case, and a more accurate common Pb correction would not

Chapter 4: Exhumational history of the Mustang and Mugu granites

yield additional age information. As a consequence, we did not attempt to measure common Pb directly using feldspars from the Mugu and Mustang granite samples we analyzed. Instead, we relied on the Stacey and Kramers (1975) model values.

In the following sections, we describe the suite of samples analyzed and the results of the U-Pb analyses. The samples include an example of the Mustang granite (00KG28) and a crosscutting, undeformed Mugu_{III} dike (00KG31) from the Thinker area, as well as two examples of Mugu_{III} granite from the Tsarang Khola area (00KG18, -20). A summary of our data is given in Table 2, and concordia plots for each of our samples are shown in Figure 11. All uncertainties are presented at the 2σ (95%) confidence level.

Mustang Granite (00KG28)

Sample 00KG28 was collected from an outcrop of porphyritic Mustang granite near Thinker village (Figure 5) that displayed $D_{3,4}$ planar and linear fabrics (e.g. Figure 3b). Five monazite crystals separated from this rock (m1-m5) were pale yellow in color with no microscopically visible inclusions. They had similar subhedral, slightly rounded morphologies and ranged in long dimension from ca. 200 μm to ca. 70 μm (Figure 12a). BSE images revealed that monazites in 00KG28 possess complex internal structure. For example, grain m1 showed nonconcentric, patchy zoning (Figure 13a), whereas m3 showed patchy, yet broadly concentric zoning (Figure 13b). All grains were free of inclusions except for monazite m1, which contained a relatively large quartz inclusion (Figure 13a).

Two xenotime crystals separated from 00KG28 (x1 and x2) were pale greenish-yellow in color, optically clear, and apparently free of inclusions (Figure 12a). Both ca.

Chapter 4: Exhumational history of the Mustang and Mugu granites

200 μm across, these grains were anhedral and displayed no obvious crystal faces. No BSE images were obtained for them and thus we have no information regarding whether or not they were chemically zoned.

On the concordia diagram (Figure 11a), both xenotimes are normally discordant, with $^{207}\text{Pb}/^{206}\text{Pb}$ dates of 36.2 ± 4.2 Ma (x1) and 464.3 ± 2.8 Ma (x2) (Table 2). Since the country rock of the Mustang granite is thought to be no older than Silurian (Colchen *et al.*, 1986; Le Fort and France-Lanord, 1995), it is certain that the x2 data indicates inheritance of pre-Himalayan xenotime in the Mustang granite. Although x1 is only slightly discordant, we regard its date as improbably old to represent the magmatic age of the sample in light of the monazite data discussed below. The most likely interpretation is that x1 is either a composite grain with a pre-36 Ma core and a post-36 Ma magmatic rim, or an entirely inherited grain that lost substantial radiogenic Pb during entrainment in the Mustang magma. In any case, the xenotime data do not provide useful information about the crystallization age of 00KG28.

As is often the case with monazites from Himalayan leucogranites, m1-m5 yield a range of near-concordant U-Pb dates that cannot be explained solely by analytical uncertainty (cf. Viskupic and Hodges, 2001) (Figure 11a; Table 2). In virtually all cases, magmatic, rather than inherited, monazites in these rocks display reversely discordant behavior which has been interpreted to be the consequence of preferential uptake of ^{230}Th during crystallization, which eventually produces “excess” ^{206}Pb (Schärer, 1984; Parrish, 1990). Because of this, we interpret the discordant monazites from 00KG28 that yield Mesozoic and Paleozoic dates (m1 and m3; Figure 11a) to reflect inheritance. Reversely-discordant grains m2, m4, and m5 yielded $^{207}\text{Pb}/^{235}\text{U}$ dates of 24.77 ± 1.42 Ma, $23.35 \pm$

Chapter 4: Exhumational history of the Mustang and Mugu granites

0.17 Ma, and 22.76 ± 1.65 Ma, respectively (Table 2; Figure 11a). The data for grains m2 and m5 represent relatively poor analyses, but the spread of reversely discordant dates is nevertheless difficult to attribute to analytical imprecision and instead suggests either multiple generations of monazite growth or Pb loss (Viskupic and Hodges, 2001). The latter possibility, however, seems less likely due to the low magmatic temperatures of Himalayan leucogranites and the lack of evidence for post-magmatic, high-temperature metamorphism in the UMM. Given the data at hand, we regard 23.35 ± 0.17 Ma – the relatively precise $^{207}\text{Pb}/^{235}\text{U}$ date of m4 – as our best estimate of the magmatic age of the Mustang pluton, although the data do not preclude a slightly younger or even slightly older age.

Mugu Granite: Mugu_{III} (00KG18)

Sample 00KG18 was collected from the edge of the main body of the Mugu pluton in the Tsarang Khola (e.g. Figure 3d), about 1 km structurally below the Dangardzong fault (Figure 5). Although in thin section this coarse-grained sample contained no obvious deformational fabrics, a crude preferred alignment of tourmaline crystals defined what we regard as a flow fabric. Monazite crystals in this rock are orange-yellow in color and typically contain inclusions visible through a binocular microscope (Figure 12b). Three grains (m1, m2, m3) with few or no inclusions were selected for U-Pb geochronology. Grain m1 was oblong with a long dimension of ca. 120 μm . Its subhedral form displayed two distinctive crystal faces (Figure 12b). BSE imaging of this grain showed no significant compositional zonation, although a band of quartz inclusions approximately bisects the crystal (Figure 13c). Grain m2 (Figure 12b)

Chapter 4: Exhumational history of the Mustang and Mugu granites

was also elongated with a maximum dimension of ca. 160 μm , but completely anhedral. No obvious zonation was evident in BSE image, but the grain contained several large quartz inclusions (Figure 13d). The optically cleanest of the 00KG18 monazites we studied was grain m3, an equant, subhedral crystal with a diameter of about 80 μm (Figure 12b). Under the binocular microscope, no inclusions were observed in this grain. In light of the apparent lack of zoning in grains m1 and m2, no BSE images were obtained for grain m3.

On a concordia diagram, all grains plot as reversely discordant (Figure 11b). The $^{207}\text{Pb}/^{235}\text{U}$ dates for m1 and m3 are statistically indistinguishable at 19.615 ± 0.046 Ma and 19.63 ± 0.11 Ma respectively (Table 2). Grain m2 is significantly younger, with a $^{207}\text{Pb}/^{235}\text{U}$ date of 19.417 ± 0.048 Ma (Table 2). Given that there is no evidence for a significant metamorphic event in this area subsequent to Mugu magmatic activity, it is unlikely that grain m2 is a post-magmatic metamorphic monazite, or that its younger apparent age is related to Pb loss. We thus tentatively interpret the 19.417 ± 0.048 Ma date as the most likely magmatic age of the rock and attribute the slightly older m1 and m3 dates to xenocrystic monazites that were perhaps derived from a slightly older phase of the Mugu suite during anatexis and emplacement of this part of the pluton.

Mugu Granite: Mugu_{III} (00KG20)

A medium-grained, undeformed, 0.5 m-wide dike of Mugu granite was sampled from an outcrop along the Tsarang Khola where it intrudes Lo Mantang gneiss and cuts across deformed Lo Mantang gneiss and deformed Mugu_I and Mugu_{II} granite sills (e.g. Figure 3e). The heavy mineral suite for this sample (00KG20) contained abundant

Chapter 4: Exhumational history of the Mustang and Mugu granites

uraninite (for details see Hurtado *et al.*, submitted – Chapter 5) as well as monazite. We analyzed two anhedral, pale yellow monazite grains (m1 and m2) (Figure 12c). Both contained a few microscopically visible inclusions that were determined to be quartz by further examination with the electron microprobe. Grain m1 was ca. 120 μm across, and BSE imaging revealed complex, non-concentric compositional zoning (Figure 13e). Grain m2 was ca. 150 μm across, with little compositional zoning (Figure 13f).

Analysis of monazite grain m1 was slightly normally discordant, with a $^{207}\text{Pb}/^{235}\text{U}$ date of 18.28 ± 0.10 Ma (Figure 11c; Table 2). Grain m2 is reversely discordant with a $^{207}\text{Pb}/^{235}\text{U}$ date of 26.04 ± 0.14 Ma (Figure 11c; Table 2). We regard the m2 date as indicative of inheritance, reflecting either a phase of the Mustang granite older than 00KG28 or a composite grain with an old core and younger rim. The fact that m1 was conspicuously zoned and plots below concordia may suggest that it contains some inherited material and younger intergrowths. If this is true, and we presume that all monazite in 00KG20 is either magmatic or inherited, then the 18.28 ± 0.10 Ma date from m1 would represent a maximum age for the sample.

Mugu Granite: Mugu_{III} (00KG31)

Sample 00KG31 is from a ca. 1-m thick, fine-grained, gray, undeformed dike that cuts deformed Mustang granite (e.g. 00KG28) in an outcrop near Thinker village (e.g. Figure 3c). Five monazite crystals were separated from this sample (Figure 12d). All five were free of visible inclusions. Four (m2, m3, m4, m5) were transparent and pale yellow in color, whereas a fifth (m1) was orange-yellow in color and slightly cloudy. Grains m3, m4, and m5 were euhedral to subhedral and equant, measuring between ca. 80

Chapter 4: Exhumational history of the Mustang and Mugu granites

μm and ca. 100 μm across. Grains m1 and m2 were subhedral and rounded, measuring ca. 70 μm across. BSE images were acquired for monazite grains m1 and m2 (Figure 13g & h). They show faint, patchy compositional zoning and some inclusions, although we could not determine the composition of the inclusions.

The oldest analyzed monazite crystal was m4, which was reversely discordant with a $^{207}\text{Pb}/^{235}\text{U}$ date of 24.73 ± 0.12 Ma (Figure 11d; Table 2). The similarity of this date with the interpreted age of Mustang sample 00KG28 – and the fact that Mustang granite is the host rock of the dike from which 00KG31 was collected – suggest that m4 is an inherited grain. The analysis of grain m1 (23.4 ± 3.1 Ma) was of poor quality and is of little value for determining the age of the sample. In contrast, grains m2, m3, and m5 yielded excellent results. All three grains clustered above concordia (Figure 11d), with a weighted mean $^{207}\text{Pb}/^{235}\text{U}$ date of 20.76 ± 0.67 Ma and MSWD (mean square of weighted deviates; Wendt and Carl, 1991) of 2.27 (Table 2). We interpret this date as the crystallization age of 00KG31.

Implications of the U-Pb data for the timing of granite intrusion and deformation in the UMM

Our ID-TIMS U-Pb analyses provide a new minimum age for the initial phases of Mugu intrusive activity of 20.76 ± 0.67 Ma (00KG31). This is substantially older than the 17.6 ± 0.3 Ma Th-Pb ion microprobe age obtained by Harrison (1997) from a Mugu granite sample from elsewhere in the Tsarang Khola area (Figure 5; Table 1). The broad range in age, however, is consistent with our mapped field relations which imply that Mugu leucogranitic plutonism in the UMM was temporally protracted. In fact, our dates,

Chapter 4: Exhumational history of the Mustang and Mugu granites

along with that of Harrison (1997), suggest that the third generation of Mugu granites (Mugu_{III}) alone intruded over a period of at least 3 million years. This study also yields the first constraint on the age of Mustang granite plutonism: 23.35 ± 0.17 Ma (00KG28). A lack of field evidence for multiple generations of Mustang granite intrusion suggest that this phase may represent a short-lived phase of anatectic melting at ca. 23.35 Ma. Since we were unable to constrain the age of Mugu_I directly, the possibility exists that the earliest Mugu granites may have intruded before that time, whereas the latest are at least six million years younger than the Mustang granite.

Although we were limited to the Mustang granite and to Mugu_{III} dikes, our U-Pb ages allow us to place some constraints on the deformational history of the UMM (Figure 6). First, the youngest dated Mugu granite sample (00KG20) implies a maximum age constraint for D₅ deformation of somewhat less than ca. 18.3 Ma. Second, the 23.35 ± 0.17 Ma age for Mustang granite (00KG28) and the 20.76 ± 0.67 Ma for the Mugu granite sample cutting the Mustang granite (00KG31) provide a relatively tight bracket for the age of D₃₋₄ extensional deformation in the Thinker area. We take this as a maximum age for the inception of east-west extension in the Upper Mustang region.

⁴⁰Ar/³⁹Ar THERMOCHRONOLOGY

In an effort to explore the cooling history of the UMM and the implications of that history for the tectonic evolution of the massif, we analyzed biotite, muscovite, and K-feldspar separated from the Mugu and Mustang granites with the ⁴⁰Ar/³⁹Ar method. In addition, we analyzed biotite separated from the Lo Mantang gneiss in the immediate footwall of the Dangardzong fault in the UMM as well as from greenschist facies

Chapter 4: Exhumational history of the Mustang and Mugu granites

metapelitic rocks of the Tibetan Sedimentary Sequence farther south near Lumpa Khola (Figure 2). Mugu granite intrusion and metamorphism in the UMM occurred at ca. 575 ± 25 °C (Guillot *et al.*, 1995c), conditions in excess of the nominal Ar closure temperatures of the phases we analyze (ca. 150 °C-400 °C; McDougall and Harrison, 1999). We therefore interpret all our $^{40}\text{Ar}/^{39}\text{Ar}$ results as cooling ages.

We categorize samples by their $^{40}\text{Ar}/^{39}\text{Ar}$ cooling ages, noting how those categories correlate with lithology and with the D₁ to D₅ deformational sequence (Figure 6) defined for the UMM. In addition, we attempt to place constraints on closure temperatures corresponding to the cooling ages using composition and grain size data and empirical calibrations (Harrison *et al.*, 1985; Hames and Bowring, 1994; Grove and Harrison, 1996). Finally, we apply the estimated closure temperatures and the $^{40}\text{Ar}/^{39}\text{Ar}$ cooling ages to a model for the cooling history of the UMM and Dangardzong fault footwall

Sample Characteristics

In Upper Mustang, the southernmost exposures of Tibetan Sedimentary Sequence that contain phases suitable for $^{40}\text{Ar}/^{39}\text{Ar}$ dating occur at Lumpa Khola (Figure 2). We separated biotite from two samples of the Tilicho Col Formation (98KG19 and -20) which we collected from the intact footwall of the Dangardzong fault, structurally below the D₅ cataclastic zone (c.f. Hurtado *et al.*, 2001). Sample 98KG19 is a very fine-grained, gray, quartz + biotite + chlorite phyllite, and 98KG20 is a medium-grained quartz + K-feldspar + biotite psammitic schist. In both samples the biotite defines the primary schistosity in the rock. Unfortunately, since Lumpa Khola lies well outside the UMM,

Chapter 4: Exhumational history of the Mustang and Mugu granites

this schistosity cannot be placed specifically in the context of the previously described deformational history (Figure 6), although it is undoubtedly older than D_5 .

Approximately 30 km farther northwest, in the Tsarang Khola, we collected a second suite of samples from both the Mugu granite and its country rock during our geologic transect into the southernmost part of the UMM (Figure 5). These include examples of the main body of the Mugu granite and a variety of deformed and undeformed Mugu_I-Mugu_{III} granite dikes and sills, and the Lo Mantang gneiss country rock. Although macroscopically deformed and classified as Mugu_I, in thin section the sample from the main part of the Mugu granite (00KG16) is isotropic, with an equigranular, interlocking, mosaic texture. Only muscovite was separated from this sample for $^{40}\text{Ar}/^{39}\text{Ar}$ analysis. Similarly, deformed Mugu_I dike 00KG12 has a comparatively weak fabric in thin section, although in outcrop it is clearly deformed, having been folded and boudinaged along with the Lo Mantang gneiss it intrudes. Both muscovite and K-feldspar were separated from this sample. Biotite and muscovite define well-developed planar fabrics in deformed Mugu_{II} sill samples 00KG06, -08, -09, and -14. Both biotite and muscovite were separated from 00KG08, while only biotite was separated from 00KG09 and only muscovite from 00KG06 and -14. Sigmoidal K-feldspar present in 00KG08 was also separated. Mugu_{III} sample 00KG20, although from a macroscopically undeformed crosscutting dike (Figure 7f), possesses a planar fabric in thin section defined by biotite, which we separated for analysis. The Lo Mantang gneiss samples (00KG10, -13, -19) crosscut by the deformed and undeformed dikes are all fine-grained with S-C fabrics defined by biotite which we separated for analysis.

Chapter 4: Exhumational history of the Mustang and Mugu granites

Finally, 11 km northwest of Tsarang Khola, along the southeastern edge of the UMM near Thinker village (Figures 2 & 5), we collected a third suite of samples that includes the Mustang granite (00KG25, -26, -28, -29, -30, and -32) and crosscutting phases of Mugu granite (00KG23, -24, and -31). These samples were collected in a steep bedrock canyon perpendicular to the Dangardzong fault, with successive samples collected at higher elevations in an effort to produce an “age-elevation” profile. The Mustang granite samples were all porphyritic and displayed well-developed $D_{3.4}$ fabrics. Most yielded pure separates of biotite, muscovite, and K-feldspar. Mugu granite samples from the Thinker area (00KG23 and -24) are from outcrops of the enigmatic, light-gray, somewhat weathered leucogranite pods that intrude the Mustang granite. Biotite, muscovite, and K-feldspar were separated from 00KG24, whereas only separates of muscovite and K-feldspar could be obtained from 00KG23. Also from the Thinker area, Mugu_{III} dike 00KG31, described previously (see U-Pb section above), yielded both biotite and muscovite.

$^{40}\text{Ar}/^{39}\text{Ar}$ Analytical Procedures

Analytical work was performed at the Massachusetts Institute of Technology CLAIR (Cambridge Laboratory for Argon Isotopic Research) facility (Hodges *et al.*, 1994b). Samples were crushed and sieved to 500 μm , and, after defiling to remove metal residue from the crushing procedures and decanting in water to remove the finest silt and dust fractions, biotite, muscovite, and K-feldspar were separated and purified using standard techniques. Minerals were separated by density using sodium polytungstate and by magnetic susceptibility using a Frantz isodynamic separator to isolate individual

Chapter 4: Exhumational history of the Mustang and Mugu granites

grains of muscovite, biotite, and K-feldspar. Paper shaking and hand picking were performed to increase the purity of the separates and to ensure sample homogeneity. Final mineral separates varied in grain size from ca. 100 μm to ca. 1 mm in diameter and were ca. 99% pure.

Before packaging for irradiation, purified mineral separates were washed with distilled water, acetone, and ethanol in an ultrasonic bath. Between 50 mg (for micas) and 100 mg (for K-feldspar) of material were sealed in ca. 1 cm^2 Al foil envelopes for irradiation. The filled Al foil envelopes were loaded into Al disks, shielded with Cd foil, and sent to the research nuclear reactor at McMaster University, Ontario, Canada where they were irradiated in core position 5C. Each of our irradiation packages (clair-88, -96, -111, and -112) consisted of a stack of 4 to 9 of the Al disks arranged in layers (see Table 3 for irradiation details). To facilitate corrections for interfering nuclear reactions, Ca, K, and Cl production factors were monitored with synthetic, reagent-grade CaF_2 , K_2SO_4 , and KCl salts distributed among the layers. Fast neutron flux was monitored with Fish Canyon-1-fine (Fcf) sanidine – a CLAIR intra-laboratory standard derived from the Fish Canyon tuff – placed in every other layer. The Fcf sanidine standard has been calibrated repeatedly at MIT against the original Fish Canyon tuff sanidine standard, the latter of which has a commonly accepted age of 28.02 Ma (Renne *et al.*, 1998). Although recent high-precision U-Pb geochronology (Schmitz and Bowring, 2001) has raised questions regarding the eruptive age of the Fish Canyon tuff, we will adopt the 28.02 Ma value for the original Fish Canyon tuff sanidine in order to facilitate comparisons with previously published Himalayan $^{40}\text{Ar}/^{39}\text{Ar}$ data from our laboratory and others. Assuming this age

Chapter 4: Exhumational history of the Mustang and Mugu granites

for the original Fish Canyon sanidine, our replicate intercalibrations yield an age of 28.38 Ma for Fcf sanidine.

J values were determined by automated Ar-ion laser total fusion analyses of the Fcf fluence monitors. For each layer containing fluence monitors, five replicate analyses of about five crystals each were analyzed and the results were used to calculate J and its uncertainty (e.g. McDougall and Harrison, 1999) (Table 3). Within a layer, flux gradients are typically negligible, so we assign the mean J and its uncertainty calculated for each layer to all samples in that layer. However, neutron flux varied significantly parallel to the long axis of the irradiation package, and because monitors were distributed throughout the layers in each irradiation package, we were able to document the resulting inter-layer gradients in J . We use a polynomial interpolation function to model J as a function of sample position within the package and to calculate J for layers without fluence monitors (Table 3). In order to account for potential errors in this model, as well as potential heterogeneities in the monitor material itself, we assign a very conservative 2% uncertainty to each J value. Ages reported in the text and figures include this propagated uncertainty.

Muscovite, biotite, and K-feldspar samples were degassed by incremental heating in a double-vacuum resistance furnace. Temperatures within the furnace are monitored with a W-Re thermocouple and controlled automatically to within ± 5 °C during the course of a heating increment via feedback loop. All samples were allowed to equilibrate with the ambient stand-by furnace temperature (250 °C) for 5 minutes prior to commencement of the heating schedule. Mica degassing experiments used monotonic step-heating schedules between 550 °C and 1550 °C (Table 4) designed to optimize the

Chapter 4: Exhumational history of the Mustang and Mugu granites

distribution of gas released among the heating steps. For the K-feldspar experiments, we employed heating schedules (Table 5) designed to provide the information necessary for multidomain diffusion modeling of the cooling history of each sample (e.g. Lovera *et al.*, 1989, 1991; Lovera *et al.*, 1993). In particular, we used duplicate isothermal heating increments at low temperatures to allow us to correct for the effects of Cl-correlated extraneous ^{40}Ar released during decrepitation of Cl-rich fluid inclusions (Harrison *et al.*, 1994). Additional long-duration, replicate isothermal steps at higher temperatures were used to maximize the quantity of gas released prior to the incongruent melting of K-feldspar. Duration of heating increments varied for K-feldspar analyses, but for biotite and muscovite analyses, all heating increments were 10 minutes long (Tables 4 & 5). These times, however, do not include an additional 10 minutes during which the evolved gas was gettered before analysis, and during which the sample re-equilibrated with the furnace stand-by temperature (250 °C). Gettering time for fluence monitor laser analyses was 5.5 minutes, which includes 30 seconds for sample lasing and degassing. Evolved gases were purified with metal-alloy getters in an automated extraction line and analyzed using an MAP 215-50 mass spectrometer (e.g. Hodges *et al.*, 1994b).

Laser analyses of monitors were performed using an electron multiplier detector. Mass discrimination resulted in a ($^{40}\text{Ar}/^{36}\text{Ar}$) of 276 for atmospheric argon measured with this instrument. The total system blank at M/e 40 for laser analyses of monitors was typically $< 5 \times 10^{-16}$ moles and $< 5 \times 10^{-17}$ moles at M/e 39, 38, 37, and 36. Blanks were re-measured automatically after every ten analyses. Gas extracted from mica, biotite, and K-feldspar unknowns was measured using a Faraday cup detector. Mass discrimination results in a ($^{40}\text{Ar}/^{36}\text{Ar}$) of 299 for atmospheric argon measured with the Faraday detector.

Chapter 4: Exhumational history of the Mustang and Mugu granites

Operational blanks for the furnace extraction line are dominated by the furnace itself and are strongly temperature- and time-dependent. Furnace blanks were measured as a function of temperature – at 800 K, 1500 K, and 1800 K – after every other sample or after a prolonged hiatus between furnace analyses. Blank corrections are typically small: in this study, signal sizes were typically two to three orders of magnitude larger than the furnace system blank at all temperatures. Typical blanks (in moles) at M/e 40, 39, 38, 37 and 36, respectively, were: (at 800 K) 2×10^{-14} , 7×10^{-17} , 5×10^{-17} , 2×10^{-17} , 8×10^{-17} ; (at 1500 K) 2×10^{-14} , 4×10^{-17} , 4×10^{-17} , 3×10^{-17} , 1×10^{-16} ; (at 1800 K) $< 3 \times 10^{-14}$, 8×10^{-17} , 4×10^{-17} , 1×10^{-16} , 3×10^{-17} . Measurements were corrected for blank, mass discrimination, and interferences prior to utilization for age calculations. Data reduction was performed using the MITAr software package (Matlab® version written by K. V. Hodges, 1999), and complete data are given in Tables 4 and 5. ^{40}K decay constants used are those recommended by Steiger and Jäger (1977). All analytical uncertainties associated with both measured and blank data were propagated through the calculations.

For each increment of gas extracted, a $^{40}\text{Ar}/^{39}\text{Ar}$ date was calculated with an assigned 2σ uncertainty that reflects propagated errors in all correction factors and J (Tables 4 & 5). In these calculations it is assumed that the initial $^{40}\text{Ar}/^{36}\text{Ar}$ value is that of modern atmosphere: $(^{40}\text{Ar}/^{36}\text{Ar})_i = 295.5$ (McDougall and Harrison, 1999). The results were plotted on conventional release spectrum diagrams as a function of cumulative $^{39}\text{Ar}_k$ release during the incremental heating experiment (Figure 14). Release spectra were tested for the presence of statistically valid plateaux by determining if the error-weighted mean of the dates of three or more contiguous steps – representing at least 50% of the total $^{39}\text{Ar}_k$ released – lies within the 2σ (95%) confidence interval for each date used in

Chapter 4: Exhumational history of the Mustang and Mugu granites

calculating the mean, exclusive of the uncertainty in the J value. The error assigned to the plateau date is twice the weighted standard error of the mean (2SE), inclusive of the uncertainty in J but exclusive of the uncertainty in the age of the Fcf fluence monitor.

The data for each experiment also were used to construct ($^{36}\text{Ar}/^{40}\text{Ar}$) vs. ($^{39}\text{Ar}/^{40}\text{Ar}$) isotope correlation diagrams (Roddick *et al.*, 1980) (e.g. Figure 15). Linear arrays of data on such diagrams are regarded as mixtures of radiogenic and non-radiogenic Ar components and, in ideal cases, provide precise $^{40}\text{Ar}/^{39}\text{Ar}$ isochron dates without the need to assume ($^{40}\text{Ar}/^{36}\text{Ar}$)_i (Roddick *et al.*, 1980). Suspected isochrons were regressed using the weighted least-squares linear method of York (1969) and tested for significance using the method of Wendt and Carl (1991), which is based on the MSWD. Regressions with MSWD values within 2σ of the expected value of 1.0 are regarded as isochrons, and their ($^{39}\text{Ar}/^{40}\text{Ar}$) intercepts were used to calculate inverse isochron dates, with 2σ errors estimated from the regression statistics and the error in J .

Biotite and Muscovite Results

Table 6 summarizes the results of plateau and inverse isochron calculations for biotite and muscovite from Upper Mustang. All experiments resulted in data that defined plateaux (Figure 14; Table 6). Similarly, a significant number of the steps – representing from 80 to 100 percent of the total ^{36}Ar released – from every experiment defined statistically significant isochrons with acceptable MSWD values (Figure 15; Table 6). The dates in bold in Table 6 are our preferred cooling ages for the micas. The selections were based largely on the ($^{40}\text{Ar}/^{36}\text{Ar}$)_i values obtained from the isochron fits. If a sample yielded ($^{40}\text{Ar}/^{36}\text{Ar}$)_i within uncertainty of the atmospheric value (295.5), we take the more

Chapter 4: Exhumational history of the Mustang and Mugu granites

precise plateau date as the best estimate of the cooling age. If the indicated $^{40}\text{Ar}/^{36}\text{Ar}_i$ is, within uncertainty, larger than 295.5, then we accept the isochron date as the best estimate of the cooling age. In these cases, we infer the presence of extraneous ^{40}Ar that makes the plateau model age unreliable (McDougall and Harrison, 1999), but the good correlations revealed by inverse isochron analysis suggest that the indicated ages are suitably corrected for the effect of the excess. In several cases, the indicated ($^{40}\text{Ar}/^{36}\text{Ar}$)_i is substantially less than 295.5. We do not regard these values as realistic – no obvious geologic process might account for such values – and we instead attribute them to the fact that most of the gas used in the isochron analysis is so highly radiogenic that the initial ratio is very poorly constrained. In such cases, the nature of the radiogenic component is nevertheless very well constrained and we regard the inverse isochron date as the best estimate for the cooling age. In Table 6, samples with multiple inverse isochron results serve to illustrate the insensitivity of the cooling age to ($^{40}\text{Ar}/^{36}\text{Ar}$)_i in these cases.

Mustang Granite Muscovite and Biotite

The four muscovite samples from the Mustang granite yield decreasing $^{40}\text{Ar}/^{39}\text{Ar}$ cooling ages with decreasing elevation (Figure 16a; Table 6). They decrease from 18.31 ± 0.25 Ma at the top of the transect to 17.35 ± 0.44 Ma at the bottom over ca. 200 m of relief. Unlike the muscovite in these rocks, the biotite does not show a variation in age correlative with elevation (Figure 16b; Table 6). Instead, our five biotite analyses yield statistically indistinguishable $^{40}\text{Ar}/^{39}\text{Ar}$ apparent ages with a mean of 17.58 ± 0.43 Ma.

Chapter 4: Exhumational history of the Mustang and Mugu granites

Mugu Granite Biotite and Muscovite

Two populations are distinguishable in the Mugu granite muscovite $^{40}\text{Ar}/^{39}\text{Ar}$ apparent ages (Figure 16c; Table 6). The four analyses in the older cluster have a mean age of 17.85 ± 0.14 Ma. These include the deformed Mugu_I sample from the main part of the Mugu pluton (00KG16) and the sample of extensively deformed Mugu_I leucogranite dike (00KG12). This set also includes the samples from the gray Mugu leucogranite intruding the Mustang granite in the Thinker area (00KG23, -24). The younger cluster of four analyses (Figure 16c; Table 6) has a mean of 17.25 ± 0.11 Ma and includes crosscutting, undeformed Mugu_{III} dikes 00KG06 and -31 as well as deformed Mugu_{II} samples 00KG08 and -14.

Biotite from the Mugu granite samples yield more scattered $^{40}\text{Ar}/^{39}\text{Ar}$ apparent ages (Figure 16d; Table 6) with a cluster of three samples (00KG08, -24, -31) that has a mean of 17.83 ± 0.18 Ma, within uncertainty of the Mustang granite mean biotite ages. Two other biotite samples are younger: 00KG09 is 16.68 ± 0.24 Ma and 00KG20 is 17.11 ± 0.84 Ma. All together, the Mugu granite biotites have a mean age of 17.46 ± 0.21 Ma.

Tibetan Sedimentary Sequence Biotite

The three Lo Mantang gneiss biotites from the Tsarang Khola area in the UMM yield a tight cluster of ages (Figure 16e; Table 6). The mean age is 17.54 ± 0.22 Ma, within uncertainty of the mean biotite ages from both the Mustang and Mugu granites.

The two biotite samples from lower-grade Tibetan Sedimentary Sequence (Tilicho Col Formation) farther south in Lumpa Khola yielded similar ages (Figure 16e; Table 6). The biotite from 98KG19 yielded a well-defined plateau with an age of $17.62 \pm$

Chapter 4: Exhumational history of the Mustang and Mugu granites

0.45 Ma, representing 79.5% of the gas (Figure 14) while the age spectrum from the 98KG20 biotite also displayed a plateau representing 89.3% of the gas and an age of 17.22 ± 0.22 Ma (Figure 14). The mean of these analyses is 17.42 ± 0.25 Ma, similar to the mean obtained for biotite from Lo Mantang gneiss samples in the UMM.

K-Feldspar Results

Although we designed our degassing experiments with the intent of constructing multi-domain diffusion models of the cooling history of the samples (e.g. Lovera *et al.*, 1989, 1991; Lovera *et al.*, 1993) our efforts were unsuccessful. One reason for this may be a violation of a basic assumption of the multi-domain diffusion theory: that the samples cooled monotonically over the Ar closure interval. Certainly, the presence of multiple generations of leucogranites in the UMM (Figure 6) makes simple monotonic cooling unlikely. Another reason may be that, despite our best efforts to minimize its impact by using heating schedules with replicate isothermal steps, extraneous ^{40}Ar contamination was too great to permit straightforward modeling (e.g. Hodges *et al.*, 1994b). For instance, most heating increments for the K-feldspar samples we studied yield $^{40}\text{Ar}/^{39}\text{Ar}$ dates (Table 5) that approach – if not exceed – the biotite and muscovite $^{40}\text{Ar}/^{39}\text{Ar}$ cooling ages for the same sample (Table 6). Our approach to this problem was to estimate the age of the least-retentive domain (LRD) for each of our feldspar samples by two methods. In the first, we evaluate the $^{39}\text{Ar}_K$ weighted mean dates of low temperature increments defining saddles in the release spectra (e.g. Copeland *et al.*, 1987; Hodges *et al.*, 1994b). In the second we consider statistically significant inverse isochron dates for selected groups of low-temperature increments.

Minimum $^{39}\text{Ar}_K$ Weighted Mean Dates

All of the analyzed K-feldspars yield release spectra (Figure 17) with broadly similar morphologies characterized by: (1) a low-temperature segment with alternating young and excessively old increments; followed by (2) a saddle-shaped segment of very young increments; and (3) a segment of increasing ages, often culminating in a near-plateau.

We infer that the LRD in each sample yields the youngest dates and consider the increments on the saddle-shaped segment of the release spectrum as representative of gas released from the LRD, although we realize that Cl-related extraneous ^{40}Ar from fluid inclusions degassed in the lowest temperature steps may obscure younger ages (Harrison *et al.*, 1994). The release spectra saddles typically include increments between ca. 400 °C and ca. 850 °C and represent between 3 and 20 percent of the total $^{39}\text{Ar}_K$ evolved during degassing (Table 5). Utilizing the $^{39}\text{Ar}_K$ weighted mean of the individual increment model dates defining the spectrum saddles, we calculated minimum spectrum dates (MSDs) (Table 7). MSD estimates for the age of the LRD for K-feldspars from both the Mustang and Mugu K-feldspars are all similar, with a mean of 15.26 ± 0.36 Ma. However, we note that – with the exception of sample 00KG32 – the mean MSDs increase slightly with increasing altitude from 15.34 ± 0.99 Ma for the highest sample (00KG30) to ca. 15.19 ± 0.79 Ma for the lowest (00KG24) (Figure 18a).

K-feldspar Isotope Correlation Diagrams

If we interpret the MSDs to be geologically meaningful indicators of the LRD age, we must assume no contamination of the saddle dates in each spectrum by extraneous ^{40}Ar . Unfortunately, the UMM K-feldspars typically display evidence of excess ^{40}Ar contamination, although it remains unclear exactly how this contamination is distributed among the diffusion domains, and thus how it evolves during step-heating experiments. As previously mentioned, the low-temperature segments of the release spectra are clearly contaminated, but the saddle and near-plateau segments may be as well. For example, the high-temperature, near-plateau segments for K-feldspar samples 00KG08 (ca. 21-20 Ma) and 00KG32 (ca. 20-19 Ma) are significantly older than the cooling ages for micas from the same samples (ca. 18.31-17.43 Ma – 00KG32; ca. 17.61-17.07 Ma – 00KG08), despite the certainty that the closure temperature of K-feldspar is substantially lower than that of either muscovite or biotite. Therefore, because of the likely presence of extraneous ^{40}Ar throughout the K-feldspar domain structure, we regard the MSD as an overestimate of the age of the LRD. As an alternative we estimate the age of the LRD with inverse isochron analysis of the K-feldspar data to calculate a minimum isochron date (MID). This approach requires no *a priori* assumption of ($^{40}\text{Ar}/^{39}\text{Ar}$), and, in theory, allows us to correct for extraneous ^{40}Ar .

For each of our K-feldspar experiments, the data define one or more statistically significant linear arrays that correspond to contiguous blocks of heating increments (Figure 19; Table 7). These arrays probably reflect the existence of multiple domains with different capacities for retaining radiogenic ^{40}Ar during cooling (Lovera *et al.*, 1991) and/or different levels of contamination by excess ^{40}Ar (Foster *et al.*, 1990). For all

Chapter 4: Exhumational history of the Mustang and Mugu granites

samples with multiple linear arrays (all but 00KG23 and -32), the inverse isochron dates follow a consistent pattern, decreasing as the temperatures of the included increments decreased (Table 7). The youngest dates, the MIDs, are obtained from the linear arrays defined by the lowest temperature heating increments.

In all cases, the MIDs calculated in this fashion are younger than the MSDs for the same sample, with $(^{40}\text{Ar}/^{36}\text{Ar})_i$ ratios significantly higher than 295.5 (Table 7). In light of evidence for pervasive extraneous ^{40}Ar contamination, we regard the MIDs as our best estimates of the LRD cooling ages for our K-feldspars. The mean MSD is 14.24 ± 0.27 Ma, although there is a substantially larger spread in the MID than in the MSD (Table 7). With one exception (00KG30), the MIDs for K-feldspars from the Thinker area increase with increasing elevation, from 12.88 ± 0.75 Ma for 00KG24 to 14.51 ± 0.42 Ma for sample 00KG29, the highest sample (Figure 18b; Table 7).

Finally, of the eight K-feldspar samples we analyzed, samples 00KG23 and -32 do not yield multiple linear arrays, and we therefore cannot define MIDs for them. Of the two, only 00KG23 has an acceptable $(^{40}\text{Ar}/^{39}\text{Ar})_i$ value (296.26 ± 16.69) (Table 7). This suggests that the corresponding inverse isochron age of 17.04 ± 0.36 Ma (MSWD = 1.44) may have geologic meaning as an estimate of the age recorded by the domain with the highest closure temperature.

CLOSURE TEMPERATURES AND COOLING RATES

Key to understanding the significance of the $^{40}\text{Ar}/^{39}\text{Ar}$ data is an understanding of the closure temperatures of the phases we have dated. Without closure temperature constraints for our specific samples, we are limited in our ability to use the

Chapter 4: Exhumational history of the Mustang and Mugu granites

thermochronologic data in developing models for the cooling and exhumational history of the UMM. For instance, if we assume that the nominal closure temperature of muscovite is ca. 415 °C to 350 °C (Robbins, 1972; Hames and Bowring, 1994; Lister and Baldwin, 1996), while that of biotite is ca. 350 °C to 300 °C (Grove and Harrison, 1996), we expect muscovite cooling ages to be consistently older than biotite ages for the same samples. For some samples (e.g. 00KG08, -24, -25, -28, -31; Table 7), however, just the opposite is true.

Muscovite and Biotite Diffusion Parameters

Anomalously old biotite $^{40}\text{Ar}/^{39}\text{Ar}$ apparent ages are often due to contamination by extraneous ^{40}Ar (McDougall and Harrison, 1999). However, isochron analysis of the UMM samples shows that the non-radiogenic Ar component in most has a $(^{40}\text{Ar}/^{39}\text{Ar})_i$ ratio approximately the same as modern atmosphere. Some biotites (e.g. 00KG24, -25, -31; Table 6) have poorly-constrained $(^{40}\text{Ar}/^{36}\text{Ar})_i$ values less than 295.5, which is also inconsistent with the presence of extraneous ^{40}Ar . As a consequence, we investigate the possibility that the closure temperatures of biotite and muscovite in our samples may be significantly different than the nominal values. In particular, might the closure temperatures of the UMM biotites approach or exceed those of coexisting muscovites? We consider the Fe/Mg compositional dependence of biotite closure temperature (e.g. Harrison et al., 1985; Grove and Harrison, 1996) as well as the dependence of both biotite and muscovite closure temperatures on grain size and cooling rate.

We assumed that ^{40}Ar diffusivity in muscovite is described adequately by the experimental data of Robbins (1972) as reinterpreted by Hames and Bowring (1994)

Chapter 4: Exhumational history of the Mustang and Mugu granites

(Table 8a). There is, as yet, no evidence of a compositional dependence on the rate of this process for simple muscovites with no substantial phengite component. On the other hand, there is evidence that composition – particularly Fe/Mg – plays a role in ^{40}Ar diffusion in the biotite group of trioctahedral micas (McDougall and Harrison, 1999). To address this effect, we employed wavelength-dispersive electron microprobe analysis of biotites from seven samples in order to determine mole fraction annite (X_{ann}). We found a relatively limited variation, with X_{ann} ranging between 0.70 and 0.83 (Table 8b). For each grain, we calculated the activation energy (E_a) and frequency factor (D_o) based on X_{ann} by a simple linear interpolation of the diffusion data published by Harrison (1985) and Grove and Harrison (1996) (Table 8b). We choose their experimental data because they are more pertinent to Fe-rich biotite like ours than are the phlogopite data of Giletti (1974). For the biotites for which we did not determine X_{ann} , we simply used the mean values for biotites from the appropriate rock unit (i.e. Mustang granite, Mugu granite, or Tibetan Sedimentary Sequence/Lo Mantang gneiss) to calculate their diffusion parameters (Table 8b)

To account for closure temperature dependence on grain size, we calculated mean half-grain size for each mineral aliquot by taking the arithmetic mean of > 20 grain half-size³ measurements per sample. In each case, we were careful to measure grains that showed intact crystal faces and thus had not been significantly broken during the crushing process. The grains measured were not the same as those irradiated for subsequent isotopic analyses, but they comprise representative aliquots taken from the

³ Defined as one-half of the longest dimension of the grain as measured in the {001} crystallographic plane.

Chapter 4: Exhumational history of the Mustang and Mugu granites

same mineral separates. Biotite half-grain sizes range from 158 μm to 630 μm (Tables 6 & 8b). Muscovite half-grain sizes range between 473 μm and 1103 μm (Table 6).

Closure temperatures based on the available information were calculated using the MacArgon 5.1.0 computer program (Lister and Baldwin, 1996), assuming an infinite cylinder geometry and a variety of cooling rates between 10 $^{\circ}\text{C}/\text{Myr}$ and 100 $^{\circ}\text{C}/\text{Myr}$ (Table 9a). Both size-dependent and size-independent closure temperatures were calculated, the former assuming the effective diffusion dimension (r) is the physical grain size (Hames and Bowring, 1994; Hodges *et al.*, 1994a; Hodges and Bowring, 1995) and the latter assuming an effective diffusion dimension of 150 μm (Harrison *et al.*, 1985; McDougall and Harrison, 1999).

Including the effect of composition into the closure temperature calculations implies that the UMM biotites are relatively retentive, with closure temperatures comparable to muscovite closure temperatures at all cooling rates (Table 9a). Similarly, including the size dependence on closure temperatures has a large effect on both muscovite and biotite closure temperatures, increasing them above the size-independent values by an average of 8 $^{\circ}\text{C}$ for biotites and 40 $^{\circ}\text{C}$ for muscovite at all cooling rates (Table 9a). We choose to include the compositional dependence on biotite closure as it offers the least arbitrary solution to the problem of anomalously old biotite and a large body of evidence suggests that the effect is real (see references in McDougall and Harrison, 1999). The choice between using size-dependent or size-independent closure temperatures for both muscovite and biotite is not as clear because we cannot devise a consistent, systematic choice regarding size dependence that simultaneously and satisfactorily explains the ages and closure temperatures for all the samples. Without

Chapter 4: Exhumational history of the Mustang and Mugu granites

better information, we choose to view the size-dependent and independent closure temperatures for each sample as upper and lower limits and use the mean in our interpretations regarding cooling and exhumation rates (see “Cooling Rate Determination” below).

We did not do detailed analysis of the pressure dependence of closure temperature, as it is a small effect. For instance, a 3 kbar pressure change translates to a ca. 10 °C change in the closure temperature assuming the activation volumes listed in Tables 8a and 8b. The final parameter controlling the closure temperatures corresponding to our $^{40}\text{Ar}/^{39}\text{Ar}$ cooling ages is our choice of cooling rate. While not a large effect, it is not insignificant and changes closure temperature by ca. 10 °C to 20 °C between cooling rates of 45 °C/Myr and 100 °C/Myr for both biotite and muscovite (Table 9a). We discuss our choice of cooling rate and our best estimates for mica closure temperatures below.

K-Feldspar Diffusion Parameters

We also seek constraints on closure temperatures corresponding to our MID estimates of the age of the LRD in our K-feldspars. Plotted on an Arrhenius diagram (Figure 20), the diffusive loss of ^{39}Ar during a K-feldspar heating experiment defines subparallel linear arrays from which E_a and D_0/r^2 values can be obtained from the slope and ordinal intercept, respectively. With an unweighted linear regression algorithm, we calculate E_a and (D_0/r^2) for the linear array corresponding to the lowest-temperature increments, making the assumption that this linear array represents diffusion from the LRD. The resulting diffusion parameters for each K-feldspar we analyzed are listed in

Chapter 4: Exhumational history of the Mustang and Mugu granites

Table 8c. Assuming an infinite slab geometry (McDougall and Harrison, 1999), we use these parameters with an assumed effective diffusion dimension of 6 μm (McDougall and Harrison, 1999) to calculate closure temperatures with the MacArgon 5.1.0 program (Lister and Baldwin, 1996) for a range of cooling rates between 10 $^{\circ}\text{C}/\text{Myr}$ and 100 $^{\circ}\text{C}/\text{Myr}$ (Table 9b). As with mica closure temperatures, K-feldspar LRD closure temperatures vary by ca. 10 $^{\circ}\text{C}$ depending on whether 45 $^{\circ}\text{C}/\text{Myr}$ or 100 $^{\circ}\text{C}/\text{Myr}$ is chosen as the cooling rate.

Cooling Rate Determination

Cooling rates were estimated iteratively. We began with the assumption that monazite and xenotime are sufficiently retentive of radiogenic Pb that their ID-TIMS dates are crystallization ages for granites from relatively low-temperature crustal melts such as those studied here (e.g. Viskupic and Hodges, 2001). We further presume that these ages reflect the final crystallization ages of the granites from which they were separated. Although we have no explicit data on the solidus temperatures of the parent magmas for the Mugu and Mustang granites, we assume for simplicity that both crystallized at ca. 700 ± 75 $^{\circ}\text{C}$, a range that is reasonable in light of experimental data for other Himalayan leucogranites (Scaillet *et al.*, 1995; Patiño Douce and Harris, 1998) and is consistent with the peak metamorphic temperature estimate of Guillot *et al.* (1995c). We infer from our available U-Pb data that Mugu granite magmatism began at ca. 20.76 Ma (Table 10) and is strictly younger than Mustang granite magmatism, which occurred at ca. 23.35. Simple thermal calculations⁴ of the conductive cooling of the Mustang

⁴ These calculations involve one-dimensional solutions of the heat equation for conductive cooling of an intrusive body including latent heat of crystallization but neither radiogenic heat production nor advection.

Chapter 4: Exhumational history of the Mustang and Mugu granites

granite (Turcotte and Schubert, 1982) predict that the UMM within 6 km of the center of the Mustang granite would have attained ca. 500-550 °C by the time Mugu granite intrusion began ca. 3 Myr later. Similar calculations predict that the same area would have been reheated to ca. 600-650 °C within ca. 1 Myr of intrusion of the main body of the Mugu granite. For simplicity, we assume that the thermal history subsequent to ca. 20.76 Ma involves no further significant re-heating, although we recognize Mugu intrusion at smaller scales continued for several million years afterward.

Other temperature-time constraints were initially provided by combining averages of our $^{40}\text{Ar}/^{39}\text{Ar}$ dating results (Table 10) with nominal closure temperatures for muscovite (ca. 400 °C), biotite (ca. 350 °C), and K-feldspar (ca. 150 °C) (McDougall and Harrison, 1999). Collectively, these age data and nominal closure temperatures defined a first approximation of the temperature-time curve as a series of linear interpolations between points. We then used the slope of this first-approximation curve to improve our estimates of cooling rates which, in turn, we used to recalculate more appropriate average $^{40}\text{Ar}/^{39}\text{Ar}$ closure temperatures (Tables 9a & b). Using the new set of closure temperatures, a second-approximation curve was constructed and the process was repeated.

After several iterations, we found the best, self-consistent cooling model to be that illustrated in Figure 21a with a cooling rate of ca. 45 °C/Myr between 20.76 Ma and 17.5 Ma, ca. 100 °C/Myr between 17.5 Ma and 15.5 Ma, and ca. 10 °C/Myr between 15.5 Ma and the present. This estimate, based on average closure temperatures and cooling ages, is consistent with the specific cooling ages and closure temperatures from individual samples with multiple thermochronometers (Figure 21b). The cooling history is also

Chapter 4: Exhumational history of the Mustang and Mugu granites

broadly consistent with the $^{40}\text{Ar}/^{39}\text{Ar}$ data from Guillot *et al.* (1999) (Table 1) which they interpret to reflect cooling through 300 °C-350 °C at ca. 17-15 Ma.

Biotite and muscovite closure temperatures (45 °C/Myr cooling rate) corresponding to our interpretive cooling history are shown in Table 6. On average⁵, biotite (ca. 403 ± 30 °C) and muscovite (393 ± 14 °C) from within the UMM have overlapping closure temperatures ranges, and may explain the cases where the biotite cooling ages match or exceed the muscovite cooling ages. Closure temperatures of ca. 390 °C for biotites from Lumpa Khola, outside of the high-grade core of the UMM, are close to the Garzanti *et al.* (1987) estimate of ca. 350 °C for the maximum metamorphic temperature at this latitude. The resulting K-feldspar LRD (MID) closure temperatures (45 °C/Myr cooling rate) are given in Table 7 and range between 96 °C and 236 °C with a mean of 157 °C. If a 100° C/Myr cooling rate is instead used, the mean is 167 °C, but the variation in mean closure temperature due to different choices of cooling rate is well within the overall dynamic range in closure temperatures among the various samples (Tables 7 & 9b).

IMPLICATIONS OF THE $^{40}\text{Ar}/^{39}\text{Ar}$ DATA

Deformational and Intrusive History of the UMM

The wide range in muscovite $^{40}\text{Ar}/^{39}\text{Ar}$ cooling ages – and generally consistent biotite cooling ages – for samples from the UMM allow us to make several inferences about the chronology of deformation and intrusion. For the Mustang granite samples, we note that both the biotite and muscovite cooling ages (Table 6) define linear arrays when

⁵ The rates in parentheses are the average of the size-dependent and -independent rates in Table 9a for 45 °C/Myr. The uncertainties are one half the total range between the size-dependent and -independent rates.

Chapter 4: Exhumational history of the Mustang and Mugu granites

plotted as functions of elevation (Figure 16a & b). Enigmatic Mugu granite samples 00KG23 and -24, however, yielded relatively old muscovite cooling ages that do not fit the age-elevation profile defined by muscovite from the Mustang granite samples they intrude (Figure 16a; Table 6). By contrast, biotite from 00KG24 (biotite from 00KG23 was not analyzed) yields an age (ca. 17.66 Ma) consistent with the Mustang granite biotite age-elevation profile (Figure 16b; Table 6). From these observations, we can infer that samples 00KG23 and -24 intruded into the Mustang granite and cooled to the closure temperature of muscovite early in the cooling history of the Thinker area, possibly pre-dating the Mustang granite. Furthermore, the similarity of muscovite cooling ages from 00KG23 and -24 to that of Mugu₁ sample 00KG12 (Figure 16c; Table 6) supports the hypothesis that 00KG23 and -24 are Mugu₁ granites. Finally, the fact that 00KG16, the sample from the main part of the Mugu granite, falls in the same cluster with 00KG12, -23, and -24 (Figure 16c; Table 6), suggests that 00KG16 also belongs to the Mugu₁ generation.

Exhumational History of the UMM

Several different approaches have been described to determine denudation rates from thermochronologic data. One method is to translate the composite cooling curve in Figure 21a into a denudation curve by assuming a geothermal gradient (e.g. Copeland *et al.*, 1987). An equivalent, but more detailed procedure, explicitly employs the “multiple mineral method” which is based upon the difference in cooling ages of multiple minerals from the same sample, assuming appropriate closure temperatures and a geothermal gradient (e.g. Benjamin, 1986; Benjamin *et al.*, 1987). Alternatively, one can use the

Chapter 4: Exhumational history of the Mustang and Mugu granites

“relief method” (e.g. Benjamin, 1986; Benjamin *et al.*, 1987) which relies on the difference in cooling ages for a single mineral in separate samples collected at different elevations and does not require knowledge of closure temperature or geothermal gradient. Moore and England (2001) demonstrate a fourth method that takes advantage of the curvature of a temperature-time path and its strong dependence on denudation rate and weak dependence on other parameters. In this section, we apply each of these methods to place constraints on the exhumational history of the UMM and the Dangardzong fault footwall.

Multiple Mineral Methods

We can calculate maximum and minimum constraints on the geothermal gradient based on existing pressure-temperature data and our thermochronologic and closure temperature results. Guillot *et al.* (1995c) report that the Mugu leucogranite was emplaced at 2.6 ± 0.6 kbar to 4.0 ± 1.0 kbar and at ambient temperatures of 575 ± 25 °C. Assuming a surface temperature and pressure of 0 kbar and 0 °C, these values result in gradients of 73.7 ± 17.3 °C/km and 47.9 ± 12.2 °C/km, respectively. We use the mean of these, ca. 60 °C/km as our best estimate for the geothermal gradient in the UMM at ca. 20.76 Ma.

Estimates of denudation rate can be obtained by dividing the cooling rate by the geothermal gradient, and, thus, denudation curves are essentially linearly scaled versions of cooling curves. Scaling the cooling curves for the UMM by 60 °C/km results in the denudation rates in Figure 21. The composite denudation curve (Figure 21a) is segmented into three intervals, with average denudation rates of ca. 0.2 mm/yr between

Chapter 4: Exhumational history of the Mustang and Mugu granites

20.76 Ma and 17.5 Ma, ca. 1.7 mm/yr between 17.5 Ma and 15.5 Ma, and ca. 0.75 mm/yr between 15.5 Ma and the present (Figure 21a). The composite denudation curve is consistent with denudation rates determined from individual samples with multiple thermochronometers (Figure 21b).

Relief Method

In the Thinker area, one of our objectives in collecting samples in a steep transect was to examine the variation in cooling age as a function of elevation among samples whose locations differ little except in height. We make the simplifying assumptions that each sample will have passed through a given closure temperature isotherm at a different time, and that the isotherms themselves remain stationary with respect to the land surface. When these conditions are reasonably satisfied⁶, the slope of an age-elevation linear array can be taken as a direct estimate of the denudation rate independent of the geothermal gradient.

As mentioned previously, muscovite, biotite, and K-feldspar cooling ages from the Thinker area all show linear trends of varying slope, each characterized by increasing age with increasing elevation. The denudation rate obtained by a linear fit to the muscovite age-elevation data is ca. 0.15 mm/yr, averaged over the interval between ca. 18.3 and ca. 17.4 Ma (Figure 16a). The biotite linear array, however, is much steeper than that defined by muscovite, although its slope cannot be well-constrained since the ages defining it are all the same within uncertainty (Figure 16b). In addition, the K-feldspar MSD ages define a linear array with a slope of ca. 0.79 mm/yr at ca. 15.25 Ma

⁶ The latter assumption is incorrect in detail since fast denudation rates will cause isotherms to be advected towards the surface, an effect the computational method described in the following section addresses.

Chapter 4: Exhumational history of the Mustang and Mugu granites

(Figure 18a). By contrast, in the interval between ca. 14.51 Ma and ca. 12.88 Ma, the linear array defined by the K-feldspar MID ages has a much shallower slope of ca. 0.05 mm/yr (Figure 18b).

Collectively, we interpret these age-elevation patterns to indicate relatively slow denudation between > 18.3 Ma and ca. 17.4 Ma, after which the cooling rate increased substantially. By ca. 15.25 Ma, it had again slowed and continued to decelerate through at least ca. 13.79 Ma. While the absolute values of the denudation rates determined by the relief method differ somewhat from those obtained from the multiminerals method, the overall shape of the denudation curve is the same, with significant changes in slope at ca. 17.5 Ma and ca. 15.5-15 Ma and rapid denudation in the interval between.

Computational Method

Moore and England (2001) developed a computational method for determining denudation rates from thermochronologic data without *a priori* knowledge of the geothermal gradient. Geometrically, the problem considers a half-space ($z > 0$; z increases with depth) containing a rock with N thermochronometers that moves upward (in the negative z direction) relative to the surface ($z = 0$) at a constant rate U as material is removed from the top. Given this scenario, Moore and England (2001) argue that the curvature of the temperature-time path for the rock undergoing rapid exhumation is sensitive only to the initial temperature (T_o) and, primarily, the denudation rate (U). Moreover, they find that the curvature is relatively insensitive to parameters such as the time when denudation began (t_o), the initial depth ($z_o = Ut_o$), or the initial geothermal gradient ($a = T_o/z_o$). Thus, U can be computed from temperature-time histories with

Chapter 4: Exhumational history of the Mustang and Mugu granites

sufficient curvature as quantified by the parameter, λ , the square root of the Péclet number. The Péclet number is the ratio of the timescale for thermal advection to that for thermal diffusion, and temperature-time paths with large Péclet numbers – e.g. those dominated by thermal advection due to rapid denudation – have greater curvature. Moore and England (2001) determined that their technique is appropriate in situations with $\lambda > 0.3$, whereas temperature-time paths with $\lambda < 0.3$ cannot yield information about denudation rate unless additional constraints on t_o , z_o , or a are available.

The basic equation to be solved is the one-dimensional heat flow equation including advection (e.g. Turcotte and Schubert, 1982):

$$\frac{\partial^2 T}{\partial z^2} + \frac{U}{\kappa} \frac{\partial T}{\partial z} - \frac{1}{\kappa} \frac{\partial T}{\partial t} = -\frac{A}{K} \quad (1),$$

where T is temperature (in K), z is depth (in m), U is denudation rate (in m s⁻¹), κ is thermal diffusivity (in m² s⁻¹), t is time elapsed (in s⁻¹) since the beginning of denudation (t_o), A is radiogenic heat production (in W m⁻³), and K is thermal conductivity (in W m⁻¹ K⁻¹). With the simplifying assumptions of constant U , linear initial temperature structure ($T_{z,t=0} = az$), negligible radiogenic heat production ($A = 0$), and constant surface temperature ($T_{z=0,t} = 0$), solution of equation (1) for T yields (Moore and England, 2001):

$$T = \frac{aU}{2} \left\{ 2t_o + (t_o - 2t) e^{-\frac{U^2(t_o-t)}{\kappa}} \operatorname{erfc} \left[\frac{U(t-t_o)}{2\sqrt{\kappa t}} \right] - t_o \operatorname{erfc} \left[\frac{Ut_o}{2\sqrt{\kappa t}} \right] \right\} \quad (2).$$

For any choice of U , T_o , and z_o , equation (2) generates a temperature-time path for which a misfit function, R , can be defined (Moore and England, 2001):

$$R(U, T_o, z_o) = \frac{1}{N} \sum_{j=1}^N \delta_j \quad (3),$$

Chapter 4: Exhumational history of the Mustang and Mugu granites

where N is the number of thermochronometers per sample. The parameter δ_j is the smallest misfit between the synthetic temperature-time curve calculated from equation (2) (T_{calc}, t_{calc}) and the closure temperature-cooling age pair (T_{obs}, t_{obs}) for the j -th thermochronometer (Moore and England, 2001):

$$\delta_j = \min \left[\left(\frac{T_{obs} - T_{calc}}{\sigma_T} \right)^2 + \left(\frac{t_{obs} - t_{calc}}{\sigma_t} \right)^2 \right] \quad (4),$$

where, σ_T (in °C) and σ_t (in Ma) are the uncertainties in the closure temperature and cooling age of the j -th thermochronometer, respectively. A search within U - T_o - z_o parameter space for the synthetic temperature-time curve with the minimum R identifies the most likely (U, T_o, z_o) given the input thermochronologic data.

Our implementation of this procedure (Matlab® program by JMH, 2001) differs from that described by Moore and England (2001) in one key respect. Whereas their analysis implicitly constraint temperature-time paths to reach $T = 0$ at $t = 0$, we consider temperature-time paths that reach $T = 0$ at $t > 0$. We accomplish this by iteratively offsetting the input cooling ages by varying amounts between zero and the age of the youngest thermochronometer. This results in a family of best-fit temperature-time paths, one for each age-offset, and in the end we pick the one with the smallest R . In this way, we make use of another degree of freedom to place a constraint on when exhumation succeeded in bringing a sample to near-surface temperature conditions.

We apply this methodology to ten samples from the Mugu and Mustang granite for which we have data from multiple thermochronometers, e.g. some permutation of monazite or xenotime U-Pb, muscovite $^{40}\text{Ar}/^{39}\text{Ar}$, biotite $^{40}\text{Ar}/^{39}\text{Ar}$, and K-feldspar (MSD and/or MID) $^{40}\text{Ar}/^{39}\text{Ar}$ (Table 11). For muscovite, biotite, and MID K-feldspar $^{40}\text{Ar}/^{39}\text{Ar}$

Chapter 4: Exhumational history of the Mustang and Mugu granites

ages, we use the closure temperatures and uncertainties calculated for the specific sample (Tables 6 & 7). In the cases of U-Pb ages and MSD K-feldspar $^{40}\text{Ar}/^{39}\text{Ar}$ ages, we use closure temperatures of 700 ± 75 °C (Scaillet *et al.*, 1995; Patiño Douce and Harris, 1998) and 250 ± 50 °C, respectively. The latter assumes that the MSDs represent more retentive domains than the least retentive domain (LRD, which we equate with MIDs), and is a reasonable estimate of the highest nominal closure temperature expected from the K-feldspar domain structure (McDougall and Harrison, 1999).

Since the Péclet number (Pe) is given by:

$$Pe = \frac{Uz_o}{\kappa} = \lambda^2 \quad (5),$$

it cannot be directly calculated without knowing U and z_o beforehand. Instead, we estimate Pe – and, by extension, the λ parameter – graphically by plotting the closure temperature-cooling age pairs for a given sample, each normalized to the closure temperature and cooling age of the oldest thermochronometer, on a graph of T/T_o (dimensionless temperature) vs. τ (dimensionless time). We compare the resulting curves to similarly constructed curves with known λ (e.g. Figure 1 in Moore and England, 2001) and find that each of our samples has $\lambda > 0.3$ (Table 11).

We illustrate the results of our modeling in contoured cross-sectional plots through U - T_o - z_o parameter space (Figure 22a-j). Generally, the region of low R values in these plots is a narrow band elongated parallel to the z_o axis, with a small irregularly-shaped cross section in the U - t_o plane (e.g. Figure 22j). We therefore place more confidence in the best-fit values for U and T_o than in the corresponding z_o (or a and t_o derived from z_o). The white circles on the plots in Figure 22 represent the best-fit (U, T_o, z_o) ; the complete results are summarized in Table 11. In all but three cases, good

Chapter 4: Exhumational history of the Mustang and Mugu granites

fits to the thermochronologic data were achieved with an age-offset ($T = 0$ intercept age) of ca. 12-14 Ma (Table 11). In general, U is constrained to be ca. 1.5-3.61 mm/yr in the interval between ca. 18.3-17.5 Ma and ca. 14-12 Ma, although two samples yielded rates in excess of 4 mm/yr (Table 11). In every sample modeled, the simulated temperature-time paths yielded values for T_o consistent with the closure temperature of the oldest thermochronometer used in the simulation (Table 11).

This methodology allows us to better constrain the denudation rate in the interval of fast denudation (post ca. 17.5 Ma) implied by the near-vertical Mustang granite biotite age-elevation profile (Figure 16b). With the Moore and England (2001) analysis we obtain an average denudation rate of 2.7 mm/yr during this interval. This result is higher than the 1.7 mm/yr rate derived from the multiminerall method, perhaps suggesting that the geothermal gradient of 60 °C/km we used in the multiminerall calculations was an overestimate. To bring the multiminerall method in line, we would have to assume a geothermal gradient of 37 °C/km, assuming the same cooling rate (ca. 100 °C/Ma) for the interval between ca. 17.5 and ca. 15.5 Ma used to construct Figure 21. This moderate to high geothermal gradient is similar to values from other areas in the Himalaya with relatively young granites experiencing fast exhumation, such as the Nanga Parbat syntaxis (George *et al.*, 1993; Moore and England, 2001).

DISCUSSION: EVOLUTION OF THE UPPER MUSTANG MASSIF AND THE THAKKHOLA GRABEN

Figure 23 summarizes our results for the variation in denudation rate in the UMM over the past 21 Ma. The curve shows slow denudation (0.2-0.15 mm/yr) between >21

Chapter 4: Exhumational history of the Mustang and Mugu granites

Ma and ca. 17.4 Ma. Rapid denudation (average of 2.7 mm/yr) occurred between ca. 17.5 Ma and ca. 15.5 Ma. Finally, denudation decelerated between ca. 15.25 Ma (0.79 mm/yr) and ca. 13 Ma (0.05 mm/yr) – and progressively until the present – with an average of 0.75 mm/yr in this interval. As a whole, our denudational history is consistent with the 1 mm/yr rate (averaged between 20 Ma and 5 Ma) estimated by Le Fort and France-Lanord (1995). Our analysis, however, gives us the capability of resolving tectonically significant details within the denudational history, such as the accelerated denudation during the ca. 17.5-15.5 Ma interval.

In addition, the 14-12 Ma age-offsets obtained from our computational analysis give an estimate for when the Mustang granite reached near-surface temperature conditions and, presumably, was exposed at the surface. We can use this information to make an estimate for the amount of rock uplift that has occurred during denudation of the UMM. A denudation rate of 2.7 mm/yr between ca. 18 Ma and ca. 13 Ma implies 13.5 km of exhumation. Taking into account the ca. 2 km of relief developed in the present-day UMM and the isostatic effects of exhumation (e.g. Molnar and England, 1990), this amount of exhumation translates into ca. 10 km of rock uplift which is consistent with independent estimates of the depth of emplacement of the Mustang and Mugu granites and high-temperature metamorphism of the country rock (Guillot *et al.*, 1995b). However, we recognize that the initial phases of rapid exhumation may well have been isothermal, so the amount of exhumation we estimate from our denudation rates is a minimum estimate.

We assume that the contribution of erosion to denudation and concomitant exhumation, cooling, and rock uplift within the UMM has been limited. Paleoclimate

Chapter 4: Exhumational history of the Mustang and Mugu granites

within the Thakkhola graben is not well-known, but the facies represented in the Thakkhola graben fill – which range between coarse alluvial fan deposits, fluvial and periglacial conglomerates, and fine lacustrine siltstones (Fort *et al.*, 1982; Garzione *et al.*, 2000a; Hurtado *et al.*, 2001) – and the paleoelevation history of the area (Garzione *et al.*, 2000b) suggest that it has not varied significantly from current, high altitude arid plateau conditions since at least 12-10 Ma. Since denudation related to the movement of a major normal fault can lead to rapid cooling of rocks in its footwall, we hypothesize that the cooling and denudational history of the UMM is due to the inception of extension in Upper Mustang. Fabrics from the earliest extensional deformational phase we describe, D₂, indicate east-directed extension along shallowly dipping planes, and our thermochronology constrains it to have begun by ca. 21 Ma. We suggest that this represents the initial episodes of extension in the UMM along a low-angle detachment structure, perhaps related to the lithologic contact discerned in the Landsat TM imagery (Figure 4). Consistent ca. 17.5 Ma cooling ages and the abrupt metamorphic break across the Dangardzong fault between Thinker village and Lumpa Khola suggest that Dangardzong fault activity was occurring by ca. 17 Ma along this stretch. For this reason, we interpret the phase of rapid cooling and denudation beginning at ca. 18.3-17.5 Ma (Figure 23) to be largely the result of activity on the Dangardzong fault. This pushes back the minimum age of the current mode of the Thakkhola graben extension from the previous minimum estimate of ca. 14 Ma (Coleman and Hodges, 1995).

Estimating the rate and amount of horizontal extension due to the Dangardzong fault since 17.5 Ma is aided by the analysis of remote sensing data. The separation distance of ca. 30 km gives a preliminary estimate for the net amount of horizontal

Chapter 4: Exhumational history of the Mustang and Mugu granites

extension in the Thakkhola graben. Assuming this separation has occurred since ca. 17.5 Ma gives an average horizontal rate of extension of about 1.7 mm/yr over the last 17.5 Ma. This rate is a maximum since offset may have initiated as early as ca. 21 Ma. It is also a maximum since the subsurface geometry of the northern Thakkhola graben is not known.

At first, our ca. 17.5 Ma estimate of the age of the Dangardzong fault may seem incompatible with the age of Thakkhola extension inferred from the age of sediments preserved within the graben. Yoshida *et al.* (1984) proposed that the presumed oldest sediments in the Thakkhola graben are ca. 11 Ma based on magnetostratigraphy, a conclusion reinforced by additional magnetostratigraphy reported by Garzione *et al.* (2000a), who also placed a ca. 8 Ma maximum age on sediments unconformably above. The problem, however, does not necessarily lie with the ages of the sediments nor with those of the granites and structures, but in the presumption that the stratigraphy of the Thakkhola graben is completely known and that the oldest part of the basin fill has been identified and dated. Unpublished observations by the JMH and KVH suggest more complexity to the stratigraphy of the Thakkhola graben than previously appreciated. For instance, some of the oldest-known sediments in the basin (ca. 12-8 Ma; Yoshida *et al.*, 1984; Garzione *et al.*, 2000a) already contain clasts of leucogranite, implying that there may be yet-undescribed, syn-extensional deposits that pre-date surface exposure of the Mugu and Mustang granites (e.g. pre-ca. 14-12 Ma; this study). We therefore suspect that the oldest sediments in the basin may be older than 12-8 Ma, perhaps approaching the time of the inception of the Dangardzong fault (ca. 17.5 Ma).

Chapter 4: Exhumational history of the Mustang and Mugu granites

Our new constraint on the timing of fast tectonic denudation due to the Dangardzong fault is similar to $^{40}\text{Ar}/^{39}\text{Ar}$ dates from Lower Mustang that suggest brittle South Tibetan fault (STF) system activity during the interval ca. 16-12 Ma (Coleman and Hodges, 1995; Vannay and Hodges, 1996; Godin, 1999). Since this time interval includes both the early development of the Thakkhola graben and ongoing STF system activity, it supports the hypothesis that the Dangardzong fault and the STF system were synchronously active in the middle Miocene (Godin, 1999; Hurtado *et al.*, 2001; Hurtado *et al.*, submitted – see Chapter 3). That the two systems were also synchronously active and kinematically linked in the Pleistocene (Hurtado *et al.*, 2001) suggests a direct relationship between the development of the Dangardzong fault and the STF system.

Informed by our structural data, geochronologic constraints, and remote sensing analyses, we can go further and propose a model for the evolution of the Thakkhola graben that incorporates the development of the UMM. Lee *et al.* (2000) outlined three possible models for origin of the North Himalayan gneiss domes: (a) core complex extension; (b) diapirism; and (c) duplex formation. They also suggested four specific criteria types of observations and predictions that can be used to distinguish between them: (1) the nature of the contact between the high grade rocks and their country rock; (2) the cooling history; (3) the relationships between metamorphism, magmatism, and deformation; and (4) structural history of the high grade rocks and the country rock.

We can rule out the duplex model because we did not observe any thrust-sense kinematics in the UMM. The fact that the UMM is cored by the Mustang granite and closely associated with Mugu granites suggests that the diapiric model may be a reasonable one. In fact, diapiric upwelling of low-viscosity, low-density material does

Chapter 4: Exhumational history of the Mustang and Mugu granites

figure prominently in the model we propose for the development of the UMM (see also Chapter 6). However, we cannot overlook the regional context of the UMM within an extensional basin closely tied to the STF system. We therefore favor a core complex scenario for the early development of the UMM. Several lines of evidence support this interpretation. First, although we did not directly observe the contact separating the amphibolite-facies Lo Mantang gneisses in the UMM from the surrounding low-grade Tibetan Sedimentary Sequence rocks, the abrupt transition between the two suggests the contact is a structural one. Second, the domical shape of the UMM and the low-angle contact observed in Figure 4 are consistent with a core complex geometry, especially given the regional extension known to be occurring in the Thakkhola graben. Third, thermobarometric studies (Guillot *et al.*, 1995a) show that the granitic rocks in the core of the UMM have been subsequently exhumed from ca. 9 km, a process which, according to our thermochronologic data, occurred rapidly over a short period of time. Although this rapid exhumation most likely occurred on the Dangardzong fault, the deformational features we document in our structural observations are kinematically consistent with the progressive exhumation of the UMM along a steepening detachment system.

Figure 6 summarizes the deformational and intrusive history of the UMM based on field relationships and our geochronologic constraints (see also Table 10). Deformational phases D_{1-2} represent initial thickening and burial of the UMM during which the amphibolite-facies metamorphism occurred. Deformational phases D_{3-5} record top-to-the-east sense of shear accommodated by progressive slip on an extensional detachment system bounding the UMM. We hypothesize that the early (pre- ca. 21 Ma) ductile deformation (D_3) occurred during slip on one or more low-angle detachment

Chapter 4: Exhumational history of the Mustang and Mugu granites

faults (e.g. Figure 4b). D_{3-4} fabrics (ca. 21 Ma) developed downdip and were progressively exhumed (and overprinted by D_5) during successive movement events (e.g. Figure 7i), and it was during the D_{4-5} interval (post- ca. 18.3 Ma) that the Dangardzong fault initiated. Thus, the UMM had an origin similar to that of the extensional metamorphic core complexes in the North American Cordillera (e.g. Davis and Coney, 1979; Coney, 1980). However, as time progressed the core-complex mode of extension evolved into the current rift-flank style of extension, a process similar to that proposed for the Panamint Mountains of Southern California (Hodges *et al.*, 1990).

As discussed in Hurtado, *et al.* (submitted – see Chapter 3), a quantitative model for core complex formation by (Chéry, 2001) may be applicable to the evolution of Upper Mustang (see Figure 14 in Chapter 3). In that model, a breakaway fault triggers the development of a “synthetic”, low-angle décollement at depth. Subsequently, upwelling of material from below the brittle-ductile transition warps the décollement upwards thinning its hanging wall. This occurs in the footwall of a new, steep normal fault antithetic to the original breakaway. In the case of Upper Mustang, Hurtado *et al.* (submitted – see Chapter 3) suggest that the breakaway structure triggering the UMM décollement, was the northwest-dipping STF system basal detachment in the Marsyandi valley which at ca. 22-18 Ma was characterized top-to-the-west motion (Coleman, 1996a). Following the Chéry (2001) model, we suggest that continued slip would have resulted in upward doming of the STF detachment surface and thinning of its hanging wall west of the proto-Thakkhola graben (Figure 24a). It is during this phase that the UMM is exhumed as a metamorphic core complex. The core-complex style of deformation continues until the steep antithetic normal fault predicted by the Chéry

Chapter 4: Exhumational history of the Mustang and Mugu granites

(2001) model initiates. This phase marks the beginning of extension along the Dangardzong fault and formation of the Thakkhola basin as the kinematics progressively shift from the core complex mode of extension to the rift mode.

Figure 24b is a block model cartoon of the architecture of the Upper Mustang region, having developed as in Figure 24a. According to this model, our geologic transects would have sampled the footwall of the southern margin of an eastward-extending low-angle detachment system. Our structural observations for D_{1-2} deformation are consistent with this model as they record subhorizontal, coaxial, north-south compression and east-west extension along south-dipping planes, consistent with the essentially transcurrent motion expected along a margin parallel to the extension direction.

Furthermore, there are three implications of the model in Figure 24b. The first is that the low-angle detachment surface active during the main core-complex phase is, in fact, the STF system basal detachment surface. The geometry we envision is not unlike that which has been proposed for the Kangmar dome and illustrated in interpretive cross-sections based on the results of the INDEPTH seismic reflection campaign (e.g. Nelson *et al.*, 1996). The second implication is that the material being exhumed in the UMM originates below the STF décollement and is related to the high grade, migmatitic gneisses of the Greater Himalayan Sequence exposed in the core of the Himalaya in the footwall of the STF system. Indeed, there are superficial as well as petrographic and geochemical similarities between the Mustang granite and the augen orthogneisses common in the uppermost part of the Greater Himalayan Sequence (Le Fort and France-Lanord, 1995). In addition, the large number of Paleozoic U-Pb ages obtained from the

Chapter 4: Exhumational history of the Mustang and Mugu granites

Mustang granite is a characteristic it shares with the Greater Himalayan Sequence orthogneisses (e.g. Hodges *et al.*, 1996b). We recognize, however, that unlike our interpretation of the Mustang granite, the preferred interpretation of the Greater Himalayan Sequence orthogneiss is that it represents a Paleozoic igneous stratum modified during the Miocene by Himalayan metamorphism rather than a Miocene intrusion (e.g. Hodges, 2000 and references therein).

Similarly, the Mugu leucogranites resemble the leucocratic dikes and sills commonly found intruding the Greater Himalayan Sequence. In particular, the Mugu pluton bears superficial, petrographic, and geochemical similarities with large leucogranite bodies elsewhere in the Himalaya – in particular the Manaslu granite (Le Fort and France-Lanord, 1995) – even though the latter are more commonly found in the immediate hanging wall of the STF system rather than tens of kilometers to the north as is the case with the Mugu pluton (see Hurtado *et al.*, submitted – Chapter 3). However, if the low-angle décollement bounding the UMM is, in fact, an exhumed portion of the STF basal detachment surface, the structural disposition of the adjacent Mugu granite would be analogous to that of the Manaslu granite.

The third implication is a kinematic link between the STF system and extensional basins, such as the Thakkhola graben, which are closely associated with North Himalayan gneiss domes. In fact, a linkage between the STF system and the Kangmar dome has been previously suggested by work in southern Tibet by Chen *et al.* (1990), and a core complex scenario was considered by Edwards *et al.* (1996) for the development of the Kula Kangri pluton in the footwall of the STF system in the Gonto La area of Tibet (Figure 1). Our model, however, has the additional feature of explicitly relating east-west

Chapter 4: Exhumational history of the Mustang and Mugu granites

extension to core-complex development, which, in turn, is affected by STF system activity. Furthermore, by applying the Chéry (2001) developmental model to the Thakkhola graben, we can hypothesize a common mechanism for the three extensional systems: flow of the Greater Himalayan Sequence within an intracrustal channel beneath the STF system décollement. In the Himalaya, southward extrusion of channel material may occur between the STF system and the Main Central thrust (MCT) system (Hodges *et al.*, 2001), and it is reasonable that variations in the timing, vigor, and orientation of this extrusion can have effects elsewhere in the orogen (see Chapter 6). A strong possibility for how this could occur is through the redistribution and removal of gravitational potential energy (GPE) via orogen-parallel and orogen-perpendicular channel flow (Hodges *et al.*, 2001; see Chapter 6). For example, areas north of the Himalayan front with an excess of GPE – due to activity (or inactivity) of the STF and MCT systems and/or erosion – could have a propensity for orogen-parallel flow to dissipate the local GPE maximum. This flow, in turn, drives extension in the crust above the channel, resulting in rifting and the development of gneiss domes (see Chapter 6).

CONCLUSION

Research in the Upper Mustang area of central Nepal has yielded new minimum U-Pb age constraints for the oldest phases of the Mugu leucogranite (20.76 ± 0.67 Ma) and the first age constraint for the Mustang granite (23.35 ± 0.17 Ma). Integrated U-Pb, $^{40}\text{Ar}/^{39}\text{Ar}$, and structural geologic work has defined a deformational and intrusive history for the Upper Mustang massif characterized by amphibolite-facies metamorphism of the Lo Mantang gneiss, protracted Mugu granite intrusion over at least 3 Myrs, and five

Chapter 4: Exhumational history of the Mustang and Mugu granites

deformational phases (Figure 6; Table 10). Kinematic indicators show that deformation in the UMM has been characterized by east-west extension along progressively steeper structures, and we suggest that the UMM originated as a core complex that transitioned into a steeply-dipping extensional rift system, forming the modern Thakkhola graben. U-Pb and $^{40}\text{Ar}/^{39}\text{Ar}$ cooling ages indicating that ductile east-west extension in the region began between ca. 23.35 Ma and ca. 20.76 Ma and that large-scale top-to-the east brittle-ductile normal-sense motion was ongoing by ca. 18.3-17.5 Ma. The latest deformational phases in the UMM are kinematically indistinguishable from the modern Dangardzong fault and are accompanied by a period of rapid cooling (ca. 100°C/Myr) and denudation (ca. 2.7 mm/yr) of the Upper Mustang Massif in the Dangardzong fault footwall between ca. 18.3-17.5 Ma and ca. 15.5-12 Ma (Figure 23). The maximum horizontal rate of extension was approximately 1.7 mm/yr, as indicated by the dismemberment of the originally circular plan form of the Mustang granite by the Dangardzong fault.

Our estimate of ca. 18.3-17.5 Ma for the age of inception of the Thakkhola graben is substantially older than the previous minimum estimate of ca. 14 Ma (Coleman and Hodges, 1995). It is also far older than the ca. 8 Ma estimate for the age of the Nyainqentanghla rift which Harrison *et al.* (1995) take as the age of Tibetan east-west extension in general. Other estimates for the age of east-west normal faulting in Tibet range between a minimum of ca. 13.5 Ma (Blisniuk *et al.*, 2001) and ca. 18.3-13.3 Ma (Williams, 2001). Based on the wide range in ages for the various grabens studied by these workers and others, we feel that the notion of a single, catastrophic event leading to east-west extension on the Tibetan plateau (e.g. Molnar and Tapponnier, 1978; England and Houseman, 1989; Harrison *et al.*, 1992; Molnar *et al.*, 1993) is unwarranted. Instead,

Chapter 4: Exhumational history of the Mustang and Mugu granites

our findings suggest that the extensional histories of Tibetan grabens situated close to the STF system are closely tied to core-complex development in associated North Himalayan gneiss domes, and, ultimately, to activity on the STF system.

ACKNOWLEDGEMENTS

This research was supported by a grant from the U. S. National Science Foundation (NSF) awarded to KVH, J. P. Grotzinger, and Kelin X Whipple (EAR-9706216) and an NSF graduate fellowship awarded to JMH. JMH thanks the Frank and Eva B. Buck Foundation for their continuing financial support. JMH also thanks: Neel Chatterjee for guidance in using the MIT Electron Microprobe; Karen Viskupic for advice regarding common Pb corrections; and Arthur White for discussions regarding biotite and muscovite closure temperature determination, $^{40}\text{Ar}/^{39}\text{Ar}$ analysis of K-feldspar, and Fcflucence monitor age calibration. Ang Phuri Sherpa, Tsering Tendi Sherpa Lama, Makar Girial, Chhatra Girial, Pasang Sherpa, Bom Magar, the “Jomsom Mule Wrangler”, Ang Shen Norbu (the “Dangardzong Yak Wrangler”), and all our friends at Magic Mountain-Sundar Himali Treks provided superb logistical support in the field. JMH and KVH thank: Mr. Hom Prasad Khatiwada for his services as government liaison; the Nepal Ministry of Home for permission to enter the Upper Mustang Restricted Area; and B. N. Upreti, Tribuvan University, and the personnel of the Department of Mines and Geology of the Government of Nepal for their assistance. JMH and KVH also send a special thanks and *tashi delek* to the King of Mustang, Raja Jigme Dorje, for his hospitality and blessing. ENVI® and Matlab® are trademarks of Research Systems, Incorporated and The MathWorks, respectively, and reference herein does not imply endorsement by the Massachusetts Institute of Technology. Use of DTED® Level 0 data does not indicate endorsement or approval by either the U. S. Secretary of Defense, the former Defense Mapping Agency, or the National Imagery and Mapping Agency (United States Code, 10 U.S.C. 445).

Chapter 4: Exhumational history of the Mustang and Mugu granites

REFERENCES CITED

- Allmendinger, R. W., 2001, StereonetPPC 6.0.2.
- Armijo, R., Tapponier, P., Mercier, J., and Han, T., 1986, Quaternary extension in Southern Tibet: Field observations and tectonic implications: *Journal of Geophysical Research*, v. 91, p. 13803-13872.
- Benjamin, M. T., 1986, *Fission-track ages on some Bolivian plutonic rocks: Implications for the Tertiary uplift and erosion history of the Altiplano-Cordillera Real* [M.S. thesis]: Dartmouth College, 58 p.
- Benjamin, M. T., Johnson, N. M., and Naeser, C. W., 1987, Recent rapid uplift in the Bolivian Andes: Evidence from fission-track dating: *Geology*, v. 15, p. 680-683.
- Blisniuk, P. M., Hacker, B. R., Glodny, J., Ratschbacher, L., Bi, S., Wu, Z., McWilliams, M. O., and Calvert, A., 2001, Normal faulting in central Tibet since at least 13.5 Myr ago: *Nature*, v. 412, p. 628-632.
- Bordet, P., Colchen, M., Krummenacher, D., LeFort, P., Mouterde, R., and Remy, M., 1971, *Recherches géologiques dans l'Himalaya du Népal, région de la Thakkhola*: Paris, Centre National de la Recherche Scientifique, 279 p.
- Brown, R. L., and Nazarchuk, J. H., 1993, Annapurna detachment fault in the Greater Himalaya of central Nepal, in Treloar, P. J., and Searle, M. P., eds., *Himalayan Tectonics*: London, Geological Society Special Publication, 47, p. 461-473.
- Buck, W. R., and Sokoutis, D., 1994, Analogue model of gravitational collapse and surface extension during continental convergence: *Nature*, v. 369, p. 737-740.
- Burchfiel, B. C., Chen, Z., Hodges, K. V., Liu, Y., Royden, L. H., Deng, C., and Xu, J., 1992, *The South Tibetan Detachment System, Himalayan Orogen: Extension Contemporaneous With and Parallel to Shortening in a Collisional Mountain Belt*, Geological Society of America Special Paper 269: Boulder, CO, Geological Society of America, 41 p.
- Burchfiel, B. C., Chen, Z., Royden, L. H., Liu, Y., and Deng, C., 1991, Extensional development of Gabo Valley, southern Tibet: *Tectonophysics*, v. 194, p. 187-193.
- Burchfiel, B. C., and Royden, L. H., 1985, North-south extension within the convergent Himalayan region: *Geology*, v. 13, p. 679-682.
- Burg, J. P., and Chen, G. M., 1984, Tectonics and structural zonation of southern Tibet, China: *Nature*, v. 311, p. 219-223.

Chapter 4: Exhumational history of the Mustang and Mugu granites

- Burg, J. P., Guiraud, M., Chen, G. M., and Li, G. C., 1984, Himalayan metamorphism and deformations in the North Himalayan belt, southern Tibet, China: *Earth and Planetary Science Letters*, v. 69, p. 391-400.
- Caby, R., Pêcher, A., and LeFort, P., 1983, Le M.C.T. himalayen: nouvelles données sur le métamorphisme inverse à la base de la Dalle du Tibet: *Revue Géogr. phys. Géol. dynam.*, v. 24, p. 89-100.
- Chen, Z., Liu, Y., Hodges, K. V., Burchfiel, B. C., Royden, L. H., and Deng, C., 1990, Structural evolution of the Kangmar dome: A metamorphic core complex in southern Xizang (Tibet): *Science*, v. 250, p. 1552-1556.
- Chéry, J., 2001, Core complex mechanics: From the Gulf of Corinth to the Snake Range: *Geology*, v. 29, no. 5, p. 439-442.
- Colchen, M., 1980, *Evolution paléogéographique et structurale du fossé de la Thakkhola-Mustang (Himalaya du Népal): implications sur l'histoire récente de la chaîne himalayenne*: C.R. Ac. Sc. Paris, v. 290, p. 311-314.
- Colchen, M., LeFort, P., and Pêcher, A., 1986, *Recherches Géologiques dans l'Himalaya du Népal: Annapurna - Manaslu - Ganesh Himal (Notice de la carte géologique au 1/200000)*: Paris, Centre National de la Recherche Scientifique, 136 p.
- Coleman, M. E., 1996a, Orogen-parallel and orogen-perpendicular extension in the central Nepalese Himalayas: *Geological Society of America Bulletin*, v. 108, p. 1594-1607.
- Coleman, M. E., 1996b, *The Tectonic Evolution of the Central Himalaya, Marsyandi Valley, Nepal* [Ph.D. thesis]: MIT, 221 p.
- Coleman, M. E., 1998, U-Pb constraints on Oligocene-Miocene deformation and anatexis, Marsyandi Valley, central Nepalese Himalaya: *American Journal of Science*, v. 298, p. 553-571.
- Coleman, M. E., and Hodges, K. V., 1995, Evidence for Tibetan plateau uplift before 14 Myr ago from a new minimum age for east-west extension: *Nature*, v. 374, p. 49-52.
- Coney, P. J., 1980, Cordilleran metamorphic core complexes: An overview, in Crittenden, M. D., Coney, P. J., and Davis, G. H., eds., *Cordilleran Metamorphic Core Complexes*: Boulder, CO, Geological Society of America Memoir 153, p. 7-34.
- Copeland, P., Harrison, T. M., Kidd, W. S. F., Xu, R., and Zhang, Y., 1987, Rapid Early Miocene acceleration of uplift in the Gangdese belt, Xizang - southern Tibet, and

Chapter 4: Exhumational history of the Mustang and Mugu granites

- its bearing on accommodation mechanisms in the India-Asia collision: *Earth and Planetary Science Letters*, v. 86, p. 240-252.
- Davis, G. H., and Coney, P. J., 1979, Geologic development of the Cordilleran metamorphic core complexes: *Geology*, v. 7, p. 120-124.
- Edwards, M. A., Kidd, W. S. F., Li, J., Yue, Y., and Clark, M., 1996, Multi-stage development of the southern Tibetan detachment system near Khula Kangri. New data from Gonto La: *Tectonophysics*, v. 260, p. 1-19.
- England, P., and Houseman, G., 1989, Extension during continental convergence, with application to the Tibetan Plateau: *Journal of Geophysical Research*, v. 94, p. 17561-17579.
- Fort, M., Freydet, P., and Colchen, M., 1982, Structural and sedimentological evolution of the Thakkhola-Mustang graben (Nepal Himalayas): *Zeitschrift für Geomorphologie*, v. 42, p. 75-98.
- Foster, D. A., Harrison, T. M., Copeland, P., and Heizler, M. T., 1990, Effects of excess argon with large diffusion domains on K-feldspar age spectra: *Geochimica et Cosmochimica Acta*, v. 54, p. 1699-1708.
- Fuchs, G., 1967, *Geological Map of the Dolpo region and the Dhaula Himal*: Osterr. Akad. Wiss., scale 1:100000.
- Fuchs, G., Widder, R., and Tuladhar, R., 1988, Contribution to the geology of the Manang area (Annapurna Himal, Nepal): *Jahrbuch der Geologischen Bundesanstalt, Wien*, v. 131, p. 593-607.
- Gansser, A., 1964, *Geology of the Himalayas*: London, Wiley Interscience, 289 p.
- Gariépy, C., Allègre, C. J., and Xu, R.-H., 1985, The Pb-isotope geochemistry of granitoids from the Himalaya-Tibet collision zone: implications for crustal evolution: *Earth and Planetary Science Letters*, v. 74, p. 220-234.
- Garzanti, E., Baud, A., and Mascle, G., 1987, Sedimentary record of the northward flight of India and its collision with Eurasia (Ladakh Himalaya, India): *Geodinamica Acta (Paris)*, v. 1, no. 4/5, p. 297-312.
- Garzanti, E., Gorza, M., Martellini, L., and Nicora, A., 1994, Transition from diagenesis to metamorphism in the Paleozoic to Mesozoic succession of the Dolpo-Manang synclinorium and Thakkhola graben (Nepal Tethys Himalaya): *Eclogae Geologicae Helvetiae*, v. 87, p. 613-632.

Chapter 4: Exhumational history of the Mustang and Mugu granites

- Garzione, C. N., Dettman, D. L., Quade, J., DeCelles, P. G., and Butler, R. F., 2000a, High times on the Tibetan Plateau: Paleoelevation of the Thakkhola graben, Nepal: *Geology*, v. 28, no. 4, p. 339-342.
- Garzione, C. N., Quade, J., DeCelles, P. G., and English, N. B., 2000b, Predicting paleoelevation of Tibet and the Himalaya from $\delta^{18}\text{O}$ vs. altitude gradients in meteoric water across the Himalaya: *Earth and Planetary Science Letters*, v. 183, p. 215-229.
- George, M., Harris, N. B. W., and butler, R. W. H., 1993, The tectonic implications of contrasting granite magmatism between the Kohistan island arc and the Nanga Parbat massif, Pakistan Himalaya, in Treloar, P. J., and Searle, M. P., eds., *Himalayan Tectonics*: London, Geological Society Special Publication, p. 173-191.
- Giletti, B. J., 1974, Studies in diffusion I: Argon in phlogopite mica, in Hofmann, A. W., Giletti, B. J., Yoder, H. S., and Yund, R. A., eds., *Geochemical Transport and Kinetics*: Washington, Carnegie Institute of Washington Publication, p. 107-115.
- Godin, L., 1999, *Tectonic Evolution of the Tethyan Sedimentary Sequence in the Annapurna Area, Central Nepal Himalaya* [Ph.D. thesis]: Carleton University, 219 p.
- Godin, L., Brown, R. L., Hanmer, S., and Parrish, R., 1999, Back folds in the core of the Himalayan orogen: An alternative interpretation: *Geology*, v. 27, p. 151-154.
- Grove, M., and Harrison, T. M., 1996, 40Ar^* diffusion in Fe-rich biotite: *American Mineralogist*, v. 81, p. 940-951.
- Guillot, S., LeFort, P., Pecher, A., Barman, M. R., and Aprahamian, J., 1995a, Contact metamorphism and depth of emplacement of the Manaslu Granite (central Nepal); implications for Himalayan orogenesis: *Tectonophysics*, v. 241, no. 1-2, p. 99-119.
- Guillot, S., Mascle, G., Lardeaux, J. M., Colchen, M., and De Sigoyer, J., 1995b, A new discovery of eclogites from the Himalaya, Tso Moriri dome unit (northwestern India): *Mitteilungen des Geologischen Instituts ETH Zürich und Universität Zürich, Neue Folge*, v. 298, p. 84-87.
- Guillot, S., Pecher, A., and LeFort, P., 1995c, Contrôles tectoniques et thermiques de la mise en place des leucogranites himalayens; Tectonic and thermal constraints on emplacement of Himalayan leucogranites: *Comptes Rendus Acad. Sci. Paris*, v. 320, no. 1, p. 55-61.
- Hagen, T., 1968, *Report on the Geological Survey of Nepal: Volume 2, Geology of the Thakkhola, including adjacent areas*, Schweiz. Naturforsch. Ges. Denschr., 160 p.

Chapter 4: Exhumational history of the Mustang and Mugu granites

- Hagen, T., 1969, *Report on the Geological Survey of Nepal: Volume 1, Preliminary reconnaissance*, Schweiz. Naturforsch. Ges. Denschr.
- Hames, W. E., and Bowring, S. A., 1994, An empirical evaluation of the argon diffusion geometry in muscovite: *Earth and Planetary Science Letters*, v. 124, p. 161-167.
- Harrison, T. M., Copeland, P., Kidd, W. S. F., and Lovera, O., 1995, Activation of the Nyainquentanghla Shear Zone: Implications for uplift of the southern Tibetan Plateau: *Tectonics*, v. 14, p. 658-676.
- Harrison, T. M., Copeland, P., Kidd, W. S. F., and Yin, A., 1992, Raising Tibet: *Science*, v. 255, p. 1663-1670.
- Harrison, T. M., Duncan, I., and McDougall, I., 1985, Diffusion of ^{40}Ar in biotite: Temperature, pressure, and compositional effects: *Geochimica et Cosmochimica Acta*, v. 49, p. 2461-2468.
- Harrison, T. M., Heizler, M. T., Lovera, O. M., Chen, W., and Grove, M., 1994, A chlorine disinfectant for excess argon released from K-feldspar during step heating: *Earth and Planetary Science Letters*, v. 123, p. 95-104.
- Harrison, T. M., Lovera, O. M., and Grove, M., 1997, New insights into the origin of two contrasting Himalayan granite belts: *Geology*, v. 25, p. 899-902.
- Hawkins, D. P., and Bowring, S. A., 1997, U-Pb systematics of monazite and xenotime: case studies from the Paleoproterozoic of the Grand Canyon, Arizona: *Contributions to Mineralogy and Petrology*, v. 127, p. 87-103.
- Herren, E., 1987, Zaskar shear zone: Northeast-southwest extension within the Higher Himalayas (Ladakh, India). *Geology*, v. 15, p. 409-413.
- Hodges, K., Bowring, S., Davidek, K., Hawkins, D., and Krol, M., 1998, Evidence for rapid displacement on Himalayan normal faults and the importance of tectonic denudation in the evolution of mountain ranges: *Geology*, v. 26, p. 483-486.
- Hodges, K. V., 2000, Tectonics of the Himalaya and southern Tibet from two perspectives: *Geological Society of America Bulletin*, v. 112, no. 3, p. 324-350.
- Hodges, K. V., Bowring, S., Hawkins, D., and Davidek, K., 1996a, The age of the Rongbuk granite and Qomolangma detachment, Mount Everest region, southern Tibet, in Macfarlane, A. M., Sorkhabi, R. B., and Quade, J., eds., *11th Himalaya-Karakoram-Tibet Workshop Abstracts*, p. 63-64.
- Hodges, K. V., and Bowring, S. A., 1995, $^{40}\text{Ar}/^{39}\text{Ar}$ thermochronology of isotopically zoned micas: Insights from the southwestern USA Proterozoic orogen: *Geochimica et Cosmochimica Acta*, v. 59, p. 3205-3220.

Chapter 4: Exhumational history of the Mustang and Mugu granites

- Hodges, K. V., Hames, W. E., and Bowring, S. A., 1994a, $^{40}\text{Ar}/^{39}\text{Ar}$ age gradients in micas from a high temperature - low pressure metamorphic terrain: Evidence for very slow cooling and implications for the interpretation of age spectra: *Geology*, v. 22, p. 55-58.
- Hodges, K. V., Hames, W. E., Olszewski, W. J., Burchfiel, B. C., Royden, L. H., and Chen, Z., 1994b, Thermobarometric and $^{40}\text{Ar}/^{39}\text{Ar}$ geochronologic constraints on Eohimalayan metamorphism in the Dinggyê area, southern Tibet: *Contributions to Mineralogy and Petrology*, v. 117, p. 151-163.
- Hodges, K. V., Hurtado, J. M., and Whipple, K. X., 2001, Southward Extrusion of Tibetan Crust and its Effect on Himalayan Tectonics: *Tectonics*, v. 20 (6), p. 799-8099.
- Hodges, K. V., McKenna, L. W., and Harding, M. B., 1990, Structural unroofing of the central Panamint Mountains, Death Valley region, SE California, in Wernicke, B. P., ed., *Basin and Range Extensional Tectonics Near the Latitude of Las Vegas, NV*: Boulder, CO, Geological Society of America Memoir 176, p. 377-390.
- Hodges, K. V., Parrish, R., Housh, T., Lux, D., Burchfiel, B. C., Royden, L., and Chen, Z., 1992, Simultaneous Miocene extension and shortening in the Himalayan orogen: *Science*, v. 258, p. 1466-1470.
- Hodges, K. V., Parrish, R. R., and Searle, M. P., 1996b, Tectonic evolution of the central Annapurna Range, Nepalese Himalayas: *Tectonics*, v. 15, p. 1264-1291.
- Hurtado, J. M., Hodges, K. V., and Whipple, K. X., 2001, Neotectonics of the Thakkhola Graben and Implications for Recent Activity on the South Tibetan Fault System in the Central Nepal Himalaya: *Geological Society of America Bulletin*, v. 113, no. 2, p. 222-240.
- Judge, A., and McNutt, M., 1991, The relationship between plate curvature and elastic plate thickness: A study of the Peru-Chile trench: *Journal of Geophysical Research*, v. 96, p. 16625-16639.
- Krummenacher, D., 1971, Géochronométrie des roches de l'Himalaya., in sci., C. n. r., ed., *Recherches géologiques dans l'Himalaya du Népal, région de la Thakkhola*: Paris, p. 187-202.
- Le Fort, P., 1975, Himalayas: the collided range: Present knowledge of the continental arc: *American Journal of Science*, v. 275-A, p. 1-44.
- Le Fort, P., and France-Lanord, C., 1995, Granites from Mustang and surrounding regions, central Nepal: *Journal of the Nepal Geological Society*, v. 10, p. 79-81.

Chapter 4: Exhumational history of the Mustang and Mugu granites

- Lee, J., Hacker, B. R., Dinklage, W. S., Yu, W., Gans, P., and Calvert, A., 2000, Evolution of the Kangmar Dome, southern Tibet: structural, petrologic, and thermochronologic constraints: *Tectonics*, v. 19, no. 5, p. 872-895.
- Lin, A., 1999, S-C cataclasite in granitic rock: *Tectonophysics*, v. 304, p. 257-273.
- Lister, G. S., and Baldwin, S. L., 1996, Modelling the effect of arbitrary P-T-t histories on argon diffusion in minerals using the MacArgon program for the Apple Macintosh: *Tectonophysics*, v. 253, p. 83-109.
- Lister, G. S., and Snoke, A. W., 1984, S-C mylonites: *Journal of Structural Geology*, v. 6, p. 617-638.
- Lovera, O. M., Heizler, M. T., and Harrison, T. M., 1993, Argon diffusion domains in K-feldspar II: kinetic properties of MH-10: *Contributions to Mineralogy and Petrology*, v. 113, p. 381-393.
- Lovera, O. M., Richter, F. M., and Harrison, T. M., 1989, $^{40}\text{Ar}/^{39}\text{Ar}$ geochronometry for slowly cooled samples having a distribution of diffusion domain size: *Journal of Geophysical Research*, v. 94, p. 17917-17936.
- Lovera, O. M., Richter, F. M., and Harrison, T. M., 1991, Diffusion domains determined by ^{39}Ar released during step heating: *Journal of Geophysical Research*, v. 96, p. 2057-2069.
- McCaffrey, K. J. W., 1996, Estimates of modern arc-parallel strain rates in forearcs: *Geology*, v. 24, p. 27-30.
- McCaffrey, R., and Nabelek, J., 1998, Role of oblique convergence in the active deformation of the Himalayas and southern Tibet plateau: *Geology*, v. 28, no. 8, p. 691-694.
- McDougall, I., and Harrison, T. M., 1999, *Geochronology and Thermochronology by the $^{40}\text{Ar}/^{39}\text{Ar}$ Method* (2nd Ed.): New York, Oxford University Press, 269 p.
- Mercier, J.-L., Armijo, R., Tapponier, P., Carey-Gailhardis, E., and Han, T. L., 1987, Change from late Tertiary compression to Quaternary extension in southern Tibet during the India-Asia collision: *Tectonics*, v. 6, p. 275-304.
- Molnar, P., and England, P., 1990, Late Cenozoic uplift of mountain ranges and global climate change: chicken or egg?: *Nature*, v. 346, p. 29-34.
- Molnar, P., England, P., and Martinod, J., 1993, Mantle dynamics, uplift of the Tibetan Plateau, and the Indian monsoon: *Reviews of Geophysics*, v. 31, p. 357-396.

Chapter 4: Exhumational history of the Mustang and Mugu granites

- Molnar, P., and Lyon-Caen, H., 1989, Fault-plane solutions of earthquakes and active tectonics of the Tibetan plateau and its margins: *Geophysical Journal International*, v. 99, p. 123-153.
- Molnar, P., and Tapponier, P., 1975, Cenozoic tectonics of Asia: Effects of a continental collision: *Science*, v. 189, p. 419-426.
- Molnar, P., and Tapponier, P., 1978, Active tectonics of Tibet: *Journal of Geophysical Research*, v. 83, p. 5361-5375.
- Moore, M. A., and England, P. C., 2001, On the inference of denudation rates from cooling ages of minerals: *Earth and Planetary Science Letters*, v. 185, p. 265-284.
- Nelson, K. D., Zhao, W., Brown, L. D., Kuo, J., Che, J., Xianwen, L., Klemperer, S., Makovsky, Y., Meissner, R., Mechie, J., Kind, R., Wenzel, F., Ni, J., Nabelek, J., Chen, L., Handong, T., Wenbo, W., Jones, A. G., Booker, J., Unsworth, M., Kidd, W. S. F., Hauk, M., Alsdorf, D., Ross, A., Cogan, M., Wu, C., Sandvol, E. A., and Edwards, M., 1996, Partially molten middle crust beneath southern Tibet: Synthesis of Project INDEPTH Results: *Science*, v. 274, p. 1684-1688.
- Ni, J., and York, J. E., 1978, Cenozoic extensional tectonics of the Tibetan Plateau: *Journal of Geophysical Research*, v. 83, p. 5277-5384.
- NIMA, 1996, *MIL-PRF-89020A: Military Performance Specification, DTED*.
- Pan, Y., and Kidd, W. S. F., 1992, Nyainqentanglha shear zone: A late Miocene extensional detachment in the southern Tibetan Plateau: *Geology*, v. 20, p. 775-778.
- Parrish, R., 1990, U-Pb dating of monazite and its application to geological problems: *Canadian Journal of Earth Sciences*, v. 27, p. 1431-1450.
- Patiño Douce, A. E., and Harris, N., 1998, Experimental Constraints on Himalayan Anatexis: *Journal of Petrology*, v. 39, no. 4, p. 689-710.
- Ratschbacher, L., Frisch, W., Liu, G., and Chen, C., 1994, Distributed deformation in southern and western Tibet during and after India-Asia collision: *Journal of Geophysical Research*, v. 99, p. 19917-19945.
- Renne, P. R., Swisher, C. C., Deino, A. L., Karner, D. B., Owens, T. L., and DePaolo, D. J., 1998, Intercalibration of standards, absolute ages and uncertainties in $^{40}\text{Ar}/^{39}\text{Ar}$ dating: *Chemical Geology*, v. 145, p. 117-152.
- Robbins, G. A., 1972, *Radiogenic argon diffusion in muscovite under hydrothermal conditions* [M.S. thesis]: Brown University, 42 p.

Chapter 4: Exhumational history of the Mustang and Mugu granites

- Roddick, J. C., Cliff, R. A., and Rex, D. C., 1980, The evolution of excess argon in Alpine biotites - A ^{40}Ar - ^{39}Ar analysis: *Earth and Planetary Science Letters*, v. 48, p. 185-208.
- RSI, 2000, *ENVI User's Guide 3.4*, Research Systems, Inc., 930 p.
- Scaillet, B., Pichavant, M., and Roux, J., 1995, Experimental crystallization of leucogranite magmas: *Journal of Petrology*, v. 36, no. 3, p. 663-705.
- Schärer, U., 1984, The effect of initial ^{230}Th disequilibrium on young U-Pb ages: the Makalu case, Himalaya: *Earth and Planetary Science Letters*, v. 67, p. 191-204.
- Schmitz, M. D., and Bowring, S. A., 2001, U-Pb zircon and titanite systematics of the Fish Canyon Tuff: an assessment of high-precision U-Pb geochronology and its application to young volcanic rocks: *Geochimica et Cosmochimica Acta*, v. 65, p. 2571-2587.
- Stacey, J. S., and Kramers, J. D., 1975, Approximation of terrestrial isotope evolution by a two-stage model: *Earth and Planetary Science Letters*, v. 26, p. 207-221.
- Steiger, R. H., and Jäger, E., 1977, Subcommittee on geochronology: convention on the use of decay constants in geo- and cosmochronology: *Earth and Planetary Science Letters*, v. 36, p. 359-362.
- Tapponier, P., Mercier, J. L., Proust, F., Andrieux, J., Armijo, R., Bassoulet, J. P., Brunel, M., Burg, J. P., Colchen, M., Dupré, B., Girardeau, J., Marcoux, J., Mascle, G., Matte, P., Nicolas, A., and Li, T. D., 1981, The Tibetan side of the India-Eurasia collision: *Nature*, v. 294, p. 405-410.
- Turcotte, D. L., and Schubert, G., 1982, *Geodynamics: applications of continuum physics to geological problems*: New York, John Wiley & Sons, 450 p.
- Vannay, J.-C., and Hodges, K. V., 1996, Tectonometamorphic evolution of the Himalayan metamorphic core between Annapurna and Dhaulagiri, central Nepal: *Journal of Metamorphic Geology*, v. 14, p. 635-656.
- Viskopic, K. M., and Hodges, K. V., 2001, Monazite-xenotime thermochronology: methodology and an example from the Nepalese Himalaya: *Contributions to Mineralogy and Petrology*, v. 141, p. 233-247.
- Wendt, I., and Carl, C., 1991, The statistical distribution of the mean squared weighted deviation: *Chemical Geology*, v. 86, p. 275-285.
- Williams, 2001, Age and composition of dikes in Southern Tibet: New constraints on the timing of east-west extension and its relationship to postcollisional volcanism: *Geology*, v. 29, no. 4, p. 339-342.

Chapter 4: Exhumational history of the Mustang and Mugu granites

Wu, C., Nelson, K. D., Wortman, G., Samson, S. D., Yue, Y., Li, J., Kidd, W. S. F., and Edwards, M. A., 1998, Yadong cross structure and South Tibetan detachment in the east central Himalaya (89°-90°E): *Tectonics*, v. 17, p. 28-45.

York, D., 1969, Least-squares fitting of a straight line with correlated errors: *Earth and Planetary Science Letters*, v. 5, p. 320-324.

Yoshida, M., Igarashi, Y., Arita, K., Hayashi, D., and Sharma, T., 1984, Magnetostratigraphic and pollen analytic studies of the Thakmar series, Nepal Himalayas: *Journal of the Nepal Geological Society*, v. 4, p. 101-120.

FIGURE CAPTIONS

Table 1.

Existing geochronologic data for the Mustang and Mugu granites.

Table 2.

ID-TIMS U-Pb data for the Mugu and Mustang granites.

Table 3.

$^{40}\text{Ar}/^{39}\text{Ar}$ irradiation details for packages clair88, -92, -111, and -112.

Table 4.

$^{40}\text{Ar}/^{39}\text{Ar}$ data for biotite and muscovite from the UMM.

Table 5.

$^{40}\text{Ar}/^{39}\text{Ar}$ data for K-feldspar from the UMM.

Table 6.

$^{40}\text{Ar}/^{39}\text{Ar}$ results for biotite and muscovite from the UMM.

Table 7.

$^{40}\text{Ar}/^{39}\text{Ar}$ results for K-feldspar from the UMM.

Chapter 4: Exhumational history of the Mustang and Mugu granites

Table 8.

- a. Diffusion parameters for UMM muscovite.
- b. Diffusion parameters for UMM biotite.
- c. Diffusion parameters for UMM K-feldspar.

Table 9.

- a. $^{40}\text{Ar}/^{39}\text{Ar}$ closure temperatures as a function of cooling rate for biotite and muscovite from the UMM.
- b. $^{40}\text{Ar}/^{39}\text{Ar}$ closure temperatures as a function of cooling rate for K-feldspar from the UMM.

Table 10.

Summary of geochronologic results for the UMM.

Table 11.

Summary of denudation rate results from Moore and England (2001) analysis of UMM thermochronologic data.

Figure 1.

Map of the Himalaya and the Tibetan Plateau showing the distribution of major structures (after Hodges, 2000). Lines denote faults with ornamentation pointing in dip-direction of fault plane: triangular barbs = thrust fault; tick marks = low-angle normal faults; stick-and-ball = steeply-dipping normal faults. Blue faults are the east-west extending grabens in Tibet. Red faults are the South Tibetan fault system. The North Himalayan gneiss domes shown are shown in yellow. Abbreviations: ITS = Indus-Tsangpo suture; STFS = South Tibetan fault system; MCTS = Main Central thrust system; MBT = Main Boundary thrust; MFT = Main Frontal thrust; UMM = Upper Mustang massif; GM = Gurla Mandhata; TM = Tso Morari; KD = Kangmar dome; GL = Gonto La area; TG = Thakkhola graben; YCS = Yadong Cross Structure.

Chapter 4: Exhumational history of the Mustang and Mugu granites

Figure 2.

Simplified geologic map of the Thakkhola graben region of the central Nepal Himalaya (see Figure 1 for location) modified from Colchen (1986) and Coleman (1996b). Abbreviations: ITS = Indus-Tsangpo suture; DF = Dangardzong fault; STFS = South Tibetan fault system; MCTS = Main Central thrust system. Triangles denote significant peaks: A1 = Annapurna I (8091 m); A2 = Annapurna II (7938 m); N = Nilgiri North (7061 m); D1 = Dhaulagiri I (8167 m). Dots denote villages and towns mentioned in text.

Figure 3.

a. Tibetan Sedimentary Sequence metamorphosed to Lo Mantang gneiss in the Tsarang Khola. Ruler for scale is 15 cm in length. Note compositional layering.

b. Outcrop of Mustang granite in the Thinker area. Note abundant, large feldspar augen, some of which are tabular, although many are sigmoidal or deltoidal in shape. Lens cap for scale is 5.5 cm in diameter.

c. Small dike of Mugu granite crosscutting Tibetan Sedimentary Sequence in the Tsarang Khola. Note that it is much more leucocratic than the Mustang granite (c.f. Figure 3b) and that, with the exception of the large tourmaline crystals, the Mugu granite is generally finer-grained than the Mustang granite. Lens cap for scale is 5.5 cm in diameter.

d. View to the west of the bedrock gorge of the upper Tsarang Khola (see Figure 5 for location). The mountain front in the background is composed entirely of Mugu granite. The top of the escarpment is ca. 1000 m above river level.

e. View to west of an undeformed Mugu_{III} dike (white) truncating compositional layering and deformational fabrics (D₁-D₄) in the Lo Mantang gneiss (gray) in the Tsarang Khola. Field book for scale is 12 cm by 19 cm.

f. View to north of boudinaged (B₃) and folded (F₄) leucocratic veins of Mugu_{II} generation within the Lo Mantang gneiss in the Tsarang Khola. Ruler for scale is 15 cm in length.

g. View to north of isoclinally folded Mugu_I sill (white) in the Lo Mantang gneiss (gray) in the Tsarang Khola. For scale, Mr. T. T. Sherpa Lama is ca. 1.5 m tall.

Chapter 4: Exhumational history of the Mustang and Mugu granites

h. First type of fine-grained Mugu granite seen in the Thinker area. Large pod of medium gray Mugu granite and small amounts of white Mugu granite in contact with small amount of darker Mustang granite. Lens cap for scale is 5.5 cm in diameter.

i. Second type of Mugu granite seen in a boulder in the Thinker area. Note the complex folding and superpositions of at least three generations of apparently syn-deformational micro-intrusions, including (1) conspicuously banded, folded gray granitic host rock, (2) tourmaline-bearing, boudinaged leucogranite sills, and (3) cross-cutting dikes of both gray and white granite. Lens cap for scale is 5.5 cm in diameter.

j. Third type of Mugu granite seen in the Thinker area. Close-up of an undeformed dike of tourmaline bearing Mugu leucogranite truncating the deformational fabrics in the Mustang granite. Lens cap for scale is 5.5 cm in diameter.

Figure 4.

Oblique, 3-dimensional visualizations of the northern end of the Thakkhola graben combining decorrelation-stretched Landsat TM images draped over co-registered DTED® (level 0: 1 km resolution) digital topography. Landsat TM bands 7 (reflected mid-infrared: 2.08-2.35 μm ; 28.5 m ground resolution) and 6 (thermal infrared: 10.4-12.5 mm; 120 m ground resolution) were chosen. Band 7 was used in the red channel and band 6 in the green and blue channels, and decorrelation stretching maximized the spectral contrast between granite and other material in the resulting RGB image. Apparent ground resolution of three-dimensional views is approximately 0.5 km.

a. View of the UMM looking northeast into the northern end of the Thakkhola graben and the enigmatic granite body on the opposite side (boxed area). The graben at this latitude is ca. 30 km across.

b. View of the east side of the Thakkhola graben looking northwest into the northern end of the graben toward the UMM. The boxed area in the foreground is the enigmatic granite body discussed in the text. The graben at this latitude is ca. 30 km across.

c. Magnified view of the enigmatic granite body on the east side of the Thakkhola graben (boxed areas in Figure 4ab). The contact between red (granite) and

Chapter 4: Exhumational history of the Mustang and Mugu granites

blue (presumably Tibetan Sedimentary Sequence) is shallow dipping and could conceivably be a low-angle normal fault. View to east. Note scale-bar.

Figure 5.

Simplified geologic map of the northern end of the Thakkhola graben after Le Fort and France-Lanord (1995) and incorporating our field observations and remote sensing work. Boxed areas show our two principal study transects in the Tsarang Khola and Thinker village areas.

Figure 6.

Deformational history of the UMM. The first column lists age constraints based on U-Pb and $^{40}\text{Ar}/^{39}\text{Ar}$ data. The second column lists the sequence of deformational events (in circles). The other columns depict the distribution of deformational fabrics (in boxes; see text for nomenclature) in the three major rock types. Horizontal lines denote our correlation of deformational fabrics among the three rock types.

Figure 7.

a. View to south of concordant Mugu_I sills within the Lo Mantang gneiss in the Tsarang Khola. Sills and compositional layering in the gneiss define S₀/S₁. Field book for scale is 12 cm by 19 cm.

b. View to south of isoclinally folded (F₂) Mugu_I sills within the Lo Mantang gneiss in the Tsarang Khola. Axial planes are sub-parallel to S₀/S₁ and are oriented ca. 270 dipping ca. 80° S. Field book for scale is 12 cm by 19 cm.

c. View to south of a boudinaged (B₃) Mugu_I sill in Lo Mantang gneiss in the Tsarang Khola. Ruler for scale is 15 cm long.

d. View to north of a folded (F₄) Mugu_{II} discordant vein that has been previously boudinaged (B₃) in the Tsarang Khola. Note axial planar schistosity developed in the Lo Mantang gneiss. Field book for scale is 12 cm by 19 cm.

e. View to north of a D₅ brittle fault plane (S₅) cutting Mugu granite in the Tsarang Khola. Arrows denote fault kinematics. For scale, Dr. K. V. Hodges is 1.8 m tall.

Chapter 4: Exhumational history of the Mustang and Mugu granites

f. Slickensides (L_5) on a D_5 fault plane in the Tsarang Khola. Slickenlines plunge ca. 25° towards 065. Arrows drawn on outcrop in the field highlight the slickenlines. Lens cap for scale is 5.5 cm in diameter.

g. View to southeast of a steeply east-dipping (ca. 60°) fault buried beneath an alluvial fan surface near Samar village. Arrows denote buried faults. Note the colluvial wedge developed against a paleo-scarp. Undisturbed alluvium buries the scarp and colluvium. Total height of outcrop is ca. 10 m.

h. View to northeast of brittle S-C fabrics in a shallowly east-dipping (ca. 30°) shear zone developed in Tibetan Sedimentary Sequence rocks buried beneath an alluvial fan surface near Samar village (adjacent to site in Figure 7g). Shear sense is top-to-the-east.

Figure 8.

Equal area stereonet depicting structural measurements from the Tsarang Khola. N denotes the number of measurements illustrated. Stereonets calculated with the program StereonetPPC 6.0.2 (Allmendinger, 2001). For planar measurements, the mean is described as both a great circle (red arc) and mean vector (open square) with 2σ (95% confidence level) error ellipse. Goodness-of-fit statistics given include: k = concentration factor; 99% cone = size of 3σ (99%) confidence cone; 95% cone = size of 2σ (95%) confidence cone. Plots are contoured with a 4.0%/1% area contour interval.

- a. Strike and dip of S_0/S_1 compositional layering in the Lo Mantang gneiss.
- b. Trend and plunge of L_3 lineations in the Lo Mantang gneiss.
- c. Strike and dip of D_5 brittle fault planes (S_5).
- d. Trend and plunge of D_5 slickenlines (L_5).

Figure 9.

Equal area stereonet depicting structural measurements from the Thinker area. N denotes the number of measurements illustrated. Stereonets calculated with the program StereonetPPC 6.0.2 (Allmendinger, 2001). For planar measurements, the mean is described as both a great circle (red arc) and mean vector (open square) with 2σ (95% confidence level) error ellipse. Goodness-of-fit statistics given include: k = concentration

Chapter 4: Exhumational history of the Mustang and Mugu granites

factor; 99% cone = size of 3σ (99%) confidence cone; 95% cone = size of 2σ (95%) confidence cone. Plots are contoured with a 4.0%/1% area contour interval.

- a. Strike and dip of S_{3-4} foliations in the Mustang granite.
- b. Trend and plunge of L_{3-4} lineations in the Mustang granite.

Figure 10.

a. View to north of mylonitic fabric characteristic of the Mustang granite in the Thinker area. Shear sense is top-to-the-east. Lens cap for scale is 5.5 cm in diameter.

b. View to south of large K-feldspar augen in the Mustang granite in the Thinker area showing top-to-the-east shear sense. Lens cap for scale is 5.5 cm in diameter.

c. View to north of top-to-the-east kinematic indicators in the Mustang granite in the Thinker area. Note the back-rotated K-feldspar augen. Lens cap for scale is 5.5 cm in diameter.

d. View to north of top-to-the-east kinematic indicators in the Mustang granite in the Thinker area. Lens cap for scale is 5.5 cm in diameter.

e. View to south of top-to-the-east kinematic indicators in the Mustang granite in the Thinker area. Lens cap for scale is 5.5 cm in diameter.

f. View to north of Mustang granite in the Thinker area. Foliation strikes to 021 and dips 70°E. Note kinematic indicators showing top-to-the-east shear sense. Lens cap for scale is 5.5 cm in diameter.

g. View to south of brittle shear zone cutting through the Mustang granite in the Thinker area. The shear zone strikes northwest and dips ca. 40°S. Field-of-view is ca. 8 m across

Figure 11.

Concordia diagrams for U-Pb samples from the UMM. Curves with numbered tic marks represent concordia with labels in units of Ma. Data points include error ellipses representing 2σ (95%) analytical uncertainties. Data points are labeled by grain identifier (m = monazite; x = xenotime).

- a. 00KG28, Mustang granite from the Thinker area.
- b. 00KG18, Mugu_{III} granite from the Tsarang Khola..

Chapter 4: Exhumational history of the Mustang and Mugu granites

- c. 00KG20, Mugu_{III} granite from the Tsarang Khola..
- d. 00KG31, Mugu_{III} granite from the Thinker area.

Figure 12.

Reflected light digital photographs of grains analyzed for U-Pb dating by ID-TIMS. Images obtained using a digital camera and a binocular microscope of grains immersed in ethanol. Magnification and scale given for each image. Grains used for analysis are labeled. Abbreviations: m = monazite; x = xenotime.

- a. 00KG28, grains m1-m5 & x1-x2.
- b. 00KG18, grains m1-m3.
- c. 00KG20, grains m1 & m2.
- d. 00KG31, grains m1-m5.

Figure 13.

Back-scattered electron (BSE) images of grains analyzed for U-Pb dating by ID-TIMS. Grains were mounted in epoxy mounts and polished to expose cross-sections through the grain centers, after which they were washed in ethanol and carbon-coated for electron microprobe analysis. The images were created with the JEOL JXA-733 electron microprobe at the Massachusetts Institute of Technology. Variations in contrast in BSE images indicate the extent of compositional zoning within the grain. Scale given for each image. Abbreviations: m = monazite.

- a. 00KG28, grain m1.
- b. 00KG28, grain m3.
- c. 00KG18, grain m1.
- d. 00KG18, grain m2.
- e. 00KG20, grain m1.
- f. 00KG20, grain m2.
- g. 00KG31, grain m1.
- h. 00KG31, grain m2.

Figure 14.

Incremental heating release spectra for UMM muscovite and biotite $^{40}\text{Ar}/^{39}\text{Ar}$ samples. Increments are plotted with uncertainties that do not include the uncertainty in J . Each spectrum is labeled with a sample identifier of the form: clxxx.yyyyyy.zz, where xxx is the irradiation number, yyyyyy is the sample number, and zz is the mineral (bt = biotite; ms = muscovite). Each spectrum is also labeled with the statistically significant plateau date and its 2σ (95% confidence level) uncertainty (inclusive of uncertainty in J), the percent ^{39}Ar represented by the plateau, the increments (steps) included in the plateau (see Table 4), and the J value used. All samples resulted in statistically significant plateaux (see Table 6).

Figure 15.

Isotope correlation diagrams for UMM muscovite and biotite $^{40}\text{Ar}/^{39}\text{Ar}$ samples. Increments are plotted as points with uncertainties that do not include the uncertainty in J . Solid points indicate those used in the isochron fit; open points are not used in the fit. The triangle labeled “air” represents the $^{36}\text{Ar}/^{40}\text{Ar}$ of modern atmosphere. Each plot is labeled with a sample identifier of the form: clxxx.yyyyyy.zz, where xxx is the irradiation number, yyyyyy is the sample number, and zz is the mineral (bt = biotite; ms = muscovite). Each spectrum is also labeled with the statistically significant inverse isochron date and its 2σ (95% confidence level) uncertainty (inclusive of uncertainty in J), the $(^{40}\text{Ar}/^{39}\text{Ar})$, and its 2σ (95% confidence level) uncertainty, the MSWD of the linear fit, the percent ^{39}Ar represented by the isochron, and the increments (steps) included in the isochron (see Table 4). All samples resulted in statistically significant isochrons (see Table 6).

Figure 16.

a. Muscovite $^{40}\text{Ar}/^{39}\text{Ar}$ cooling age vs. elevation for samples from the Thinker area. Note the increase in age with increasing elevation. A linear fit through the Mustang granite samples (00KG32, -30, -28, and -25) implies a cooling rate (slope) of 0.15 mm/yr. The Mugu granite samples from this area do not fit the trend. Error bars denote 2σ (95% confidence level) uncertainties in cooling ages.

Chapter 4: Exhumational history of the Mustang and Mugu granites

b. Biotite $^{40}\text{Ar}/^{39}\text{Ar}$ cooling age vs. elevation. Note the clustering of ages at ca. 17.6 Ma. These data lack a correlation between elevation and cooling age similar to that seen for muscovite from the same rocks (Figure 16a). Error bars denote 2σ (95% confidence level) uncertainties in cooling ages.

c. Cluster diagram showing the distribution of Tsarang Khola and Thinker area Mugu granite muscovite $^{40}\text{Ar}/^{39}\text{Ar}$ cooling ages. Two groups are evident, one with a mean of 17.85 Ma. The younger group has a mean of 17.25 Ma. Error bars denote 2σ (95% confidence level) uncertainties in cooling ages.

d. Cluster diagram showing the distribution of Tsarang Khola and Thinker area Mugu granite biotite $^{40}\text{Ar}/^{39}\text{Ar}$ cooling ages. Error bars denote 2σ (95% confidence level) uncertainties in cooling age.

e. Cluster diagram showing the distribution of Tibetan Sedimentary Sequence biotite $^{40}\text{Ar}/^{39}\text{Ar}$ cooling ages. Their mean is ca. 17.5 Ma. Error bars denote 2σ (95% confidence level) uncertainties in cooling ages.

Figure 17.

Incremental heating release spectra for UMM K-feldspar $^{40}\text{Ar}/^{39}\text{Ar}$ samples. Increments are plotted with uncertainties that do not include the uncertainty in J . Each spectrum is labeled with a sample identifier of the form: clxxx.yyyyyy.zz, where xxx is the irradiation number, yyyyyy is the sample number, and zz is the mineral (bt = biotite; ms = muscovite). When applicable, each spectrum is also labeled with the statistically significant plateau date and its 2σ (95% confidence level) uncertainty (inclusive of uncertainty in J), the percent ^{39}Ar represented by the plateau, the increments (steps) included in the plateau (see Table 4), and the J value used. Only samples 00KG08 and -23 resulted in statistically significant plateaux. Note the form of each release spectrum. Each shows a near-plateaux above ca. 20% ^{39}Ar released. In most cases, this part of the spectrum is saddle-shaped. Each also shows another saddle-shaped section below ca. 20% ^{39}Ar released (labeled with arrows). The low-temperature saddles are interpreted in terms of minimum spectrum dates (MSDs) (see Tables 5 & 7).

Figure 18.

a. $^{40}\text{Ar}/^{39}\text{Ar}$ K-feldspar minimum spectrum dates (MSD) vs. elevation for samples from the Thinker area. Note the increase in age with increasing elevation. A linear fit through the data implies a cooling rate (slope) of 0.79 mm/yr. Error bars denote 2σ (95% confidence level) uncertainties in cooling age.

b. $^{40}\text{Ar}/^{39}\text{Ar}$ K-feldspar minimum isochron dates (MID) vs. elevation for samples from the Thinker area. Note the increase in age with increasing elevation. A linear fit through the data implies a cooling rate (slope) of 0.05 mm/yr. Error bars denote 2σ (95% confidence level) uncertainties in cooling age.

Figure 19.

Isotope correlation diagrams for UMM K-feldspar $^{40}\text{Ar}/^{39}\text{Ar}$ samples. Increments are plotted as points with uncertainties that do not include the uncertainty in J . Solid points indicate those used in the isochron fit; open points are not used in the fit. The triangle labeled “air” represents the $^{36}\text{Ar}/^{40}\text{Ar}$ of modern atmosphere. Each plot is labeled with a sample identifier of the form: clxxx.yyyyyy.zz, where xxx is the irradiation number, yyyyyy is the sample number, and zz is the mineral (kf = K-feldspar). Each spectrum is also labeled with the statistically significant inverse isochron date and its 2σ (95% confidence level) uncertainty (inclusive of uncertainty in J), the $(^{40}\text{Ar}/^{39}\text{Ar})_i$ and its 2σ (95% confidence level) uncertainty, the MSWD of the linear fit, the percent ^{39}Ar represented by the isochron, and the increments (steps) included in the isochron (see Table 4). Note that each sample (except 00KG23 and -32) has multiple plots with isochrons calculated for different sets of points. The sets of points were chosen as contiguous blocks that define conspicuous linear arrays in the isotope correlation diagrams. In all cases illustrated, these linear arrays yield statistically significant isochrons. We interpret them as distinct diffusion domains within each sample, each with different closure temperatures. We interpret the arrays corresponding to the lower temperature increments in terms of minimum isochron dates (MIAs) (see Table 7).

Figure 20.

$^{40}\text{Ar}/^{39}\text{Ar}$ K-feldspar Arrhenius diagrams. Blue triangles represent experimental data (39ArK release during step-heating). Red squares indicate data points used for determination of Arrhenius parameters (E_a and D_0/r^2). Line and equation show the results of the linear fit to the data. Symbols: E_a = activation energy; D = diffusivity; D_0 = diffusivity at infinite temperature; T = temperature; r = effective diffusion dimension.

- a. 00KG08.
- b. 00KG12.
- c. 00KG23.
- d. 00KG24.
- e. 00KG26.
- f. 00KG29.
- g. 00KG30.
- h. 00KG32.

Figure 21.

a. Composite cooling (denudation) curve. Left vertical axis shows temperature. Right vertical axis shows corresponding depth assuming a geotherm of 60 °C/km. Points denote mean age constraints representative of the UMM thermochronologic data as a whole with error bars depicting appropriate propagated errors (cooling age) and range of reasonable values (closure temperature). The blue curve is a piecewise spline fit to the average thermochronologic data.

b. Multimineral cooling curves. Each panel corresponds to an individual sample. The points are the actual cooling age-closure temperature data pairs for specific thermochronometers with uncertainties. Abbreviations: upb = U-Pb on monazite and/or xenotime; ms = muscovite $^{40}\text{Ar}/^{39}\text{Ar}$; bt = biotite $^{40}\text{Ar}/^{39}\text{Ar}$; kf = K-feldspar $^{40}\text{Ar}/^{39}\text{Ar}$, either msd (minimum spectrum date) or mid (minimum isochron date). Horizontal error bars denote 2σ (95% confidence level) uncertainties in cooling age. Vertical error bars denote the minimum-maximum range of closure temperatures (see Table 9). The red curve is the composite cooling curve depicted in Figure 21a.

Chapter 4: Exhumational history of the Mustang and Mugu granites

Figure 22.

Plots showing the results of the Moore and England (2001) analysis for each of the ten samples modeled. For each sample, there are four graphs. In the upper left is a plot of temperature vs. time. In this panel, the points are cooling age-closure temperature data pairs for specific thermochronometers with uncertainties. Abbreviations: upb = U-Pb on monazite and/or xenotime; ms = muscovite $^{40}\text{Ar}/^{39}\text{Ar}$; bt = biotite $^{40}\text{Ar}/^{39}\text{Ar}$; kf = K-feldspar $^{40}\text{Ar}/^{39}\text{Ar}$, either msd (minimum spectrum date) or mid (minimum isochron date). Horizontal error bars denote 2σ (95% confidence level) uncertainties in cooling age. Vertical error bars denote the minimum-maximum range of closure temperatures (see Table 9). Also plotted in this panel is the best-fit synthetic cooling curve resulting from the model. Note that the synthetic cooling curve has a different form than that of the cooling curves in Figure 21. This results from the assumption built-in to the Moore and England (2001) methodology of a constant U throughout the denudational history of a given sample. The cooling curves in Figure 21 are not subject to this assumption. As a result, the U obtained from the Moore and England (2001) analysis may be thought of as an average rate over the time interval represented by the thermochronologic data. In the other three panels are contour plots of R as seen along three cross-sections through U - T_o - z_o space. The white circle in each panel shows the best-fit point in the parameter space.

Figure 23

Best interpretation of the denudational history of the UMM as shown in a plot of denudation rate vs. time. Blue curve derived from results of analysis in Figures 21 & 22 and Table 11, as well as the thermochronologic data summarized in Table 10

Figure 24

a. Schematic cross-sections showing the development of the UMM. All views are to the north along of an east-west cross-section at the latitude of Thinker village. Only the bottom panel is to scale and uses the modern-day topographic profile. Depicted in the top panel is the initial condition at $>$ ca. 24 Ma showing the Tibetan Sedimentary Sequence (TSS) in the hanging wall of the South Tibetan fault system (STFS) and the Greater Himalayan Sequence (GHS) in the footwall prior to intrusion of the Mustang granite.

Chapter 4: Exhumational history of the Mustang and Mugu granites

Circles with crosses denote motion of the top plate into the page. The second panel depicts the condition at ca. 21 Ma, after Mustang granite (MG) intrusion and at the time when east-west extension began in the Thakkhola area (horizontal arrows). The vertical arrow depicts warping upward of the interface between the MG and TSS. Note shown is the synchronous north-south oriented compression inferred from $D_{1,2}$ fabrics. Two interpretations of the MG-TSS contact are possible: (a) it is the STFS fault plane or (b) it is an intrusive contact that has modified the STFS. In either case, the MG and associated Lo Mantang gneiss are interpreted to originate from below the STFS. The third panel depicts the situation at ca. 18.5 Ma by which time the low-angle detachment predecessor to the Dangardzong fault is active, exhuming the Mustang granite in a core complex fashion along the MG-TSS interface (i.e. the STFS). The bottom panel depicts the situation after ca. 17.5 Ma. During this time, the Dangardzong fault has become active and extension in the Thakkhola region has shifted from the core complex mode to the modern-day rift mode.

b. Block-diagram cartoon of the Thakkhola graben looking from above and towards the southwest. Abbreviations: STF = South Tibetan fault system; TSS = Tibetan Sedimentary Sequence; GHS = Greater Himalayan Sequence; Fill = Thakkhola graben Tertiary fill sediments; DF = Dangardzong fault. Note the three-dimensional topology of the STF. In particular, note that the DF roots into the STF such that, at the latitude of the UMM where the MG has been exhumed, the STF and DF form a curved surface bounding the UMM along its southeastern edge. Note that this model predicts that GHS and MG underlie the Thakkhola graben fill in the northern part of the graben. This is not the case in the southern part of the graben where TSS underlies the fill. This is the result of the scissors geometry of the Dangardzong fault (e.g. Hurtado *et al.*, 2001 – see Chapter 2) – as well as pre-Dangardzong fault upper-plate thinning in Upper Mustang – which has allowed the graben to completely excise the TSS in the north but not the south.

Chapter 4: Exhumational history of the Mustang and Mugu granites

TABLE 1. PREVIOUS AGE CONSTRAINTS FROM THE MUSTANG AND MUGU GRANITES

Sample*	Location†	Age $\pm 2\sigma$ § (Ma)	Mineral & Technique	Reference
(Mustang?) pegmatite	terrace gravel; locality unknown	24	muscovite; conventional K-Ar	Krummenacher (1971)
(Mugu?) granite	terrace gravel; locality unknown	15	muscovite; conventional K-Ar	Krummenacher (1971)
Mugu leucogranite <i>LO68isp2</i>	Tsarang Khola N083°48' W029°07'	17.6 \pm 0.3	monazite; ion microprobe Th-Pb	Harrison <i>et al.</i> (1997)
Mugu leucogranite <i>LO93</i>	Tsarang Khola	15.8 (100%) 15.9 \pm 0.2 (82%, 3.0, 297 \pm 2)	muscovite; ⁴⁰ Ar/ ³⁹ Ar step- heating	Guillot <i>et al.</i> (1999)
Mugu leucogranite <i>LO93</i>	Tsarang Khola	16.6 \pm 0.2 (72%) 16.7 \pm 0.2 (92%, 2.1, 294 \pm 8)	biotite; ⁴⁰ Ar/ ³⁹ Ar step- heating	Guillot <i>et al.</i> (1999)
Mugu leucogranite <i>LO94</i>	Tsarang Khola	15.3 (100%) 15.4 \pm 0.4 (60%, 2.3, 300 \pm 3)	muscovite; ⁴⁰ Ar/ ³⁹ Ar step- heating	Guillot <i>et al.</i> (1999)
Mugu leucogranite <i>LO94</i>	Tsarang Khola	15.7 (100%) 16.0 \pm 0.8 (59%, 15.0, 297 \pm 20)	biotite; ⁴⁰ Ar/ ³⁹ Ar step- heating	Guillot <i>et al.</i> (1999)

Note: For specific details of the samples listed, see references to the original publications.

* Description of sample lithology. Queries denote our interpretation of sample lithology if unclear from the original publication. Where available, original sample numbers given in italics.

† Description of sample localities with coordinates, if available. See Figure 5.

§ Ages as reported by original authors along with 2 σ (95%) uncertainties, if reported. For ⁴⁰Ar/³⁹Ar analyses, two dates are listed. The first is the plateau (bold) or total gas date (plain type) with the % ³⁹Ar_K in parentheses. The second is the inverse isochron date with % ³⁹Ar_K, MSWD, and (⁴⁰Ar/³⁶Ar)_{initial} (with 2 σ uncertainty), respectively, in parentheses. See text and McDougall and Harrison (1999) for general information on ⁴⁰Ar/³⁹Ar thermochronology.

Table 1

TABLE 2. ID-TIMS DATA AND RESULTS FOR THE MUGU AND MUSTANG GRANITES

Grain†	Mass§ (µg)	U# (ppm)	Pb# (ppm)	Th/U#	Common Pb‡ (pg)	Common			Correlation Coefficient	²⁰⁶ Pb/ ²³⁸ U		²⁰⁷ Pb/ ²³⁵ U		²⁰⁷ Pb/ ²⁰⁶ Pb	
						²⁰⁶ Pb*/ ²⁰⁶ Pb§§	²⁰⁶ Pb/ ²⁰⁶ Pb##	²⁰⁶ Pb/ ²³⁸ U†††		²⁰⁷ Pb/ ²³⁵ U†††	²⁰⁷ Pb/ ²⁰⁶ Pb†††	Date\$\$\$ (Ma)	±	2σ\$\$\$ (Ma)	Date\$\$\$ (Ma)
<i>00KG28 (Thinker area Mustang granite)</i>															
m1	11.8	2478	111.0	18.939	4.1	3291.1	6.139	0.007194(0.17)	0.0471(0.22)	0.04749(0.13)	0.792	46.21 ± 0.08	46.74 ± 0.10	73.9 ± 3.2	
m2	1.8	1127	42.8	26.262	16.3	49.7	8.332	0.003892(2.26)	0.0247(5.74)	0.04601(5.02)	0.497	25.04 ± 0.57	24.77 ± 1.42	-2.1 ± 121.0	
m3	0.7	1918	765.7	14.557	41.0	87.9	11.756	0.033426(0.49)	0.2679(1.71)	0.05813(1.56)	0.443	211.96 ± 1.03	241.01 ± 4.12	534.6 ± 34.1	
m4	0.6	3303	112.6	30.460	1.2	404.6	9.607	0.003692(0.50)	0.0233(0.73)	0.04570(0.50)	0.723	23.75 ± 0.12	23.35 ± 0.17	-18.0 ± 12.1	
m5	0.7	1603	58.0	32.448	4.6	78.9	10.047	0.003665(5.70)	0.0227(7.25)	0.04486(4.14)	0.822	23.58 ± 1.35	22.76 ± 1.65	-63.4 ± 101.0	
x1	4.9	5365	31.0	0.817	3.1	2869.7	0.262	0.005130(0.11)	0.0331(0.21)	0.04675(0.18)	0.561	32.98 ± 0.04	33.03 ± 0.07	36.2 ± 4.2	
x2	2.5	7152	488.0	0.736	28.7	2214.2	0.301	0.057132(0.22)	0.4435(0.26)	0.05630(0.13)	0.869	358.16 ± 0.80	372.73 ± 0.96	464.3 ± 2.8	
<i>00KG18 (Tsarang Khola Mugu granite dike)</i>															
m1	1.3	42006	143.0	0.599	7.1	1568.5	0.186	0.003150(0.16)	0.0195(0.23)	0.04491(0.16)	0.729	20.28 ± 0.03	19.62 ± 0.05	-60.7 ± 3.9	
m2	2.1	27618	116.2	1.646	9.1	1221.7	0.525	0.003033(0.16)	0.0193(0.25)	0.04617(0.18)	0.682	19.52 ± 0.03	19.42 ± 0.05	6.4 ± 4.4	
m3	0.7	26831	102.8	0.940	7.8	467.9	0.297	0.003102(0.47)	0.0195(0.57)	0.04565(0.32)	0.832	19.97 ± 0.09	19.63 ± 0.11	-21.1 ± 7.7	
<i>00KG20 (Tsarang Khola Mugu granite dike)</i>															
m1	16.0	4789	56.5	10.114	100.6	156.3	3.258	0.002829(0.14)	0.0182(0.52)	0.04657(0.49)	0.382	18.21 ± 0.03	18.28 ± 0.10	27.4 ± 11.7	
m2	7.7	4272	92.8	14.867	44.9	212.3	4.673	0.004132(0.19)	0.0260(0.55)	0.04560(0.50)	0.411	26.58 ± 0.05	26.04 ± 0.14	-23.3 ± 12.2	
<i>00KG31 (Thinker area Mugu granite dike)</i>															
m1	0.9	2970	109.0	11.703	58.5	28.0	4.025	0.003391(1.31)	0.0233(13.08)	0.04984(12.48)	0.504	21.82 ± 0.29	23.39 ± 3.06	187.4 ± 290.4	
m2	0.9	4344	67.3	12.942	7.6	130.5	3.878	0.003391(1.80)	0.0203(2.36)	0.04336(1.45)	0.791	21.83 ± 0.39	20.38 ± 0.48	-146.8 ± 35.9	
m3	1.3	7005	98.8	12.127	4.3	489.2	3.737	0.003387(0.81)	0.0208(0.90)	0.04460(0.36)	0.918	21.79 ± 0.18	20.93 ± 0.19	-77.2 ± 8.7	
m4	1.6	4579	47.4	6.391	3.5	549.2	2.019	0.003903(0.36)	0.0246(0.50)	0.04581(0.33)	0.757	25.11 ± 0.09	24.73 ± 0.12	-12.5 ± 7.9	
m5	1.6	1402	22.2	14.143	1.5	358.2	4.282	0.003440(0.57)	0.0208(1.44)	0.04382(1.26)	0.501	22.14 ± 0.13	20.89 ± 0.30	-120.6 ± 31.0	

Notes:
† Fractions designated by mineral m = monazite, x = xenotime
§ Sample weights, estimated using sample dimensions determined from a calibrated graded video monitor, are known to within 40% based on comparisons of estimated and measured weights
Compositions expressed as ppm U, ppm total Pb, and Th/U Th/U ratios calculated from the ²⁰⁶Pb/²⁰⁶Pb ratios
‡ Total common Pb in analyses
§§ Measured ratio corrected for fractionation and spike only, Pb fractionation is 0.12 ± 0.04% per a.m.u. (atomic mass unit) for multicollector (dynamic) Faraday analyses and 0.15 ± 0.04% per a.m.u. for single collector Daly analysis based on repeated analyses of NBS-981
Radiogenic Pb See ††† for analytical details
††† Isotopic ratios are corrected for fractionation, spike, blank, and initial common Pb Total procedural U blank < 0.1 pg ± 50% Data were reduced using a total procedural Pb blank of 3.5 pg ± 50% except for analyses with < 3.5 pg total common Pb, in which case this value was used as blank and the uncertainty reduced to 20% Pb blank composition ²⁰⁶Pb/²⁰⁶Pb = 19.10 ± 0.1%, ²⁰⁷Pb/²⁰⁶Pb = 15.71 ± 0.1%, ²⁰⁸Pb/²⁰⁶Pb = 38.65 ± 0.1% (uncertainties at the 1σ level) Initial common Pb composition used is that of Stacey and Kramers (1975) and the interpreted age of the sample Numbers in parentheses are the % error reported at the 2σ (95%) confidence level
\$\$\$ Uncertainties in millions of years (Ma) at the 2σ (95%) confidence level Age calculations based on the decay constants of Steiger and Jäger (1977) 0.4947e-10 yr⁻¹ (²³²Th), 9.8485e-10 yr⁻¹ (²³⁵U), 1.55125e-10 yr⁻¹ (²³⁸U)

Table 2

TABLE 3. ⁴⁰Ar/³⁹Ar IRRADIATION PACKAGE DATA

Irradiation Package	Date Irradiated	Duration (hours)	Power (MW)	Layer Numbers†	Samples Included§	Fluence Monitors#	J Value‡ ±	2σ‡
clair-88	8/24/98	10	2	6	98KG20 (bt)	FCf	0.002731 ±	0.000051
clair-96	3/10/99	7	2	4	98KG19 (bt)	FCf	0.001706 ±	0.000022
clair-111	9/21/00	12	2	6	00KG12 (ms), -27 (ms),	interpolated	0.003177 ±	0.000001
					7 00KG09 (bt), -23 (ms), -24 (ms), 31 (ms)	FCf	0.003129 ±	0.000032
					8 00KG06 (ms), -10 (bt), -19 (bt), -24 (bt), -28 (bt), -28 (ms), -31 (bt)	interpolated	0.003087 ±	0.000001
					9 00KG08 (bt), -08 (ms), -14 (ms), -16 (ms), -20 (bt)	FCf	0.003111 ±	0.000001
clair-112	9/21/00	12	2	1	00KG13 (bt), -25 (ms), -26 (bt), 30 (bt), -30 (ms), -32 (bt)	FCf	0.003101 ±	0.000001
					2 00KG25 (bt), -32 (ms), -26 (kf), -30 (kf),	interpolated	0.003170 ±	0.000018
					3 00KG12 (kf), -23 (kf), -24 (kf), -32 (kf)	FCf	0.003211 ±	0.000045
					4 00KG08 (kf), -29 (kf),	interpolated	0.003224 ±	0.000019

Notes :

† Only layers with samples analyzed for this project are listed.

§ Hyphenated sample numbers have the same "xxKG" prefix. Abbreviations: ms = muscovite; bt = biotite; kf = K-feldspar.

FCf = Fish Canyon-1 fine-grained sanidine. This is an internal age standard used at CLAIR. Its age is assumed to be 28.38 Ma as calibrated against the original Fish Canyon anidine assuming the latter is 28.02 Ma (Renne *et al.*, 1998). "Interpolated" denotes layers with no flux monitor. J is calculated for these layers by interpolating between the adjacent layers with a polynomial function.

‡ J is calculated using the equation: $J = (\exp(\lambda t) - 1) / ({}^{40}\text{Ar} / {}^{39}\text{Ar}_k)$. Uncertainty is quoted at the 2σ (95%) confidence level and includes both analytical error and propagated error in polynomial interpolation.

Table 3

Chapter 4: Exhumational history of the Mustang and Mugu granites

TABLE 4. ⁴⁰Ar/³⁹Ar STEP HEATING DATA FOR BIOTITE AND MUSCOVITE FROM THE UPPER MUSTANG REGION, CENTRAL NEPAL

Sample†	T§ (°C)	Duration# (minutes)	³⁷ Ar/ ³⁹ Ar ±	³⁶ Ar/ ³⁹ Ar 2σ ±	³⁷ Ar/ ³⁹ Ar ±	³⁶ Ar/ ³⁹ Ar 2σ ±	³⁷ Ar,‡ (moles)	³⁶ Ar, Released§§ (cumulative %)	³⁷ Ar## (%)	Date††† (Ma)	Date 2σ§§§ (Ma)	Date 2σ## (Ma)
98KG19 Biotite CLAIR 96, Layer 4 J = 0.001706 ± 0.00022 Weight = 0.0322 g	825	10	0.00177 ±	0.00028 ±	0.12866 ±	0.00079 ±	6.31E-14	5.4	47.7	11.39 ±	1.99 ±	1.98 ±
	850	10	0.00115 ±	0.00074 ±	0.14032 ±	0.01214 ±	5.45E-14	10.1	65.9	14.40 ±	5.10 ±	5.09 ±
	875	10	0.00136 ±	0.00105 ±	0.14556 ±	0.00273 ±	5.32E-14	14.7	59.9	12.63 ±	6.50 ±	6.50 ±
	900	10	0.00125 ±	0.00048 ±	0.16263 ±	0.00801 ±	6.71E-14	20.5	62.9	11.89 ±	2.82 ±	2.81 ±
	925	10	0.00091 ±	0.00100 ±	0.11914 ±	0.00405 ±	2.20E-14	22.4	73.2	18.82 ±	7.58 ±	7.58 ±
	950	10	0.00069 ±	0.00024 ±	0.13653 ±	0.00067 ±	7.08E-14	28.5	79.5	17.84 ±	1.60 ±	1.59 ±
	975	10	0.00063 ±	0.00024 ±	0.14383 ±	0.00160 ±	6.56E-14	34.2	81.3	17.33 ±	1.55 ±	1.53 ±
	1000	10	0.00067 ±	0.00016 ±	0.14082 ±	0.00227 ±	5.86E-14	39.2	80.1	17.44 ±	1.13 ±	1.11 ±
	1050	10	0.00053 ±	0.00030 ±	0.14700 ±	0.00309 ±	1.67E-13	53.6	84.2	17.57 ±	1.88 ±	1.86 ±
	1075	10	0.00031 ±	0.00011 ±	0.15593 ±	0.00333 ±	1.68E-13	68.2	90.9	17.87 ±	0.79 ±	0.75 ±
	1100	10	0.00025 ±	0.00028 ±	0.15742 ±	0.00119 ±	1.26E-13	79.0	92.5	18.01 ±	1.64 ±	1.62 ±
	1150	10	0.00035 ±	0.00017 ±	0.15592 ±	0.00017 ±	1.62E-13	93.0	89.7	17.64 ±	1.09 ±	1.07 ±
	1200	10	0.00046 ±	0.00032 ±	0.15649 ±	0.00126 ±	7.31E-14	99.3	86.3	16.91 ±	1.85 ±	1.84 ±
	1250	10	0.00241 ±	0.00125 ±	0.14300 ±	0.01390 ±	8.32E-15	100.0	28.9	6.22 ±	8.04 ±	8.04 ±
³⁷ Ar, Weighted Mean Date ± 2σ††† (Ma)										16.53 ±	0.62 ±	
98KG20 Biotite CLAIR 88, Layer 6 J = 0.002731 ± 0.00051 Weight = 0.0616 g	850	10	0.00335 ±	0.00044 ±	0.16209 ±	0.00464 ±	1.66E-13	3.1	1.1	0.35 ±	3.96 ±	3.96 ±
	875	10	0.00161 ±	0.00023 ±	0.23570 ±	0.00477 ±	3.55E-13	9.7	52.4	10.93 ±	1.46 ±	1.43 ±
	900	10	0.00058 ±	0.00012 ±	0.22357 ±	0.00664 ±	3.30E-13	15.9	82.7	18.17 ±	1.08 ±	1.05 ±
	925	10	0.00029 ±	0.00015 ±	0.27202 ±	0.00689 ±	6.29E-13	27.6	91.2	16.47 ±	0.98 ±	0.93 ±
	950	10	0.00027 ±	0.00010 ±	0.26932 ±	0.00033 ±	4.36E-13	35.7	91.8	16.75 ±	0.62 ±	0.54 ±
	975	10	0.00032 ±	0.00090 ±	0.26088 ±	0.00824 ±	1.17E-13	37.9	90.6	17.05 ±	5.04 ±	5.03 ±
	1000	10	0.00026 ±	0.00021 ±	0.27730 ±	0.00239 ±	2.77E-13	43.1	92.2	16.33 ±	1.14 ±	1.10 ±
	1050	10	0.00019 ±	0.00014 ±	0.27437 ±	0.00139 ±	3.60E-13	49.8	94.2	16.86 ±	0.81 ±	0.75 ±
	1075	10	0.00006 ±	0.00020 ±	0.27987 ±	0.00645 ±	2.97E-13	55.3	98.1	17.21 ±	1.16 ±	1.11 ±
	1100	10	0.00018 ±	0.00012 ±	0.27059 ±	0.00052 ±	4.94E-13	64.5	94.7	17.18 ±	0.70 ±	0.62 ±
	1150	10	0.00019 ±	0.00004 ±	0.26244 ±	0.00195 ±	7.95E-13	79.2	84.4	17.54 ±	0.43 ±	0.27 ±
	1160	10	0.00019 ±	0.00004 ±	0.26244 ±	0.00195 ±	7.85E-13	83.8	93.1	17.33 ±	0.47 ±	0.34 ±
	1200	10	0.00023 ±	0.00006 ±	0.26371 ±	0.00193 ±	7.85E-13	93.8	93.1	17.33 ±	0.47 ±	0.34 ±
	1215	10	0.00017 ±	0.00046 ±	0.25441 ±	0.01076 ±	1.38E-13	96.4	94.7	18.28 ±	2.77 ±	2.75 ±
	1230	10	0.00042 ±	0.00055 ±	0.22801 ±	0.00812 ±	8.39E-14	97.9	87.4	18.80 ±	3.57 ±	3.55 ±
	1245	10	0.00093 ±	0.00131 ±	0.26777 ±	0.01738 ±	5.70E-14	99.0	72.5	13.31 ±	7.15 ±	7.15 ±
	1250	10	0.00316 ±	0.00207 ±	0.30860 ±	0.02199 ±	2.41E-14	99.4	6.6	1.05 ±	9.78 ±	9.78 ±
	1275	10	0.00083 ±	0.00265 ±	0.30398 ±	0.02833 ±	3.09E-14	100.0	75.2	12.17 ±	12.67 ±	12.67 ±
³⁷ Ar, Weighted Mean Date ± 2σ††† (Ma)										16.11 ±	0.32 ±	
00KG06 Muscovite CLAIR 111, Layer 8 J = 0.003087 ± 0.00001 Weight = 0.0536 g	650	10	0.00153 ±	0.00051 ±	0.14141 ±	0.00127 ±	2.89E-14	0.8	54.7	21.44 ±	5.88 ±	5.88 ±
	700	10	0.00237 ±	0.00007 ±	0.09893 ±	0.00089 ±	1.22E-13	4.4	30.0	18.51 ±	1.31 ±	1.31 ±
	750	10	0.00158 ±	0.00007 ±	0.17620 ±	0.00111 ±	5.88E-13	21.6	53.2	16.74 ±	0.67 ±	0.67 ±
	800	10	0.00041 ±	0.00004 ±	0.27958 ±	0.00059 ±	7.28E-13	42.9	87.8	17.43 ±	0.27 ±	0.26 ±
	850	10	0.00059 ±	0.00016 ±	0.26860 ±	0.00034 ±	5.10E-13	57.8	82.3	17.01 ±	0.94 ±	0.94 ±
	900	10	0.00098 ±	0.00009 ±	0.22606 ±	0.00184 ±	2.62E-13	65.5	70.8	17.39 ±	0.68 ±	0.68 ±
	950	10	0.00106 ±	0.00010 ±	0.22317 ±	0.00274 ±	2.22E-13	72.0	68.7	17.08 ±	0.81 ±	0.80 ±
	1000	10	0.00086 ±	0.00010 ±	0.23925 ±	0.00263 ±	3.02E-13	80.8	74.5	17.29 ±	0.73 ±	0.73 ±
	1050	10	0.00051 ±	0.00024 ±	0.28432 ±	0.00263 ±	2.47E-13	88.1	84.8	16.56 ±	1.39 ±	1.39 ±
	1100	10	0.00036 ±	0.00033 ±	0.30286 ±	0.00434 ±	1.42E-13	92.2	89.1	16.33 ±	1.77 ±	1.77 ±
	1200	10	0.00010 ±	0.00016 ±	0.30763 ±	0.00451 ±	1.88E-13	97.7	96.9	17.48 ±	0.90 ±	0.90 ±
	1300	10	0.00049 ±	0.00044 ±	0.29979 ±	0.00241 ±	4.70E-14	99.1	85.4	15.82 ±	2.40 ±	2.40 ±
	1350	10	0.00057 ±	0.00247 ±	0.31261 ±	0.00239 ±	2.06E-14	99.7	83.0	14.75 ±	12.91 ±	12.91 ±
	1550	10	0.00223 ±	0.00498 ±	0.26909 ±	0.00537 ±	9.77E-15	100.0	34.1	7.05 ±	30.35 ±	30.35 ±
³⁷ Ar, Weighted Mean Date ± 2σ††† (Ma)										17.11 ±	0.29 ±	
00KG08 Biotite CLAIR 111, Layer 9 J = 0.003111 ± 0.00001 Weight = 0.0842 g	550	10	0.00246 ±	0.00004 ±	0.09063 ±	0.00158 ±	2.05E-13	13.0	27.2	16.75 ±	0.92 ±	0.92 ±
	650	10	0.00035 ±	0.00007 ±	0.28712 ±	0.00404 ±	4.08E-13	39.0	89.6	17.47 ±	0.46 ±	0.46 ±
	750	10	0.00006 ±	0.00026 ±	0.31484 ±	0.00427 ±	3.21E-13	59.4	98.0	17.41 ±	1.38 ±	1.38 ±
	800	10	0.00035 ±	0.00037 ±	0.30110 ±	0.00477 ±	7.93E-14	64.5	89.6	16.65 ±	2.03 ±	2.03 ±
	900	10	0.00015 ±	0.00009 ±	0.29972 ±	0.00281 ±	2.78E-13	82.2	95.5	17.81 ±	0.50 ±	0.50 ±
	1000	10	0.00011 ±	0.00015 ±	0.29216 ±	0.00182 ±	2.66E-13	99.1	96.7	18.50 ±	0.84 ±	0.83 ±
	1100	10	0.00229 ±	0.00211 ±	0.26275 ±	0.00894 ±	1.31E-14	99.9	32.4	6.91 ±	13.28 ±	13.28 ±
	1550	10	0.00253 ±	0.05303 ±	0.12801 ±	0.02785 ±	1.26E-15	100.0	25.3	11.07 ±	682.88 ±	682.88 ±
³⁷ Ar, Weighted Mean Date ± 2σ††† (Ma)										17.46 ±	0.68 ±	
00KG08 Muscovite CLAIR 111, Layer 9 J = 0.003111 ± 0.00001 Weight = 0.0168 g	550	10	0.00314 ±	0.00010 ±	0.02147 ±	0.00012 ±	3.89E-14	0.7	7.2	18.80 ±	7.67 ±	7.67 ±
	650	10	0.00293 ±	0.00004 ±	0.04144 ±	0.00012 ±	1.04E-13	2.7	13.5	18.23 ±	1.66 ±	1.66 ±
	700	10	0.00264 ±	0.00006 ±	0.07023 ±	0.00045 ±	2.38E-13	7.1	22.1	17.57 ±	1.40 ±	1.40 ±
	750	10	0.00120 ±	0.00012 ±	0.20479 ±	0.00041 ±	1.18E-12	29.0	64.4	17.58 ±	0.93 ±	0.93 ±
	800	10	0.00036 ±	0.00008 ±	0.29094 ±	0.00089 ±	1.14E-12	50.2	89.3	17.17 ±	0.48 ±	0.48 ±
	850	10	0.00061 ±	0.00009 ±	0.27443 ±	0.00076 ±	7.02E-13	63.3	81.9	16.70 ±	0.57 ±	0.56 ±
	900	10	0.00094 ±	0.00017 ±	0.23203 ±	0.00174 ±	3.30E-13	69.5	72.1	17.38 ±	1.21 ±	1.20 ±
	950	10	0.00112 ±	0.00012 ±	0.23123 ±	0.00173 ±	2.89E-13	74.5	66.8	16.16 ±	0.89 ±	0.88 ±
	1000	10	0.00089 ±	0.00013 ±	0.24150 ±	0.00033 ±	3.82E-13	81.6	73.6	17.04 ±	0.90 ±	0.89 ±
	1050	10	0.00049 ±	0.00011 ±	0.28327 ±	0.00204 ±	3.75E-13	88.6	85.3	16.94 ±	0.65 ±	0.65 ±
	1100	10	0.00023 ±	0.00013 ±	0.29406 ±	0.00386 ±	2.05E-13	92.4	93.2	17.72 ±	0.77 ±	0.77 ±
	1200	10	0.00011 ±	0.00012 ±	0.31515 ±	0.00467 ±	2.62E-13	97.3	96.7	17.17 ±	0.66 ±	0.66 ±
1300	10	0.00024 ±	0.00076 ±	0.31004 ±	0.00553 ±	8.76E-14	98.9	92.7	16.72 ±	4.05 ±	4.05 ±	
1350	10	0.00062 ±	0.00064 ±	0.32055 ±	0.00238 ±	3.26E-14	99.6	81.5	14.23 ±	3.30 ±	3.30 ±	
1550	10	0.00103 ±	0.00498 ±	0.27310 ±	0.00274 ±	2.41E-14	100.0	69.4	14.22 ±	30.01 ±	30.01 ±	
³⁷ Ar, Weighted Mean Date ± 2σ††† (Ma)										17.16 ±	0.32 ±	
00KG09 Biotite CLAIR 111, Layer 7 J = 0.003129 ± 0.00032 Weight = 0.0424 g	550	10	0.00299 ±	0.00009 ±	0.06817 ±	0.00112 ±	1.19E-13	3.9	11.6	9.55 ±	2.20 ±	2.20 ±
	600	10	0.00137 ±	0.00004 ±	0.20305 ±	0.00297 ±	2.60E-13	12.4	59.5	16.47 ±	0.43 ±	0.40 ±
	650	10	0.00033 ±	0.00010 ±	0.30055 ±	0.00747 ±	4.43E-13	26.8	90.0	16.85 ±	0.65 ±	0.63 ±
	700	10	0.00008 ±	0.00008 ±	0.32091 ±	0.00692 ±	5.26E-13	44.0	97.5	17.10 ±	0.55 ±	0.52 ±
	750	10	0.00010 ±	0.00012 ±	0.32249 ±	0.00912 ±	1.80E-13	49.9	96.9	16.92 ±	0.73 ±	0.71 ±
	800	10	0.00026 ±	0.00028 ±	0.31892 ±	0.00912 ±	1.59E-13	55.0	92.3	16.29 ±	1.53 ±	1.52 ±
	850	10	0.00023 ±	0.00								

Chapter 4: Exhumational history of the Mustang and Mugu granites

00KG10	550	10	0.00196	±	0.00013	0.12972	±	0.00200	2.00E-13	16.4	41.9	17.92	±	1.64	1.63
Biotite	650	10	0.00023	±	0.00011	0.29821	±	0.00138	1.99E-13	32.6	93.2	17.34	±	0.60	0.60
CLAIR 111, Layer 8	750	10	0.00015	±	0.00023	0.31322	±	0.00085	1.88E-13	47.9	95.5	16.93	±	1.22	1.22
J = 0.003087 ± 0.00001	850	10	0.00025	±	0.00023	0.30561	±	0.00142	1.15E-13	57.3	92.4	16.78	±	1.25	1.25
Weight = 0.0144 g	850	10	0.00010	±	0.00011	0.30892	±	0.00211	4.08E-13	90.7	96.9	17.42	±	0.58	0.58
	1050	10	0.00005	±	0.00026	0.29679	±	0.00187	1.14E-13	100.0	98.3	18.38	±	1.43	1.43
*Ar, Weighted Mean Date ± 2σ (Ma)												17.44	±	0.43	
00KG12	550	10	0.00332	±	0.00027	0.03825	±	0.00029	4.46E-14	0.8	1.9	2.78	±	11.94	11.94
Muscovite	650	10	0.00286	±	0.00023	0.06842	±	0.00062	1.28E-13	3.2	15.5	12.94	±	5.73	5.73
CLAIR 111, Layer 6	700	10	0.00242	±	0.00009	0.10498	±	0.00068	3.71E-13	9.9	28.4	15.43	±	1.39	1.39
J = 0.003177 ± 0.00001	750	10	0.00081	±	0.00009	0.23744	±	0.00302	1.04E-12	28.8	76.0	18.28	±	0.68	0.67
Weight = 0.0132 g	800	10	0.00004	±	0.00020	0.31009	±	0.00501	6.05E-13	39.9	98.6	18.17	±	1.11	1.11
	850	10	0.00028	±	0.00010	0.28809	±	0.00096	7.38E-13	53.4	91.5	18.14	±	0.59	0.58
	900	10	0.00072	±	0.00016	0.25984	±	0.00054	4.32E-13	61.2	78.7	17.30	±	1.06	1.06
	950	10	0.00064	±	0.00008	0.26022	±	0.00044	4.26E-13	69.0	80.9	17.75	±	0.51	0.51
	1000	10	0.00059	±	0.00004	0.26840	±	0.00036	5.86E-13	79.7	82.5	17.56	±	0.29	0.28
	1050	10	0.00028	±	0.00003	0.29563	±	0.00121	4.30E-13	87.6	91.6	17.71	±	0.22	0.21
	1100	10	0.00004	±	0.00003	0.31140	±	0.00184	2.20E-13	91.6	98.7	18.10	±	0.21	0.20
	1200	10	0.00006	±	0.00019	0.31548	±	0.00303	2.73E-13	96.5	98.0	17.75	±	1.02	1.02
	1300	10	0.00026	±	0.00122	0.31489	±	0.00458	1.41E-13	99.1	92.2	16.73	±	6.53	6.53
	1350	10	0.00012	±	0.00083	0.30429	±	0.00953	3.31E-14	99.7	96.4	18.09	±	4.61	4.61
	1550	10	0.00107	±	0.00130	0.17712	±	0.00467	1.60E-14	100.0	68.3	21.97	±	12.32	12.32
*Ar, Weighted Mean Date ± 2σ (Ma)												17.50	±	0.34	
00KG13	550	10	0.00130	±	0.00054	0.19751	±	0.00483	3.14E-14	4.3	61.6	17.39	±	4.50	4.50
Biotite	650	10	0.00135	±	0.00014	0.17623	±	0.00098	1.68E-13	26.9	60.1	18.99	±	1.34	1.34
CLAIR 112, Layer 1	750	10	0.00017	±	0.00024	0.26678	±	0.00112	1.00E-13	40.6	94.7	18.46	±	1.38	1.38
J = 0.003101 ± 0.00001	850	10	0.00028	±	0.00022	0.27482	±	0.00221	1.02E-13	54.5	91.6	18.57	±	1.34	1.34
Weight = 0.0100 g	950	10	0.00027	±	0.00013	0.29879	±	0.00158	3.17E-13	97.9	91.9	17.15	±	0.70	0.70
	1050	10	0.00163	±	0.00011	0.22751	±	0.00637	1.54E-14	100.0	51.8	12.70	±	0.98	0.98
*Ar, Weighted Mean Date ± 2σ (Ma)												17.86	±	0.54	
00KG14	650	10	0.00285	±	0.00006	0.05434	±	0.00055	7.53E-14	1.9	15.6	16.10	±	2.01	2.01
Muscovite	700	10	0.00215	±	0.00022	0.11881	±	0.00088	1.83E-13	6.4	36.5	17.17	±	3.00	3.00
CLAIR 111, Layer 9	750	10	0.00118	±	0.00011	0.22324	±	0.00051	7.91E-13	26.1	64.9	16.27	±	0.84	0.84
J = 0.003111 ± 0.00001	800	10	0.00026	±	0.00008	0.30185	±	0.00089	8.94E-13	48.4	92.3	17.10	±	0.45	0.45
Weight = 0.0620 g	850	10	0.00027	±	0.00005	0.29440	±	0.00041	5.46E-13	62.0	91.8	17.44	±	0.28	0.28
	900	10	0.00048	±	0.00018	0.28678	±	0.00271	2.80E-13	69.0	85.8	17.98	±	1.14	1.14
	950	10	0.00084	±	0.00053	0.25911	±	0.00300	2.04E-13	74.0	75.2	16.23	±	3.39	3.39
	1000	10	0.00068	±	0.00033	0.26846	±	0.00285	2.81E-13	81.0	79.7	16.61	±	2.03	2.03
	1050	10	0.00041	±	0.00032	0.29767	±	0.00309	2.42E-13	87.1	87.8	16.51	±	1.75	1.75
	1100	10	0.00017	±	0.00039	0.32157	±	0.00434	1.52E-13	90.8	94.8	16.50	±	2.01	2.01
	1200	10	0.00007	±	0.00024	0.31873	±	0.00485	2.17E-13	96.3	97.9	17.19	±	1.27	1.27
	1300	10	0.00021	±	0.00048	0.31653	±	0.00555	8.58E-14	98.4	93.7	16.56	±	2.50	2.50
	1350	10	0.00067	±	0.00109	0.32183	±	0.00220	3.03E-14	99.1	79.9	13.91	±	5.57	5.57
	1550	10	0.00079	±	0.00142	0.29713	±	0.00455	3.44E-14	100.0	76.6	14.43	±	7.86	7.86
*Ar, Weighted Mean Date ± 2σ (Ma)												16.84	±	0.38	
00KG16	650	10	0.00270	±	0.00011	0.05909	±	0.00065	5.33E-14	2.0	20.3	19.19	±	3.06	3.06
Muscovite	750	10	0.00057	±	0.00006	0.26118	±	0.00031	6.25E-13	25.3	83.0	17.78	±	0.40	0.39
CLAIR 111, Layer 9	800	10	0.00001	±	0.00021	0.31248	±	0.00218	6.11E-13	48.0	99.5	17.82	±	1.13	1.13
J = 0.003111 ± 0.00001	850	10	0.00011	±	0.00017	0.30609	±	0.00122	3.31E-13	60.3	96.7	17.67	±	0.89	0.89
Weight = 0.0375 g	900	10	0.00028	±	0.00023	0.29484	±	0.00608	1.77E-13	66.9	91.7	17.40	±	1.35	1.35
	950	10	0.00020	±	0.00009	0.28829	±	0.00116	1.93E-13	74.1	93.8	18.20	±	0.53	0.53
	1000	10	0.00013	±	0.00017	0.30105	±	0.00481	2.71E-13	84.2	96.1	17.86	±	0.98	0.98
	1075	10	0.00001	±	0.00013	0.31407	±	0.00451	2.05E-13	91.9	99.6	17.73	±	0.73	0.73
	1250	10	0.00027	±	0.00018	0.29498	±	0.00423	1.06E-13	95.8	91.9	17.42	±	1.06	1.06
	1350	10	0.00040	±	0.00137	0.34974	±	0.00827	9.11E-14	99.2	88.0	14.09	±	6.45	6.45
	1550	10	0.00178	±	0.00127	0.31366	±	0.00540	2.09E-14	100.0	47.4	8.48	±	6.66	6.66
*Ar, Weighted Mean Date ± 2σ (Ma)												17.60	±	0.41	
00KG19	550	10	0.00298	±	0.00007	0.04117	±	0.00068	8.00E-14	2.1	12.0	16.12	±	2.89	2.89
Biotite	600	10	0.00151	±	0.00008	0.18614	±	0.00301	3.04E-13	10.2	55.3	16.49	±	0.79	0.78
CLAIR 111, Layer 8	650	10	0.00040	±	0.00005	0.28132	±	0.00664	6.27E-13	26.9	88.2	17.39	±	0.43	0.43
J = 0.003087 ± 0.00001	700	10	0.00019	±	0.00011	0.30241	±	0.00768	5.20E-13	40.7	94.2	17.28	±	0.68	0.67
Weight = 0.0541 g	750	10	0.00015	±	0.00009	0.30670	±	0.01051	2.19E-13	46.5	95.6	17.29	±	0.84	0.83
	800	10	0.00000	±	0.00025	0.30057	±	0.00422	1.84E-13	51.4	99.8	18.43	±	1.37	1.37
	850	10	0.00020	±	0.00021	0.29726	±	0.00431	2.18E-13	57.2	93.8	17.51	±	1.14	1.14
	900	10	0.00015	±	0.00007	0.30570	±	0.00537	3.94E-13	67.7	95.4	17.32	±	0.43	0.42
	950	10	0.00009	±	0.00053	0.30167	±	0.00841	4.65E-13	80.1	97.2	17.87	±	2.87	2.87
	1000	10	0.00014	±	0.00008	0.29379	±	0.00486	5.78E-13	95.5	95.7	18.07	±	0.51	0.51
	1050	10	0.00037	±	0.00029	0.29413	±	0.00863	1.11E-13	98.4	88.9	16.77	±	1.65	1.65
	1100	10	0.00006	±	0.00089	0.29275	±	0.00556	4.30E-14	99.6	97.4	18.46	±	4.94	4.94
	1150	10	0.00136	±	0.00243	0.30423	±	0.01188	1.62E-14	100.0	59.8	10.93	±	13.09	13.09
*Ar, Weighted Mean Date ± 2σ (Ma)												17.45	±	0.42	
00KG20	550	10	0.00293	±	0.00004	0.04969	±	0.00085	6.22E-14	4.4	13.4	15.12	±	1.57	1.57
Biotite	650	10	0.00038	±	0.00071	0.24522	±	0.00233	9.28E-14	10.9	88.6	20.19	±	4.77	4.77
CLAIR 111, Layer 9	750	10	0.00015	±	0.00005	0.31388	±	0.00378	3.57E-13	35.9	95.5	17.03	±	0.30	0.29
J = 0.003111 ± 0.00001	800	10	0.00002	±	0.00014	0.31784	±	0.00304	1.55E-13	46.8	99.2	17.46</			

Chapter 4: Exhumational history of the Mustang and Mugu granites

	900	10	0.00078	±	0.00012	0.24421	±	0.00057	5.42E-13	71.2	76.8	17.69	±	0.81	0.79	
	950	10	0.00097	±	0.00010	0.22624	±	0.00134	3.12E-13	77.6	71.2	17.69	±	0.76	0.74	
	1000	10	0.00087	±	0.00013	0.23253	±	0.00219	3.63E-13	84.9	74.2	17.95	±	0.97	0.96	
	1050	10	0.00050	±	0.00053	0.28154	±	0.00442	2.47E-13	90.0	85.1	17.00	±	3.14	3.13	
	1100	10	0.00022	±	0.00018	0.29934	±	0.00259	1.23E-13	92.5	93.4	17.56	±	1.02	1.01	
	1200	10	0.00012	±	0.00090	0.30245	±	0.00563	1.47E-13	95.5	96.3	17.92	±	4.94	4.93	
	1300	10	0.00008	±	0.00052	0.31026	±	0.00524	1.43E-13	98.4	97.4	17.66	±	2.80	2.79	
	1350	10	0.00020	±	0.00073	0.30979	±	0.00364	6.30E-14	99.7	93.9	17.06	±	3.88	3.88	
	1550	10	0.00176	±	0.00071	0.26356	±	0.00678	1.68E-14	100.0	47.9	10.25	±	4.50	4.50	
			*Ar, Weighted Mean Date ± 2σ (Ma)									17.42	±	0.36		
	00KG24	550	10	0.00309	±	0.00019	0.05865	±	0.00175	8.00E-14	2.4	8.8	9.34	±	5.40	5.40
		600	10	0.00113	±	0.00011	0.20769	±	0.00330	3.41E-13	12.7	66.4	17.74	±	0.91	0.91
		650	10	0.00024	±	0.00007	0.28646	±	0.00361	7.47E-13	35.2	92.9	17.99	±	0.44	0.43
		700	10	0.00007	±	0.00009	0.30969	±	0.00544	5.03E-13	50.3	97.9	17.55	±	0.53	0.53
		750	10	0.00016	±	0.00045	0.30939	±	0.00602	1.70E-13	55.4	95.1	17.07	±	2.37	2.37
		800	10	0.00019	±	0.00092	0.30607	±	0.00542	1.44E-13	59.8	94.1	17.07	±	4.88	4.88
		900	10	0.00013	±	0.00015	0.29847	±	0.00353	7.79E-13	83.2	95.9	17.84	±	0.84	0.83
		950	10	0.00009	±	0.00006	0.30300	±	0.00603	4.99E-13	98.2	97.2	17.80	±	0.41	0.41
		1000	10	0.00073	±	0.00060	0.28963	±	0.00743	4.21E-14	99.5	78.2	15.00	±	3.37	3.37
		1100	10	0.00213	±	0.00184	0.30674	±	0.00638	1.64E-14	100.0	36.9	6.69	±	9.85	9.85
			*Ar, Weighted Mean Date ± 2σ (Ma)									17.42	±	0.38		
	00KG24	550	10	0.00286	±	0.00018	0.05634	±	0.00045	9.02E-14	2.0	15.5	15.50	±	5.26	5.26
		650	10	0.00215	±	0.00010	0.11031	±	0.00111	5.83E-14	3.3	36.4	18.56	±	1.59	1.57
		750	10	0.00124	±	0.00003	0.20419	±	0.00032	9.62E-13	24.9	63.4	17.47	±	0.30	0.24
		800	10	0.00008	±	0.00010	0.30454	±	0.00311	9.15E-13	45.5	97.4	17.99	±	0.58	0.55
		850	10	0.00020	±	0.00006	0.29277	±	0.00156	6.01E-13	59.0	93.9	18.03	±	0.40	0.36
		900	10	0.00049	±	0.00019	0.27353	±	0.00131	2.66E-13	65.0	85.5	17.58	±	1.17	1.15
		950	10	0.00037	±	0.00065	0.27345	±	0.00069	2.87E-13	71.4	89.0	18.30	±	3.90	3.90
		1000	10	0.00032	±	0.00012	0.29158	±	0.00516	4.47E-13	81.5	90.3	17.43	±	0.79	0.77
		1050	10	0.00008	±	0.00002	0.30835	±	0.00624	2.71E-13	87.6	97.5	17.79	±	0.43	0.39
		1100	10	0.00005	±	0.00030	0.32670	±	0.00731	1.58E-13	91.1	98.4	16.95	±	1.56	1.55
		1200	10	0.00015	±	0.00021	0.31844	±	0.00648	1.98E-13	95.5	95.4	16.96	±	1.16	1.15
		1300	10	0.00031	±	0.00033	0.31833	±	0.00620	1.05E-13	97.9	90.8	16.06	±	1.76	1.75
		1350	10	0.00070	±	0.00061	0.32139	±	0.00997	4.82E-14	99.0	79.3	13.90	±	3.20	3.20
		1550	10	0.00033	±	0.00062	0.28208	±	0.00715	4.49E-14	100.0	90.1	17.97	±	3.67	3.66
			*Ar, Weighted Mean Date ± 2σ (Ma)									17.59	±	0.34		
	00KG25	650	10	0.00182	±	0.00006	0.15571	±	0.00329	1.76E-13	15.1	46.1	16.86	±	0.84	0.83
		700	10	0.00021	±	0.00012	0.29152	±	0.00469	2.58E-13	37.2	93.7	18.32	±	0.75	0.74
		750	10	0.00008	±	0.00028	0.30519	±	0.00442	1.20E-13	47.5	97.5	18.20	±	1.56	1.56
		800	10	0.00039	±	0.00061	0.29526	±	0.00237	6.25E-14	52.8	88.4	17.07	±	3.48	3.48
		850	10	0.00020	±	0.00028	0.28827	±	0.00329	7.88E-14	59.6	94.0	18.57	±	1.62	1.62
		900	10	0.00037	±	0.00011	0.27996	±	0.00229	1.55E-13	72.9	88.8	18.54	±	0.72	0.71
		950	10	0.00030	±	0.00020	0.27811	±	0.00260	1.72E-13	87.6	91.1	18.65	±	1.23	1.22
		1000	10	0.00029	±	0.00067	0.28844	±	0.00650	9.01E-14	95.3	91.3	18.03	±	3.92	3.92
		1050	10	0.00055	±	0.00082	0.29222	±	0.01224	3.47E-14	98.3	83.6	16.31	±	4.73	4.72
		1100	10	0.00036	±	0.00114	0.29095	±	0.00800	1.42E-14	99.5	89.2	17.47	±	6.57	6.57
		1200	10	0.00014	±	0.00428	0.27435	±	0.01616	5.91E-15	100.0	95.9	19.90	±	26.11	26.11
			*Ar, Weighted Mean Date ± 2σ (Ma)									18.03	±	0.54		
	00KG25	550	10	0.00331	±	0.00048	0.03286	±	0.00012	1.51E-14	0.4	2.3	3.92	±	24.10	24.10
		650	10	0.00299	±	0.00025	0.05231	±	0.00003	3.18E-14	1.4	11.6	12.40	±	7.91	7.90
		700	10	0.00267	±	0.00060	0.08742	±	0.00137	5.55E-14	3.0	21.1	13.45	±	11.20	11.20
		750	10	0.00161	±	0.00006	0.17911	±	0.00228	3.26E-13	12.5	52.4	16.87	±	0.70	0.69
		800	10	0.00035	±	0.00003	0.29057	±	0.00366	6.31E-13	31.0	89.5	17.18	±	0.31	0.30
		850	10	0.00043	±	0.00009	0.27887	±	0.00246	4.75E-13	44.9	87.1	17.41	±	0.58	0.57
		900	10	0.00060	±	0.00010	0.25672	±	0.00135	2.90E-13	53.4	92.5	17.84	±	0.66	0.66
		950	10	0.00046	±	0.00011	0.27389	±	0.00095	3.72E-13	64.3	86.2	17.54	±	0.40	0.40
		1000	10	0.00025	±	0.00007	0.29655	±	0.00110	4.88E-13	78.5	92.5	17.38	±	0.40	0.40
		1050	10	0.00009	±	0.00028	0.30732	±	0.00141	2.03E-13	84.5	97.3	17.66	±	1.51	1.51
		1100	10	0.00004	±	0.00023	0.30822	±	0.00279	1.15E-13	87.8	98.7	17.86	±	1.22	1.22
		1200	10	0.00012	±	0.00015	0.30627	±	0.00115	1.18E-13	91.3	96.3	17.54	±	0.78	0.78
		1300	10	0.00022	±	0.00065	0.30351	±	0.00295	7.11E-14	93.4	93.3	17.13	±	3.54	3.54
		1350	10	0.00014	±	0.00030	0.31925	±	0.00364	8.13E-14	95.7	95.6	16.70	±	1.58	1.58
		1550	10	0.00002	±	0.00013	0.30150	±	0.00261	1.46E-13	100.0	99.2	18.35	±	0.71	0.71
			*Ar, Weighted Mean Date ± 2σ (Ma)									17.24	±	0.31		
	00KG26	550	10	0.00286	±	0.00017	0.05635	±	0.00044	4.41E-14	1.1	15.6	15.41	±	5.04	5.04
		650	10	0.00172	±	0.00003	0.16278	±	0.00104	2.19E-13	6.8	49.2	16.85	±	0.33	0.32
		700	10	0.00047	±	0.00014	0.28785	±	0.00186	4.99E-13	19.7	85.6	16.63	±	0.81	0.81
		750	10	0.00005	±	0.00001	0.31486	±	0.00485	4.09E-13	30.2	98.2	17.40	±	0.20	0.20
		800	10	0.00023	±	0.00014	0.30052	±	0.00451	2.84E-13	37.5	92.9	17.24	±	0.76	0.76
		850	10	0.00027	±	0.00007	0.29090	±	0.00368	3.24E-13	45.9	92.0	17.63	±	0.46	0.45
		900	10	0.00049	±	0.00005	0.27960	±	0.00403	5.30E-13	59.5	85.3	17.01	±	0.35	0.34
		950	10	0.00029	±	0.00012	0.29828	±	0.00404	1.01E-12	85.5	91.3	17.07	±	0.67	0.66
		1000	10	0.00023	±	0.00010	0.30229	±	0.00366	3.51E-13	94.6	93.1	17.18	±	0.59	0.59
		1050	10	0.00013	±	0.00016	0.30236	±	0.00207	1.48E-13	98.4	96.2	17.73	±	0.86</	

Chapter 4: Exhumational history of the Mustang and Mugu granites

00KG28	550	10	0 00302 ± 0 00015	0 04383 ± 0 00043	5 45E-14	1 1	10 8	13 85 ± 5 57	5 57	5 57
Muscovite	650	10	0 00251 ± 0 00009	0 07740 ± 0 00087	7 97E-14	2 8	25 8	18 45 ± 1 84	1 84	1 84
CLAIR 111, Layer 8	700	10	0 00221 ± 0 00015	0 10277 ± 0 00182	1 45E-13	5 9	34 6	18 67 ± 2 42	2 42	2 42
J = 0 003087 ± 0 00001	750	10	0 00140 ± 0 00006	0 19247 ± 0 00068	6 89E-13	20 3	53 6	16 89 ± 0 49	0 49	0 49
Weight = 0 0739 g	800	10	0 00025 ± 0 00007	0 29348 ± 0 00117	9 72E-13	40 7	92 5	17 49 ± 0 40	0 40	0 40
	850	10	0 00021 ± 0 00013	0 29382 ± 0 00154	8 43E-13	58 4	93 5	17 68 ± 0 73	0 73	0 73
	900	10	0 00062 ± 0 00032	0 27006 ± 0 00313	4 85E-13	68 2	81 6	16 77 ± 1 96	1 96	1 96
	950	10	0 00079 ± 0 00013	0 25549 ± 0 00384	2 61E-13	73 6	76 6	16 64 ± 0 85	0 85	0 85
	1000	10	0 00034 ± 0 00007	0 28232 ± 0 00411	3 31E-13	80 6	89 9	17 67 ± 0 47	0 47	0 47
	1050	10	0 00028 ± 0 00065	0 30252 ± 0 00193	1 81E-13	84 4	91 7	16 83 ± 3 49	3 49	3 49
	1100	10	0 00008 ± 0 00015	0 31120 ± 0 00742	1 47E-13	87 5	97 4	17 38 ± 0 82	0 82	0 82
	1200	10	0 00007 ± 0 00003	0 31117 ± 0 00549	1 92E-13	91 5	97 7	17 43 ± 0 25	0 25	0 25
	1300	10	0 00009 ± 0 00016	0 31308 ± 0 00668	1 99E-13	95 7	97 2	17 24 ± 0 85	0 85	0 85
	1350	10	0 00016 ± 0 00050	0 31368 ± 0 00800	1 21E-13	98 2	95 0	16 81 ± 2 62	2 62	2 62
	1550	10	0 00033 ± 0 00038	0 30646 ± 0 00717	8 53E-14	100 0	90 2	16 34 ± 2 05	2 05	2 05
									⁴⁰ Ar, Weighted Mean Date ± 2σ _{int} (Ma)	17 26 ± 0 32
00KG30	550	10	0 00278 ± 0 00019	0 06191 ± 0 00023	5 05E-14	1 3	17 8	16 01 ± 4 97	4 97	4 97
Biotite	650	10	0 00112 ± 0 00011	0 21352 ± 0 00126	5 06E-13	14 6	66 8	17 45 ± 0 82	0 82	0 82
CLAIR 112, Layer 1	700	10	0 00021 ± 0 00011	0 30574 ± 0 00397	6 82E-13	32 4	93 6	17 08 ± 0 63	0 63	0 63
J = 0 003101 ± 0 00001	750	10	0 00004 ± 0 00006	0 30359 ± 0 00468	3 25E-13	41 0	98 6	18 11 ± 0 37	0 37	0 37
Weight = 0 0503 g	800	10	0 00007 ± 0 00020	0 31015 ± 0 00476	1 75E-13	45 6	97 9	17 60 ± 1 05	1 05	1 05
	850	10	0 00014 ± 0 00011	0 30703 ± 0 00316	2 18E-13	51 3	95 7	17 38 ± 0 60	0 60	0 60
	900	10	0 00026 ± 0 00005	0 29806 ± 0 00256	6 19E-13	67 5	92 3	17 27 ± 0 29	0 29	0 29
	950	10	0 00017 ± 0 00018	0 30378 ± 0 00254	8 29E-13	89 2	94 8	17 40 ± 0 98	0 98	0 98
	1000	10	0 00021 ± 0 00009	0 30632 ± 0 00156	2 51E-13	95 8	93 7	17 06 ± 0 48	0 48	0 48
	1050	10	0 00007 ± 0 00053	0 30693 ± 0 00160	1 09E-13	98 6	97 7	17 75 ± 2 82	2 82	2 82
	1150	10	0 00006 ± 0 00653	0 29643 ± 0 00326	4 66E-14	99 8	98 0	18 42 ± 36 07	36 07	36 07
	1350	10	0 00191 ± 0 00453	0 19411 ± 0 00777	6 01E-15	100 0	43 4	12 48 ± 38 31	38 31	38 31
									⁴⁰ Ar, Weighted Mean Date ± 2σ _{int} (Ma)	17 37 ± 0 53
00KG30	650	10	0 00330 ± 0 00029	0 03858 ± 0 00066	2 67E-14	1 1	2 6	3 76 ± 12 28	12 28	12 28
Muscovite	700	10	0 00247 ± 0 00028	0 08329 ± 0 00103	4 77E-14	3 1	27 0	18 07 ± 5 61	5 61	5 61
CLAIR 112, Layer 7	750	10	0 00124 ± 0 00008	0 19862 ± 0 00290	4 04E-13	19 7	63 3	17 77 ± 0 79	0 79	0 79
J = 0 003101 ± 0 00001	800	10	0 00020 ± 0 00005	0 28966 ± 0 00308	5 49E-13	42 2	93 8	18 05 ± 0 37	0 37	0 37
Weight = 0 0254 g	850	10	0 00035 ± 0 00007	0 27962 ± 0 00172	4 28E-13	59 8	89 5	17 84 ± 0 41	0 41	0 41
	900	10	0 00061 ± 0 00008	0 25099 ± 0 00064	1 96E-13	67 9	81 9	18 19 ± 0 51	0 51	0 51
	950	10	0 00056 ± 0 00017	0 24881 ± 0 00123	1 65E-13	74 7	83 3	18 65 ± 1 10	1 10	1 10
	1000	10	0 00003 ± 0 00017	0 28113 ± 0 00128	2 30E-13	84 1	99 0	19 51 ± 0 98	0 98	0 98
	1050	10	0 00004 ± 0 00029	0 29855 ± 0 00343	1 28E-13	89 4	98 6	18 41 ± 1 57	1 57	1 57
	1100	10	0 00005 ± 0 00026	0 29993 ± 0 00450	8 40E-14	92 8	98 4	18 28 ± 1 45	1 45	1 45
	1200	10	0 00019 ± 0 00028	0 30223 ± 0 00116	1 07E-13	97 2	94 2	17 38 ± 1 54	1 54	1 54
	1300	10	0 00043 ± 0 00132	0 30353 ± 0 00231	4 35E-14	99 0	87 2	16 01 ± 7 13	7 13	7 13
	1350	10	0 00106 ± 0 01629	0 31550 ± 0 01233	1 10E-14	99 5	68 5	12 12 ± 84 80	84 80	84 80
	1550	10	0 00066 ± 0 00485	0 27095 ± 0 00872	1 32E-14	100 0	80 4	16 54 ± 29 35	29 35	29 35
									⁴⁰ Ar, Weighted Mean Date ± 2σ _{int} (Ma)	17 94 ± 0 53
00KG31	600	10	0 00326 ± 0 00013	0 04297 ± 0 00088	1 45E-13	4 1	3 8	4 86 ± 4 95	4 95	4 95
Biotite	650	10	0 00111 ± 0 00016	0 21675 ± 0 00238	4 94E-13	18 2	67 1	17 16 ± 1 22	1 22	1 22
CLAIR 111, Layer 8	700	10	0 00025 ± 0 00011	0 29119 ± 0 00371	7 21E-13	38 8	92 6	17 65 ± 0 65	0 65	0 65
J = 0 003087 ± 0 00001	800	10	0 00002 ± 0 00009	0 29389 ± 0 00362	3 20E-13	49 9	96 3	18 98 ± 0 55	0 55	0 55
Weight = 0 0524 g	850	10	0 00027 ± 0 00034	0 29958 ± 0 00535	1 71E-13	54 8	91 9	17 03 ± 1 87	1 87	1 87
	875	10	0 00021 ± 0 00009	0 28018 ± 0 00697	2 47E-13	61 8	93 6	17 89 ± 0 65	0 65	0 65
	900	10	0 00022 ± 0 00007	0 28700 ± 0 00425	8 83E-13	87 0	93 4	18 05 ± 0 46	0 46	0 46
	925	10	0 00013 ± 0 00018	0 29188 ± 0 00545	3 50E-13	97 0	96 1	18 26 ± 1 06	1 06	1 06
	950	10	0 00073 ± 0 00059	0 27507 ± 0 00569	6 37E-14	98 8	78 3	15 80 ± 3 49	3 49	3 49
	975	10	0 00208 ± 0 00180	0 27673 ± 0 00748	2 31E-14	100 0	38 5	7 74 ± 10 68	10 68	10 68
									⁴⁰ Ar, Weighted Mean Date ± 2σ _{int} (Ma)	17 18 ± 0 37
00KG31	650	10	0 00286 ± 0 00023	0 05998 ± 0 00073	5 15E-14	1 2	15 5	14 51 ± 6 26	6 26	6 26
Muscovite	700	10	0 00268 ± 0 00018	0 07932 ± 0 00119	1 09E-13	3 7	20 7	14 65 ± 3 70	3 70	3 70
CLAIR 111, Layer 7	750	10	0 00138 ± 0 00011	0 19539 ± 0 00136	6 20E-13	18 2	59 1	16 95 ± 0 92	0 92	0 92
J = 0 003129 ± 0 000032	800	10	0 00029 ± 0 00010	0 29328 ± 0 00136	1 07E-12	43 2	91 3	17 51 ± 0 57	0 57	0 57
Weight = 0 0670 g	850	10	0 00037 ± 0 00014	0 29022 ± 0 00071	7 08E-13	59 7	88 8	17 21 ± 0 82	0 82	0 82
	900	10	0 00065 ± 0 00043	0 26141 ± 0 00179	3 29E-13	67 4	80 7	17 36 ± 2 73	2 73	2 73
	950	10	0 00056 ± 0 00014	0 26069 ± 0 00396	2 26E-13	72 6	83 3	17 97 ± 0 93	0 93	0 93
	1000	10	0 00051 ± 0 00025	0 27718 ± 0 00504	2 80E-13	79 2	84 9	17 23 ± 1 54	1 54	1 54
	1050	10	0 00025 ± 0 00007	0 30146 ± 0 00347	2 10E-13	84 1	92 6	17 27 ± 0 45	0 45	0 45
	1100	10	0 00002 ± 0 00014	0 31286 ± 0 00811	1 65E-13	87 9	99 4	17 87 ± 0 81	0 79	0 79
	1200	10	0 00003 ± 0 00030	0 31478 ± 0 00522	2 41E-13	93 6	98 9	17 67 ± 1 58	1 58	1 58
	1300	10	0 00008 ± 0 00050	0 31652 ± 0 00523	1 77E-13	97 7	97 4	17 31 ± 2 63	2 63	2 63
	1350	10	0 00010 ± 0 00060	0 31716 ± 0 00492	6 14E-14	99 1	97 0	17 21 ± 3 15	3 15	3 15
	1550	10	0 00053 ± 0 00078	0 29621 ± 0 00464	3 66E-14	100 0	84 1	15 99 ± 4 37	4 37	4 37
									⁴⁰ Ar, Weighted Mean Date ± 2σ _{int} (Ma)	17 25 ± 0 39
00KG32	550	10	0 00289 ± 0 00014	0 05882 ± 0 00043	1 14E-13	2 5	14 6	13 87 ± 3 96	3 96	3 96
Biotite	650	10	0 00100 ± 0 00010	0 22516 ± 0 00120	5 45E-13	14 3	70 4	17 42 ± 0 77	0 77	0 77
CLAIR 112, Layer 1	700	10	0 00018 ± 0 00006	0 30573 ± 0 00113	7 12E-13	29 8	94 6	17 26 ± 0 34	0 34	0 34
J = 0 003101 ± 0 00001	750	10	0 00005 ± 0 00008	0 31886 ± 0 00581	4 22E-13	38 9	98 5	17 22 ± 0 49	0 49	0 49
Weight = 0 0679 g	800	10	0 00007 ± 0 00025	0 29928 ± 0 00476	2 25E-13	43 8	97 8	18 22 ± 1 40	1 40	1 40
	850	10	0 00003 ± 0 00016	0 31205 ± 0 00512	2 85E-13	50 0	99 0	17 69 ± 0 86	0 86	0 86
	900	10	0 00013 ± 0 00001	0 30602 ± 0 00314	8 24E-13	67 9	96 0	17 48 ± 0 16	0 16	0 16
	950	10	0 00021 ± 0 00003	0 29918 ± 0 00326	8 89E-13	87 2	93 5	17 43 ± 0 23	0 22	0 22
	1000	10	0 00022 ± 0 00015	0 29755 ± 0 00327	3 77E-13	95 4	93 4	17 50 ± 0 82	0 82	0 82
	1050	10	0 00022 ± 0 00018	0 29995 ± 0 00127	1 41E-13	98 5	93 5	17 38 ± 1 00	1 00	1 00
	1150	10	0 00001 ± 0 00094	0 29165 ± 0 00588	6 42E-14	99 9	99 6	19 04 ± 5 29	5 29	5 29
	1350	10	0 00089 ± 0 00335	0 15664 ± 0 01282	6 13E-15	100 0	73 8	26 18 ± 34 83	34 83	34 83
									⁴⁰ Ar, Weighted Mean Date ± 2σ _{int} (Ma)	17 40 ± 0 21
00KG32	550	10	0 00311 ± 0 00050	0 03363 ± 0 00013	1 53E-14	0 5	8 0	13 53 ± 25 02	25 02	25 02
Muscovite	650	10	0 00309 ± 0 00036	0 04545 ± 0 00018	3 81E-14	1 8	8 7	10 88 ± 13 14	13 14	13 14
CLAIR 112, Layer 2	700	10	0 00214 ± 0 00038	0 12175 ± 0 00093	9 14E-14	4 9	36 9	17 25 ± 5 17	5 17	5 17
J = 0 0										

Chapter 4: Exhumational history of the Mustang and Mugu granites

1000	10	0.00019	± 0.00010	0.28994	± 0.00140	3.20E-13	85.3	94.4	18.54	± 0.62	0.61
1050	10	0.00020	± 0.00035	0.30847	± 0.00056	1.78E-13	91.4	93.8	17.34	± 1.90	1.90
1100	10	0.00019	± 0.00034	0.30909	± 0.00082	8.99E-14	94.4	94.2	17.38	± 1.83	1.83
1200	10	0.00015	± 0.00073	0.30655	± 0.00457	6.24E-14	96.6	95.5	17.75	± 3.99	3.99
1300	10	0.00014	± 0.00129	0.31936	± 0.00691	2.10E-14	97.3	95.7	17.09	± 6.79	6.79
1350	10	0.00173	± 0.00211	0.36230	± 0.00596	1.53E-14	97.8	48.7	7.69	± 9.79	9.79
1550	10	0.00125	± 0.00205	0.29123	± 0.00633	6.50E-14	100.0	62.8	12.32	± 11.80	11.80
									³⁹ Ar, Weighted Mean Date ± 2σ ^{††} (Ma)	17.88	± 0.46

Note Sample preparation, irradiation, and flux monitor procedures are described in the text and follow procedures outlined by Hodges *et al.* (1994). Ar isotopic determinations were conducted at the MIT CLAIR facility. Data are for step heating experiments conducted in a double vacuum resistance furnace. A Faraday detector was used. Mass discrimination results in a (⁴⁰Ar/³⁹Ar) of 299 for atmospheric argon measured with the Faraday detector. Operational blanks vary with time and temperature and were usually measured after every other unknown. Typical blanks (in moles) at M/e 40, 39, 38, 37 and 36, respectively, were (800 K) 2e-14, 7e-17, 5e-17, 2e-17, 8e-17, (1500 K) 2e-14, 4e-17, 4e-17, 3e-17, 1e-16, (1800 K) < 3e-14, 8e-17, 4e-17, 1e-16, 3e-17. Uncertainties quoted at 2σ (95%) confidence level. Asterisk denotes radiogenic component.

† This column lists the sample number, mineral analyzed, irradiation package number and layer, J value (± 2σ uncertainty), and weight (in g).

‡ Temperature of release increment (± 5 C) as monitored by W-Re thermocouple.

Heating time Does not include additional 10 minutes of getting before gas is analyzed during which time the sample re-equilibrates to the furnace standby temperature (250° C).

‡ Number of moles of K-derived ³⁹Ar released during each heating increment. Calculated from measured signal size and instrumental sensitivity as calibrated against air aliquots of known volume.

§ Cumulative percent of K-derived ³⁹Ar after each increment.

Percentage of the total ³⁹Ar in each heating increment that is radiogenic.

†† Incremental model dates calculated by assuming (⁴⁰Ar/³⁹Ar) = 295.5.

§§ Includes propagated uncertainty in irradiation parameter J.

Excludes uncertainty in irradiation parameter J. Indicates contribution of analytical error to the overall uncertainty.

††† ³⁹Ar, weighted mean date is calculated by summing the product of the increment date and moles ³⁹Ar, released for each step and normalizing by the total moles of ³⁹Ar, released. Shown with propagated 2σ uncertainty including uncertainty in J.

Table 4 <continued>

Chapter 4: Exhumational history of the Mustang and Mugu granites

TABLE 5 ⁴⁰Ar/³⁹Ar STEP HEATING DATA FOR K-FELDSPAR FROM THE UPPER MUSTANG REGION, CENTRAL NEPAL

Sample †	T‡ (°C)	Duration# (minutes)	³⁹ Ar/ ³⁹ Ar ±	³⁹ Ar/ ³⁹ Ar 2σ	⁴⁰ Ar/ ³⁹ Ar ±	⁴⁰ Ar/ ³⁹ Ar 2σ	³⁹ Ar, ‡ (moles)	³⁹ Ar, Released§ (cumulative %)	⁴⁰ Ar/## (%)	Date†† (Ma)	Date 2σ§§ (Ma)	Date 2σ### (Ma)
00KG08 CLAIR 112, Layer 4 J = 0.003224 ± 0.000019 Weight = 0.0500 g	400	28	0.00121 ±	0.00004	0.02044 ±	0.00014	3.93E-14	0.7	64.2	174.08 ±	3.88	3.76
	400	36	0.00145 ±	0.00119	0.21615 ±	0.00330	2.51E-14	1.1	57.1	15.33 ±	9.42	9.42
	450	28	0.00109 ±	0.00065	0.26639 ±	0.00280	4.00E-14	1.7	67.6	14.72 ±	4.17	4.17
	450	36	0.00077 ±	0.00174	0.29962 ±	0.00288	3.43E-14	2.3	77.1	14.93 ±	9.91	9.91
	500	28	0.00150 ±	0.00074	0.27208 ±	0.00268	5.33E-14	3.2	55.6	11.87 ±	4.65	4.65
	500	36	0.00077 ±	0.00094	0.31763 ±	0.00433	5.00E-14	4.0	77.0	14.07 ±	5.03	5.03
	550	28	0.00086 ±	0.00040	0.30300 ±	0.00304	7.54E-14	5.3	74.3	14.24 ±	2.24	2.24
	550	36	0.00018 ±	0.00065	0.35596 ±	0.00135	6.91E-14	6.4	94.4	15.39 ±	3.11	3.11
	600	28	0.00176 ±	0.00015	0.14816 ±	0.00031	9.44E-14	8.0	47.9	18.72 ±	1.69	1.69
	600	36	0.00130 ±	0.00050	0.25028 ±	0.00064	8.56E-14	9.4	61.5	14.26 ±	3.40	3.40
	650	28	0.00024 ±	0.00018	0.32294 ±	0.00089	1.23E-13	11.4	92.7	16.66 ±	0.97	0.96
	650	36	0.00029 ±	0.00023	0.35209 ±	0.00515	8.96E-14	12.9	91.3	15.05 ±	1.15	1.15
	700	28	0.00009 ±	0.00067	0.32507 ±	0.00494	8.51E-14	14.3	97.1	17.33 ±	3.51	3.51
	700	36	0.00056 ±	0.00095	0.32938 ±	0.01000	5.31E-14	15.2	83.2	14.66 ±	4.94	4.94
Minimum ³⁹ Ar, Weighted Mean Spectrum Date and 2σ†† (Ma)										15.49 ±	0.95	
750	28	0.00049 ±	0.00140	0.30263 ±	0.00846	5.56E-14	16.1	85.3	16.35 ±	7.88	7.87	
750	36	0.00020 ±	0.00160	0.30577 ±	0.00995	4.22E-14	16.8	93.8	17.79 ±	8.94	8.94	
780	28	0.00022 ±	0.00057	0.25436 ±	0.00801	3.68E-14	17.4	93.4	21.27 ±	3.87	3.87	
780	36	0.00027 ±	0.00098	0.27616 ±	0.00911	3.23E-14	18.0	91.9	19.28 ±	6.09	6.09	
810	28	0.00015 ±	0.00074	0.26117 ±	0.00830	3.86E-14	18.6	95.4	21.15 ±	4.84	4.84	
810	36	0.00021 ±	0.00109	0.27051 ±	0.00897	4.43E-14	19.3	93.6	20.05 ±	6.89	6.89	
840	28	0.00015 ±	0.00078	0.25958 ±	0.00805	4.65E-14	20.1	95.3	21.27 ±	5.18	5.17	
840	36	0.00036 ±	0.00039	0.27448 ±	0.00829	4.23E-14	20.8	89.1	18.81 ±	2.53	2.53	
880	25	0.00018 ±	0.00052	0.20650 ±	0.00527	3.97E-14	21.5	94.5	26.45 ±	4.34	4.33	
900	25	0.00007 ±	0.00043	0.23695 ±	0.00523	5.68E-14	22.4	97.9	23.91 ±	3.15	3.15	
960	25	0.00027 ±	0.00017	0.22414 ±	0.00249	1.97E-13	25.7	91.9	23.72 ±	1.30	1.30	
980	25	0.00045 ±	0.00015	0.24188 ±	0.00186	2.40E-13	29.6	86.7	20.77 ±	1.06	1.06	
1000	25	0.00023 ±	0.00009	0.25310 ±	0.00146	2.93E-13	34.5	93.0	21.28 ±	0.66	0.65	
1050	25	0.00017 ±	0.00006	0.26376 ±	0.00122	5.48E-13	43.6	94.9	20.85 ±	0.42	0.40	
1075	25	0.00004 ±	0.00005	0.27166 ±	0.00141	4.32E-13	50.7	98.8	21.06 ±	0.35	0.32	
1075	40	0.00007 ±	0.00021	0.27449 ±	0.00141	4.23E-13	57.7	97.9	20.66 ±	1.31	1.31	
1075	80	0.00004 ±	0.00006	0.27127 ±	0.00097	5.11E-13	66.2	98.6	21.05 ±	0.41	0.39	
1075	150	0.00009 ±	0.00006	0.26639 ±	0.00084	5.32E-13	75.0	97.2	21.13 ±	0.39	0.37	
1075	300	0.00016 ±	0.00008	0.25958 ±	0.00049	4.90E-13	83.1	95.2	21.23 ±	0.56	0.55	
1100	20	0.00085 ±	0.00190	0.25195 ±	0.00871	1.96E-14	83.4	74.8	17.22 ±	12.85	12.85	
1100	40	0.00031 ±	0.00259	0.25324 ±	0.00428	5.47E-14	84.3	90.9	20.78 ±	17.36	17.35	
1100	80	0.00008 ±	0.00037	0.25401 ±	0.00307	1.21E-13	86.4	97.6	22.24 ±	2.52	2.51	
1100	120	0.00012 ±	0.00026	0.25315 ±	0.00210	1.51E-13	88.9	96.3	22.02 ±	1.76	1.76	
1125	20	0.00069 ±	0.00213	0.25102 ±	0.00435	2.50E-14	89.3	79.5	18.35 ±	14.47	14.47	
1125	40	0.00026 ±	0.00109	0.25185 ±	0.00350	6.78E-14	90.4	92.3	21.23 ±	7.39	7.39	
1150	15	0.00055 ±	0.00039	0.25585 ±	0.00547	3.33E-14	90.9	83.7	18.95 ±	2.64	2.64	
1200	15	0.00001 ±	0.00018	0.25827 ±	0.00164	2.63E-13	95.3	99.6	22.33 ±	1.22	1.22	
1250	15	0.00004 ±	0.00004	0.25495 ±	0.00245	1.76E-13	98.2	98.8	22.44 ±	0.37	0.35	
1300	15	0.00155 ±	0.00180	0.26842 ±	0.00444	1.29E-14	98.4	54.3	11.74 ±	11.45	11.45	
1350	15	0.00011 ±	0.00327	0.24593 ±	0.00443	1.52E-14	98.7	96.7	22.76 ±	22.60	22.60	
1550	15	0.00032 ±	0.00041	0.26056 ±	0.00366	8.04E-14	100	90.5	20.11 ±	2.72	2.72	
00KG12 CLAIR 112, Layer 3 J = 0.003211 ± 0.000045 Weight = 0.0840 g	400	28	0.00257 ±	0.00006	0.00860 ±	0.00009	4.04E-14	0.4	24.2	155.95 ±	11.79	11.61
	400	36	0.00265 ±	0.00030	0.04757 ±	0.00025	2.39E-14	0.6	21.6	26.13 ±	10.64	10.63
	450	28	0.00244 ±	0.00046	0.05750 ±	0.00047	1.90E-14	0.7	27.8	27.81 ±	13.44	13.44
	450	36	0.00237 ±	0.00026	0.06507 ±	0.00029	2.16E-14	0.9	30.0	26.52 ±	6.81	6.80
	500	28	0.00260 ±	0.00022	0.06892 ±	0.00029	4.52E-14	1.3	23.1	19.29 ±	5.51	5.51
	500	36	0.00205 ±	0.00073	0.08747 ±	0.00054	3.29E-14	1.6	39.4	25.89 ±	14.14	14.14
	550	28	0.00227 ±	0.00022	0.06341 ±	0.00021	8.96E-14	2.4	32.8	29.70 ±	5.92	5.90
	550	36	0.00239 ±	0.00015	0.10804 ±	0.00026	7.47E-14	3.1	29.3	15.67 ±	2.31	2.30
	600	28	0.00228 ±	0.00009	0.07467 ±	0.00005	1.48E-13	4.4	32.7	25.17 ±	2.13	2.10
	600	36	0.00154 ±	0.00042	0.16746 ±	0.00097	1.01E-13	5.3	54.4	18.72 ±	4.22	4.21
	650	28	0.00198 ±	0.00010	0.10657 ±	0.00009	1.73E-13	6.8	41.5	22.41 ±	1.60	1.57
	650	36	0.00123 ±	0.00028	0.23898 ±	0.00109	1.30E-13	8.0	63.7	15.39 ±	2.02	2.01
	700	28	0.00203 ±	0.00013	0.12832 ±	0.00016	2.01E-13	9.7	40.0	17.96 ±	1.71	1.69
	700	36	0.00090 ±	0.00030	0.29291 ±	0.00113	1.36E-13	11.0	73.4	14.47 ±	1.78	1.77
750	28	0.00125 ±	0.00018	0.21425 ±	0.00058	1.94E-13	12.7	63.1	17.00 ±	1.46	1.44	
750	36	0.00066 ±	0.00028	0.32146 ±	0.00272	1.32E-13	13.8	80.4	14.45 ±	1.48	1.47	
780	28	0.00074 ±	0.00033	0.29622 ±	0.00331	1.01E-13	14.7	78.0	15.21 ±	1.90	1.89	
780	36	0.00081 ±	0.00046	0.30269 ±	0.00361	8.61E-14	15.5	76.0	14.50 ±	2.61	2.60	
810	28	0.00080 ±	0.00032	0.27940 ±	0.00376	8.31E-14	16.2	76.2	15.74 ±	2.00	1.99	
810	36	0.00057 ±	0.00054	0.31063 ±	0.00458	7.55E-14	16.9	82.9	15.42 ±	2.96	2.96	
840	28	0.00056 ±	0.00039	0.29558 ±	0.00638	7.71E-14	17.6	83.5	16.31 ±	2.29	2.28	
840	36	0.00060 ±	0.00057	0.28948 ±	0.00474	8.21E-14	18.3	82.0	16.36 ±	3.34	3.33	
880	25	0.00070 ±	0.00034	0.27986 ±	0.00450	9.87E-14	19.2	79.1	16.33 ±	2.10	2.09	
900	25	0.00092 ±	0.00048	0.26684 ±	0.00345	1.27E-13	20.3	72.7	15.74 ±	3.05	3.05	
Minimum ³⁹ Ar, Weighted Mean Spectrum Date and 2σ†† (Ma)										15.51 ±	0.82	
940	25	0.00051 ±	0.00021	0.24096 ±	0.00126	2.89E-13	22.9	84.7	20.27 ±	1.50	1.47	
960	25	0.00047 ±	0.00006	0.23239 ±	0.00097	3.42E-13	25.9	86.0	21.33 ±	0.56	0.47	
980	25	0.00041 ±	0.00006	0.21857 ±	0.00035	5.00E-13	30.3	87.8	23.15 ±	0.58	0.48	
1000	25	0.00037 ±	0.00003	0.22134 ±	0.00023	7.33E-13	36.8	88.8	23.13 ±	0.41	0.26	
1025	25	0.00040 ±	0.00007	0.21720 ±	0.00032	5.46E-13	41.7	88.0	23.35 ±	0.61	0.52	
1050	25	0.00042 ±	0.00004	0.22983 ±	0.00034	5.44E-13	46.5	87.3	21.91 ±	0.42	0.29	
1060	25	0.00034 ±	0.00008	0.25039 ±	0.00102	3.43E-13	49.5	89.9	20.71 ±	0.62	0.55	
1075	25	0.00037 ±	0.00024	0.25317 ±	0.01502	2.98E-13	52.2	88.9	20.25 ±	2.11	2.09	
1075	40	0.00029 ±	0.00009	0.25672 ±	0.00145	3.24E-13	55.1	91.3	20.51 ±	0.69	0.63	
1075	80	0.00033 ±	0.00005	0.25171 ±	0.00086	4.46E-13	59.0	90.2	20.67 ±	0.47	0.37	
1075	150	0.00038 ±	0.00010	0.24266 ±	0.00046	5.34E-13	63.7	88.7	21.08 ±	0.74	0.68	
1075	300	0.00051 ±	0.00014	0.23207 ±	0.00027	6.06E-13	69.1	85.0	21.11 ±	1.0		

Chapter 4: Exhumational history of the Mustang and Mugu granites

	1125	20	0.00068	±	0.00041	0.22050	±	0.00538	4.15E-14	74.5	79.9	20.89	±	3.24	3.23
	1125	40	0.00054	±	0.00047	0.21626	±	0.00342	1.02E-13	75.4	84.0	22.37	±	3.73	3.71
	1150	15	0.00066	±	0.00111	0.21190	±	0.00497	5.48E-14	75.9	80.5	21.90	±	8.87	8.86
	1175	15	0.00059	±	0.00017	0.21004	±	0.00222	1.54E-13	77.3	82.5	22.63	±	1.42	1.39
	1200	15	0.00065	±	0.00005	0.21450	±	0.00026	5.54E-13	82.2	80.8	21.73	±	0.51	0.42
	1225	15	0.00095	±	0.00002	0.20457	±	0.00033	1.25E-12	93.2	71.9	20.26	±	0.32	0.15
	1250	15	0.00099	±	0.00026	0.19416	±	0.00017	6.15E-13	98.7	70.6	20.96	±	2.32	2.30
	1300	15	0.00113	±	0.00036	0.19225	±	0.00384	7.36E-14	99.3	66.6	19.97	±	3.26	3.24
	1350	15	0.00044	±	0.00073	0.23454	±	0.00323	2.47E-14	99.5	86.8	21.34	±	5.28	5.27
	1550	10	0.00096	±	0.00101	0.20703	±	0.00177	5.19E-14	100	71.5	19.93	±	8.23	8.22
00KG23	400	28	0.00233	±	0.00004	0.00942	±	0.00005	6.49E-14	0.6	31.0	181.33	±	6.89	6.46
CLAIR 112, Layer 3	400	36	0.00190	±	0.00021	0.15193	±	0.00160	3.87E-14	1.0	43.8	16.65	±	2.41	2.40
J = 0.003211 ± 0.000045	450	28	0.00164	±	0.00013	0.15523	±	0.00111	6.04E-14	1.6	51.6	19.15	±	1.47	1.45
Weight = 0.0700 g	450	36	0.00140	±	0.00037	0.21738	±	0.00118	5.15E-14	2.1	58.5	15.54	±	2.94	2.93
	500	28	0.00144	±	0.00022	0.19818	±	0.00082	8.28E-14	2.9	57.4	16.71	±	1.87	1.86
	500	36	0.00074	±	0.00079	0.27316	±	0.00184	7.74E-14	3.6	78.1	16.51	±	4.94	4.93
	550	28	0.00119	±	0.00036	0.22150	±	0.00058	1.27E-13	4.8	64.8	16.88	±	2.74	2.72
	550	36	0.00026	±	0.00248	0.31748	±	0.00163	1.07E-13	5.8	92.2	16.78	±	13.24	13.24
	600	28	0.00162	±	0.00012	0.17058	±	0.00040	1.70E-13	7.5	52.2	17.66	±	1.25	1.23
	600	36	0.00039	±	0.00013	0.34233	±	0.00058	1.47E-13	8.9	88.3	14.91	±	0.68	0.65
	650	28	0.00080	±	0.00028	0.27363	±	0.00036	2.16E-13	11.0	76.3	16.11	±	1.78	1.77
	650	36	0.00022	±	0.00024	0.35895	±	0.00149	1.61E-13	12.5	93.2	15.01	±	1.14	1.12
	700	28	0.00051	±	0.00023	0.29985	±	0.00120	2.01E-13	14.4	84.9	16.35	±	1.33	1.31
	700	36	0.00011	±	0.00141	0.35495	±	0.00340	1.35E-13	15.7	96.5	15.71	±	6.75	6.75
	750	28	0.00058	±	0.00024	0.28984	±	0.00242	1.54E-13	17.2	82.7	16.47	±	1.43	1.41
	750	36	0.00069	±	0.00147	0.35193	±	0.00549	1.06E-13	18.2	79.4	13.04	±	7.11	7.11
	780	28	0.00049	±	0.00013	0.32243	±	0.00551	8.66E-14	19.1	85.4	15.29	±	0.78	0.75
Minimum ⁴⁰ Ar, Weighted Mean Spectrum Date and 2σ± (Ma)												15.53	±	1.09	
	780	36	0.00035	±	0.00093	0.32499	±	0.00574	7.94E-14	19.8	89.6	15.93	±	4.88	4.87
	810	28	0.00045	±	0.00031	0.28687	±	0.00370	8.07E-14	20.6	86.6	17.43	±	1.88	1.86
	810	36	0.00033	±	0.00084	0.32146	±	0.00530	7.64E-14	21.3	90.2	16.20	±	4.43	4.43
	840	28	0.00056	±	0.00081	0.26895	±	0.00459	8.28E-14	22.1	83.3	17.87	±	5.15	5.14
	840	36	0.00058	±	0.00040	0.29657	±	0.00511	8.48E-14	22.9	82.8	16.13	±	2.34	2.33
	880	25	0.00113	±	0.00014	0.22837	±	0.00299	1.09E-13	24.0	66.5	16.81	±	1.08	1.06
	900	25	0.00083	±	0.00019	0.25017	±	0.00272	1.24E-13	25.2	75.4	17.40	±	1.35	1.33
	960	25	0.00109	±	0.00010	0.23038	±	0.00158	3.54E-13	28.6	67.6	16.93	±	0.78	0.74
	980	25	0.00105	±	0.00009	0.24025	±	0.00090	4.03E-13	32.4	68.9	16.56	±	0.69	0.65
	1000	25	0.00106	±	0.00011	0.24706	±	0.00094	5.36E-13	37.6	68.7	16.06	±	0.78	0.74
	1025	25	0.00080	±	0.00006	0.26127	±	0.00107	6.59E-13	43.9	76.3	16.86	±	0.47	0.41
	1050	25	0.00064	±	0.00006	0.27989	±	0.00101	6.05E-13	49.7	80.9	16.69	±	0.44	0.38
	1075	25	0.00048	±	0.00008	0.29467	±	0.00111	5.00E-13	54.5	85.8	16.81	±	0.50	0.44
	1075	40	0.00020	±	0.00024	0.29909	±	0.00101	5.16E-13	59.5	93.9	18.11	±	1.39	1.36
	1075	80	0.00046	±	0.00007	0.29263	±	0.00079	6.51E-13	65.7	86.4	17.05	±	0.46	0.39
	1075	150	0.00051	±	0.00004	0.28389	±	0.00041	6.95E-13	72.4	84.9	17.26	±	0.34	0.24
	1075	300	0.00054	±	0.00002	0.27562	±	0.00057	7.17E-13	79.2	84.0	17.60	±	0.28	0.12
	1100	20	0.00038	±	0.00081	0.27629	±	0.00756	3.30E-14	79.6	88.6	18.51	±	5.03	5.02
	1100	40	0.00059	±	0.00076	0.26780	±	0.00209	8.93E-14	80.4	82.4	17.77	±	4.84	4.83
	1100	80	0.00060	±	0.00021	0.26402	±	0.00202	1.87E-13	82.2	82.1	17.94	±	1.36	1.34
	1100	120	0.00054	±	0.00009	0.26201	±	0.00128	2.36E-13	84.5	84.0	18.49	±	0.63	0.57
	1125	20	0.00055	±	0.00080	0.26050	±	0.00283	3.89E-14	84.9	83.7	18.53	±	5.19	5.18
	1125	40	0.00067	±	0.00018	0.25715	±	0.00287	1.05E-13	85.9	80.1	17.98	±	1.22	1.20
	1150	15	0.00043	±	0.00072	0.25669	±	0.00537	5.40E-14	86.4	87.3	19.61	±	4.78	4.77
	1175	15	0.00086	±	0.00021	0.25785	±	0.00288	1.63E-13	88.0	74.6	16.70	±	1.41	1.39
	1200	15	0.00067	±	0.00013	0.25872	±	0.00147	4.27E-13	92.1	80.1	17.88	±	0.89	0.85
	1225	15	0.00071	±	0.00008	0.25318	±	0.00105	4.13E-13	96.0	78.9	17.98	±	0.57	0.52
	1250	15	0.00063	±	0.00022	0.25391	±	0.00406	1.36E-13	97.3	81.3	18.48	±	1.52	1.50
	1300	15	0.00020	±	0.00043	0.25177	±	0.00524	5.17E-14	97.8	94.0	21.52	±	2.94	2.93
	1350	15	0.00063	±	0.00147	0.26470	±	0.00428	5.98E-14	98.4	81.3	17.73	±	9.43	9.43
	1550	10	0.00060	±	0.00025	0.25436	±	0.00281	1.67E-13	100	82.1	18.63	±	1.71	1.69
00KG24	400	28	0.00170	±	0.00010	0.01997	±	0.00008	5.61E-14	0.6	49.8	138.95	±	8.46	8.25
CLAIR 112, Layer 3	400	36	0.00175	±	0.00099	0.17381	±	0.00179	2.83E-14	0.9	48.3	16.05	±	9.72	9.71
J = 0.003211 ± 0.000045	450	28	0.00119	±	0.00046	0.23834	±	0.00216	5.14E-14	1.4	64.7	15.67	±	3.29	3.28
Weight = 0.0650 g	450	36	0.00123	±	0.00045	0.28564	±	0.00113	4.66E-14	1.9	63.5	12.85	±	2.67	2.67
	500	28	0.00073	±	0.00031	0.26569	±	0.00075	7.98E-14	2.8	78.2	16.99	±	1.98	1.97
	500	36	0.00103	±	0.00076	0.33566	±	0.00149	7.44E-14	3.6	69.3	11.94	±	3.85	3.84
	550	28	0.00063	±	0.00007	0.29312	±	0.00171	1.23E-13	4.8	81.2	16.00	±	0.49	0.44
	550	36	0.00028	±	0.00033	0.35601	±	0.00445	1.00E-13	5.9	91.7	14.88	±	1.58	1.56
	600	28	0.00137	±	0.00013	0.21158	±	0.00035	1.54E-13	7.5	59.5	16.23	±	1.10	1.08
	600	36	0.00008	±	0.00052	0.36517	±	0.00178	1.22E-13	8.8	97.6	15.45	±	2.44	2.43
	650	28	0.00056	±	0.00023	0.34424	±	0.00158	1.70E-13	10.6	83.3	13.99	±	1.18	1.16
	650	36	0.00003	±	0.00110	0.36842	±	0.00487	1.32E-13	12.0	98.9	15.51	±	5.07	5.07
	700	28	0.00029	±	0.00030	0.35033	±	0.00321	1.59E-13	13.7	91.2	15.04	±	1.47	1.46
	700	36	0.00015	±	0.00026	0.36820	±	0.00695	1.03E-13	14.8	95.4	14.98	±	1.26	1.24
	750	28	0.00034												

Chapter 4: Exhumational history of the Mustang and Mugu granites

1050	25	0.00025	±	0.00004	0.29303	±	0.00133	3.90E-13	35.8	92.5	18.22	±	0.37	0.27
1075	25	0.00033	±	0.00006	0.29808	±	0.00115	4.46E-13	40.6	90.2	17.47	±	0.43	0.35
1075	40	0.00027	±	0.00011	0.30205	±	0.00116	4.82E-13	45.6	92.0	17.58	±	0.68	0.63
1075	80	0.00022	±	0.00007	0.30092	±	0.00100	6.34E-13	52.3	93.4	17.92	±	0.46	0.39
1075	150	0.00022	±	0.00004	0.29567	±	0.00050	6.97E-13	59.7	93.3	18.21	±	0.33	0.22
1075	300	0.00031	±	0.00003	0.29049	±	0.00067	7.64E-13	67.7	90.8	18.05	±	0.31	0.19
1100	20	0.00005	±	0.00483	0.28944	±	0.00772	3.36E-14	68.1	98.4	19.62	±	28.26	28.26
1100	40	0.00017	±	0.00058	0.28733	±	0.00482	8.94E-14	69.0	94.7	19.03	±	3.43	3.42
1100	80	0.00023	±	0.00015	0.28585	±	0.00251	1.91E-13	71.0	93.1	18.79	±	0.94	0.90
1100	120	0.00030	±	0.00014	0.28570	±	0.00178	2.63E-13	73.8	91.0	18.38	±	0.90	0.86
1125	20	0.00034	±	0.00078	0.28470	±	0.00719	4.36E-14	74.3	89.8	18.20	±	4.66	4.66
1125	40	0.00039	±	0.00034	0.28375	±	0.00397	1.21E-13	75.5	88.4	17.99	±	2.09	2.08
1150	15	0.00002	±	0.00151	0.28202	±	0.00554	6.42E-14	76.2	99.2	20.29	±	9.10	9.09
1175	15	0.00029	±	0.00013	0.28541	±	0.00265	2.02E-13	78.3	91.2	18.44	±	0.86	0.82
1200	15	0.00030	±	0.00003	0.30271	±	0.00108	8.69E-13	87.5	91.1	17.38	±	0.31	0.19
1225	15	0.00014	±	0.00010	0.30123	±	0.00073	7.19E-13	95.1	95.8	18.35	±	0.62	0.56
1250	15	0.00030	±	0.00041	0.30004	±	0.00433	1.42E-13	96.6	91.0	17.51	±	2.34	2.32
1300	15	0.00015	±	0.00101	0.30091	±	0.00614	6.88E-14	97.3	95.4	18.30	±	5.72	5.71
1350	15	0.00039	±	0.00039	0.30829	±	0.00535	6.91E-14	98.0	88.5	16.57	±	2.20	2.19
1550	10	0.00035	±	0.00019	0.29647	±	0.00259	1.86E-13	100	89.5	17.42	±	1.15	1.13
00KG26														
400	28	0.00189	±	0.00042	0.00615	±	0.00007	1.21E-14	0.1	44.1	369.81	±	93.42	93.40
400	36	0.00299	±	0.00068	0.03192	±	0.00034	4.66E-15	0.1	11.7	20.77	±	35.63	35.63
450	28	0.00193	±	0.00026	0.03452	±	0.00021	1.45E-14	0.2	42.8	69.59	±	12.15	12.14
450	36	0.00413	±	0.00109	0.10482	±	0.00181	1.30E-14	0.3	-21.9	-11.99	±	17.68	17.68
500	28	0.00176	±	0.00030	0.05264	±	0.00042	3.98E-14	0.6	48.1	51.52	±	9.51	9.51
500	36	0.00152	±	0.00175	0.19215	±	0.00097	2.97E-14	0.8	55.1	16.34	±	15.22	15.22
550	28	0.00139	±	0.00028	0.10991	±	0.00049	6.87E-14	1.3	58.9	30.40	±	4.27	4.27
550	36	0.00156	±	0.00170	0.25065	±	0.00184	5.02E-14	1.7	53.8	12.25	±	11.37	11.37
600	28	0.00110	±	0.00028	0.17406	±	0.00027	1.07E-13	2.4	67.5	22.05	±	2.64	2.64
600	36	0.00095	±	0.00029	0.30404	±	0.00485	7.26E-14	2.9	71.7	13.46	±	1.64	1.63
650	28	0.00082	±	0.00015	0.22618	±	0.00166	1.55E-13	4.1	75.7	19.06	±	1.12	1.12
650	36	0.00037	±	0.00031	0.34026	±	0.00342	1.05E-13	4.8	89.0	14.92	±	1.56	1.56
700	28	0.00169	±	0.00020	0.16155	±	0.00096	1.74E-13	6.0	50.1	17.65	±	2.07	2.06
700	36	0.00036	±	0.00017	0.34407	±	0.00509	1.34E-13	7.0	89.3	14.81	±	0.88	0.88
750	28	0.00058	±	0.00018	0.28476	±	0.00206	2.57E-13	8.8	82.8	16.58	±	1.04	1.04
750	36	0.00026	±	0.00021	0.35478	±	0.00420	1.74E-13	10.1	92.1	14.80	±	1.00	1.00
780	28	0.00027	±	0.00060	0.34387	±	0.00562	1.19E-13	10.9	92.0	15.25	±	2.94	2.93
780	36	0.00026	±	0.00048	0.34329	±	0.00537	9.83E-14	11.6	92.0	15.29	±	2.36	2.36
810	28	0.00032	±	0.00028	0.31133	±	0.00466	9.41E-14	12.3	90.5	16.57	±	1.52	1.52
810	36	0.00017	±	0.00064	0.34468	±	0.00673	7.76E-14	12.9	94.9	15.71	±	3.15	3.15
840	28	0.00089	±	0.00084	0.30049	±	0.00460	8.54E-14	13.5	73.4	13.95	±	4.68	4.68
840	36	0.00040	±	0.00049	0.32929	±	0.00607	7.57E-14	14.0	88.1	15.26	±	2.53	2.53
Minimum ⁴⁰ Ar, Weighted Mean Spectrum Date and 2σ (Ma)											15.22	±	0.96	
880	25	0.00046	±	0.00036	0.29095	±	0.00497	8.47E-14	14.6	86.3	16.91	±	2.09	2.09
900	25	0.00014	±	0.00197	0.28271	±	0.00374	1.18E-13	15.5	95.9	19.31	±	11.68	11.67
940	25	0.00064	±	0.00011	0.27127	±	0.00347	1.99E-13	16.9	81.1	17.04	±	0.76	0.75
960	25	0.00066	±	0.00056	0.26834	±	0.00167	2.81E-13	18.9	80.3	17.05	±	3.47	3.47
980	25	0.00059	±	0.00002	0.26365	±	0.00123	3.68E-13	21.5	82.5	17.83	±	0.19	0.16
1000	25	0.00061	±	0.00019	0.25821	±	0.00088	5.24E-13	25.3	81.9	18.08	±	1.25	1.25
1025	25	0.00058	±	0.00004	0.25888	±	0.00042	6.71E-13	30.1	82.6	18.18	±	0.27	0.25
1050	25	0.00061	±	0.00008	0.26282	±	0.00033	8.69E-13	36.3	81.8	17.73	±	0.53	0.52
1080	25	0.00049	±	0.00004	0.27554	±	0.00035	7.02E-13	41.3	85.5	17.67	±	0.28	0.26
1075	25	0.00034	±	0.00025	0.28495	±	0.00042	6.19E-13	45.7	89.8	17.96	±	1.49	1.49
1075	40	0.00027	±	0.00005	0.29438	±	0.00080	6.42E-13	50.3	91.8	17.76	±	0.31	0.30
1075	80	0.00021	±	0.00007	0.29664	±	0.00048	6.00E-13	54.6	93.7	18.00	±	0.42	0.40
1075	150	0.00019	±	0.00007	0.28815	±	0.00041	6.98E-13	59.6	94.3	18.65	±	0.44	0.43
1075	300	0.00020	±	0.00005	0.27740	±	0.00037	8.21E-13	65.5	94.0	19.30	±	0.31	0.29
1100	20	0.00002	±	0.00259	0.26984	±	0.00545	5.52E-14	65.9	99.3	20.95	±	16.04	16.04
1100	40	0.00019	±	0.00029	0.26909	±	0.00456	1.15E-13	66.7	94.3	19.96	±	1.87	1.87
1100	80	0.00014	±	0.00040	0.26815	±	0.00254	2.07E-13	68.2	95.7	20.32	±	2.48	2.48
1100	120	0.00029	±	0.00023	0.26583	±	0.00172	2.67E-13	70.1	91.4	19.57	±	1.43	1.42
1125	20	0.00008	±	0.00061	0.26294	±	0.00540	5.24E-14	70.4	97.5	21.11	±	3.92	3.92
1125	40	0.00030	±	0.00034	0.26439	±	0.00393	1.38E-13	71.4	91.1	19.62	±	2.19	2.19
1150	15	0.00013	±	0.00033	0.26164	±	0.00471	7.06E-14	71.9	95.9	20.87	±	2.17	2.17
1175	15	0.00027	±	0.00015	0.25999	±	0.00327	1.56E-13	73.0	91.8	20.11	±	1.00	1.00
1200	15	0.00035	±	0.00012	0.25734	±	0.00083	3.91E-13	75.8	89.6	19.83	±	0.78	0.77
1225	15	0.00026	±	0.00005	0.25384	±	0.00030	6.86E-13	82.0	91.6	20.55	±	0.35	0.33
1250	15	0.00029	±	0.00002	0.26034	±	0.00036	1.23E-12	90.9	91.2	19.95	±	0.18	0.14
1300	15	0.00025	±	0.00001	0.26929	±	0.00033	6.66E-13	95.6	92.4	19.55	±	0.14	0.08
1350	15	0.00024	±	0.00010	0.27424	±	0.00195	2.34E-13	97.3	92.7	19.25	±	0.62	0.61
1550	10	0.00019	±	0.00016	0.27815	±	0.00087	3.77E-13	100	94.3	19.30	±	1.00	0.99
00KG29														
400	28	0.00208	±	0.00007	0.00297	±	0.00004	2.79E-14	0.2	38.7	632.46	±	30.10	29.95
400	36	0.00277	±	0.00035	0.03669	±	0.00005	1.13E-14	0.2	18.1	28.43	±	16.08	16.08
450	28	0.03114	±	0.18098	-0.00003	±	0.00001	-2.44E-20	0.2	844.8	12243.30	±	11741.30	11741.30
450	36	0.00162	±	0.00287	0.08181	±	0.00079	1.87E-14	0.3	52.0	36.63	±	59.19	59.19
550	28	0.00168	±	0.00016	0.04849	±	0.00036	2.54E-13	1.9	50.4	59.45	±	5.45	5.44
550	36	0.00153	±	0.00057	0.23145	±	0.00244	1.17E-13	2.6	54.7	13.72	±	4.24	4.24
600	28	0.00146	±	0.00013	0.18541	±	0.00195	2.66E-13	4.1	56.8	17.75	±	1.28	1.27
600	36	0.00096	±	0.00035	0.28805	±	0.00299	1.42E-13	5.0	71.4	14.39	±	2.06	2.06
650	28	0.00116	±	0.00003	0.18595	±	0.00122	3.99E-13	7.3	65.7	20.47	±	0.39	0.37
650	36	0.00085	±	0.00017	0.29998	±	0.00095	2.52E-13	8.8	74.6	14.44	±	0.99	0.99
700	28	0.00169	±	0.00006	0.17553	±	0.00032	2.56E-13	10.4	50.1	16.54	±	0.57	0.56
700	36	0.00049	±	0.00007	0.33265	±	0.00138	2.02E-13	11.6	85.4	14.90	±	0.38	0.37
750	28	0.00072	±	0.00005	0.25386	±	0.00064	3.64E-13	13.7	78.5	17.92	±	0.38	0.37
750	36	0.00041	±	0.00038	0.33507	±	0.00097	2.55E-13						

Chapter 4: Exhumational history of the Mustang and Mugu granites

	840	36	0.00084 ± 0.00022	0.28788 ± 0.00067	1.31E-13	19.5	75.0	15.12 ± 1.31	1.30	
	880	25	0.00127 ± 0.00049	0.23991 ± 0.00057	1.60E-13	20.4	62.4	15.10 ± 3.49	3.48	
	Minimum ⁴⁰ Ar, Weighted Mean Spectrum Date and 2σ± (Ma)								15.21 ± 0.96	
	900	25	0.00098 ± 0.00015	0.23402 ± 0.00071	2.06E-13	21.6	70.9	17.57 ± 1.11	1.10	
	940	25	0.00092 ± 0.00005	0.21715 ± 0.00040	4.78E-13	24.5	72.8	19.43 ± 0.43	0.41	
	960	25	0.00085 ± 0.00010	0.22006 ± 0.00035	5.06E-13	27.5	74.8	19.69 ± 0.75	0.74	
	980	25	0.00083 ± 0.00003	0.21464 ± 0.00049	6.22E-13	31.2	75.3	20.33 ± 0.29	0.27	
	1000	25	0.00073 ± 0.00017	0.21635 ± 0.00076	9.69E-13	36.9	78.4	20.99 ± 1.33	1.33	
	1025	25	0.00063 ± 0.00002	0.22913 ± 0.00099	1.34E-12	44.9	81.3	20.56 ± 0.24	0.21	
	1050	25	0.00049 ± 0.00005	0.24552 ± 0.00120	1.14E-12	51.7	85.5	20.17 ± 0.38	0.36	
	1060	25	0.00037 ± 0.00007	0.26433 ± 0.00119	7.16E-13	56.0	89.0	19.51 ± 0.49	0.47	
	1075	25	0.00034 ± 0.00011	0.26822 ± 0.00091	6.21E-13	59.7	89.8	19.40 ± 0.74	0.73	
	1075	40	0.00026 ± 0.00009	0.26591 ± 0.00125	6.72E-13	63.6	92.1	20.07 ± 0.62	0.61	
	1075	80	0.00035 ± 0.00002	0.26055 ± 0.00114	8.12E-13	68.5	89.5	19.90 ± 0.22	0.18	
	1075	150	0.00032 ± 0.00002	0.24480 ± 0.00094	8.82E-13	73.7	90.5	21.41 ± 0.22	0.19	
	1075	300	0.00035 ± 0.00004	0.23207 ± 0.00077	9.49E-13	79.4	89.5	22.32 ± 0.33	0.30	
	1100	20	0.00053 ± 0.00081	0.22316 ± 0.00110	6.38E-14	79.7	84.4	21.88 ± 6.16	6.16	
	1100	40	0.00036 ± 0.00013	0.22239 ± 0.00055	1.51E-13	80.6	89.3	23.24 ± 0.99	0.98	
	1100	80	0.00047 ± 0.00007	0.22018 ± 0.00085	2.76E-13	82.3	86.0	22.60 ± 0.57	0.55	
	1100	120	0.00030 ± 0.00032	0.22050 ± 0.00024	3.29E-13	84.2	91.0	23.86 ± 2.50	2.50	
	1125	20	0.00036 ± 0.00022	0.21503 ± 0.00066	5.90E-14	84.6	89.4	24.05 ± 1.76	1.76	
	1125	40	0.00042 ± 0.00016	0.21371 ± 0.00042	1.49E-13	85.5	87.5	23.69 ± 1.26	1.25	
	1150	15	0.00053 ± 0.00057	0.20790 ± 0.00220	8.14E-14	85.9	84.3	23.45 ± 4.69	4.69	
	1175	15	0.00046 ± 0.00015	0.20243 ± 0.00089	2.60E-13	87.5	86.3	24.67 ± 1.26	1.25	
	1200	15	0.00046 ± 0.00003	0.21440 ± 0.00028	6.76E-13	91.5	86.4	23.33 ± 0.26	0.23	
	1225	15	0.00047 ± 0.00005	0.22243 ± 0.00024	5.50E-13	94.8	86.1	22.40 ± 0.42	0.40	
	1250	15	0.00042 ± 0.00007	0.22558 ± 0.00042	2.68E-13	96.4	87.4	22.42 ± 0.52	0.50	
	1300	15	0.00060 ± 0.00025	0.23566 ± 0.00047	2.09E-13	97.6	82.2	20.19 ± 1.80	1.79	
	1350	15	0.00042 ± 0.00036	0.23233 ± 0.00120	1.33E-13	98.4	87.4	21.77 ± 2.67	2.67	
	1550	10	0.00052 ± 0.00017	0.20257 ± 0.00051	2.71E-13	100	84.6	24.16 ± 1.45	1.44	
	00KG30									
	400	28	0.00126 ± 0.00001	0.00531 ± 0.00001	1.74E-14	0.1	62.7	573.38 ± 4.53	3.58	
	400	36	0.00302 ± 0.00348	0.10366 ± 0.00439	1.05E-14	0.2	10.8	5.93 ± 56.53	56.53	
	450	28	0.00165 ± 0.00068	0.06927 ± 0.00149	1.56E-14	0.3	51.2	41.78 ± 16.28	16.28	
	450	36	0.00320 ± 0.00225	0.18455 ± 0.00525	1.22E-14	0.4	5.3	1.65 ± 20.59	20.59	
	500	28	0.00125 ± 0.00019	0.05424 ± 0.00086	4.24E-14	0.7	63.0	65.27 ± 5.98	5.97	
	500	36	0.00138 ± 0.00136	0.27352 ± 0.01133	2.35E-14	0.8	8.9	12.37 ± 8.37	8.37	
	550	28	0.00117 ± 0.00030	0.09083 ± 0.00145	7.22E-14	1.3	65.3	40.68 ± 5.55	5.54	
	550	36	0.00098 ± 0.00070	0.31383 ± 0.01068	4.57E-14	1.7	70.9	12.89 ± 3.80	3.80	
	600	28	0.00078 ± 0.00088	0.17067 ± 0.00167	1.32E-13	2.6	76.9	25.60 ± 8.58	8.58	
	600	36	0.00073 ± 0.00095	0.34532 ± 0.00416	1.06E-13	3.3	78.3	12.94 ± 4.60	4.60	
	650	28	0.00102 ± 0.00017	0.22754 ± 0.00519	1.85E-13	4.6	69.9	17.51 ± 1.40	1.39	
	650	36	0.00056 ± 0.00102	0.31097 ± 0.00476	1.31E-13	5.5	83.4	15.30 ± 5.51	5.51	
	700	28	0.00080 ± 0.00019	0.26754 ± 0.00682	2.18E-13	7.0	76.1	16.22 ± 1.28	1.28	
	700	36	0.00032 ± 0.00035	0.36317 ± 0.00629	1.91E-13	8.3	90.4	14.20 ± 1.62	1.62	
	750	28	0.00049 ± 0.00027	0.31181 ± 0.00598	2.60E-13	10.1	85.5	15.63 ± 1.51	1.51	
	750	36	0.00017 ± 0.00025	0.35237 ± 0.00448	1.41E-13	11.1	94.7	15.33 ± 1.23	1.23	
	780	28	0.00037 ± 0.00055	0.34295 ± 0.00516	7.98E-14	11.6	88.9	14.79 ± 2.72	2.72	
	780	36	0.00030 ± 0.00058	0.33617 ± 0.00466	7.05E-14	12.1	90.9	15.42 ± 2.90	2.90	
	810	28	0.00009 ± 0.00043	0.32905 ± 0.00254	6.14E-14	12.5	97.2	16.85 ± 2.17	2.17	
	810	36	0.00052 ± 0.00238	0.31914 ± 0.00143	5.74E-14	12.9	84.6	15.12 ± 12.50	12.50	
	840	25	0.00079 ± 0.00091	0.31019 ± 0.00087	6.53E-14	13.4	76.5	14.07 ± 4.90	4.89	
	Minimum ⁴⁰ Ar, Weighted Mean Spectrum Date and 2σ± (Ma)								15.34 ± 0.99	
	880	25	0.00024 ± 0.00151	0.28940 ± 0.00101	1.39E-13	14.3	92.8	18.27 ± 8.74	8.74	
	920	25	0.00028 ± 0.00048	0.27966 ± 0.00119	2.12E-13	15.8	91.6	18.66 ± 2.89	2.89	
	960	25	0.00045 ± 0.00009	0.25660 ± 0.00041	4.43E-13	18.9	86.7	19.24 ± 0.60	0.59	
	1000	25	0.00042 ± 0.00007	0.25351 ± 0.00060	9.30E-13	25.3	87.3	19.62 ± 0.47	0.46	
	1020	25	0.00048 ± 0.00010	0.24747 ± 0.00032	8.12E-13	30.9	85.6	19.69 ± 0.66	0.65	
	1050	25	0.00047 ± 0.00003	0.25422 ± 0.00042	1.05E-12	38.1	85.9	19.25 ± 0.22	0.19	
	1060	25	0.00038 ± 0.00004	0.27396 ± 0.00047	8.05E-13	43.7	88.7	18.44 ± 0.26	0.26	
	1075	25	0.00033 ± 0.00005	0.27792 ± 0.00037	7.77E-13	49.1	90.0	18.45 ± 0.35	0.33	
	1075	40	0.00030 ± 0.00008	0.28332 ± 0.00063	7.81E-13	54.5	91.0	18.30 ± 0.46	0.45	
	1075	80	0.00023 ± 0.00003	0.27633 ± 0.00148	9.50E-13	61.0	93.1	19.18 ± 0.22	0.19	
	1075	150	0.00023 ± 0.00001	0.26514 ± 0.00144	8.88E-13	67.2	93.1	20.00 ± 0.17	0.12	
	1075	300	0.00023 ± 0.00003	0.25094 ± 0.00177	9.76E-13	73.9	93.2	21.13 ± 0.27	0.25	
	1100	20	0.00021 ± 0.00028	0.24432 ± 0.00173	7.17E-14	74.4	93.8	21.86 ± 1.92	1.91	
	1100	40	0.00012 ± 0.00022	0.24816 ± 0.00123	1.90E-13	75.7	96.3	22.08 ± 1.48	1.47	
	1100	80	0.00014 ± 0.00034	0.24912 ± 0.00176	3.59E-13	78.2	95.6	21.85 ± 2.30	2.30	
	1100	120	0.00021 ± 0.00007	0.24921 ± 0.00146	4.25E-13	81.1	93.7	21.41 ± 0.48	0.46	
	1125	20	0.00018 ± 0.00043	0.24466 ± 0.00147	8.36E-14	81.7	94.7	22.02 ± 2.91	2.90	
	1125	40	0.00023 ± 0.00012	0.24786 ± 0.00072	2.58E-13	83.5	93.0	21.35 ± 0.79	0.78	
	1150	15	0.00022 ± 0.00036	0.24497 ± 0.00042	1.62E-13	84.6	93.4	21.69 ± 2.46	2.46	
	1175	15	0.00018 ± 0.00012	0.23780 ± 0.00033	4.21E-13	87.5	94.6	22.63 ± 0.84	0.83	
	1200	15	0.00014 ± 0.00006	0.23686 ± 0.00078	7.27E-13	92.5	95.6	22.96 ± 0.60	0.58	
	1225	15	0.00021 ± 0.00017	0.24275 ± 0.00037	5.12E-13	96.1	93.7	21.96 ± 1.17	1.16	
	1250	15	0.00005 ± 0.00022	0.25483 ± 0.00053	1.68E-13	97.2	98.3	21.94 ± 1.42	1.42	
	1300	15	0.00017 ± 0.00045	0.26121 ± 0.00162	1.05E-13	98.0	94.9	20.68 ± 2.88	2.88	
	1350	15	0.00010 ± 0.00013	0.24965 ± 0.00083	2.49E-13	99.7	96.9	22.09 ± 0.86	0.86	
	1550	10	0.00041 ± 0.00061	0.19488 ± 0.00080	4.78E-14	100	87.7	25.58 ± 5.19	5.19	
	00KG32									
	400	28	0.00132 ± 0.00005	0.01949 ± 0.00006	6.10E-14	0.5	60.8	172.36 ± 4.60	3.98	
	400	36	0.00092 ± 0.00157	0.19330 ± 0.00264	3.15E-14	0.8	72.7	21.68 ± 13.74	13.74	
	450	28	0.00078 ± 0.00031	0.20844 ± 0.00166	5.54E-14	1.2	76.9	21.28 ± 2.51	2.49	
	450	36	0.00061 ± 0.00048	0.28526 ± 0.00063	4.31E-14	1.6	81.8	16.55 ± 2.84	2.83	
	500	28	0.00064 ± 0.00026	0.18319 ± 0.00029	9.20E-14	2.4	81.0	25.47 ± 2.45	2.43	
	500	36	0.00030 ± 0.00055	0.30573 ± 0.00375	7.93E-14	3.1	90.9	17.16 ± 3.05	3.04	
	550	28	0.00075 ± 0.00030	0.22789 ± 0.00131	1.34E-13	4.2	77.7	19.66 ± 2.24	2.23	
	550	36	0.00021 ± 0.00027	0.33637 ± 0.00495	1.02E-13	5.1	93.5	16.06 ± 1.42	1.40	
	600	28	0.00104 ± 0.00011	0.21550 ± 0.00188	1.29E-13	6.2	69.3	18.55 ± 0.90	0.87	
	600	36	0.00040 ± 0.00050	0.34785 ± 0.00370	1.16E-13	7.1	88.2	14.66 ± 2.45	2.44	

Table 5 <continued>

Chapter 4: Exhumational history of the Mustang and Mugu granites

650	28	0 00073 ±	0 00030	0 31094 ±	0 00267	1 71E-13	8 6	78 3	14 56 ±	1 66	1 64
Minimum ⁴⁰ Ar _r Weighted Mean Spectrum Date and 2σ ^{†††} (Ma)										14 60 ±	1 40
650	36	0 00007 ±	0 00053	0 35505 ±	0 00462	1 21E-13	9 6	97 7	15 91 ±	2 54	2 53
700	28	0 00042 ±	0 00024	0 32005 ±	0 00285	1 32E-13	10 7	87 3	15 76 ±	1 30	1 28
700	36	0 00018 ±	0 00042	0 34458 ±	0 00428	8 08E-14	11 4	94 5	15 84 ±	2 08	2 07
750	28	0 00037 ±	0 00119	0 31625 ±	0 00357	8 23E-14	12 1	89 1	16 27 ±	6 37	6 36
750	36	0 00018 ±	0 00080	0 34427 ±	0 00500	5 99E-14	12 6	94 4	15 84 ±	3 97	3 96
780	28	0 00012 ±	0 00252	0 32706 ±	0 00717	5 44E-14	13 1	96 4	17 02 ±	13 06	13 06
780	36	0 00012 ±	0 00041	0 33390 ±	0 00606	5 40E-14	13 5	96 3	16 65 ±	2 14	2 12
810	28	0 00024 ±	0 00067	0 30408 ±	0 00551	5 59E-14	14 0	92 7	17 60 ±	3 78	3 77
810	36	0 00041 ±	0 00070	0 31249 ±	0 00611	6 07E-14	14 5	87 9	16 24 ±	3 80	3 79
840	28	0 00009 ±	0 00107	0 28016 ±	0 00612	6 77E-14	15 1	97 3	20 04 ±	6 51	6 50
840	36	0 00047 ±	0 00038	0 28548 ±	0 00598	7 86E-14	15 7	85 8	17 36 ±	2 30	2 29
880	25	0 00061 ±	0 00032	0 26239 ±	0 00405	1 05E-13	16 6	82 0	18 04 ±	2 11	2 09
900	25	0 00048 ±	0 00014	0 26423 ±	0 00313	1 33E-13	17 8	85 8	18 73 ±	0 95	0 92
960	25	0 00060 ±	0 00010	0 25424 ±	0 00173	4 04E-13	21 2	82 2	18 66 ±	0 75	0 70
980	25	0 00055 ±	0 00010	0 25922 ±	0 00104	4 36E-13	24 9	83 5	18 59 ±	0 72	0 67
1000	25	0 00052 ±	0 00005	0 26791 ±	0 00101	5 32E-13	29 4	84 4	18 19 ±	0 41	0 32
1025	25	0 00047 ±	0 00003	0 27895 ±	0 00126	6 44E-13	34 8	86 1	17 82 ±	0 31	0 19
1050	25	0 00042 ±	0 00005	0 28804 ±	0 00100	6 69E-13	40 5	87 6	17 56 ±	0 41	0 33
1075	25	0 00029 ±	0 00004	0 29076 ±	0 00079	7 19E-13	46 5	91 4	18 15 ±	0 34	0 23
1075	40	0 00022 ±	0 00008	0 29103 ±	0 00056	7 77E-13	53 1	93 5	18 54 ±	0 52	0 45
1075	80	0 00017 ±	0 00003	0 28607 ±	0 00046	1 00E-12	61 6	94 9	19 15 ±	0 31	0 16
1075	150	0 00024 ±	0 00004	0 27830 ±	0 00038	1 06E-12	70 6	92 8	19 23 ±	0 35	0 23
1075	300	0 00023 ±	0 00003	0 27017 ±	0 00037	1 04E-12	79 4	92 9	19 85 ±	0 33	0 19
1100	40	0 00025 ±	0 00037	0 26446 ±	0 00400	1 17E-13	80 4	92 5	20 18 ±	2 43	2 41
1100	80	0 00017 ±	0 00005	0 26406 ±	0 00163	2 56E-13	82 5	94 8	20 71 ±	0 44	0 34
1100	120	0 00019 ±	0 00015	0 26474 ±	0 00180	3 25E-13	85 3	94 4	20 57 ±	0 99	0 95
1125	20	0 00014 ±	0 00085	0 26347 ±	0 00539	5 58E-14	85 8	95 6	20 93 ±	5 48	5 48
1125	40	0 00021 ±	0 00011	0 26131 ±	0 00263	1 57E-13	87 1	93 6	20 66 ±	0 82	0 77
1150	15	0 00016 ±	0 00033	0 25869 ±	0 00591	8 14E-14	87 8	95 1	21 20 ±	2 26	2 24
1175	15	0 00026 ±	0 00020	0 25314 ±	0 00167	2 35E-13	89 8	92 3	21 03 ±	1 39	1 36
1200	15	0 00023 ±	0 00009	0 26465 ±	0 00079	5 28E-13	94 2	93 1	20 30 ±	0 62	0 55
1225	15	0 00022 ±	0 00012	0 26911 ±	0 00131	3 43E-13	97 1	93 5	20 05 ±	0 84	0 79
1250	15	0 00045 ±	0 00128	0 25719 ±	0 00426	8 58E-14	97 9	86 5	19 40 ±	8 42	8 41
1300	15	0 00058 ±	0 00098	0 25123 ±	0 00617	4 96E-14	98 3	82 8	19 01 ±	6 63	6 62
1350	15	0 00010 ±	0 00067	0 25623 ±	0 00501	4 95E-14	98 7	96 8	21 78 ±	4 47	4 46
1550	10	0 00025 ±	0 00010	0 26173 ±	0 00251	1 54E-13	100	92 6	20 41 ±	0 76	0 71

Note Sample preparation, irradiation, and flux monitor procedures are described in the text and follow the procedures outlined by Hodges *et al.* (1994). Ar isotopic determinations were conducted at the MIT CLAIR facility. Data are for step heating experiments conducted in a double vacuum resistance furnace. A Faraday detector was used. Mass discrimination results in a (⁴⁰Ar/³⁹Ar) of 293 for atmospheric argon measured with the Faraday detector. Operational blanks vary with time and temperature and were usually measured after every other unknown. Typical blanks (n moles) at M/e 40, 39, 38, 37 and 36, respectively, were as follows (800 K) 2e-14, 7e-17, 5e-17, 2e-17, 8e-17, (1500 K) 2e-14, 4e-17, 4e-17, 3e-17, 1e-16, (1800 K) < 3e-14, 8e-17, 4e-17, 1e-16, 3e-17. Uncertainties quoted at the 2σ (95%) confidence level. Asterisk designates radiogenic component.

† This column lists the sample number, irradiation package number and layer, J value (± 2σ uncertainty), and weight (in g)

§ Temperature of release increment (± 5 K) as monitored by W-Re thermocouple

Heating time Does not include additional 10 minutes of getting before gas is analyzed during which time the sample re-equilibrates to the furnace stand-by temperature (250° C)

‡ Number of moles of K-derived ⁴⁰Ar released during each heating increment. Calculated from measured signal size and instrumental sensitivity as calibrated against air aliquots of known volume

§§ Cumulative percent of K-derived ⁴⁰Ar after each increment

Percentage of the total ⁴⁰Ar in each heating increment that is radiogenic

††† Incremental model dates calculated by assuming (⁴⁰Ar/³⁹Ar) = 295.5

§§§ Includes propagated uncertainty in irradiation parameter J

Excludes uncertainty in irradiation parameter J. Indicates contribution of analytical error to the overall uncertainty

‡‡ Minimum spectrum date (MSD) ⁴⁰Ar_r weighted mean date calculated by summing the product of the increment date and moles ⁴⁰Ar_r released for each step and normalizing by the total moles of ⁴⁰Ar_r released. Shown with propagated 2σ uncertainty including uncertainty in J. Steps chosen by inspection of the release spectra and identification of "saddles" in the spectra (Figure 17)

Table 5 <continued>

Chapter 4: Exhumational history of the Mustang and Mugu granites

TABLE 6. SUMMARY OF BIOTITE AND MUSCOVITE ⁴⁰Ar/³⁹Ar STEP HEATING RESULTS FROM THE UPPER MUSTANG REGION, CENTRAL NEPAL

Sample	Mineral	Description†	Location§			Plateau#			Inverse Isochron ‡			MSWD	Average Grain Half-Size¶ (µm)	Average Composition # (X _m)	Grainsize Dependent Closure T ^{***} (°C)	Grainsize Independent Closure T ^{§§§} (°C)
			Latitude (°N, WGS-84)	Longitude (°E, WGS-84)	Altitude (m)	Date (Ma)	2σ (Ma)	³⁹ Ar (%)	Date (Ma)	2σ (Ma)	³⁹ Ar (%Ar/ ³⁹ Ar)					
<i>Lumpa Khola</i>																
98KG19	Biotite	TSS in DF fw	28° 53' 656"	083° 46' 133"	2918	17.62 ± 0.45	79.5	17.89 ± 1.07	79.5	287.46 ± 98.43	1.18	268	0.77	401	380	
98KG20	Biotite	TSS in DF fw	28° 53' 656"	083° 46' 133"	2918	17.22 ± 0.22	89.3	16.65 ± 0.79	89.8	455.65 ± 158.50	1.09	335	0.77	408	380	
<i>Tsarang Khola</i>																
00KG06	Muscovite	Mugu, sill xc LMG	29° 08' 504"	083° 53' 285"	-	17.30 ± 0.20	100.0	17.23 ± 0.25	100.0	299.55 ± 8.32	1.17	630	-	429	373	
00KG08	Muscovite	Mugu, sill xc LMG	29° 08' 520"	083° 53' 257"	-	17.07 ± 0.23	100.0	17.00 ± 0.25	100.0	298.31 ± 3.51	1.11	945	-	446	373	
00KG12	Muscovite	Mugu, sill xc LMG	29° 07' 836"	083° 53' 142"	-	17.85 ± 0.12	90.1	17.98 ± 0.14	100.0	274.57 ± 8.00	1.19	1103	-	453	373	
00KG14	Muscovite	Mugu, sill xc LMG	29° 07' 851"	083° 53' 118"	-	17.23 ± 0.21	100.0	17.28 ± 0.23	100.0	290.72 ± 6.48	1.09	630	-	429	373	
00KG16	Muscovite	Mugu, main part of pluton	29° 08' 149"	083° 52' 953"	-	17.82 ± 0.25	100.0	17.78 ± 0.27	100.0	301.14 ± 12.08	1.38	788	-	438	373	
00KG08	Biotite	Mugu, sill xc LMG	29° 08' 520"	083° 53' 257"	-	17.61 ± 0.29	100.0	17.74 ± 0.32	100.0	288.90 ± 5.93	1.43	394	0.83	431	400	
00KG09	Biotite	Mugu, sill xc LMG	29° 08' 735"	083° 52' 954"	-	16.68 ± 0.24	96.1	16.77 ± 0.36	96.1	288.16 ± 15.04	1.48	394	0.77	411	380	
00KG10	Biotite	LMG xc by 00KG09	29° 08' 735"	083° 52' 954"	-	17.38 ± 0.36	100.0	17.33 ± 0.40	100.0	303.01 ± 21.18	0.84	158	0.77	382	380	
00KG13	Biotite	LMG xc by 00KG12	29° 07' 836"	083° 53' 142"	-	17.82 ± 0.52	97.9	17.39 ± 0.76	97.9	335.12 ± 43.08	1.51	236	0.77	397	383	
00KG19	Biotite	LMG xc by 00KG16 & 20	29° 08' 149"	083° 52' 953"	-	17.42 ± 0.21	100.0	17.48 ± 0.24	100.0	289.73 ± 6.55	1.32	315	0.77	406	383	
00KG20	Biotite	Mugu, dike xc LMG	29° 08' 149"	083° 52' 953"	-	17.07 ± 0.20	98.5	17.12 ± 0.22	98.5	289.44 ± 4.46	0.86	238	0.70	374	361	
17.11 ± 0.84								87.7	291.33 ± 247.00	0.85						
<i>Thinker Village</i>																
00KG23	Muscovite	Mugu, granite	29° 13' 870"	083° 52' 945"	4425	17.67 ± 0.28	97.0	17.99 ± 0.36	99.7	285.39 ± 4.60	0.99	1103	-	453	373	
00KG24	Muscovite	Mugu, granite	29° 13' 870"	083° 52' 945"	4425	17.66 ± 0.18	100.0	17.73 ± 0.28	100.0	290.95 ± 7.93	1.79	788	-	438	373	
00KG25	Muscovite	D., def Mustang granite	29° 13' 890"	083° 52' 888"	4436	17.40 ± 0.18	100.0	17.52 ± 0.21	100.0	282.02 ± 11.22	1.1	473	-	417	373	
00KG28	Muscovite	D., def Mustang granite	29° 13' 979"	083° 52' 751"	4516	17.38 ± 0.16	100.0	17.38 ± 0.21	100.0	293.83 ± 7.05	1.18	551	-	423	373	
00KG30	Muscovite	D., def Mustang granite	29° 14' 065"	083° 52' 641"	4567	18.09 ± 0.21	100.0	18.21 ± 0.25	100.0	282.16 ± 15.48	1.46	630	-	429	373	
00KG31	Muscovite	Mugu, dike xc 00KG30	29° 14' 065"	083° 52' 641"	4567	17.40 ± 0.26	100.0	17.50 ± 0.32	100.0	282.70 ± 12.87	0.37	551	-	423	373	
00KG32	Muscovite	D., def Mustang granite	29° 14' 060"	083° 52' 659"	4620	18.31 ± 0.25	100.0	18.38 ± 0.30	100.0	286.56 ± 22.29	0.92	551	-	423	373	
00KG24	Biotite	Mugu, granite	29° 13' 870"	083° 52' 945"	4425	17.77 ± 0.24	97.6	17.88 ± 0.27	100.0	271.72 ± 15.16	1.72	473	0.77	417	380	
00KG25	Biotite	D., def Mustang granite	29° 13' 890"	083° 52' 888"	4436	18.08 ± 0.38	100.0	18.54 ± 0.45	100.0	270.64 ± 13.65	0.28	315	0.80	415	391	
00KG26	Biotite	D., def Mustang granite	29° 13' 911"	083° 52' 827"	4452	17.23 ± 0.13	100.0	17.32 ± 0.19	100.0	287.29 ± 6.03	0.93	394	0.73	399	369	
00KG28	Biotite	D., def Mustang granite	29° 13' 979"	083° 52' 751"	4516	17.67 ± 0.16	95.5	17.62 ± 0.18	99.6	304.36 ± 4.25	1.5	512	0.74	412	373	
00KG30	Biotite	D., def Mustang granite	29° 14' 065"	083° 52' 641"	4567	17.45 ± 0.17	100.0	17.45 ± 0.21	100.0	290.01 ± 16.80	1.55	394	0.76	408	378	
00KG31	Biotite	Mugu, dike xc 00KG30	29° 14' 065"	083° 52' 641"	4567	17.97 ± 0.26	95.3	18.11 ± 0.26	100.0	283.46 ± 10.30	1.12	394	0.77	411	380	
00KG32	Biotite	D., def Mustang granite	29° 14' 060"	083° 52' 659"	4620	17.43 ± 0.11	100.0	17.47 ± 0.15	100.0	284.61 ± 13.03	0.48	630	0.76	424	378	

Note: Double vacuum resistance furnace step heating experiments. Sample preparation, irradiation, and flux monitor procedures are described in the text and follow the procedures outlined by Hodges *et al.* (1994). Sample analysis and data reduction procedures are described in the text. Complete step-heating data is given in Table 4. All uncertainties quoted at the 2σ (95%) confidence level. Age uncertainties include uncertainty in irradiation parameter J (Table 3). Boldface indicates preferred ages.

† See text for lithologic descriptions and details of the D-, D₁/Mugu-Mugu, deformational/intrusive sequence (Fig. 6). Abbreviations: def = deformed, unde = undeformed, xc = crosscutting or crosscut, TSS = Tibetan Sedimentary Sequence, LMG = Lo Manthang grass, fw = footwall, DF = Dangdzong Fault.

‡ Location determined with a handheld GPS receiver with ca. 7-15 m horizontal precision. Note that these measurements were made after Selective Availability was deactivated in May, 2000. Altitude measured with an electronic barometric altimeter with ca. ±10 m precision. A differential technique was used with the Kal Gandaki River at Kagbeni village (Fig. 2) as the datum (2773 m above mean sea level).

Plateau dates are defined as three or more consecutive heating increments, constituting at least 50% of the total ³⁹Ar, for the sample, with individual increment model ages (Table 4) overlapping their combined ³⁹Ar, weighted mean date at the 2σ (95% confidence) level. Plateau dates are dependent on the assumption that the initial ratio of ⁴⁰Ar to ³⁹Ar is that of modern atmosphere (i.e. ⁴⁰Ar/³⁹Ar = 295.5 (McDougall and Harrison 1999)). See Fig. 14 for included increments.

‡ Inverse isochron dates are calculated from linear fits to the isotopic data (Table 4) as plotted on (³⁹Ar/³⁹Ar) vs. (⁴⁰Ar/³⁹Ar) isotope correlation diagrams (see Fig. 15 for included increments) (Roddick *et al.*, 1980). The linear regression techniques of York (1969) were used. The date thus calculated is directly related to the abscissa intercept, and (⁴⁰Ar/³⁹Ar) is calculated from the ordinal intercept. The latter is used to evaluate the plateau date assumption that (⁴⁰Ar/³⁹Ar) = 295.5. MSWD (mean square of weighted deviates) is a measure of the goodness-of-fit. MSWD = 1 for a perfect fit (Wendt and Carl, 1991). Samples with multiple inverse isochron results serve to illustrate the insensitivity of the inverse isochron date to (⁴⁰Ar/³⁹Ar) in cases where the data distribution precludes reliable determination of (⁴⁰Ar/³⁹Ar) e.g. calculated (⁴⁰Ar/³⁹Ar) < 295.5 (Fig. 15, see text for details).

§§ Calculated by taking the arithmetic mean of > 20 grain radius measurements per sample. For each sample, the grains measured are not the same as those irradiated and used in isotopic analyses, but they comprise a representative aliquot taken from the same mineral separate. Radii measured under magnification using an optical picking microscope with calibrated eyepiece reticule.

Only biotite compositions were measured. Mole fraction anorthite (X_{an}) compositions determined using wavelength-dispersive electron microprobe analysis. X_{an} values for samples not analyzed with the electron microprobe – but whose X_{an} is estimated from the mean of similar samples that were analyzed – are italicized.

††† Calculated from the equations in Dodson (1973) as implemented in MacArgon 5.10 (Lister and Baldwin, 1996). We assume a nominal cooling rate of 45 °C between ca. 20 Ma and ca. 17.5 Ma (see text). We use our average grain half-sizes as the effective diffusion dimension for both micas (Hames and Bowring, 1994; Hodges *et al.*, 1994; Hodges and Bowring 1995). For biotites, we also account for compositional dependence (Harrison *et al.*, 1985; Grove and Harrison, 1996). Diffusion parameters are given in Tables 8a and 8b. An infinite cylinder geometry is assumed for both micas (Hames and Bowring, 1994; Harrison *et al.*, 1995).

§§§ Calculated from the equations in Dodson (1973) as implemented in MacArgon 5.10 (Lister and Baldwin, 1996), assuming a sub-grain diffusion domain of 150 µm for both micas (Harrison *et al.*, 1985; McDougall and Harrison, 1999). We assume a nominal cooling rate of 45 °C between ca. 20 Ma and ca. 17.5 Ma (see text). For biotites, we also account for compositional dependence (Harrison *et al.*, 1985; Grove and Harrison, 1996). Diffusion parameters are given in Tables 8a and 8b. An infinite cylinder geometry is assumed for both micas (Hames and Bowring, 1994; Harrison *et al.*, 1995).

Table 6

TABLE 7 SUMMARY OF K-FELDSPAR ⁴⁰Ar/³⁹Ar STEP HEATING RESULTS FROM THE UPPER MUSTANG REGION, CENTRAL NEPAL

Sample	Description†	Location§			Minimum Spectrum Date (MSD)#				Minimum Isochron Date (MID)‡					LRD Arrhenius Parameters§§				
		Latitude (°N, WGS-84)	Longitude (°E, WGS-84)	Altitude (m)	Age ± 2σ (Ma)	2σ (Ma)	³⁹ Ar (%)	Steps	Age ± 2σ (Ma)	2σ (Ma)	³⁹ Ar (%)	(⁴⁰ Ar/ ³⁹ Ar), ± 2σ	MSWD	Steps	³⁹ Ar (%)	E _a (kcal/mol)	D ₀ /r ² (s ⁻¹)	T _c (°C)
<i>Tsarang Khola</i>																		
00KG08	D3 def Mugu dike xc TSS	29° 08 520'	083° 53 257'	-	15.29 ± 0.95	14.5	2-1-4	20.63 ± 0.50	81.9	495.51 ± 163.58	1.10	15-41,43-45	11.4	1-11	21.8	2.93E-01	96	
								15.35 ± 0.84	14.5	340.16 ± 32.61	1.26	2-14						
00KG12	D1 def Mugu dike xc TSS	29° 07 836'	083° 53 142'	-	15.51 ± 0.51	7.6	16-24	19.94 ± 0.77	52.9	421.14 ± 62.46	1.15	25,26,30-45,47-50	6.1	4-11	29.6	9.24E+00	172	
								13.62 ± 0.75	19.0	374.11 ± 7.24	1.23	1-4,7,9-24						
<i>Thinker Village</i>																		
00KG23	Mugu granite	29° 13 870'	083° 52 945'	4425	15.53 ± 1.09	10.2	10-17	17.04 ± 0.36	81.4	296.26 ± 16.69	1.44	2,4-9,11,13-16,18-33,35-37,39,41-44,47	11.0	1-11	22.4	3.81E-04	103	
00KG24	Mugu granite	29° 13 870'	083° 52 945'	4425	15.19 ± 0.79	20.4	2-23	17.13 ± 1.47	69.9	465.43 ± 245.01	1.57	24-42,44-48	10.6	1-11	23.1	5.63E-01	109	
								12.88 ± 0.75	19.4	555.26 ± 33.54	1.10	1-8,10-23						
00KG26	D3 def Mustang granite	29° 13 911'	083° 52 827'	4452	15.22 ± 0.96	5.2	16-22	16.87 ± 0.25	29.6	797.40 ± 365.57	0.54	42-50	2.3	3-9	37.1	3.14E+02	231	
								17.63 ± 0.42	42.2	316.07 ± 36.51	1.73	23-34,37,38,41						
								13.98 ± 0.80	12.7	490.32 ± 38.76	1.45	1-3,5-12,14-22						
00KG29	undef Mugu dike xc Mustang	29° 13 979'	083° 52 751'	4516	15.21 ± 0.96	6.7	14-21	18.49 ± 1.20	31.5	684.95 ± 120.08	0.94	33-48	8.6	4-10	40.0	3.96E+03	236	
								19.52 ± 0.33	41.4	346.10 ± 22.58	1.96	25-32,35						
								14.51 ± 0.42	14.2	333.00 ± 14.33	0.65	2-4,6-8,10-12,14-21						
00KG30	D3 def Mustang granite	29° 14 065'	083° 52 641'	4567	15.34 ± 0.99	8.8	12-21	19.14 ± 0.43	35.4	778.85 ± 8.40	1.21	1,22,23,33-47	9.8	3-15	32.6	1.91E+01	206	
								10.97 ± 1.55	12.1	784.06 ± 8.54	1.40	1-10,12-21						
00KG32	D3 def Mustang granite	29° 14 060'	083° 52 659'	4620	14.60 ± 1.40	2.4	10-11	19.14 ± 0.33	37.6	288.60 ± 29.17	1.39	2,3,6,7,9,15-26,32,33,35,38,44-46	8.6	1-11	22.1	2.09E-01	105	

Note Double vacuum resistance furnace step heating experiments Sample preparation, irradiation, and flux monitor procedures are described in the text and follow the procedures outlined by Hodges *et al.* (1994) Sample analysis and data reduction procedures are described in the text Complete step-heating data is given in Table 5 All uncertainties quoted at the 2σ (95%) confidence level Age uncertainties include uncertainty in irradiation parameter *J* (Table 3)

† See text for lithologic descriptions and details of the D₁-D₂/Muqu₁-Muqu₂ deformational/intrusive sequence (Fig 6) Abbreviations def = deformed, undef = undeformed, xc = crosscutting or crosscut, LMG = Lo Mantang gneiss

§ Location determined with a handheld GPS receiver with ca 7-15 m horizontal precision Note that these measurements were made after Selective Availability was deactivated in May, 2000 Altitude measured with an electronic barometric altimeter with ca ±10 m precision A differential technique was used with the Kali Gandaki River at Kagbeni village (Fig 2) as the datum (2773 m above mean sea level)

³⁹Ar, weighted mean date calculated by summing the product of the incremental date and moles ³⁹Ar, released for each step and normalizing by the total moles of ³⁹Ar, released (Table 5) Shown with propagated 2σ uncertainty including uncertainty in *J* Minima are identified by inspection of the release spectra (Fig 17) The increments included in the minima are contiguous and define linear arrays in Arrhenius plots (Fig 20)

‡ Inverse isochron dates are calculated from linear fits to the isotopic data (Table 5) as plotted on (⁴⁰Ar/³⁹Ar) vs (³⁹Ar/³⁹Ar) isotope correlation diagrams (Fig 19) (Roddick *et al.*, 1980) The linear regression techniques of York (1969) were used The age thus calculated is directly related to the abscissal intercept, and (⁴⁰Ar/³⁹Ar)₀ is calculated from the ordinal intercept MSWD (mean square of weighted deviates) is a measure of the goodness-of-fit, MSWD = 1 for a perfect fit (Wendt and Carl, 1991) "Steps" indicates the heating increment numbers (Table 5) included in the linear regression Samples with multiple inverse isochron results reflect our interpretation of the presence of multiple trapped Ar components (see text for details) Bold indicates our best estimate of the age recorded by the least retentive domain (LRD) in the sample

§§ LRD = Least retentive domain In all cases, the MID is used to estimate the age of the LRD LRD diffusion parameters calculated for the first linear array in the Arrhenius plots (Fig 20) Diffusion parameters (*E_a* and [*D₀*/r²]) are calculated and then used to determine closure temperature (*T_c*) using data in Table 8c and the program MacArgon 5.10 (Lister and Baldwin, 1996) A cooling rate of 45 °C/Myr (see text), activation volume (*V_a*) of 10 cm³, effective diffusion dimension (*r*) of 6 μm, and slab geometry are assumed (McDougall and Harrison, 1999)

Table 7

TABLE 8a. MUSCOVITE DIFFUSION PARAMETERS

E_a † (kcal/mol)	D_0 † (cm ² /s)	V_a § (cm ³)	Diffusion Geometry #	r ‡ (μm)	Cooling Rate§§ (°C/Myr)
43	3.20E-04	10	cylindrical	150	45

Notes :

† Values are those of Robbins (1972) as quoted in Hames and Bowring (1994).

§ Activation volume. Value used is that advocated by Lister and Baldwin (1996).

Infinite cylinder diffusion geometry advocated by Hames and Bowring (1994).

‡ Effective diffusion dimension (McDougall and Harrison, 1999).

§§ Details of cooling rate determination given in text.

Table 8a

Chapter 4: Exhumational history of the Mustang and Mugu granites

TABLE 8b. BIOTITE DIFFUSION PARAMETERS

Sample	Composition † (X_{ann})	E_a § (kcal/mol)	D_o § (cm^2/s)	V_a # (cm^3)	Diffusion Geometry ‡	Half-Grain Size §§ (μm)	Cooling Rate ## ($^{\circ}C/Myr$)
98KG19	<i>0.77</i>	52.58	0.54	14	cylindrical	268	45
98KG20	<i>0.77</i>	52.58	0.54	14	cylindrical	335	45
00KG08	0.83	54.32	0.67	14	cylindrical	394	45
00KG09	<i>0.77</i>	52.32	0.52	14	cylindrical	394	45
00KG10	<i>0.77</i>	52.32	0.52	14	cylindrical	158	45
00KG13	<i>0.77</i>	52.58	0.54	14	cylindrical	236	45
00KG19	<i>0.77</i>	52.58	0.54	14	cylindrical	315	45
00KG20	0.70	50.30	0.38	14	cylindrical	236	45
00KG24	<i>0.77</i>	52.32	0.52	14	cylindrical	473	45
00KG25	0.80	53.45	0.61	14	cylindrical	315	45
00KG26	0.73	51.14	0.44	14	cylindrical	394	45
00KG28	0.74	51.63	0.47	14	cylindrical	512	45
00KG30	<i>0.76</i>	52.07	0.51	14	cylindrical	394	45
00KG31	<i>0.77</i>	52.35	0.53	14	cylindrical	394	45
00KG32	<i>0.76</i>	52.07	0.51	14	cylindrical	630	45

Notes :

† Mole fraction annite (X_{ann}) measured using wavelength-dispersive electron microprobe analysis (see text for details). X_{ann} values for samples not analyzed with the electron microprobe – but whose X_{ann} is estimated from the mean of similar samples that were analyzed – are italicized. Means: Tibetan Sedimentary Sequence/Lo Mantang gneiss = 0.77; Mugu granite = 0.77; Mustang granite = 0.76.

§ Calculated from compositional data using experimental results of Grove and Harrison (1996) and Harrison *et al.* (1985). E_a = activation energy; D_o = frequency factor.

Activation volume. Value used is that for annite advocated by Harrison *et al.* (1985). Same value used for all samples as they are closer to the annite endmember composition than to the phlogopite endmember composition.

‡ Infinite cylinder diffusion geometry advocated by Harrison *et al.* (1985).

§§ Calculated by taking the arithmetic mean of >20 grain radius measurements per sample. For each sample, the grains measured are not the same as those irradiated and used in isotopic analyses, but they comprise a representative aliquot taken from the same mineral separate. Radii measured under magnification using an optical picking microscope with calibrated eyepiece reticule. For grain-size-independent closure temperature calculation, an effective diffusion dimension (r) of 150 μm was used (Harrison *et al.*, 1985).

Details of cooling rate determination given in text.

Table 8b

TABLE 8c: K-FELDSPAR DIFFUSION PARAMETERS

Sample	Heating Increments†	E_a § (kcal/mol)	D_o/r^2 § (cm ² /s)	V_a # (cm ³)	Diffusion Geometry ‡	r §§ (μm)	Cooling Rate ## (°C/Myr)
00KG08	1 - 11	21.8	2.93E-01	10	slab	6	100
00KG12	4 - 11	29.6	9.24E+00	10	slab	6	100
00KG23	1 - 11	22.4	3.81E-01	10	slab	6	100
00KG24	1 - 11	23.1	5.63E-01	10	slab	6	100
00KG26	3 - 9	37.1	3.14E+02	10	slab	6	100
00KG29	4 - 10	40.0	3.96E+03	10	slab	6	100
00KG30	3 - 15	32.6	1.91E+01	10	slab	6	100
00KG32	1 - 11	22.1	2.09E-01	10	slab	6	100

Notes :

† Heating increments included in linear regression in Arrhenius diagram.

§ Activation energy (E_a) calculated from the slope, and (D_o/r^2) calculated from ordinal intercept on Arrhenius diagrams.

Activation volume.

‡ Slab or plane-sheet diffusion geometry (McDougall and Harrison, 1999).

§§ Effective diffusion dimension (McDougall and Harrison, 1999). Assumed to be representative of the smallest diffusion domain. In practice, since we have a value for (D_o/r^2) (as opposed to simply D_o), the diffusion dimension (r) assumed does not affect the closure temperature calculation.

Details of cooling rate determination given in text.

Table 8c

Chapter 4: Exhumational history of the Mustang and Mugu granites

TABLE 9a. MICA CLOSURE TEMPERATURE AS A FUNCTION OF COOLING RATE

Sample	10°C/Myr		45°C/Myr		100°C/Myr	
	T _c (SD)† (°C)	T _c (SI)§ (°C)	T _c (SD)† (°C)	T _c (SI)§ (°C)	T _c (SD)† (°C)	T _c (SI)§ (°C)
<i>Muscovite</i>						
00KG06	398	347	429	373	446	387
00KG08	414	347	446	373	464	387
00KG12	421	347	453	373	471	387
00KG14	398	347	429	373	445	387
00KG16	407	347	438	373	456	387
00KG23	421	347	453	373	471	387
00KG24	407	347	438	373	456	387
00KG25	387	347	417	373	433	387
00KG28	393	347	423	373	440	387
00KG30	398	347	429	373	446	387
00KG31	393	347	423	373	440	387
00KG32	393	347	423	373	440	387
<i>averages #</i>	<i>403</i>	<i>347</i>	<i>433</i>	<i>373</i>	<i>451</i>	<i>387</i>
<i>Biotite</i>						
98KG19	377	360	401	383	414	395
98KG20	384	360	408	383	421	395
00KG08	407	378	431	400	445	413
00KG09	387	358	411	380	424	392
00KG10	359	358	382	380	394	392
00KG13	374	360	397	383	410	395
00KG19	382	360	406	383	419	395
00KG20	352	339	374	361	387	373
00KG24	392	358	417	380	430	392
00KG25	391	369	415	391	428	404
00KG26	375	347	399	369	412	381
00KG28	388	351	412	373	426	385
00KG30	384	356	408	378	422	390
00KG31	387	358	411	380	424	393
00KG32	399	356	424	378	438	390
<i>averages #</i>	<i>383</i>	<i>358</i>	<i>406</i>	<i>380</i>	<i>420</i>	<i>392</i>

Note : The cooling rates shown are representative of the range of values tested: 10°C/Myr, 45°C/Myr, 60°C/Myr, 100°C/Myr, and 120°C/Myr. Closure temperatures (T_c) calculated using the diffusion parameters in Tables 8a and 8b and the program MacArgon 5.10 (Lister and Baldwin, 1996).
† SD = size dependent. Uses measured average grain half-sizes as the effective diffusion dimension.
§ SI = size independent. Uses effective diffusion dimension of 150 μ m.
Column averages (arithmetic means). For a given cooling rate, we take the average size dependent and size independent closure temperatures as upper and lower bounds on closure temperatures for all samples.

Table 9a

TABLE 9b. K-FELDSPAR CLOSURE TEMPERATURE
AS A FUNCTION OF COOLING RATE

Sample	10°C/Myr	45°C/Myr	100°C/Myr
	T_c † (°C)	T_c † (°C)	T_c † (°C)
00KG08	80	96	105
00KG12	155	172	183
00KG23	86	103	112
00KG24	93	109	118
00KG26	212	231	241
00KG29	218	236	246
00KG30	187	206	217
00KG32	88	105	114
<i>averages §</i>	140	157	167

Notes :

† The cooling rates listed are representative of the range of values considered: 10°C/Myr, 45°C/Myr, 60°C/Myr, 100°C/Myr, and 120°C/Myr. Closure temperatures (T_c) calculated using the diffusion parameters in Table 8c and the program MacArgon 5.10 (Lister and Baldwin, 1996).

§ Column averages (arithmetic means).

Table 9b

Chapter 4: Exhumational history of the Mustang and Mugu granites

TABLE 10. SUMMARY OF GEOCHRONOLOGIC RESULTS

Description†		Age (Ma)	±	2σ (Ma)	Remarks§
Mustang granite	U-Pb	23.35	±	0.17	00KG28; similar ages from 00KG31 (m5), 00KG20 (m5)
Mugu granite	U-Pb	20.76	±	0.67	00KG31; minimum age for Mugu _{III}
Mugu granite	U-Pb	18.28	±	0.10	00KG20; youngest dated Mugu _{III}
Mustang granite	ms maximum	18.31	±	0.25	00KG32; see Fig. 16a
	ms minimum	17.35	±	0.44	00KG25; see Fig. 16a
Mugu granite	ms average	17.85	±	0.14	average of older age cluster; see Fig 16c
Mustang granite	bt average	17.58	±	0.43	see Fig. 16b
Mugu granite	ms average	17.25	±	0.11	average of younger age cluster; see Fig.16c
Mugu granite	bt average	17.46	±	0.21	see Fig. 16d
TSS in UMM	bt average	17.54	±	0.22	see Fig. 16e
TSS at LK	bt average	17.42	±	0.25	98KG19, -20; in immediate DF footwall
Mustang & Mugu granites at Thinker	MSD maximum	15.34	±	0.99	00KG30; see Fig. 18a
	MSD minimum	15.19	±	0.79	00KG24; see Fig. 18a
Mustang & Mugu granites at Thinker	MID maximum	14.51	±	0.42	00KG29; see Fig. 18b
	MID minimum	12.88	±	0.75	00KG24; see Fig. 18b

Notes :

† Lithology and type of geochronologic constraint. U Pb = ID TIMS analyses of monazite or xenotime; ms = ⁴⁰Ar/³⁹Ar analysis of muscovite; bt = ⁴⁰Ar/³⁹Ar analysis of biotite; MSD = ⁴⁰Ar/³⁹Ar minimum spectrum date for K-feldspar (see text for details); MID = ⁴⁰Ar/³⁹Ar minimum isochron date for K-feldspar (see text for details). MIDs are our best estimate for the age of the LRD (least retentive domain; see text for details). UMM = Upper Mustang massif; LK = Lumpa Khola; Thinker = Thinker area. See Fig. 2 for locations.

§ Specific samples are listed where appropriate. For samples pertinent to constraining the U-Pb age of the Mustang granite, the code in parentheses denotes a specific grain (m = monazite). Note that neither 00KG31 or -20 are Mustang granite samples; the grains in question are likely inherited. See text and Fig. 6 for explanation of deformational and intrusive phases mentioned. Figures cited illustrate age-elevation or age cluster relationships in the data. DF = Dangardzong Fault.

Table 10

TABLE 11. DENUDATION RATE RESULTS*

Sample	Thermochronometers†	λ §	R#	U** (mm/yr)	T_o ‡ (°C)	z_o §§ (km)	t_o ## (Ma)	a*** (°C/km)	Max. Age††† (Ma)	Min. Age§§§ (Ma)	Intercept#### (Ma)
00KG08	ms, bt, MID****	0.6	0.17	2.21	425	5	17.61	85	17.61	15.35	15.35
00KG12	ms, MSD, MID	1.2	0.35	1.91	475	25	25.35	19	17.97	13.62	12.26
00KG20	upb, bt	1.1	0.72	4.01	700	10	18.81	70	18.28	17.11	16.32
00KG23	ms, MSD	0.8	0.03	2.01	425	10	18.95	43	17.93	15.53	13.98
00KG24	ms, bt, MSD, MID	0.9	0.19	1.71	425	15	20.69	28	17.66	12.88	11.92
00KG26	bt, MSD, MID	1.0	0.19	2.01	400	15	19.95	27	17.47	13.98	12.49
00KG28	upb, ms****	1.0	0.80	1.51	625	20	26.25	31	23.25	17.38	13.00
00KG30	ms, bt, MSD	1.5	0.07	3.61	400	20	19.35	20	18.09	15.34	13.81
00KG31	upb, ms	2.3	0.03	4.81	700	35	23.85	20	20.76	17.40	16.58
00KG32	ms, MSD****	1.5	0.02	3.41	400	20	18.94	20	18.31	14.60	13.08

Notes :

* Calculated using the methodology of Moore and England (2001).

† Abbreviations: upb = U-Pb from monazite (00KG28 and -31) or uraninite (00KG20); ms = $^{40}\text{Ar}/^{39}\text{Ar}$ from muscovite; bt = $^{40}\text{Ar}/^{39}\text{Ar}$ from biotite; MSD = $^{40}\text{Ar}/^{39}\text{Ar}$ K-feldspar minimum spectrum date (see text for details); MID = $^{40}\text{Ar}/^{39}\text{Ar}$ K-feldspar minimum isochron date (see text for details). MIDs are our best estimate for the age of the LRD (least retentive domain; see text for details).

§ Curvature parameter equal to the square root of the Péclet number. Moore and England (2001) determined that $\lambda > 0.3$ is necessary for their technique to be applicable.

Misfit value (see equation(3)) for the best fit temperature-time solution to equation (2).

** Best fit uplift rate. It is well-constrained by this analysis.

‡ Best fit initial temperature. It is well-constrained by this analysis.

§§ Initial depth corresponding the the best fit U and T_o . It is poorly constrained by this analysis.

Age for beginning of denudation. Calculated by dividing z_o by U , it is poorly constrained by this analysis.

*** Initial geothermal gradient. Calculated by dividing T_o by z_o , it is poorly constrained by this analysis.

††† Cooling age of the oldest thermochronometer used as input.

§§§ Cooling age of the youngest thermochronometer used as input.

Projected age at which the calculated cooling curve intersects $T = 0$.

**** Anomalous biotite (00KG28 & -32) or MSD (00KG08) data were excluded from the analysis of these samples.

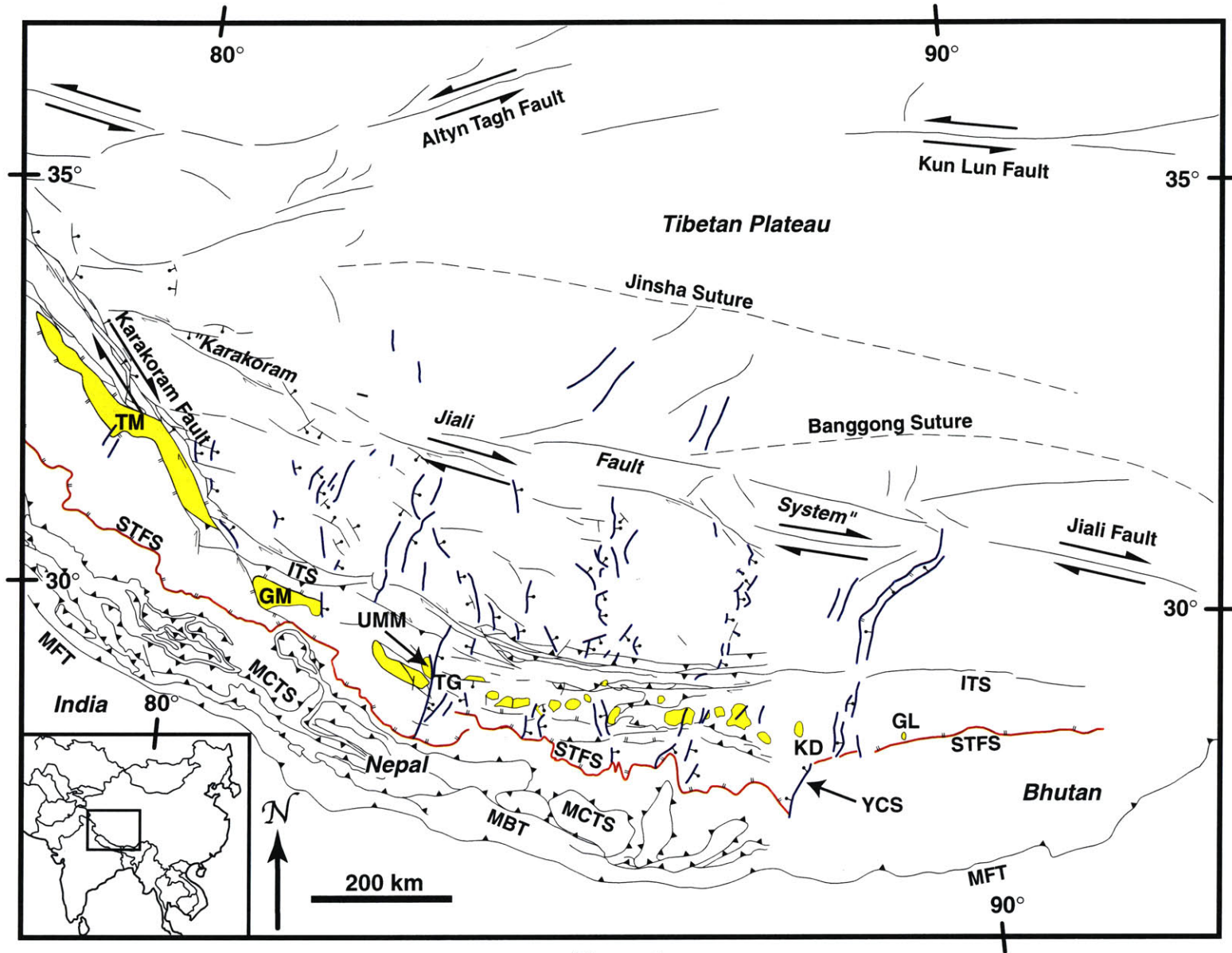


Figure 1

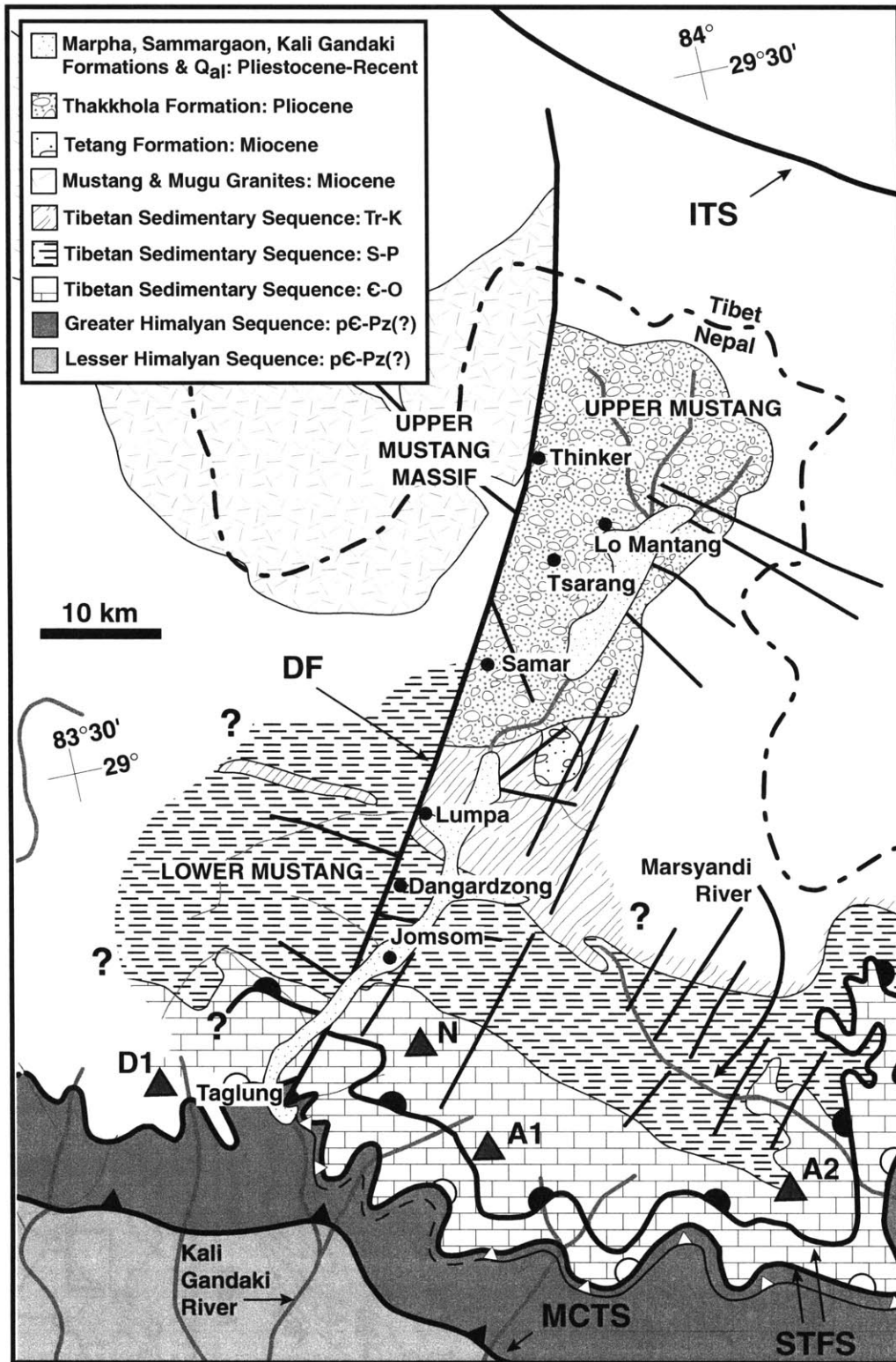


Figure 2

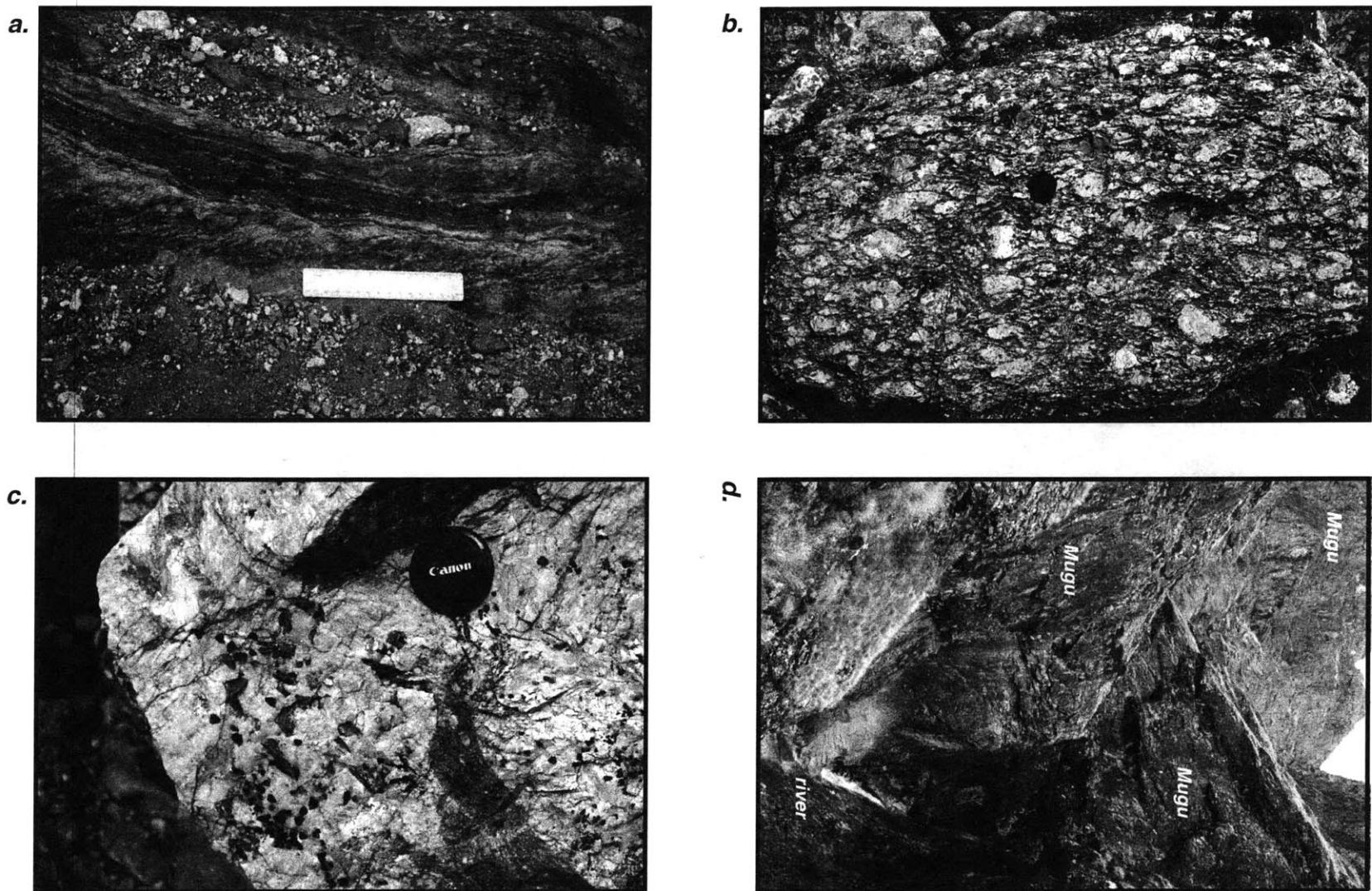


Figure 3

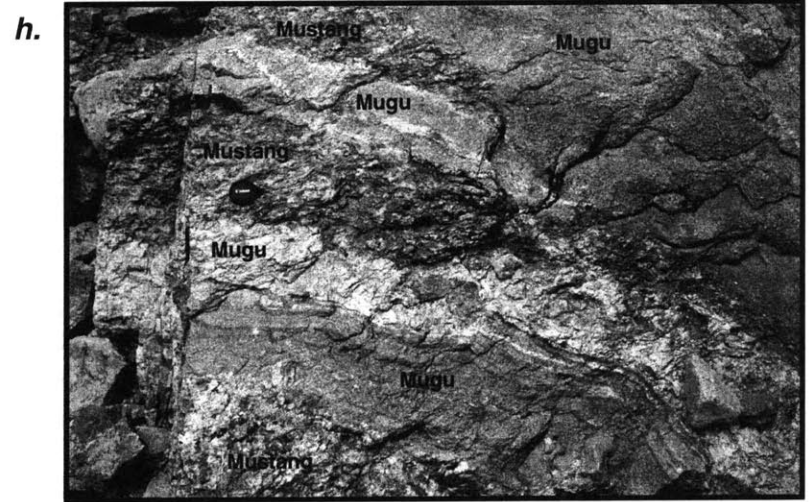
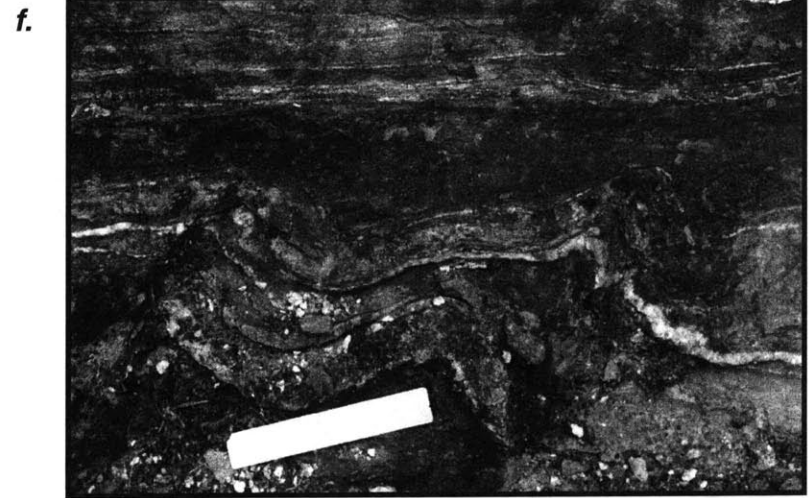
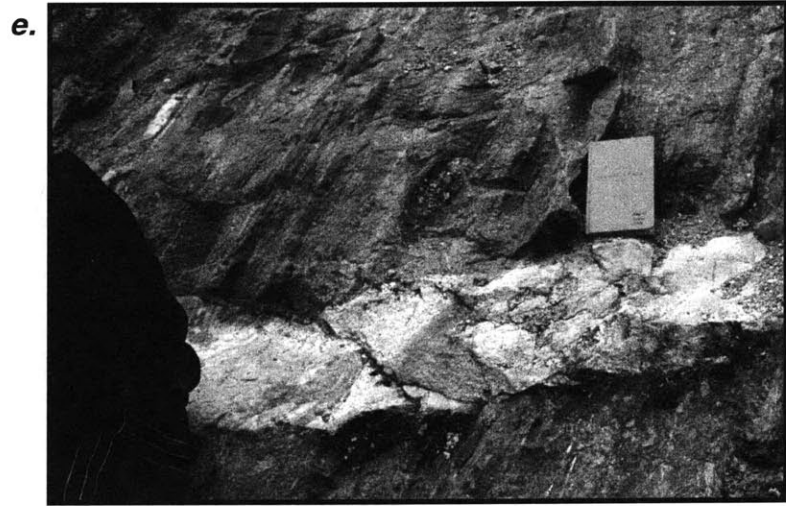


Figure 3 <continued>

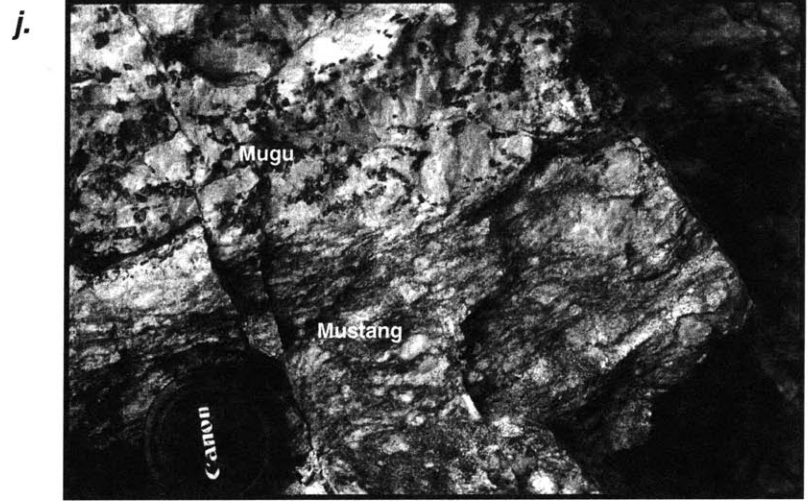
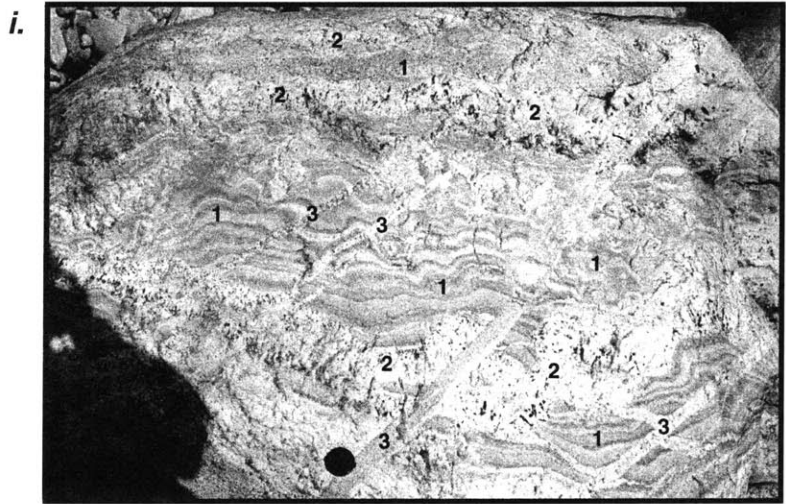


Figure 3 <continued>

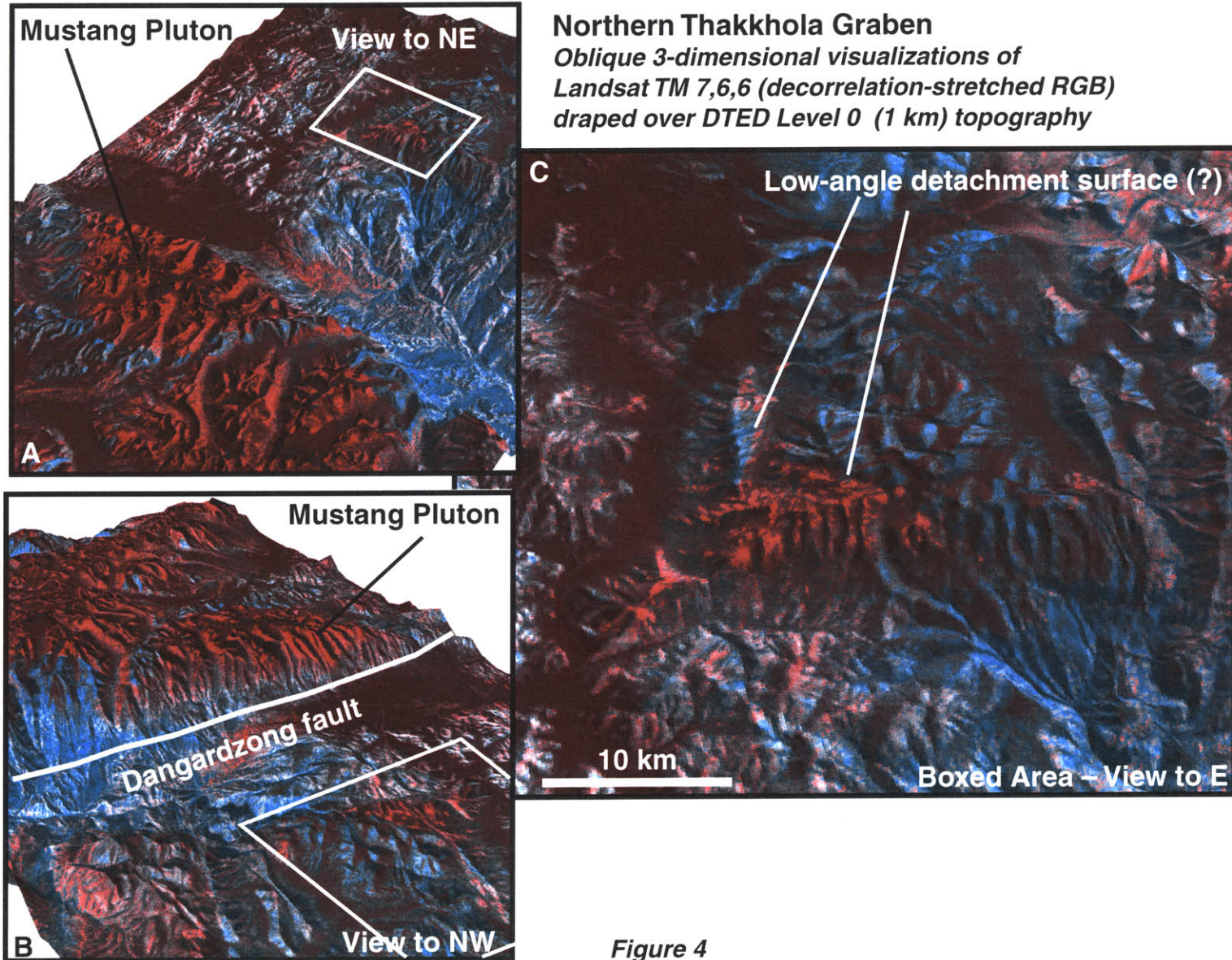


Figure 4

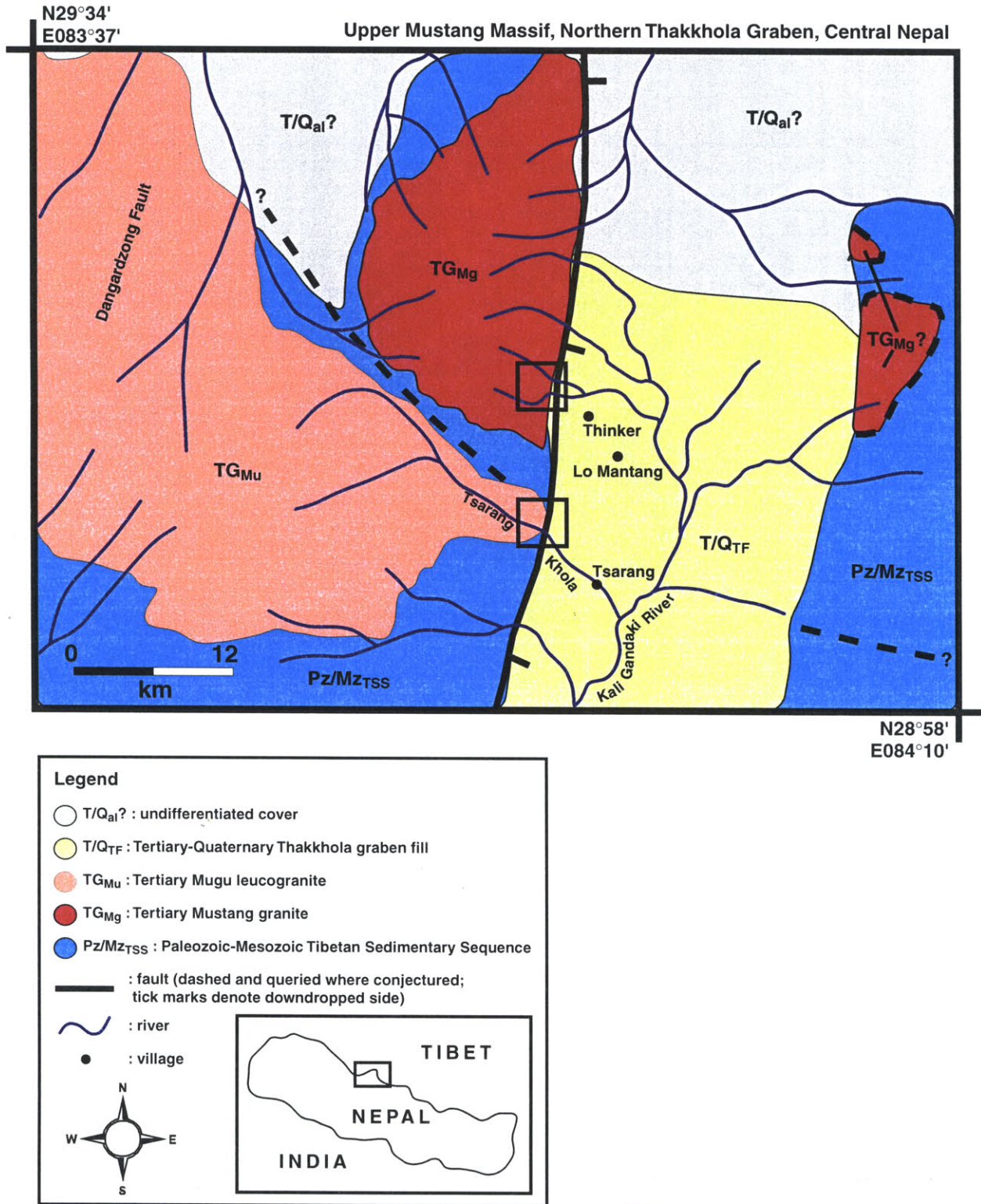


Figure 5

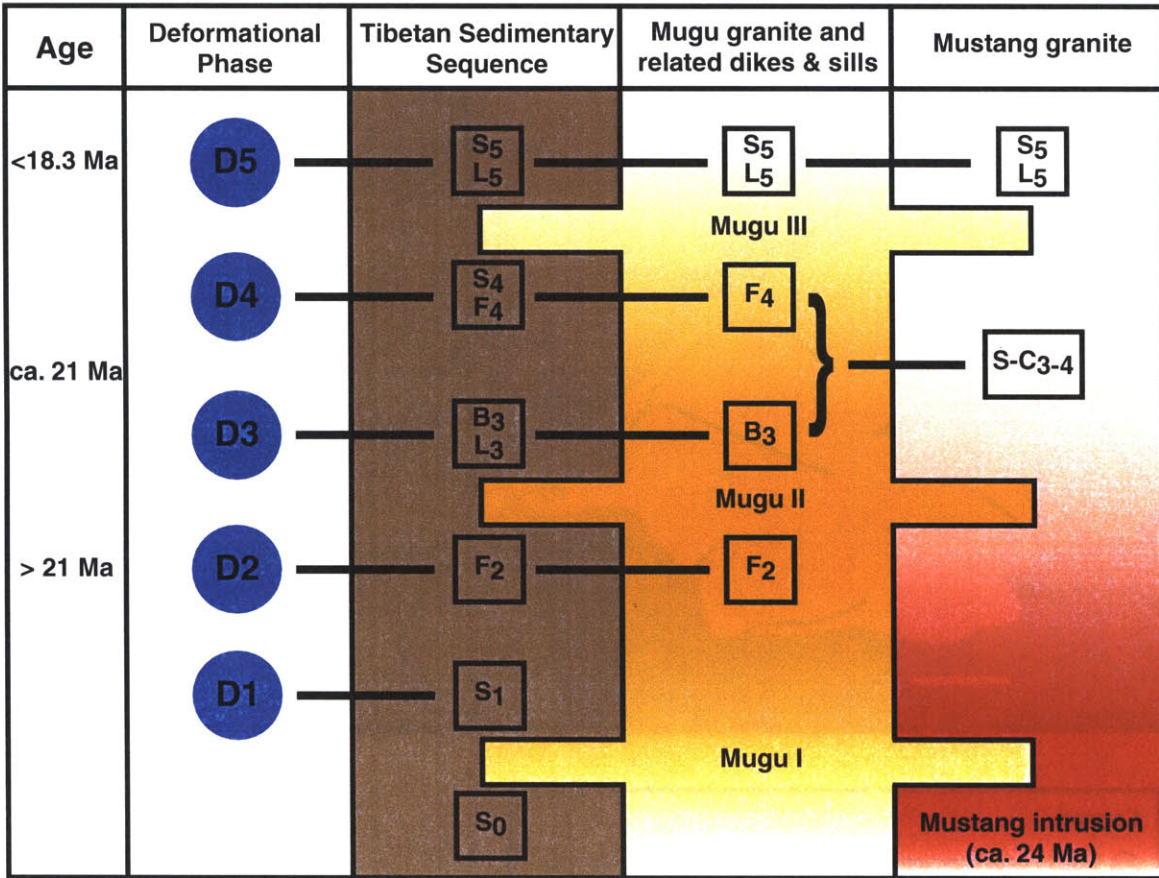


Figure 6

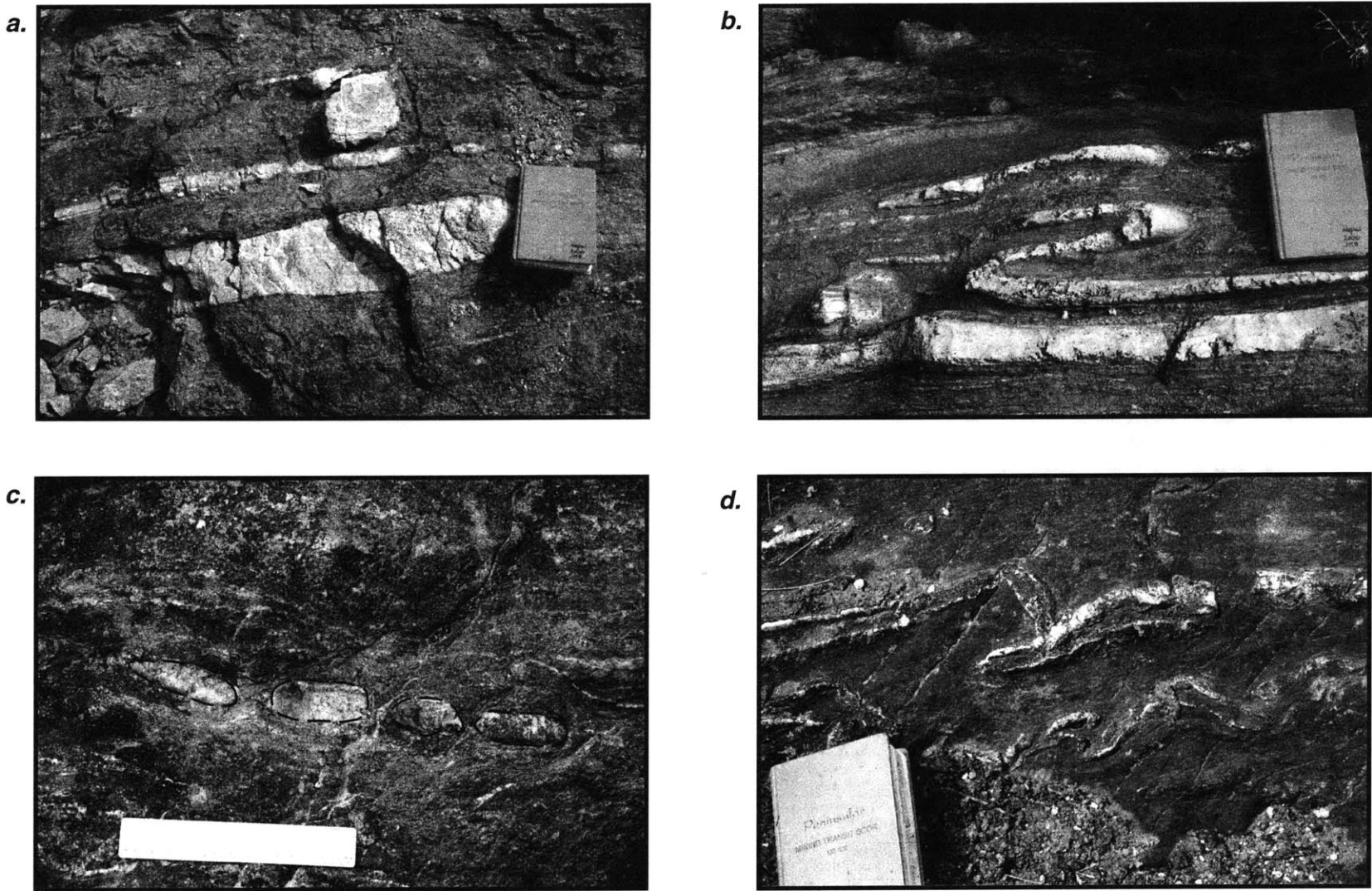


Figure 7

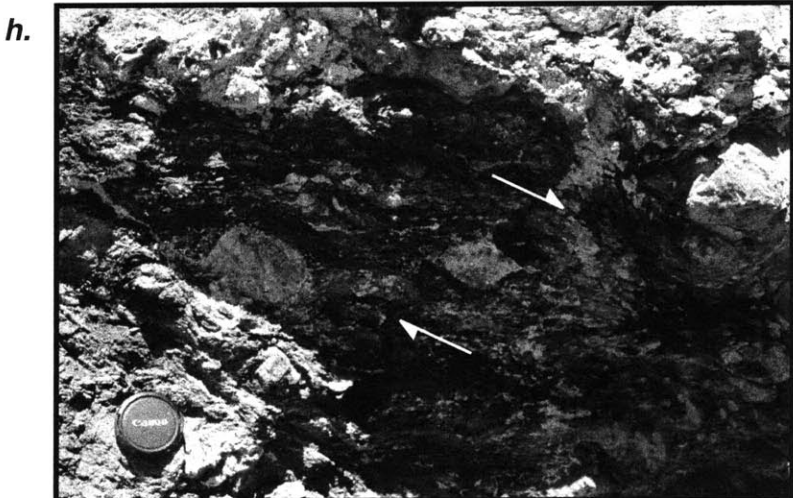
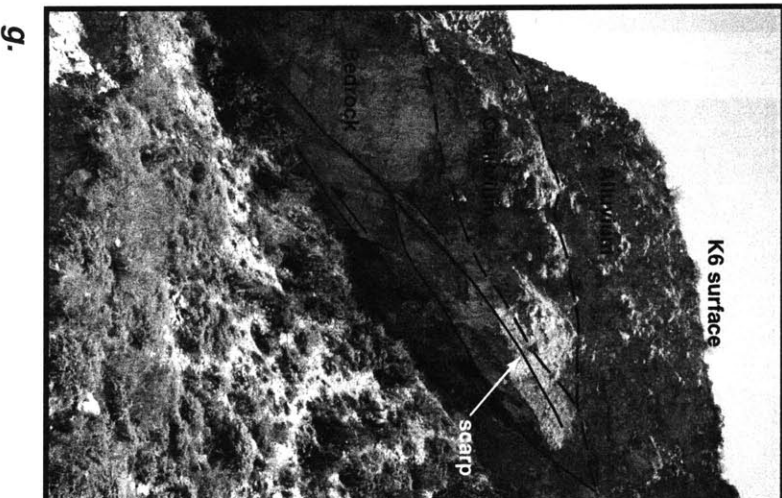
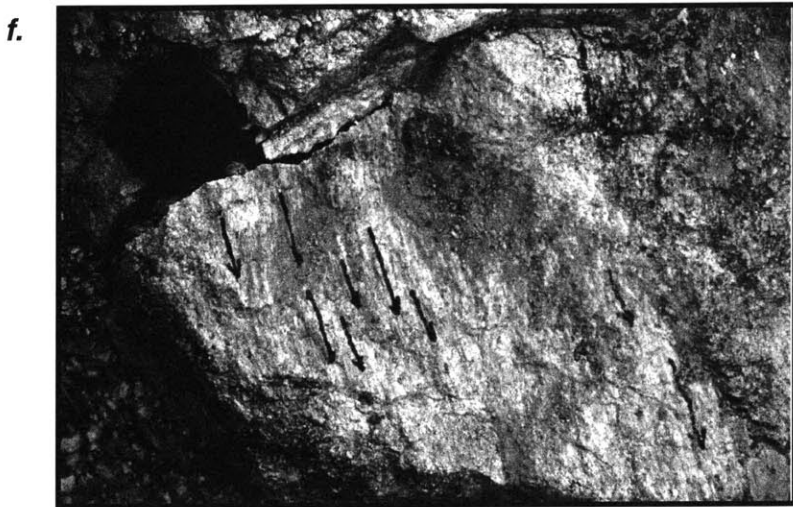
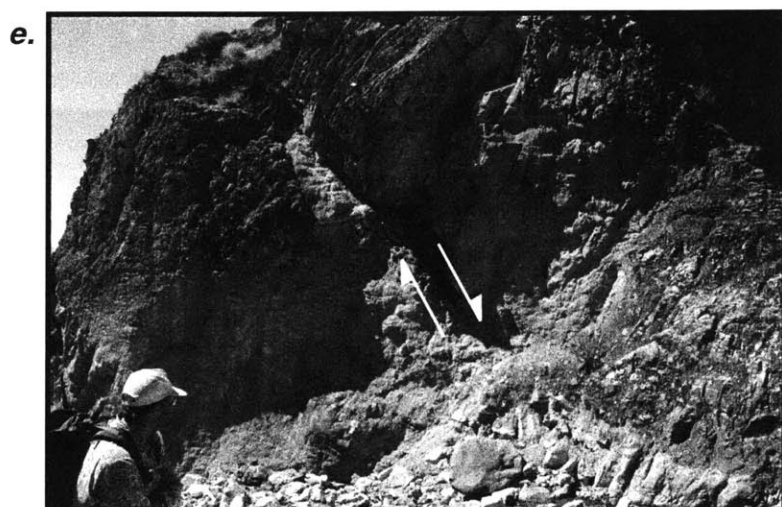
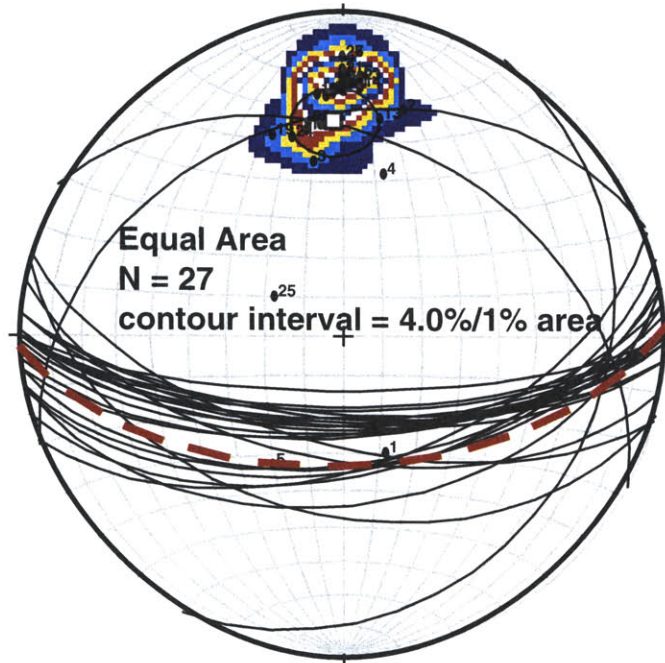


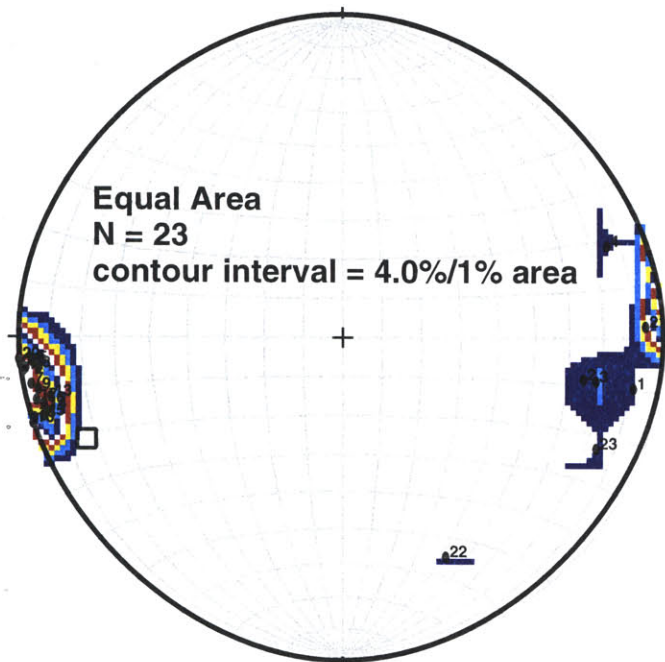
Figure 7 <continued>

a.



- ▣ Great circle strike & dip = $87.6^\circ, 56.8^\circ$ S
- Mean vector trend & plunge = $357.8^\circ, 33.3^\circ$
 $k = 9.1$; 99% cone = 12.3° , 95% cone = 9.8°

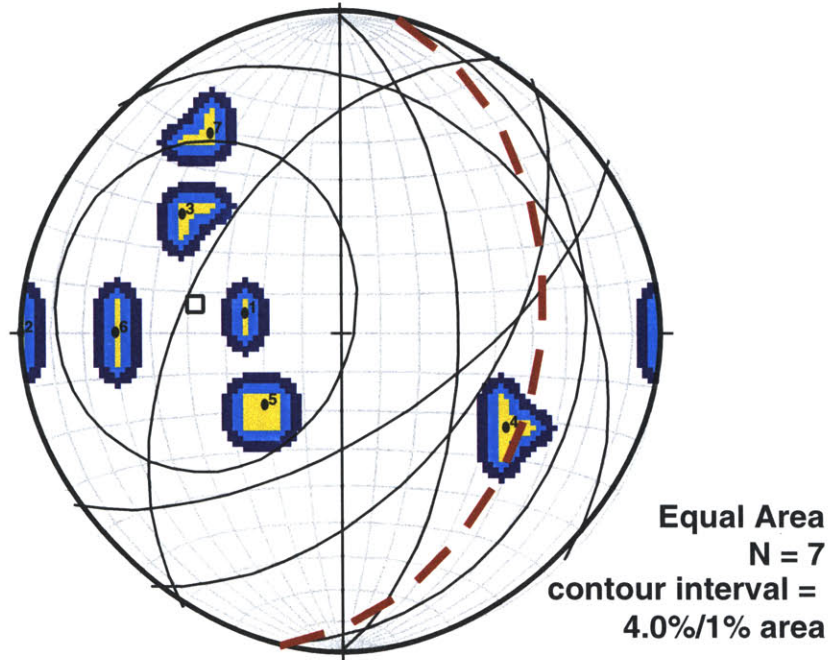
b.



- Mean vector trend & plunge = $247.7^\circ, 15.6^\circ$

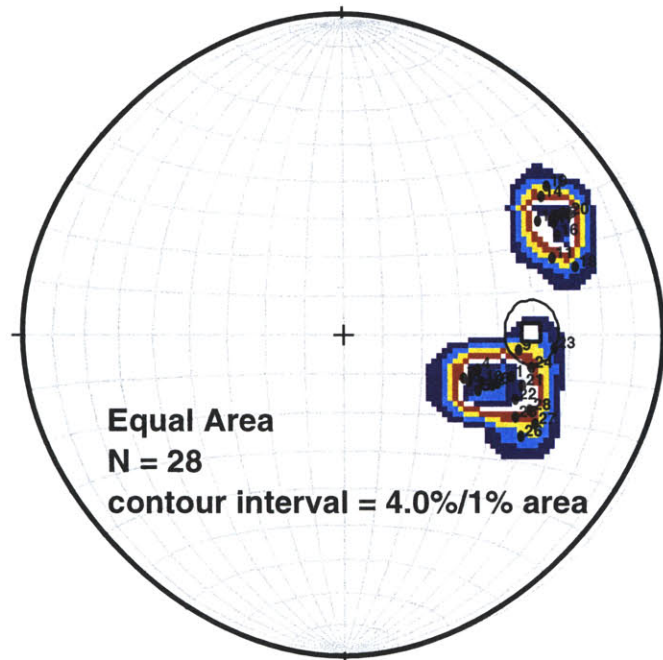
Figure 8

c.



/// Great circle strike & dip = 11.0° , 38.3° E
□ Mean vector trend & plunge = 281.3° , 52.0°

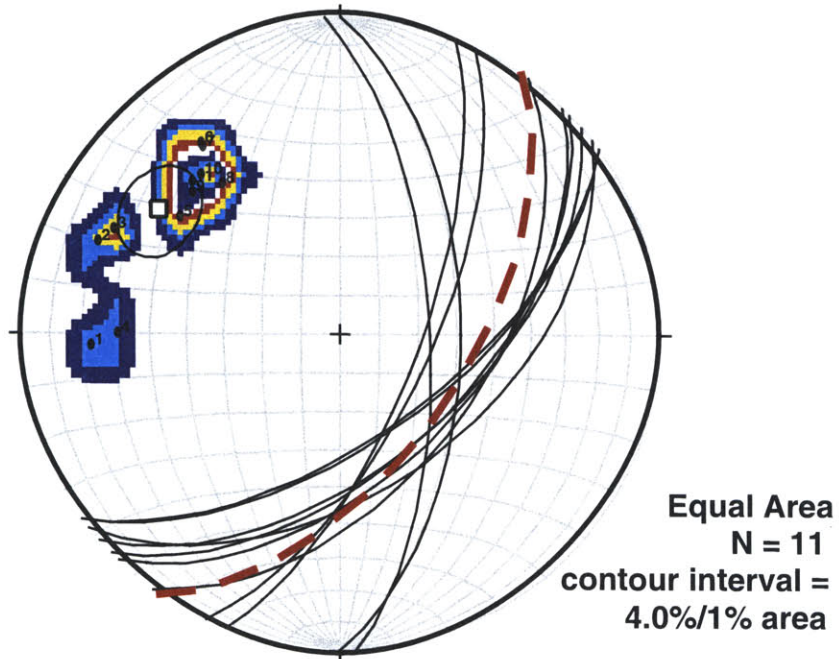
d.



□ Mean vector trend & plunge = 89.2° , 40.8°
k = 14.1; 99% cone = 9.5° , 95% cone = 7.5°

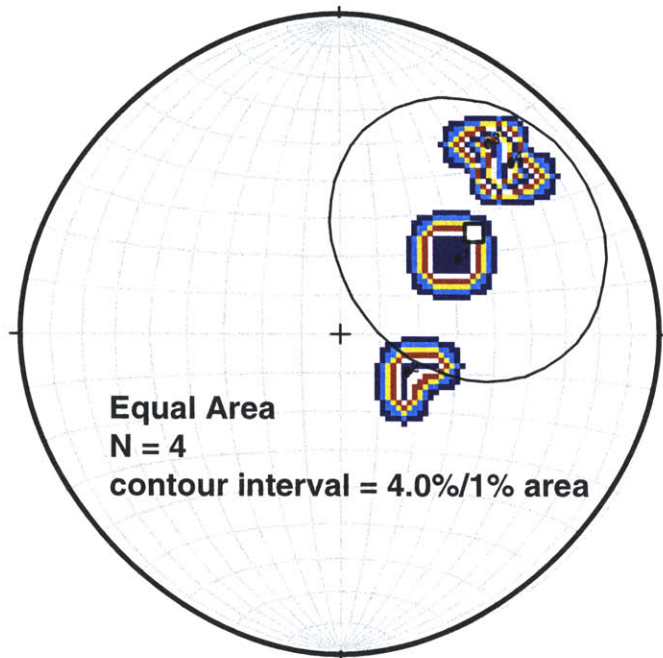
Figure 8 <continued>

a.



- Great circle strike & dip = $34.5^\circ, 58.2^\circ$ E
- Mean vector trend & plunge = $304.1^\circ, 31.9^\circ$
k = 19.8; 99% cone = 14.3° , 95% cone = 11.1°

b.



- Mean vector trend & plunge = $53.1^\circ, 46.1^\circ$
k = 9.9; 99% cone = 53.7° , 95% cone = 36.1°

Figure 9

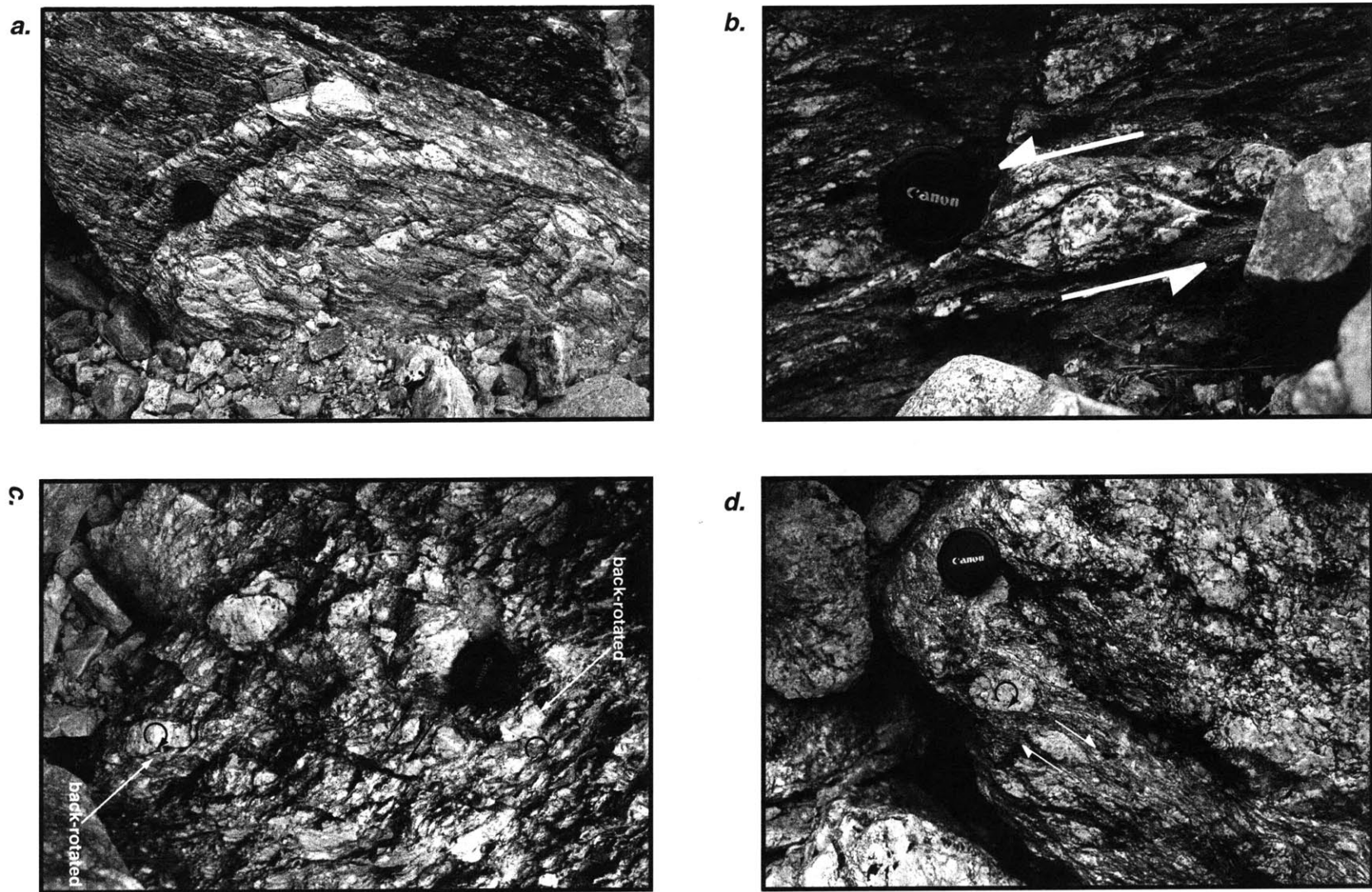


Figure 10

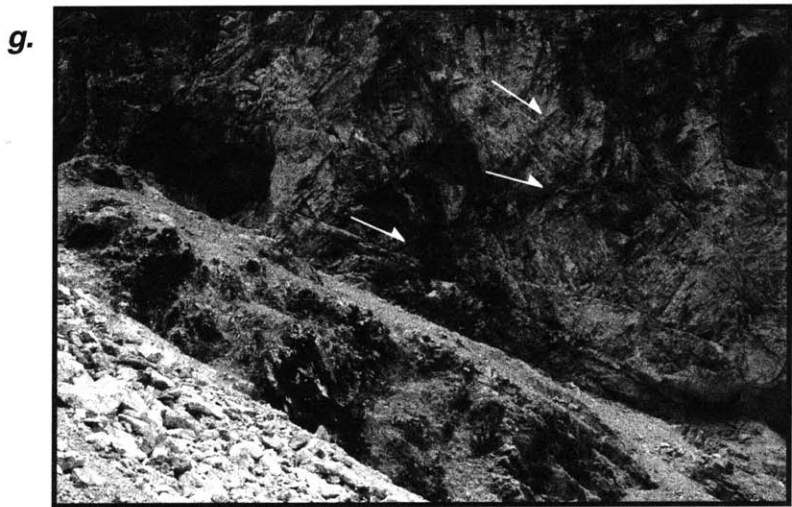
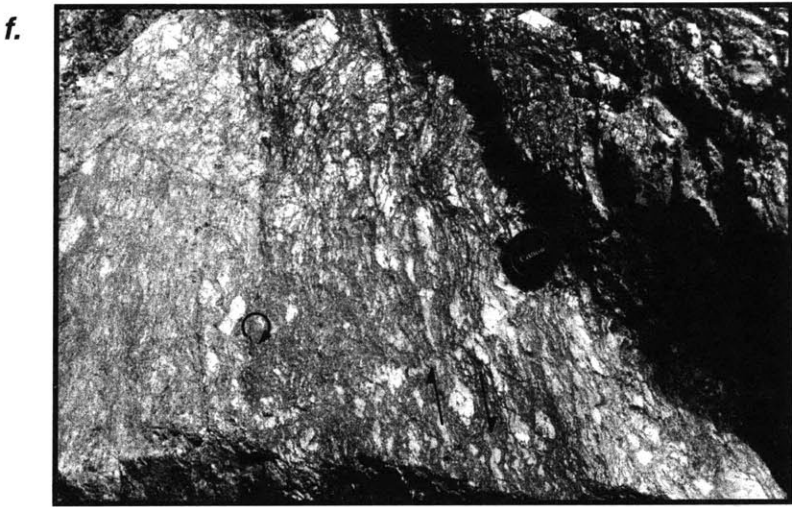
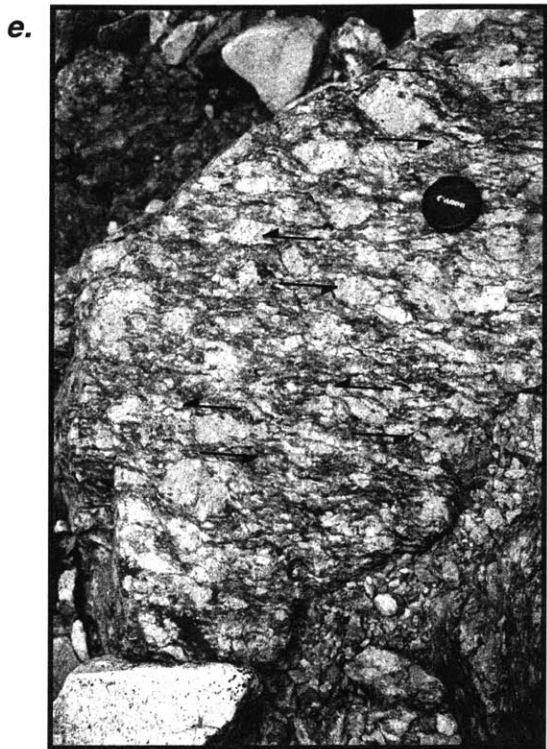


Figure 10 <continued>

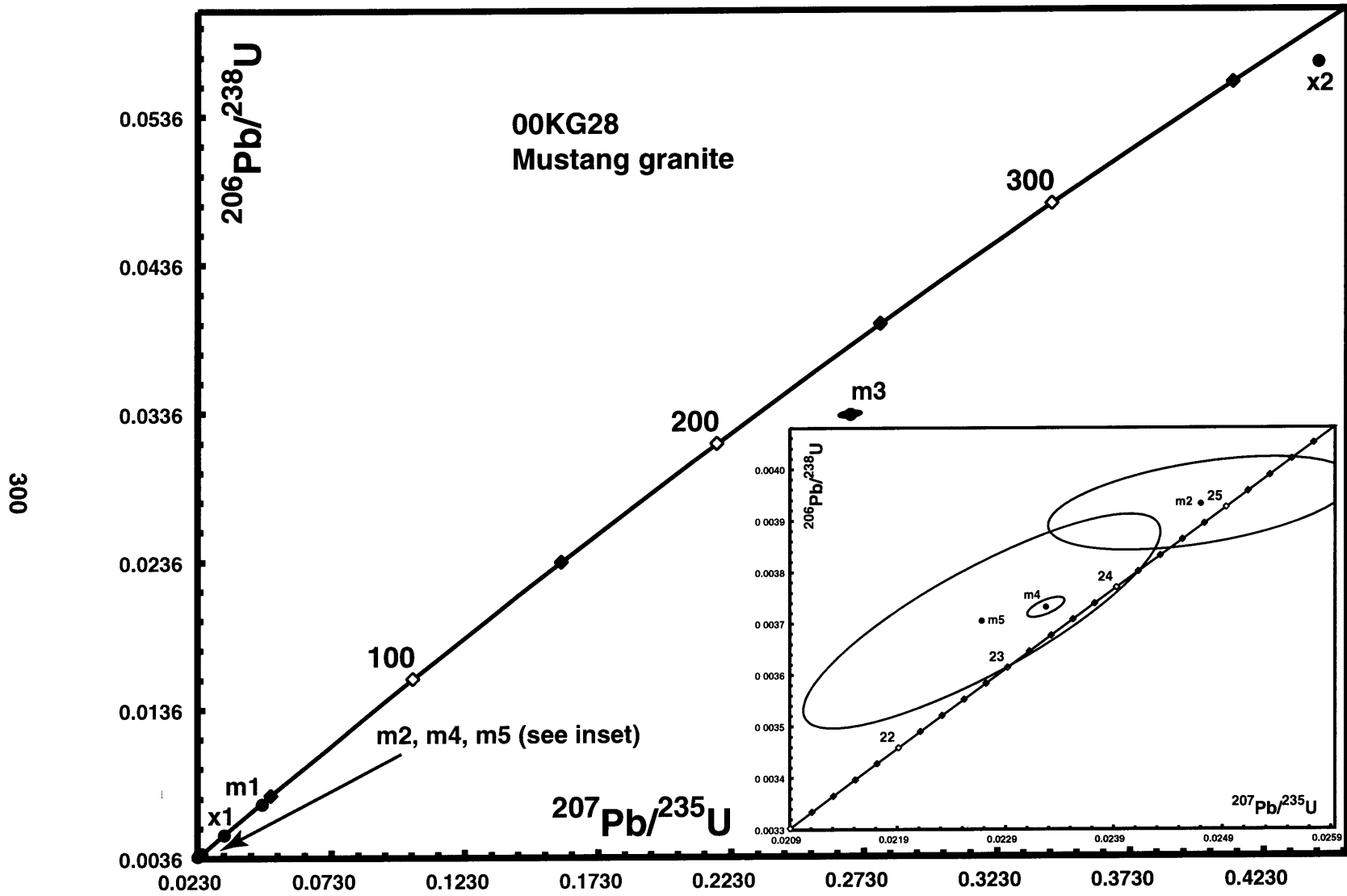


Figure 11a

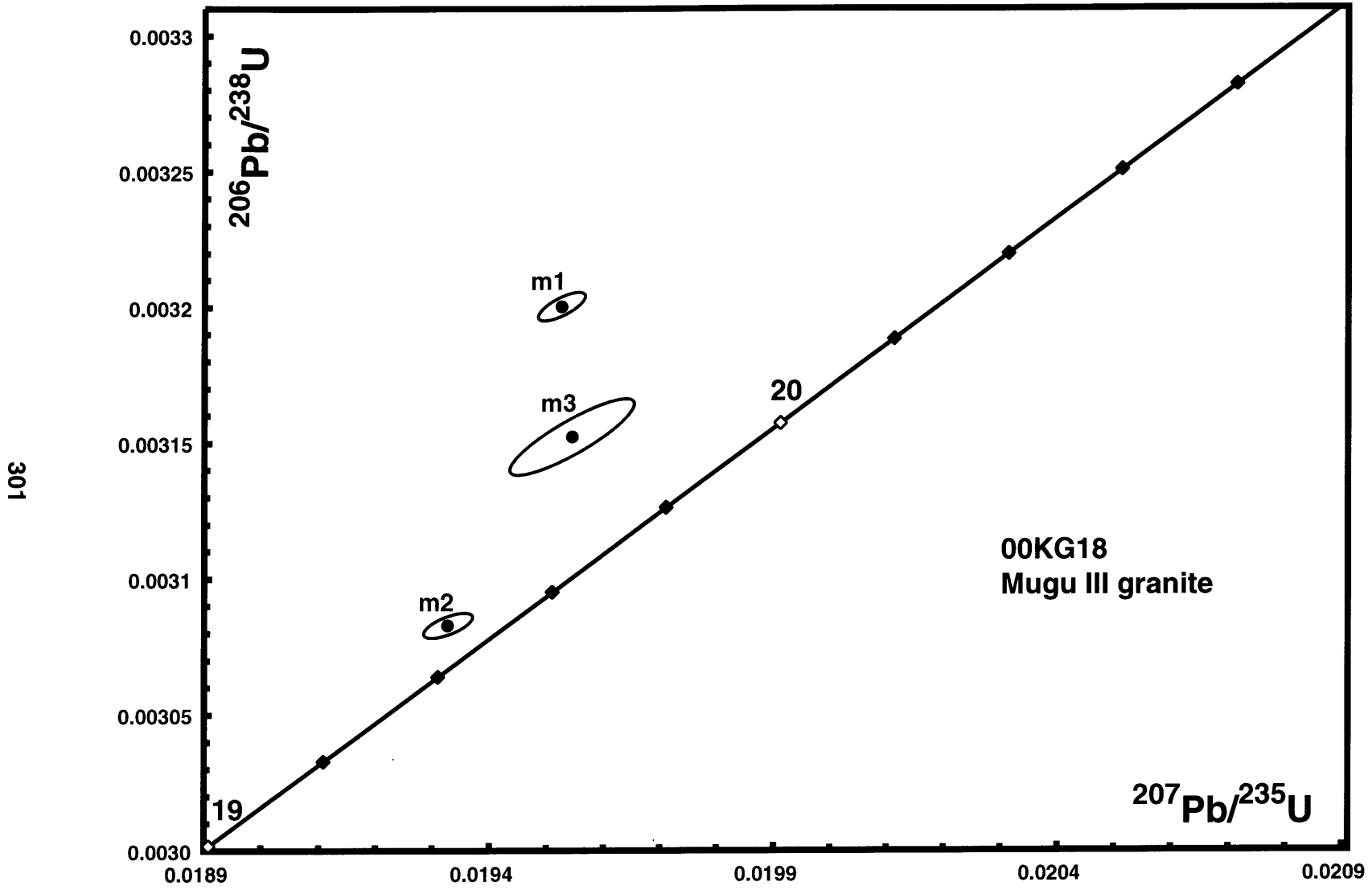


Figure 11b

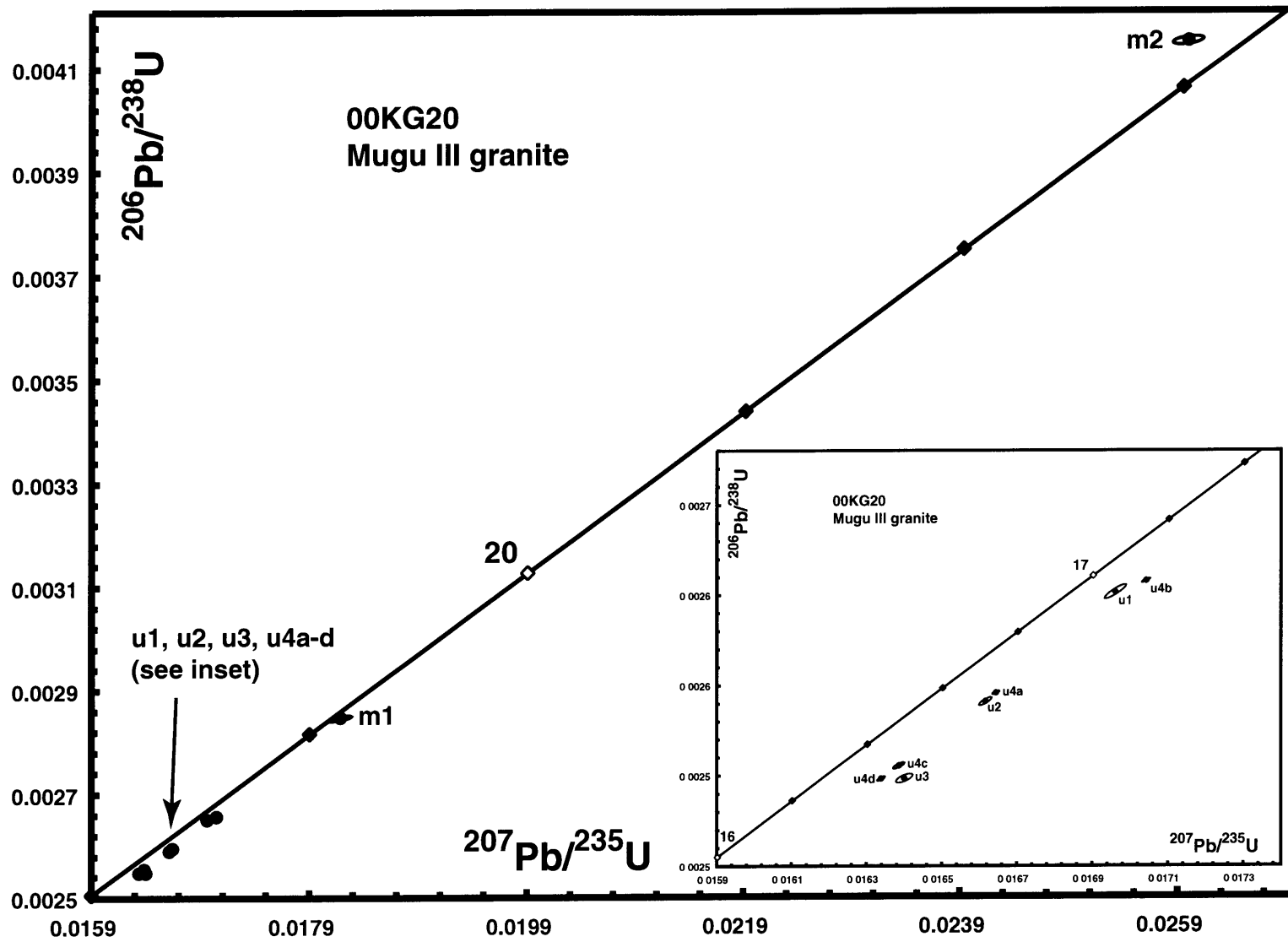


Figure 11c

303

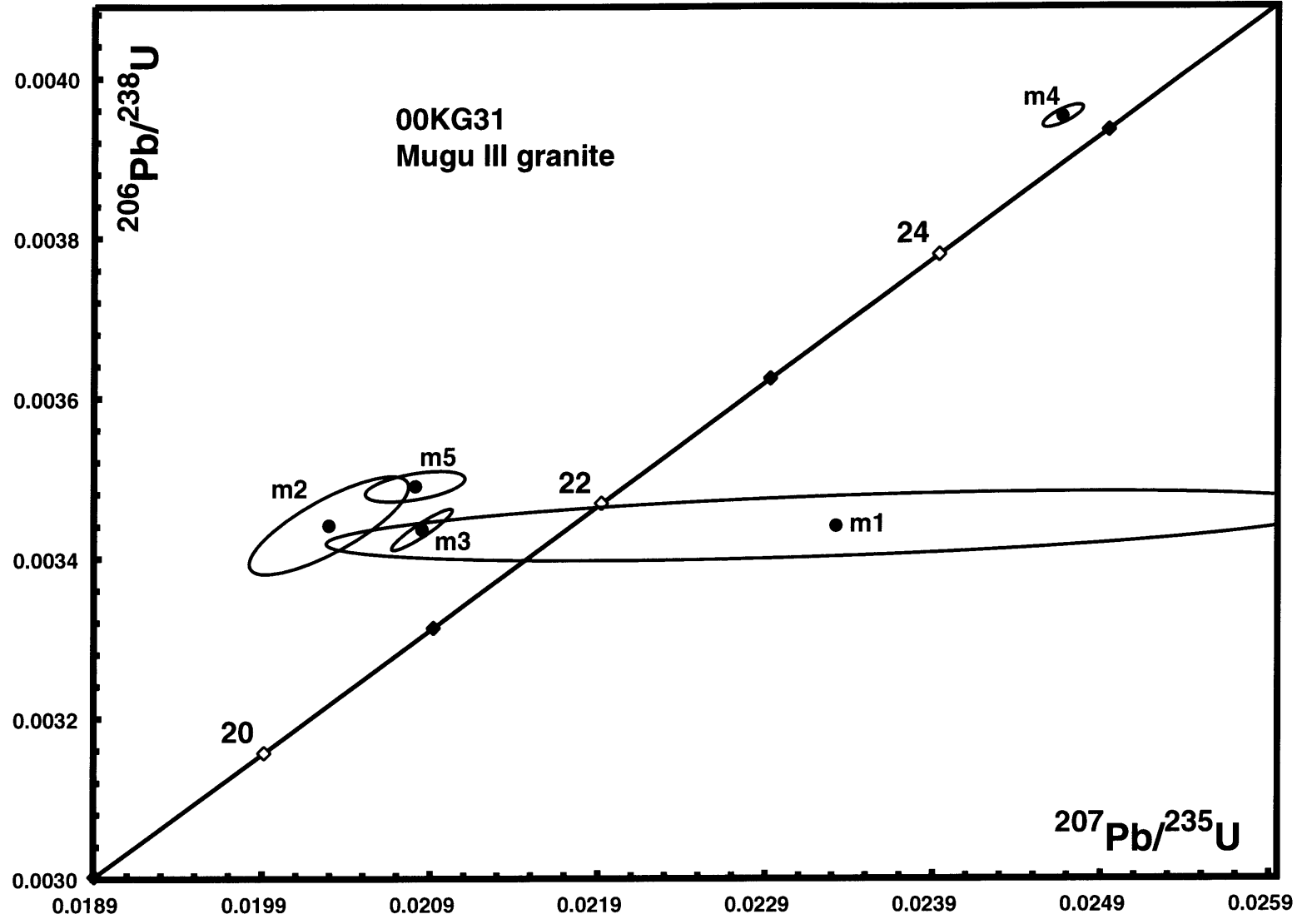


Figure 11d

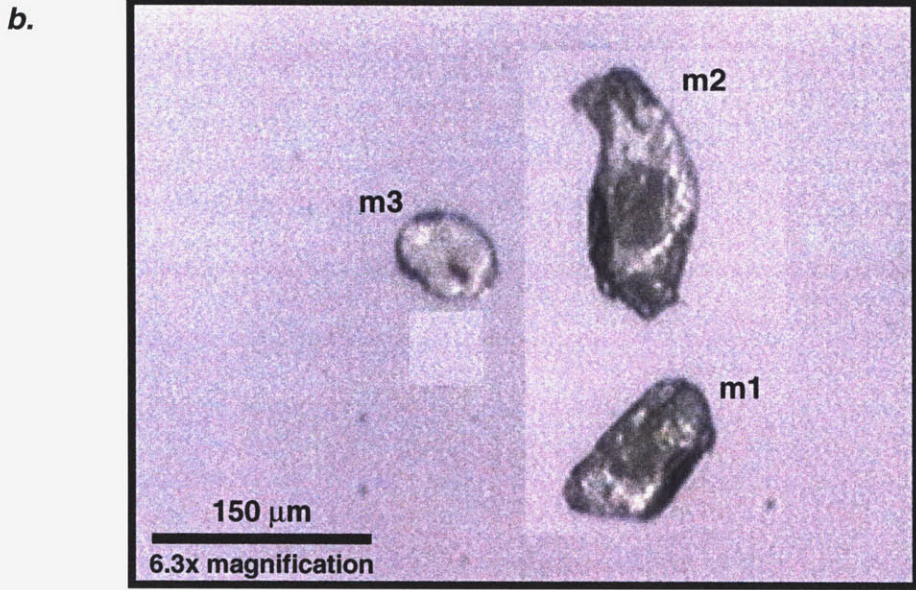
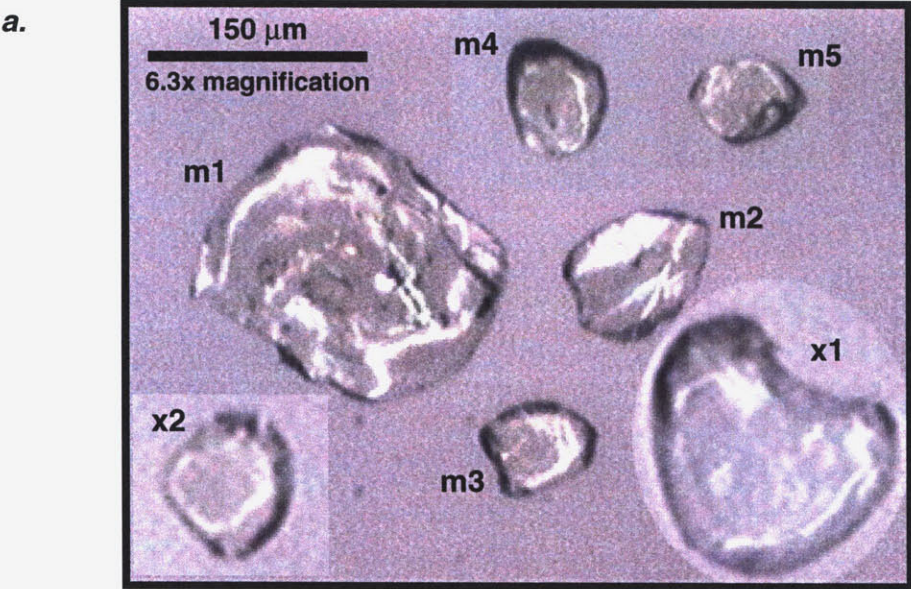
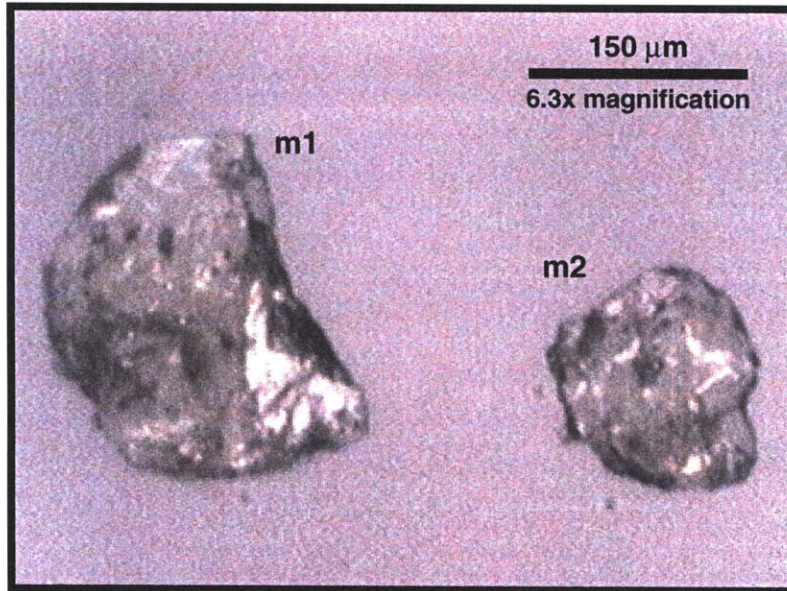


Figure 12

c.



d.

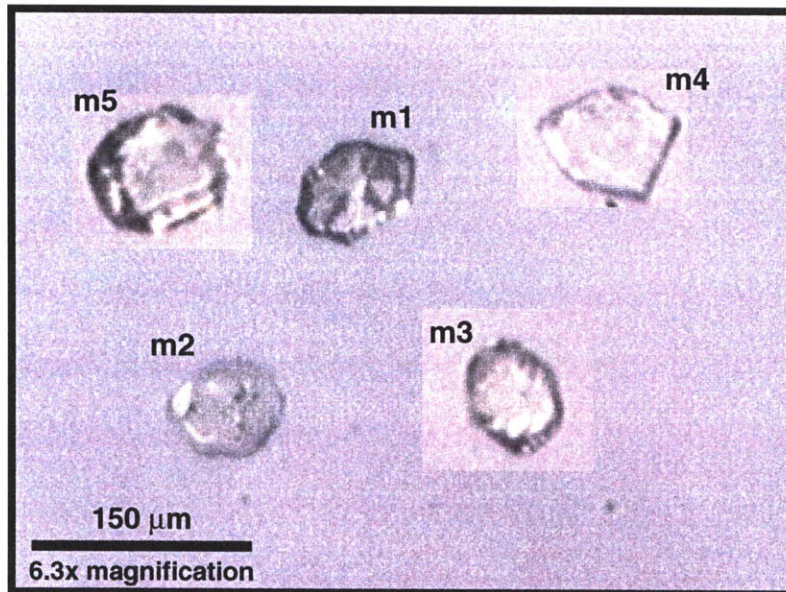
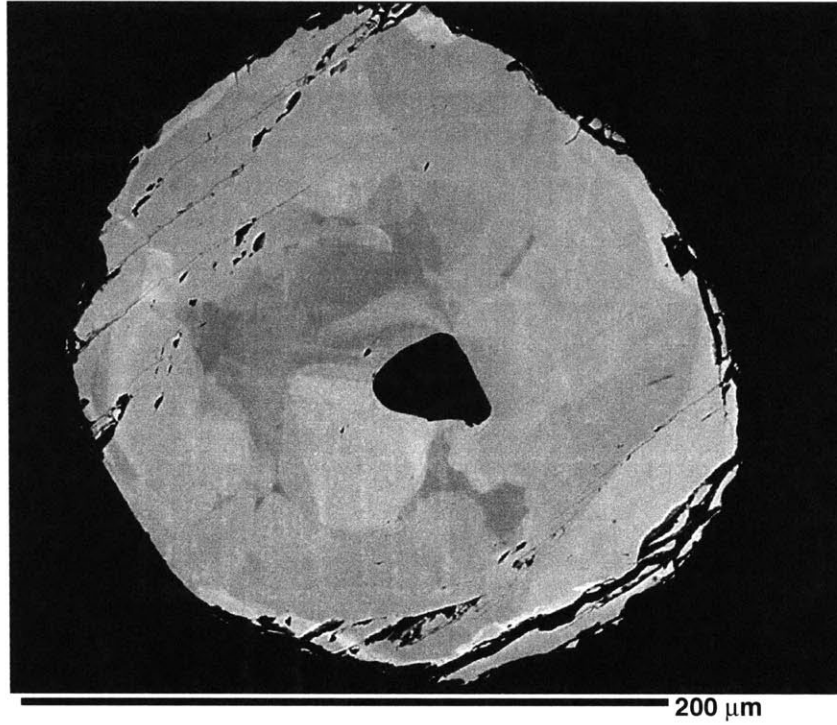


Figure 12 <continued>

a. Back-scattered Electron Image: 00KG28 m1



b. Back-scattered Electron Image: 00KG28 m3

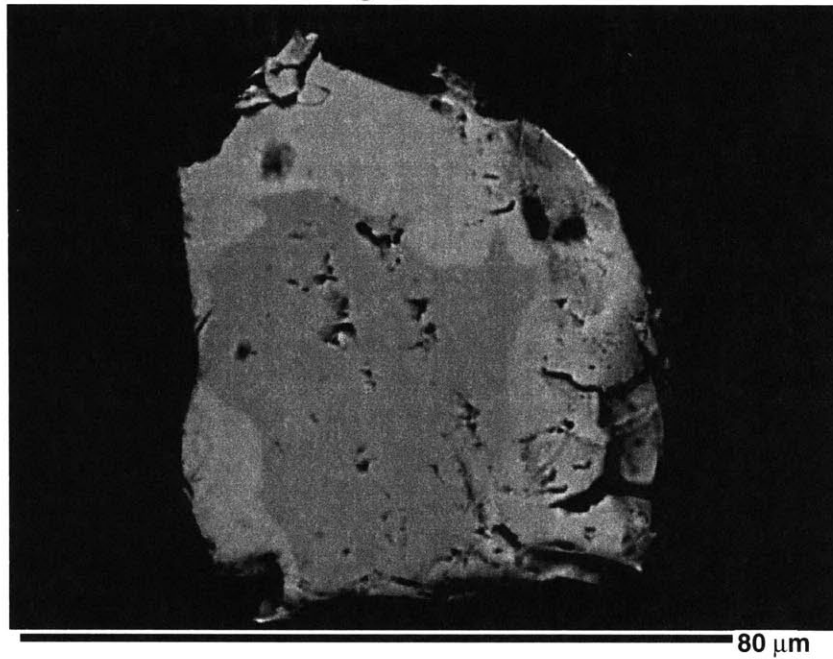
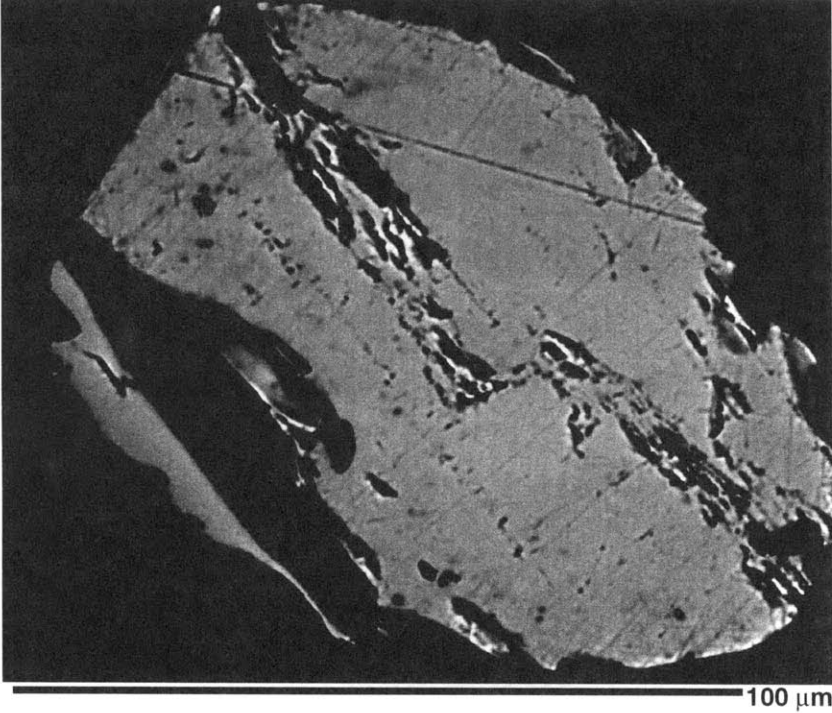


Figure 13

c. Back-scattered Electron Image: 00KG18 m1



d. Back-scattered Electron Image: 00KG18 m2

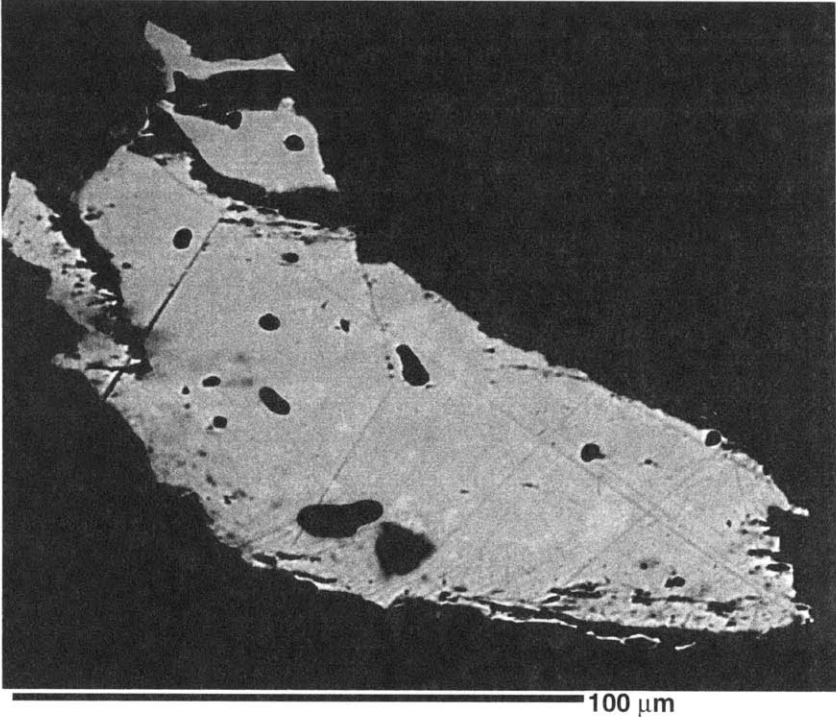
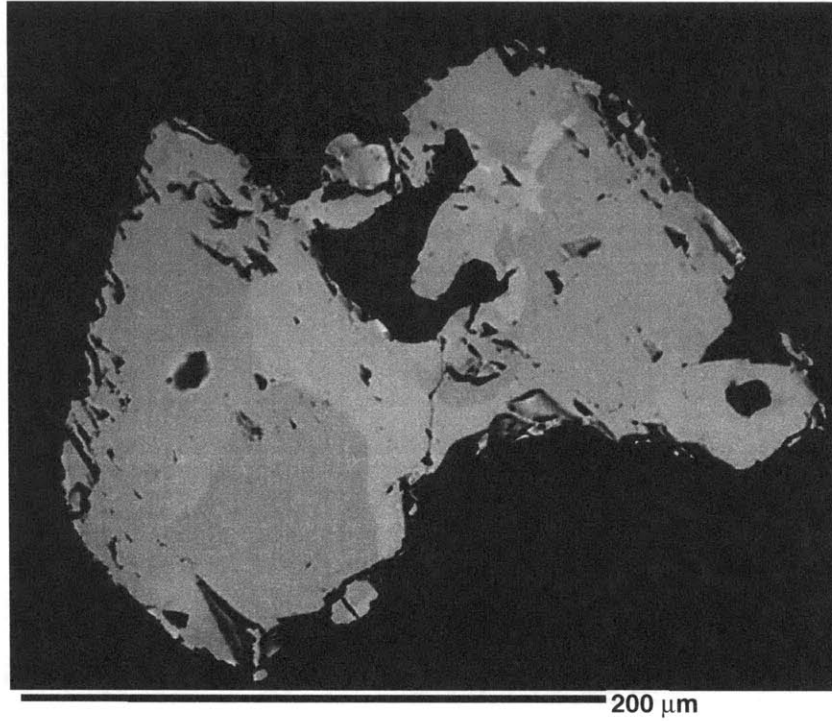


Figure 13 <continued>

e. Back-scattered Electron Image: 00KG20 m1



f. Back-scattered Electron Image: 00KG20 m2

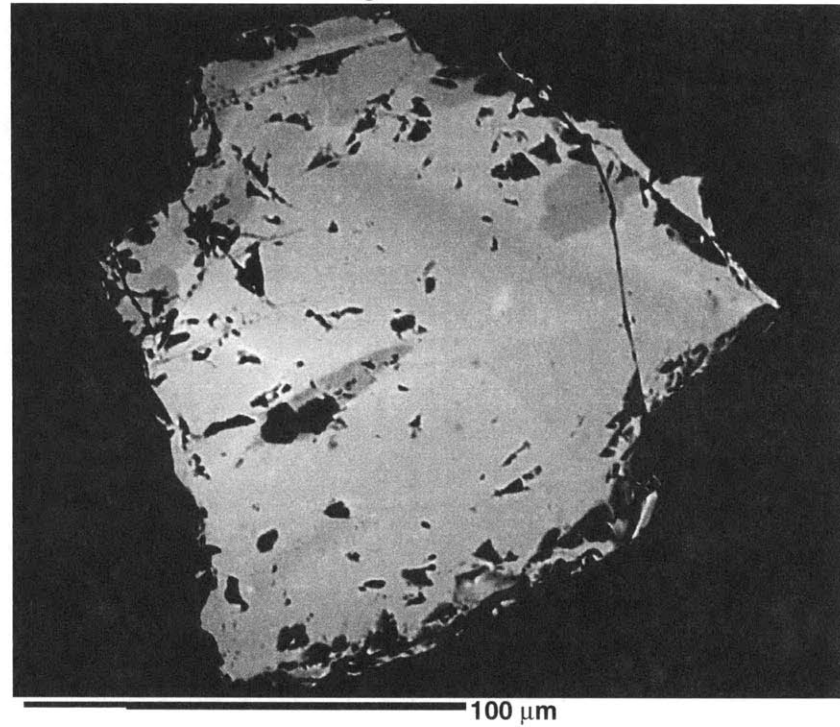
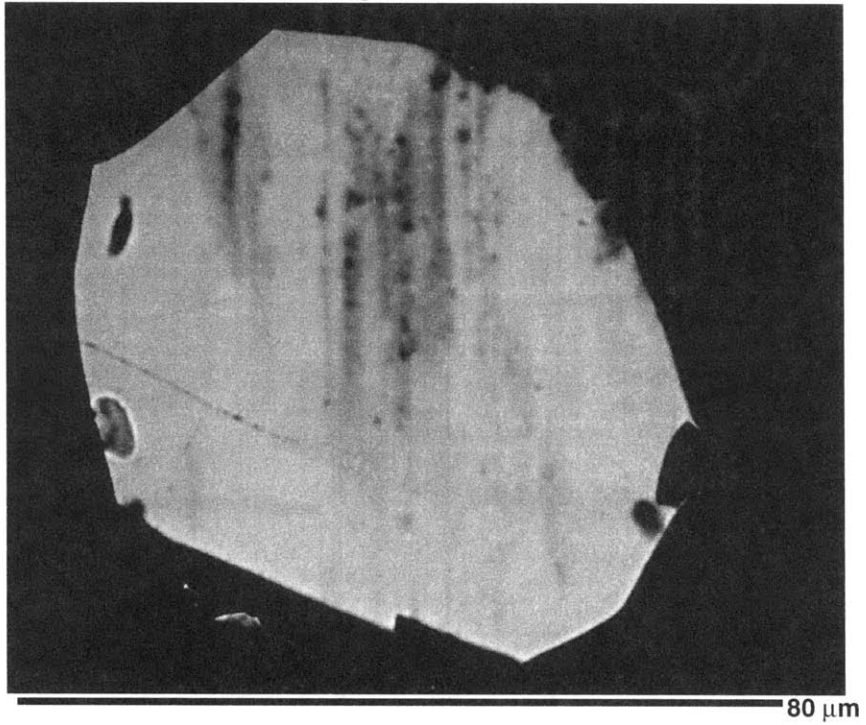


Figure 13 <continued>

g. Back-scattered Electron Image: 00KG31 m1



h. Back-scattered Electron Image: 00KG31 m2

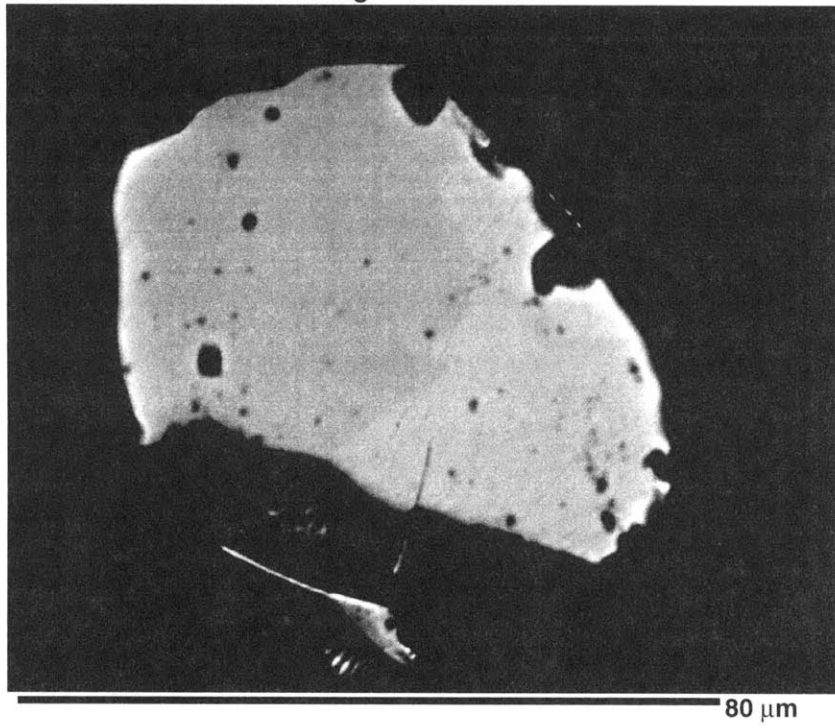


Figure 13 <continued>

Chapter 4: Exhumational history of the Mustang and Mugu granites

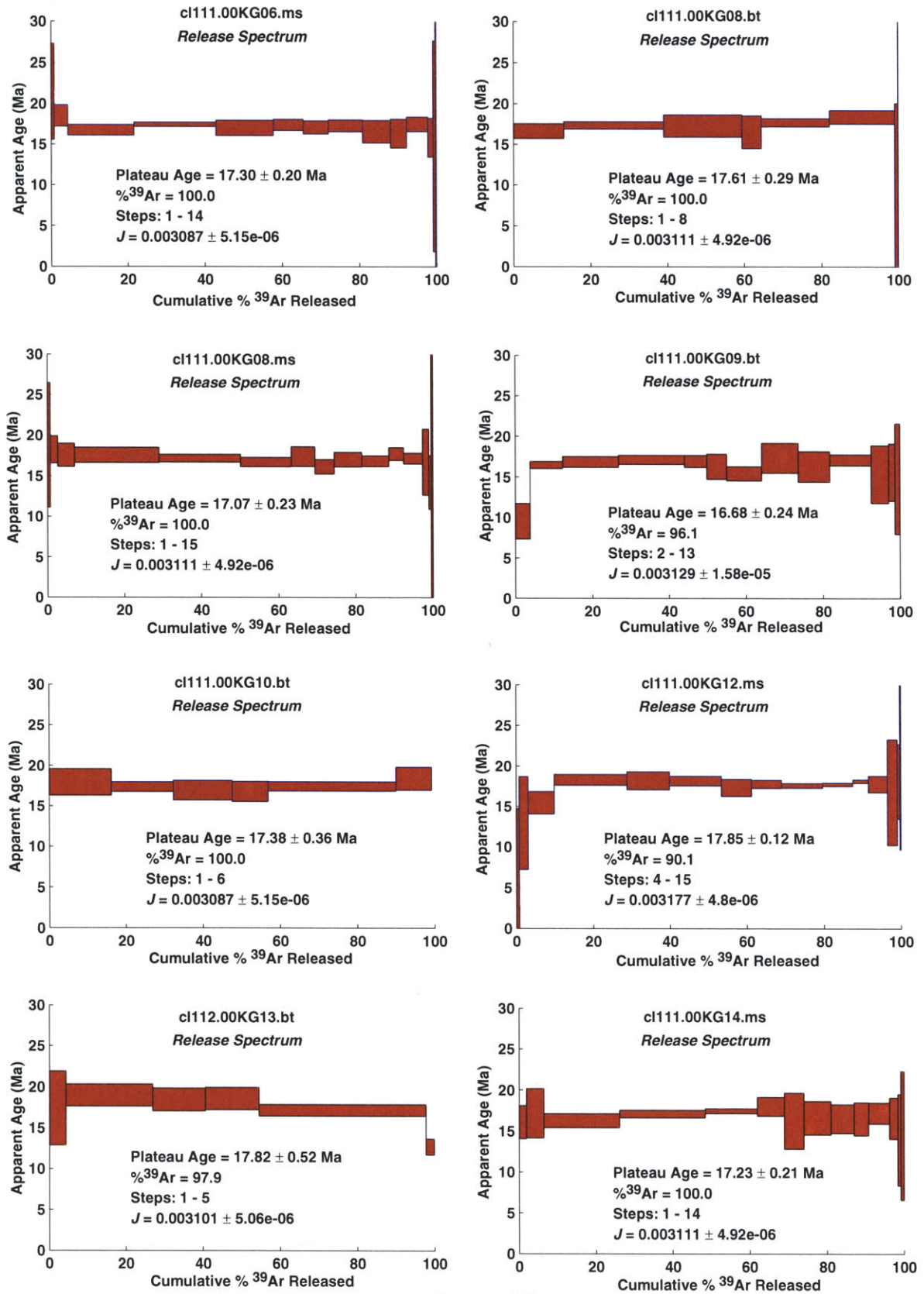


Figure 14

Chapter 4: Exhumational history of the Mustang and Mugu granites

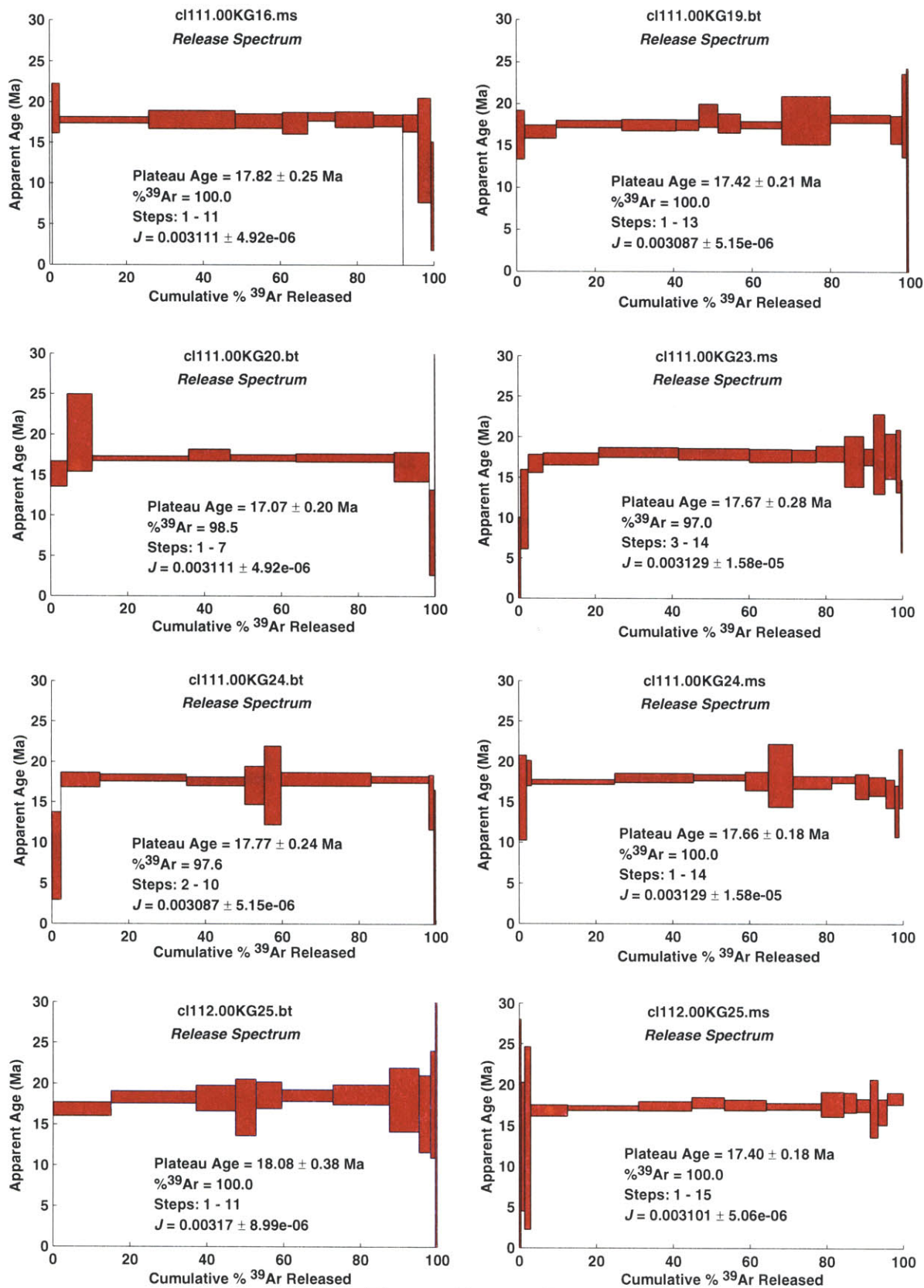


Figure 14 <continued>

Chapter 4: Exhumational history of the Mustang and Mugu granites

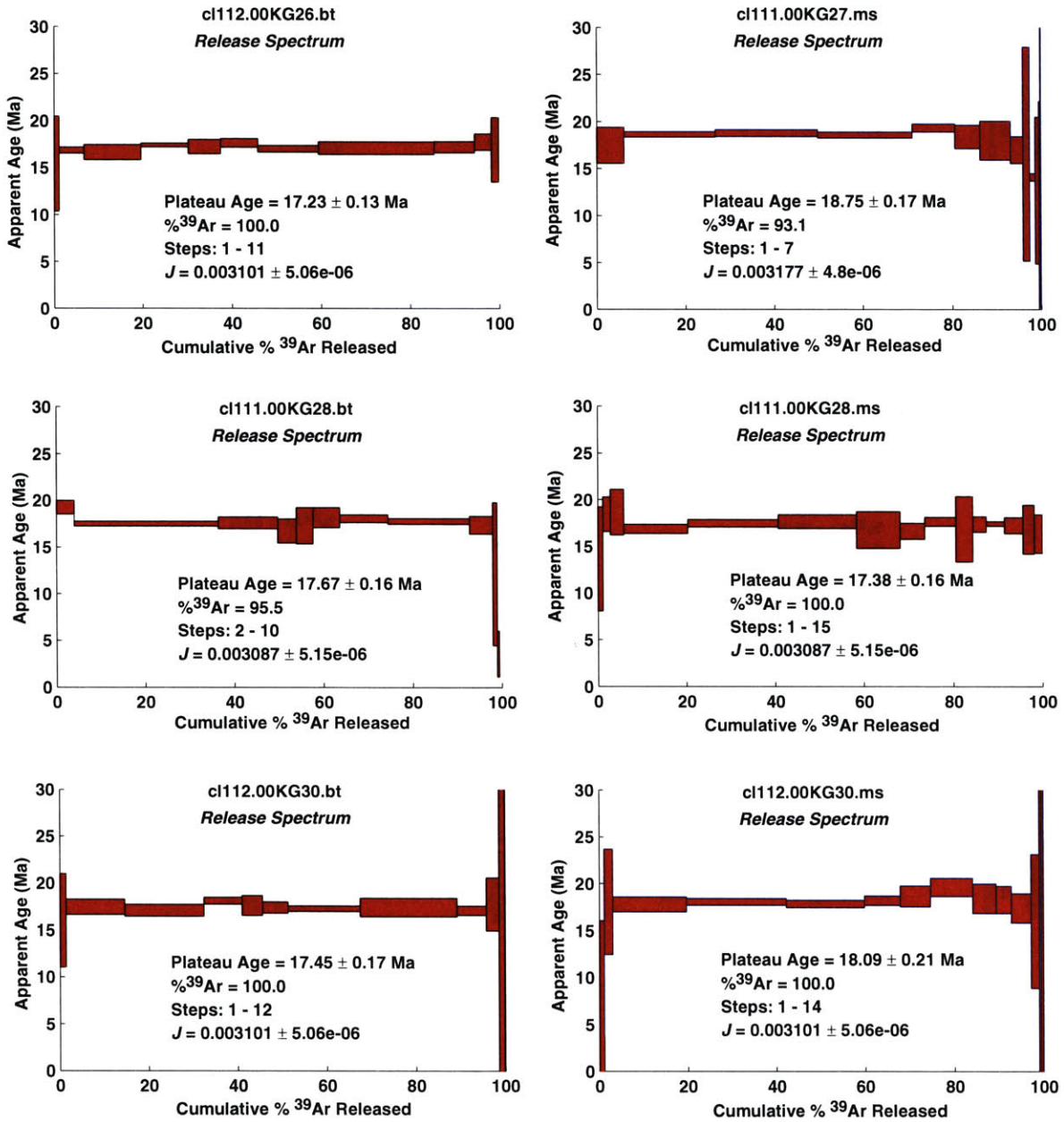


Figure 14 <continued>

Chapter 4: Exhumational history of the Mustang and Mugu granites

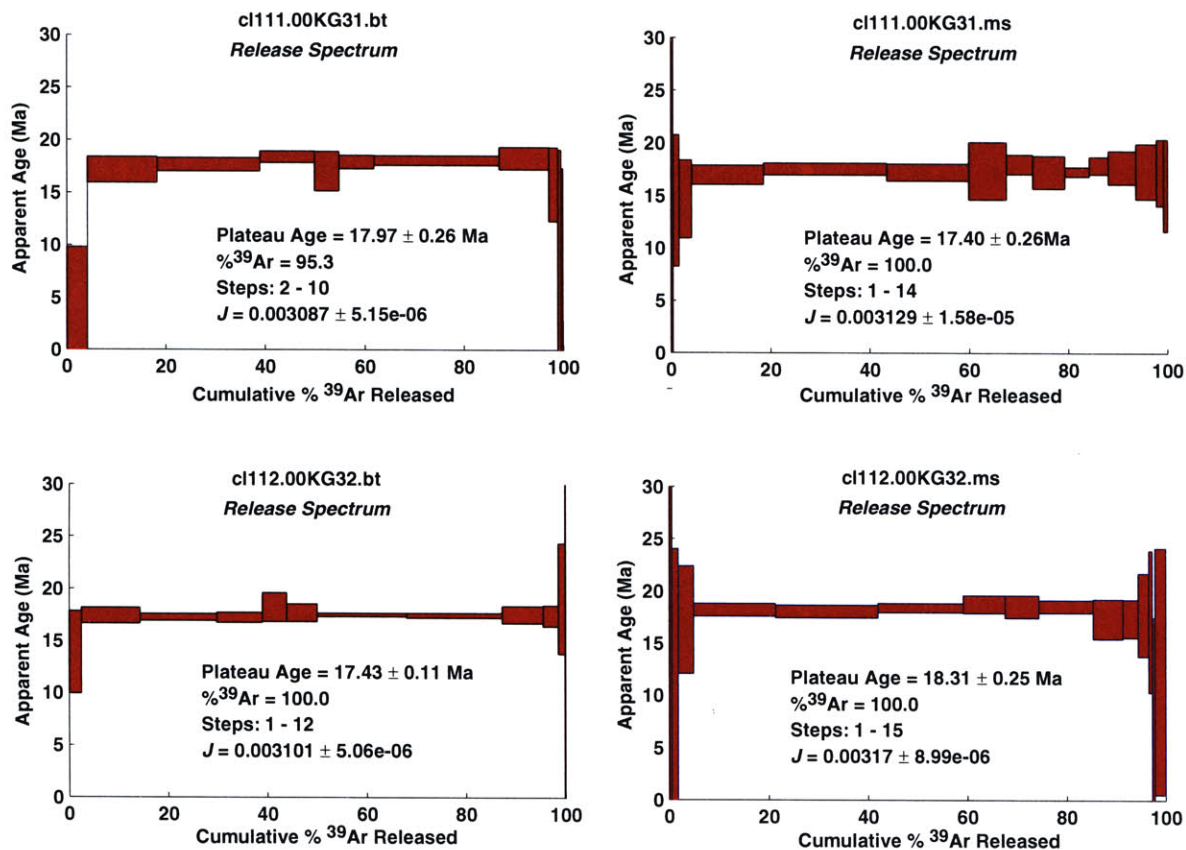


Figure 14 <continued>

Chapter 4: Exhumational history of the Mustang and Mugu granites

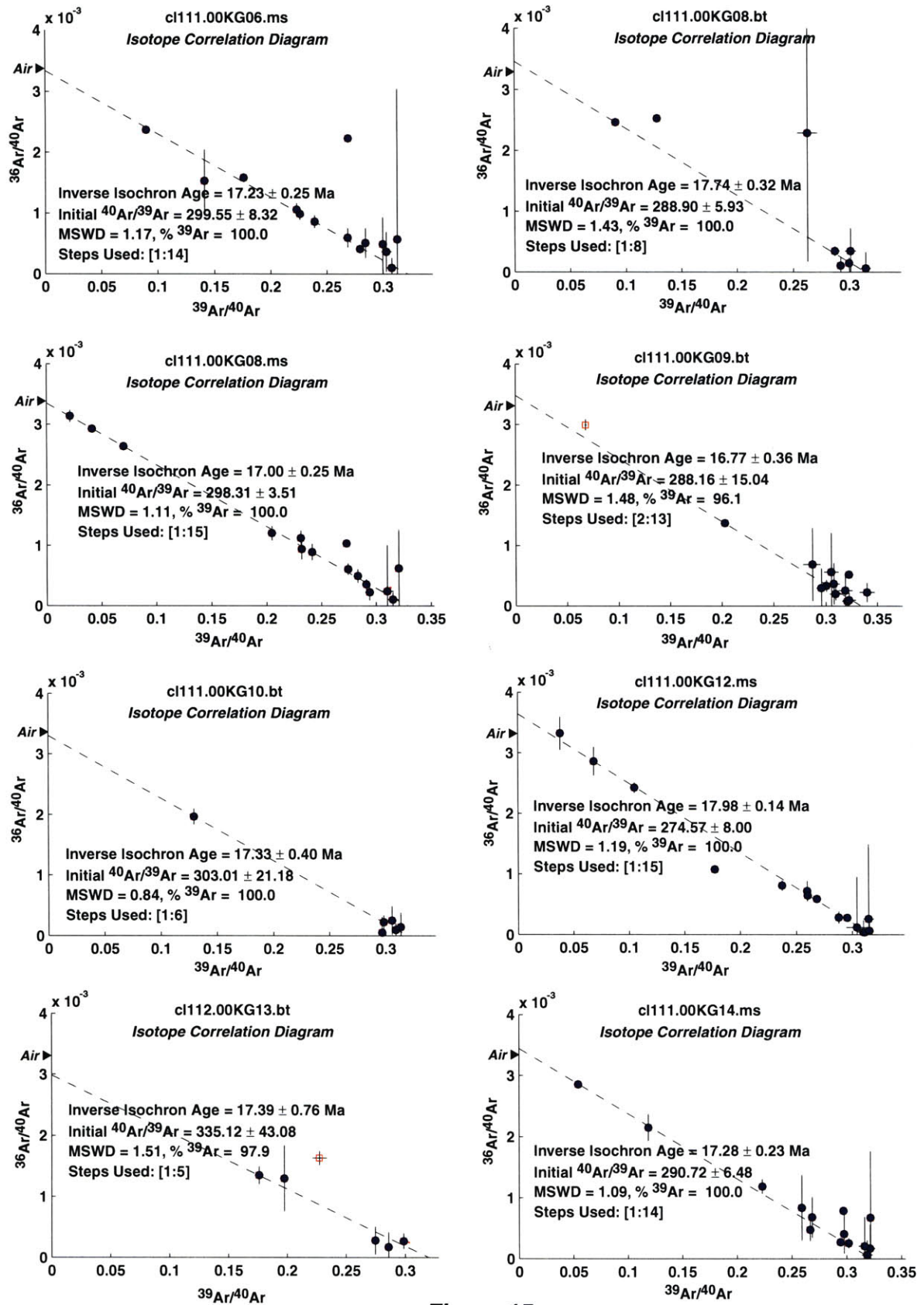


Figure 15

Chapter 4: Exhumational history of the Mustang and Mugu granites

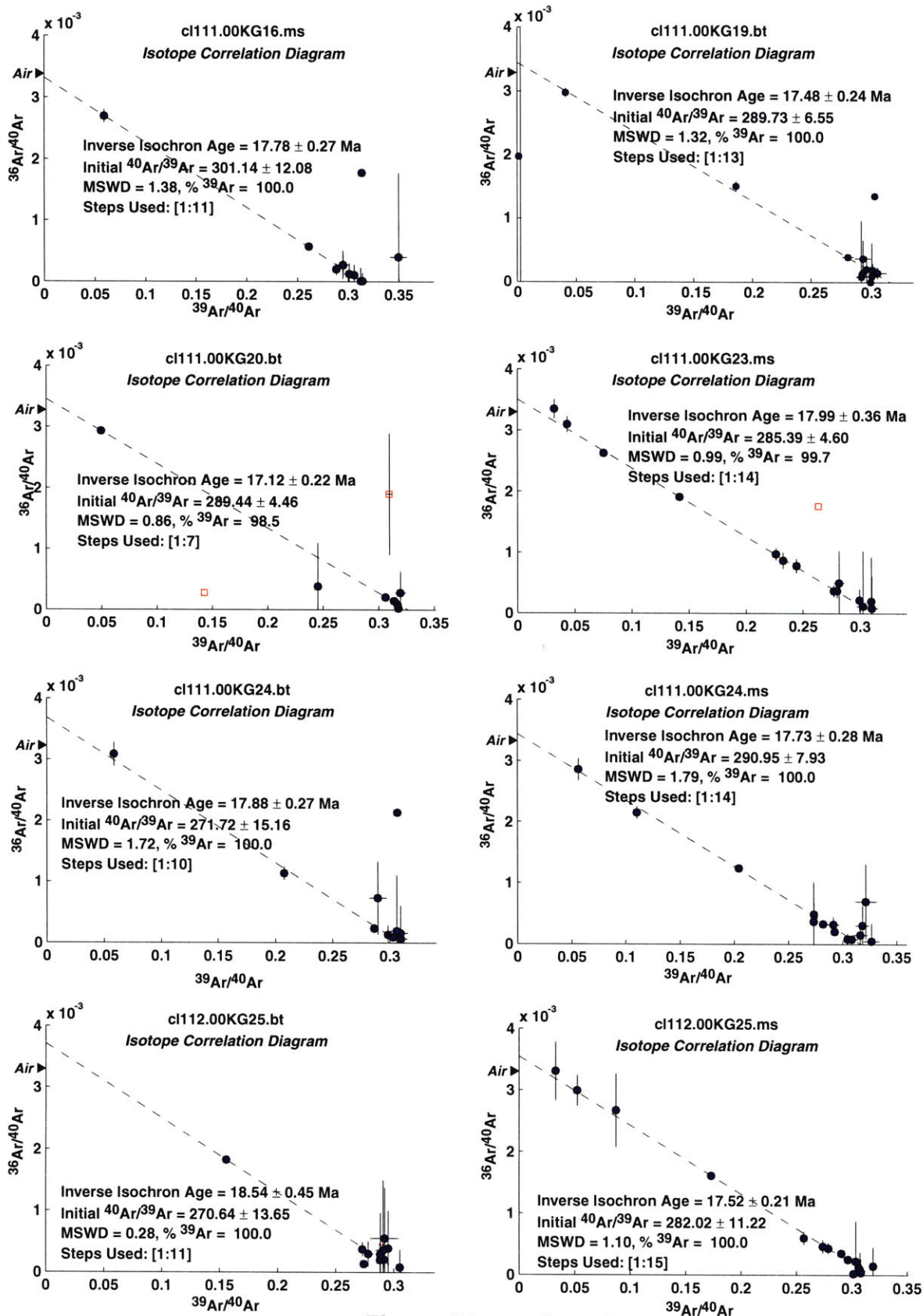


Figure 15 <continued>

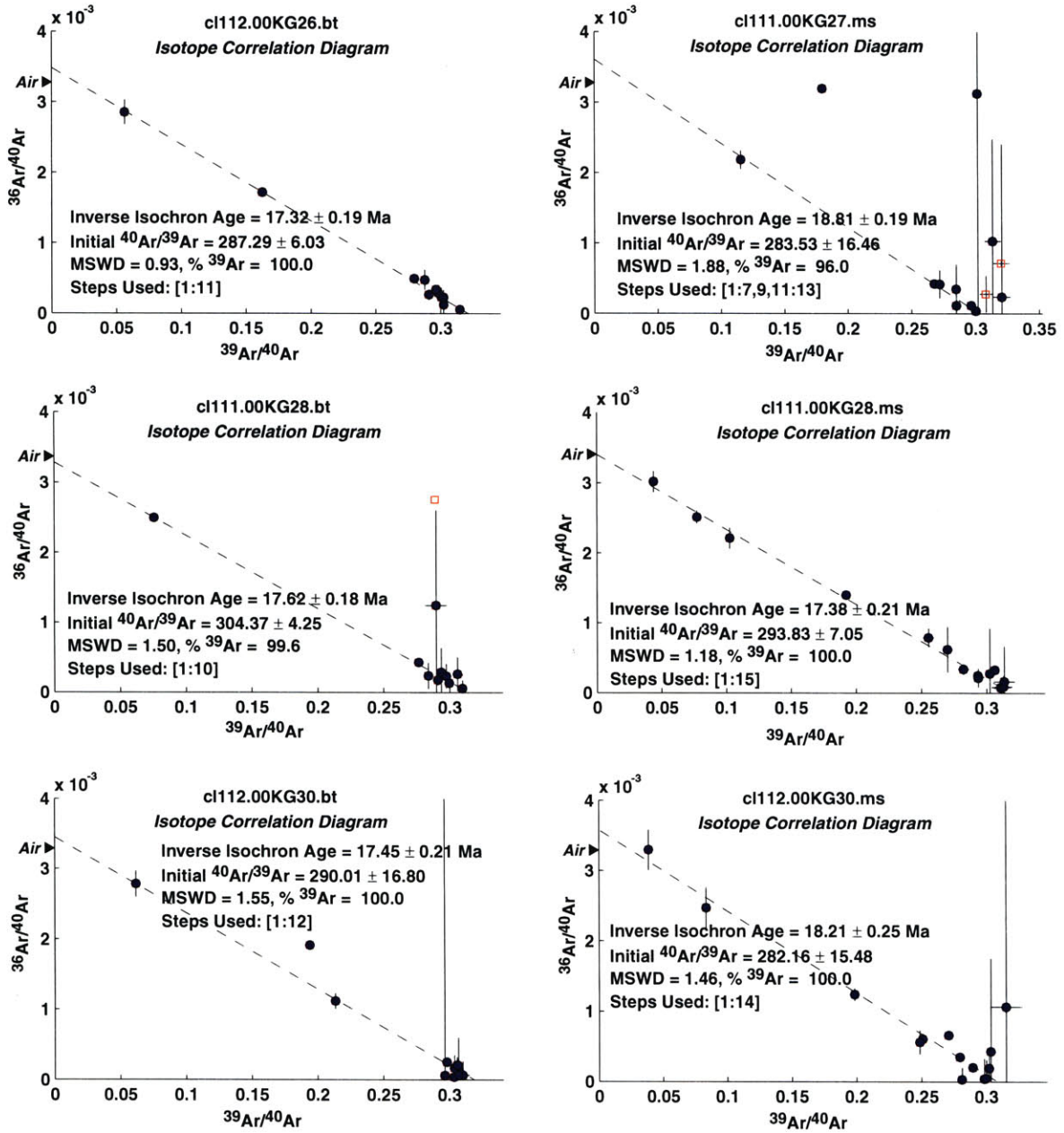


Figure 15 <continued>

Chapter 4: Exhumational history of the Mustang and Mugu granites

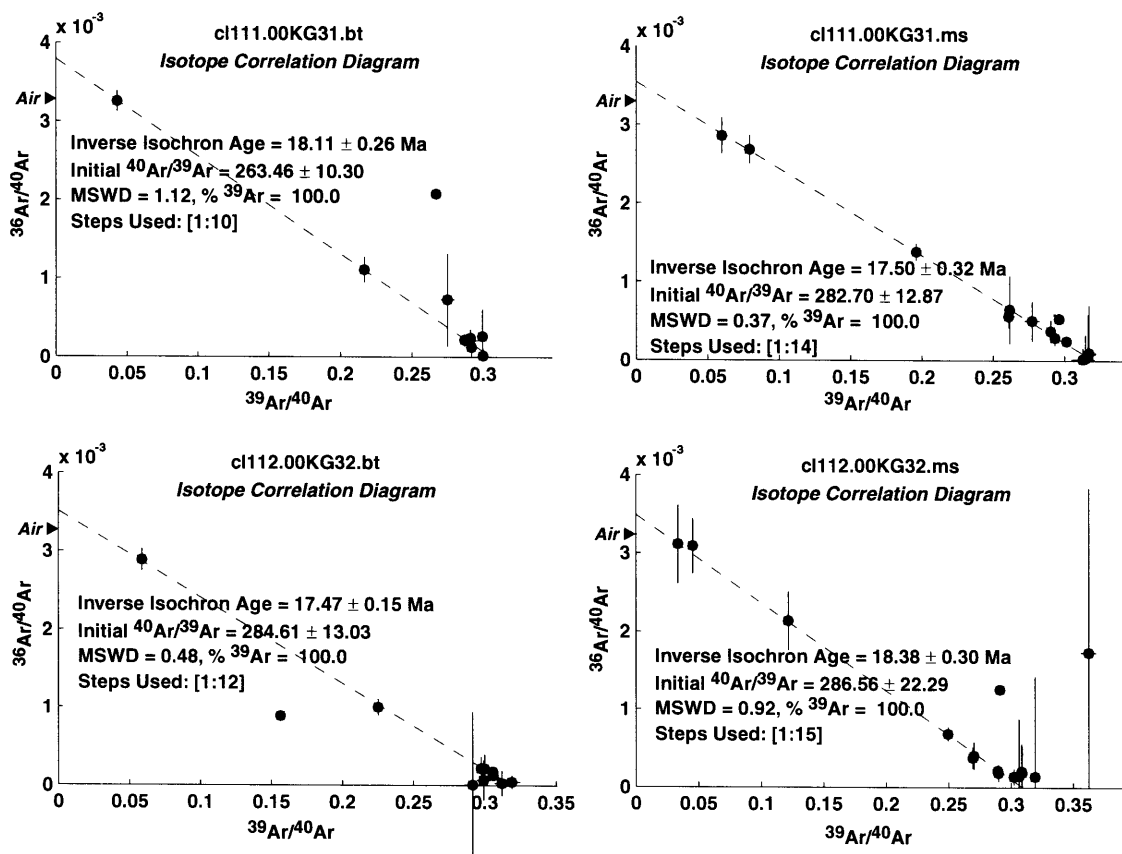


Figure 15 <continued>

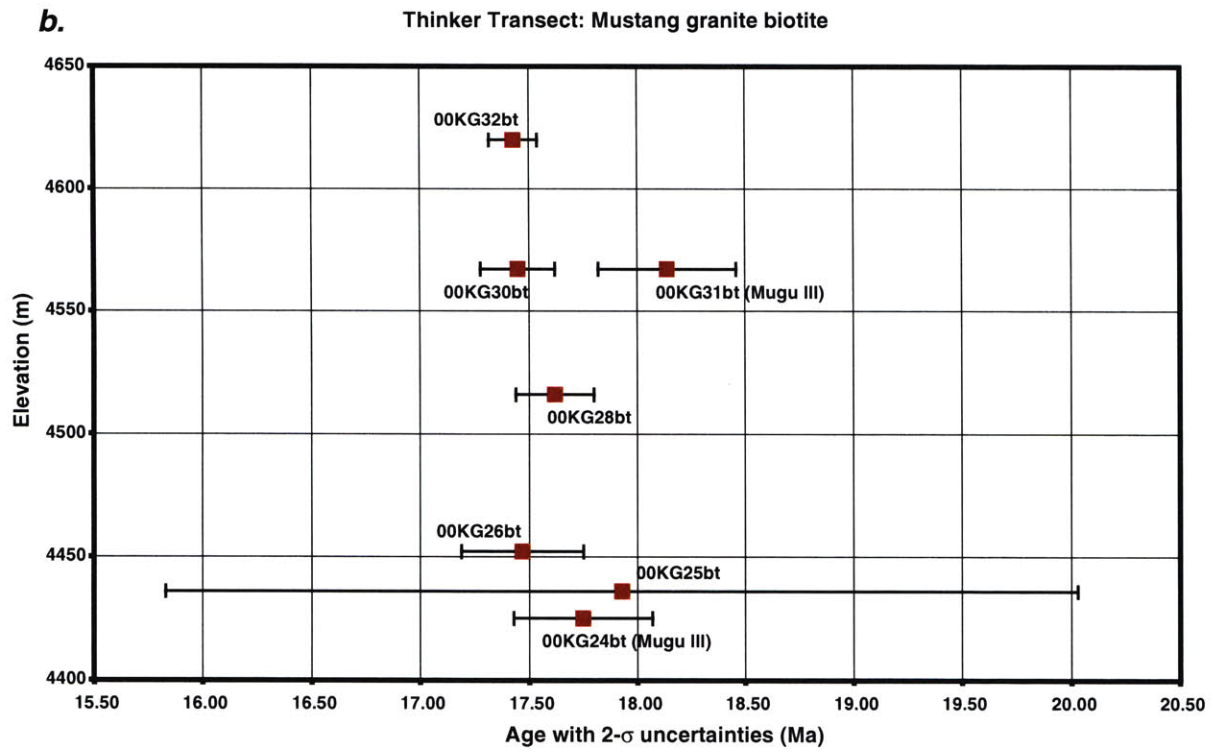
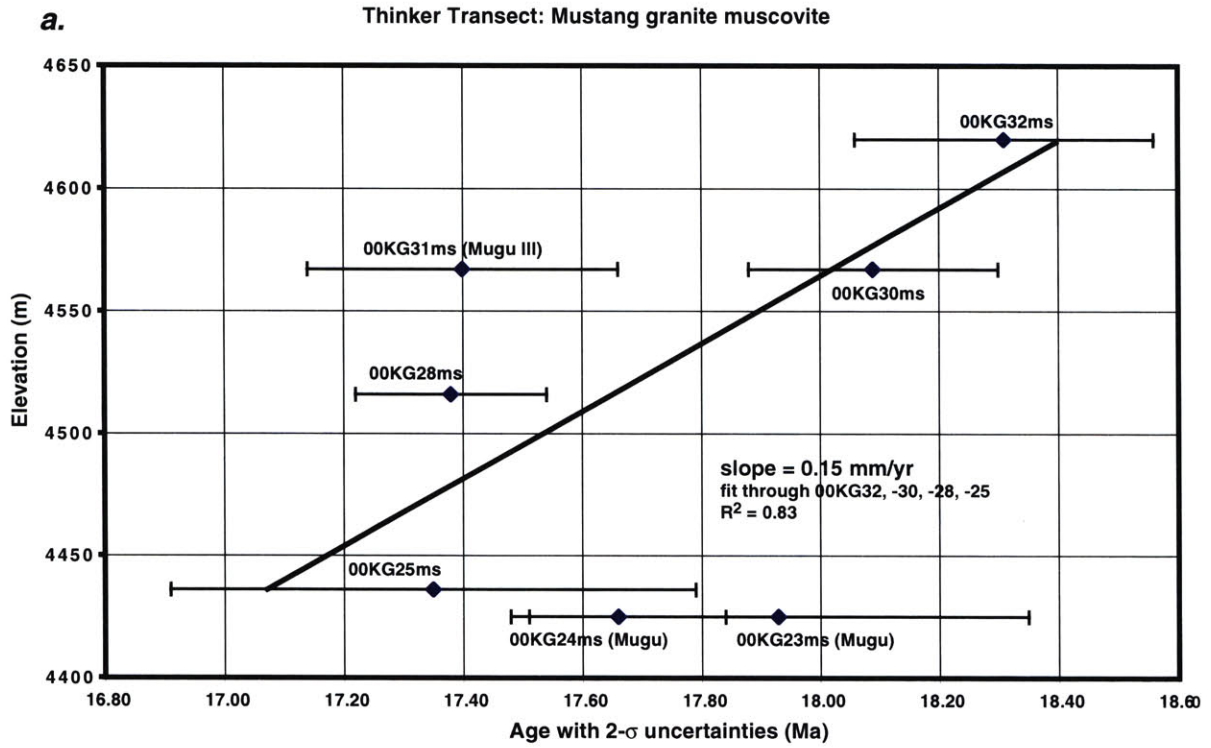


Figure 16

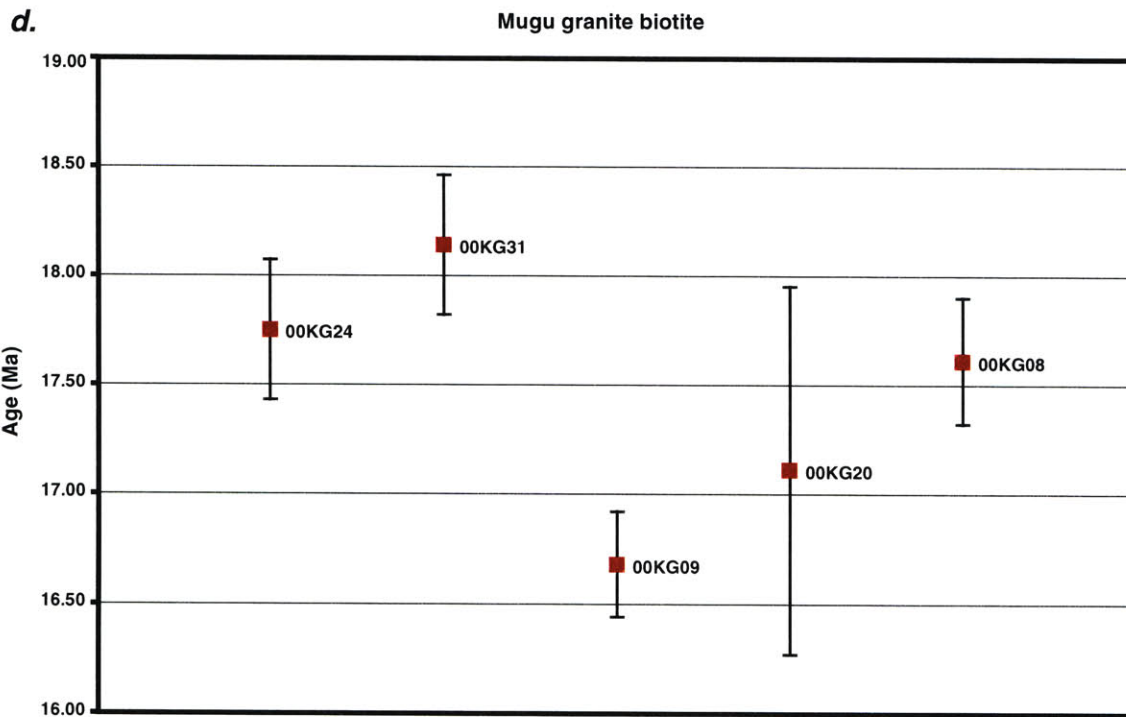
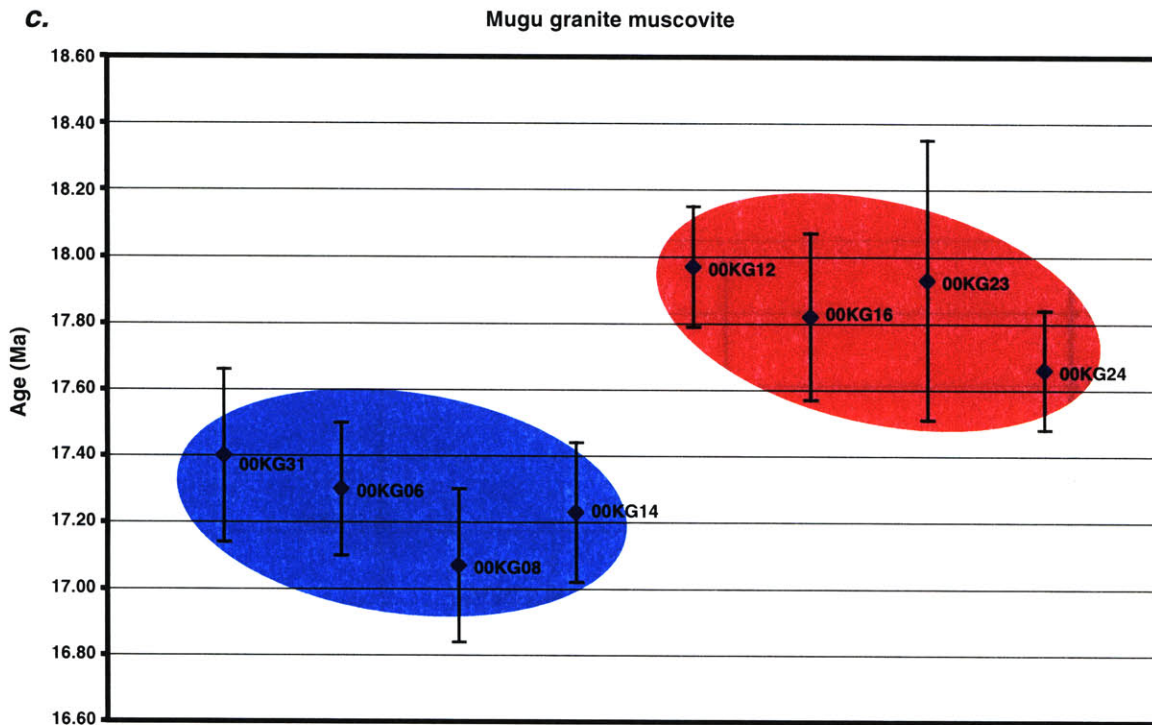


Figure 16 <continued>

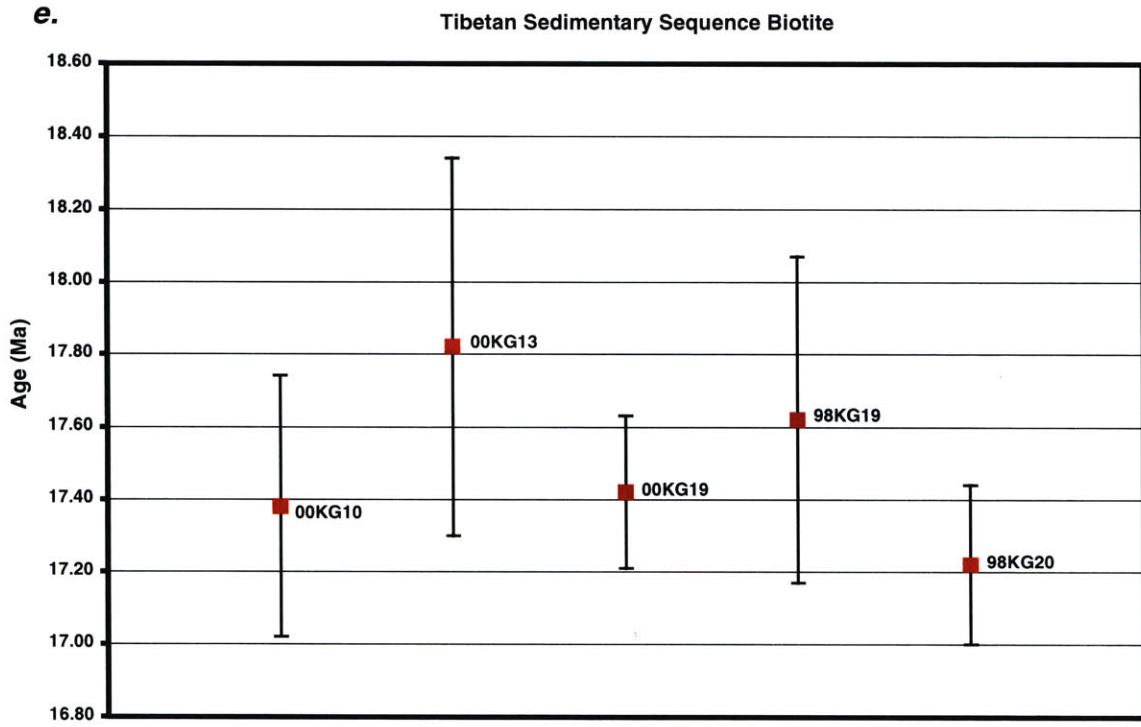


Figure 16 <continued>

Chapter 4: Exhumational history of the Mustang and Mugu granites

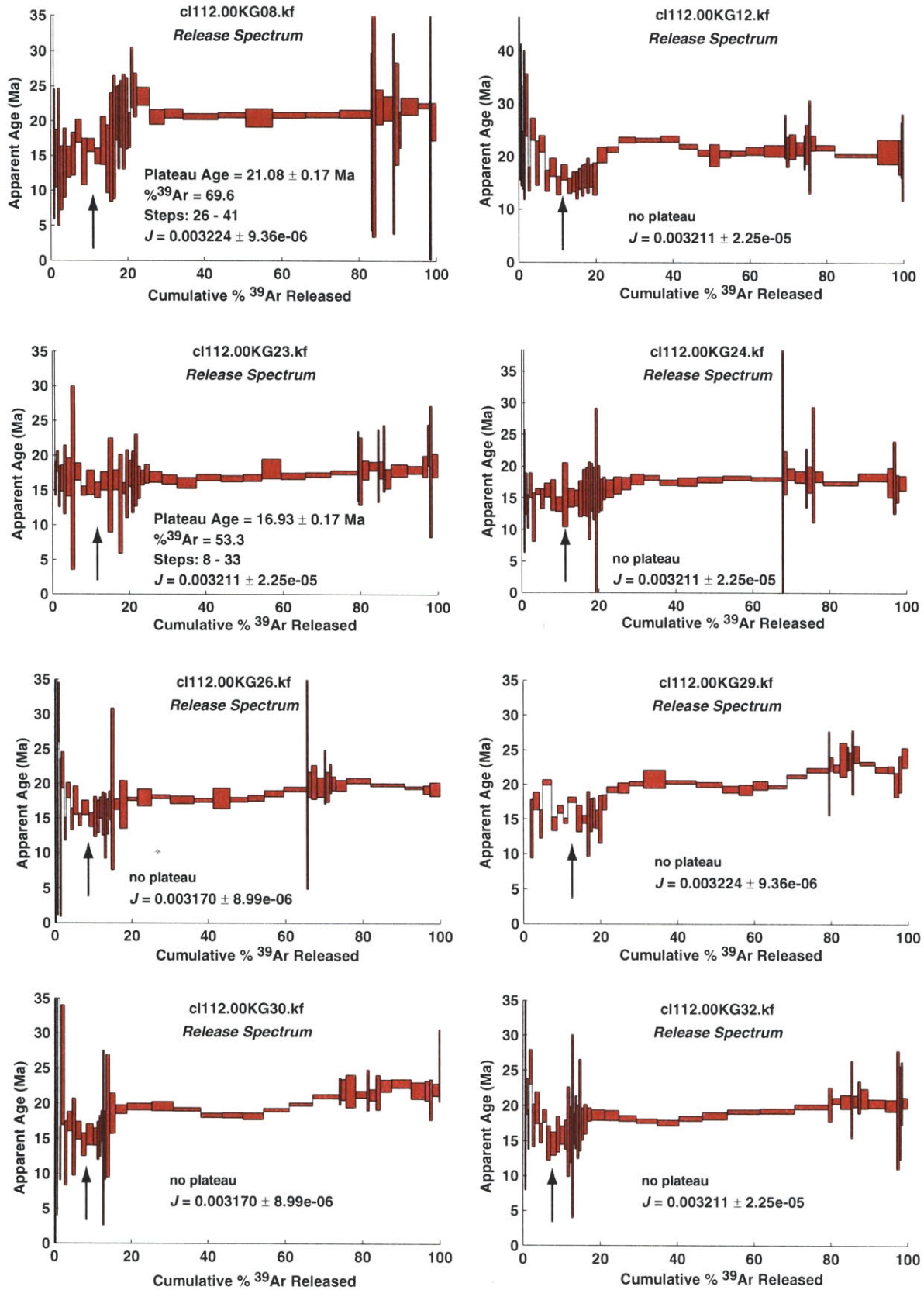


Figure 17

Chapter 4: Exhumational history of the Mustang and Mugu granites

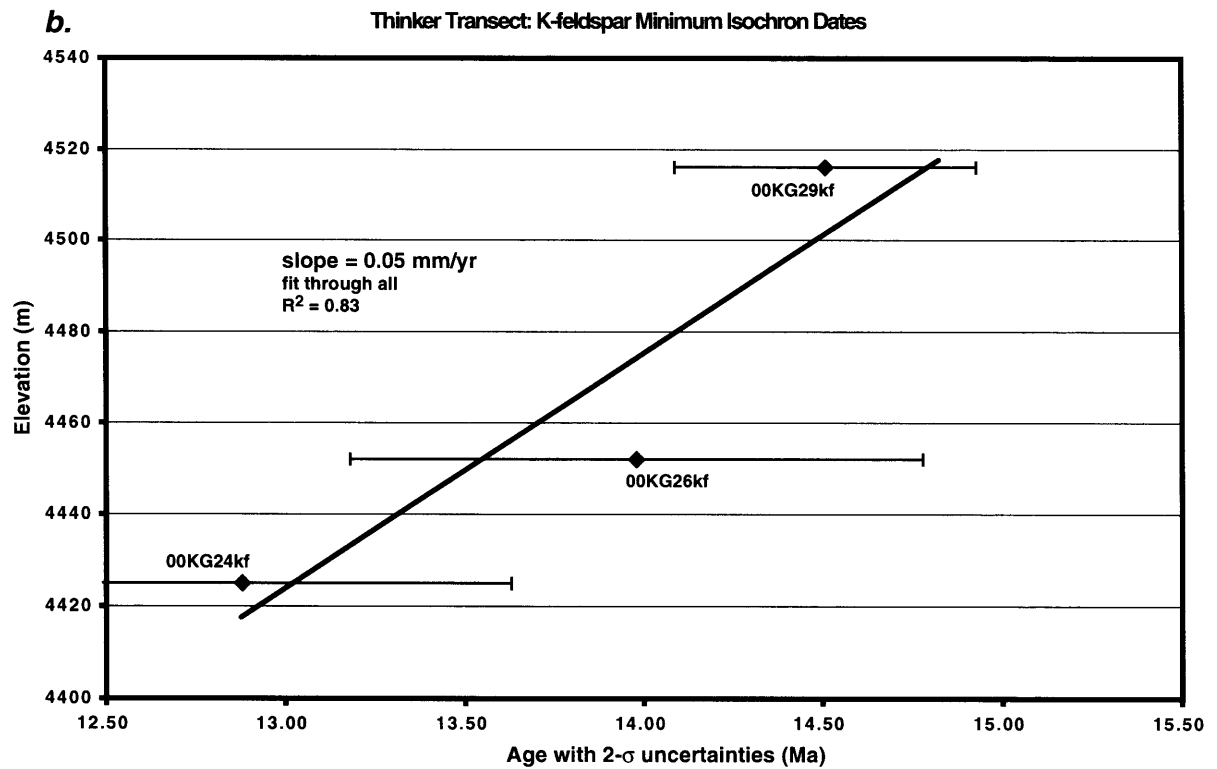
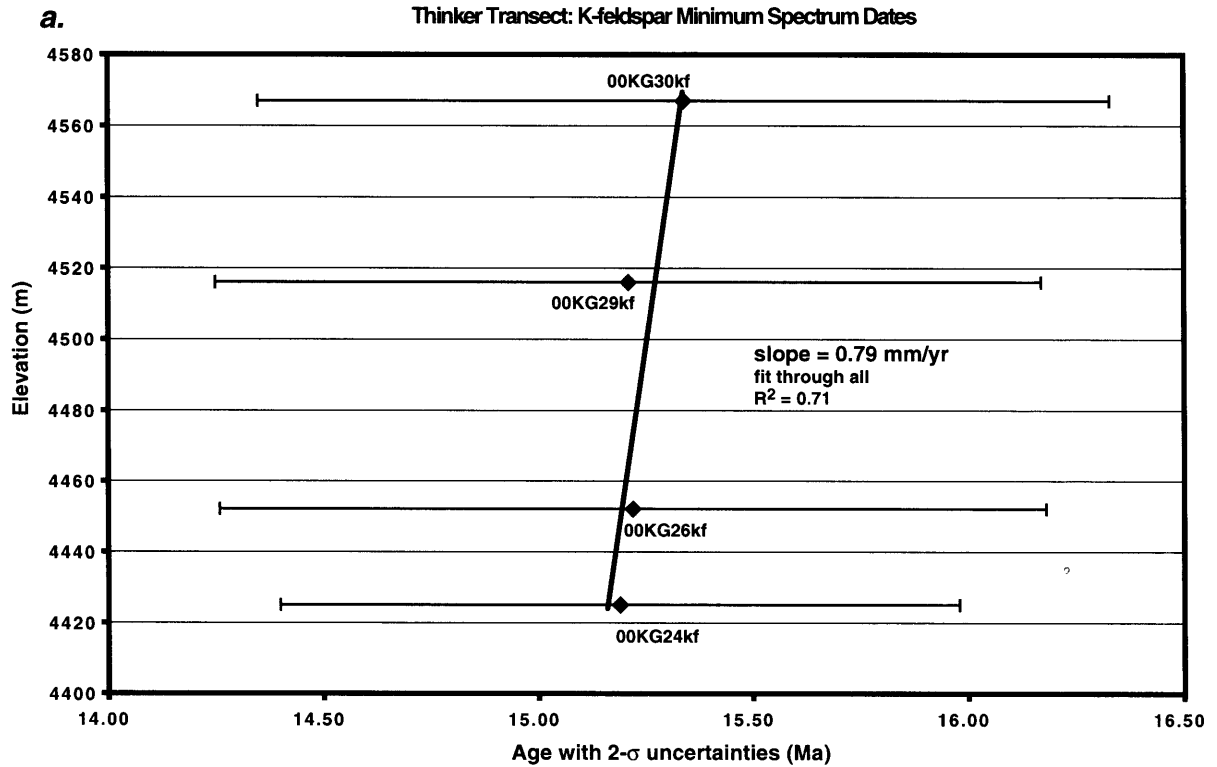


Figure 18

Chapter 4: Exhumational history of the Mustang and Mugu granites

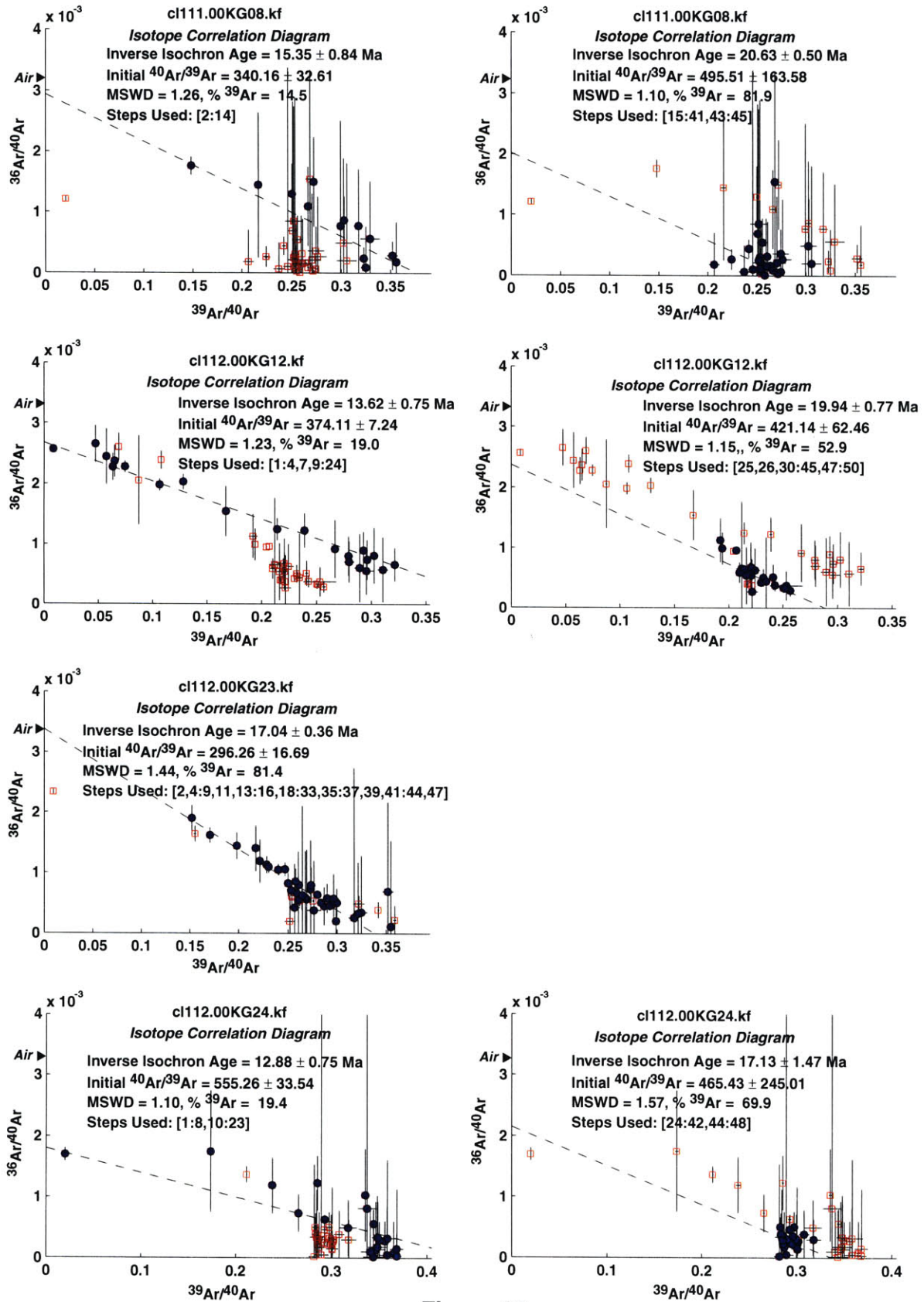


Figure 19

Chapter 4: Exhumational history of the Mustang and Mugu granites

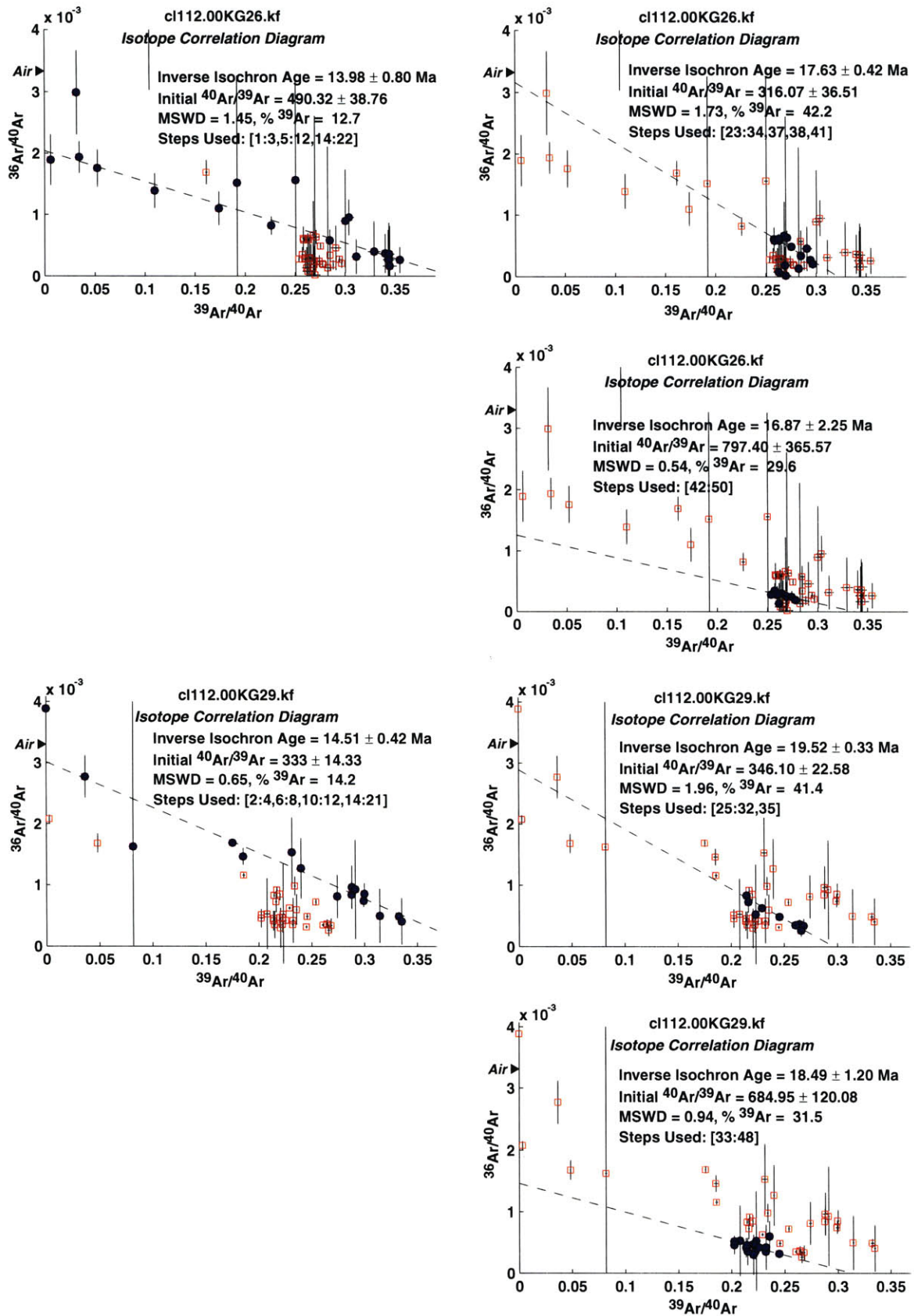


Figure 19 <continued>

Chapter 4: Exhumational history of the Mustang and Mugu granites

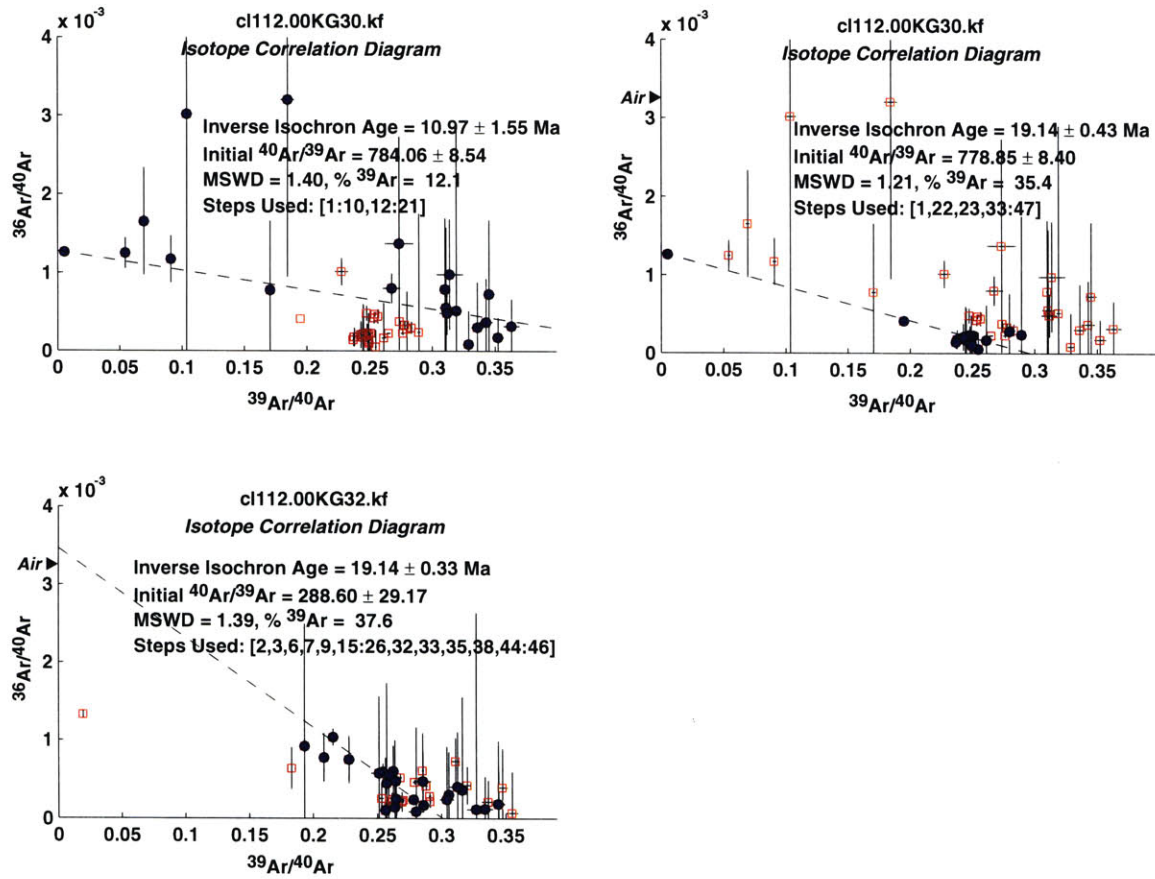


Figure 19 <continued>

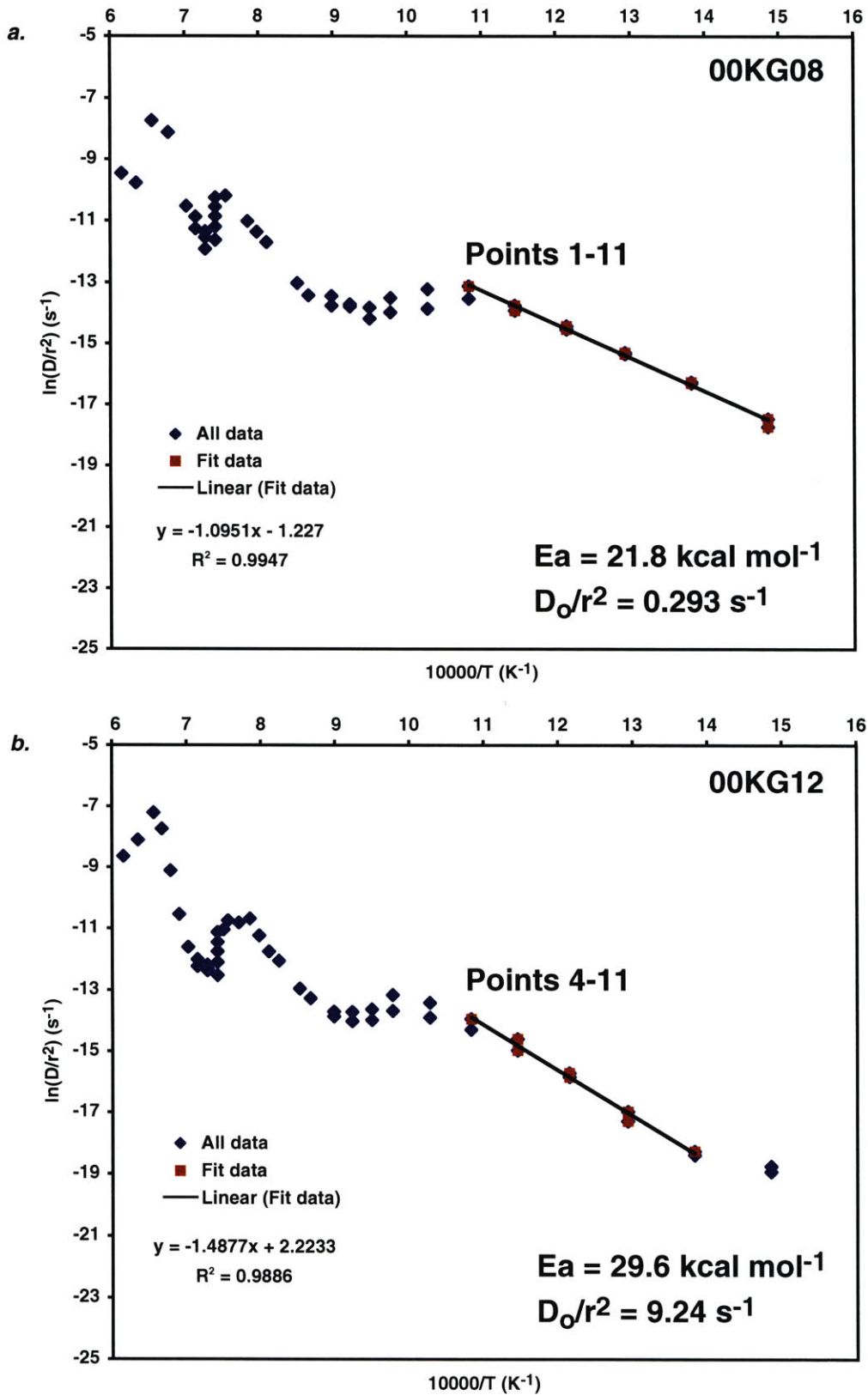


Figure 20

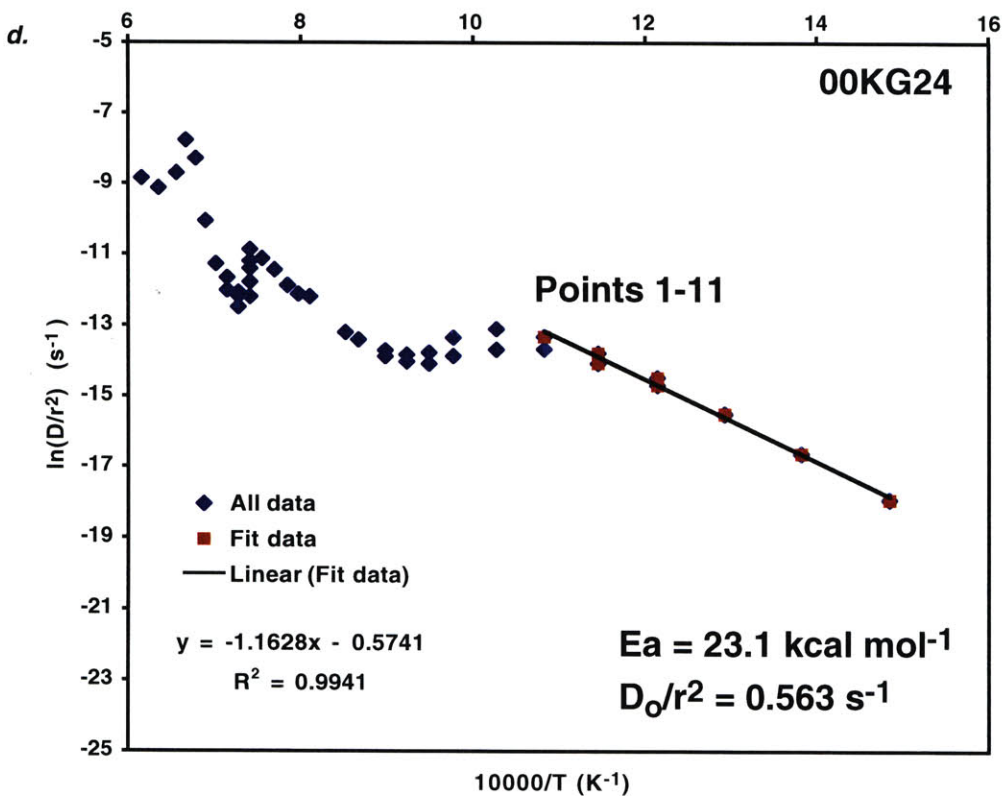
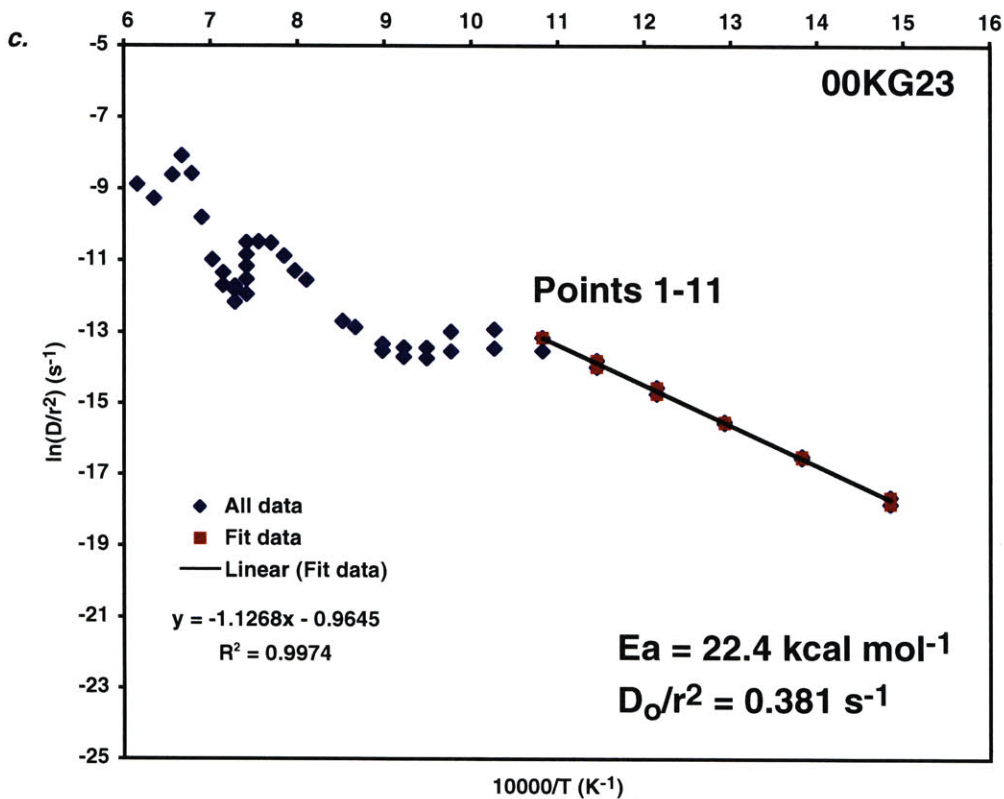


Figure 20 <continued>

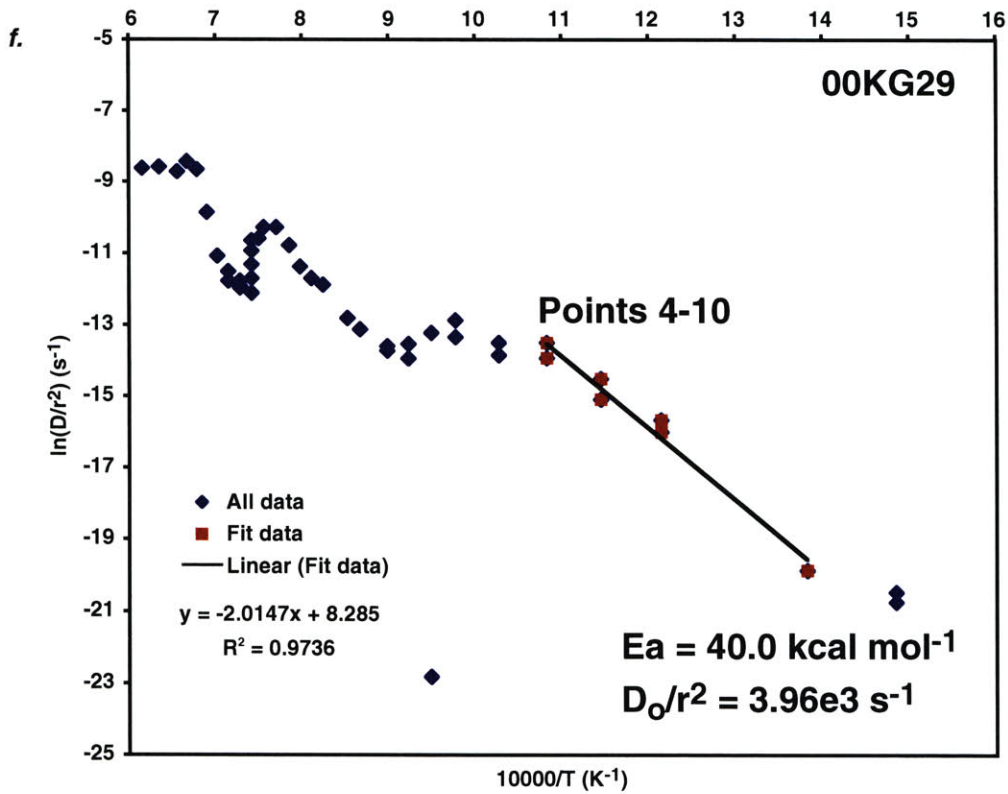
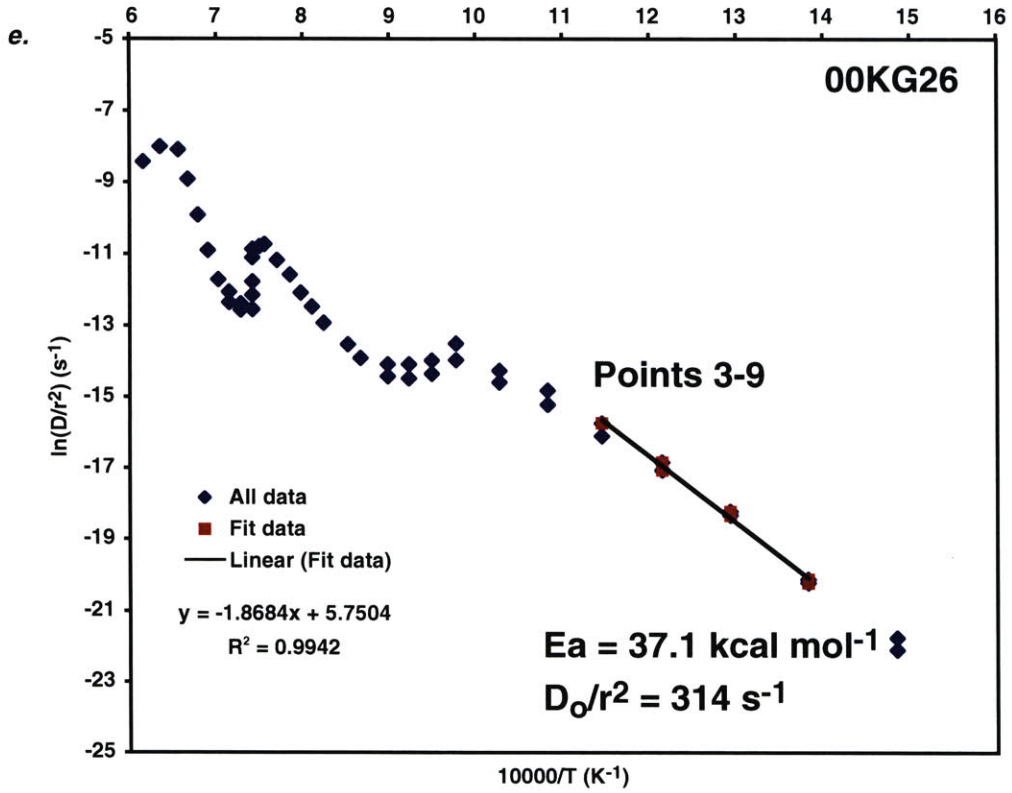


Figure 20 <continued>

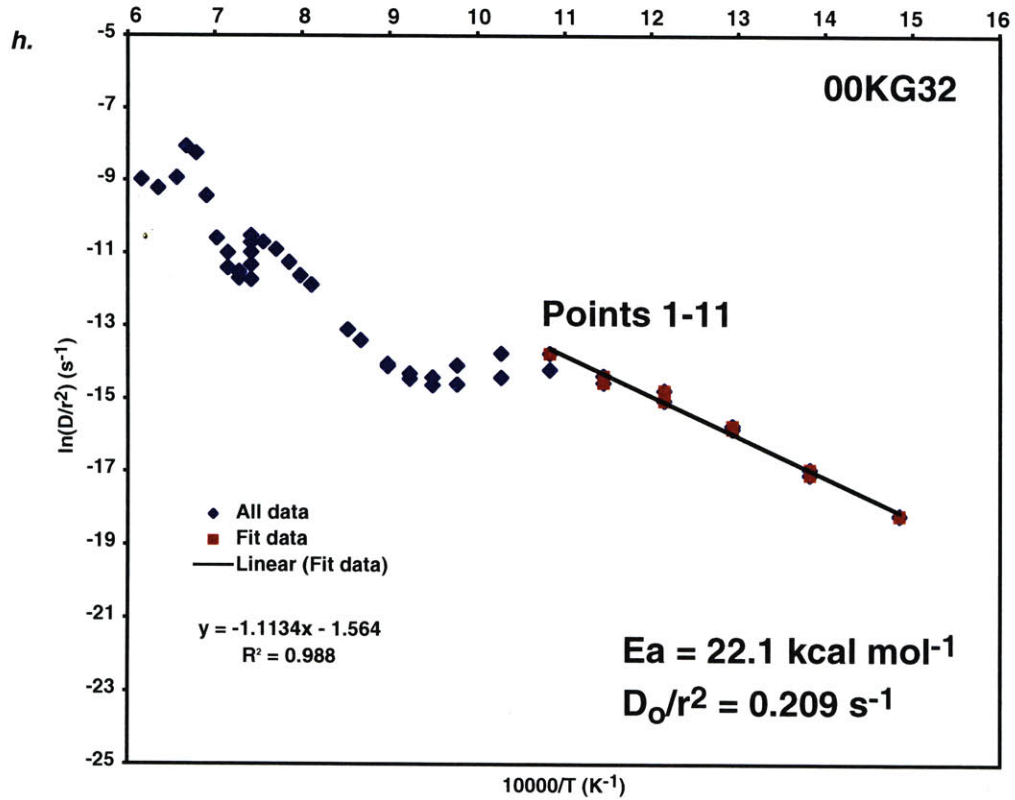
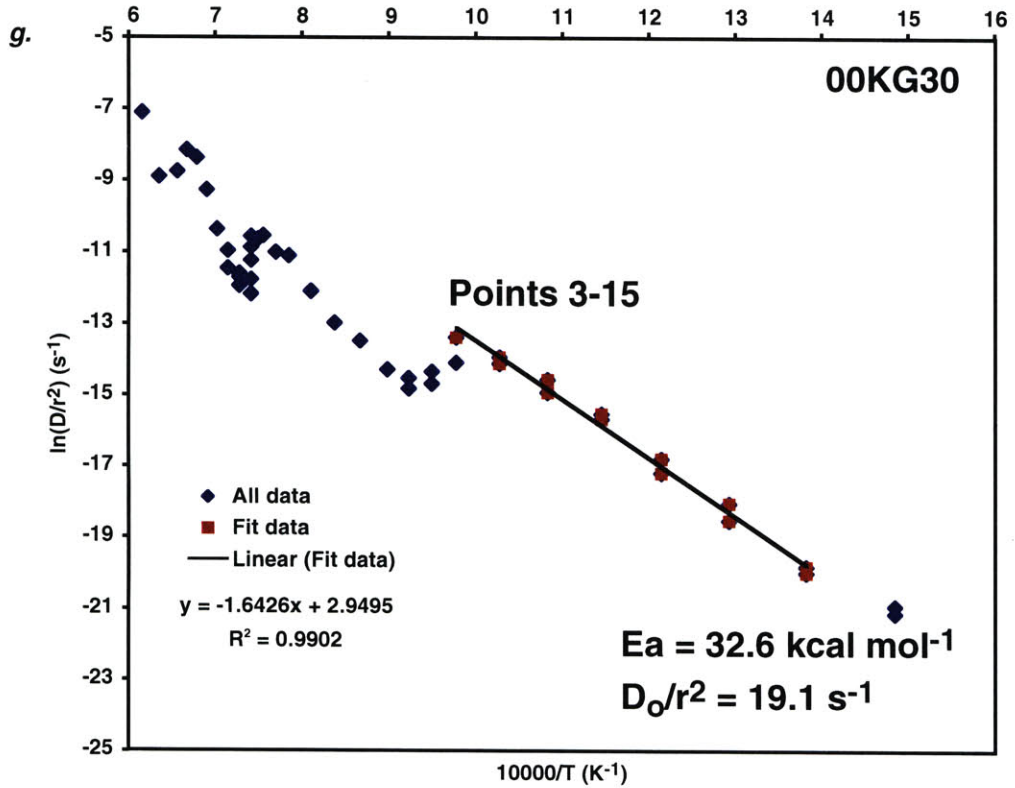


Figure 20 <continued>

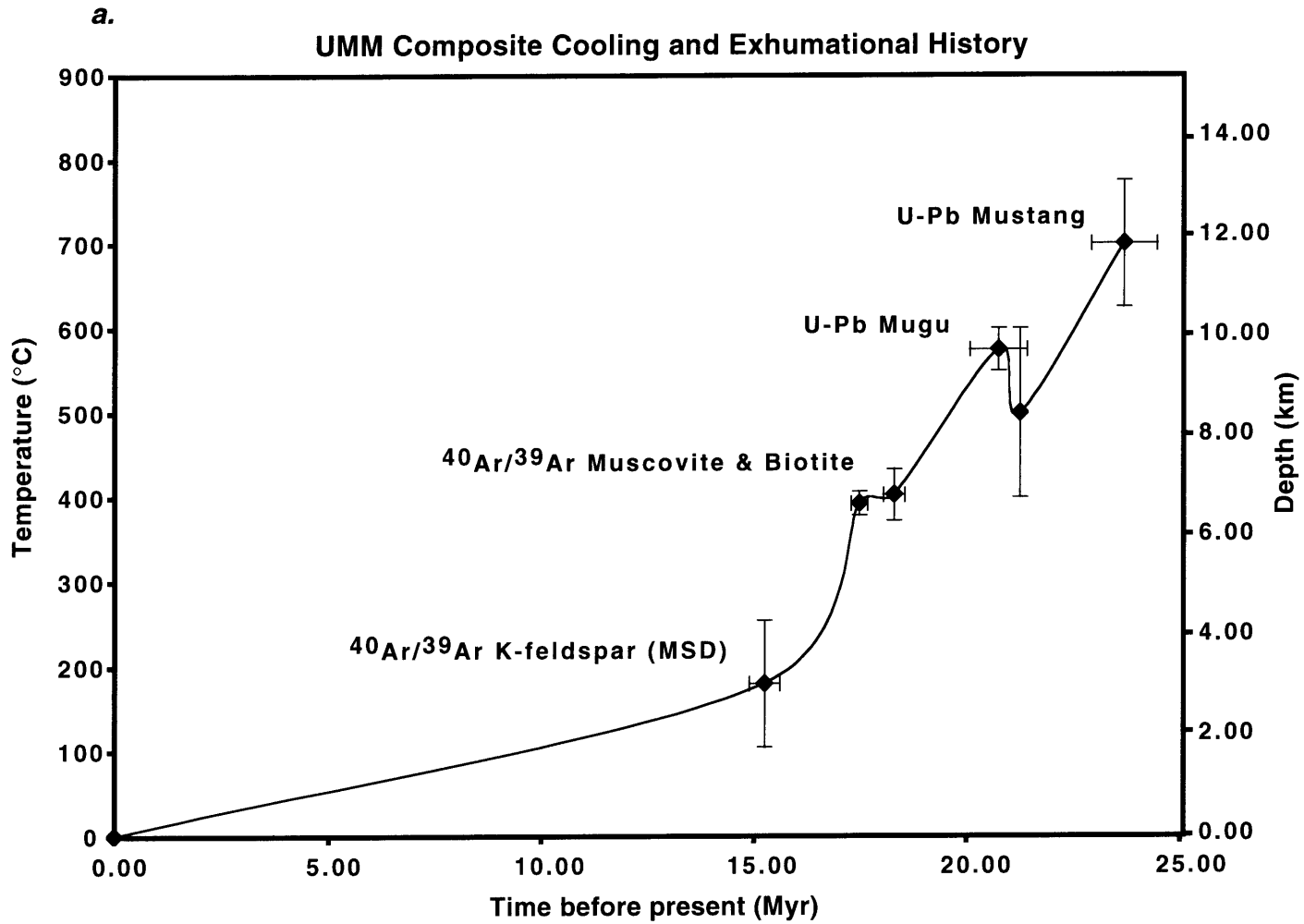


Figure 21

b.

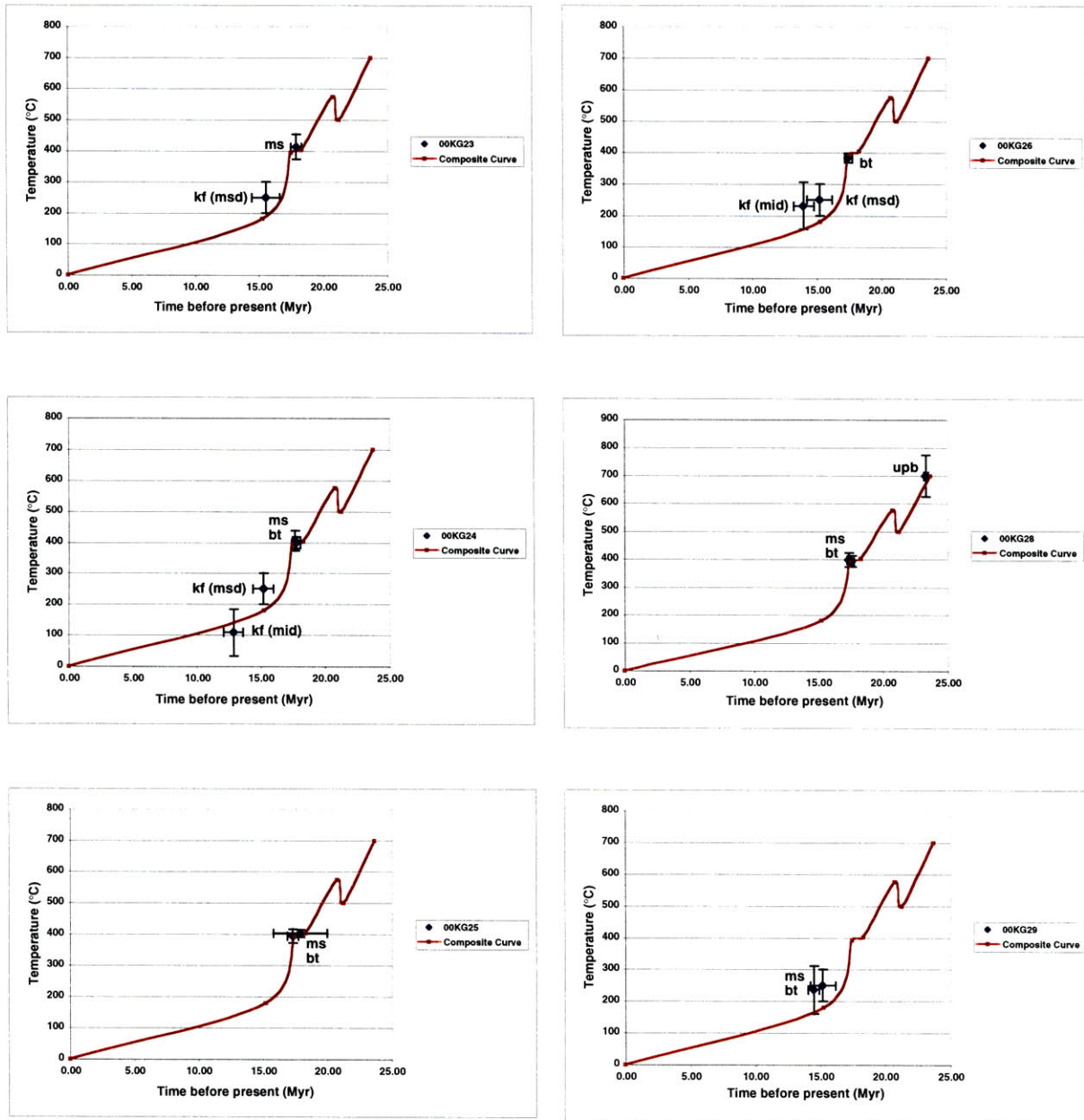


Figure 21 <continued>

b. <continued>

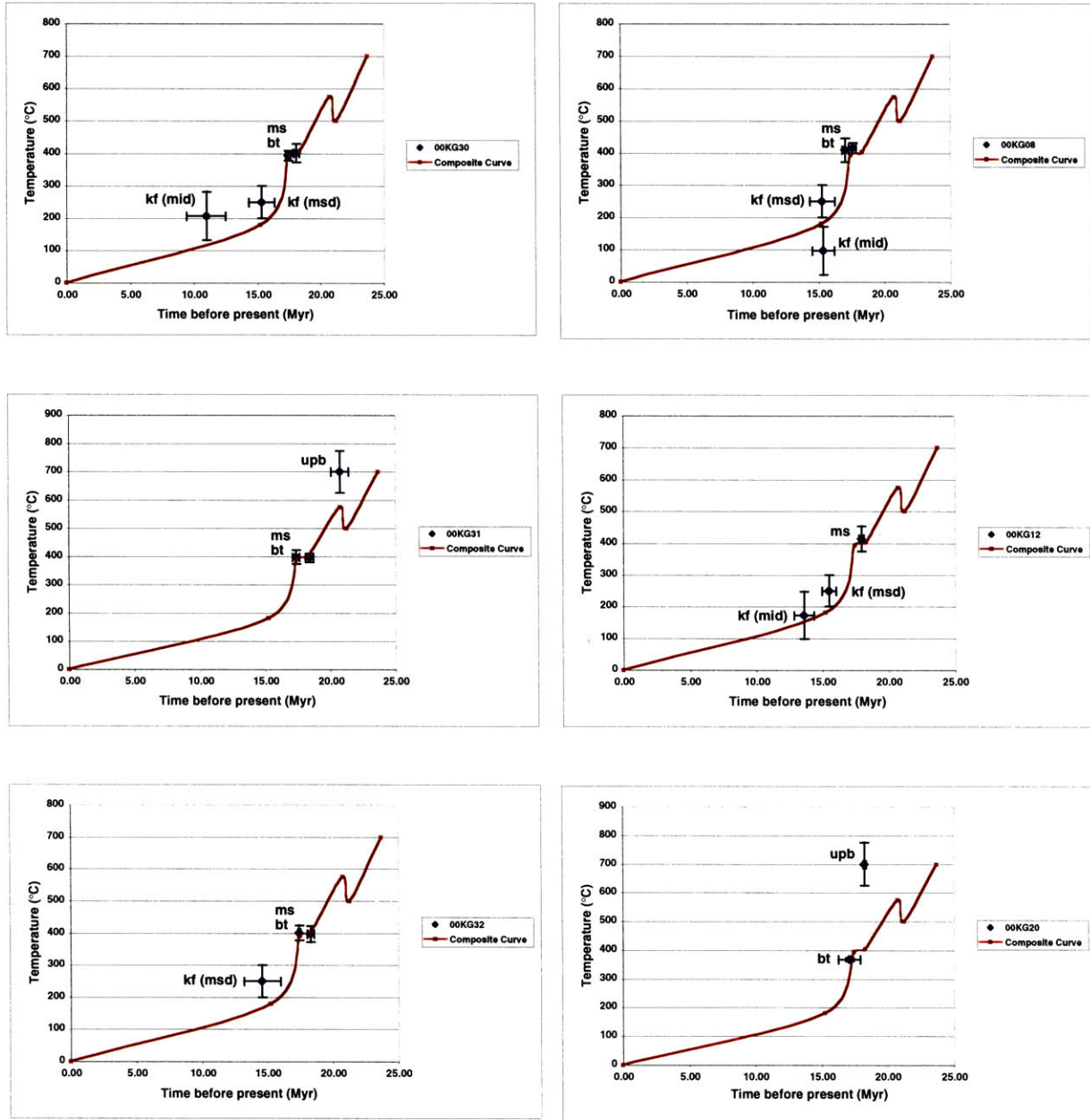


Figure 21 <continued>

Figure 22

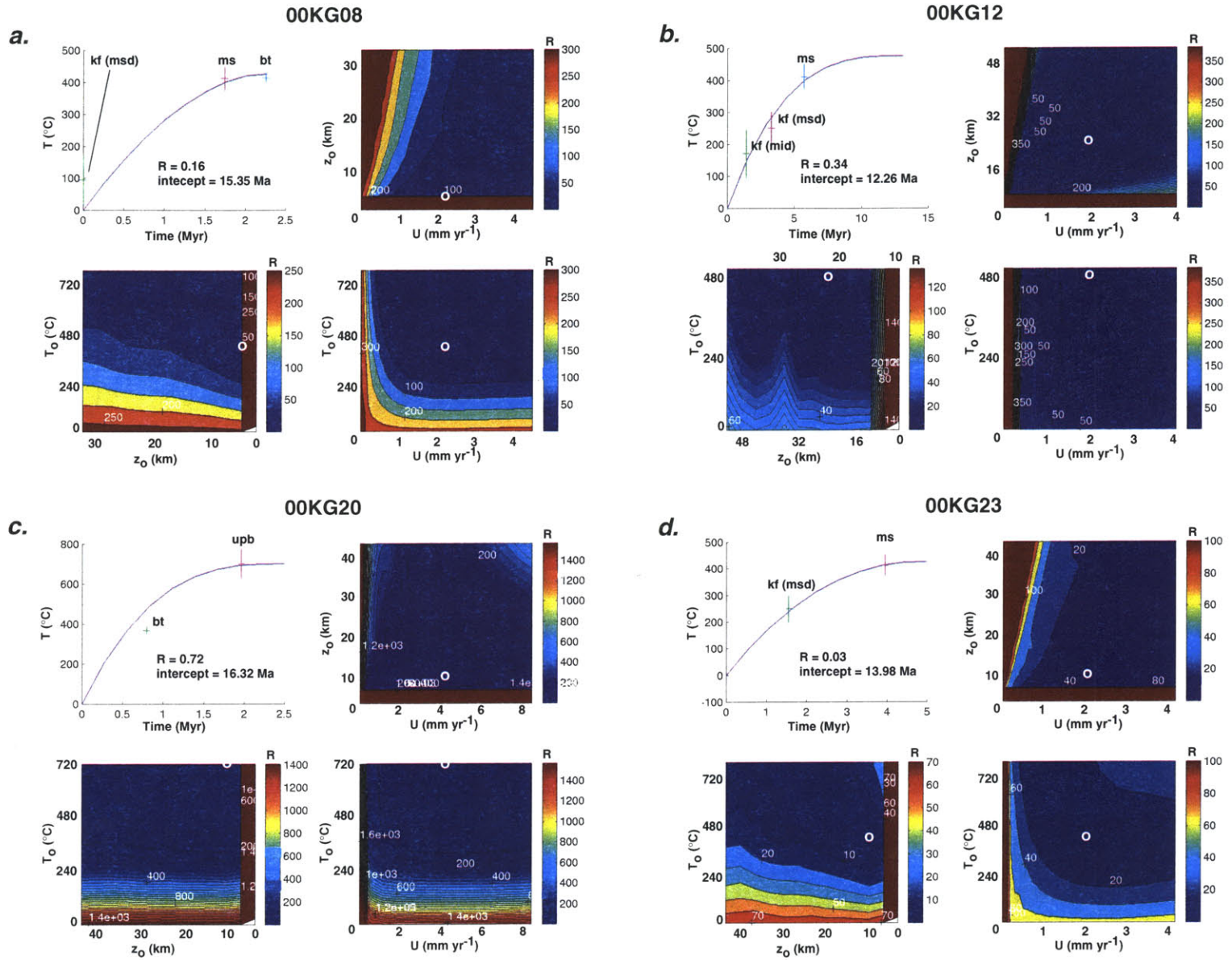
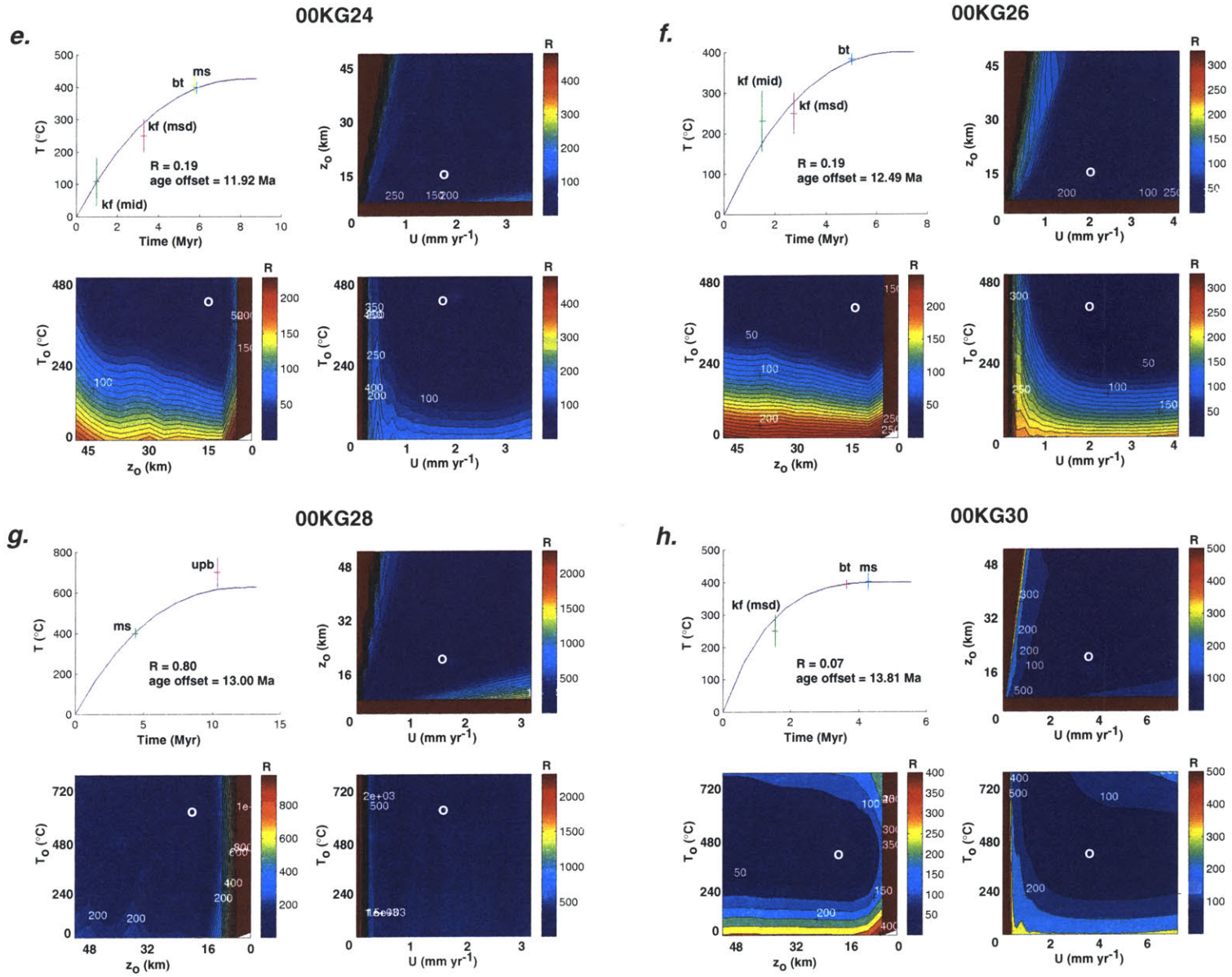


Figure 22 <continued>



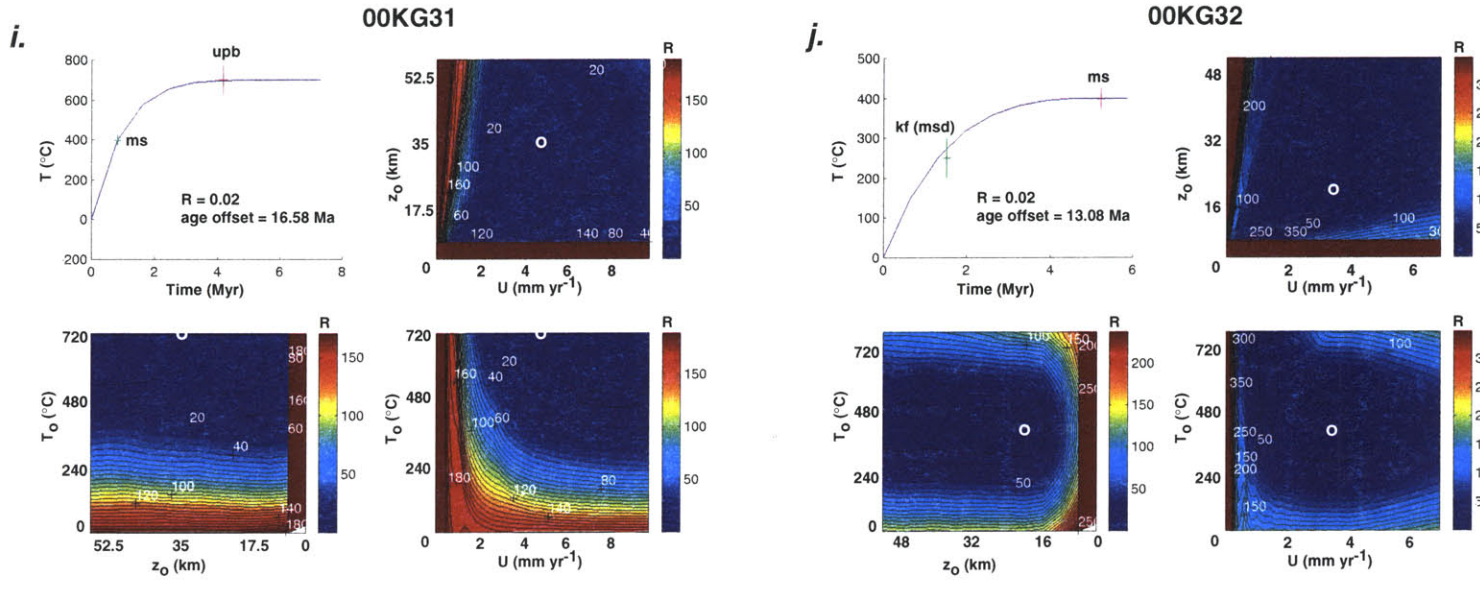


Figure 22 <continued>

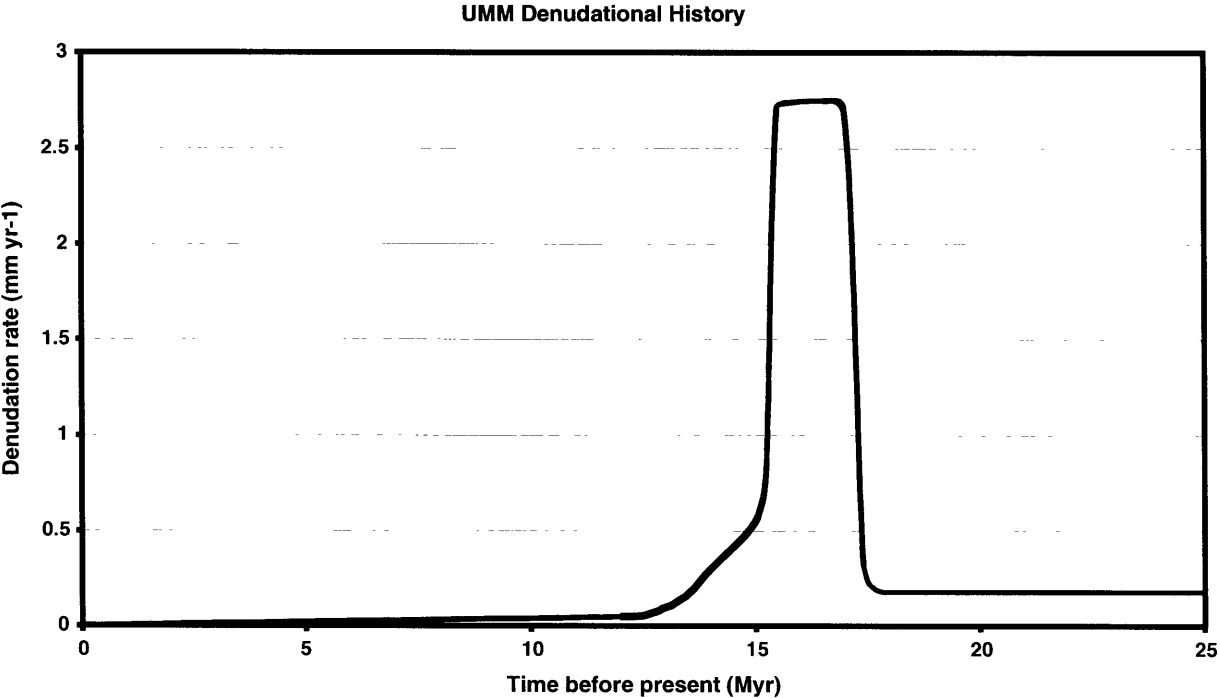
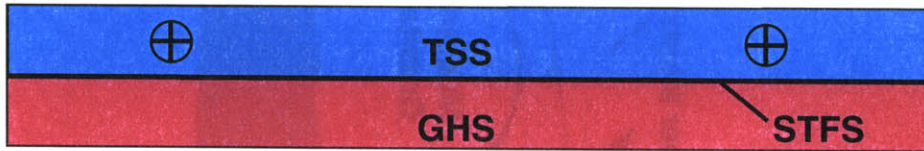
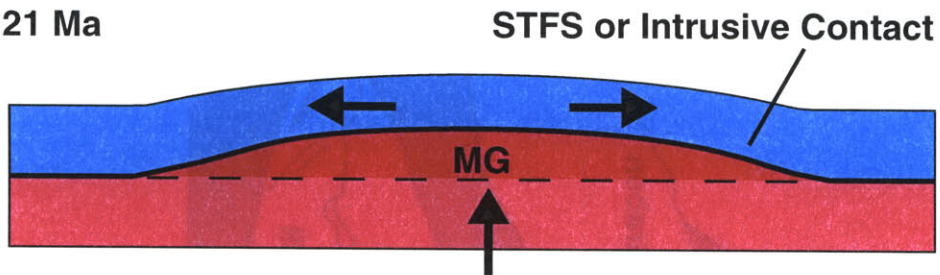


Figure 23

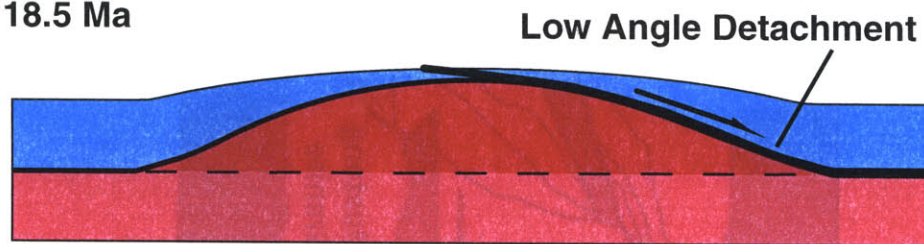
> ca. 24 Ma



by ca. 21 Ma



by ca. 18.5 Ma



post ca. 17.5 Ma

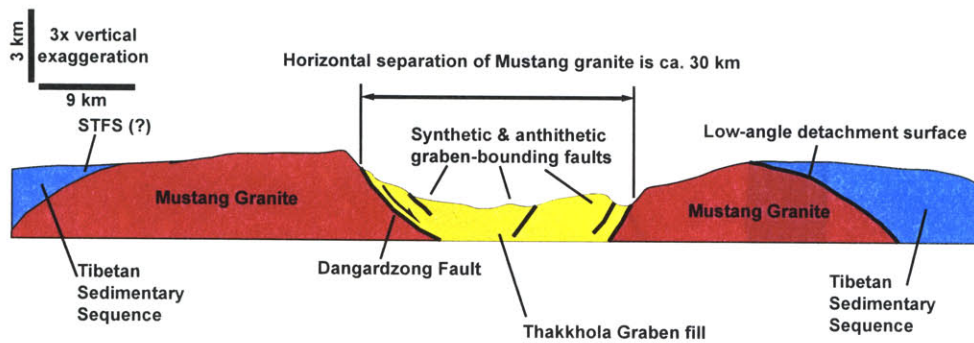


Figure 24a

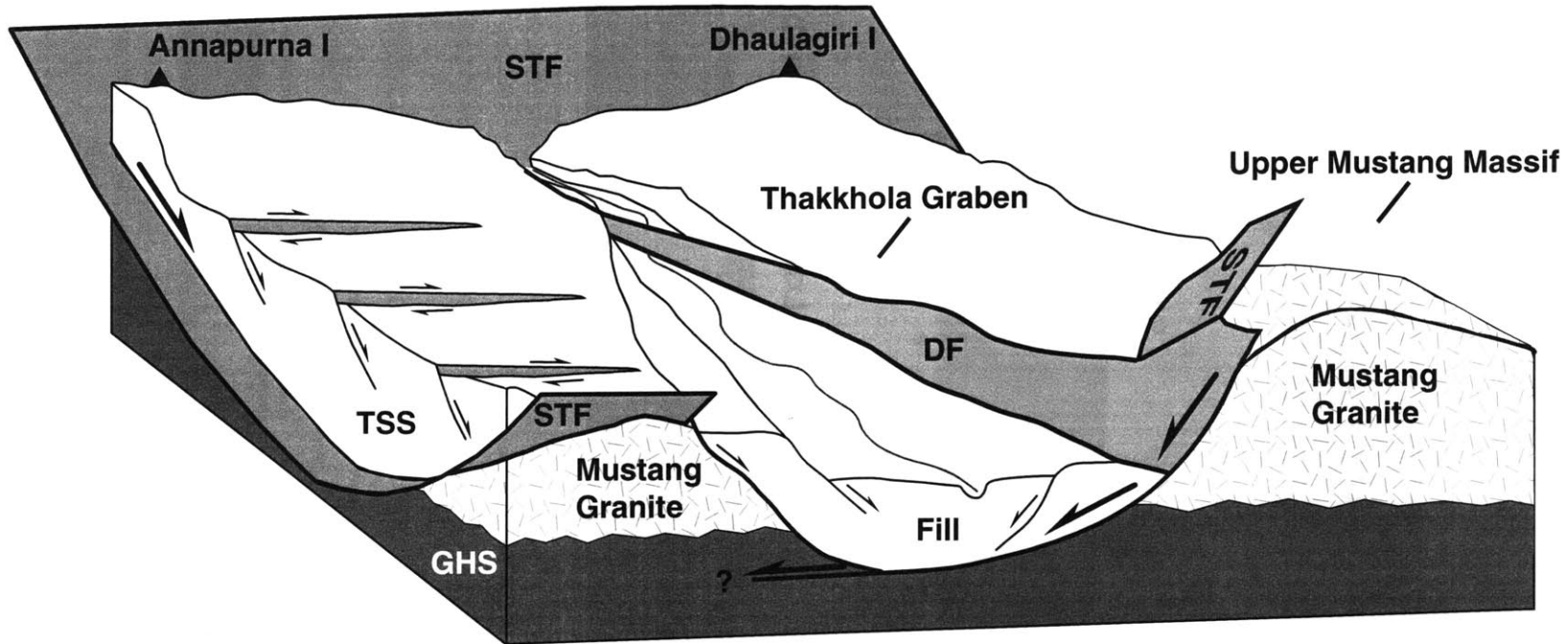


Figure 24b

Chapter 5:

***Electron microprobe chemical dating of
uraninite as a reconnaissance tool for
leucogranite geochronology***

For submission to *Earth and Planetary Science Letters*

Chapter 5: Electron microprobe chemical dating of uraninite as a reconnaissance tool for leucogranite geochronology

José M. Hurtado, Jr. *
Nilanjan Chatterjee
Jahandar Ramezani
Kip V. Hodges
Samuel A. Bowring

Department of Earth, Atmospheric, and Planetary Sciences
Massachusetts Institute of Technology
Cambridge, Massachusetts

* address: MIT EAPS 54-1022, 77 Massachusetts Avenue, Cambridge, MA 02139-4307
email: hurtado@MIT.EDU

ABSTRACT

We suggest that electron microprobe techniques may be employed to date Tertiary samples of uraninite (UO_2) which can contain very high concentrations of radiogenic Pb after only a few million of years of U and Th decay. Although uraninite is regarded as a rare accessory mineral, it is relatively abundant in leucogranitic rocks such as those found in the Himalayan orogen. We apply the U-Th-total Pb electron microprobe chemical dating method to a uraninite crystal from a ca. 18.3 Ma dike of the Mugu granite from the Upper Mustang region of central Nepal. With this technique, we calculate a mean chemical date that is consistent with isotope-dilution thermal ionization mass spectrometry (ID-TIMS) U-Pb dates obtained from seven other uraninite grains and a monazite crystal from the same sample. Electron microprobe chemical dating yields results that typically will be an order of magnitude less precise than conventional dates: in the specific case of the Mugu granite, single point chemical dates each have ca. 1.5 Ma 2σ (95%) confidence level uncertainties. However, the mean chemical date of 15 point analyses of the crystal we study has a 2SE (standard error) uncertainty of ca. 400 ka, comparable to uncertainties obtained with ID-TIMS. These results show that electron microprobe chemical dating of uraninite has substantial promise as a reconnaissance tool for the geochronology of young granitic rocks. However, electron microprobe work also

Chapter 5: Electron microprobe chemical dating of uraninite

reveals substantial chemical complexity within uraninite that must be taken into account. The analyzed crystal displays a texturally and chemically distinctive core and rim that suggests episodic growth. Concentration gradients in U, Th, and Y across the boundary imply diffusive modification with $D_{nU} \approx D_{nTh} \approx \frac{1}{3} D_{nY}$. We estimate the diffusivity of U, Th, and Y in uraninite at ca. 700 °C to be $> 10^{-7} \text{ cm}^2 \text{ s}^{-1}$. In contrast, Pb shows no distinctive concentration gradient across the core-rim boundary, implying that Pb has a much higher diffusivity in uraninite than U, Th, or Y. We estimate that Pb loss of as much as ca. 8.9% has occurred in the uraninite grains we analyzed by ID-TIMS.

INTRODUCTION

Leucogranitic rocks produced by crustal melting are frequently found in collisional orogenic settings. These granites have the potential to provide important constraints on the absolute ages of deformational events that occurred during anatexis. For example, various studies (as reviewed by Hodges, 2000) have demonstrated spatial and temporal relationships between anatexis and both contractional and extensional deformation in the Himalayan orogen. High-precision U-Pb geochronology of pre-, syn-, and post-kinematic granites utilizing traditional isotope-dilution, thermal-ionization mass spectrometry (ID-TIMS) has proved to be a powerful tool for unraveling the complex geologic history of the Himalaya (e.g. Schärer, 1984; Noble and Searle, 1995; Searle *et al.*, 1997; Coleman, 1998; Hodges *et al.*, 1998). However, the existence of numerous generations of anatexites in the Himalaya and the complexity of accessory mineral suites in these rocks (e.g. Viskupic and Hodges, 2001) requires painstaking, systematic effort for geochronology to be effective. It is therefore useful to explore reconnaissance methods of U-Pb geochronology that, while inherently less precise, might better inform and facilitate detailed ID-TIMS work.

Chapter 5: Electron microprobe chemical dating of uraninite

One reconnaissance method that has been used to great effect in the Himalaya is Th-Pb ion microprobe isotopic dating of monazite (Harrison *et al.*, 1995; Harrison *et al.*, 1996; Harrison *et al.*, 1997). A second, high spatial resolution, reconnaissance approach to dating monazite employs chemical rather than isotopic data. This method presumes that essentially all Pb in monazite is derived from the *in situ* decay of U and (in particular) Th, such that the concentration of Pb in a specific sample is proportional to its age (Montel *et al.*, 1996). For monazites that are sufficiently old – typically Paleozoic or older – the necessary measurements can be made with electron microprobe equipment, instruments that are more widely available than ion microprobes and that provide an order-of-magnitude better spatial resolution than is commonly realized in most ion microprobe studies. Although electron microprobe chemical dating of monazite has proved to be an important tool for tectonic studies in older orogenic settings (e.g. Williams *et al.*, 1999), the concentrations of radiogenic Pb in Tertiary monazites – such as those found in the Himalaya – are sufficiently low to limit usefulness of the technique using currently available technology. However, we show in this paper how another common leucogranite accessory mineral – uraninite (UO₂) – is a more useful target for electron microprobe chemical dating studies of young samples.

THEORY

The radioactive decay of ²³⁵U, ²³⁸U, and ²³²Th in a mineral produces ²⁰⁷Pb, ²⁰⁶Pb, and ²⁰⁸Pb, respectively. If the mineral incorporates no common Pb at the time of crystallization, the concentration of Pb in the mineral after an elapsed time (*t*) is due

Chapter 5: Electron microprobe chemical dating of uraninite

solely to the radioactive parent U and Th isotopes and is governed by the composite decay equation:

$$C_{Pb} = C_{Th} \left[0.897 \left(e^{\lambda_{232}t} - 1 \right) \right] + C_U \left[0.859 \left(e^{\lambda_{238}t} - 1 \right) + 0.006 \left(e^{\lambda_{235}t} - 1 \right) \right] \quad (1),$$

where C_{Pb} , C_{Th} , and C_U are concentrations (in ppm) of Pb, Th, and U, respectively; λ_{232} , λ_{238} , and λ_{235} are the decay constants (in yr^{-1}) for ^{232}Th , ^{238}U , and ^{235}U , respectively (Steiger and Jäger, 1977); and t is age (in yr). The coefficient preceding the first exponential term in equation (1) is the mass ratio of ^{208}Pb to ^{232}Th (i.e. $208/232 \approx 0.897$); the coefficients preceding the second and third exponential terms are the ratios of the abundance fractions of the respective U isotopes to the mean atomic mass of U (i.e. $0.9928/238.04 \approx 0.859$ for ^{238}U ; $0.0072/238.04 \approx 0.006$ for ^{235}U). An iterative solution to equation (1) forms the basis for published electron microprobe chemical dating studies of monazite (e.g. Montel *et al.*, 1996; Cocherie *et al.*, 1998; Williams *et al.*, 1999; Terry *et al.*, 2000).

As equation (1) shows, the decay of ^{235}U makes relatively little contribution to the total concentration of radiogenic Pb in a mineral. It is also evident that the relative contributions of the decays of ^{238}U and ^{232}Th depend on both the Th/U ratio of the mineral and a sample's age since $\lambda_{235} > \lambda_{238} > \lambda_{232}$. Thus, a higher proportion of the radiogenic Pb in an older mineral will be derived from U decay than from Th decay, even if the concentrations of U and Th are the same. However, the dependence on the Th concentration is much greater than the dependence on the decay constants. For a sample of a given age, the Th contribution to the radiogenic Pb content is significant (e.g. $\geq 10\%$ of the U contribution) if Th/U is greater than approximately 0.33 (Figure 1a). For a fixed

Chapter 5: Electron microprobe chemical dating of uraninite

Th/U ratio, the proportional Th contribution is essentially constant, if slightly decreasing with age (Figure 1a).

However, ignoring the Th contribution to the total Pb in uraninite has a limited effect on the apparent age. Neglecting Th, one can iteratively calculate approximate, maximum dates (t_{max}) using a modified form of equation (1):

$$C_{Pb-U} = C_U [0.859(e^{\lambda_{238} t_{max}} - 1) + 0.006(e^{\lambda_{235} t_{max}} - 1)] \quad (2),$$

where C_{Pb-U} is the concentration (in ppm) of Pb, all of which is assumed to be produced exclusively by U decay. For samples with equal amounts of Th and U (Th/U = 1.0), the discrepancy between dates calculated from equation (1) and those calculated from equation (2) will be ca. 25% (Figure 1b).

APPLICATION TO LEUCOGRANITE FROM THE NEPAL HIMALAYA

We illustrate the use of this approach for uraninite with a sample of Himalayan leucogranite collected in the Upper Mustang region of north central Nepal (Figure 2). The northwestern flank of a major N-S rift in this region – the Thakkhola graben – consists of a metamorphic massif which is dominated by exposures of Mesozoic siliciclastic and carbonate rocks metamorphosed to greenschist and amphibolite facies during the Tertiary (e.g. Hurtado *et al.*, submitted – see Chapter 4). These rocks are intruded by two suites of granites: porphyritic and sometimes megacrystic granite of the Mustang pluton; and fine- to medium-grained, more leucocratic bodies of the Mugu leucogranite (e.g. Hurtado *et al.*, submitted – see Chapter 4; Le Fort and France-Lanord,

Chapter 5: Electron microprobe chemical dating of uraninite

1995). Based on their field relationships with respect to deformational fabrics, it appears that the Mugu leucogranites represent several distinctive episodes of anatectic melting (Hurtado *et al.*, submitted – see Chapter 4). Previously published Th-Pb (Harrison *et al.*, 1997) and recently obtained ID-TIMS U-Pb dates for accessory minerals (Hurtado *et al.*, submitted – see Chapter 4) demonstrate that the Mugu leucogranites range from > ca. 20.76 Ma to at least ca. 17.6 Ma.

The particular sample of Mugu granite we examine in this study, 00KG20, was collected from a late-phase, 0.5 m-wide dike that intrudes both an earlier Mugu granite dike and dark, calc-pelitic metamorphosed country rock (Figure 3a) (Hurtado *et al.*, submitted – see Chapter 4). In addition to monazite, the accessory mineral suite for this sample included relatively abundant, black, euhedral crystals of uraninite (Figure 3b). Pure accessory mineral separates were obtained from a crushed aliquot of 00KG20 using standard magnetic and gravimetric separation techniques. One uraninite crystal from 00KG20 (u5) was selected for electron microprobe chemical dating, while seven other grains (u1-u3, u4a-d) were dissolved for comparative ID-TIMS geochronology. Two monazites from 00KG20 (m1 and m2) were also measured with ID-TIMS (see also Hurtado *et al.*, submitted – Chapter 4).

Electron Microprobe Analytical Methods

Crystal u5 is a cubic crystal approximately 200 μm across. We mounted it in epoxy, and we ground and polished the mount to expose a rectangular cross section through the core of the grain. The polished section was then washed with ethanol and

Chapter 5: Electron microprobe chemical dating of uraninite

carbon-coated for electron microprobe analysis at the Massachusetts Institute of Technology with a JEOL JXA-733 instrument. Back-scattered electron (BSE) and secondary electron (SE) images of the grain (Figure 3c & d) were produced in order to evaluate the extent of compositional zoning of u5 in a crude fashion and as an aid to selecting spots for quantitative analysis. Semi-quantitative energy dispersive spectrometry (EDS) analyses were also performed on inclusions within the grain to identify their mineralogy. Quantitative measurements of U, Th, Pb, and Y concentrations were made along two core-to-rim transects of grain u5 (Figure 3c & d): Transect 1 (circles) which comprises 14 semi-equally-spaced spot analyses and Transect 2 (crosses) which comprises 10 spots. This approach was chosen in order to evaluate, in a quantitative way, the magnitude of chemical zoning in the grain. This is valuable information since gradients in U, Th, and Pb concentrations, perhaps related to polyphase uraninite growth, may result in spatial variations in calculated chemical dates.

Quantitative point analyses were performed by wavelength dispersive spectrometry (WDS) using PET diffracting crystals and sealed Xe-proportional counters. Prior to quantitative analysis, the WD spectrometers were calibrated with respect to U, Th, Pb, and Y using UO_2 , ThO_2 , ThSiO_4 , PbTiO_3 , and YAG (Y-Al-garnet: $\text{Y}_3\text{Al}_5\text{O}_{12}$) standards. All measurements were made with an accelerating voltage of 20 kV, a beam current of 100 nA, and a dwell time of 240 seconds per element measured to maximize analytical precision. The minimum detection limits under these conditions were ca. 525 ppm for U, ca. 151 ppm for Th, ca. 273 ppm for Pb, and ca. 263 ppm for Y. The spot size was ca. 1 μm . The X-ray lines used for concentration measurements were $\text{PbM}\alpha$, $\text{ThM}\alpha$, $\text{UM}\alpha$, and $\text{YL}\alpha$. Matrix corrections were performed with the CITZAF program

Chapter 5: Electron microprobe chemical dating of uraninite

(Armstrong, 1995) using the atomic number correction of Ducumb and Reed (1968), tabulated mass absorption coefficients (Heinrich, 1969), and the fluorescence correction of Reed (1965).

For the calculation of chemical dates, concentrations of U, Th, and Pb in grain u5 were measured simultaneously using three different WD spectrometers equipped with PET diffracting crystals. We measured $PbM\alpha$ and $ThM\alpha$ sequentially with the best WD spectrometer. The other two WD spectrometers were used to simultaneously measure $UM\alpha$ and $YL\alpha$. After each measurement, the k-ratios for U and Pb were corrected for spectral interferences from the overlapping $ThM\beta$ and $YL\gamma$ lines, respectively (e.g. Montel *et al.*, 1996; Cocherie *et al.*, 1998; Terry *et al.*, 2000). This was done by measuring the x-ray intensities of $ThM\beta$ in the U-free $ThSiO_4$ standard and of $YL\gamma$ in the Pb-free YAG standard. These measurements, scaled by multiplying them by the k-ratios of Th and Y in grain u5, were subtracted from the measured intensities of U and Pb in grain u5 to yield corrected U and Pb intensities. We find that Th interference creates an average U content overestimate of ca. 16 ppm, and Y interference creates an average Pb content overestimate of ca. 35 ppm. Oxygen concentrations were calculated from stoichiometry of the oxides of U, Th, Pb and Y. We assume that there is negligible common lead and that mass transfer has not significantly altered the elemental concentrations in the uraninite (e.g. Montel *et al.*, 1996; Cocherie *et al.*, 1998) and use the U, Th, and Pb concentrations and equation (1) to calculate U-Th-total Pb chemical dates. Uncertainties in the dates were estimated by propagating analytical uncertainties in U, Th, and Pb concentrations through equation (1) using a modified Monte Carlo method (Anderson, 1976; Terry *et al.*, 2000; White, 2001), and, for individual points,

Chapter 5: Electron microprobe chemical dating of uraninite

they are reported at the 2σ (95%) confidence level. The uncertainties do not include geologic uncertainty or uncertainty in the calibration standards, although according to Montel (1996) the latter only contributes ca. 1% to the total uncertainty. Concentration data and calculated chemical dates are given in Table 1.

Grain Characteristics

When uraninite crystals from 00KG20 are examined under a binocular microscope, their crystal faces display a specular patina that suggests the presence of microinclusions (Figure 3b). BSE and SE imagery of grain u5 confirm the presence of abundant inclusions, many of which were plucked during sample polishing, leaving a large number of pockmarks and voids on the surface (Figure 3c & d). Some of the void space left by excavated inclusions forms a conspicuous, 8 μm wide, octahedrally-symmetric, concentric band that has the form of crystal faces (Figure 3c). EDS analyses demonstrate that many of the inclusions still remaining in the grain are quartz, although a few were found to be fayalite, aluminosilicate, and diopside. Aluminosilicate and diopside both occur in the calc-pelitic country rocks of Upper Mustang (and specifically in the host rock to 00KG20) so the inclusions are therefore regarded as xenocrystic. The presence of fayalite and diopside inclusions in u5 is petrologically significant because xenocrystic diopside would be expected to dissolve quickly in a leucogranitic magma.

ID-TIMS Analytical Methods

For comparison with the electron microprobe chemical dates, we selected four

Chapter 5: Electron microprobe chemical dating of uraninite

euohedral, cubic uraninite crystals (u1-u4) ranging in size from 75 μm to 150 μm on a side (Figure 3b) for conventional U-Pb analysis. We fractured grain u4 and selected four pieces (u4a, -b, -c, and d) for individual analyses. The seven grains selected for analysis were photographed and measured using a binocular microscope with calibrated reticule and video display in order to estimate their weights. Experience in our facility suggests that the estimated values have a nominal error of roughly 20%. Prior to analysis, the grains were thoroughly washed in de-ionized water in an ultrasonic bath on a hot plate. Grains u4a and u4b were washed briefly in 4N HNO_3 at 80 $^\circ\text{C}$. Washed and rinsed grains were loaded into FEP Teflon® microcapsules, spiked with a mixed ^{205}Pb - ^{233}U - ^{235}U tracer solution, and dissolved in concentrated HF at 220 $^\circ\text{C}$ within pressure vessels for 48-60 hours. Dissolution was followed by conversion to chloride form using 6N HCl at 180 $^\circ\text{C}$ for 12 hours. Pb and U were isolated and extracted from the samples using a miniaturized HCl-based anion-exchange chromatography procedure modified after Krogh (1973). U and Pb were then loaded separately on single, degassed Re filaments with a silica gel- H_3PO_4 emitter solution. Isotopic compositions were measured by isotope-dilution, thermal-ionization mass spectrometry (ID-TIMS) on a VG Sector 54 multi-collector mass spectrometer at the Massachusetts Institute of Technology.

Pb isotopic measurements were made in dynamic mode using four Faraday cup detectors and an axial, ion-counting Daly detector. An internal Daly-Faraday gain calibration was obtained by peak-switching the ^{205}Pb isotope peak into the axial position. U isotopes were measured as oxide ions in static mode on three Faraday cup detectors with an average $^{235}\text{U}^{16}\text{O}_2^+$ ion-beam intensity of 100 mV. Measured isotopic ratios were corrected for mass-dependant isotope fractionation in the mass spectrometer, as well as

Chapter 5: Electron microprobe chemical dating of uraninite

for U and Pb contributions from the spike, laboratory blanks and the initial Pb in the sample. U-Pb isotopic dates and their associated uncertainties (Table 2) were calculated using the decay constants of Steiger and Jäger (1977) and the error propagation algorithm of Ludwig (1980) See Table 2 for further details, including fractionation, total procedural blanks, and complete isotopic data for each grain analyzed.

With the exception of u3, the isotopic composition of Pb in the grains we analyzed was highly radiogenic (Table 2), such that calculated U-Pb dates are not strongly dependent on our choice of a common Pb correction scheme. Moreover, using Pb isotopic compositions of HF-leached feldspars from other Himalayan leucogranites that display a relatively wide range of common Pb compositions (e.g. Gariépy *et al.*, 1985; Hodges *et al.*, 1998; Viskupic and Hodges, 2001) produced insignificant changes in the plotting coordinates in concordia space of the 00KG20 uraninites. As a consequence, we did not attempt to measure common Pb for 00KG20 directly and relied instead on the Stacey and Kramers (1975) model values.

RESULTS

After matrix and Y and Th interference corrections were applied, elemental concentrations of U, Th, Pb, Y, and O (in weight %) were re-normalized to sum to 100% and the elemental concentrations were recast in ppm (Table 1). In most cases, the sum total of U, Th, Pb, Y, and O was close to 100% by weight before re-normalization (Table 1) indicating that these species comprise the bulk composition of grain u5. The significant (i.e. ppm level) amounts of Th and Y are consistent with previous measurements of natural uraninite (Snetsinger and Polkowski, 1977). Generally, the 0-

Chapter 5: Electron microprobe chemical dating of uraninite

3% unaccounted for may be due to trace amounts of Nd, Ra, Ce, N, He, A, and/or OH commonly present in uraninite that we did not measure (e.g. Snetsinger and Polkowski, 1977; Klein and Hurlbut, 1993). Those analyses with anomalously low totals (e.g. $\leq 96\%$; italicized in Table 1) may also have been adversely affected by non-idealities (i.e. pits and roughness) on the polished grain surface (Figure 3c & d). Those points were excluded from the calculation of mean chemical dates.

Spatial Variations in U, Th, Pb, and Y Concentrations

The lack of contrast variations in the BSE image (Figure 3d) implies that no significant variations in mean atomic weight occur within grain u5. This preliminary observation belies textural and other chemical evidence for significant variability within the grain. For instance, the prominent, octahedrally-symmetric intra-grain boundary visible in the SE (Figure 3c) and BSE (Figure 3d) images strongly suggests concentric structural zonation and allows us to define a core and a rim which we interpret to be the result of episodic crystal growth.

Moreover, our point chemical data indicate that the rim and core of u5 have significantly different U, Th, and Y concentrations (Table 2). Superimposed on Figure 3c & d is a map of the twenty-four spots analyzed for the calculation of total U-Th-Pb chemical dates. Concentration profiles – plots of elemental concentration as a function of position outwards from the center of the crystal – display discontinuities that coincide exactly with the structural break between the core and rim (Figure 4). Average U concentration along Transects 1 and 2 is ca. 85,0000 ppm in the core compared to ca. 81,0000 ppm in the rim (Figure 4a & b). The core and rim are very well defined by the U

Chapter 5: Electron microprobe chemical dating of uraninite

distribution, and the chemical discontinuity between them is fairly sharp, occurring over a distance of ca. 25 μm . Conversely, Th concentration along Transect 1 rises from an average of ca. 27,000 ppm in the core to ca. 63,000 ppm in the rim, a profile that is the mirror image of that for U and equally well defined (Figure 4c). Although Th concentrations are slightly different along Transect 2, averaging ca. 24,000 ppm in the core vs. ca. 63,000 ppm in the rim, the pattern is the same as that along Transect 1 (Figure 4d). Y concentration is closely correlated with Th concentration along both transects. Average Y concentration in Transect 1 rises from ca. 3,500 ppm in the core to ca. 8,700 ppm in the rim (Figure 4e), whereas along Transect 2, core Y concentration averages ca. 3,200 ppm, which rises to ca. 8,900 ppm in the rim (Figure 4f). When contoured and superimposed on the SE image of grain u5, the elemental concentration data from Transects 1 and 2 match exactly the structural zonation of the crystal, exhibiting a high U-low Th-low Y core, and a low U-high Th-low Y rim (Figure 4e).

By contrast, Pb concentration (Table 2) along either transect does not display simple systematics. Along Transect 1, there is no discontinuity in Pb concentration at the structural break (Figure 4g). Instead, a group of five points within the core has an elevated average Pb concentration of ca. 2600 ppm compared to an average of ca. 2100 ppm along the rest of the transect. Along Transect 2, three points – the centermost point and two at the rim – have anomalously high Pb concentration, averaging ca. 2300 ppm compared to an average of ca. 2100 ppm along the rest of the transect (Figure 4h). The contour plot of Pb concentrations bears little resemblance to those for U, Th, and Y and does not conform to any morphologic features visible on the imaged surface of u5 (Figure 4e).

Electron Microprobe Chemical Dates

Table 2 summarizes the total U- Pb-Th chemical dates calculated with equation (1) and the electron microprobe data for each point along both transects through grain u5. Dates along Transect 1 vary substantially between 23.00 Ma and 17.34 Ma. Similarly, dates along Transect 2 vary between 20.28 Ma and 16.79 Ma. For every point analysis, the propagated 2σ (95% confidence level) uncertainty is ca. 1.50 Ma.

A contour plot of the chemical dates along both transects does not conform to crystal morphology (Figure 4e), and when plotted as age profiles as a function of distance from the center of the crystal (Figure 4i & j), it is apparent that the chemical dates are closely correlated with Pb concentration and not with the distributions of U, Th, or Y (c.f. Figure 4a-h). Chemical dates along Transect 1 are anomalously old for the same group of five points within the core of u5 that have elevated Pb concentrations (Figure 4i). Similarly, those points along Transect 2 which had high Pb concentrations are also anomalously old (Figure 4j). In either case, the distribution of chemical dates is not consistent with simple, concentric growth zonation of the crystal.

With the exception of the clusters of older points with anomalously high Pb concentrations, chemical dates are otherwise consistent from point to point along both transects (Figure 4k). We calculated separate mean chemical dates for each transect, as well as a mean chemical date considering all the point analyses. These averages excluded the older outlier points, as well as those with low totals (Table 1). Uncertainty in the average chemical dates is taken as two standard errors (2SE) of the mean. For Transect 1, the mean chemical date is 18.17 ± 0.52 Ma (Table 1; Figure 4i). The seven

Chapter 5: Electron microprobe chemical dating of uraninite

reliable dates included in the average are statistically indistinguishable, with a mean squared weighted deviation (MSWD) of 1.07, well within uncertainty of the ideal value of 1.0 (Wendt and Carl, 1991). The mean chemical date for the eight reliable dates along Transect 2 is 17.77 ± 0.59 Ma, although with a larger MSWD of 2.01 (Table 1; Figure 4j). Taken as a whole, these fifteen chemical dates have an average of 17.96 ± 0.40 Ma (MSWD = 1.22) (Table 1; Figure 4k) which we regard as a reliable estimate of the age of grain u5. By comparison, the mean age of the total of seven outlier points along both transects¹ is 21.12 ± 0.97 Ma, although it has an unacceptably high MSWD of 3.47.

ID-TIMS Dates

Monazite grain m1 plots nearly concordantly (Figure 5) with a $^{207}\text{Pb}/^{235}\text{U}$ date of 18.28 ± 0.10 Ma (Table 2; Hurtado *et al.*, submitted – see Chapter 4). Although uraninite grains u1-u4a-d yielded very precise ID-TIMS dates, all were substantially normally discordant when plotted on a concordia diagram, and their significance with respect to the crystallization age of 00KG20 is not obvious (Figure 5a & b). Individual $^{207}\text{Pb}/^{235}\text{U}$ dates range between 17.139 Ma and 16.436 Ma (Table 2), and the seven analyses define a linear array in $^{206}\text{Pb}/^{238}\text{U}$ vs. $^{207}\text{Pb}/^{235}\text{U}$ space that is essentially parallel to concordia (Figure 5a & b).

Given such a linear array of data, one way to estimate a crystallization age is to calculate the upper intercept of the chord defined by the array with concordia. Before doing so, it is appropriate to consider the effect of ^{230}Th deficiency within extremely U

¹ This only includes those points that are anomalously old and does not include points with low totals.

Chapter 5: Electron microprobe chemical dating of uraninite

enriched phases such as uraninite. Deficiency in initial ^{230}Th will, in turn, cause deficiency in ^{206}Pb , resulting in anomalously low $^{206}\text{Pb}/^{238}\text{U}$ dates and normally discordant data points. One approach is to apply the correction described by Parrish (1990):

$$\left(\frac{^{206}\text{Pb}}{^{238}\text{U}}\right)_{\text{corrected}} = \left(\frac{^{206}\text{Pb}}{^{238}\text{U}}\right)_{\text{measured}} - \left\{ \left[\frac{\left(\frac{\text{Th}}{\text{U}}\right)_{\text{mineral}}}{\left(\frac{\text{Th}}{\text{U}}\right)_{\text{magma}}} - 1 \right] \left[\frac{\lambda_{238}}{\lambda_{230}} \right] \right\} \quad (3),$$

where the “corrected” subscript refers to the ^{230}Th deficiency corrected value, the “measured” subscript indicates the value from the ID-TIMS analyses, the “mineral” subscript indicates the Th/U ratio of the uraninite grain, the “magma” subscript indicates the Th/U ratio of the source magma, and λ_{238} and λ_{230} are the decay constants (in yr^{-1}) for ^{238}U , and ^{230}Th , respectively (Steiger and Jäger, 1977). For this correction, we must assume a value for the Th/U ratio parent magma. Although that specific data is not available for the Mugu granite, we use the Th/U ratio determined for the parent magma of a similar intrusion, the Manaslu pluton (0.689 – Le Fort *et al.*, 1987). The effect of the correction is to shift the $^{206}\text{Pb}/^{238}\text{U}$ of each analysis by ca. 0.000015 (Table 3), moving the data point upward along the $^{206}\text{Pb}/^{238}\text{U}$ axis towards concordia (Figure 5a & b). Thus corrected, the seven uraninite ID-TIMS analyses do not yield a statistically significant linear correlation (MSWD = 19.8), but linear regression of these data using a modified version of the algorithm derived by York (1969) – specifically Model 2 of Ludwig (1991) – yields an upper concordia intercept corresponding to a date of $17.63^{+108}_{-0.63} \text{ Ma}$ (Figure 5c).

However, while correcting for ^{230}Th deficiency (Schärer, 1984; Parrish, 1990) results in a small change in $^{206}\text{Pb}/^{238}\text{U}$ (Figure 5a & b; Table 3), it significantly affects the

Chapter 5: Electron microprobe chemical dating of uraninite

result of the linear regression through the data. For instance, regressing the uncorrected data yields an upper intercept of $19.22_{-1.55}^{+95.21}$ Ma (MSWD = 16.5) (Figure 5d). Since the upper intercept is dependent on an assumption of a magmatic Th/U, a value for which we have no specific constraint, and because the quality of both linear regressions is poor, we suggest that the grain with the oldest $^{207}\text{Pb}/^{235}\text{U}$ date (u4b; 17.139 ± 0.011 Ma [2σ]; Table 2) gives the best minimum constraint on the crystallization age of uraninite in 00KG20.

DISCUSSION

Comparison of Chemical Dating and ID-TIMS Results

Table 4 summarizes the U-Th-Pb geochronologic constraints resulting from our analysis of monazite and uraninite from sample 00KG20. Within uncertainty, all three mean chemical dates agree with each other and with the monazite $^{207}\text{Pb}/^{235}\text{U}$ ID-TIMS date, falling in the range between 18.69 Ma and 17.18 Ma. Within uncertainty, the mean chemical dates also agree with the 17.63 upper intercept resulting from linear regression of the ^{230}Th deficiency corrected uraninite ID-TIMS data, although the uncertainties in question are rather large (Table 4). The very precise 17.139 Ma $^{207}\text{Pb}/^{235}\text{U}$ ID-TIMS date we interpret as a minimum constraint on uraninite crystallization, falls just outside of the range of the other constraints (Table 4). We however, attribute this, and the linear array the ID-TIMS uraninite data describe, to varying degrees of Pb loss.

Because we do not know the specific Th/U of the magma from which the Mugu granite crystallized, the absolute significance of the uraninite ID-TIMS upper intercept date is uncertain. However, the similarity it has to the mean chemical dates may suggest

Chapter 5: Electron microprobe chemical dating of uraninite

that the Th/U ratio we use is a reasonable estimate. In any case, the simplest interpretation of the ID-TIMS results is that the linear array in Figure 5 represents substantial, but variable, Pb loss subsequent to crystallization and prior to the $^{207}\text{Pb}/^{235}\text{U}$ date of the oldest grain (u4b: 17.139 ± 0.011 Ma [2σ]; Table 2). Moreover, the fact that individual fragments of the same crystal (u4a-d) neither yield identical dates (Table 2) nor plot identically on the concordia diagram (Figure 5) suggests that Pb loss was complex and occurred on both inter- and intra-grain scales, a hypothesis we explore in more detail below.

Since it is the oldest date obtained from the sample, we take the 18.28 ± 0.10 Ma $^{207}\text{Pb}/^{235}\text{U}$ date from monazite grain m1 as our best estimate of a minimum age for 00KG20 (see also Hurtado *et al.*, submitted – Chapter 4). That this age is within uncertainty of the upper intercept of the uraninite ID-TIMS data supports this conclusion if we interpret the uraninite data to reflect Pb loss. The similarity between both of these ID-TIMS results and the mean chemical dates, despite the large uncertainties, is encouraging because it shows that the chemical dating technique may be an expedient method for reconnaissance geochronology of leucogranites.

Chemical Zonation and Episodic Growth of Uraninite

Strictly speaking, uraninite, UO_2 , refers to the U-rich end-member of a solid solution series in which U and Th substitute for one another, with thoraninite, ThO_2 , as the Th-rich end-member. The chemical difference between the core and rim of grain u5 suggests a change in magmatic conditions during uraninite growth that signaled a transition from uraninite crystallization in the core of grain u5 to thoraninite

Chapter 5: Electron microprobe chemical dating of uraninite

crystallization at the rim. At the same time, the marked increase in Y concentration in the rim suggests that the magma from which grain u5 crystallized became more enriched in REE (rare earth elements) as time progressed. However, in both the cases of U and Th as well as REE, the fact that the concentration profiles (Figures 4a-f) are abrupt step-functions rather than more gradual ones suggests that there may have been a hiatus in uraninite growth during which the changes in magmatic chemistry occurred. However, the lack of any similar pattern among the chemical dates within grain u5 (e.g. Figures 3e & 4i-k) also suggests that any such hiatus was not prolonged, lasting no more than ca. 1.5 Ma, the uncertainty in our chemical dates (Table 1). That the entire growth history of the uraninite in sample 00KG20 was a short one is also hinted at by the peculiar mineralogy of some of the inclusions within grain u5. The lack of a simple core to edge chemical age gradient in both Transects 1 and 2 (Figure 4i & j) and the preservation of inclusions of diopside and fayalite, both expected to dissolve quickly in a leucogranitic melt, suggest that encapsulation of the inclusions within the uraninite was a rapid process. Furthermore, these observations suggest that uraninite was an early solidus phase in the melt that crystallized as the 00KG20 dike.

U, Th, Pb and Y Diffusion in Uraninite

The hypothesis that Pb mobility in uraninite is an important contributor to the U-Th-Pb systematics of grain u5 is supported by the spatial patterns of elemental concentrations we measured with the electron microprobe. We note that the spatial distribution of Pb is completely unlike that of U, Th, and Y and that it does not match the grain morphology (e.g. Figure 3e). Moreover, the pattern of chemical dates in grain u5 –

Chapter 5: Electron microprobe chemical dating of uraninite

which mirrors that of Pb concentration – is not compatible with the simple concentric growth zonation suggested by grain morphology and the distributions of U, Th, and Y (e.g. Figure 3e). This is especially true along Transect 2 where the oldest chemical dates are found in the rim of u5 (Figure 4j). These observations suggest to us that the process responsible for the distribution of Pb is different than that responsible for the distribution of U, Th, and Y. In addition, we can infer that the measured distribution of Pb likely came about at some point after crystallization of the grain. Quantitative examination of the distributions of U, Th, and Y can give us a framework for understanding the process at work.

Although the structural interface between the chemically distinct core and rim of grain u5 marks relatively sharp discontinuities in U, Th, and Y, the geometry of the concentration profiles across the boundary are suggestive of diffusive transfer patterns that developed during post-crystallization cooling (Figure 4a-f). We model this process using the equations for an infinite composite medium for the case of two infinite halfspaces, each with diffusivity, D_n (in $\text{cm}^2 \text{s}^{-1}$) at a given temperature, in contact along an interface at $x = 0$, (Crank, 1975):

$$\frac{C_1}{C_0} = \frac{1}{2} \left\{ 1 + \operatorname{erf} \left(\frac{x}{2\sqrt{D_n t}} \right) \right\}, \quad \text{for } x > 0 \quad (4a)$$

$$\frac{C_2}{C_0} = \frac{1}{2} \left\{ \operatorname{erfc} \left(\frac{|x|}{2\sqrt{D_n t}} \right) \right\}, \quad \text{for } x < 0 \quad (4b),$$

where x is the spatial coordinate (in cm), t is time (in s); c_1 is the concentration in the region $x > 0$ (in ppm), c_2 is the concentration in the region $x < 0$ (in ppm), and c_0 is the initial concentration in the region $x > 0$ (in ppm). It is assumed that the initial

Chapter 5: Electron microprobe chemical dating of uraninite

concentration in the region $x < 0$ is zero, and that the equilibrium concentrations in both regions are equal (e.g. $\frac{c_1}{c_2} = 1$, for all x when $t = t_{equilibrium}$).

We use two methods to fit equations (4ab) to the measured U, Th, and Y concentration profiles. The first method employs a parameter search method (e.g. Moore and England, 2001; Hurtado *et al.*, submitted – see Chapter 4) to find the best fit values for both $D_n t$, which describes the shape of the diffusion profile, as well as for the interface position, x'_b . With the latter we can perform the coordinate transformation:

$$x = x' - x'_b \quad (5),$$

where the x' coordinate frame has its origin at the first point of the concentration profile and the x coordinate frame has its origin at the interface position. The results of these calculations are summarized in Figure 6. With this method, we find that $D_n t$ is $1 \times 10^{-6} \text{ cm}^2$ for U, Th, and Y in Transect 1, whereas $D_n t$ is an order of magnitude smaller ($1 \times 10^{-7} \text{ cm}^2$) in Transect 2.

In the second method, we linearize equations (4ab) by inverting through the error function:

$$\frac{x}{2\sqrt{D_n t}} = \text{erf}^{-1} \left[\left(2 \frac{c_1}{c_0} \right) - 1 \right], \quad \text{for } x > 0 \quad (6a)$$

$$\frac{|x|}{2\sqrt{D_n t}} = \text{erf}^{-1} \left[1 - \left(2 \frac{c_1}{c_0} \right) \right], \quad \text{for } x < 0 \quad (6b).$$

For U, Th, and Y, we take c_0 as the maximum concentration along the profile and we plot

$\text{erf}^{-1} \left[\left(2 \frac{c_1}{c_0} \right) - 1 \right]$ as a function of x . The slope of the best fit line through the data is

then proportional to $\frac{1}{2\sqrt{D_n t}}$ while the x intercept is equal to x'_b . Unfortunately, along

Chapter 5: Electron microprobe chemical dating of uraninite

Transect 2 there are too few points in the transitional section of the concentration profiles to yield good fits with this method, so we focus on the results from Transect 1 (Figure 7a, c, & e). The U and Th concentration profiles in Transect 1 yield similar $D_n t$ values of $2.76 \times 10^{-6} \text{ cm}^2$ and $2.99 \times 10^{-6} \text{ cm}^2$, respectively. For Y, $D_n t$ is $6.19 \times 10^{-6} \text{ cm}^2$, about a factor of 2 higher. From these results we can make a general statement about the relative diffusivity of U, Th, and Y in grain u5 and infer that:

$$D_{nU} \approx D_{nTh} \approx \frac{1}{3} D_{nY} \quad (7),$$

assuming that the profiles are diffusive and were established under uniform cooling conditions over the same length of time. Furthermore, presuming that all Pb in the sample is radiogenic, the comparative homogeneity of its concentration across the core-rim interface in grain u5 (Figure 4g & h) – despite a significant difference in U/Th ratio across the interface (Table 2) – suggests that Pb is substantially more mobile in the uraninite structure than U, Th, or Y. Therefore, elaborating on equation (7), we can infer that:

$$D_{nPb} > 3 D_{nU} = 3 D_{nTh} = D_{nY} \quad (8).$$

Few previous workers have studied UO_2 , although early studies did arrive at estimates for Pb diffusivity in uraninite as well as models for the structure of uraninite and its effect on diffusion through the material. Yershov (1974) advocated a complex structure for natural uraninite wherein Pb resides in either “stable” or “unstable” sites. In this model, uraninite is made up of a secondary structure of stable, or ordered, lattice sites called “crystallites” within an unstable, or disordered, matrix. The structure is produced during self-oxidation of uraninite (U^{4+} to U^{6+} – Ellsworth, 1924; Berman, 1957) which triggers exsolution of tabular PbO domains along unit-cell boundaries. The resulting

Chapter 5: Electron microprobe chemical dating of uraninite

laminar structure was described by (Berman, 1957) as a “...mosaic of crystallites in parallel position...separated along cube planes by ‘spacers’, monomolecular layers of ...orthorhombic Pb.” Whereas Yershov (1974) estimated the diffusivity of Pb in stable zones at 700 °C to be ca 10^{-17} cm² s⁻¹, he suggested that the unstable zones could serve as faster diffusion pathways with diffusivities at least 1000 times greater (10^{-13} cm² s⁻¹). Based on these estimates, the ca. 100 μm scale redistribution of Pb within grain u5 could have been produced within ca. 0.3 Ma at a temperature of 700 °C, a reasonable estimate of the magmatic temperature of the Mugu granite. Furthermore, based on equation (8), we can estimate that the diffusivity of U, Th, and Y should be no greater than 10^{-17} cm² s⁻¹ at 700 °C.

Estimates of diffusivity of U in natural uraninite do not exist, although some estimates exist for U diffusivity in artificial, metallic UO₂. Interest in this material stems from its importance as a fuel in nuclear reactors. Most recently, Sabioni *et al.* (1998) published an Arrhenius relationship for U in near-optimum density, synthetic UO₂:

$$\begin{aligned} D_n &= D_0 \exp\left[\frac{E_a}{RT}\right] \\ D_0 \text{ (cm}^2 \text{ s}^{-1}\text{)} &= 8.54 \times 10^{-7} \\ E_a \text{ (kJmol}^{-1}\text{)} &= 425.54 \end{aligned} \quad (9)$$

where D_n is the diffusivity (in cm² s⁻¹) at temperature T (in K), D_0 is the diffusivity at infinite temperature, E_a is the activation energy, and R is the gas constant (8.31451 J mol⁻¹ K⁻¹). If we use equation (9) in conjunction with our measured value of $D_n t$ for U in uraninite u5 (2.76×10^{-6} cm² s⁻¹), we can make an estimate of the time required to develop the U concentration profiles we observe given a reasonable range of temperatures, or *vice versa*. We find that for any reasonable choice of temperature, the time required is

Chapter 5: Electron microprobe chemical dating of uraninite

geologically unrealistic (Table 5). Similarly, for any geologically reasonable period of time, the required temperature is impossibly high (Table 6).

There are several possible explanations for this. The most likely is that the Arrhenius parameters of Sabioni *et al.* (1998) are not applicable to natural uraninite, although the possibility exists that the concentration profiles we observe in grain u5 are not due to diffusion at all and may reflect another process. However, in addition to the parameters in equation (9), Sabioni *et al.* (1998) reviewed several previous estimates of the Arrhenius parameters for U in UO_2 . All of these have substantially larger D_0 . For instance Yajima *et al.* (1966) suggests that $D_0 = 1 \times 10^{-4} \text{ cm}^2 \text{ s}^{-1}$ and $E_a = 290 \text{ kJ mol}^{-1}$. Using these values instead of those of Sabioni *et al.* (1998) results in more realistic temperatures and times (Tables 5 & 6). In addition, we note that D_n at 700 °C (ca. $10^{-20} \text{ cm}^2 \text{ s}^{-1}$) using the Arrhenius parameters of Yajima *et al.* (1966) is consistent with our estimate ($< 10^{-17} \text{ cm}^2 \text{ s}^{-1}$) based on the relative diffusivity of U and Pb and the estimated diffusivity of Pb at 700 °C (Yershov, 1974).

Estimating the Degree of Pb Loss

We have shown that within the large uncertainties that inherent to the technique that the resulting chemical dates are consistent with ID-TIMS dates. In detail, however, it is clear that Pb loss will affect both ID-TIMS and chemical dates, making the dates we measure less than the actual age of the grain. The question remain: to what extent has Pb loss from uraninite affected the dates we measure? Our electron microprobe study of grain u5 allows us to make an estimate of the degree of Pb loss. Figure 8 is a plot of the relationship between chemical age and Pb concentration as described by equation (1),

Chapter 5: Electron microprobe chemical dating of uraninite

assuming that the concentrations of U and Th are equal to the mean concentrations from grain u5 (U: ca. 837,227 ppm, Th: ca. 36,539 ppm; Table 1). The relationship is a linear one with a slope of 0.084 Ma per ppm.

If we assume that the ca. 17.63 Ma ID-TIMS upper intercept date for uraninites u1-u3 & u4a-d is indicative of the true crystallization age of uraninite in 00KG20 and apply the linear relationship in Figure 8, Pb loss ranges between ca. 58 ppm (for u4b) and 142 ppm (for u4d). Assuming that the mean concentration of Pb (ca. 2242 ppm; Table 1) in grain u5 is applicable to the other uraninite grains in 00KG20, this translates into Pb loss of between ca. 2.5% (for u4b) and ca. 5.9% (for u4d). These estimates are based on the discrepancies between the individual uraninite $^{207}\text{Pb}/^{235}\text{U}$ dates (Table 1) and the uraninite upper intercept date (Table 4). According to this scheme, grain u5 has essentially no Pb loss since its mean chemical date is within uncertainty (actually older than) the upper intercept age. Alternatively, if we use the ca. 18.3 Ma ID-TIMS date from monazite m1 as the true uraninite crystallization age, we surmise between ca. 135 ppm, or ca. 5.7%, (u4b) and ca. 219 ppm, or ca. 8.9%, (u4d) Pb loss for uraninites u1-u3 & u4a-d. According to this scheme grain u5 has experienced ca. 38 ppm (ca 1.7%) of Pb loss.

CONCLUSION

Comparison between the results of the electron microprobe work and ID-TIMS dating of uraninite from the same sample of Mugu leucogranite suggests that electron microprobe chemical dating of uraninite may be a useful reconnaissance tool for the geochronology of rocks containing this mineral. The calculated mean chemical dates are

Chapter 5: Electron microprobe chemical dating of uraninite

within uncertainty of other estimates for the crystallization age of the granite as determined by more precise ID-TIMS measurements. Nevertheless, gaining the high spatial resolution of electron microprobe geochronology comes at a price: losing some analytical precision. ID-TIMS U-Pb geochronology of uraninite may, under the best circumstances, yield results with a precision that is up to two orders of magnitude greater than that for electron microprobe chemical dating of uraninite. However, we have shown that uraninite as young as ca. 18.3 Ma can be successfully dated by chemical means with an uncertainty of less than a million years, which is adequate to address many tectonic problems.

Examination of chemical data from uraninite u5 reveals spatial patterns in U, Th, and Y concentrations indicative of diffusion across the structural interface between a chemically distinct core and rim. By contrast, Pb concentration does not display any such diffusive profile. From the form of the concentration profiles, we infer that the diffusivity of Pb is much higher than those of U, Th, or Y in the uraninite family of minerals. Quantitative modeling of the U, Th, and Y concentration profiles, combined with previous estimates for the Arrhenius parameters governing U diffusion in synthetic UO_2 and the diffusivity of Pb in uraninite, suggest that the diffusivity of U, Th, and Y is less than $10^{-7} \text{ cm}^2 \text{ s}^{-1}$ at ca. 700 °C. Pb diffusivity is substantially higher and suggests the possibility that mobility and loss of Pb has affected ID-TIMS analyses of other grains from sample 00KG20. We estimate the amount of Pb loss to be as much as 8.9%.

Bearing the complexities in mind, we advocate the integrated use of electron microprobe and ID-TIMS methods whenever feasible. Electron microprobe chemical dating can be applied quickly and cheaply to uraninites from numerous samples, and the

Chapter 5: Electron microprobe chemical dating of uraninite

results may be used to select appropriate samples for higher precision ID-TIMS work. In addition, the high spatial resolution of the electron microprobe may help with the interpretation of ID-TIMS results for the many leucogranite samples that contain multiple generations of accessory minerals. In older samples, electron microprobe chemical dating of accessory minerals such as monazite may add an additional dimension to such research. Finally, as we have shown, detailed electron microprobe work can also illuminate situations wherein Pb loss or mobility has affected ID-TIMS analyses

ACKNOWLEDGEMENTS

This research was supported by a grant from the U. S. National Science Foundation (NSF) awarded to KVH, J. P. Grotzinger, and Kelin X Whipple (EAR-9706216) and an NSF graduate fellowship awarded to JMH. JMH thanks the Frank and Eva B. Buck Foundation for their continuing financial support.

REFERENCES CITED

- Anderson, G. M., 1976, Error propagation by the Monte Carlo method in geochemical calculations: *Geochimica et Cosmochimica Acta*, v. 40, p. 1533-1538.
- Armstrong, J. T., 1995, A package of correction programs for the quantitative electron microbeam x-ray analysis of thick polished materials, thin-films, and particles: *Microbeam Analysis*, v. 4, p. 177-200.
- Berman, R. M., 1957, The role of lead and excess oxygen in uraninite: *American Mineralogist*, v. 42, no. 11 & 12, p. 705-729.
- Cocherie, A., Legendre, O., Peucat, J. J., and Kouamelan, A. N. 1998, Geochronology of polygenetic monazites constrained by in situ electron microprobe Th-U total lead determination - implications for lead behavior in monazite: *Geochimica et Cosmochimica Acta*, v. 62, p. 2475-2497.

Chapter 5: Electron microprobe chemical dating of uraninite

- Colchen, M., LeFort, P., and Pêcher, A., 1986, *Recherches Géologiques dans l'Himalaya du Népal: Annapurna - Manaslu - Ganesh Himal (Notice de la carte géologique au 1/200000)*: Paris, Centre National de la Recherche Scientifique, 136 p.
- Coleman, M. E., 1998, U-Pb constraints on Oligocene-Miocene deformation and anatexis, Marsyandi Valley, central Nepalese Himalaya: *American Journal of Science*, v. 298, p. 553-571.
- Crank, J., 1975, *The Mathematics of Diffusion*: London, Oxford University Press, 414 p.
- Duncumb, P., and Reed, S. J. B., 1968, Quantitative Electron Probe Microanalysis, in Heinrich, K. F. J., ed., *National Bureau of Standards Special Publication 298*, p. 133.
- Ellsworth, H. V., 1924, *Pan. Am. Geol.*, v. 42, p. 273.
- Gariépy, C., Allègre, C. J., and Xu, R.-H., 1985, The Pb-isotope geochemistry of granitoids from the Himalaya-Tibet collision zone: implications for crustal evolution: *Earth and Planetary Science Letters*, v. 74, p. 220-234.
- Guillot, S., Pecher, A., and LeFort, P., 1995, Contrôles tectoniques et thermiques de la mise en place des leucogranites himalayens; Tectonic and thermal constraints on emplacement of Himalayan leucogranites: *Comptes Rendus Acad. Sci. Paris*, v. 320, no. 1, p. 55-61.
- Harrison, T. M., Lovera, O. M., and Grove, M., 1997, New insights into the origin of two contrasting Himalayan granite belts: *Geology*, v. 25, p. 899-902.
- Harrison, T. M., McKeegan, K. D., and LeFort, P., 1995, Detection of inherited monazite in the Manaslu leucogranite by $^{208}\text{Pb}/^{232}\text{Th}$ ion microprobe dating: Crystallization age and tectonic implications: *Earth and Planetary Science Letters*, v. 133, p. 271-282.
- Harrison, T. M., Ryerson, F. J., McKeegan, K. D., Le Fort, P., and Yin, A., 1996, Th-Pb monazite ages of Himalayan metamorphic and leucogranitic rocks: Constraints on the timing of inverted metamorphism and slip on the MCT and STD, in Macfarlane, A. M., Sorkhabi, R. B., and Quade, J., eds., *11th Himalaya-Karakoram-Tibet Workshop Abstracts*, p. 58-59.
- Heinrich, K. F. J., 1969, *National Bureau of Standards, Technical Note 521*.
- Hodges, K., Bowring, S., Davidek, K., Hawkins, D., and Krol, M., 1998, Evidence for rapid displacement on Himalayan normal faults and the importance of tectonic denudation in the evolution of mountain ranges: *Geology*, v. 26, p. 483-486.

Chapter 5: Electron microprobe chemical dating of uraninite

- Hodges, K. V., 2000, Tectonics of the Himalaya and southern Tibet from two perspectives: *Geological Society of America Bulletin*, v. 112, no. 3, p. 324-350.
- Klein, C., and Hurlbut, C. S. J., 1993, *Manual of Mineralogy* (after James D. Dana): New York, John Wiley & Sons, Inc., 681 p.
- Krogh, T. E., 1973, A low-contamination method for hydrothermal decomposition of zircon and extraction of U and Pb for isotopic age determinations: *Geochimica et Cosmochimica Acta*, v. 37, no. 3, p. 485-494.
- Le Fort, P., Cuney, M., Deniel, C., France-Lanord, C., Sheppard, S. M. F., Upreti, B. N., and Vidal, P., 1987, Crustal generation of Himalayan leucogranites: *Tectonophysics*, v. 134, p. 39-57.
- Le Fort, P., and France-Lanord, C., 1995, Granites from Mustang and surrounding regions, central Nepal: *Journal of the Nepal Geological Society*, v. 10, p. 79-81.
- Ludwig, K. R., 1980, Calculation of uncertainties of U-Pb isotope data: *Earth and Planetary Science Letters*, v. 46, p. 212-220.
- Ludwig, K. R., 1991, Isoplot; a plotting and regression program for radiogenic-isotope data; version 2.53: *U.S. Geological Survey Open File Report 91-0445*, p. 39p.
- Montel, J.-M., Foret, S., Veschambre, M., Nicollet, C., and Provost, A., 1996, Electron microprobe dating of monazite: *Chemical Geology*, v. 131, p. 37-53.
- Moore, M. A., and England, P. C., 2001, On the inference of denudation rates from cooling ages of minerals: *Earth and Planetary Science Letters*, v. 185, p. 265-284.
- Noble, S. R., and Searle, M. P., 1995, Age of crustal melting and leucogranite formation from U-Pb zircon and monazite dating in the western Himalaya, Zaskar, India: *Geology*, v. 23, no. 12, p. 1135-1138.
- Parrish, R., 1990, U-Pb dating of monazite and its application to geological problems: *Canadian Journal of Earth Sciences*, v. 27, p. 1431-1450.
- Patiño Douce, A. E., and Harris, N., 1998, Experimental Constraints on Himalayan Anatexis: *Journal of Petrology*, v. 39, no. 4, p. 689-710.
- Reed, S. J. B., 1965, Characteristic fluorescence correction in electron-probe microanalysis: *British Journal of Applied Physics*, v. 16, no. 913-926.
- Sabioni, A. C. S., Ferraz, W. B., and Millot, F., 1998, First study of uranium self-diffusion in UO₂ by SIMS: *Journal of Nuclear Materials*, v. 257, p. 180-184.

Chapter 5: Electron microprobe chemical dating of uraninite

- Scailliet, B., Pichavant, M., and Roux, J., 1995, Experimental crystallization of leucogranite magmas: *Journal of Petrology*, v. 36, no. 3, p. 663-705.
- Schärer, U., 1984, The effect of initial ^{230}Th disequilibrium on young U-Pb ages: the Makalu case, Himalaya: *Earth and Planetary Science Letters*, v. 67, p. 191-204.
- Searle, M. P., Parrish, R. R., Hodges, K. V., Hurford, A., Ayers, M. W., and Whitehouse, M. J., 1997, Shisha Pangma leucogranite, South Tibetan Himalaya: Field relations, geochemistry, age, origin, and emplacement: *Journal of Geology*, v. 105, p. 295-317.
- Snetsinger, K. G., and Polkowski, G., 1977, Rare accessory uraninite in a Sierran granite: *American Mineralogist*, v. 62, p. 587-588.
- Stacey, J. S., and Kramers, J. D., 1975, Approximation of terrestrial isotope evolution by a two-stage model: *Earth and Planetary Science Letters*, v. 26, p. 207-221.
- Steiger, R. H., and Jäger, E., 1977, Subcommittee on geochronology: convention on the use of decay constants in geo- and cosmochronology: *Earth and Planetary Science Letters*, v. 36, p. 359-362.
- Terry, M. P., Robinson, P., Hamilton, M. A., and Jercinovic, M. J., 2000, Monazite geochronology of UHP and HP metamorphism, deformation, and exhumation, Nordoyane, Western Gneiss region, Norway: *American Mineralogist*, v. 85, no. 11-12, p. 1651-1664.
- Viskupic, K. M., and Hodges, K. V., 2001, Monazite-xenotime thermochronology: methodology and an example from the Nepalese Himalaya: *Contributions to Mineralogy and Petrology*, v. 141, p. 233-247.
- Wendt, I., and Carl, C., 1991, The statistical distribution of the mean squared weighted deviation: *Chemical Geology*, v. 86, p. 275-285.
- White, A. P., 2001, *Extensional Evolution of the Central East Greenland Caledonides* [Ph.D. thesis]: Massachusetts Institute of Technology, 301 p.
- Williams, M. L., Jercinovic, M. J., and Terry, M. P., 1999, Age mapping and dating of monazite on the electron microprobe: deconvoluting multistage tectonic histories: *Geology*, v. 27, no. 11, p. 1023-1026.
- Yajima, S., Furuya, H., and Hiroi, T., 1966, *Journal of Nuclear Materials*, p. 162.
- Yershov, V. M., 1974, A method of examining the diffusion parameters of lead in uranium minerals: *Geochemistry International*, v. 11, p. 1099-1101.

Chapter 5: Electron microprobe chemical dating of uraninite

York, D., 1969, Least-squares fitting of a straight line with correlated errors: *Earth and Planetary Science Letters*, v. 5, p. 320-324.

FIGURE CAPTIONS

Table 1.

Electron microprobe data for sample 00KG20 (grain u5).

Table 2.

Isotope dilution, thermal-ionization mass spectrometry (ID-TIMS) data for sample 00KG20 (grains m1-2 & u1-u4a-d).

Table 3.

Summary of ^{230}Th deficiency correction (Schärer, 1984; Parrish, 1990) of 00KG20 uraninites.

Table 4.

Summary of U-Th-Pb geochronologic results for sample 00KG20.

Table 5.

Times required for diffusion to create U diffusion profile in Figure 6a for a variety of reasonable temperatures, given the appropriate Arrhenius parameters and the modeled $D_n t$ parameter for U from Figure 7a.

Table 6.

Temperatures required for diffusion to create U diffusion profile in Figure 6a for a variety of reasonable times, given the appropriate Arrhenius parameters and the modeled $D_n t$ parameter for U from Figure 7a.

Figure 1.

a. Plot of $[Pb]_{Th}/[Pb]_U$ versus sample age (in Ma). The quantity $[Pb]_{Th}/[Pb]_U$ is the ratio of the portion of the total Pb concentration derived from ^{232}Th decay to that derived from ^{235}U and ^{238}U decay. It is calculated by taking the ratio of the two summed terms on the right hand side of equation (1). Labeled curves shown are for a range of Th/U ratios between 0.05 and 1.0 (equal concentrations of Th and U). Uraninites from sample 00KG20 have a mean Th/U of approximately 0.05 (see Tables 1 & 2).

b. Plot showing the effect of Th/U on calculated electron microprobe chemical dates for sample 00KG20. We assume appropriate mean concentrations of U (837226.86 ppm) and Pb (2241.46 ppm) for grain u5 (Table 1). The solid curve shows how the chemical date of grain u5 calculated with equation (1) varies with Th concentration (and thus Th/U). The dashed horizontal line shows the chemical date of grain u5 calculated with equation (2) (ca. 19.2 Ma) which is independent of Th/U. The dash-dotted curve shows the percent deviation of the date calculated from equation (1) with respect to that calculated from equation (2) as a function of Th/U for grain u5. The dotted vertical line shows the mean Th/U for 00KG20 (ca. 0.05; see Tables 1 & 2). The intersection of this vertical line with the other curves indicates a date of ca. 18.9 using equation (1), which amounts to a mean deviation of ca. 1.6% from the ca. 19.2 Ma date calculated with equation (2).

Figure 2.

Map showing the location of the Thakkhola graben and Upper Mustang Massif (UMM) (inset) and generalized geology of the region.

Figure 3.

a. Photograph of the Mugu granite dike from which sample 00KG20 was taken. View to the southwest. Field book for scale is 12 cm by 19 cm. The country rock is deformed Silurian to Devonian calcic pelitic schist of the Tibetan Sedimentary sequence (Colchen *et al.*, 1986; Le Fort and France-Lanord, 1995) metamorphosed to lower-amphibolite facies. Compositional layering in the country rock strikes east and dips moderately south, whereas the dike strikes north and dips steeply west. The dike is

Chapter 5: Electron microprobe chemical dating of uraninite

undeformed and cuts across older, deformed Mugu granite dikes (not shown) and the deformational fabrics in the country rock. Further details are given in Hurtado *et al.* (submitted – see Chapter 4).

b. Photomicrographs of uraninite crystals from 00KG20. Grains u1-u4a-d were used for ID-TIMS analysis, and grain u5 (not shown, but similar in size and appearance to the unbroken u4) was used for electron microprobe work. Note the specular patina on the uraninite grains (e.g. light colored patches on u1, u3, and u4) indicative of pervasive inclusions. Images taken with a digital camera mounted to a binocular microscope. The grains, immersed in an ethanol bath, were imaged with a digital camera under reflected light at a magnification of 6.3x (see scale bar).

c. Secondary electron (SE) image of grain u5. Note the abundant pits and voids due to excavated inclusions. Some form a concentric band parallel to the crystal faces. Labeled circles denote locations of spot analyses in Transect 1. Crosses denote spot analyses in Transect 2. Spot sizes (ca. 1 μm) are smaller than the diameter of the symbols.

d. Back-scattered electron (BSE) image of grain u5. Note the lack of any obvious variation in grayscale within the grain, suggesting a lack of intra-grain gradients in chemical composition. Labeled circles denote locations of spot analyses in Transect 1. Crosses denote spot analyses in Transect 2. Spot sizes (ca. 1 μm) are smaller than the diameter of the symbols.

e. Contour plots of U, Th, Y, Pb, and chemical age superimposed on the SE image for u5. Contours of U, Th, and Y concentrations conform closely to the structural zonation visible in the crystal. Contours of Pb and chemical age do not conform to crystal morphology. Labeled circles and crosses denote locations of spot analyses. Spot sizes (ca. 1 μm) are smaller than the diameter of the symbols. Plain SE image in lower right corner is for reference.

Figure 4.

Along-transect profiles of elemental concentrations and chemical dates. Units along the x-axis are in μm from the center of the grain. The center of the grain ($x = 0$ μm) is taken as the position of the first point in the transect. The core region of the grain

Chapter 5: Electron microprobe chemical dating of uraninite

is that closest to the center, and the rim is on the periphery. See Figure 3c & d. Concentration is in ppm. Dates are in Ma. Error bars denote the 2σ (95%) confidence intervals.

- a. U concentration profile along Transect 1.
- b. U concentration profile along Transect 2.
- c. Th concentration profile along Transect 1.
- d. Th concentration profile along Transect 2.
- e. Y concentration profile along Transect 1.
- f. Y concentration profile along Transect 2.
- g. Pb concentration profile along Transect 1.
- h. Pb concentration profile along Transect 2.
- i. Chemical age profile along Transect 1.
- j. Chemical age profile along Transect 2.
- k. Plot of combined chemical dates for both transects.

Figure 5.

Concordia diagrams for sample 00KG20. Curves with numbered tic marks represent concordia with labels in units of Ma. Data points include error ellipses representing 2σ (95%) analytical uncertainties. Data points are labeled by grain identifier (m = monazite; u = uraninite).

a. Uraninite analyses u1-u4a-d. Uncorrected for ^{230}Th deficiency (Schärer, 1984; Parrish, 1990). Note that the uraninite analyses form a linear array essentially parallel to concordia

b. Uraninite analyses u1-u4-d. Corrected for ^{230}Th deficiency (Schärer, 1984; Parrish, 1990). Note that the correction moves the data points upward toward concordia slightly.

c. Uraninite analyses u1-u4a-d and monazite m1. Uraninite data have been corrected for ^{230}Th deficiency (Schärer, 1984; Parrish, 1990). A York (1969) regression – specifically Model 2 of Ludwig (1991) – through the corrected uraninite analyses yields an upper concordia intercept corresponding to a date of $17.63^{+108}_{-0.63}{}^{72}$ Ma (MSWD = 19.8).

Chapter 5: Electron microprobe chemical dating of uraninite

d. Uraninite analyses u1-u4a-d and monazite m1. Uraninite data have not been corrected for ^{230}Th deficiency (Schärer, 1984; Parrish, 1990). A York (1969) regression – specifically Model 2 of Ludwig (1991) – through the uncorrected uraninite analyses yields an upper concordia intercept corresponding to a date of $19.22^{+95}_{-155} \text{ Ma}$ (MSWD = 16.5)

Figure 6.

Concentration profiles normalized to the maximum concentration along the transect (C/C_0). Error bars denote 2σ (95%) confidence intervals. Dashed line is best-fit model diffusion profile to the concentration data using equations (4ab). The shape of the curve is determined by the quantity $D_n t$. Units along the x-axis are in μm from the first point in the transect (see Figure 3c & d).

- a. Transect 1 uranium.
- b. Transect 2 uranium.
- c. Transect 1 thorium.
- d. Transect 2 thorium.
- e. Transect 1 yttrium.
- f. Transect 2 yttrium.

Figure 7.

Inversion of concentration profiles through the inverse error function using equations (6ab). Diamonds are point analyses. Solid line is least squares linear fit through the data (equation and R^2 fit criterion given). The slope of the best-fit line is proportional to the quantity $D_n t$.

- a. Transect 1 uranium.
- b. Transect 2 uranium.
- c. Transect 1 thorium.
- d. Transect 2 thorium.
- e. Transect 1 yttrium.
- f. Transect 2 yttrium.

Chapter 5: Electron microprobe chemical dating of uraninite

Figure 8.

Plot showing the relationship between Pb concentration and chemical age according to equation (1). We assume that the concentrations of U and Th are equal to the mean concentrations from grain u5 (U: ca. 837,227 ppm, Th: ca. 36,539 ppm; Table 1). The relationship is a linear one with a slope of 0.084 Ma per ppm.

TABLE 1. ELECTRON MICROPROBE POINT DATA AND RESULTS FOR 00KG20 u5

Point†	X§ (μm)	U# (ppm)	\pm	2 σ # (ppm)	Th# (ppm)	\pm	2 σ # (ppm)	Pb# (ppm)	\pm	2 σ # (ppm)	Y# (ppm)	\pm	2 σ # (ppm)	O# (ppm)	Total‡ (wt %)	Date§§ (Ma)	\pm	2 σ §§ (Ma)				
<i>Transect 1</i>																						
1	0.0	851402	35	\pm 1907	14	23949	01	\pm 187	28	2197	86	\pm 166	.77	3536	97	\pm 243	77	118918	92	98	18.32	\pm 1.43
2	8.9	851337	34	\pm 1941	05	24113.62		\pm 187	60	2274	52	\pm 169	00	3440	80	\pm 240	99	118909	39	96	18.96	\pm 1.45
3	15.0	852592	90	\pm 1909	81	22853.21		\pm 184	65	2132	50	\pm 166	59	3486	12	\pm 240	68	118926	09	98	17.76	\pm 1.43
4	24.0	850194	55	\pm 1921	44	24997	95	\pm 189	98	2491	30	\pm 172	10	3457	92	\pm 248	35	118881	83	98	20.78	\pm 1.48
5	35.4	849428	76	\pm 1987	66	26083.21		\pm 197	71	2731	19	\pm 178	62	3027	59	\pm 242	51	118775	60	93	22.79	\pm 1.54
6	47.5	847579	39	\pm 1932	.48	27475.27		\pm 197	82	2382.09		\pm 173	.80	3613	74	\pm 250	29	118896	41	96	19.91	\pm 1.50
7	51.5	839720	54	\pm 1914	56	34624.47		\pm 211	21	2514.13		\pm 170	01	4094	32	\pm 246	23	118976	68	97	21.15	\pm 1.48
8	54.9	848176	87	\pm 1950	81	26797.99		\pm 196	70	2753	56	\pm 176	12	3397	95	\pm 248	59	118818	11	95	23.00	\pm 1.52
9	62.9	840221	77	\pm 1898	90	34879	03	\pm 209	27	2061	49	\pm 165	08	3834	68	\pm 242	12	118951	61	99	17.34	\pm 1.43
10	77.1	826913	25	\pm 1885	36	46081	54	\pm 233	17	2069	07	\pm 164	95	5771	94	\pm 264	24	119239	81	98	17.60	\pm 1.45
11	83.0	814998	48	\pm 1874	50	56269	61	\pm 250	96	2225.48		\pm 164	.51	7139	97	\pm 278	32	119421	11	99	19.13	\pm 1.46
12	94.2	806348	88	\pm 1870	73	62975	14	\pm 264	50	2082	39	\pm 165	01	8918	22	\pm 293	77	119683	58	97	18.04	\pm 1.47
13	103.9	806932	26	\pm 1904	36	62665.12		\pm 268	21	2019	44	\pm 167	05	8688	58	\pm 299	06	119623	80	95	17.49	\pm 1.49
14	115.9	806055	73	\pm 1853	93	63575	09	\pm 261	93	2193	94	\pm 166	39	8543	41	\pm 292	01	119605	67	99	19.01	\pm 1.49
<i>Transect 1 mean \pm 2SE ##</i>																18.17	\pm	0.52				
<i>Transect 2</i>																						
1	0.0	851264	86	\pm 1906	83	24201.97		\pm 187	32	2269	63	\pm 168	09	3339	43	\pm 244	11	118866	20	98	18.91	\pm 1.45
2	8.9	851658	82	\pm 1890	68	23926	03	\pm 185	19	2040	69	\pm 165	50	3479	00	\pm 241	30	118873	41	100	17.00	\pm 1.42
3	18.4	851480	18	\pm 1907	32	24295	03	\pm 186	.10	2157	55	\pm 167	.56	3207	23	\pm 239	19	118815	86	100	17.98	\pm 1.44
4	26.2	852249	70	\pm 1909	04	23360	36	\pm 184	08	2199	03	\pm 166	55	3315.77		\pm 240	33	118869	07	99	18.31	\pm 1.43
5	42.4	852562	81	\pm 1892	69	23197.99		\pm 183	73	2138	69	\pm 166	18	3235	18	\pm 240	83	118894	47	100	17.81	\pm 1.43
6	47.4	852841	.48	\pm 1893	31	23257	23	\pm 182	34	2016	95	\pm 164	87	3115	65	\pm 231	56	118843	47	100	16.79	\pm 1.41
7	60.8	850680	10	\pm 1905	52	24764	74	\pm 187	72	2013	10	\pm 166	44	3650	38	\pm 243	41	118891	69	99	16.79	\pm 1.43
8	73.2	826923	08	\pm 1901	92	45968	74	\pm 233	52	2383	79	\pm 169	.82	5525	50	\pm 264	89	119189	63	97	20.28	\pm 1.49
9	80.8	806150	69	\pm 1870	.27	63249	62	\pm 264	38	2144	54	\pm 165	64	8827.27		\pm 294	83	119630	96	98	18.58	\pm 1.48
10	89.5	805729	90	\pm 1853	18	63373	15	\pm 262	36	2302	09	\pm 166	44	8943	11	\pm 293	87	119659	85	99	19.95	\pm 1.49
<i>Transect 2 mean \pm 2SE ##</i>																17.77	\pm	0.59				
<i>All points mean \pm 2SE ##</i>																17.96	\pm	0.40				

Notes

† See Fig 3c-d for maps of the points superimposed on the back-scattered and secondary electron images. For Transect 1, Point 1 is near the center of the grain and Point 14 is at the edge. Similarly, for Transect 2, Point 1 is near the center and Point 10 is at the edge.

§ Radial distance outward from the center of the grain. The "center" is taken to be the position of the innermost point analysis. Note that Point 1 for Transect 1 is not in the same place as Point 1 for Transect 2, although both are in the approximate center of the grain (Fig 3c-d). For Transect 1, the structural break between core and rim is between Points 9 and 10. For Transect 2 the structural break between core and rim is between Points 7 and 8.

Concentrations determined by wavelength dispersive spectrometry (WDS) using PET diffracting crystals calibrated with UO_2 , ThO_2 , ThSiO_4 , PbTiO_3 , and YAG (Y-Al garnet $\text{Y}_3\text{Al}_5\text{O}_{12}$) standards. Measured intensities converted to concentrations using the CITZAF matrix correction (Armstrong, 1995). O concentration determined stoichiometrically. Raw concentrations (in weight %, not shown) of U, Th, Pb, Y, and O were re-normalized to sum to 100% and then recast in ppm (values listed in table). YL γ interference with the PbM α line causes Pb contents to be overestimated by ca. 35 ppm, and ThM β interference with the UM α line causes U contents to be overestimated by ca. 16 ppm. The concentrations listed have been corrected accordingly (see text). Analytical uncertainties listed are at the 2 σ (95%) confidence level and reflect errors due to the counting statistics only.

‡ Un-normalized, Y- and Th-interference corrected (see #) totals for each point analysis in weight percent (wt. %). In most cases, the totals are close to 100% before being re-normalized (re-normalized % totals not given, see #). Generally, the 0-3% unaccounted for may be due to trace amounts of Nd, Ra, Ce, N, He, A, and/or OH commonly present in uraninite that we did not measure (e.g. Snetsinger and Polkowki, 1977; Klein and Hurlbut, 1993). Those analyses with anomalously low totals (e.g. $\leq 96\%$, italicized) may also have been adversely affected by non-idealities (i.e. pits and roughness) on the polished grain surface (see Fig 3c-d). These points were excluded from calculation of the mean chemical date (see ##).

§§ Dates calculated using equation (1). Uncertainties given are at the 2 σ (95%) confidence level. Uncertainties estimated by propagating analytical uncertainties in U, Th, and Pb concentrations through equation (1) using a modified Monte Carlo method (e.g. Anderson, 1976; Terry *et al.*, 2000; White, 2001). Calculations use the decay constants of Steiger and Jäger (1977): $0.4947\text{e-}10 \text{ yr}^{-1}$ (^{235}U), $9.8485\text{e-}10 \text{ yr}^{-1}$ (^{238}U), $1.55125\text{e-}10 \text{ yr}^{-1}$ (^{230}U).

Mean chemical date excludes both points with low totals (italicized dates, see ‡) and anomalously old points (dates in plain type, see text & Fig 4k). Dates in boldface are those used in mean calculations. Uncertainties given are 2 standard errors of the mean chemical dates (2SE).

TABLE 2. ID-TIMS DATA AND RESULTS FOR 00KG20 u1-u4a-d & m1-2

Grain†	Mass§ (µg)	U# (ppm)	Pb# (ppm)	Th/U#	Common Pb‡ (pg)	Uranium					Correlation Coefficient	²⁰⁶ Pb/ ²³⁸ U		²⁰⁷ Pb/ ²³⁵ U		²⁰⁷ Pb/ ²⁰⁶ Pb	
						²⁰⁶ Pb/ ²⁰⁴ Pb§§	²⁰⁶ Pb/ ²⁰⁸ Pb##	²⁰⁶ Pb/ ²³⁸ U†††	²⁰⁷ Pb/ ²³⁵ U†††	²⁰⁷ Pb/ ²⁰⁶ Pb†††		Date§§§ (Ma)	2σ§§§ (Ma)	Date§§§ (Ma)	2σ§§§ (Ma)	Date§§§ (Ma)	2σ§§§ (Ma)
<i>Uraninite</i>																	
u1	2.5	411002	991.9	0.062	4.5	38691.3	0.020	0.002632(0.15)	0.01694(0.17)	0.04669(0.08)	0.864	16.942 ± 0.025	17.058 ± 0.029	33.4 ± 2.0			
u2	1.2	734695	1740.6	0.070	8.4	17243.4	0.023	0.002571(0.09)	0.01660(0.10)	0.04682(0.05)	0.857	16.552 ± 0.015	16.713 ± 0.018	39.9 ± 1.3			
u3	1.4	517929	1230.8	0.069	41.4	2849.6	0.022	0.002528(0.10)	0.01638(0.14)	0.04698(0.09)	0.736	16.279 ± 0.017	16.497 ± 0.023	48.4 ± 2.3			
u4a	1.2	351631	827.8	0.051	0.4	181580.6	0.017	0.002576(0.05)	0.01662(0.06)	0.04681(0.04)	0.736	16.583 ± 0.008	16.742 ± 0.011	39.5 ± 1.0			
u4b	2.5	267762	644.0	0.044	0.6	198820.6	0.014	0.002638(0.05)	0.01702(0.07)	0.04680(0.04)	0.782	16.982 ± 0.009	17.139 ± 0.011	39.2 ± 1.0			
u4c	1.2	425932	986.4	0.049	0.9	95393.5	0.016	0.002536(0.07)	0.01637(0.09)	0.04681(0.05)	0.806	16.324 ± 0.012	16.483 ± 0.015	39.7 ± 1.3			
u4d	1.2	535167	1237.8	0.054	0.6	187062.8	0.018	0.002528(0.06)	0.01632(0.07)	0.04681(0.04)	0.800	16.279 ± 0.009	16.436 ± 0.012	39.5 ± 1.0			
<i>Monazite</i>																	
m1	16.0	4789	56.5	10.114	100.6	156.3	3.258	0.002829(0.14)	0.01820(0.52)	0.04657(0.49)	0.382	18.21 ± 0.03	18.28 ± 0.10	27.4 ± 11.7			
m2	7.7	4272	92.8	14.867	44.9	212.3	4.673	0.004132(0.19)	0.02600(0.55)	0.04560(0.50)	0.411	26.58 ± 0.05	26.04 ± 0.14	-23.3 ± 12.2			

Notes

† Fractions designated by mineral m = monazite; u = uraninite All fractions were single crystals, except for u4a-d which were single fragments of a larger crystal
 § Sample weights, estimated using sample dimensions determined from a calibrated gnded video monitor, are known to within 40% based on comparisons of estimated and measured weights
 # Compositions expressed as ppm U, ppm total Pb, and Th/U Th/U ratios calculated from the ²⁰⁸Pb/²⁰⁶Pb ratios
 ‡ Total common Pb in analyses
 §§ Measured ratio corrected for fractionation and spike only, Pb fractionation is 0.12 ± 0.04% per a m u (atomic mass unit) for multicollector (dynamic) Faraday analyses and 0.15 ± 0.04% per a m u for single collector Daly analysis based on repeated analyses of NBS-981
 ## Radiogenic Pb See ††† for analytical details
 ††† Isotopic ratios corrected for fractionation, spike, blank, and initial common Pb Total procedural U blank < 0.1 pg ± 50% Data were reduced using a total procedural Pb blank of 3.5 pg ± 50% except for analyses with < 3.5 pg total common Pb, in which case this value was used as blank and the uncertainty reduced to 20% Pb blank composition ²⁰⁶Pb/²⁰⁴Pb = 19.10 ± 0.1%, ²⁰⁷Pb/²⁰⁴Pb = 15.71 ± 0.1%, ²⁰⁸Pb/²⁰⁴Pb = 38.65 ± 0.1% (uncertainties at the 1σ level) Initial common Pb composition used is based on the model of Stacey and Kramers (1975) and the interpreted age of the sample, see Hurtado *et al.* (submitted – Chapter 4) for details Numbers in parentheses are the % error reported at the 2σ (95%) confidence level
 §§§ Uncertainties in millions of years (Ma) at the 2σ (95%) confidence level Age calculations based on the decay constants of Steiger and Jäger (1977): 0.4947e-10 yr⁻¹ (²³²Th), 9.8485e-10 yr⁻¹ (²³⁵U), 1.55125e-10 yr⁻¹ (²³⁸U)

Table 2

TABLE 3. ²³⁰Th DEFICIENCY CORRECTION†

Grain	(²⁰⁶ Pb/ ²³⁸ U) _{uc} §	(Th/U) _{mineral} #	(²⁰⁶ Pb/ ²³⁸ U) _c ‡
u1	0.002632	0.062	0.002647
u2	0.002571	0.070	0.002586
u3	0.002528	0.069	0.002543
u4a	0.002576	0.051	0.002592
u4b	0.002638	0.044	0.002654
u4c	0.002536	0.049	0.002552
u4d	0.002528	0.054	0.002544

Notes :

† Uses equation from Parrish (1990): (²⁰⁶Pb/²³⁸U)_c = (²⁰⁶Pb/²³⁸U)_{uc} - ([(Th/U)_{mineral}/(Th/U)_{magma}]-1) * {λ₂₃₈ / λ₂₃₀ }.

Decay constants: λ₂₃₈ = 1.5513e⁻¹⁰ yr⁻¹; λ₂₃₀ = 9.22e⁻⁶ yr⁻¹.
(Th/U)_{magma} = 0.689 (Manaslu pluton; Le Fort *et al.* , 1987).

§ uc = uncorrected.

Th/U ratio of the grain as determined by ID-TIMS analysis (see Table 2).

‡ c = corrected.

TABLE 4. SUMMARY OF U-Pb-Th GEOCHRONOLOGIC RESULTS FOR 00KG20

Technique†	Mineral	Date (Ma)	±	Uncertainty (Ma)
ID-TIMS§	monazite	18.28	±	0.10
ID-TIMS§	uraninite	17.139	±	0.011
ID-TIMS	isochron#	17.63	±	+108.72/-0.63
Chemical‡	uraninite	18.17	±	0.52
Chemical§§	uraninite	17.77	±	0.59
Chemical##	uraninite	17.96	±	0.40

Notes :

† ID-TIMS = isotope-dilution, thermal ionization mass spectrometry. Chemical = electron microprobe total U-Th-Pb chemical dating.

§ Monazite ID-TIMS date is ²⁰⁷Pb/²³⁵U date of grain m1 (Hurtado *et al.* , submitted – see Chapter 4). Uraninite ID-TIMS date is ²⁰⁷Pb/²³⁵U date of grain u4b (Table 1). ID-TIMS uncertainties are given at the 2σ (95%) confidence level.

York 2 regression (York, 1969; Ludwig, 1991) through uraninites u1-u4ad (Fig. 5c). Data corrected for ²³⁰Th deficiency.

‡ Transect 1 mean and 2 standard errors of the mean (Table 2).

§§ Transect 2 mean and 2 standard errors of the mean (Table 2).

All points mean and 2 standard errors of the mean (Table 2).

Tables 3 & 4

Chapter 5: Electron microprobe chemical dating of uraninite

TABLE 5. U DIFFUSIVITY: TIME CALCULATIONS

T† (°C)	T† (K)	D _o § (cm ² s ⁻¹)	t# (Ma)
Sabioni <i>et al.</i> (1998)‡			
500	773	1.78E-35	4.91E+15
525	798	1.41E-34	6.21E+14
550	823	9.83E-34	8.90E+13
575	848	6.12E-33	1.43E+13
600	873	3.43E-32	2.55E+12
625	898	1.75E-31	5.01E+11
650	923	8.14E-31	1.07E+11
675	948	3.50E-30	2.50E+10
700	973	1.40E-29	6.27E+09
725	998	5.19E-29	1.68E+09
750	1023	1.81E-28	4.82E+08
Yajima <i>et al.</i> (1966)§§			
500	773	2.56E-24	3.42E+04
525	798	1.05E-23	8.32E+03
550	823	3.96E-23	2.21E+03
575	848	1.38E-22	6.33E+02
600	873	4.48E-22	1.95E+02
625	898	1.36E-21	6.41E+01
650	923	3.90E-21	2.24E+01
675	948	1.06E-20	8.27E+00
700	973	2.72E-20	3.22E+00
725	998	6.67E-20	1.31E+00
750	1023	1.57E-19	5.58E-01

Notes :

† Range of reasonable temperatures, between the metamorphic temperature of the country rock (ca. 500 °C – Hurtado *et al.*, submitted – see Chapter 4) and the temperature of a leucogranitic melt (ca. 700 °C – Scaillet *et al.*, 1995; Patiño Douce and Harris, 1998).

§ $D_n = D_o \exp(-E_a/RT)$. D_o = diffusivity at infinite temperature (in cm² s⁻¹); E_a = activation energy (in kJ mol⁻¹); R = gas constant (8.31451 J mol⁻¹ K⁻¹); T = temperature (in K); D_n = diffusivity (in cm² s⁻¹) at temperature T .

Required time to develop the diffusion profiles in Fig. 6, at a given temperature (see †), based on the modeled $D_n t$ value (2.76e-6 cm²) and the appropriate Arrhenius parameters (see ‡ and §§).

‡ $D_o = 8.54e-7$ cm² s⁻¹. $E_a = 425.54$ kJ mol⁻¹.

§§ $D_o = 1e-4$ cm² s⁻¹. $E_a = 290$ kJ mol⁻¹.

TABLE 6. U DIFFUSIVITY: TEMPERATURE CALCULATIONS

t† (Ma)	t† (sec)	D _o § (cm ² s ⁻¹)	T# (°C)
Sabioni <i>et al.</i> (1998)‡			
1	3.16E+13	8.74E-20	1434
2	6.31E+13	4.37E-20	1395
3	9.47E+13	2.91E-20	1373
4	1.26E+14	2.19E-20	1358
5	1.58E+14	1.75E-20	1347
6	1.89E+14	1.46E-20	1337
7	2.21E+14	1.25E-20	1330
8	2.52E+14	1.09E-20	1323
9	2.84E+14	9.72E-21	1317
10	3.16E+14	8.74E-21	1312
11	3.47E+14	7.95E-21	1307
12	3.79E+14	7.29E-21	1303
13	4.10E+14	6.73E-21	1299
14	4.42E+14	6.25E-21	1296
15	4.73E+14	5.83E-21	1292
16	5.05E+14	5.47E-21	1289
17	5.36E+14	5.14E-21	1286
18	5.68E+14	4.86E-21	1284
Yajima <i>et al.</i> (1966)§§			
1	3.16E+13	8.74E-20	733
2	6.31E+13	4.37E-20	713
3	9.47E+13	2.91E-20	702
4	1.26E+14	2.19E-20	694
5	1.58E+14	1.75E-20	688
6	1.89E+14	1.46E-20	683
7	2.21E+14	1.25E-20	679
8	2.52E+14	1.09E-20	676
9	2.84E+14	9.72E-21	673
10	3.16E+14	8.74E-21	670
11	3.47E+14	7.95E-21	668
12	3.79E+14	7.29E-21	666
13	4.10E+14	6.73E-21	663
14	4.42E+14	6.25E-21	662
15	4.73E+14	5.83E-21	660
16	5.05E+14	5.47E-21	658
17	5.36E+14	5.14E-21	657
18	5.68E+14	4.86E-21	655

Notes :

† Range of reasonable times, between 1 Ma and the age of 00KG20.

§ $D_n = D_o \exp(-E_a/RT)$. D_o = diffusivity at infinite temperature (in cm² s⁻¹); E_a = activation energy (in kJ mol⁻¹); R = gas constant (8.31451 J mol⁻¹ K⁻¹); T = temperature (in K); D_n = diffusivity (in cm² s⁻¹) at temperature T .

Required temperature to develop the diffusion profiles in Fig. 6, over a given period of time (see †), based on the modeled $D_n t$ value (2.76e-6 cm²) and the appropriate Arrhenius parameters (see ‡ and §§).

‡ $D_o = 8.54e-7$ cm² s⁻¹. $E_a = 425.54$ kJ mol⁻¹.

§§ $D_o = 1e-4$ cm² s⁻¹. $E_a = 290$ kJ mol⁻¹.

Tables 5 & 6

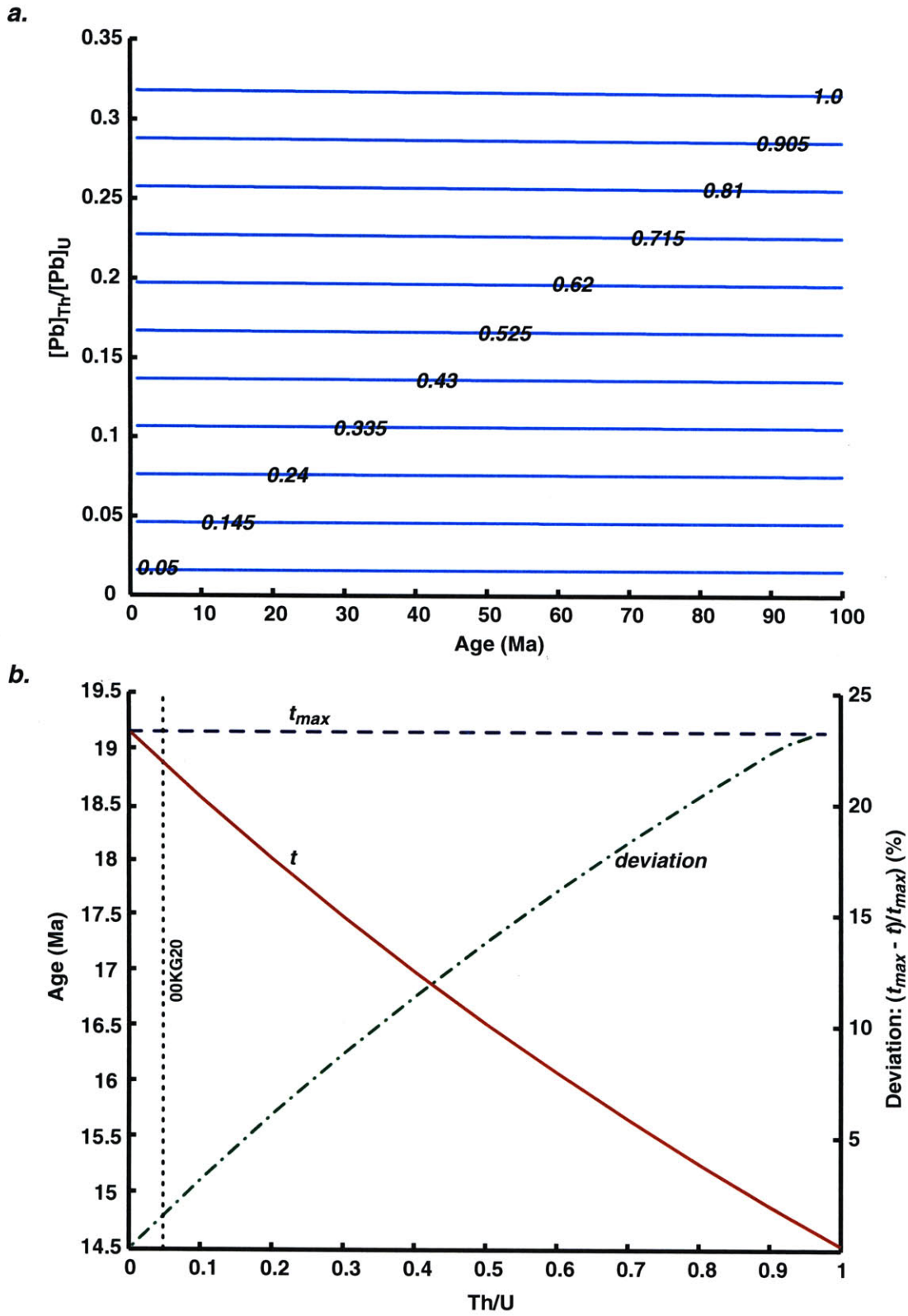


Figure 1

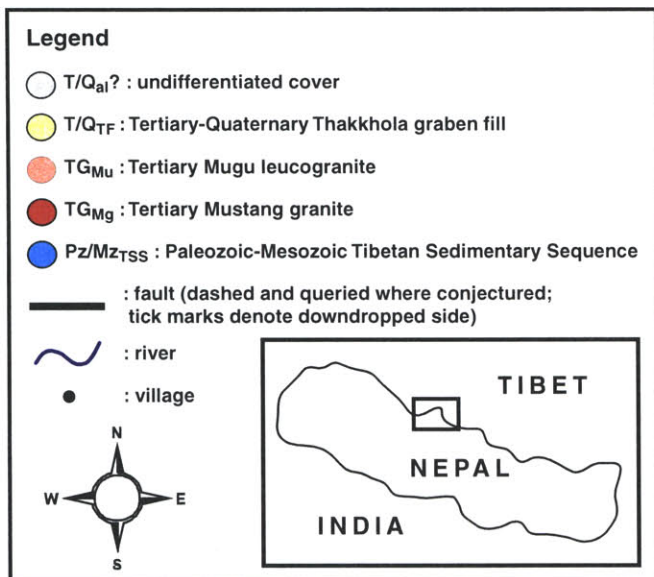
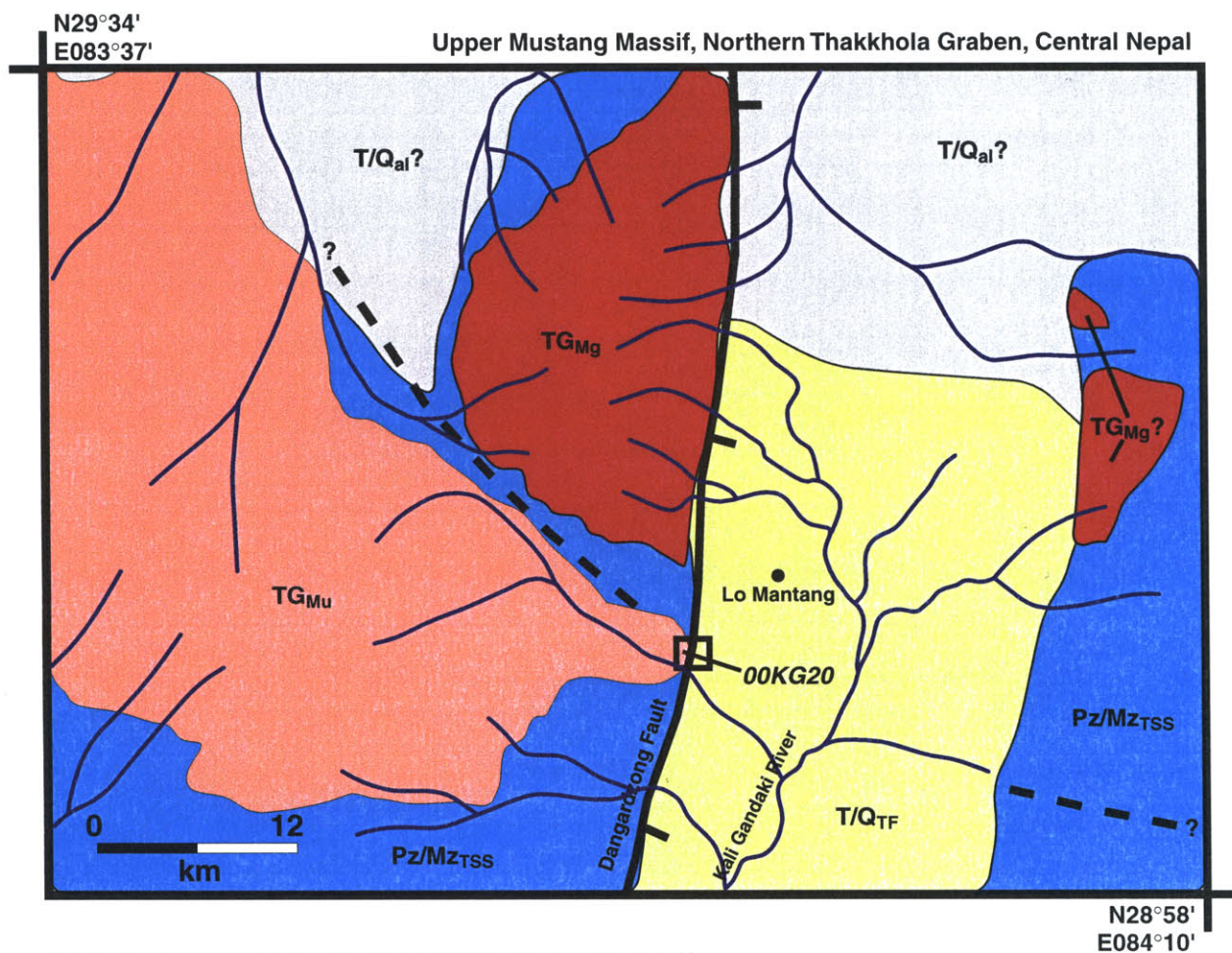
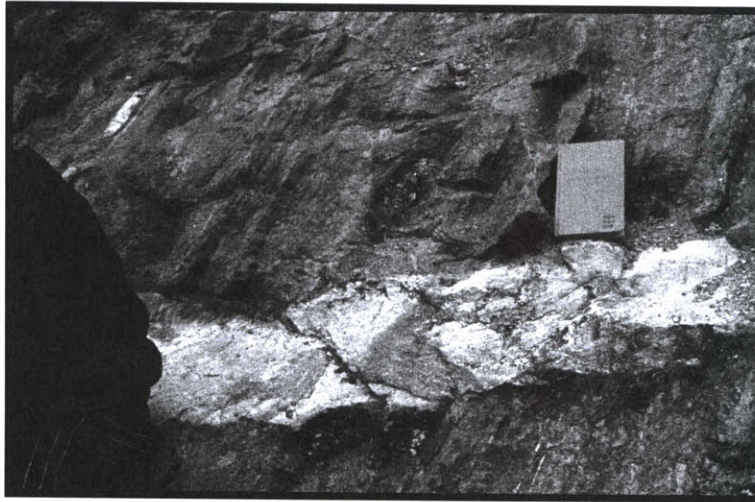


Figure 2

a.



b.

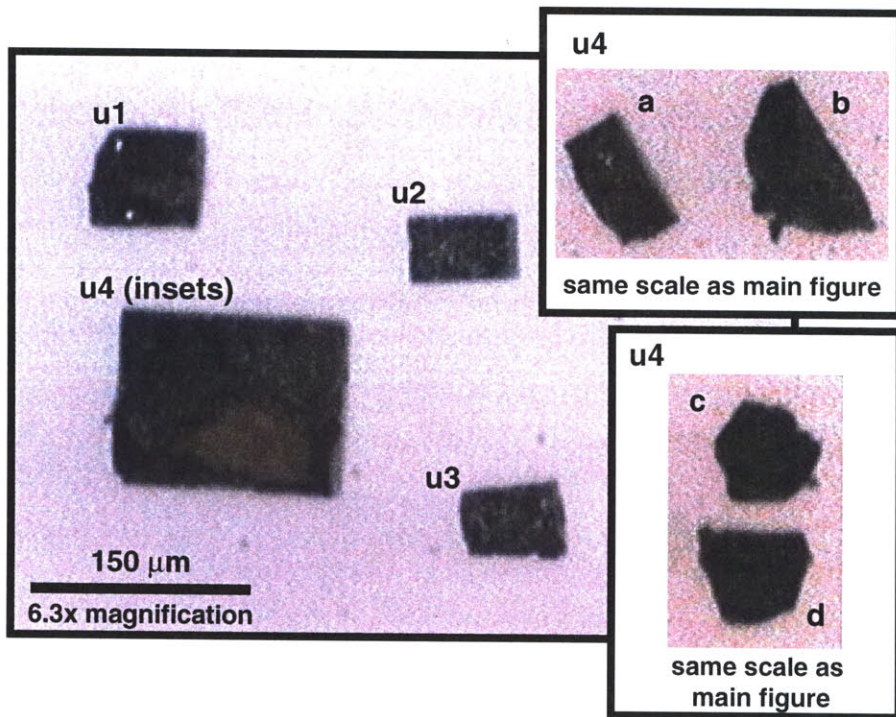
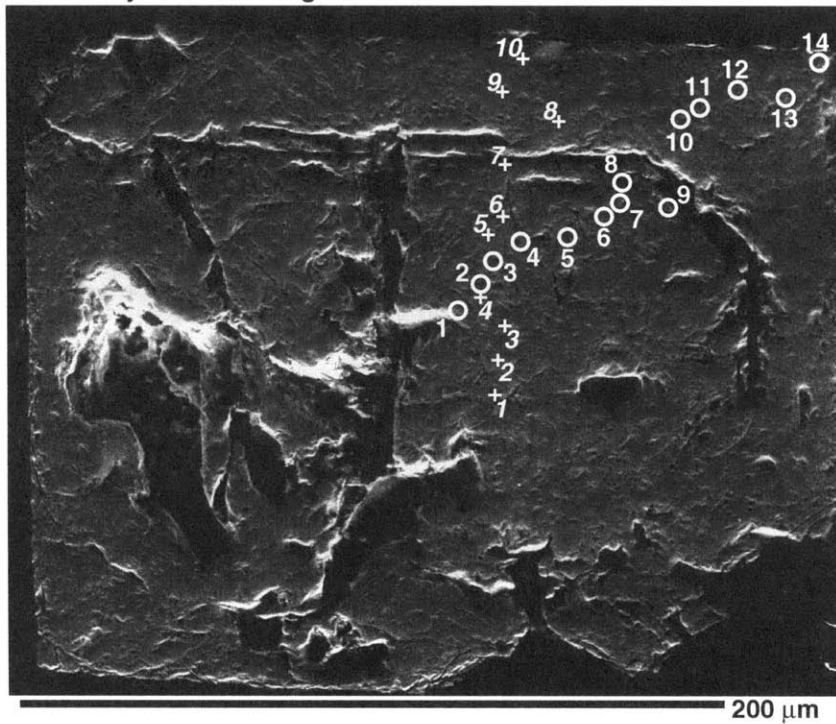


Figure 3

c. Secondary Electron Image: 00KG20 u5



d. Back-scattered Electron Image: 00KG20 u5

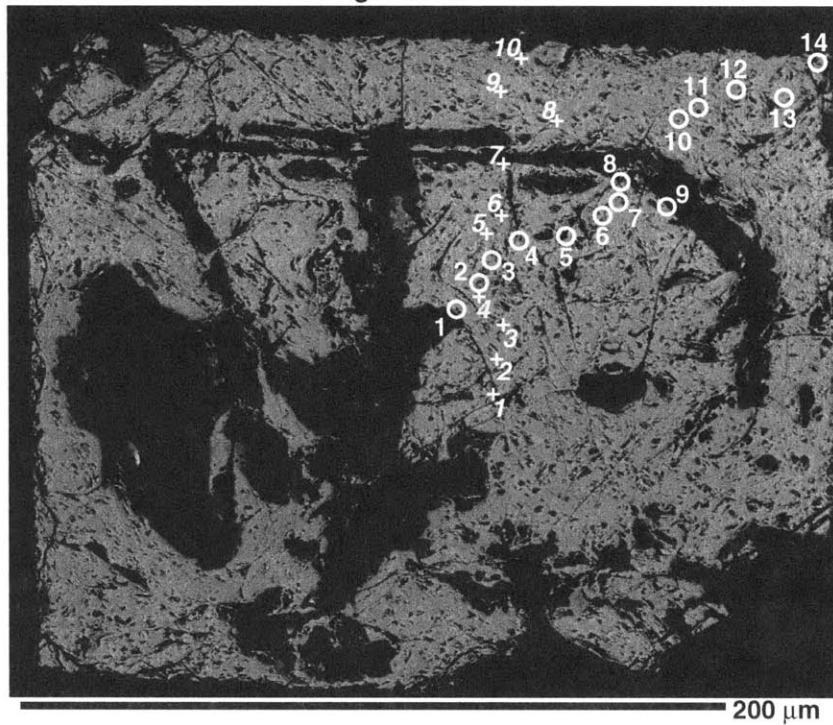


Figure 3

e.

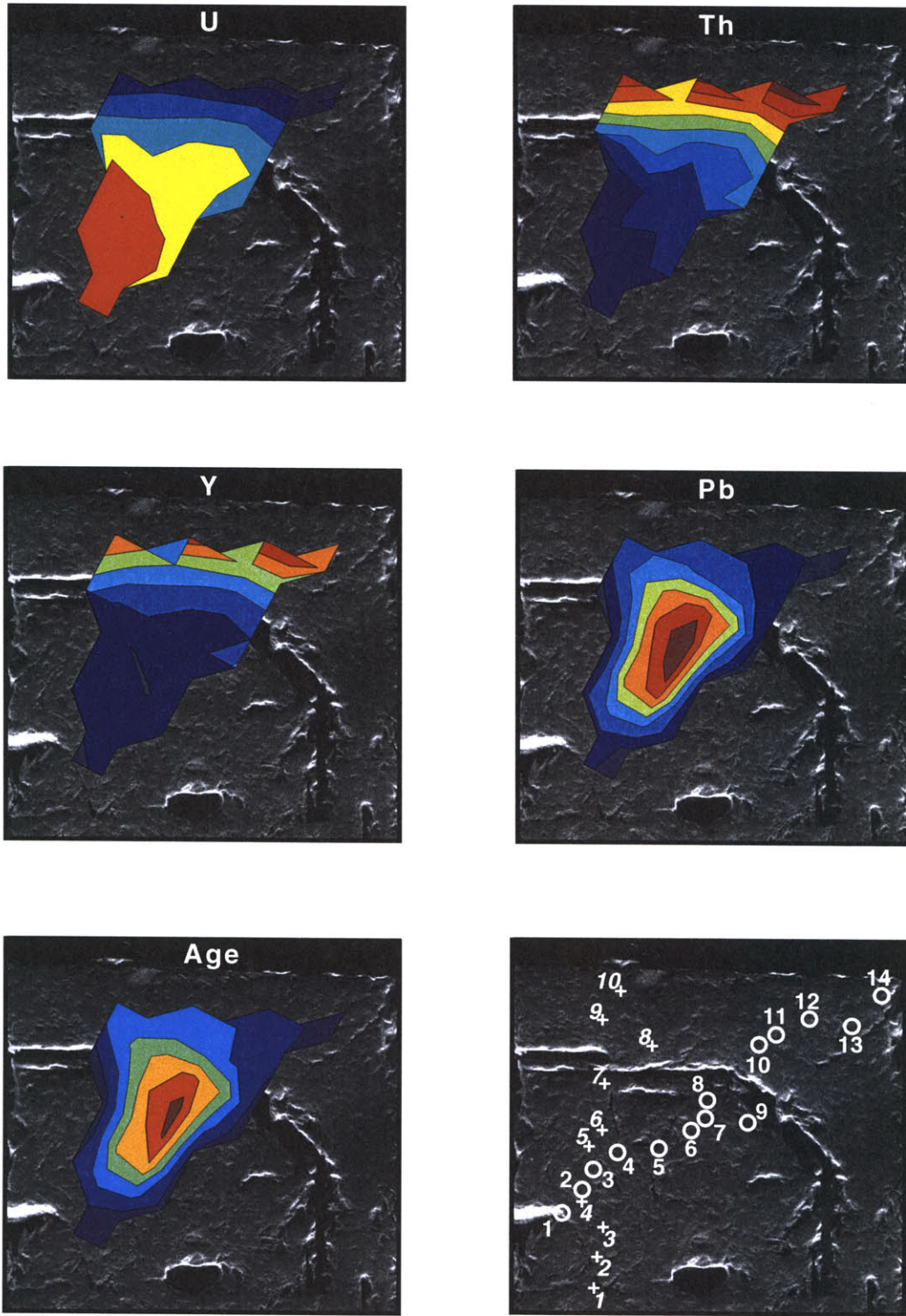


Figure 3

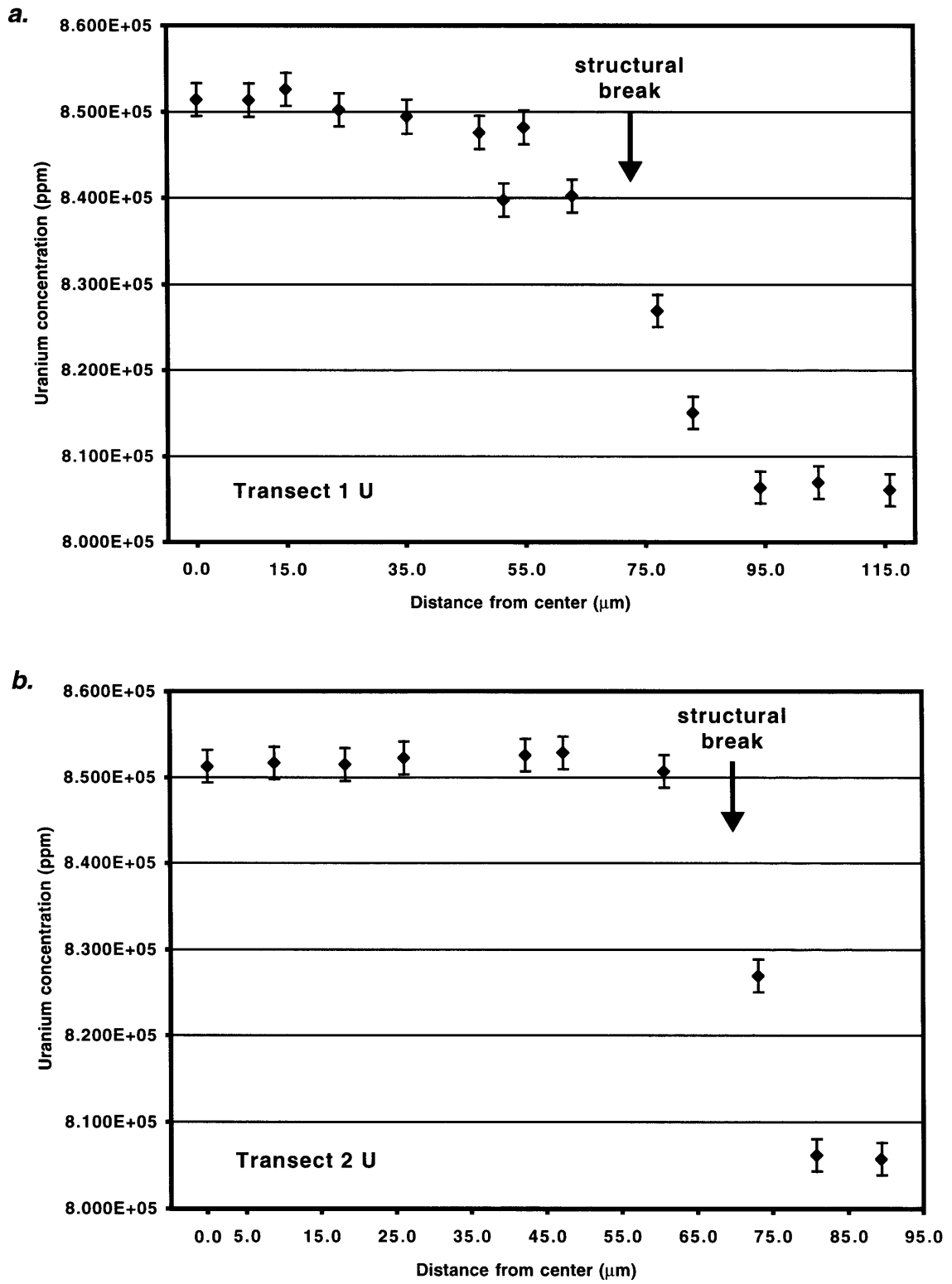


Figure 4

Chapter 5: Electron microprobe chemical dating of uraninite

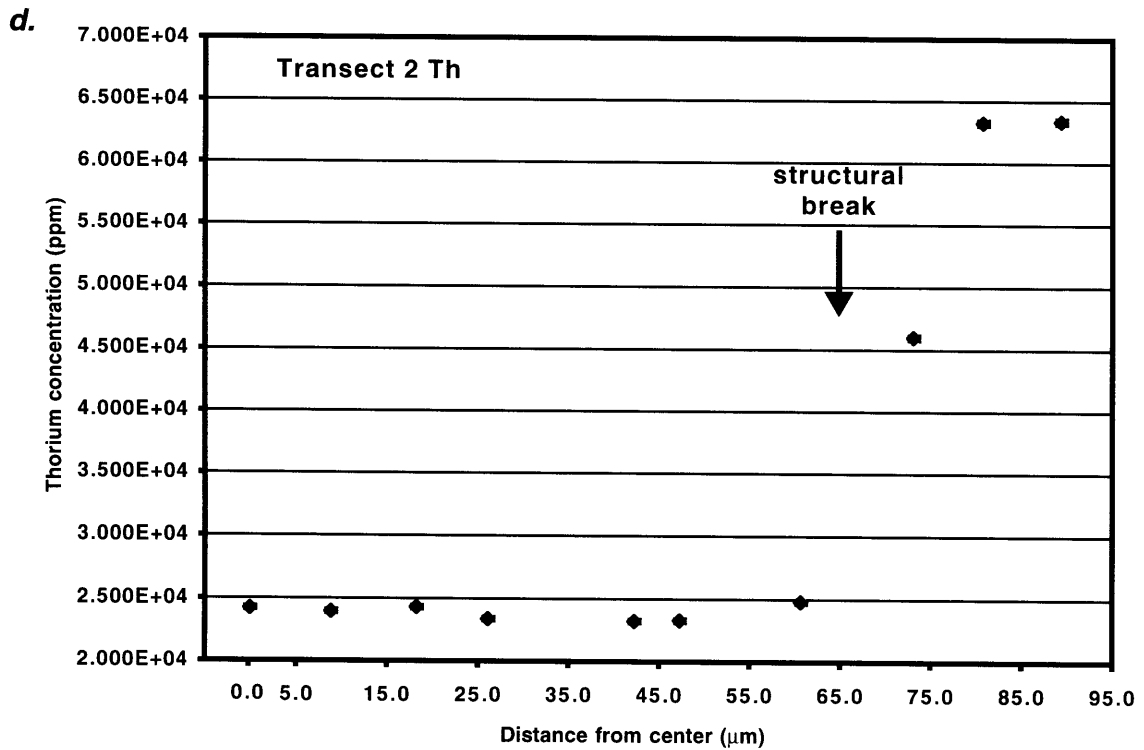
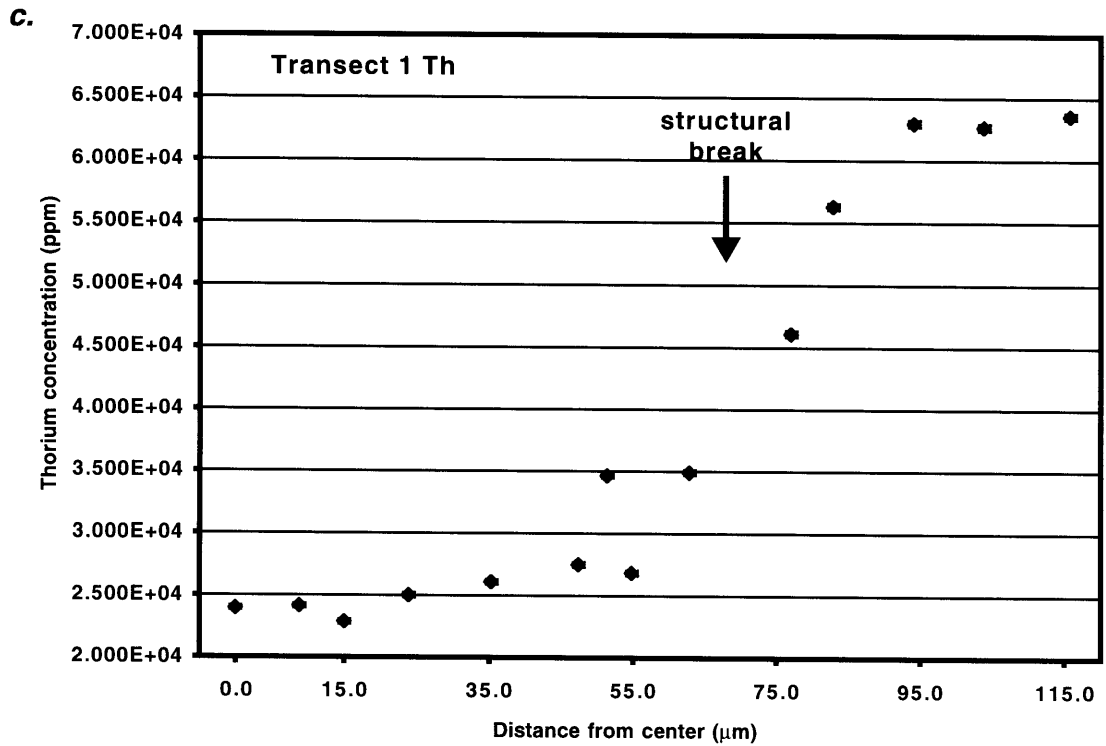


Figure 4 <continued>

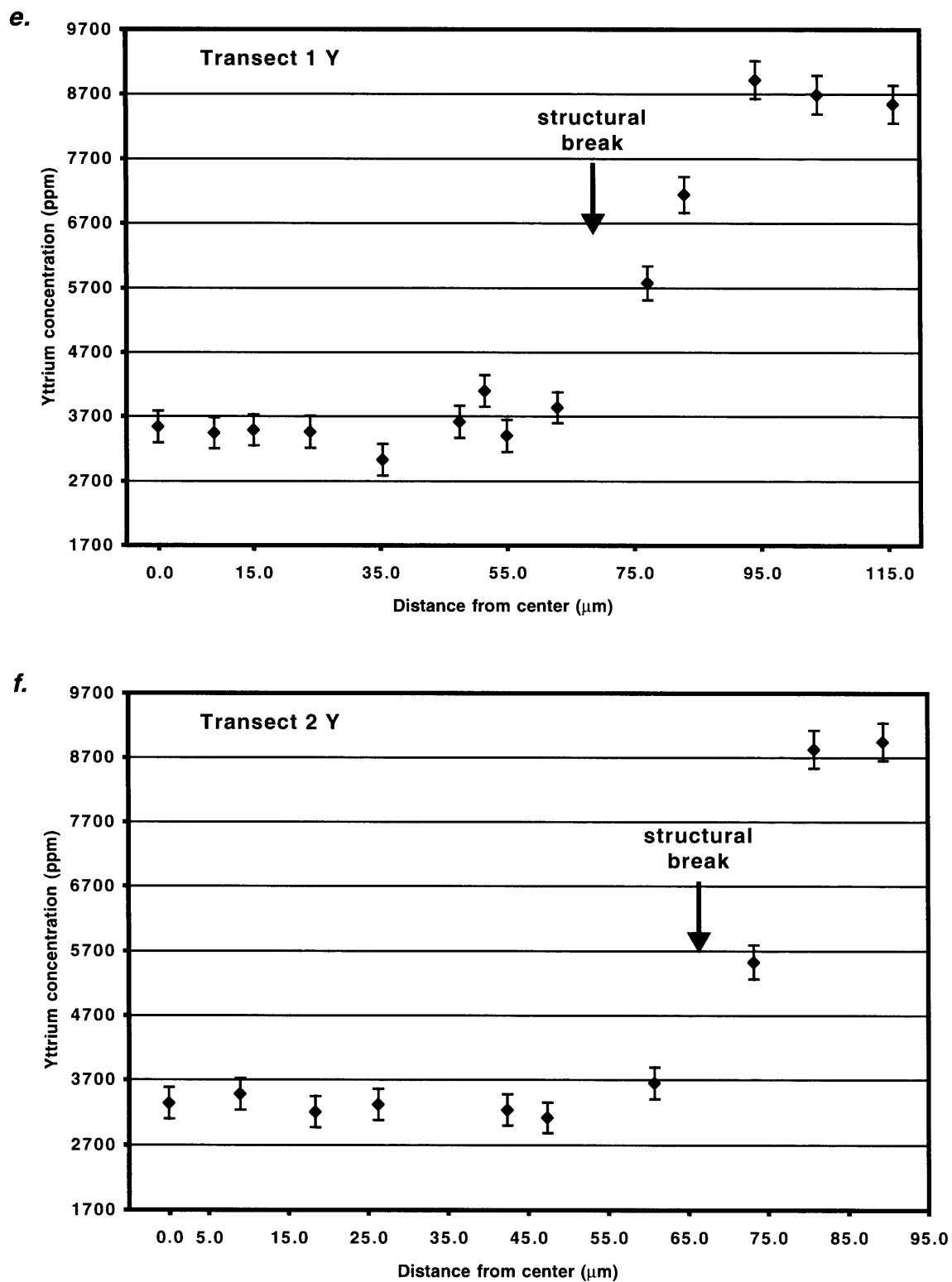


Figure 4 <continued>

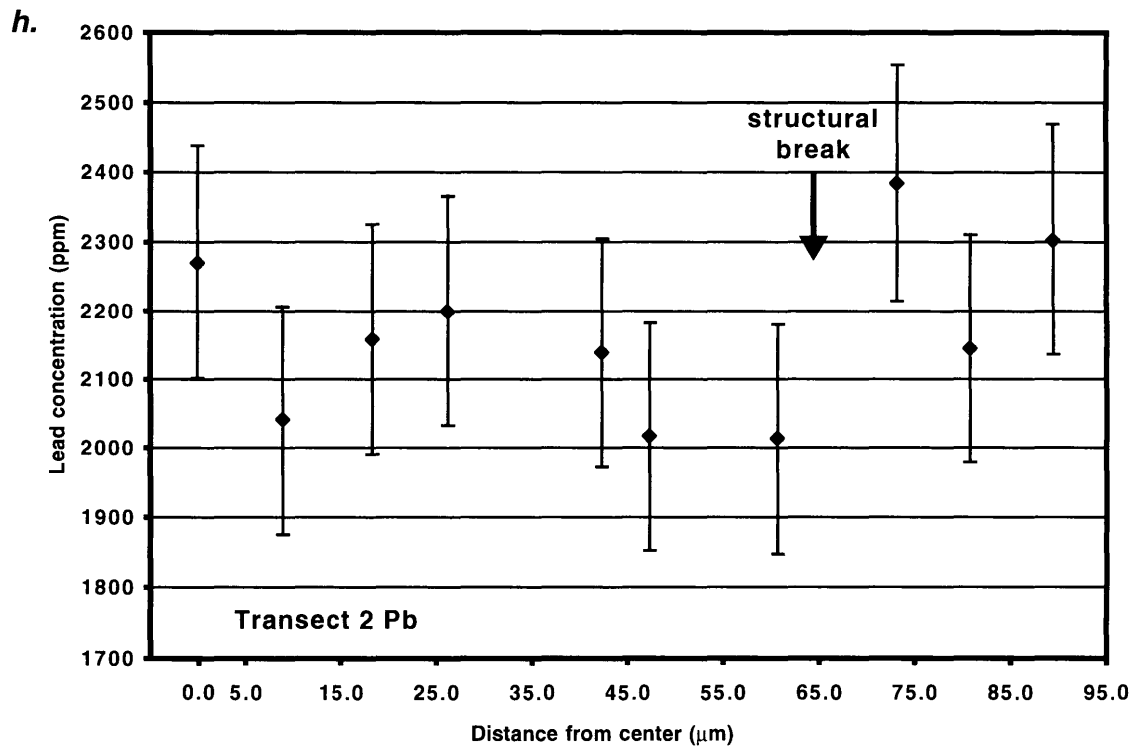
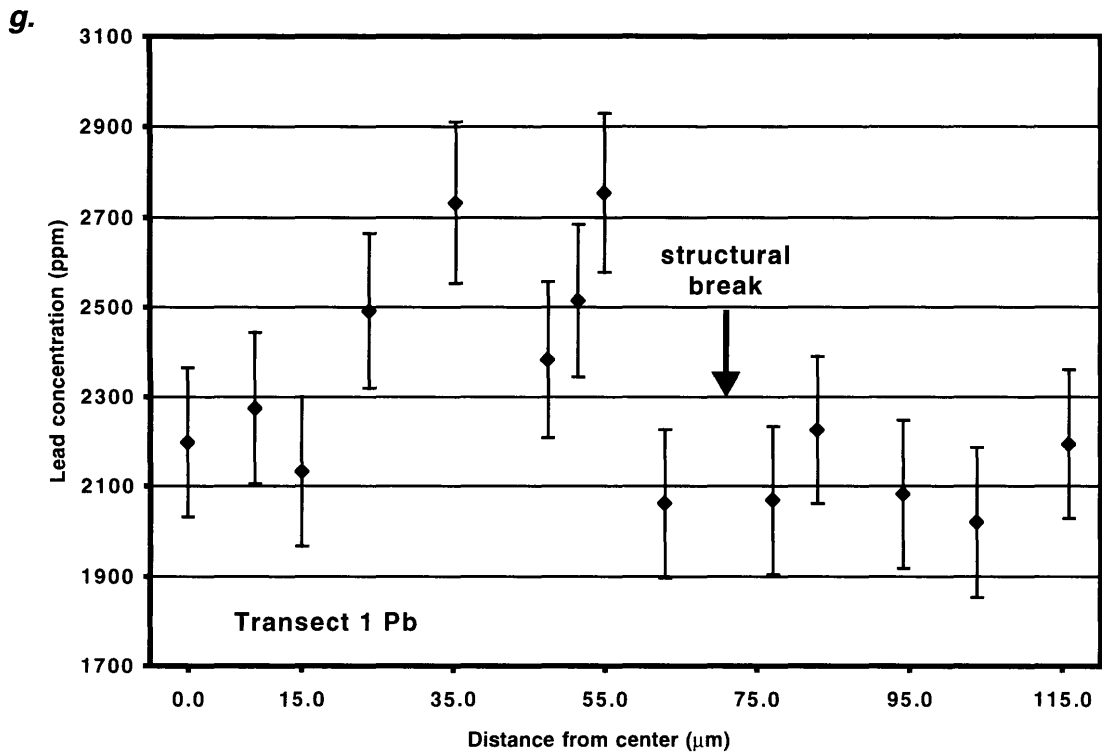


Figure 4 <continued>

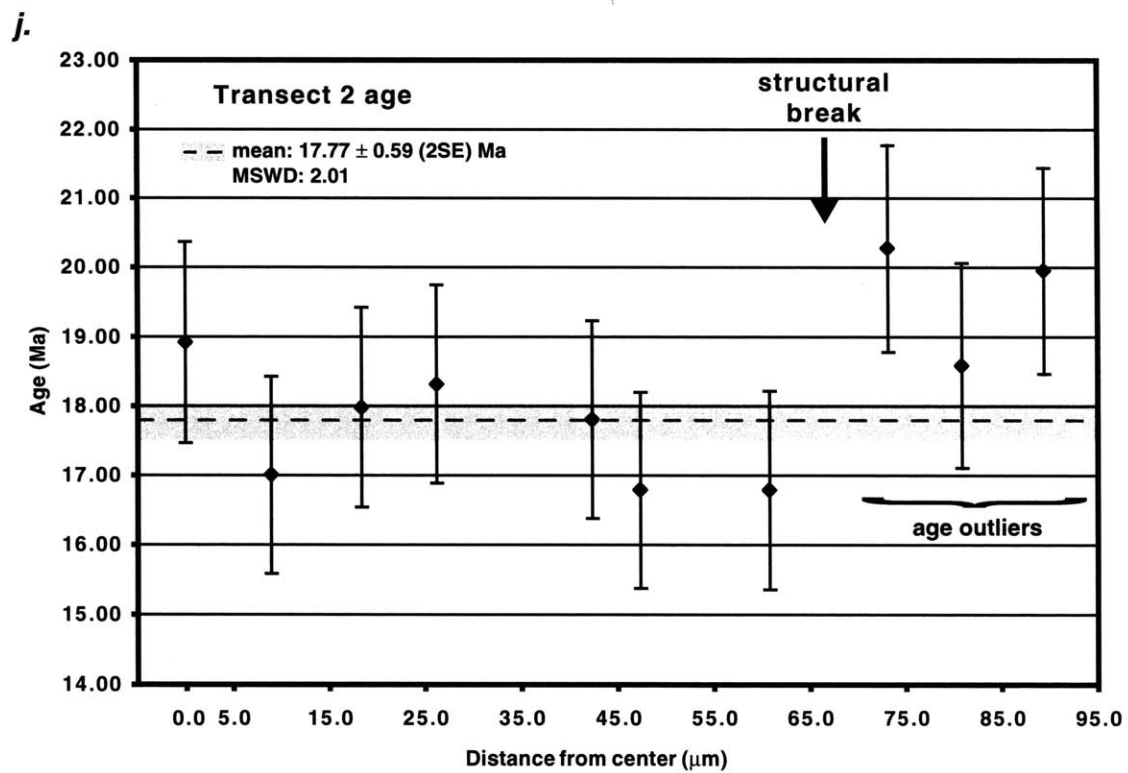
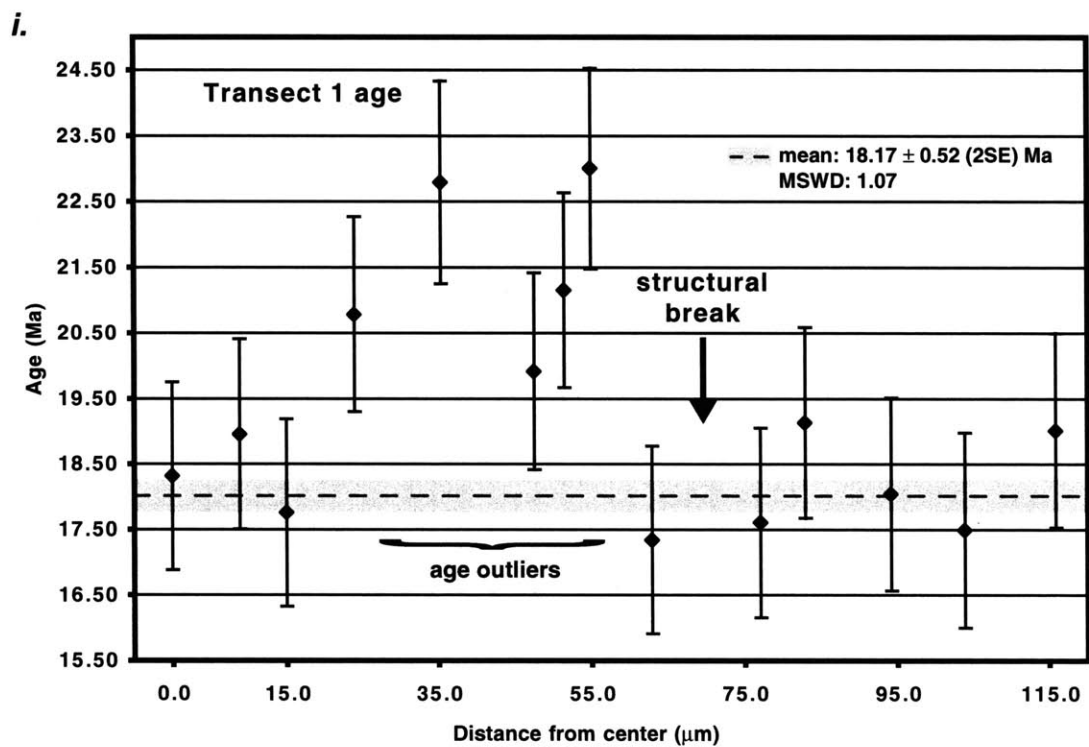


Figure 4 <continued>

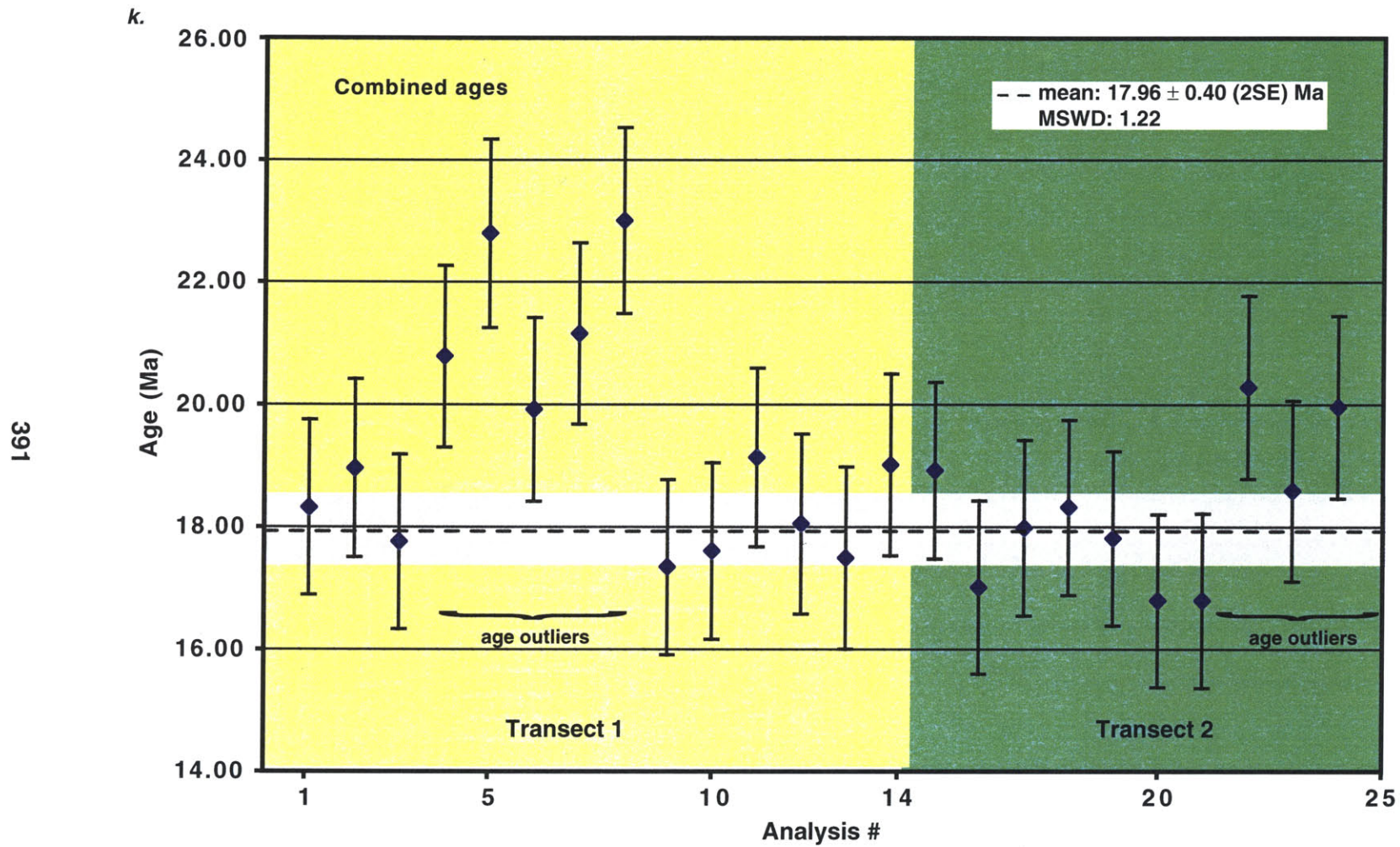


Figure 4

391

Chapter 5: Electron microprobe chemical dating of uraninite

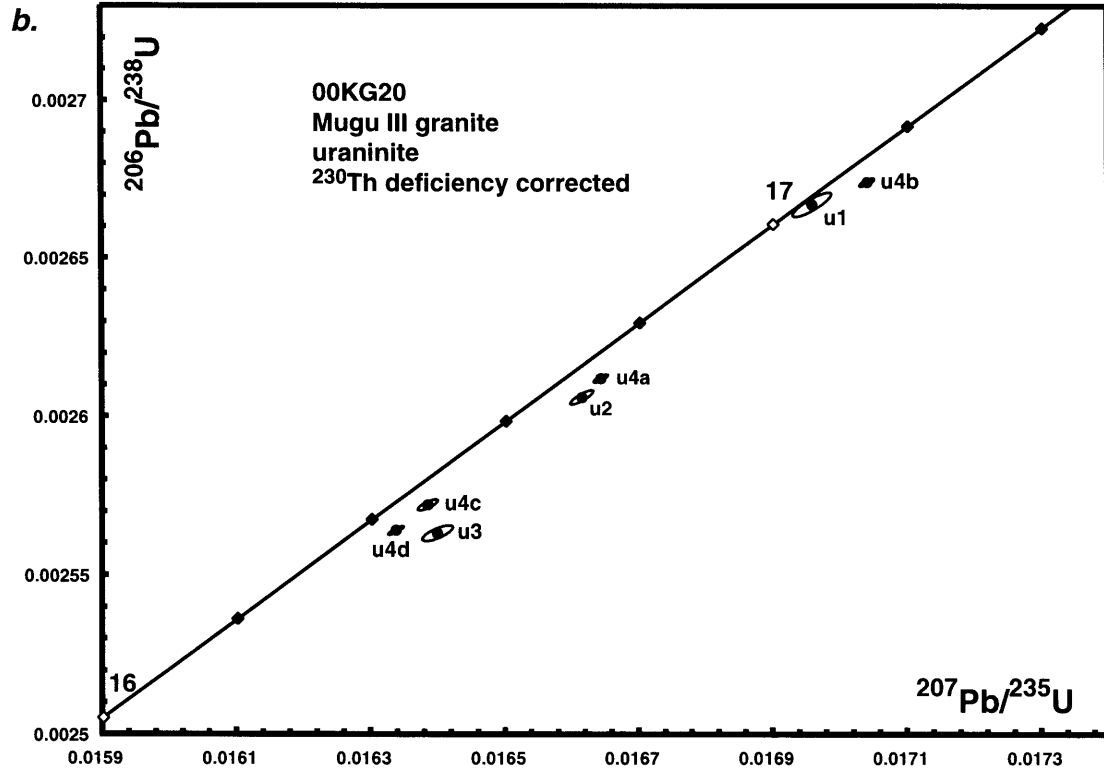
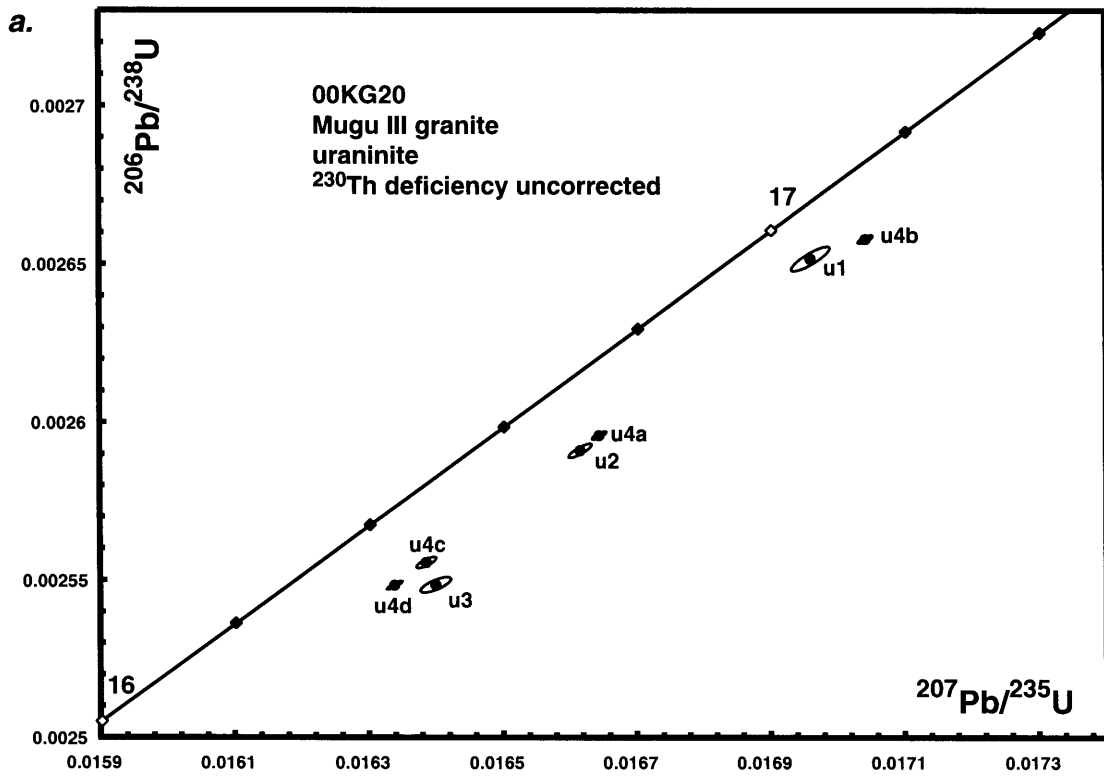


Figure 5

Chapter 5: Electron microprobe chemical dating of uraninite

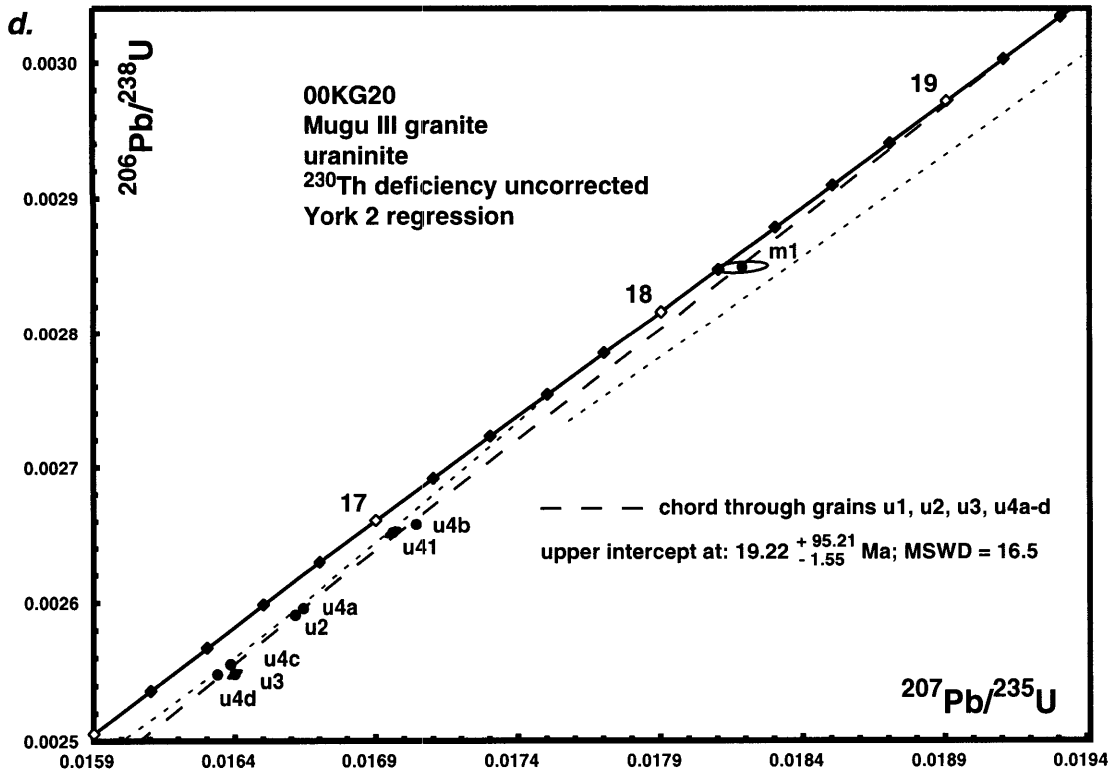
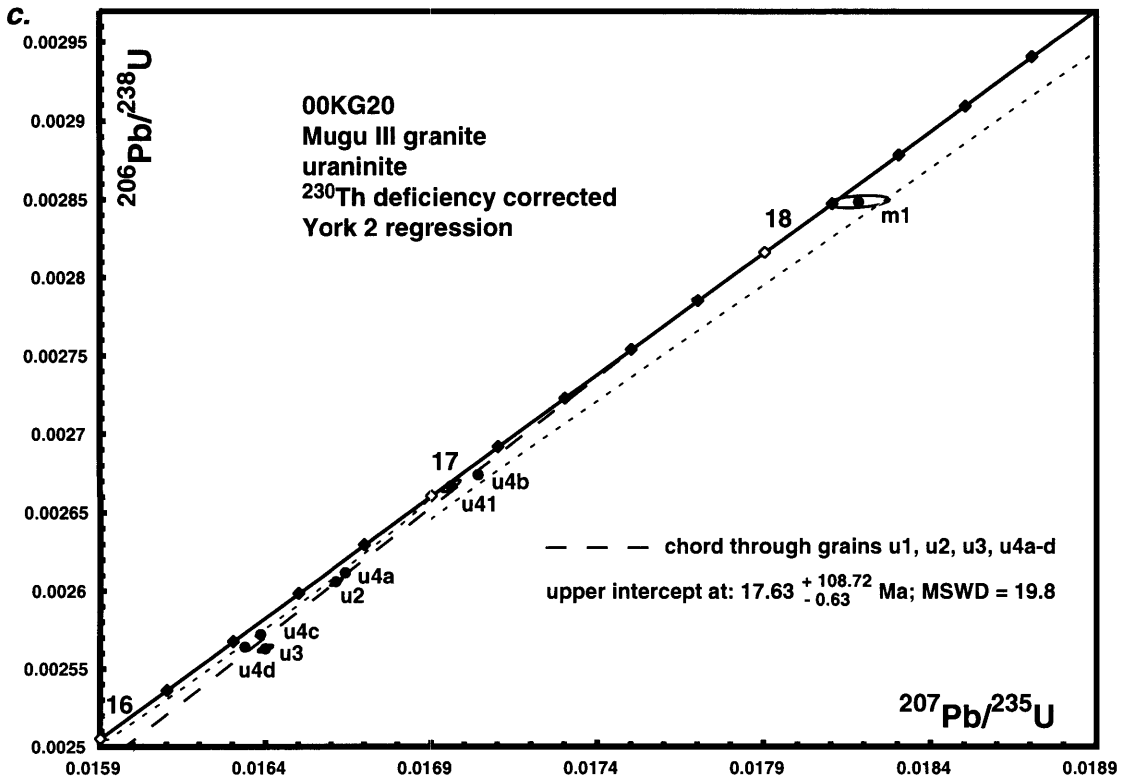


Figure 5 <continued>

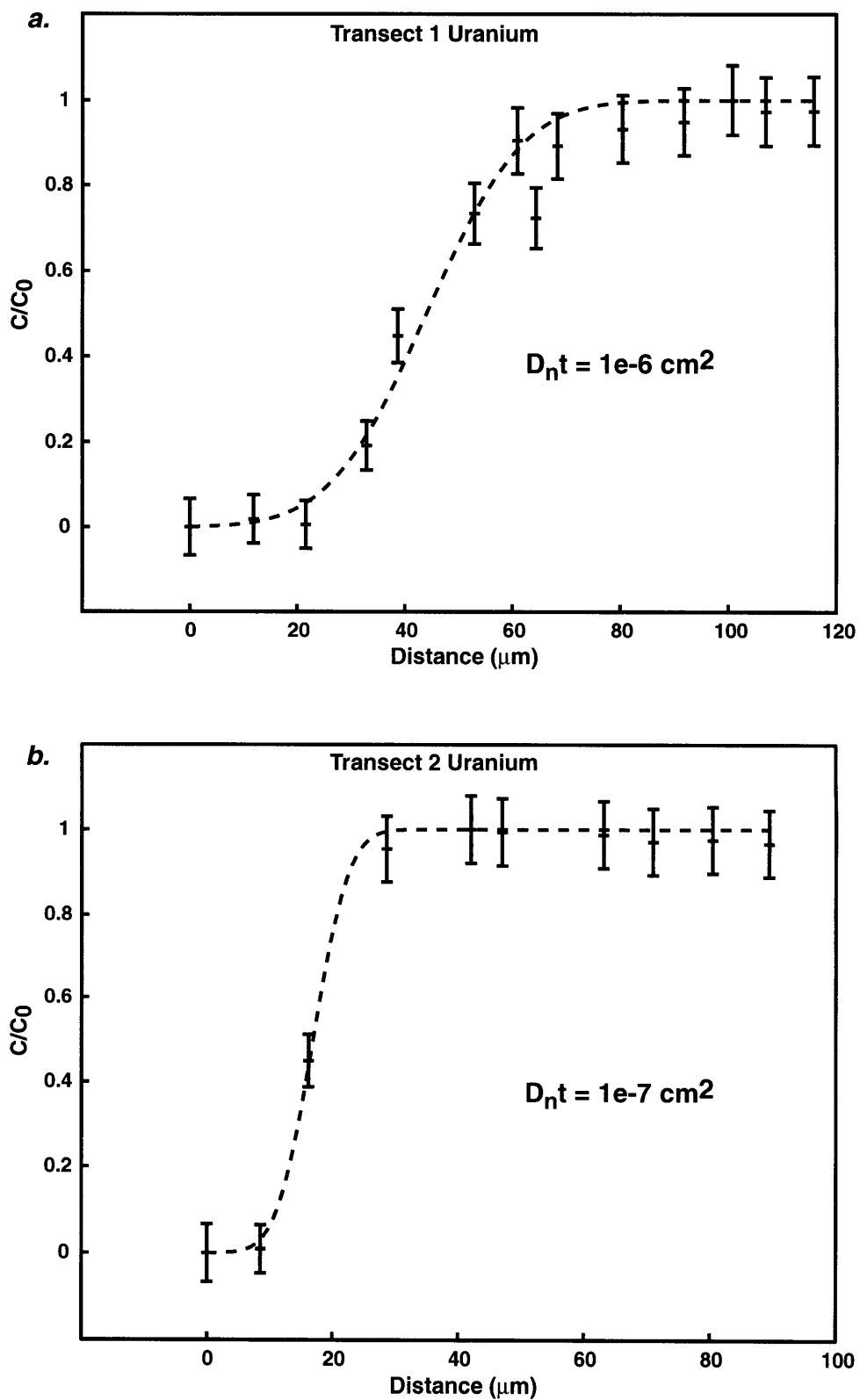


Figure 6

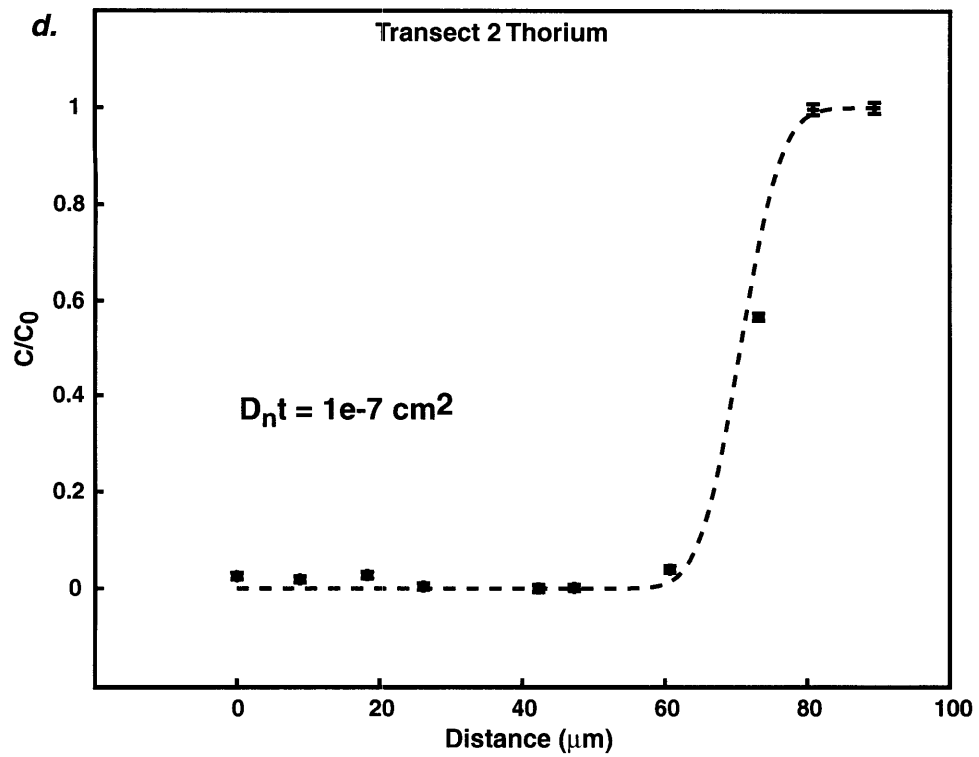
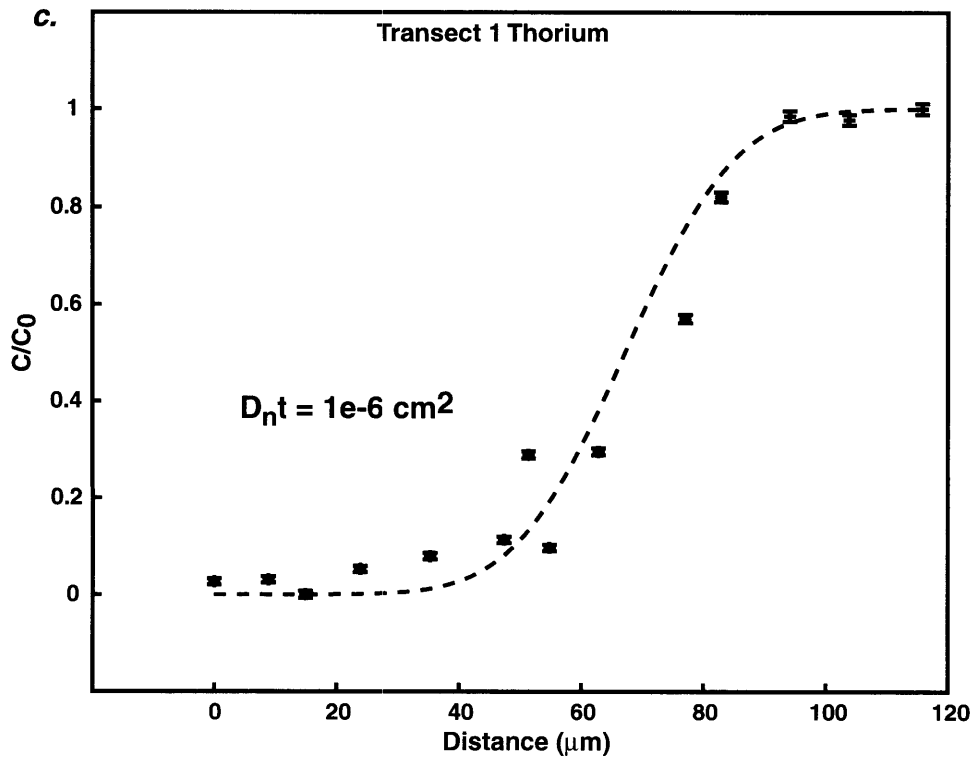


Figure 6 <continued>

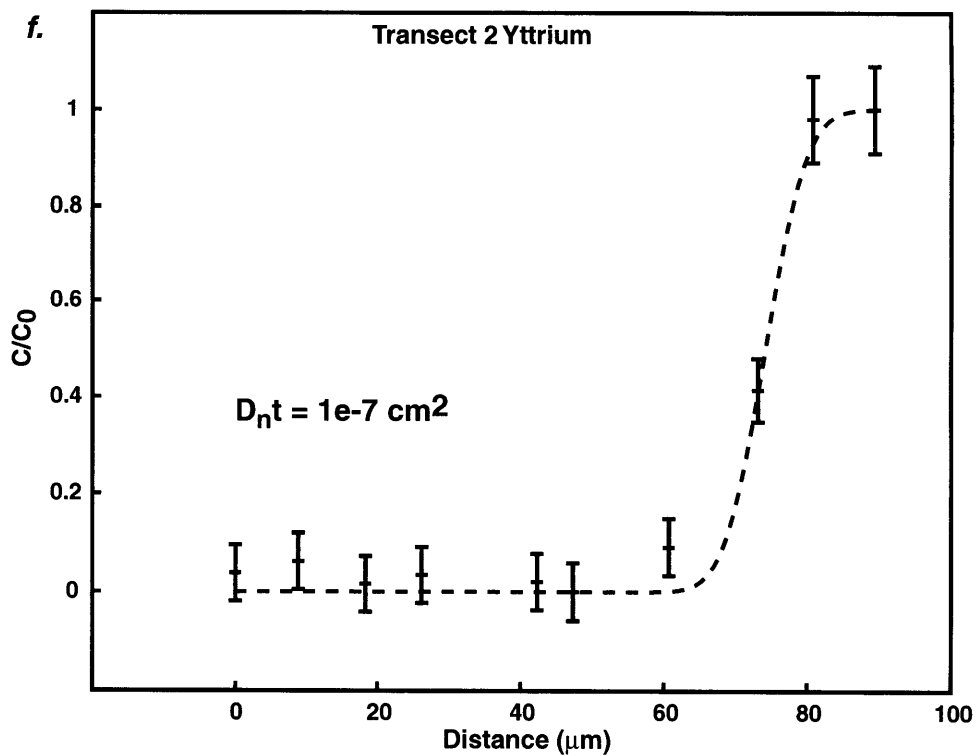
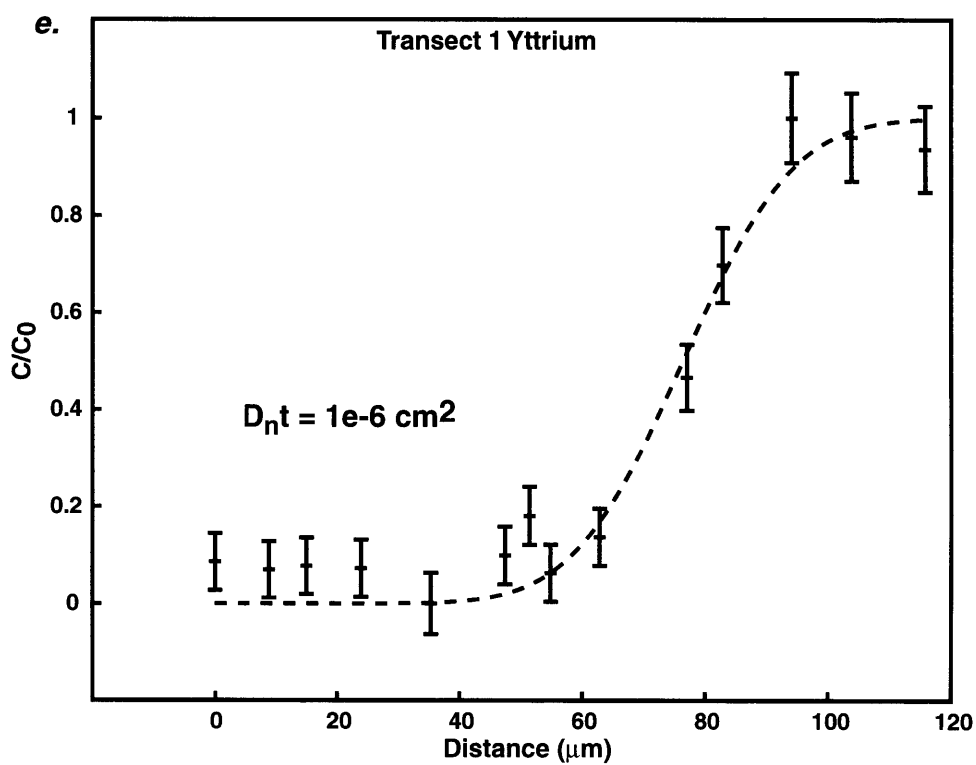


Figure 6 <continued>

Chapter 5: Electron microprobe chemical dating of uraninite

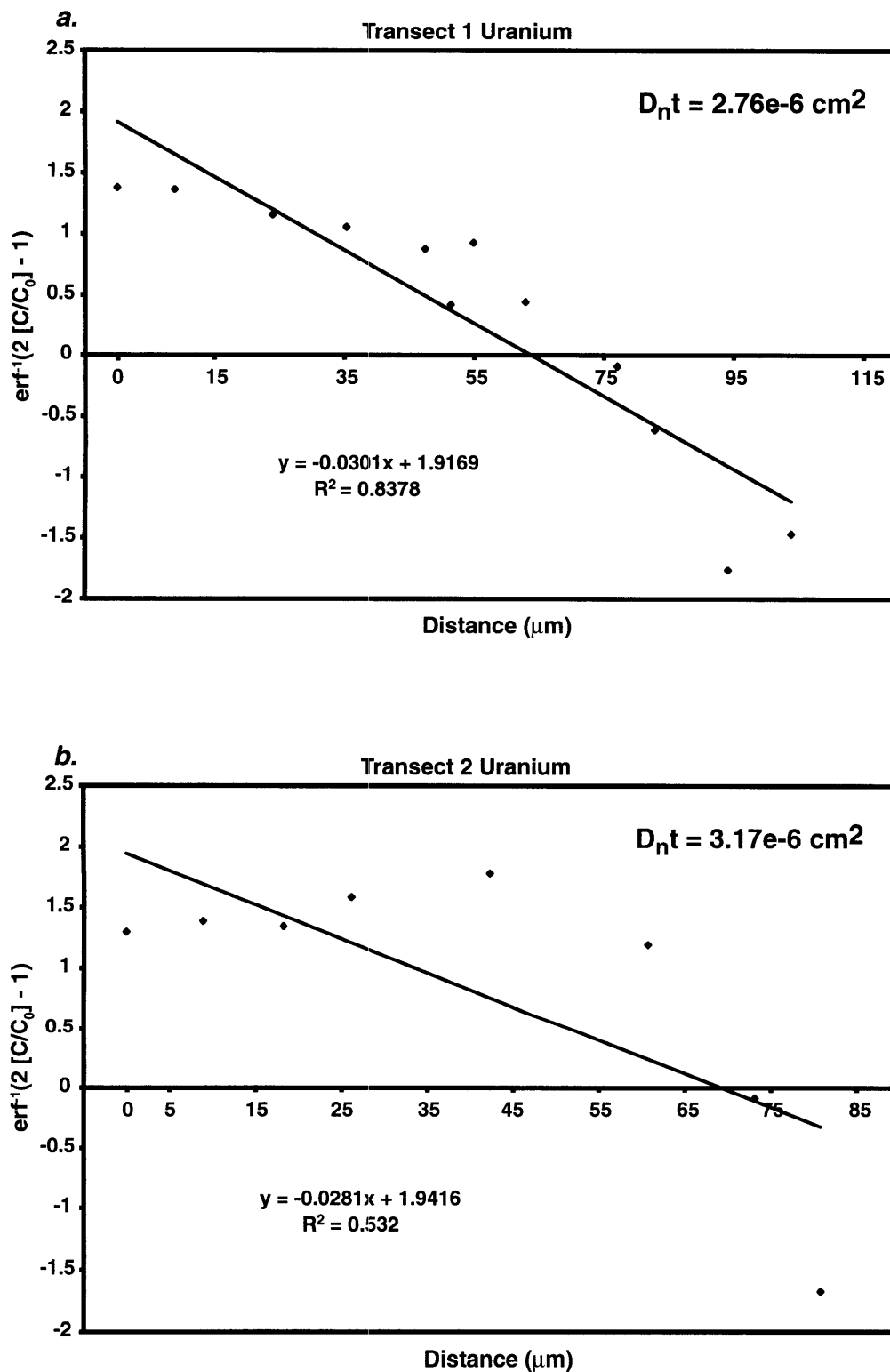


Figure 7

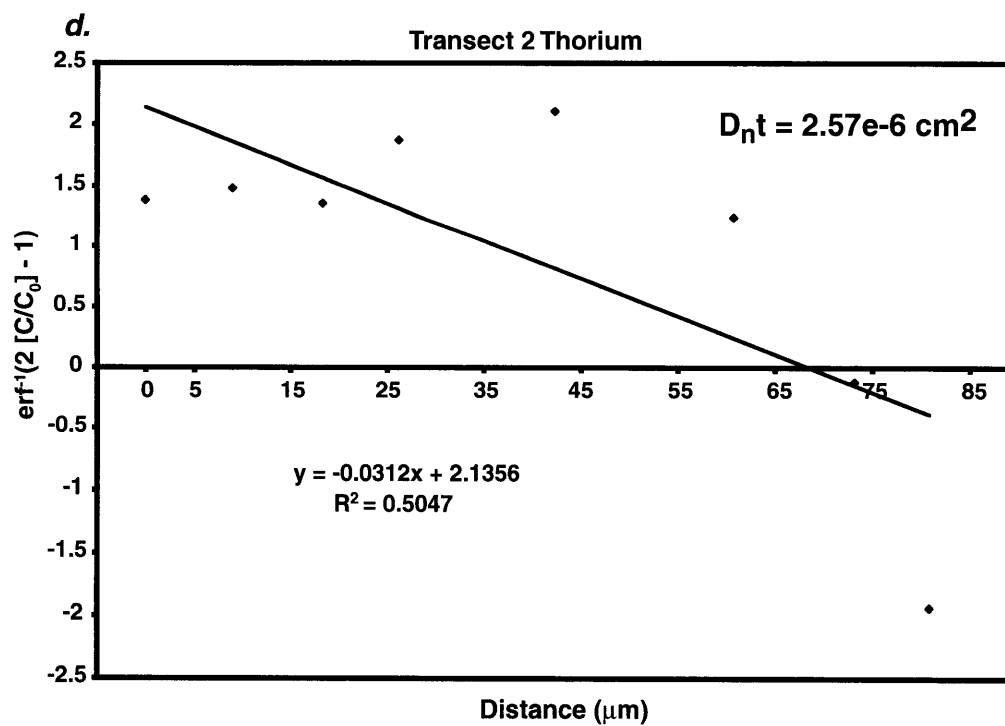
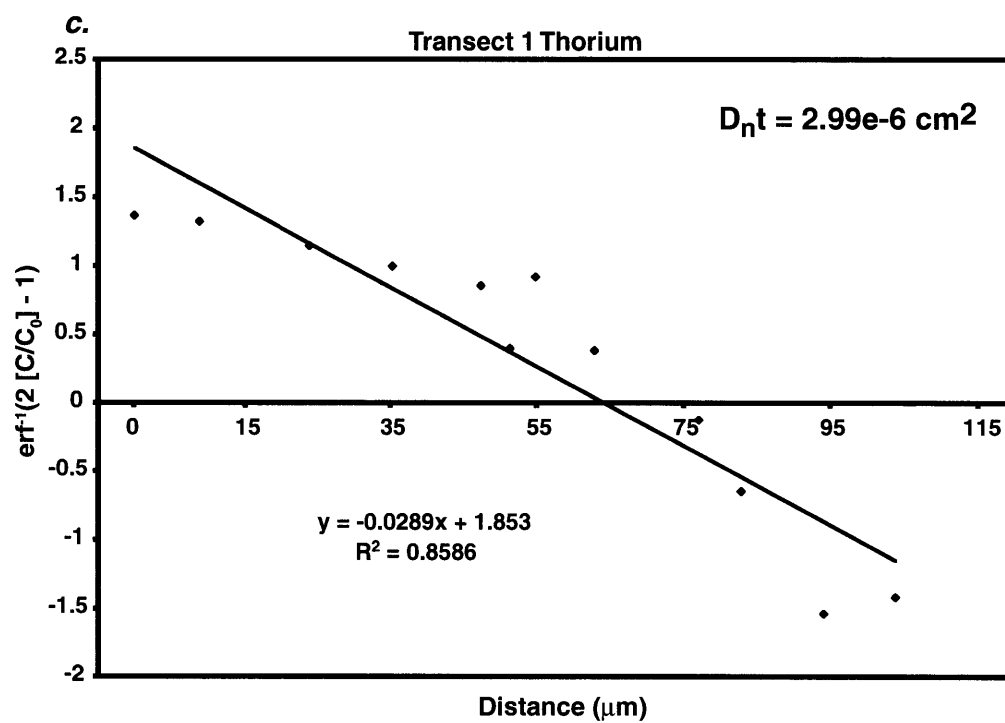


Figure 7 <continued>

Chapter 5: Electron microprobe chemical dating of uraninite

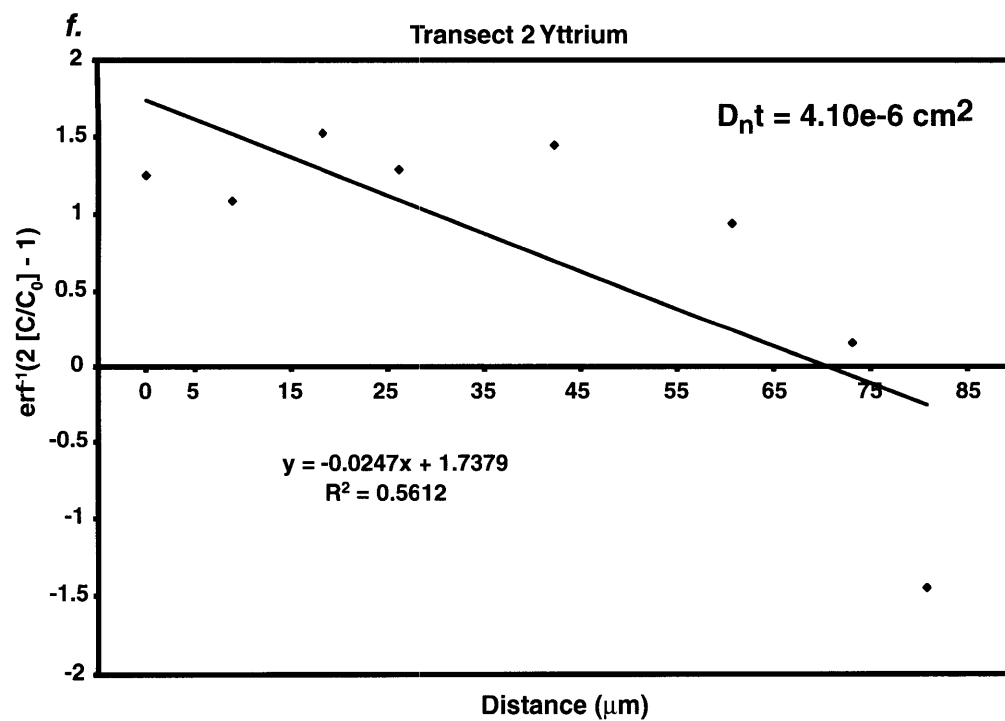
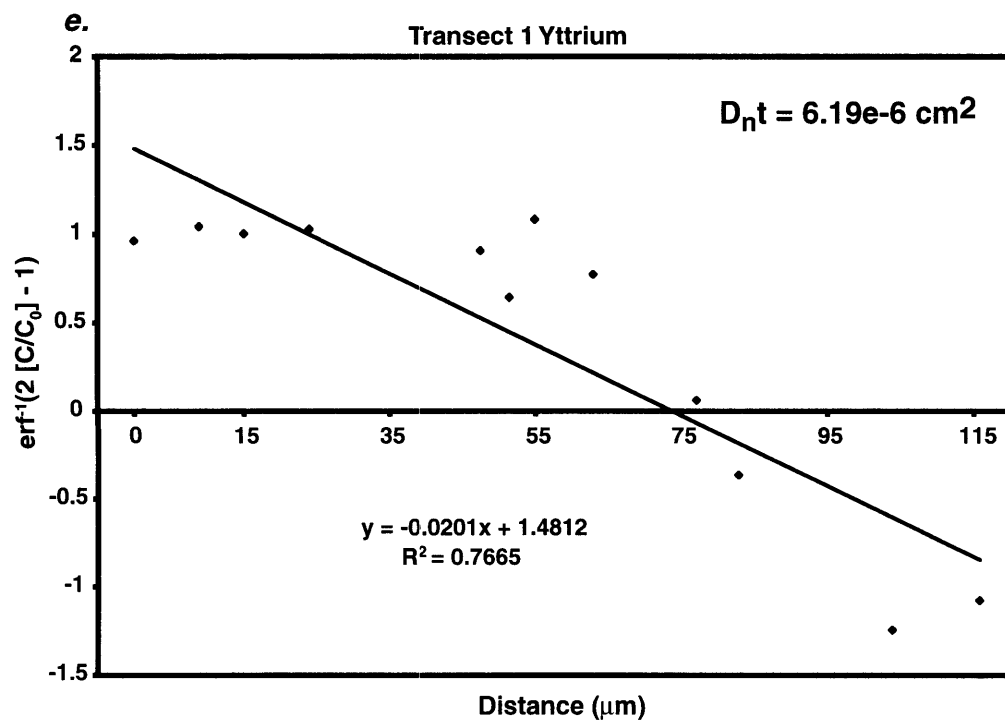


Figure 7 <continued>

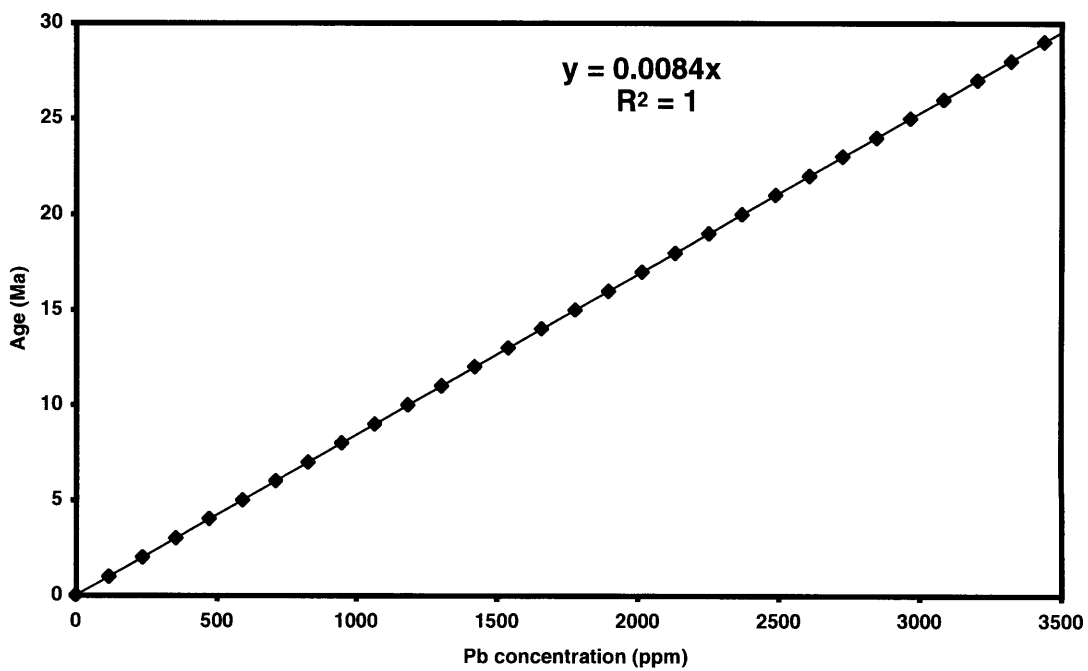


Figure 8

Chapter 6:

***Synthesis – Intracrustal channel flow,
gravitational potential energy, and the
tectonic development of the Himalaya***

Chapter 6: Synthesis – Intracrustal channel flow, gravitational potential energy, and the tectonic development of the Himalaya

The data in the preceding chapters – in particular Chapters 2-4 – imply a close linkage between three modes of extension prevalent in southern Tibet. The first mode is characterized by east-west rifting localized in north-striking grabens bound by steeply-dipping normal faults (Figure 1a). The prototypical feature development as a consequence of this mode is the Thakkhola graben itself. The second mode of extension led to core complex development and associated doming, exhumation, and denudation, as exemplified by the Upper Mustang massif (UMM) and similar metamorphic and igneous culminations among the North Himalayan gneiss domes (Figure 1a). Normal-sense displacement at a range of structural levels on various strands of the South Tibetan fault (STF) system (Figure 1a) comprises the third extensional mode. In Chapters 2-4, I describe kinematic models for the relationships among these extensional styles. In this chapter, I present a more comprehensive model of tectonic development of the Thakkhola and Dhaulagiri regions.

INTRACRUSTAL CHANNEL FLOW

The model I present for the tectonics of the Himalayan margin of the Tibetan plateau combines the ideas of deformation driven by gravitational potential energy (GPE) contrasts and channelized flow of crustal material. I interpret the GPE structure of the southern margin of the Tibetan plateau in terms of pressure gradients and hypothesize that the vertically-averaged stresses one can infer from lateral gradients in gravitational potential energy can drive channel flow (e.g. Clark and Royden, 2000; McQuarrie and

Chapter 6: Synthesis

Chase, 2000; Hodges *et al.*, 2001). Southward flow of lower crustal material out from the Tibetan interior can account for many of the features of Himalayan tectonics, including the kinematics of the STF system. Spatial and temporal variations in the efficiency of the flow can result in orogen-parallel flow and affect core-complex and rift development in southern Tibet.

Arguments for an Intracrustal Channel

Just north of the Kangmar dome in east-central Tibet (Figure 1a), “bright spots” in the INDEPTH seismic reflection profile have been reported (Nelson *et al.*, 1995; Brown *et al.*, 1996; Makovski *et al.*, 1996) (Figure 1b). Combining seismic data indicating low mid-crustal velocities (Kind *et al.*, 1996) with magnetotelluric data suggesting anomalously high conductivities (Chen *et al.*, 1996) and measurements of high surface heat flow (Francheteau *et al.*, 1984). Nelson *et al.* (1995) hypothesized that such bright spots in southern Tibet represent a layer of conductive fluid, most likely partial melt, at a depth of ca. 20 km. Similarly, in central and northern Tibet, low S-wave velocities and high Poisson (McNamara *et al.*, 1994; Owens and Zandt, 1997), as well as widespread Neogene alkalic volcanism (e.g. Turner *et al.*, 1993) suggest that the middle to lower crust under that part of the plateau also contains partial melts. Some researchers (e.g. Nelson *et al.*, 1996; Clark and Royden, 2000) have suggested that this zone of partial melt is an intracrustal channel of mobile crust, and Hodges *et al.* (2001) and others (e.g. Grujic *et al.*, 1996; Wu, *et al.*, 1998; Searle, 1999; Beaumont *et al.*, 2001; Hodges *et al.*, 2001) have speculated that the southern leading edge of the intracrustal channel is now exposed in the Himalaya as the Greater Himalayan Sequence (Figure 1b). In tectonic models based on this interpretation, southward extrusion in the Himalaya would have

Chapter 6: Synthesis

been accommodated by both coeval slip along the STF and the MCT systems as well as removal of the exhumed material by vigorous erosion at the range front (Figure 1b) (e.g. Beaumont *et al.*, 2001; Hodges *et al.*, 2001). Such models are consistent with many geological observations in the Himalaya, especially evidence of the broad synchronicity of STF and MCT system displacement at various times since the Miocene, pervasive ductile fabrics indicative of southward extrusion, and the inversion of metamorphic isograds in the Greater Himalayan Sequence, as reviewed by Hodges (2000).

Beaumont *et al.* (2001) showed that thermomechanical models simulating channel flow are capable of reproducing many of the geologic features of the Himalaya and southern Tibet, including the pressure-temperature-time characteristics of the Greater Himalayan Sequence. An important feature of these models is that they indicate the spontaneous development of an intracrustal channel given the dynamical boundary conditions that likely pertained in the Himalayan-Tibetan orogenic system over the Miocene-Recent interval (Beaumont *et al.*, 2001; Jamieson *et al.*, 2002). This intracrustal ductile layer is tectonically significant because it can serve to decouple deformation in the upper crust from that in the lower crust, maintaining regional strain compatibility in the face of variable strain with depth. Such decoupling of the upper crust from the lower crust is precisely the situation observed with respect to the east-west extending grabens in Tibet and the shortening occurring in the Himalaya structurally below the STF system (e.g. Hurtado *et al.*, 2001).

Mathematical Description of Channel Flow

Flow in a channel can be modeled with an equation describing one-dimensional

Chapter 6: Synthesis

flow in a two-dimensional channel (e.g. Turcotte and Schubert, 1982):

$$v(\zeta) = \frac{1}{2\mu} \frac{\partial P}{\partial x} (\zeta^2 - h\zeta) + \frac{v_2 - v_1}{h} \zeta + v_1 \quad (1),$$

where x' is the horizontal coordinate within the channel (in m); ζ is the depth coordinate within the channel (in m); $v(\zeta)$ is the depth-dependent velocity profile (in m s^{-1}); μ is the spatially uniform and temporally constant viscosity of material in the channel (in Pa s); h is the channel thickness (in m); $\frac{\partial P}{\partial x}$ is the pressure gradient driving Poiseuille flow (in Pa per m); and v_1 and v_2 are the applied velocities (in m s^{-1}) at the top and bottom of the channel, respectively, which drive Couette flow. As noted by Grujic *et al.* (1996), Poiseuille flow exhibits a velocity structure consistent with the observed deformation in the Greater Himalayan Sequence, with the highest southward velocities in the center of the channel and reversals in the flow direction at the top and bottom. The Couette term takes into account “return flow” due to shear tractions along the STF and MCT systems at the top and bottom of the channel, respectively.

Thermomechanical modeling by Beaumont *et al.* (2001) has shown that outward flow in an intracrustal channel is driven entirely by gravitational forces and shear tractions. In terms of the pressure gradient in equation (1), the gravitational forces can be thought of as resulting from the thickness and density structure of the crust. From an observational standpoint, the problem of estimating the magnitude of these forces can be approached in a variety of ways. Clark and Royden (2000) and McQuarrie and Chase (2000) used pressure gradients estimated from variations in crustal thickness as inferred from topography. Alternatively, I and Hodges *et al.* (2001) describe a method by which pressure gradients arising from the vertically averaged normal stresses acting on the

Chapter 6: Synthesis

channel can be inferred from GPE anomalies calculated from the geoid. This approach is motivated by the observation that, in the Himalayan-Tibetan orogen, the most extreme gradients in the GPE anomaly coincide with the outcrop area of the Greater Himalayan Sequence, the proposed surface expression of the intracrustal channel (Hodges *et al.*, 2001).

GRAVITATIONAL POTENTIAL ENERGY ANOMALIES

Based on analogies to more familiar potential-driven flow laws such as heat flow, Hodges *et al.* (2001) suggest that the pressure gradient in equation (1) is proportional to gradients in geoid-derived GPE anomaly, ϵ_u :

$$\frac{\partial P}{\partial x} \propto \frac{\partial \epsilon_u}{\partial x} \quad (2),$$

where

$$\epsilon_N = \frac{2\pi G}{g^2} \epsilon_u \quad (3),$$

G is the gravitational constant (6.6732×10^{-11} N m² kg⁻²), and ϵ_N is the geoid height anomaly (e.g. Coblenz *et al.*, 1994; Jones *et al.*, 1996). Following Hodges *et al.* (2001), I use the NASA-NIMA joint geopotential model EGM-96 (Lemoine *et al.*, 1998) for the area between N50°15'/E66°30' and N18°15'/E114°00', a region that includes Tibet and surrounding parts of central and south Asia (Figure 2a & b). In order to ensure that only lithospheric geoid anomalies are considered, spherical harmonic terms to degree and order 7 are removed and a cosine taper function is applied to terms between degree and order 7 and 11 (Sheehan and Solomon, 1991; Jones *et al.*, 1996). Then, by applying equation (3) to the filtered geoid height anomalies, a map of ϵ_u for the Tibetan plateau is

Chapter 6: Synthesis

generated (Figure 2a). It should be noted that the ϵ_u distribution is due to the cumulative density structure of the lithosphere from the surface to a depth of approximately 70-100 km. This provides the ability to infer something about subsurface processes such as intracrustal flow, but makes precise spatial correlation with surface structures and morphology difficult despite best efforts towards co-registering the available geologic, topographic, and gravity data. The inherent coarseness of the EGM-96 data (15' per pixel) also contributes to this difficulty.

Previous workers (e.g. Molnar and Tapponnier, 1978; Molnar, 1988; England and Houseman, 1989; England and Molnar, 1997) have noted the profound GPE contrast between the Tibetan plateau and its surroundings, and seismic activity data implies that the region is actively dissipating that energy (e.g. Tanimoto and Okamoto, 2000). As implied by equations (1) and (2), one way to dissipate GPE is by material flux (Hodges *et al.*, 2001). In this respect, a useful way to visualize and understand the GPE structure of Tibet and its role in driving intracrustal flow is to look at a map of gradients in ϵ_u , for those gradients illustrate the pathways via which the most efficient mass flux will occur (e.g. Hodges *et al.*, 2001). Figure 2b shows such a map depicting the first spatial derivative of ϵ_u , a quantity referred to as $\Delta \epsilon_u$ (in N m^{-1} per km). The map was computed with the image analysis software package ENVI® (RSI, 2000) by using a modified topographic slope-modeling algorithm. The algorithm computes $\Delta \epsilon_u$ for a 3 x 3 pixel box centered on each pixel in the ϵ_u map (RSI, 2000). Displayed in this fashion, a great deal of complexity is apparent in the GPE structure of southern Tibet, with gradients and heterogeneities in both orogen-parallel and orogen-perpendicular directions (Figure 2c & d).

APPLICATION TO THE TECTONIC DEVELOPMENT OF SOUTHERN TIBET AND THE HIMALAYA

The maps in Figure 2 show that the Himalaya is the site of some of the highest ϵ_u and $\Delta\epsilon_u$ values in south-central Asia. Because large $\Delta\epsilon_u$ implies large pressure gradients, and, thus, enhanced channel flow, it is reasonable to expect that dissipation of GPE has had a significant influence on Himalayan tectonics. In detail, I find that the spatial distribution of suspected core complexes north of the Himalaya coincides with the distribution of local maxima in ϵ_u . In addition, there is a close correlation between a band of steep $\Delta\epsilon_u$ and the topographically steep Greater Himalayan Sequence, the metamorphic core of the orogen.

Gravitational Potential Energy Features of Tibet

Figure 2a shows that the interior of the Tibetan plateau has large, positive ϵ_u consistent with the observation that the region topographically high and is undergoing active extension (Molnar and Tapponnier, 1975; Molnar and Tapponnier, 1978; Ni and York, 1978; Armijo *et al.*, 1986). In Figure 2a, low ϵ_u values ($< \text{ca. } -2 \times 10^{12} \text{ N m}^{-1}$) are found in the Indian craton and foreland areas south of the Himalayan-Tibetan system as well as in the Tarim and Qaidam basins north of the Tibetan plateau. These are areas that are either in compression, as is the case south of the Himalayan foreland, or comprise old, dense, cold lithosphere with less buoyancy-driven potential energy than their surroundings, as is the case in the Indian craton and the Tarim and Qaidam basins (Molnar and Tapponnier, 1981; England and Houseman, 1985).

Chapter 6: Synthesis

The highest ϵ_u ($> \text{ca. } 5 \times 10^{12} \text{ N m}^{-1}$), is concentrated in a triangular anomaly that encompasses a large portion of the northwestern sector of the Tibetan plateau and extends north to the Altyn Tagh and west to the Karakoram-Pamir ranges (Figure 2a). The eastern edge of this anomaly is a sharp, enigmatic boundary that is orthogonal to all known sutures, active faults, and other structures on the plateau (c.f. Figure 1a). A possible explanation is that this large positive anomaly is the result of incomplete filtering of sub-lithospheric contributions to ϵ_u . In the case of the Karakoram-Pamir area, the deep subduction of continental crust in the Pamir (Burtman and Molnar, 1993) may be a dominant factor.

In general, ϵ_u on the Tibetan plateau has a broad, N-S gradient, with the values decreasing to the north, as well as a broad, E-W gradient with values increasing to the west (Figure 2a). Outside of the northwestern part of the plateau, very high ϵ_u ($> \text{ca. } 4 \times 10^{12} \text{ N m}^{-1}$), is concentrated along the Himalayan front (Figure 2a). Although the Sichuan-Longmenshan and Tarim margins of the Tibetan plateau are as topographically steep – and in some places steeper – than the Himalaya (Clark and Royden, 2000) and have comparable elevations, it is noteworthy that they do not have comparably high ϵ_u . Moderate values ($\text{ca. } 2 \times 10^{12} \text{ to } 4 \times 10^{12} \text{ N m}^{-1}$) characterize the northern margin of Tibet and the Longmenshan margin to the east (Figure 2a). Low ϵ_u ($< \text{ca. } 2 \times 10^{12} \text{ N m}^{-1}$ per km) is present along the southeastern margin (Figure 2a).

When visualized as $\Delta \epsilon_u$ (Figure 2b), the GPE distribution along the southeastern margin mimics the long-wavelength, gentle topographic slope noted by Clark and Royden (2000). This area is characterized by very low $\Delta \epsilon_u$ values ($< \text{ca. } 1 \times 10^{10} \text{ N m}^{-1}$ per km) compared to the other plateau margins. By far, the highest $\Delta \epsilon_u$ values ($> \text{ca.}$

Chapter 6: Synthesis

4×10^{10} N m⁻¹ per km) are found along the Himalayan margin (Figure 2b). As is the case with ϵ_u , $\Delta \epsilon_u$ is much higher along the Himalayan margin than along the topographically similar northern and central-eastern margins of the Tibetan plateau. Moderate $\Delta \epsilon_u$ (ca. 2×10^{10} to 3×10^{10} N m⁻¹ per km) occurs along the northern margin of Tibet and the Longmenshan margin to the east (Figure 2b).

Interestingly, when ϵ_u is visualized as a three-dimensional surface (Figure 3a), it is clear that ϵ_u along the Himalayan margin has complicated along-strike structure apparently unrelated to topography or surface geology. For instance, the central Himalaya between 78° 6' E and 88° 6' E longitude is very steep in ϵ_u space, mirroring the topographic steepness (Figure 3a & b). In contrast, the Himalayan margin to the immediate east and west of this zone has a lobate shape in ϵ_u space although topographically it is just as steep as it is in the central Himalaya (Figure 3a & b). The shape of these lobate ϵ_u areas along the Himalayan margin resemble the ϵ_u characteristics of Tibet's southeastern margin, although in the latter case the profile in ϵ_u space mirrors similarly gentle topography (e.g. Clark and Royden, 2000).

Gravitational Potential Energy Features of the Himalaya

There is little doubt that the high ϵ_u within the Tibetan interior reflects crustal thickening due to the India-Eurasia collision. It is worth noting, however, that there is a great deal of fine structure in ϵ_u , particularly along the Himalayan margin, with several prominent concentrations of and lateral variations in both ϵ_u and $\Delta \epsilon_u$ (Figures 2 & 4). I argue that the details of the GPE distribution reflect not only the India-Asia collision, but also density anomalies due to material in the intracrustal channel.

Chapter 6: Synthesis

A discontinuous chain of ϵ_u maxima with values in excess of ca. $4.5 \times 10^{12} \text{ N m}^{-1}$ extends in northwest-southeast direction across Tibet south of the Indus-Tsangpo suture (Figure 2c). These maxima are found north of the crest of the Himalayan ranges, between the traces of the South Tibetan fault system and the Indus-Tsangpo suture, and from the longitude of Gurla Mandahta to the longitude of the Namche Barwa syntaxis. This area encompasses the outcrop pattern of the North Himalayan gneiss domes (c.f. Figure 1a). The easternmost of these ϵ_u maxima (Figures 2c & 4c) include those associated with the Tso-Morari, Gurla Mandahta, and Upper Mustang massifs, the latter two of which are suspected core complexes and sites of Tertiary rapid exhumation of middle to lower crustal gneisses and granitoids (Murphy, 2000; Hurtado *et al.*, submitted – see Chapter 4). Two other prominent concentrations of high ϵ_u correspond to the gneiss domes between the Giyrong basin and the area north of the Khumbu Himalaya and to those between the Khumbu Himalaya and the Kangmar dome (another suspected core complex; Chen *et al.*, 1990) (Figures 2c & 4c). Moderately high ϵ_u (ca. $3 \times 10^{12} \text{ N m}^{-1}$) also occurs in the eastern syntaxis, southwest of the rapidly exhuming Namche Barwa massif (Figure 2c). In the western syntaxis region, another site of reported rapid exhumation of mid-crustal rocks, there is an ϵ_u anomaly of similar magnitude located southeast of the Nanga Parbat massif (Figure 2c). All of these culminations in ϵ_u , however, have small amplitudes compared to the dramatic step in ϵ_u coincident with the Himalayan front on which they are superimposed (e.g. Figures 3 & 5).

The region of high $\Delta \epsilon_u$ values along the Himalayan front also defines a prominent band, although with distinct gaps, most notably at the longitudes of both the Thakkhola graben and the Yadong-Gulu rift (Figure 2d). West of the Thakkhola graben, the

Chapter 6: Synthesis

$\Delta \varepsilon_u$ band is not well defined and is diminished in magnitude, with values about one half of those to the east, a trend that continues towards the Nanga Parbat area (Figure 2d). However, throughout the rest of the range front, and in particular the central Nepal Himalaya (Figure 4d), the northern extent of high $\Delta \varepsilon_u$ values is marked by the trace of the STF system, and the southern extent is marked by the trace of the MCT, matching the spatial distribution of the Greater Himalayan Sequence in the metamorphic core of the orogen. In the central Himalaya, the band of high $\Delta \varepsilon_u$ also correlates well with the high slope region in the topographic slope map (c.f. Figure 4b & d) (Hodges *et al.*, 2001).

These observations suggest a relationship between tectonic activity, $\Delta \varepsilon_u$, and the morphology of the range front. This hypothesis is supported by more detailed observations of the Thakkhola graben and the surrounding Annapurna and Dhaulagiri Himalaya (Figure 4). This region is the site of one of the prominent gaps in the high $\Delta \varepsilon_u$ band along the range front ($\Delta \varepsilon_u = \text{ca. } 3.5 \times 10^{10} \text{ N m}^{-1}$ per km) (Figure 4d), and it coincides with the eastern edge of the ε_u maximum which includes the Upper Mustang massif and Gurla Mandahta core complex (Figure 4c). Along this same stretch of range front, the Greater Himalayan Sequence is anomalously thin. The western and eastern edges of the $\Delta \varepsilon_u$ gap correspond to the transitions between thin and thick stretches of Greater Himalayan Sequence and the locations of anomalous N-S orientations of the STF system (Hurtado *et al.*, submitted – see Chapter 3) (Figure 4d). In this area of pronounced variations in the thickness of the Greater Himalayan Sequence there is geologic evidence for orogen-parallel flow of that material (Pêcher, 1991; Coleman, 1996; Hurtado *et al.*, submitted – see Chapter 3) as well as evidence for recent activity of both the MCT and the STF systems (Hurtado *et al.*, 2001; Hurtado *et al.*, submitted – see Chapter 3). One

Chapter 6: Synthesis

recently active strand of the STF system, the Dhaulagiri Southwest fault, follows the topographic break in the western Dhaulagiri range (Figure 4a & b) (Hurtado *et al.*, submitted – see Chapter 3). In places, it reactivates traces of the MCT system, although it is ultimately contiguous with the detachment faults in the Gurla Mandahta area (Murphy, 2000; Hurtado, *et al.*, submitted – see Chapter 3) (Figure 4a). The trace of the fault also correlates well with the northern extent of the zone of high $\Delta \varepsilon_u$ where it reappears in the western Dhaulagiri range (Figure 4c) (Hodges *et al.*, 2001; Hurtado *et al.*, submitted – see Chapter 3).

If one examines the Yadong-Gulu rift, the site of another prominent $\Delta \varepsilon_u$ gap in the Himalaya (Figures 3d & 4d), similar relationships are apparent. The $\Delta \varepsilon_u$ gap at the Yadong-Gulu rift is coincident with an apparent left-lateral offset of the STF system (e.g. the “Yadong Cross Structure” – Wu *et al.*, 1998). While $\Delta \varepsilon_u$ is low at the mouth of the Yadong-Gulu rift (ca. 2.5×10^{10} N m⁻¹ per km), within the graben further north there is a ε_u maximum between the northern and southern traces of the offset STF system (Figure 4c & d). This bears many similarities to the situation at the Thakkhola graben. In both places, we have an east-west extending graben with an apparent kinematic link to the STF system (Wu *et al.*, 1998; Hurtado *et al.*, 2001; Hurtado *et al.*, submitted – see Chapter 4) that is closely associated with adjacent gneiss domes – the Mustang massif in the case of the Thakkhola graben and Kangmar dome in the case of the Yadong-Gulu rift. The gneiss domes are coincident with local ε_u maxima, and the low- $\Delta \varepsilon_u$ gaps coincide with the mouths of the graben and/or areas where it is likely that post-Miocene tectonic activity has occurred.

Maps such as those in Figures 3 & 4 only offer a static snapshot of the *present-*

Chapter 6: Synthesis

day distribution of potential energy. Deconvolving the dynamic evolution of that distribution from the present day one is challenging at best. Despite this, note two things. First, the geologic record can give insights into what the GPE structure may have been like (e.g. Hurtado *et al.*, submitted – see Chapter 3). Second, if one assumes that the magnitudes of $\Delta \varepsilon_u$ and ε_u in the past were comparable to those today, predictions can be made regarding the importance of GPE to the tectonic and flow processes responsible for tectonism in the Himalaya. For instance, I can take orogen-perpendicular and orogen parallel transects through the ε_u data and use linear regressions to estimate $\Delta \varepsilon_u$ (Figures 3, 5 & 6). Using the resulting $\Delta \varepsilon_u$ values as proxies for the pressure gradient available to drive channel flow (e.g. equations (1)-(2)), I find that the amount of orogen-parallel material flux that could occur is within an order of magnitude of the possible orogen-perpendicular flux. However, the question remains: How do heterogeneities in the GPE field develop?

Accumulation and Dissipation of Gravitational Potential Energy

Within an orogenic plateau system, plate tectonic processes accumulate GPE in the system and act in competition with other processes that dissipate that energy, either moving it out of the system or redistributing it within the system. In the Himalaya, accumulation of GPE occurs principally by plate collisional forces. These shorten and thicken the crust and, in the case of the Tibetan-Himalayan system, have doubled its thickness. Molnar and Lyon-Caen (1988) showed that processes which double the thickness of a crustal column will more than double the GPE of that column with respect to a given reference (Figure 7). They also demonstrated that increasing the width of the

Chapter 6: Synthesis

column without increasing its thickness, would merely double the GPE of the column (Figure 7).

When viewed from another perspective, (e.g. Hodges, 1998), the relationships in Figure 7 demonstrate that GPE can be dissipated by widening the thickened column, i.e. laterally displacing its mass, at the expense of crustal thickness. Dissipative processes, therefore, are those that can either reduce crustal thickness or laterally redistribute crustal mass. Some of these processes, such as erosion, remove GPE from a system entirely by removing that mass from the system. Other processes, such as tectonic denudation along structures such as the South Tibetan fault, effectively lower and widen the orogen, and, therefore, chiefly serve to redistribute GPE within the system. Channel flow bridges the gap between these two endmember processes. Aided by the motion of faults at its upper and lower boundaries, channel flow moves mass laterally within the orogen, contributing to the outward propagation of the orogen and reduction of GPE. When impinging on a mountain front at (or close to) a flux steady state (Willett and Brandon, 2002), channel flow in conjunction with erosion can efficiently remove mass and its associated GPE entirely from the orogen.

Consider a simple column of crust with uniform density, ρ_{column} . If I assume that the column thickness changes at a rate \dot{L}_{column} , I can write an expression for the rate of GPE change:

$$\dot{U}_{column} = g\rho_{column} \frac{\dot{L}_{column}^2}{2} \quad (4).$$

A simple estimate of the magnitude of potential energy accumulation by crustal shortening in the Himalaya can be made if we take the horizontal shortening rate of ca. 20 mm yr⁻¹ (Bilham *et al.*, 1997), assume it is being accommodated on a ca. 30° N

Chapter 6: Synthesis

dipping fault plane, and calculate the vertical rate of uplift, in this case ca. 10 mm yr⁻¹. For a uniform density of 2750 kg m⁻³, and using equation (4), the rate of GPE accumulation is ca. +1.3x10¹² N m⁻¹ per Myr. A similar calculation for the dissipation of GPE by erosion at the Himalayan front yields a minimum of ca. -0.4x10¹² N m⁻¹ per Myr, for an erosion rate of >5 mm yr⁻¹ (e.g. Copeland and Harrison, 1990; Hubbard *et al.*, 1991) and regional topographic slope of 20°. Rates of tectonic denudation on the STF system are poorly constrained, and are likely to be variable within the Himalaya in both space and time. An estimate based on available data from the Everest region of Nepal suggests a rate of between 5 and 47 mm yr⁻¹ assuming that the Qomolangma detachment strand of the STF system has ≥ 30 km of displacement (Burchfiel *et al.*, 1992; Carosi *et al.*, 1998; Hodges *et al.*, 1998; Murphy and Harrison, 1999; Searle, 1999). Along a ca. 30° N dipping fault, these rates of displacement imply GPE dissipation between -0.2x10¹² N m⁻¹ per Myr and -7.4x10¹² N m⁻¹ per Myr.

These calculations show that the contributions of these three processes – shortening, erosion, and tectonic denudation – to the GPE of the orogen are similar in magnitude and that accumulation and dissipation may balance, implying that a steady-state condition may be possible. However, relatively short wavelength and high frequency spatial and temporal variations in accumulative and/or dissipative processes are likely – almost assuredly so in the case of erosion and demonstrably so in the case of tectonic denudation (e.g. Coleman, 1996; Hodges *et al.*, 1996; Hurtado *et al.*, submitted – see Chapter 3). Those circumstances suggest that a persistent, steady state channel flux condition may be hard to attain and that quasi-steady state conditions – such as attractor states – may be attained instead (e.g. Hodges *et al.*, 2001). More importantly, these

Chapter 6: Synthesis

conditions are likely to vary along strike in the orogen, such that some stretches are accumulating GPE while others are simultaneously dissipating GPE, with the potential for lateral GPE redistribution in between.

In a generic sense, the scope of the system in question and the scale of observation are important factors in the distinction between “removing” and “redistributing” GPE. For instance, normal faulting can reduce the GPE of one crustal column by moving overburden away from the footwall, but it may increase the GPE in the direction of throw. Similarly, erosion, while it can be the ultimate dissipater by removing material from a system entirely, can redistribute GPE if the resulting sediment is re-deposited elsewhere within the system. In the same way, while channel flow towards a plateau margin may dissipate the GPE of the plateau interior, the redistribution of material may increase the GPE of the margin, particularly if the flow is impeded such that the erosive removal of material is not realized. It is the prospect of local breakdowns of the flux steady state condition at the Himalayan margin that offers an explanation for the heterogeneity observed in the distribution of ε_e in southern Tibet and a link between channel flow, the efficiency of erosion and tectonic denudation, and core complex initiation.

Impediments to Intracrustal Channel Flow

Before discussing this hypothesis, it is useful to discuss the nature and estimate the magnitudes of impediments to channel flow. As even cursory fieldwork shows, the Himalayan front is not literally the leading edge of a semi-molten channel. In a more sophisticated view of the intracrustal channel, the Greater Himalayan Sequence, Lesser

Chapter 6: Synthesis

Himalayan Sequence, and other allochthonous blocks juxtaposed by the major Himalayan thrusts can be thought of as a "leading wedge" of metamorphic rocks, partially permeated and migmatized by intracrustal channel material, that is being exhumed as it is pushed out in front of the channel (e.g. Hodges *et al.*, 2001). In contrast to ductile flow in the channel *sensu stricto*, the nature of deformation within the leading wedge will be dominated by localized brittle deformation along faults. As such, one impediment to the channel flow is the effective yield stress of the leading wedge ahead of it.

Within the channel itself, flow of material is further impeded by two additional factors. The first factor, as described by Clark and Royden (2000), results from retarding forces arising from lateral gradients in crustal viscosity. Where there is a sufficiently large increase in viscosity in the direction of material flux, flow is impeded. The second impediment to flow is the far-field plate tectonic stress experienced by the lithosphere at a convergent plate boundary such as the Himalaya. The combined effect of yield stresses, far-field stresses, and viscosity contrasts serves to stop the flow of material when they dominate over the pressure gradient. Conversely, flow will occur where the pressure gradient dominates the retarding forces. Naturally, however, the thermal evolution is a key factor and an open question remains regarding which of the impeding factors is rate limiting.

Within this framework and for a given leading wedge yield stress and pressure gradient, several noteworthy cases can be identified. For instance, where shortening is minimal and viscosity gradients are low, the intra-crustal material can flow for long distances, forming plateau margins with subdued, ramp like topography as seen in southeast Asia (Clark and Royden, 2000). Where there is minimal far-field plate tectonic

Chapter 6: Synthesis

stress normal to the plateau margin, but a significant lateral increase in viscosity imparting a retarding force in excess of the pressure gradient, material will “pile up”. The result is a steep plateau margin characterized by regional tilting in the absence of surface breaking deformation as seen along the central-eastern Tibetan margin e.g. the Longmenshan (Clark and Royden, 2000; Kirby, 2001).

Where shortening due to far field stresses is high, one would expect to see a similar “piling up” of the intracrustal flow. In these settings, plate tectonic forces are of the order 1×10^{12} to 1×10^{13} N m⁻¹, approximately equivalent to – or an order of magnitude more than – the horizontal stresses implied by ϵ_i . Ironically, however, viscosity contrasts and far-field plate forces may have a diminished effect at convergent margins, particularly those that are the sites of focused orographic precipitation and attendant intense erosion. Modeling done by Jamieson *et al.* (2002) shows that, in orogens like the Himalaya, material and heat are very efficiently advected upwards to the surface and outwards towards the foreland due to the combined effects of surface, metamorphic, and deformational processes. The result is that the intracrustal channel is diverted upwards, towards the surface, and exhumed. Therefore, the intracrustal channel in the Himalaya need not impinge on the strong lithosphere surrounding Tibet as it does in the Longmenshan, but, instead, it can flow towards a free face where it is unaffected by retarding viscous and convergent forces (c.f Hodges *et al.*, 2001).

Erosional processes, therefore are important not just in dissipating potential energy, but also for establishing and sustaining the advection of material toward the surface in settings like the Himalaya. This allows intracrustal flow to continue in spite of

Chapter 6: Synthesis

viscous and far-field retarding forces. Erosion also accommodates that flux of material by removing it from the system.

Implications for Himalayan Deformation

The relative magnitudes of GPE-dissipative vs. GPE-accumulative processes and the effects of retarding forces will determine whether or not GPE increases or decreases in a particular area at a particular time. I define three main modes of potential energy dynamics and their relationship to ongoing tectonic processes.

The first mode is net energy accumulation (Figure 8, top). Periods of enhanced shortening at the Himalayan front – along structures such as the MCT and, at times, even the STF system – will result in GPE increase due to crustal thickness increases. Periods of diminished erosion at the range front may also contribute to GPE increase since the addition of mass to the range front by orogen-perpendicular channel flow would not be balanced by erosive removal. It is worth noting, however, that, since erosion plays a major role in sustaining channel flow (e.g. Beaumont *et al.*, 2001), the response time of the channel to changes in erosion rate is a critical, although unknown factor. It is unclear whether orogen-perpendicular channel flow would stop entirely or if GPE gradients alone would be sufficient to maintain flow towards the range front. Also unknown is how the timescale for erosive response compares to the timescale for reorganization of the channel flow.

The second mode is net GPE dissipation due to tectonic denudation and concomitant orogen-perpendicular channel flow and erosion at the range front (Figure 8, middle). Note that shortening may or may not continue in parallel with the dissipatory

Chapter 6: Synthesis

processes illustrated. Whether or not shortening occurs will affect the efficiency of GPE dissipation and the maintenance of a topographic steady state at the range front.

The third mode is GPE redistribution (Figure 8, bottom) and is the mode most directly applicable to the relationships between Tibetan rifts, north Himalayan gneiss domes, and the STF system. This mode is characterized by orogen-parallel flow locally dominating orogen-perpendicular flow. While this mode may or may not be responsible for the creation of localized GPE maxima (e.g. Figures 2c & 4c), it is influenced by the existence of GPE gradients, including those associated with such local maxima.

At least three scenarios may be responsible for the organization of the third dynamical mode (Figure 8, bottom). In all cases, orogen-parallel flow is driven by lateral gradients in GPE, but is rate-limited by the relative magnitudes of orogen-perpendicular and orogen-parallel retarding forces. One possibility is that orogen-parallel flow may occur when sufficient impediments to orogen-perpendicular flow exist. For example diminished erosion at the range front or periods of locally enhanced shortening could lead to local GPE maxima that cannot be accommodated by orogen-perpendicular GPE dissipation alone. In a similar scenario, orogen-parallel flow could occur when and where the impediments to orogen-parallel flow are significantly less than those opposing orogen-perpendicular flow. This could allow the former to dominate without necessarily stopping the latter altogether. Finally, orogen-parallel channel flow could occur in one area due to enhanced orogen-perpendicular channel flow in adjacent areas. In this case, the fluid flow would diverge towards those areas, resulting in orogen-parallel flow. The first of these scenarios suggests a mechanism for creating local GPE maxima (e.g. Figures 2c & 4c), while the other two do not.

Chapter 6: Synthesis

Alternatively, the mechanism for the development of GPE maxima (e.g. Figures 2c & 4c) may lie with the natural evolution of the relatively low-viscosity fluid in the channel, without regard to the complexities of GPE dissipatory processes at the range front. Natural fluid-dynamical instabilities in the channel flow, similar to those seen at the interface between two fluids of significantly different density may have caused local variations in the thickness of the intracrustal channel and undulations in the channel interfaces. This could explain the existence of local GPE maxima (Figures 2c & 4c), thickness variations of the Greater Himalayan Sequence, and the geometries of the STF and MCT systems (e.g. Hurtado *et al.*, submitted – see Chapter 3).

In the specific case of the STF system, shifts between these three modes of behavior in response to local GPE maxima could account for the complex geologic record of STF system activity in central Nepal. These phenomena include: the top-to-the-west displacement on the Chame detachment and structural evidence for orogen parallel deformation of the Greater Himalayan Sequence (Pêcher, 1991; Coleman, 1996); and lateral variations in the thickness of the Greater Himalayan sequence without disruption of the Formations within it (Coleman, 1996; Hurtado *et al.*, submitted – see Chapter 3); and shortening structures such as the Kalopani and Modi Khola shear zones (Hodges *et al.*, 1996; Vannay and Hodges, 1996). Interestingly, the transitions in displacement kinematics of the South Tibetan fault (e.g. from normal sense to thrust) are observed to occur over relatively short timescales (e.g. Hodges *et al.*, 1996) – outpacing changes in the plate convergence vector – and during intervals when there is no evidence for changes in the India-Asia plate convergence vector. The implication is that GPE heterogeneity

Chapter 6: Synthesis

due to intra-crustal channel flow may even be more important than far field plate interactions in determining the tectonic behavior of the orogen and the faults within it.

DEVELOPMENTAL SCENARIO FOR THE THAKKHOLA GRABEN AND DHAULAGIRI HIMALAYA

With this framework in mind, I suggest the following timeline for the tectonic evolution of the Thakkhola-Dhaulagiri region.

- *pre-22 Ma*: Crustal thickening and development of the intracrustal channel (Greater Himalayan Sequence) began during this time. The STF and MCT systems began activity by ca. 22 Ma. The STF basal detachment in the Annapurna Himalaya experienced top-to-the-north sense motion (Coleman, 1996), during orogen-perpendicular channel flow. Dissipation of GPE via erosive removal of channel mass and tectonic denudational orogen widening (Figure 8) began.
- *22-18 Ma*: By this time, circumstances had developed that favored orogen-parallel flow of the Greater Himalayan Sequence in the Annapurna Himalaya (Coleman, 1996) and, presumably, in the Dhaulagiri Himalaya (Hurtado *et al.*, submitted – see Chapter 3), at the expense of orogen-perpendicular flow (see previous section for a discussion of possible causes). Activity on the STF basal detachment in the Marsyandi valley of the Annapurna Himalaya was top-to-the-west (Coleman, 1996), implying eastward flow of channel material structurally below. Geometrically, the STF system in the Dhaulagiri Himalaya suggests top-to-east kinematics (Hurtado *et al.*, submitted – see Chapter 3), implying westward flow of channel material. It was during this time that the modern-day, variable-thickness outcrop patterns of the Greater Himalayan sequence and anomalous orientations of the STF basal detachment

Chapter 6: Synthesis

were developed (Hurtado *et al.*, submitted – see Chapter 3; see discussion in the previous section).

Lateral flow during this period triggered kinematics similar to those predicted by the generic model of Chéry (2001; e.g. Chapter 3, Figure 14). Continued lateral flow, and therefore orogen-parallel, low-angle STF system activity, had several effects. First, thinning and extension of the Tibetan Sedimentary Sequence in the hanging wall of the STF system in both the Annapurna and Dhaulagiri Himalaya resulted, the effects of which are observed by Hurtado *et al.* (submitted – see Chapter 3). Second, continued slip resulted in upward doming of the STF basal detachment surface and further thinning of its hanging wall (Chéry, 2001).

Another factor related to channel flow may have also caused upward doming of the STF décollement and extension of the crust above the channel. Given any number of forces impeding channel flow, the length-scale of lateral flow will be finite, and orogen-parallel flow will only transport material so far before the retarding forces cause “ponding” and the creation of a new GPE high. In the case of westward flow towards the UMM, lateral retarding forces may have been sufficient to not allow the flow to travel very far from the initial GPE maximum (near the site of the present-day Thakkhola graben). The excess channel pressure may have been sufficient to contribute to the uplift and exhumation of channel material, resulting in a component of dynamic uplift.

- *ca. 21-18.3 Ma*: Core complex extension due to the above processes marked the beginning of the development of the UMM. Decompression melting led to development of the Mustang granite and early Mugu granites (Hurtado *et al.*, submitted – see Chapter 3; Hurtado *et al.*, submitted – see Chapter 4). To the east, a minimum amount of upper plate extension, doming, and

Chapter 6: Synthesis

decompression melting (due to less excess channel pressure) may have resulted in the Manaslu pluton and the “Chako dome” (Godin, 2001).

- *ca. 18.3-17.5 Ma*: Following the Chéry (2001) model, upward doming of the STF décollement in the UMM triggered the formation of a steeply-dipping normal fault system antithetic to the STF faults in the Marsyandi valley (see Chapter 3, Figure 14). The principal structure of this new system is the Dangardzong fault, and its formation marked the beginning of the rift mode of Thakkhola graben extension, leading to rapid exhumation of the UMM in its footwall and dismemberment of the Mustang granite (Hurtado *et al.*, submitted – see Chapter 4). An additional consequence was further extension of the Tibetan Sedimentary Sequence above the thinned intracrustal channel. The scissors-geometry of the Dangardzong fault (e.g. Hurtado *et al.*, 2001) suggests that the graben propagated from north to south starting at this time.
- *ca. 17.5-15 Ma*: This interval marked an important phase of rapid cooling and exhumation of the Dangardzong fault footwall (Hurtado *et al.*, submitted – see Chapter 4). I predict that deposition of the earliest basin fill sediments in the Thakkhola graben began by the end of this interval. Note that although the Thakkhola graben *sensu stricto* “formed” at this time, east-west extension in the region began significantly earlier (as early as ca. 21 Ma with UMM core complex development). Note also that the extension in the Thakkhola graben during this time was accommodated on the STF system since the Dangardzong fault soles into the STF décollement at depth.
- *post-15 Ma*: By ca. 15 Ma, very rapid exhumation along the Dangardzong fault had subsided (Hurtado *et al.*, submitted – see Chapter 4), although development of the Thakkhola graben continued. Transcurrent “segmentational faults” (e.g. the Lupra and Tilicho Lake faults; Hurtado *et al.*, submitted – see Chapter 3), and antithetic normal faults related to Thakkhola graben extension and/or continuing STF system activity were active at ca. 14

Chapter 6: Synthesis

Ma (Coleman and Hodges, 1995; Hurtado *et al.*, submitted – see Chapter 3). By ca. 12 Ma, the Mustang and Mugu granites had been brought to the surface (Hurtado *et al.*, submitted – see Chapter 4) and were beginning to be eroded. The Tetang formation was deposited at ca. 11 Ma (Garzzone *et al.*, 2000). Clasts of both granites were being incorporated into the Thakkhola formation by ca. 8 Ma (Garzzone *et al.*, 2000). Extensional faults disrupting both the Thakkhola and Tetang Formations indicates that Thakkhola extension persisted subsequent to ca. 8 Ma (Hurtado *et al.*, 2001 – see Chapter 2).

- *ca. 35-7 ka*: Deposition of the Marpha and Sammargaon Formations in Lower Mustang, perhaps controlled, in part, by periodic damming of the Kali Gandaki river by landslides, glaciers, or seismic activity. The most recent Dangardzong fault activity in Lower Mustang occurred subsequent to Marpha Formation deposition, but prior to the rapid incision that produced the Kali Gandaki river terraces (Hurtado *et al.*, 2001 – see Chapter 2). The most recent STF system activity on the Dhumpu detachment and activity on the Dhaulagiri Southwest fault in the Dhaulagiri Himalaya also took place during this time (Hurtado *et al.*, 2001 – see Chapter 2; Hurtado *et al.*, submitted – see Chapter 3).
- *Present*: Renewed STF system activity is consistent with the dissipation of GPE maxima developed as a consequence of the preceding 22 million years of Himalayan tectonics. Based on the GPE distribution in Figures 2 & 4, the most likely areas for current and future vigorous tectonic activity are the areas between Gurla Mandahta and the Dhaulagiri Himalaya and between the Ganesh Himalaya and the Khumbu Himalaya. These regions possess the highest GPE gradients in the central Himalaya.

OUTSTANDING ISSUES AND FUTURE WORK

A number of avenues of investigation can extend our understanding of the tectonics of the Thakkhola graben and Dhaulagiri Himalaya beyond the model I present above. In addition, there are other facets to the geologic and geomorphic evolution of the region that can enhance, hopefully challenge, and ultimately refine my tectonic model.

The foremost of these possibilities and problems include:

- 1) Paleoseismology of the Dangardzong and Dhaulagiri Southwest faults: Trenching studies and detailed geochronology is critical to develop precise constraints on the Quaternary slip histories of these two structures and the seismic risk they pose. Sites in Upper Mustang have already been identified as promising with regard to cosmogenic nuclide dating of the Dangardzong fault and preliminary work has been started.
- 2) Modern seismicity: There is a lack of major seismic activity in the Thakkhola, Dhaulagiri and Annapurna areas, despite the growing evidence for Quaternary activity on the STF and MCT systems. Microseismic data for Nepal is available (e.g. Pandey *et al.*, 1995), and reveals clusters of activity near the MCT system, in particular north of Kathmandu. Although not as intense and localized, some microseismic activity also occurs in the Annapurna and Dhaulagiri areas and throughout the Thakkhola graben. Expansion of the seismic database for Nepal, in particular western Nepal, is necessary to better map out the extent of earthquake activity and its correlation to potentially active structures.
- 3) Geodetic surveys: A more extensive network of GPS stations, particularly in the northern part of the Thakkhola graben would provide data on the current rate of extension. Similarly a GPS campaign in the Dhaulagiri Himalaya can confirm whether or not STF system extension is occurring now.

Chapter 6: Synthesis

- 4) Remote sensing: Using soon-to-be-available, high-resolution ASTER hyperspectral imagery and SRTM digital topography, the techniques employed in Chapter 3 can be extended and refined. As always, detailed ground-truth fieldwork is a critical component of this type of analysis.

- 5) Basin analysis and mapping of the northern Thakkhola graben: Unfortunately, the remote northern part of the graben is hard to reach, yet may well contain the most important and complete record of basin development. As of this writing, almost all of knowledge on the Thakkhola graben basin fill is based upon the exposed Thakkhola and Tetang Formations in the southern part of Upper Mustang. Yet, vast areas of poorly mapped basin fill lie to the north, and most workers assume it is all Thakkhola Formation. As mentioned in Chapter 4, observations and reconnaissance mapping by myself and K. V. Hodges during our work on the UMM in the Tsarang and Lo Mantang areas suggests to us that this assumption is too simplistic and ignores significant complexity within the Thakkhola graben basin fill. Units older than the Tetang Formation may exist, a hypothesis motivated by the thermochronologic results in Chapter 4. Refining the internal stratigraphy of the Thakkola Formation is certainly also possible. Finally, the possibility that datable material, such as volcanic tuff, is intercalated with the basin fill is reason enough to more completely explore Upper Mustang as such material would provide timing constraints both more precise and more accurate than those previously obtained.

- 6) Structural geology of the Upper Mustang massif: A complete understanding of the history of the UMM and its evolution as a core complex requires field work and sample collection further into its interior, as well as along its northern and western edges, all of which lie within Chinese-occupied Tibet. An especially critical area is the portion of suspected Mustang granite identified with Landsat imagery in the eastern Thakkhola graben (Chapter 4, Figure 4). Confirmation that it is indeed the Mustang granite and that it is capped by a low-angle detachment are key issues to be resolved.

Chapter 6: Synthesis

- 7) Thermobarometric study of the UMM: Pressure-temperature data to complement the thermochronologic data I generated is necessary to test and refine the exhumational history I propose in Chapter 4.
- 8) Field work in the western Dhaulagiri Himalaya: Detailed fieldwork is required to test the interpretations and hypotheses made using remote sensing data. A critical issue is verifying the kinematics of the STF system in the Burbang Khola, which I predict will be top to the east, mirroring the orogen-parallel kinematics observed in the Marsyandi valley in the Annapurna area (e.g. Pêcher, 1991; Coleman, 1996). Equally important is field verification of the trace of the Tibetan Sedimentary Sequence-Greater Himalayan Sequence contact west of Gurja Himal. Finally, field mapping of the Dhaulagiri Southwest fault is necessary in order to verify its relationship with the STF and MCT systems.
- 9) Quantitative geomorphology: The unfortunate lack of 90-m resolution DTED digital topography for most of the Thakkhola graben will soon be rectified with the release of SRTM data for the region. High-quality, high-resolution topography can be applied to drainage network analysis, landscape evolution models, and bedrock incision models. Of particular interest are the headwaters of the Kali Gandaki river at the latitude of Thinker village in Upper Mustang. In this area, an enigmatic, east-striking ridge separates the Kali Gandaki valley to the south from a basin to the north that is drained by a tributary of the Indus-Tsangpo (Brahmaputra) river. The interplay between Thakkhola extension, northward incision into the highlands by the Kali Gandaki river, and possible river capture are fertile grounds for research.
- 10) Quantitative analysis of GPE: The goal of this analysis would be to derive an exact, analytical expression for the relationship between $\Delta \varepsilon_i$ and the pressure gradient driving intracrustal flow. Having developed this formalism, it could be applied to the GPE of the Himalaya to compute fluxes of intracrustal material which can be compared to independent estimates of the volume of sediment removed from the Himalayan margin, erosion rates, and long term slip rates on the STF and MCT

Chapter 6: Synthesis

systems. Other possibilities include deconvolving ε_u into components, one attributable to crustal thickness variations and a residual due to things like lateral density variations, thermal structure, and shear tractions. This analysis could be used to determine the reliability of using topographic data alone to model the pressure gradients driving channel flow.

REFERENCES CITED

- Armijo, R., Tapponier, P., Mercier, J., and Han, T., 1986, Quaternary extension in Southern Tibet: Field observations and tectonic implications: *Journal of Geophysical Research*, v. 91, p. 13803-13872.
- Beaumont, C., Jamieson, R. A., Nguyen, M. H., and Lee, B., 2001, Himalayan tectonics explained by extrusion of a low-viscosity crustal channel coupled to focused surface denudation: *Nature*, v. 414, p. 738-742.
- Bilham, R., Larson, K., Freymuller, J., and Members, P. I., 1997, GPS measurements of present-day convergence across the Nepal Himalaya: *Nature*, v. 386, p. 61-64.
- Brown, L. D., Zhao, W., Nelson, K. D., Hauck, M., Alsdorf, D., Ross, A., Cogan, M., Clark, M., Liu, X., and Che, J., 1996, Bright spots, structure and magmatism in southern Tibet from INDEPTH seismic reflection profiling: *Science*, v. 274, p. 1688-1690.
- Burchfiel, B. C., Chen, Z., Hodges, K. V., Liu, Y., Royden, L. H., Deng, C., and Xu, J., 1992, *The South Tibetan Detachment System, Himalayan Orogen: Extension Contemporaneous With and Parallel to Shortening in a Collisional Mountain Belt*, Geological Society of America Special Paper 269: Boulder, CO, Geological Society of America, 41 p.
- Burtman, V. S., and Molnar, P., 1993, *Geological and Geophysical Evidence for Deep Subduction of Continental Crust Beneath the Pamir*, Geological Society of America Special Paper 281: Boulder, CO, Geological Society of America, 76 p.
- Carosi, R., Lombardo, B., Molli, G., Musumeci, G., and Pertusati, P. C., 1998, The South Tibetan Detachment System in the Rongbuk Valley, Everest Region - Deformation Features and Geological Implications: *Journal of Asian Earth Sciences*, v. 16, no. 2-3, p. 299-311.
- Chen, L., Booker, J. L., Jones, A. G., Wu, N., Unsworth, M. J., Wei, W., and Tan, H., 1996, Electrically conductive crust in southern Tibet from INDEPTH magnetotelluric surveying: *Science*, v. 274, p. 1694-1696.

Chapter 6: Synthesis

- Chen, Z., Liu, Y., Hodges, K. V., Burchfiel, B. C., Royden, L. H., and Deng, C., 1990, Structural evolution of the Kangmar dome: A metamorphic core complex in southern Xizang (Tibet): *Science*, v. 250, p. 1552-1556.
- Chéry, J., 2001, Core complex mechanics: From the Gulf of Corinth to the Snake Range: *Geology*, v. 29, no. 5, p. 439-442.
- Clark, M. K., and Royden, L. H., 2000, Topographic ooze: Building the eastern margin of Tibet by lower crustal flow: *Geology*, v. 28, no. 8, p. 703-706.
- Coblentz, D. D., Richardson, R. M., and Sandiford, M., 1994, On the gravitational potential of the Earth's lithosphere: *Tectonics*, v. 13, no. 4, p. 929-945.
- Coleman, M. E., 1996, Orogen-parallel and orogen-perpendicular extension in the central Nepalese Himalayas: *Geological Society of America Bulletin*, v. 108, p. 1594-1607.
- Coleman, M. E., and Hodges, K. V., 1995, Evidence for Tibetan plateau uplift before 14 Myr ago from a new minimum age for east-west extension: *Nature*, v. 374, p. 49-52.
- Copeland, P., and Harrison, T. M., 1990, Episodic rapid uplift in the Himalaya revealed by $^{40}\text{Ar}/^{39}\text{Ar}$ analysis of detrital K-feldspar and muscovite, Bengal Fan: *Geology*, v. 18, p. 354-357.
- England, P., and Houseman, G., 1989, Extension during continental convergence, with application to the Tibetan Plateau: *Journal of Geophysical Research*, v. 94, p. 17561-17579.
- England, P., and Molnar, P., 1997, Active deformation of Asia: from kinematics to dynamics: *Science*, v. 278, p. 647-650.
- England, P. C., and Houseman, G., 1985, Role of lithospheric strength heterogeneities in the tectonics of Tibet and neighbouring regions: *Nature*, v. 315, p. 297-301.
- Francheteau, J., Jaupart, C., Shen, X. J., Kang, W.-H., Lee, D.-L., Bai, J.-C., Wei, H.-P., and Deng, H.-Y., 1984, High heat flow in southern Tibet: *Nature*, v. 307, no. 5946, p. 32-36.
- Garzzone, C. N., Dettman, D. L., Quade, J., DeCelles, P. G., and Butler, R. F., 2000, High times on the Tibetan Plateau: Paleoelevation of the Thakkhola graben, Nepal: *Geology*, v. 28, no. 4, p. 339-342.
- Godin, L., 2001, The Chako dome: an enigmatic structure in the hanging wall of the South Tibetan detachment, Nar valley, central Nepal, in *16th Himalaya-Karakoram-Tibet Workshop, Gratz, Austria*.

Chapter 6: Synthesis

- Grujic, D., Casey, M., Davidson, C., Hollister, L. S., Kündig, R., Pavlis, T., and Schmid, S., 1996, Ductile extrusion of the Higher Himalayan crystalline in Bhutan: evidence from quartz microfabrics: *Tectonophysics*, v. 260, p. 21-43.
- Hauck, M. L., Nelson, K. D., Brown, L. D., Zhao, W., and Ross, A. R., 1998, Crustal structure of the Himalayan Orogen at ~90° east longitude from Project INDEPTH deep reflection profiles: *Tectonics*, v. 17, no. 4, p. 481-500.
- Hodges, K., Bowring, S., Davidek, K., Hawkins, D., and Krol, M., 1998, Evidence for rapid displacement on Himalayan normal faults and the importance of tectonic denudation in the evolution of mountain ranges: *Geology*, v. 26, p. 483-486.
- Hodges, K. V., 1998, The thermodynamics of Himalayan orogenesis, in Treloar, P. J., and O'Brien, P., eds., *What Drives Metamorphism and Metamorphic Reactions?*: London, Geological Society, p. 7-22.
- Hodges, 2000, Tectonics of the Himalaya and southern Tibet from two perspectives: *Geological Society of America Bulletin*, v. 112, no. 3, p. 324-350.
- Hodges, K. V., Hurtado, J. M., and Whipple, K. X., 2001, Southward extrusion of Tibetan crust and its effect on Himalayan tectonics: *Tectonics*, v. 20, no. 6, p. 799-809.
- Hodges, K. V., Parrish, R. R., and Searle, M. P., 1996, Tectonic evolution of the central Annapurna Range, Nepalese Himalayas: *Tectonics*, v. 15, p. 1264-1291.
- Hubbard, M., Royden, L., and Hodges, K., 1991, Constraints on unroofing rates in the High Himalaya, Eastern Nepal: *Tectonics*, v. 10, p. 287-298.
- Hurtado, J. M., Hodges, K. V., and Whipple, K. X., 2001, Neotectonics of the Thakkhola Graben and Implications for Recent Activity on the South Tibetan Fault System in the Central Nepal Himalaya: *Geological Society of America Bulletin*, v. 113, no. 2, p. 222-240.
- Jamieson, R. A., Beaumont, C., Nguyen, M. H., and Lee, B., 2002, Interaction of metamorphism, deformation, and exhumation in large convergent orogens: *Journal of Metamorphic Geology*, v. 20, p. 1-16.
- Jones, C. H., Unruh, J. R., and Sonder, L. J., 1996, The role of gravitational potential energy in active deformation in the southwestern United States: *Nature*, v. 381, p. 37-41.
- Kind, R., Ni, J., Zhao, W., Wu, J., Yuan, X., Zhao, L., Sandvol, E., Reese, C., Nabelek, J., and Hearn, T., 1996, Evidence from earthquake data for a partially molten crustal layer in southern Tibet: *Science*, v. 274, p. 1692-1694.

Chapter 6: Synthesis

- Kirby, E., 2001, *Structural, Thermal, and Geomorphic Evolution of the Eastern Margin of the Tibetan Plateau* [Ph.D. thesis]: MIT, 211 p.
- Lemoine, F. G., Kenyon, S. C., Factor, J. K., Trimmer, R. G., Pavlis, N. K., Chinn, D. S., Cox, S. M., Klosko, S. M., Luthcke, S. B., Torrence, M. H., Wang, Y. M., Williamson, R. G., Pavlis, E. C., Rapp, R. H., and Olson, T. R., 1998, *The development of the joint NASA GSFC and the National Imagery and Mapping Agency (NIMA) geopotential model EGM96*, NASA Technical Paper NASA/TP-1998-206861: Greenbelt, MD, Goddard Space Flight Center, p. 600.
- Makovski, Y., Klemperer, S., Ratschbacher, L., Brown, L. D., Li, M., Zhao, W., and Meng, F., 1996, INDEPTH wide-angle reflection observation of P-wave to S-wave conversion from crustal bright spots in Tibet: *Science*, v. 274, p. 1690-1691.
- McNamara, D. E., Owens, T. J., Silver, P. G., and Wu, F. T., 1994, Shear wave anisotropy beneath the Tibetan Plateau: *Journal of Geophysical Research*, v. 99, p. 13655-13665.
- McQuarrie, N., and Chase, C. G., 2000, Raising the Colorado Plateau: i, v. 28, no. 1, p. 91-94.
- Molnar, P., 1988, A review of geophysical constraints on the deep structure of the Tibetan Plateau, the Himalaya and the Karakoram, and their tectonic implications: *Philosophical Transactions of the Royal Society of London*, v. A 326, p. 33-88.
- Molnar, P., and Lyon-Caen, H., 1988, Some simple physical aspects of the support, structure, and evolution of mountain belts, in Clark, S., Burchfiel, B. C., and Suppe, J., eds., *Processes in Continental Lithospheric Deformation*: Boulder, CO, Geological Society of America Special Paper 218, p. 179-207.
- Molnar, P., and Tapponnier, P., 1975, Cenozoic tectonics of Asia: Effects of a continental collision: *Science*, v. 189, p. 419-426.
- Molnar, P., and Tapponnier, P., 1978, Active tectonics of Tibet: *Journal of Geophysical Research*, v. 83, p. 5361-5375.
- Molnar, P. and Tapponnier, P., 1981, A possible dependence of tectonic strength on the age of the crust in Asia: *Earth and Planetary Science Letters*, v. 52, no. 107-114.
- Murphy, M. A., 2000, *Tectonic Evolution of southwest Tibet* [Ph.D. thesis]: University of California, Los Angeles, 216 p.
- Murphy, M. A., and Harrison, T. M., 1999, The relationship between leucogranites and the South Tibetan detachment system, Rongbuk Valley, southern Tibet: *Geology*, v. 27, no. 9, p. 831-834.

Chapter 6: Synthesis

- Nelson, K. D., Brown, L. D., Hauk, M. L., Alsdorf, D., Clark, M., Cogan, M., Wu, C., Makovsky, Y., Klemperer, S., Kidd, W. S. F., Edwards, M., Ni, J., Sandvol, E. A., Kind, R., Nabelek, J., Mechie, J., Steentoft, H., Wenzel, F., Meissner, R., Kuo, J. T., and Zhao, W., 1995, Initial results of INDEPTH II (1994) deep crustal profiling in southern Tibet, in Spencer, D. A., Burg, J.-P., and Spencer-Cervato, C., eds., *10th Himalaya-Karakoram-Tibet Workshop Abstract Volume: Zürich, Mitteilungen aus dem Geologischen Institut der ETH und der Universität Zürich*, No. 298.
- Nelson, K. D., Zhao, W., Brown, L. D., Kuo, J., Che, J., Xianwen, L., Klemperer, S., Makovsky, Y., Meissner, R., Mechie, J., Kind, R., Wenzel, F., Ni, J., Nabelek, J., Chen, L., Handong, T., Wenbo, W., Jones, A. G., Booker, J., Unsworth, M., Kidd, W. S. F., Hauk, M., Alsdorf, D., Ross, A., Cogan, M., Wu, C., Sandvol, E. A., and Edwards, M., 1996, Partially molten middle crust beneath southern Tibet: Synthesis of Project INDEPTH Results: *Science*, v. 274, p. 1684-1688.
- Ni, J., and York, J. E., 1978, Cenozoic extensional tectonics of the Tibetan Plateau: *Journal of Geophysical Research*, v. 83, p. 5277-5384.
- Owens, t. J., and Zandt, G., 1997, Implications of crustal property variations for models of Tibetan plateau evolution: *Nature*, v. 387, p. 37-43.
- Pandey, M. R., Tandukar, R. P., Avouac, J. P., Lavé, J., and Massot, J. P., 1995, Interseismic strain accumulation on the Himalayan crustal ramp (Nepal): *Geophysical Research Letters*, v. 22, p. 751-754.
- Pêcher, A., 1991, The contact between the Higher Himalyan crystallines and the Tibetan sedimentary series: Miocene large-scale dextral shearing: *Tectonics*, v. 10, p. 587-599.
- RSI, 2000, *ENVI User's Guide 3.4*, Research Systems, Inc., 930 p.
- Searle, M. P., 1999, Extensional and compressional faults in the Everest-Lhotse massif, Khumbu Himalaya, Nepal: *Journal of the Geological Society of London*, v. 156, p. 227-240.
- Sheehan, A. F., and Solomon, S. C., 1991, Joint Inversion of Shear Wave Travel Time Residuals and Geoid and Depth Anomalies for Long-Wavelength Variations in Upper Mantle Temperature and Composition Along the Mid-Atlantic Ridge: *Journal of Geophysical Research*, v. 96, no. B12, p. 19,981-20,009.
- Tanimoto, T., and Okamoto, T., 2000, Change of crustal potential energy by earthquakes: an indicator for extensional and compressional tectonics: *Geophysical Research Letters*, v. 27, p. 2313-2316.

Chapter 6: Synthesis

- Turcotte, D. L., and Schubert, G., 1982, *Geodynamics: applications of continuum physics to geological problems*: New York, John Wiley & Sons, 450 p.
- Turner, S., Hawkesworth, C., Liu, J., Rogers, N., Kelley, S., and van Calsteren, P., 1993, Timing of Tibetan uplift constrained by analysis of volcanic rocks: *Nature*, v. 364, p. 50-54.
- USGS, 1993, *Digital elevation models, data user guide, 5*: Reston, Virginia, United States Geological Survey, p. 1-50.
- Vannay, J.-C., and Hodges, K. V., 1996, Tectonometamorphic evolution of the Himalayan metamorphic core between Annapurna and Dhaulagiri, central Nepal: *Journal of Metamorphic Geology*, v. 14, p. 635-656.
- Willett, S. D., and Brandon, M. T., 2002, On steady states in mountain belts: *Geology*, v. 30, no. 2, p. 175-178.
- Wu, C., Nelson, K. D., Wortman, G., Samson, S. D., Yue, Y., Li, J., Kidd, W. S. F., and Edwards, M. A., 1998, Yadong cross structure and South Tibetan detachment in the east central Himalaya (89°-90°E): *Tectonics*, v. 17, p. 28-45.

FIGURE CAPTIONS

Figure 1.

a. Map of the Himalaya and the Tibetan plateau showing the distribution of major structures (after Hodges, 2000). Lines denote faults with ornamentation pointing in dip-direction of fault plane: triangular barbs = thrust fault; tick marks = low-angle normal faults; stick-and-ball = steeply-dipping normal faults. Blue faults are the east-west extending grabens in Tibet. Red faults are the South Tibetan fault system. The North Himalayan gneiss domes shown are shown in yellow. Abbreviations: ITS = Indus-Tsangpo suture; STFS = South Tibetan fault system; MCTS = Main Central thrust system; MBT = Main Boundary thrust; MFT = Main Frontal thrust; UMM = Upper Mustang massif; GM = Gurla Mandahta; TM = Tso Morari; KD = Kangmar dome; GL = Gonto La area; TG = Thakkhola graben; YCS = Yadong Cross Structure. Dashed green line denotes line of section depicted in Figure 1b.

b. Representative cross-section through southern Tibet and the Himalaya, from the Indus-Tsangpo suture (ITS) in the north to the Main Frontal thrust (MFT) in the south (dashed green line in Figure 1a). Adapted from Hauck *et al.* (1998), Nelson *et al.* (1995),

Chapter 6: Synthesis

and Hodges *et al.* (2001). Abbreviations: KD = Kangmar dome; STF = South Tibetan fault system; MCT = Main Central thrust system; MBT = Main Boundary thrust; HST = Himalayan Sole thrust. “S” and “A” denote the synform-antiform pair within the Lesser Himalayan zone in Central Nepal. Small arrows along faults denote shear sense. Large arrows denote convergence between the Indian plate (white region between the MOHO and HST) and the Asian plate (patterned and shaded region above HST). The total thickness of the Tibetan-Himalayan lithosphere above the MOHO is ca. 60-70 km. Note that the northward extent of the Greater Himalayan zone beneath Tibet is interpreted to be the intracrustal channel. The channel coincides with the zone of “bright spots” imaged by the INDEPTH project (e.g. Nelson *et al.*, 1995). The thickness of this zone is shown to be ca. 30 km (Hauck *et al.*, 1998). Note also the warped subsurface geometry of the STF décollement and its relationship to the Kangmar dome, and, I suspect, other North Himalayan gneiss domes (e.g. Hurtado *et al.*, submitted – see Chapter 4).

Figure 2.

Gravitational potential energy maps for the Tibetan plateau and surrounding regions of central and south Asia (Figure 2ab after Hodges *et al.*, 2001). Maps are derived from the NASA-NIMA joint geopotential model EGM-96, a global geoid dataset with 0.25° (ca. 30 km) resolution and referenced to the WGS-84 datum (Lemoine *et al.*, 1998). The potential energy maps are in un-projected geographic coordinates. The inset of Figure 2a shows the political geography of the region and is in Albers conical projection. Abbreviations: A = Afghanistan; BA = Bangladesh; BH = Bhutan; K = Kyrgyzstan; L = Laos; N = Nepal; R = Russia; TA = Tajikistan; TU = Turkmenistan; TH = Thailand; U = Uzbekistan; V = Vietnam.

a. Gravitational potential energy anomaly, ϵ_u . Abbreviations: I = India; K = Karakoram range; T = Tibetan plateau; S = Sichuan basin; TA = Tarim basin; Q = Qaidam basin. The box denotes the area shown in more detail in Figures 2c & d.

b. Gravitational potential energy anomaly gradient, and $\Delta \epsilon_u$ computed from the ϵ_u map using ENVI® image processing software (RSI, 2000). Note the high gradients along the southern margin of the Tibetan plateau between the eastern and western syntaxes (ES and WS). Moderately high gradients also exist along the western and

Chapter 6: Synthesis

eastern Kunlun mountains (WK and EK) as well as along the Longmenshan range (L) in eastern Tibet. Clark and Royden (2000) argued that the low gradient areas to the north and south of L are pathways for flow of intracrustal material around obstacles such as the Sichuan and Qaidam Basins (Figure 1a).

c. Detail of Figure 2a showing the ϵ_u structure of the Himalayan margin of Tibet. Abbreviations: NP = Nanga Parbat; TM = Tso Morari; GM = Gurla Mandahta; UMM = Upper Mustang Massif; TG = Thakkhola graben; GB = Giyrong basin; KH = Khumbu Himalaya; YCS = Yadong-Gulu rift/Yadong Cross Structure; KD = Kangmar dome; NB = Namche Barwa. Note the spatial correspondence between local ϵ_u maxima and the North Himalayan gneiss domes. The box denotes the area shown in Figure 4.

d. Detail of Figure 2b showing the $\Delta\epsilon_u$ structure of the Himalayan margin of Tibet. Abbreviations as in Figure 2c. Note the band of high $\Delta\epsilon_u$ along the Himalayan front and the prominent gaps at the TG and YCS.

Figure 3.

a. Three-dimensional visualizations of ϵ_u (*upper left, upper right*) and GTOPO-30 digital topography (USGS, 1993) (*bottom*) for the area shown in Figure 2a. Visualizations created with ENVI® image processing software (RSI, 2000). Topography is shown with 200 times vertical exaggeration, and the ϵ_u surface is scaled to maximize visibility of the gravitational potential energy structure. Grayscale values in the ϵ_u visualizations correspond to the magnitude of ϵ_u in N m^{-1} as shown by the color-ramp. Topography is shown for reference. Note the very steep ϵ_u gradient in the central Himalaya that mirrors the steep topography. This zone, however, is flanked by more diffuse and shallow ϵ_u on either side, despite the unchanged topographic steepness. Note also the ϵ_u gradients elsewhere in Tibet, including the moderate northeasterly gradient in the plateau interior and the shallow, diffuse ϵ_u gradient along the southeastern margin.

b. Topographic profiles across the western (top), central (middle), and eastern (bottom) Himalaya. Each frame shows profiles of the maximum (top curve), mean (middle curve), and minimum (bottom curve) topography averaged along 100-km wide swaths (Matlab® algorithm by E. Kirby, M. Clark, and P. Dodds, 1999 – e.g. Clark and Royden, 2000; Kirby, 2001) extracted from the GTOPO-30 digital elevation model

Chapter 6: Synthesis

(DEM) (USGS, 1993). Image at top shows the same area in the three-dimensional visualizations in Figure 3a. White boxes denote the swaths used in the profile calculations (W = western; C = central; E = eastern). The areas chosen for analysis are representative of the topography in each sector of the range front. Mean topographic gradients are taken as the least squares slope of the steepest part of the mean profile between ca. 5 km and 1 km elevation. Although the topographic gradient of the central Himalaya is the steepest (ca. 31 m per km), those of the western (ca. 25 m per km) and eastern (ca. 28 m per km) Himalaya are not significantly shallower.

c. Profiles of ϵ_u across the western (top), central (middle), and eastern (bottom) Himalaya. Profiles extracted from Figure 2a along the same transects used for the topographic swath profiles (Figure 3b; see image at top). GPE gradient is calculated with a least squares linear fit. Multiple fits are shown for the complex western and eastern Himalayan GPE profiles. The central Himalaya has a GPE gradient almost twice that of the western or eastern Himalaya, which exceeds the variation present in the mean topographic gradients (Figure 3b).

Figure 4.

a. Shaded relief map derived from the GTOPO-30 digital elevation model (DEM) (USGS, 1993) showing the portion of the central Nepal Himalaya and southernmost Tibetan plateau indicated in Figure 2c. Red dashed red lines denote the orogen-perpendicular transects considered. Blue dashed blue lines denote the orogen-parallel transects considered. Black ornamented and labeled lines show the traces of the South Tibetan fault (STF) and Main Central thrust (MCT) systems and yellow areas represent the outcrop pattern of the North Himalayan gneiss domes (after Hodges, 2000). Abbreviations: GM = Gurla Mandakata; UMM = Upper Mustang Massif; TG = Thakkhola graben; KD = Kangmar dome; YCS = Yadong-Gulu rift/Yadong Cross Structure; DSWF = Dhaulagiri Southwest fault.

b. Topographic slope map derived from the GTOPO-30 data for the area shown in Figure 4a. Note the spatial correspondence between the topographic breaks at the top and bottom of the band of high slopes and the STF and MCT systems, respectively. Annotations as in Figure 4a.

Chapter 6: Synthesis

c. Map of the gravitational potential energy anomaly (ϵ_u) for the area shown in Figure 4a. Note spatial correspondence between local ϵ_u maxima and the North Himalayan gneiss domes (white outlines).

d. Map of the gravitational potential energy anomaly gradient ($\Delta \epsilon_u$) for the area shown in Figure 4a. Note band of high $\Delta \epsilon_u$ along the Himalayan front coincident with the Greater Himalayan Sequence between the STF and MCT systems. Note also the prominent gaps in the band of high $\Delta \epsilon_u$ at the TG and YCS. White outlines denote the North Himalayan gneiss domes.

Figure 5.

Representative north-to-south ϵ_u transects across the central Nepal Himalaya, from the latitude of the Indus-Tsangpo suture to the outcrop trace of the Main Central Thrust (red dashed lines in Figure 4). The slope of the least squares linear fit through these data yields the average gravitational potential energy anomaly gradient ($\Delta \epsilon_u$) perpendicular to the plateau margin. STF and MCT denote the positions of the South Tibetan fault and Main Central thrust, respectively.

- a. Western Dhaulagiri Himalaya.
- b. Eastern Dhaulagiri Himalaya.
- c. Annapurna Himalaya.
- d. Ganesh Himalaya.
- e. Langtang Himalaya.
- f. Khumbu Himalaya.
- g. Yadong-Gulu rift.

Figure 6.

Representative east-west ϵ_u transects parallel to the central Nepal Himalaya, just south of the Indus-Tsangpo suture (blue dashed lines in Figure 4). The slope of the least squares linear fit through these data yields the average gravitational potential energy anomaly gradient ($\Delta \epsilon_u$) parallel to the plateau margin.

a. West-to-east, from the Upper Mustang Massif towards the Giyrong Basin (UMM-GB, Figure 4a).

Chapter 6: Synthesis

b. East-to-west from the Khumbu Himalaya towards the Gyirong Basin (KH-GB, Figure 4a).

c. West to east, from the Khumbu Himalaya towards the Yadong-Gulu rift (KH-YCS, Figure 4a).

d. East to west, from the Yadong-Gulu rift towards the Khumbu Himalaya (YCS-KH, Figure 4a).

Figure 7.

Potential energy changes associated with thickening and widening of a crustal column after (after Molnar and Lyon-Caen, 1988). Variables: a = topographic height; b = thickness of reference column; c = thickness of compensating root; f = width of orogen; ρ_{column} = uniform density of crustal column; g = gravitational acceleration; ΔU = potential energy difference between shaded and unshaded columns. *Top*: Initial condition with a crustal column (shaded) in isostatic equilibrium with a reference column (unshaded). ΔU for this condition is defined as ΔU_o . *Middle*: Thickened – e.g. mass and/or thickness increased due to shortening and/or influx of material in a channel (see Figure 9) – crustal column (shaded), now with twice the topographic height and compensating root. ΔU for this situation is substantially more than twice ΔU_o . *Bottom*: Thickened crustal column after lowering and widening – due to tectonic denudation, channel flow, erosion. ΔU for this situation is twice ΔU_o , but substantially less than that of the middle frame. Expression at bottom defines $\Delta U_{dissipated}$, the potential energy decrease between the middle and bottom frames due to dissipatory processes (see Figure 9).

Figure 8.

Schematic cross-sections through the Himalaya and southern Tibet illustrating three main modes of potential energy dynamics and their relationship to ongoing tectonic processes (after Hodges, 1998). *Top*: North-to-south cross-section depicting potential energy increase due to shortening along structures such as the Main Central thrust (MCT) and the addition of mass to the range front by channel flow. *Middle*: North-to-south cross-section depicting potential energy decrease due to tectonic denudation and concomitant channel flow and erosion at the range front. Note that shortening may or

Chapter 6: Synthesis

may not continue in parallel with the dissipatory processes illustrated. Whether or not shortening occurs will affect the efficiency of potential energy dissipation and the maintenance of a topographic steady state at the range front. *Bottom:* West-to-east cross-section depicting potential energy redistribution due to lateral channel flow. Potential energy highs may occur along stretches of the orogen where orogen-perpendicular dissipatory processes are ineffective in removing potential energy. Orogen-parallel flow of material (arrows) will locally thin the channel, as well as the crust above, and may trigger rift and core-complex extension (e.g. Chéry, 2001; Hurtado *et al.*, submitted – see Chapter 3; Hurtado *et al.*, submitted – see Chapter 4). While it thins the channel in one place, lateral flow will thicken it in another, forming new potential energy highs associated with the North Himalayan gneiss domes (NHGD) such as the Upper Mustang massif. The thinned site of the original potential energy high is now an east-west extending rift system (EWRS) with substantially less potential energy. Such is the case in the Thakkhola graben and Yadong-Gulu rifts (Figure 4).

Figure 9.

Microseismicity map of central Nepal recorded between 1985 and 1993 (from Pandey *et al.*, 1995). Most events are shallow with magnitudes below 4. Only one moderate-sized earthquake was recorded during this time interval. It was of magnitude 6 and occurred on 8/21/1988 at a depth of 57 km at 26.78°N, 86.61°E, with a fault plane solution indicative of thrusting on a southeast-striking reverse fault. Apparent from the map is the paucity of seismic activity in the sub-Himalaya along the “active” Main Frontal and Main Boundary thrusts (MFT and MBT). The bulk of activity has occurred in the greater Himalaya near the surface trace of the Main Central thrust (MCT), in particular along the stretch north of Kathmandu. Note also the activity in the Annapurna and Dhawalgiri Himalaya and the north-striking, diffuse zone of microseismicity that delineates the Thakkhola graben.

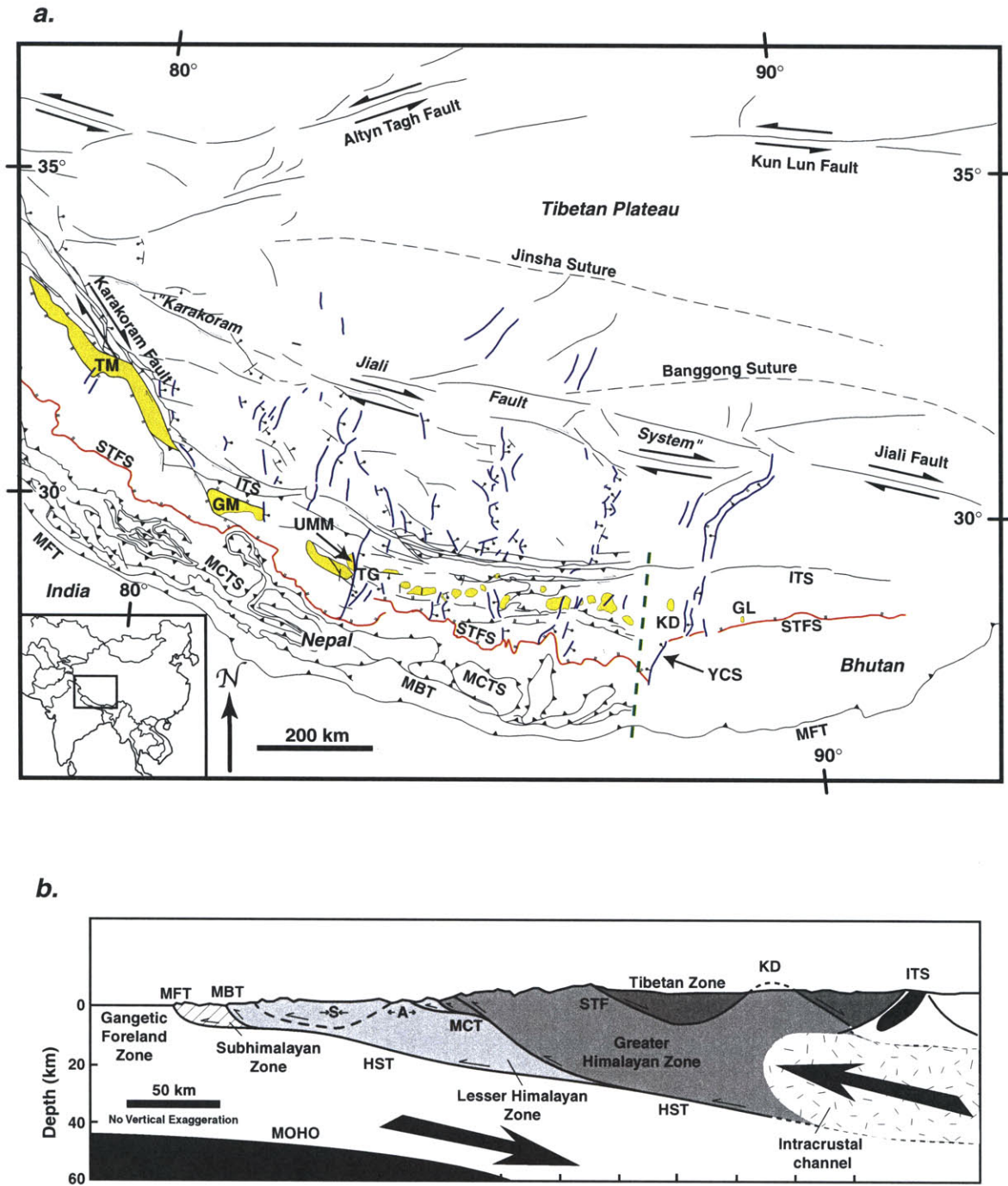


Figure 1

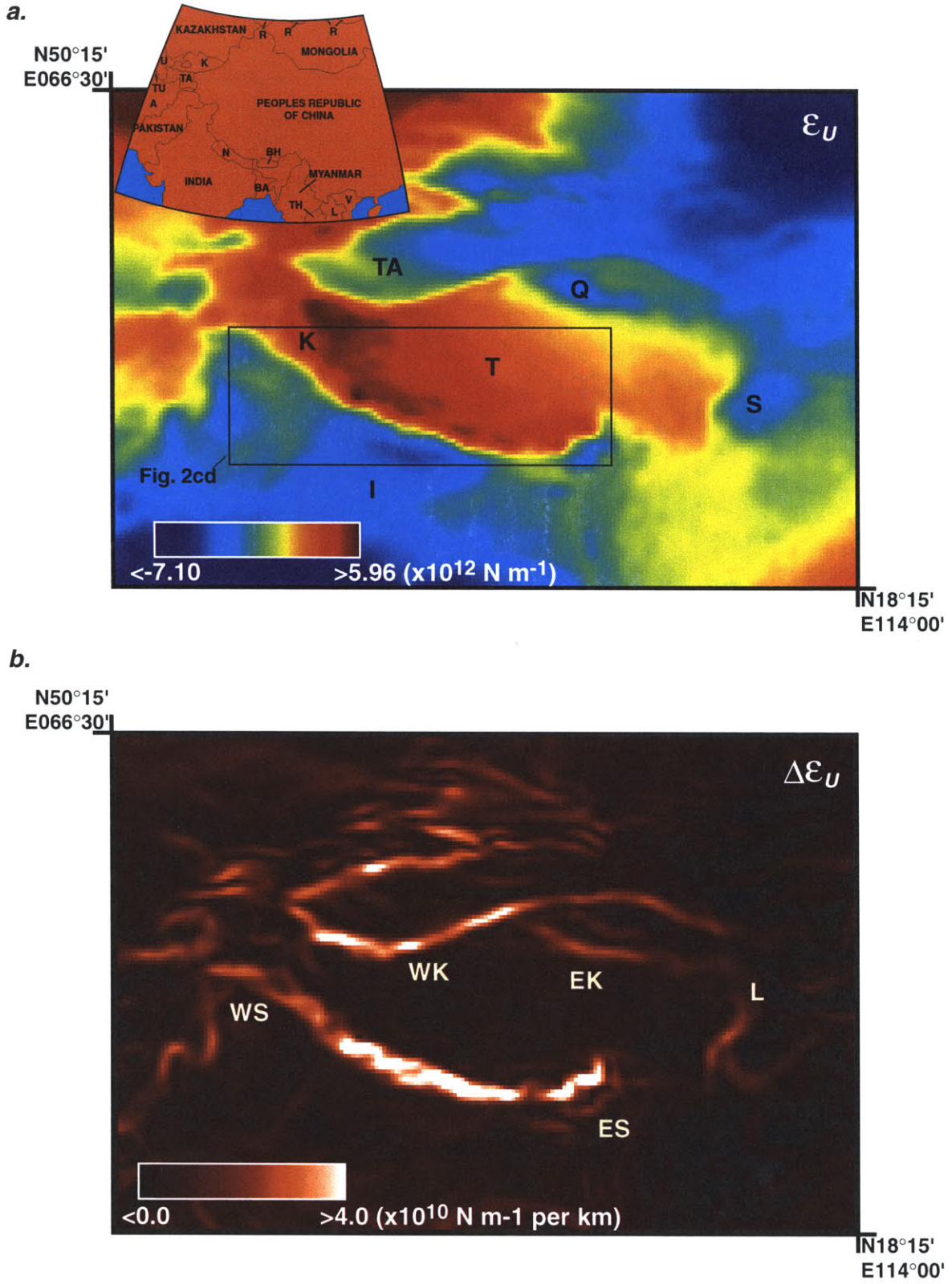


Figure 2

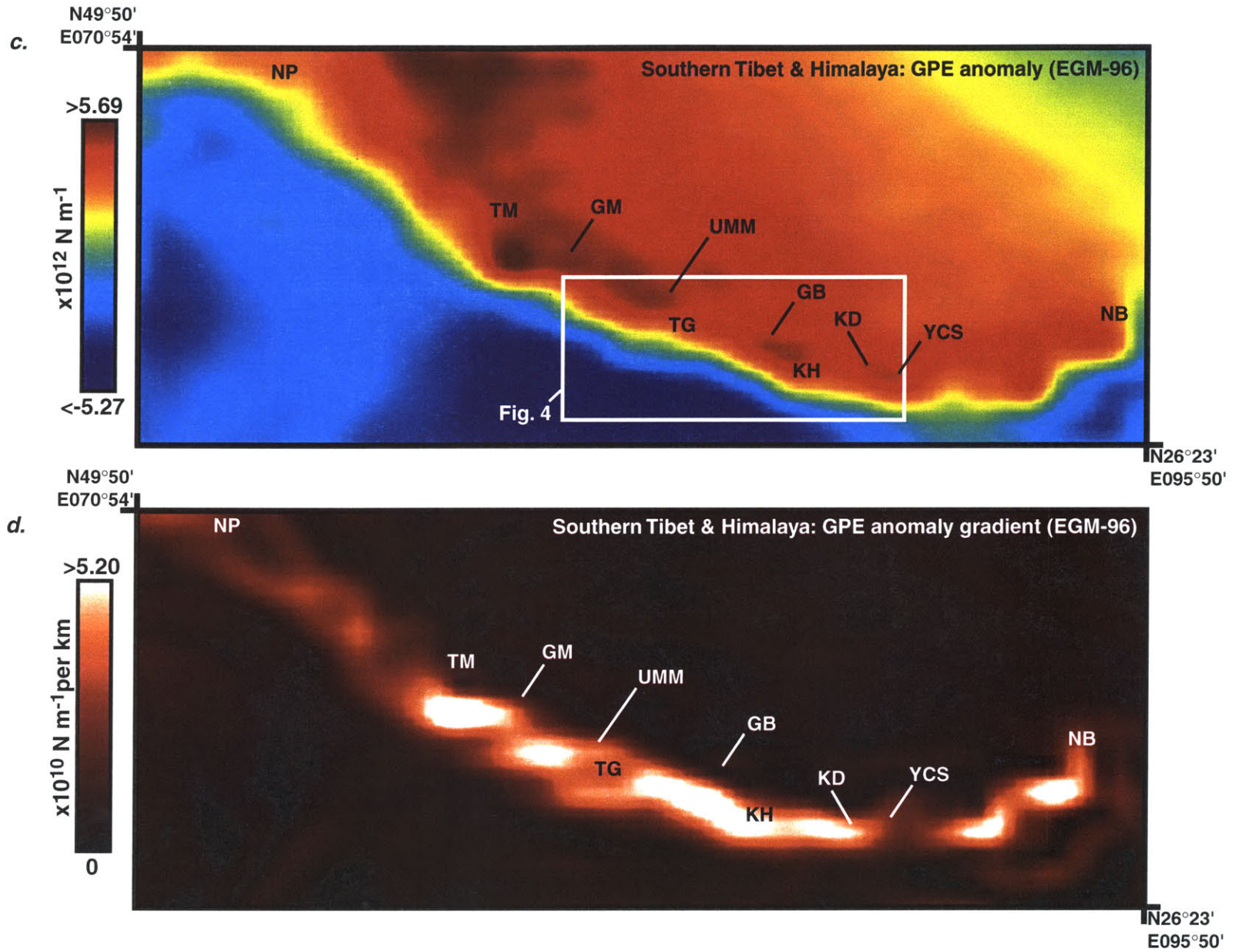


Figure 2 <continued>

a.

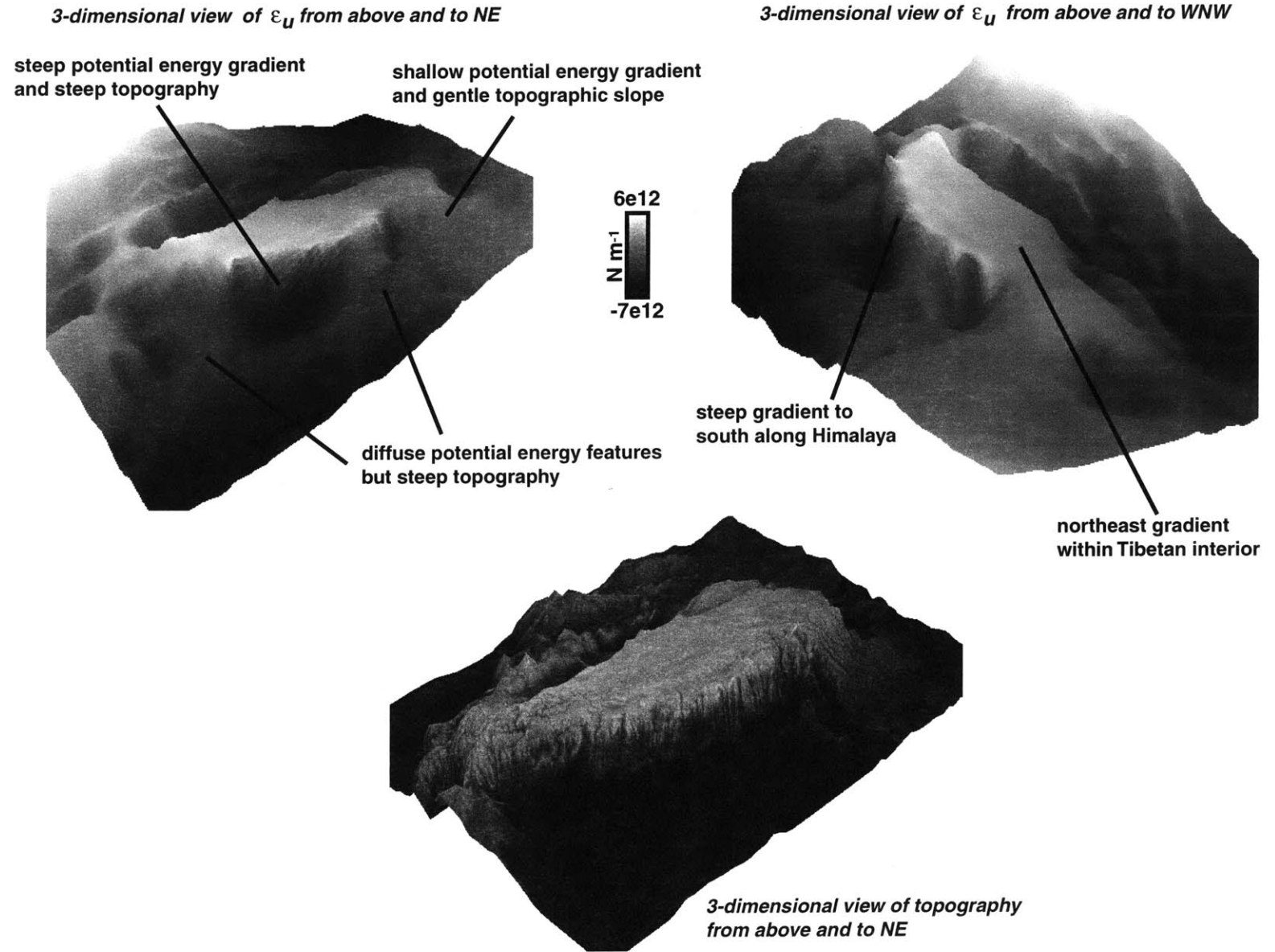
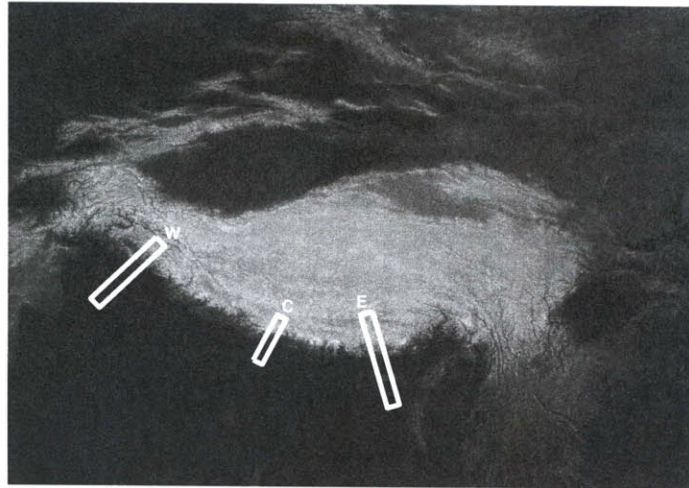
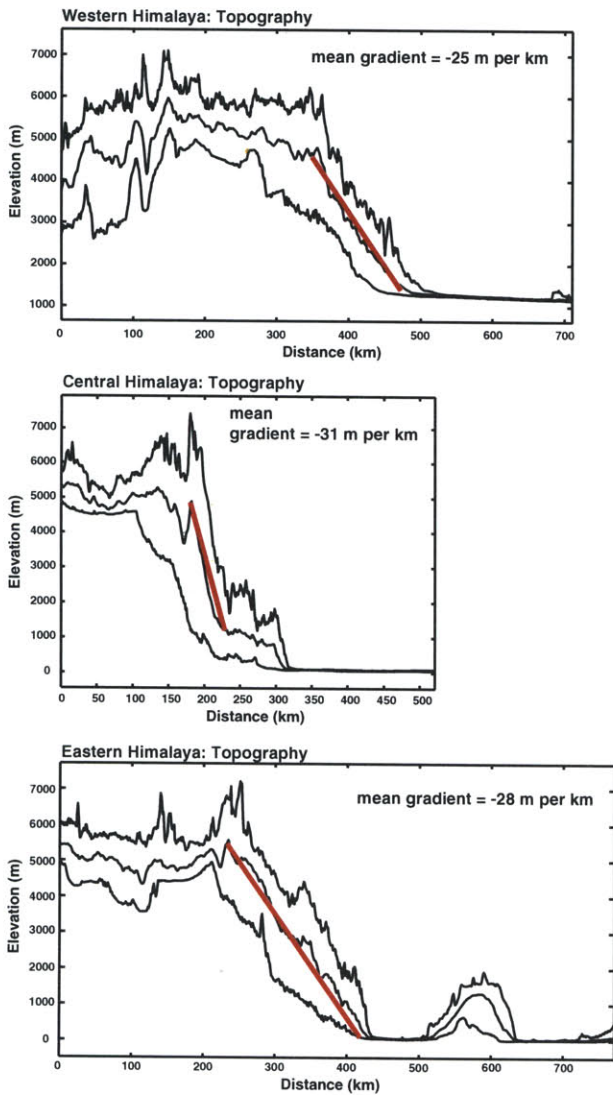


Figure 3



b.



c.

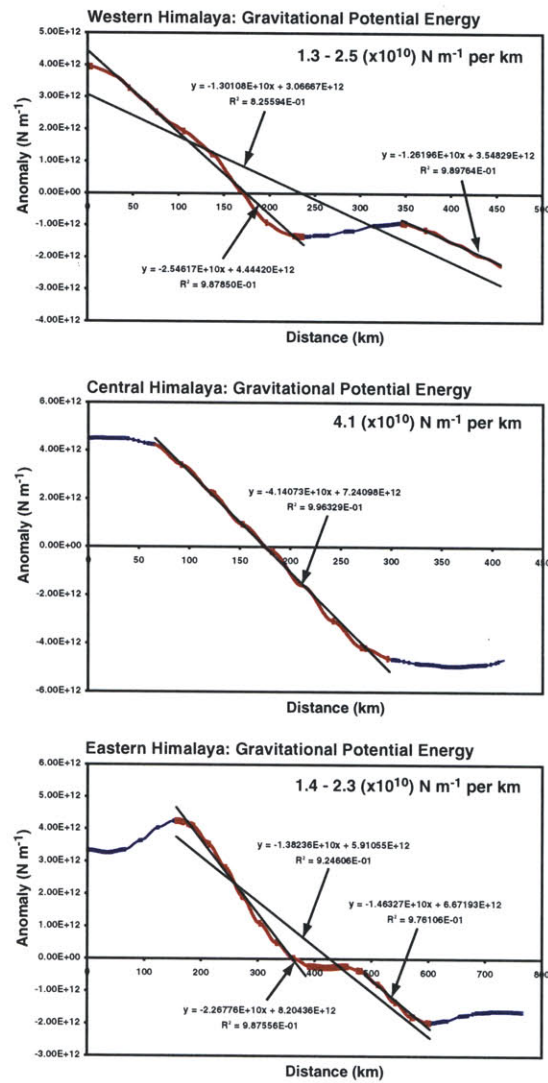


Figure 3 <continued>

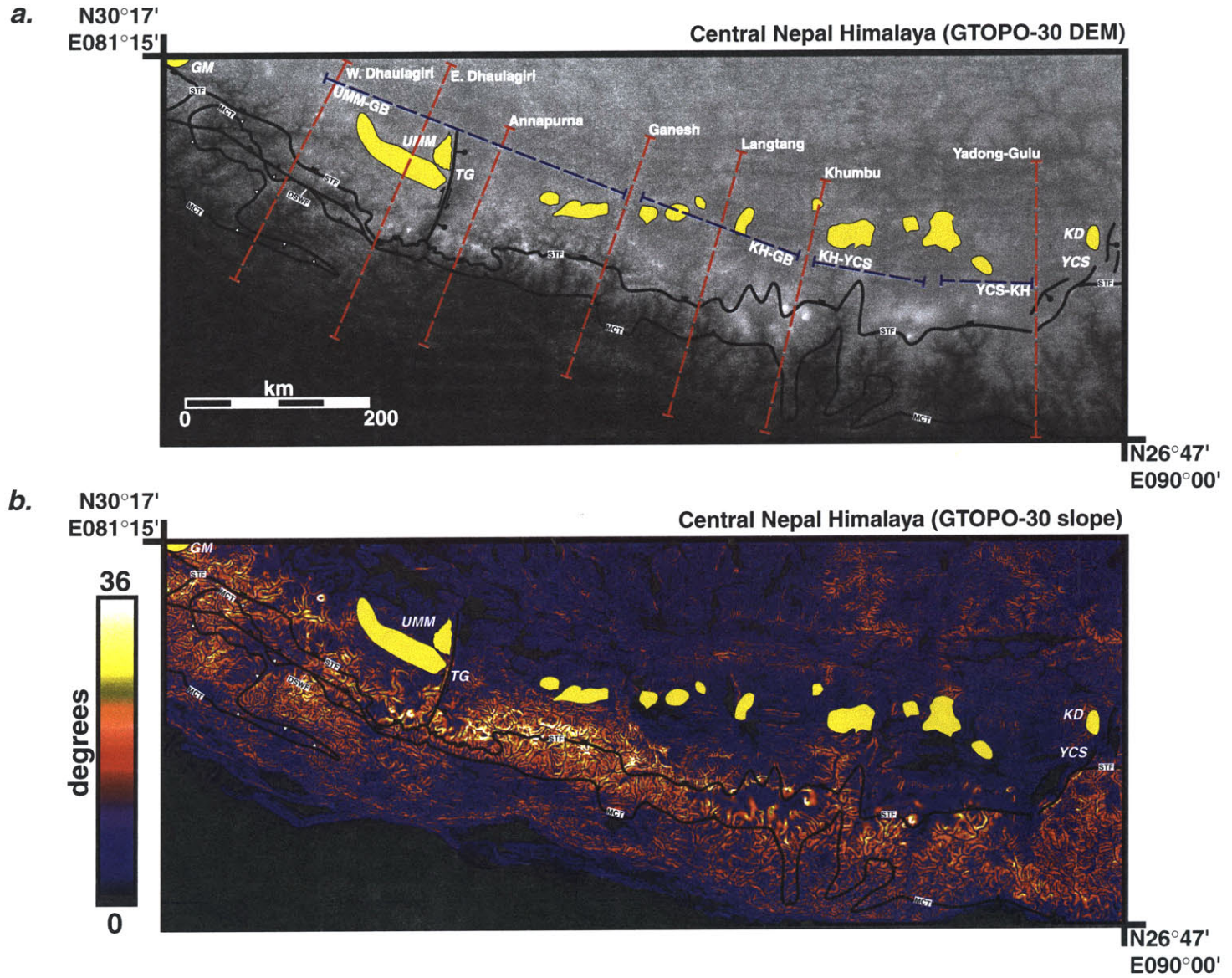


Figure 4

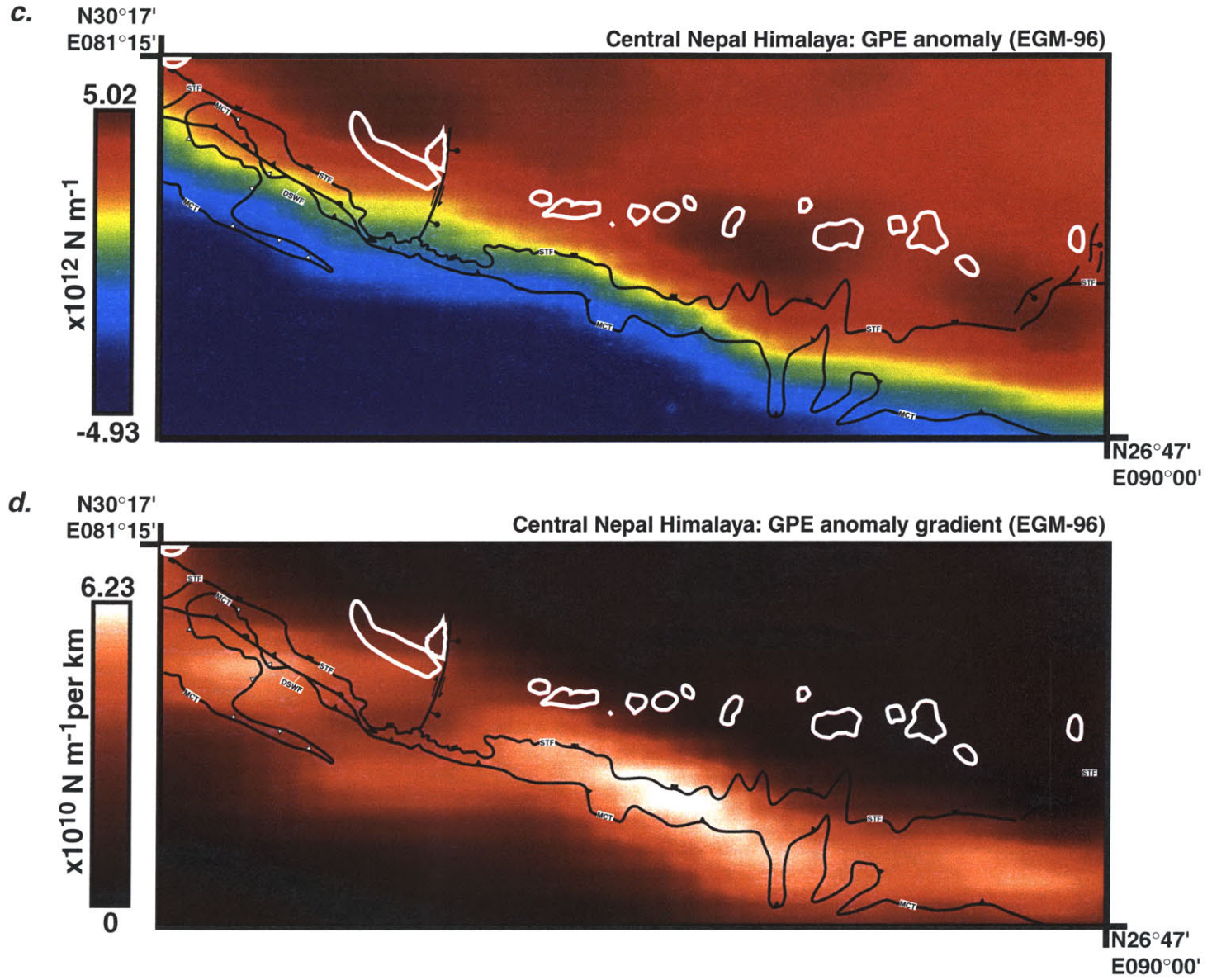


Figure 4 <continued>

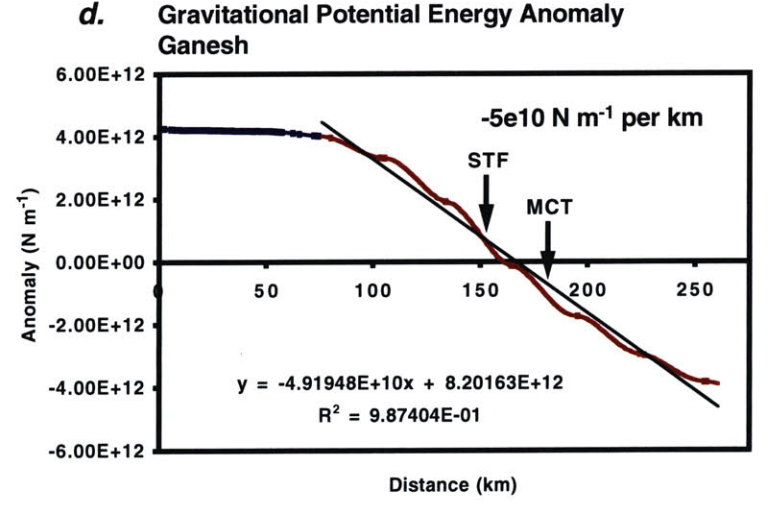
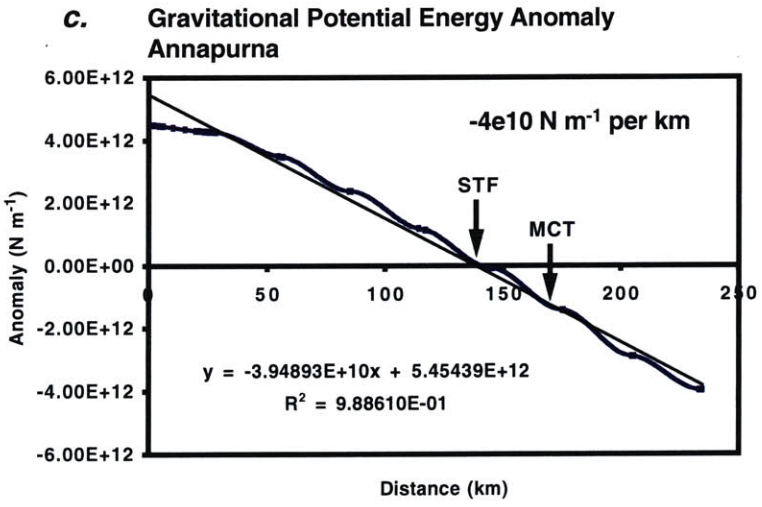
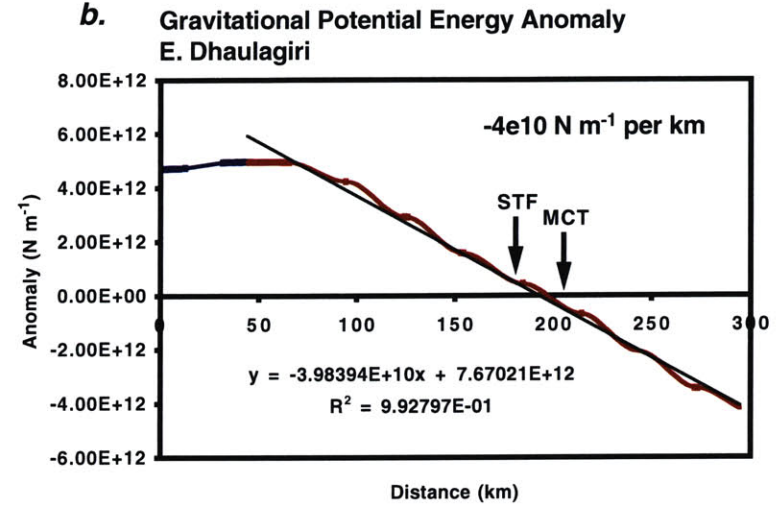
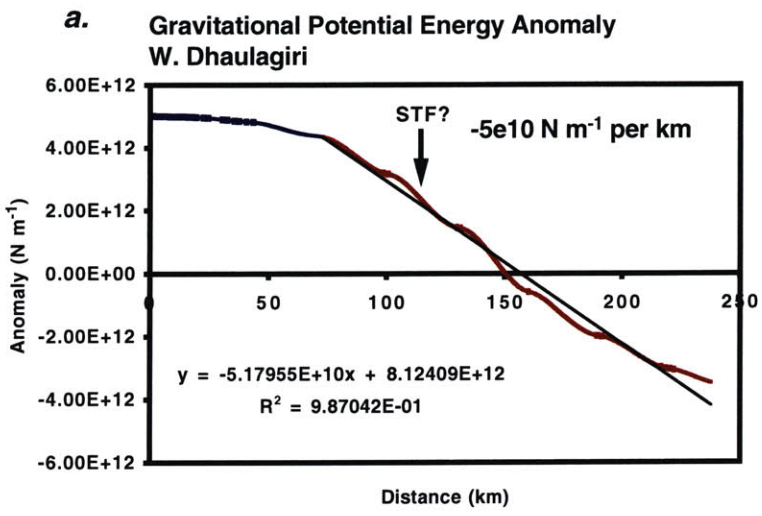


Figure 5

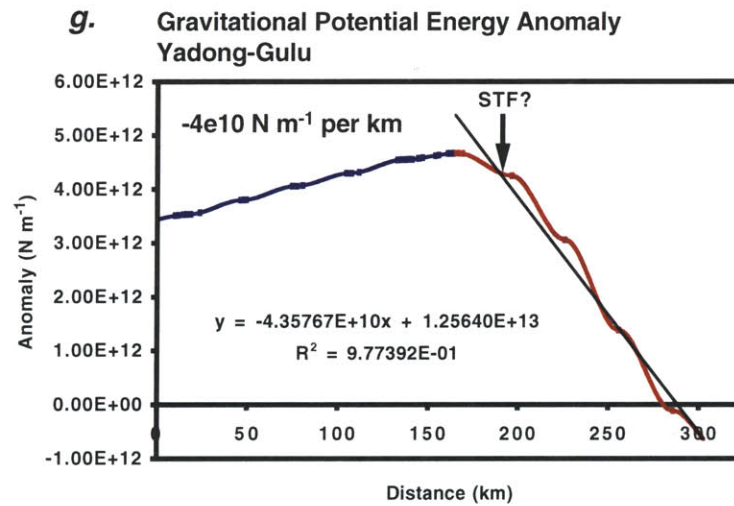
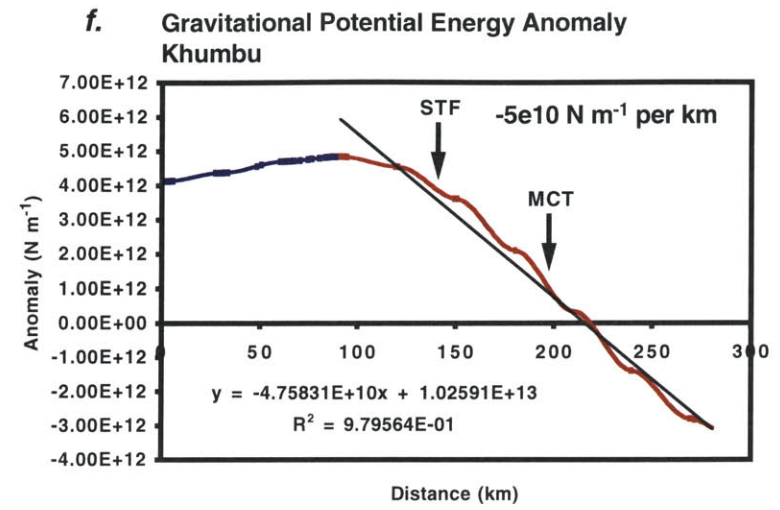
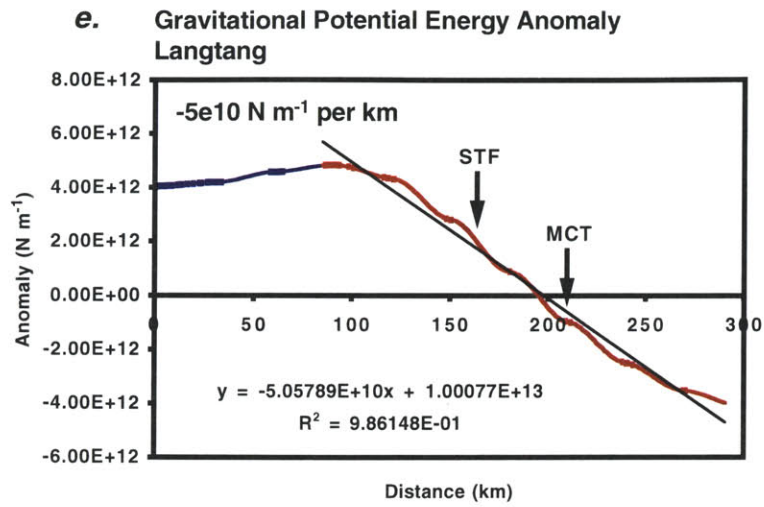
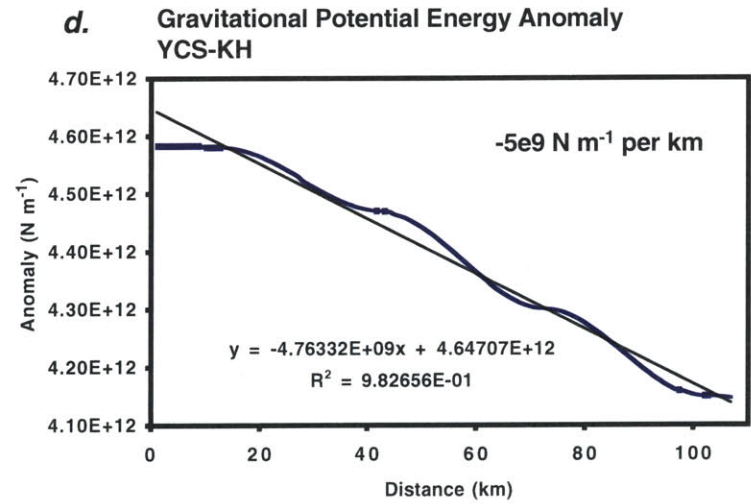
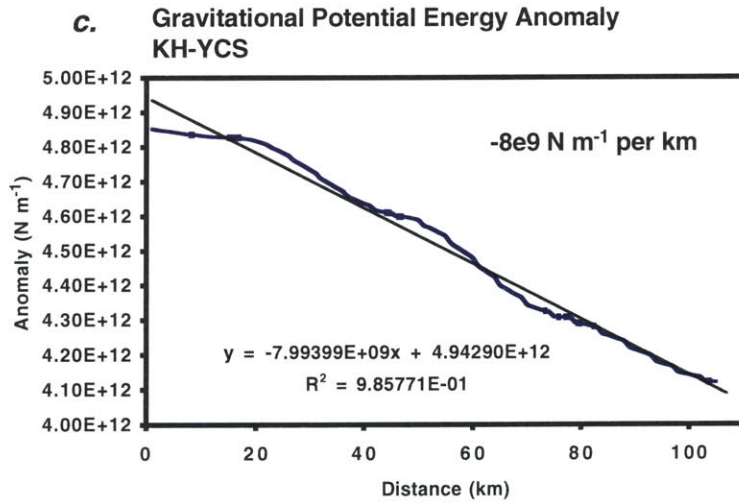
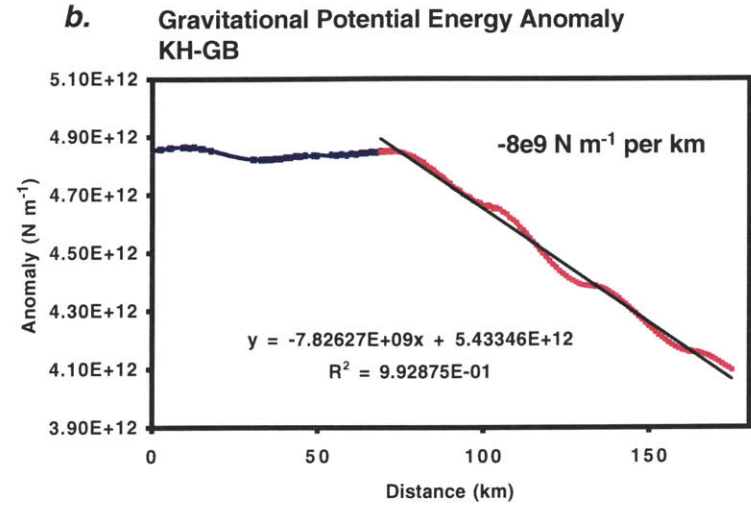
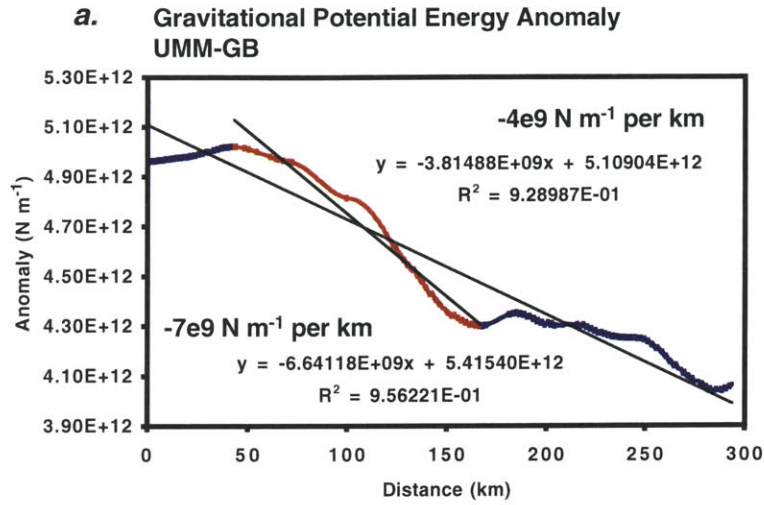
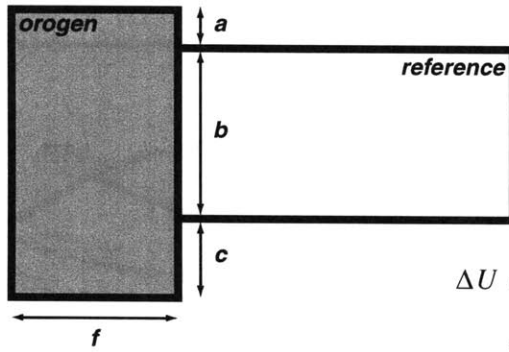


Figure 5 <continued>

Figure 6



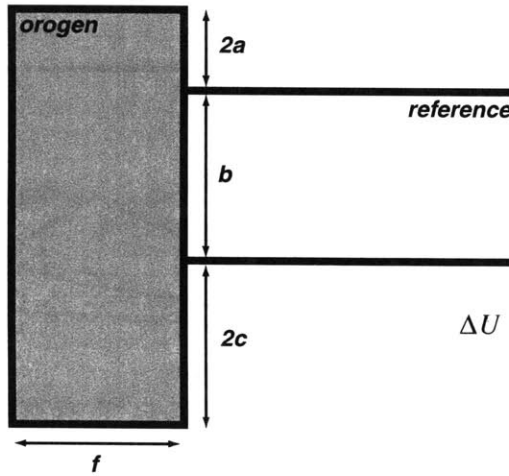
unthickened



$$\Delta U = \rho_{\text{column}} gfa \left[\frac{a}{2} + \frac{c}{2} + b \right]$$

$$= \Delta U_o$$

thickened: high, narrow

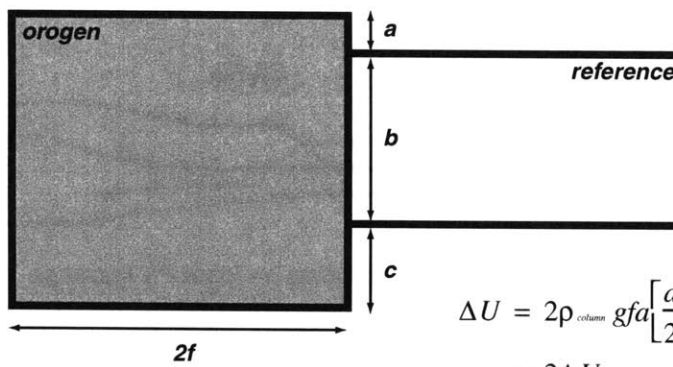


$$\Delta U = 2\rho_{\text{column}} gfa[a + c + b]$$

$$= 2\Delta U_o + \rho_{\text{column}} gfa[a + c]$$

$$> 2\Delta U_o$$

thickened: lowered, widened



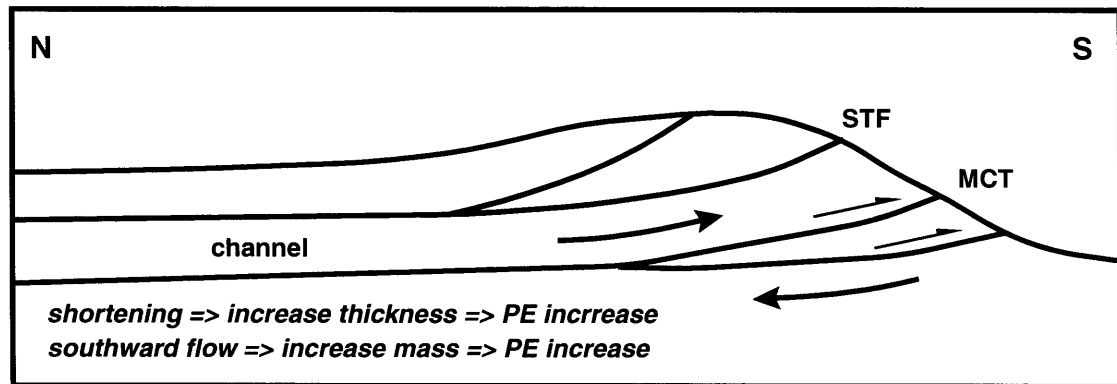
$$\Delta U = 2\rho_{\text{column}} gfa \left[\frac{a}{2} + \frac{c}{2} + b \right]$$

$$= 2\Delta U_o$$

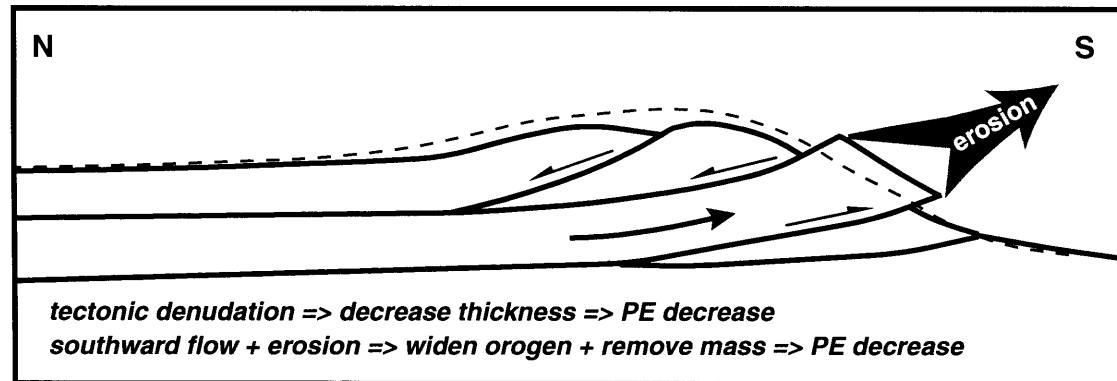
$$\Delta U_{\text{dissipated}} = \rho_{\text{column}} gfa[a + c]$$

Figure 7

Potential Energy Accumulation



Potential Energy Dissipation



Potential Energy Redistribution

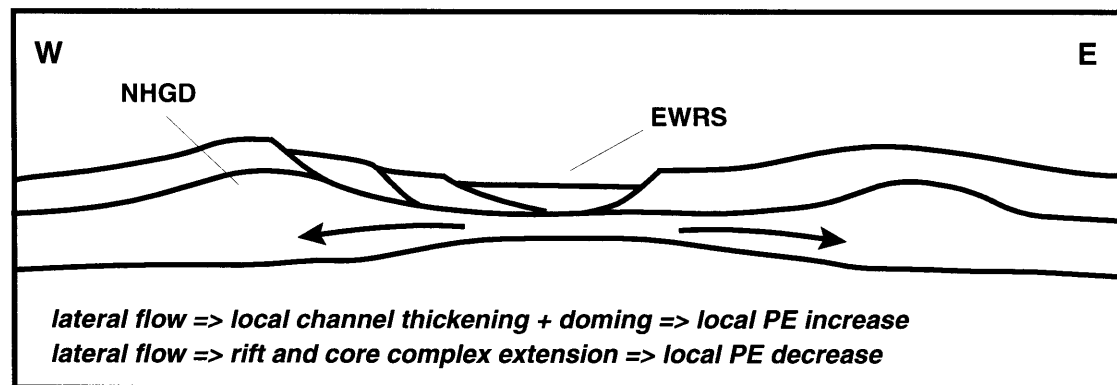


Figure 8

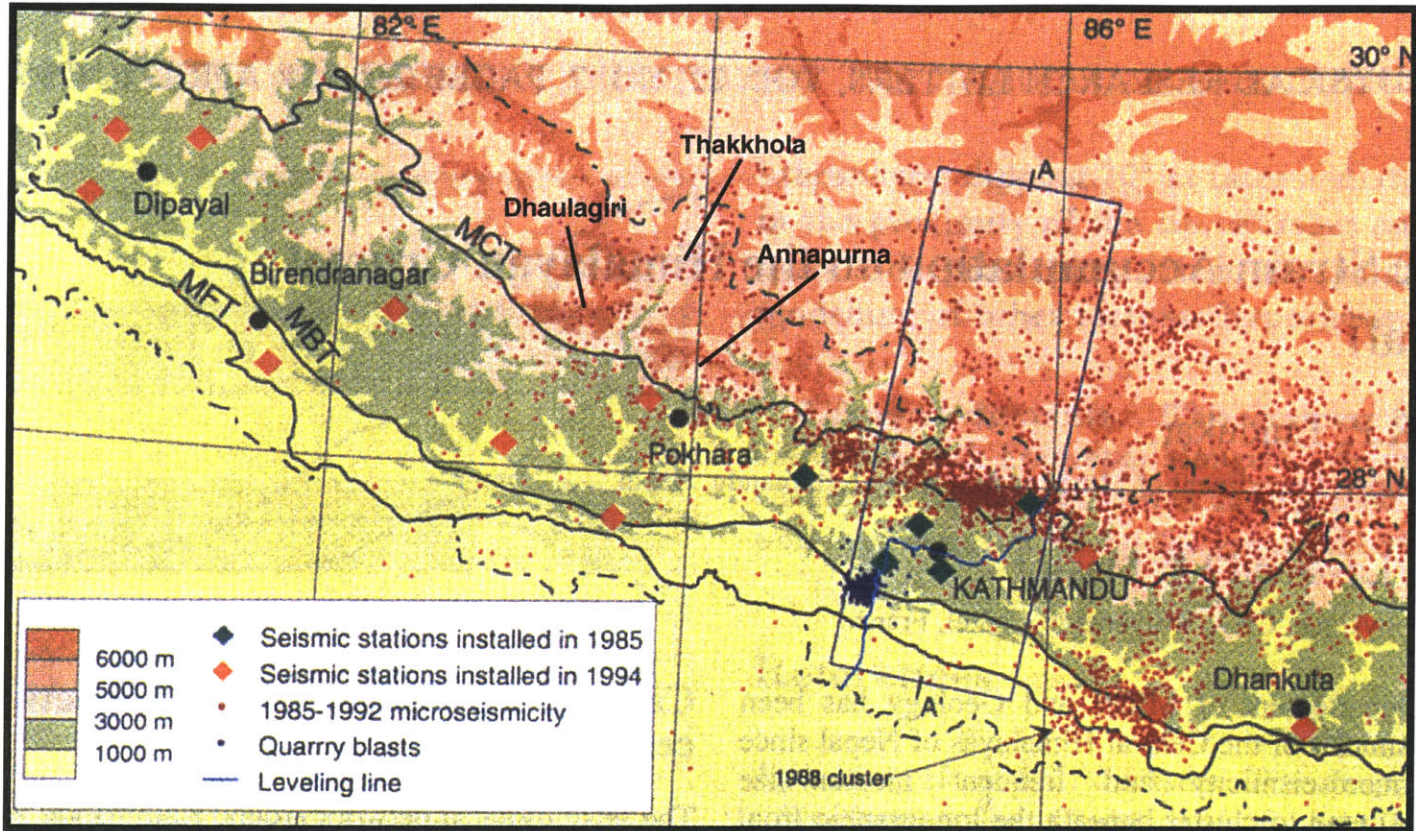


Figure 9

Biographical Note

I was born February 22, 1974 in Springfield, Massachusetts. My father was stationed at Westover Air Force Base (AFB) at the time, but being a military family we have called many places home: Castle AFB, California; Homestead AFB, Florida; RAF Lakenheath, England; Dover AFB, Delaware; Inçirlik Air Base, Turkey; and Travis AFB, California. My dad retired from the Air Force in 1991 while stationed at Travis AFB, and we settled in neighboring Fairfield, California where my parents still live.

I graduated from Vanden High School on June 11, 1992 as Valedictorian. In 1991, I received the Frank H. Buck Memorial Scholarship, which financed my undergraduate education at the California Institute of Technology (Caltech) in Pasadena, California. My intention was to study aerospace engineering, but I chose to major in planetary science instead, only to later switch to geology. I was member of Lloyd House at Caltech, and my undergraduate research was advised by alumnus and former “Lloydie”, Joseph L. Kirschvink, Ph.D.. In his lab, I worked on a variety of projects including magnetic monopole detection with superconducting quantum interference devices (SQUIDs), human and animal magnetosensitivity, and paleomagnetism and magnetostratigraphy. I graduated from Caltech with a B.S. with Honors and a M.S. in Geology on June 14, 1996. My M.S. research was on the paleomagnetism of the Cretaceous Nanaimo Group in British Columbia, Canada, a subject that has contributed to the “Baja-British Columbia” controversy. Part of this work was published in the journal *Science*:

Ward, P. D., **Hurtado, J. M. (Jr.)**, Kirschvink, J. L., and Verosub, K. L., 1997, Measurements of the Cretaceous paleolatitude of Vancouver Island: Consistent with the Baja-British Columbia Hypothesis: *Science*, v. 277 (12 Sept., 1997), pp. 1642-1645.

I won a National Science Foundation Minority Graduate Fellowship in 1996 and began graduate school at the Massachusetts Institute of Technology (MIT) in Cambridge, Massachusetts under the supervision of Kip V. Hodges, Ph.D.. In return for doing this thesis, I had the good fortune of travelling to Asia for fieldwork, leading four field expeditions to the Annapurna, Dhaulagiri, and Mustang regions of Nepal during 1997-2000. I also accompanied my friend Arthur White to East Greenland as his field assistant in 1997. In addition to months of field experience, I have also gained expertise in the diverse set of fields incorporated into this dissertation, in particular $^{40}\text{Ar}/^{39}\text{Ar}$ geochronology, neotectonics and tectonic geomorphology, and satellite remote sensing. My side occupations have included extensive work in the MIT $^{40}\text{Ar}/^{39}\text{Ar}$ laboratory and system administration for a cluster of Silicon Graphics® workstations.

While at MIT, I have been an author on eight public presentations at national and international meetings, five as first author and presenter:

Hodges, K. V., Whipple, K. X, and **Hurtado, J. M. (Jr.)**, 2000 Himalayan Neotectonics may imply active southward extrusion of Tibetan middle crust [abs. for poster]: Eos (Transactions, American Geophysical Union) (Dec., 2000 Fall Meeting, San Francisco, CA), v. 81, No. 48, p. 1094.

- Hurtado, J. M. (Jr.)**, and Hodges, K. V., 2000, Exhumational history of the Mustang and Mugu granites of the central Nepal Himalaya [abs. for poster]: *Eos* (Transactions, American Geophysical Union) (Dec., 2000 Fall Meeting, San Francisco, CA), v. 81, No. 48, p. 1070.
- Hurtado, J. M. (Jr.)**, and Hodges, K. V., 1999, The persistence of fault systems in an orogenic setting [abs. for talk]: *GSA Abstracts with Programs* (Oct., 1999 Annual Meeting, Denver, CO), v. 31, no. 7, p. 428.
- Rowley, D. B., Pierrehumbert, R. T., Currie, B. S., Hossman, A., Clayton, R. N., **Hurtado, J. M. (Jr.)**, Whipple, K. X., and Hodges, K. V., 1999, Stable isotope-based paleoaltimetry and the elevation history of the high Himalaya since the Late Miocene [abs. for poster]: *GSA Abstracts with Programs* (Oct., 1999 Annual Meeting, Denver, CO), v. 31, no. 7, p. 119.
- Hurtado, J. M. (Jr.)**, Hodges, K. V., and Whipple, K. X., 1999, Evidence for ongoing tectonic activity at the position of the South Tibetan Fault System and the Main Central Thrust in the recent past [abs. for talk], in 14th Himalaya-Karakoram-Tibet Workshop, Kloster Ettal, Germany (March, 1999): *Terra Nostra*, no.2, pp. 73-75.
- Hodges, K. V., and **Hurtado, J. M. (Jr.)**, 1998, Dynamics of the southern margin of the Tibetan plateau [abs. for talk]: *GSA Abstracts with Programs* (Oct., 1998 Annual Meeting, Toronto, Canada), v. 30, no. 7, p. 270.
- Hurtado, J. M. (Jr.)**, and Hodges, K. V., 1998, The South Tibetan System in the Kali Gandaki Valley, Annapurna Himalaya, North Central Nepal: A synthesis of structural geology and neotectonics [abs. for talk]: *GSA Abstracts with Programs* (Oct., 1998 Annual Meeting, Toronto, Canada), v. 30, no. 7, pp. 269-270.
- Hurtado, J. M. (Jr.)**, and Hodges, K. V., 1997, The relationship between E-W extension and N-S deformation in southern Tibet: Data from the Thakkhola Graben [abs. for poster]: *Eos* (Transactions, American Geophysical Union) (Dec., 1997 Fall Meeting, San Francisco, CA), v. 78, no. 46, p. 652.

In addition to the manuscripts that comprise my dissertation, I have contributed to an additional paper as second author:

- Hodges, K. V., **Hurtado, J. M. (Jr.)**, and Whipple, K. X., submitted (2001), Southward extrusion of Tibetan crust and its effect on Himalayan tectonics: *Tectonics*, v. 20 (6), p. 799-809.

During my time at MIT, I have been a teaching assistant for three courses: a graduate level writing class; undergraduate field camp in the Big Maria Mountains, California; and Mission 2004: The Search for Life on Mars. The latter, brainchild of Dr. Hodges (then MIT Dean of Undergraduate Education), was a successful experiment in teaching and tasked a group of fifty freshman with designing a mission to Mars to look for life. Their final product can be seen at <http://www.mission2004.org>.

I am a member of the Harvard Travellers Club, the Himalayan Explorers Connection, and the Mars Society (among other space-related organizations). Currently, I have 40 hours of flight time towards a private pilot certificate and I intend to attain an instrument rating. Outside of earth science and aviation, my interests include space science and exploration, world travel, 20th Century history, running, tennis, and popular culture. My penultimate goal is to be selected as a Mission Specialist astronaut. Of course, the ultimate goal is to live a happy and good life!

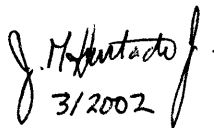
Colophon

This thesis has been prepared as required by MIT Libraries' Institute Archives and Special Collections and as described in "Specifications for Thesis Preparation 2000-2001" (<http://libraries.mit.edu/archives/thesis-specs>). Chapter 2 – which has been previously published – is included as a journal reprint with permission from the Geological Society of America. In general, *Geological Society of America Bulletin* referencing and organizational style (as of 2001) is used throughout the text.

Text and tables were composed on Apple Macintosh® computers using Microsoft® Word 98 and Excel 98. EndNote® 4.0.1 was used as the bibliographic database and for formatting of references. The font used throughout the text is Times. Helvetica is used in the tables and figures as well as for headers and page numbers. Greek letters and mathematical symbols are in Symbol. Microsoft® Equation Editor was used to format equations. Figures were created using Adobe Photoshop® 5.5 and Adobe Illustrator® 9.0.2 on Macintosh computers. Photographs, 35-mm slides, and other images on physical media were digitized into Photoshop format using a Polaroid SprintScan® 35 slide scanner and an Adara Megastar II® flatbed scanner with transparency adapter. Scans were edited in Photoshop and finished in Illustrator. Maps and remote sensing imagery were compiled, manipulated, and analyzed on Silicon Graphics® workstations using ArcView® 3.2, ArcInfo® 7.1, Matlab® 5.3, PCI® 7.0, and ENVI® 3.4 software. Interpretive maps were output as either TIFF (Tagged Image File Format) or Adobe PostScript® files for finishing in Illustrator. Likewise, plots from Matlab computer models, Excel spreadsheets, geochronologic data reduction programs, and other analytical software packages were output as PostScript files for finishing in Illustrator.

Before printing, all components of the thesis were translated into Adobe PDF® (Portable Document Format) format and compiled into a single PDF document using Adobe Acrobat® 4.0 on a Macintosh computer. Final collation, page numbering, and proofing was done in Acrobat using the Enfocus PitStop Professional® plug-in. Three archival copies were printed on Xerox Image Elite® acid-neutral paper with a Xerox Document Centre® CS 50 printer/color-photocopier. Binding was done by MIT Document Services. The PDF of the thesis (as well as the Microsoft® PowerPoint 2001 file used in the March 13, 2001 thesis defense) is included on a ISO-9660 format CD-ROM accompanying the archival copies. Electronic material, including additional remote sensing imagery, is also available from the author by contacting hurtado@alumni.caltech.edu.

This is original copy # 2 of 3.

 J. Hurtado
3/2002

